The Evaluation of Multichannel Shortwave Infrared (SWIR) Optical Data from the Japanese Earth Resources Satellite (JERS-1), for Geological Applications

Thesis

UNRESTRICTED

The evaluation of multichannel shortwave infrared (SWIR) optical data from the Japanese Earth Resources Satellite (JERS-1), for geological applications

A thesis presented for the degree of Doctor of Philosophy by

Anthony Maurice Denniss BSc (Hons), MSc

1997

Department of Earth Sciences, The Open University

DATE OF SUBMISSION: 22 DECEMBER 1997
DATE OF AWARD: 10 SEPTEMBER 1998

The evaluation of multichannel shortwave infrared (SWIR) optical data from the Japanese Earth Resources Satellite (JERS-1), for geological applications

Volume 1 of 2

****

Chapters 1 to 4

Abstract

The primary objective of this thesis is to evaluate data from the Japanese Earth Resources Satellite (JERS-1), particularly multi-channel shortwave infrared (SWIR) data. These data are to be evaluated in comparison with Landsat Thematic Mapper (TM) data for geological applications, in particular lithological discrimination in an arid environment (Oman) and volcano monitoring (Lascar, Chile).

JERS-1 is the first satellite purposely designed for geological remote sensing. Optical data (OPS) acquired by JERS-1 is of a higher spatial and spectral resolution than that from Landsat TM. Unfortunately the immediate benefits of this higher resolution are lost due to the low quality of all OPS data. All seven OPS channels are affected by along- and across-track striping, image blur at spectral boundaries, poor dynamic ranges, random speckle and inter-channel misregistration. Poor data quality greatly reduces the geological potential of these data, especially as the most severely corrupted channels are OPS 6 and OPS 7, two of the new narrow SWIR channels. However, despite poor data quality the majority of the noise artefacts associated with these data can be either removed or significantly reduced by processing in the frequency domain. A number of frequency domain techniques have been developed which separate noise features from real image data. These techniques greatly improve the quality of most OPS channels, although OPS 6 and OPS 7 are sometimes beyond recovery.

The spectral characteristics of the lithologies comprising the Oman ophiolite complex are used to demonstrate the increased discrimination potential of 'cleaned' multichannel OPS data. High resolution lab spectra of the ophiolite lithologies were degraded to TM and OPS spectral resolutions in order to determine the influence of spectral resolution on lithologic discrimination. The results of this comparison indicated that a lot of discrimination information seen at lab resolution is lost at OPS and TM resolution. This results in the reflectance spectra of some ophiolite lithologies appearing very similar, especially at TM resolution. More discrimination information is preserved at OPS resolution due to the sub-division of the wavelength range equivalent to TM 7 into three

narrow discrete channels. Analysis of resampled spectra at OPS resolution shows that OPS 8 contributes new spectral information not discernible at TM resolution.

Resampled lab spectra at OPS resolution were used to try to develop effective band combinations and image processing techniques capable of discriminating ophiolite lithologies. Tests of OPS band composites indicated that the best composite was one which combined three bands from spectrally distinct parts of the spectrum. OPS 852 proved to be the most effective OPS composite, discriminating the majority of ophiolite lithologies. Analysis of both spectral and image data showed that OPS 6 and OPS 7 are highly correlated for ophiolite lithologies. Composites combining both of these channels were very poor, however combining one channel (usually OPS 6 due to quality) with OPS 8 and OPS 2 produced a reasonable composite (OPS 862). OPS 852 is the most informative composite, and would remain so even if OPS 6 and OPS 7 were of a higher quality. Comparisons with the best TM composite (TM 754 decorrelation stretched) showed that the OPS data discriminated more lithologies and often allowed previously mapped units to be sub-divided.

To test the potential of OPS data for volcano monitoring a time series of four OPS scenes, straddling the April 1993 eruption of Lascar (Chile), were analysed. This study showed that the higher spatial resolution of the OPS sensor was capable of detecting smaller thermal features than possible with TM. This resulted in four intra-crater maps of thermal anomolies being produced, showing thermal variations associated with periods of dome growth and collapse. These data also demonstrated their usefulness for mapping the extent of pyroclastic deposits emplaced during this eruption, and also their subsequent rapid erosion.

Overall OPS data are shown to offer significant improvements with respect to lithological mapping and volcano monitoring despite their greatly reduced quality compared with Landsat TM. Extensive tests of various band combinations and processing techniques show that some of the most informative images derived of the ophiolite lithologies consist simply of cleaned channels of data combined as false colour composites. The effectiveness and possible advantages of advanced image processing techniques are often negligible due to the rapid degradation of the data when subjected to intensive processing. OPS 8 is the channel mainly responsible for contributing additional new valuable spectral information, that is not available from Landsat TM. The slight increases in spatial and spectral resolution offered by OPS data result in significantly more geological information being discernible from an OPS composite than on the equivalent TM composite.

Acknowledgements

I wish to express my thanks to the following individuals and organisations without whom this work would not have been possible; the Science and Engineering Research Council who initially funded this project; the Natural Environmental Research Council who took over funding part way through the project and to the National Aeronautical and Space Development Agency of Japan for supplying the Japanese Earth Resources Satellite data.

I am indebted to my supervisor Dr. Dave Rothery for his advice and guidance throughout this project, not to mention his extreme patience. I would also like to thank Dr. Steve Drury and Dr. Peter Francis for their informal help and advice throughout this project. Dick Carlton is also greatly acknowledged for his informal advice on all subjects, especially remote sensing. Thanks for all of your computing help.

Outside of the Open University I would like to thank Dr. George Ceuleneer and Dr. Isma Amri for their excellent guidance whilst in the field in Oman. Thank you for introducing me to the wonders of the Oman ophiolite and the rigors of field work, French style. Whilst in Oman my grateful thanks go to Dr. Hilal Al-Azri from the Ministry of Petroleum of Minerals, who supported my field visits. I would also like to thank Tony Shelton and his family for his help and hospitality whilst in Oman. Special thanks go to Dr. Takashi Nishidai for his extreme interest in this project and for his help in acquiring additional OPS data. Thanks also for inviting me to Japan to present my results at the JERS-1 Principal Investigatorship meeting (Tokyo, December 1994).

Whilst at the Open University I benefited both scientifically and socially from a great number of colleagues, too many to mention by name, but particular thanks go to Andy, Martin, Jason, Josanne, Richard, Linda, Mike and Clive. Apologies to all those I haven't mentioned by name ! Not forgetting my two USA travelling buddies Beto and Theresa, who turned going to a conference into a trip of a lifetime. A trip I will always remember ! Beto, thanks for having time to listen to me, I'm sure I would never have made it without you - hurry back ! Speaking of encouragement - thanks also go to Tony and Anne for all of theirs.

Part of this thesis has been written since I started working for the British Geological Survey so it is only fair that I thank my colleagues, Dave, Andrew, Stuart, Doug and Eugene, who have had to put up with me during this stressful time. Thanks for all of your help, advice and encouragement. Thanks also go to Dave Emery and Liz Rollin at NERC-EPFS, as well as Steve Matthews for the loan of Lascar samples. Thanks to John McM Moore who started me down the Ph.D. path in the first place.

Finally I would like to thank my family for their continued support, especially the encouragement from overseas. That only leaves one special person whom I have to thank for giving me the motivation to get this thesis finished, motivation which I may not have found on my own. Rachel, thank you.

Table of Contents - Volumes 1 & 2

Chapter 1 - Volume 1

Chapter 2 - Volume 1

Chapter 3 - Volume 1

Chapter 4 - Volume 1

Chapter 5 - Volume 2

Chapter 6 - Volume 2

Chapter 7 - Volume 2

List of Tables - Volumes 1 & 2

Chapter 2 - Volume 1

Chapter 3 - Volume 1

Chapter 4 - Volume 1

Chapter 5 - Volume 2

Chapter 6 - Volume 2

Chapter 7 - Volume 2

Appendix 1 - Volume 2

Appendix 2 - Volume 2

Appendix 3 - Volume 2

List of Figures -Volumes 1 & 2

Chapter 1 - Volume 1

Chapter 2 - Volume 1

Chapter 3 - Volume 1

Chapter 4 - Volume 1

Chapter 5 - Volume 2

Chapter 6 - Volume 2

Chapter 7 - Volume 2

Appendix 1 - Volume 2

List of Plates - Volumes 1 & 2

Chapter 2 - Volume 1

Chapter 3 - Volume 1

Chapter 5 - Volume 2

Chapter 6 - Volume 2

1.0 Introduction

1.1 Statement of objectives

This study evaluates data from the Japanese Earth Resources Satellite-1 (JERS-1), which is the first satellite platform to carry an optical scanner sub-dividing the geologically important 2.0 - 2.4 μm part of the short wavelength infrared (SWIR) spectrum into more than one channel. Landsat Thematic Mapper (TM) data are also used where applicable so that direct comparisons can be made between the multichannel JERS-1 SWIR data and the broad band TM SWIR data. Study areas within the Oman ophiolite are chosen to try to establish if any additional geological information can be observed on the JERS-1 data. The Oman ophiolite provides an ideal test area to evaluate OPS data as the region is semi arid with a wide range of lithologies well exposed, soil and vegetation cover are minimal.

The main objectives of this thesis are:

- to establish what geological information can be obtained by satellite remote sensing using three short wavelength infrared channels in the 2.0 - 2.4 μm region of the spectrum;
- to determine to what extent, if any, this is an improvement over the use of only one broad band at these wavelengths; and
- to determine the reasons for any improvement and to develop efficient methodologies for multichannel data use.

The geological aspect of this study is primarily concerned with improving lithological discrimination within the ophiolite. Lithological differences encountered between the OPS and TM data are verified, wherever possible, by direct field checks. A separate study of the Lascar volcano, Chile, is conducted to see if the subdivision of the SWIR into three narrow channels is an advantage when considering a geologically dynamic target; in particular, whether multiple SWIR channels can be used to determine quantitative information about the thermal structure of Lascar.

In this chapter I briefly introduce the reasons why the sub-division of the 2.0 - 2.4 μm region of the spectrum into multiple channels is of importance for both geological mapping and volcano monitoring. I also outline a rationale for the thesis and discuss the approaches taken to meet the above objectives.

1.2 Application of JERS-1 OPS data to geology

1.2.1 Lithological mapping

Remotely sensed data have been used in geological projects for a number of decades, initially with the analysis of black and white aerial photography for structural interpretation and colour photography for lithological discrimination. With the advent of new technology, such as satellite platforms and multispectral scanners, new geological applications have developed. Sensors onboard orbiting satellite platforms provided the first synoptic images of the Earth, allowing geological structures to be viewed over vast areas. Meanwhile the development of multispectral scanning capabilities greatly enhanced lithological discrimination from remotely sensed data.

The Multispectral Scanner (MSS) onboard the Landsat 1 platform, launched in 1972, is generally regarded as the first satellite sensor to acquire useful geological information. However, the location of the four channels at visible to near-infrared (0.5 - 1.1 μm) wavelengths (Figure 1.1) and the coarse 80 metre pixel size limited the geological uses of the data (Rothery, 1982). It was not until 1982 when the Thematic Mapper (TM) sensor was launched onboard Landsat 4, that spectral data tailored for geological needs began to be acquired from orbiting platforms. Like the MSS, the TM sensor was primarily designed for agricultural applications so it had four channels in the visible near-infrared (0.4 - 0.9 μm). However, it also had two channels in the SWIR, TM 5 (1.55 - 1.75 μm) and TM 7 (2.08 - 2.35 μm) and a third channel in the thermal infrared; TM 6 (10.4 - 12.5 μm), see Figure 1.1. TM 7 was a late addition to the sensor, primarily for the geological community. Spectral studies (Hunt, 1977, Blom, 1980) had shown that the 2.0 - 2.4 μm region of the spectrum was geologically important because hydroxyl, sulphate and carbonate absorption features occur at these wavelengths (Blom, 1980). The inclusion of TM 7, combined with the 30 metre pixel size (except TM 6), greatly improved satellite based geological mapping.

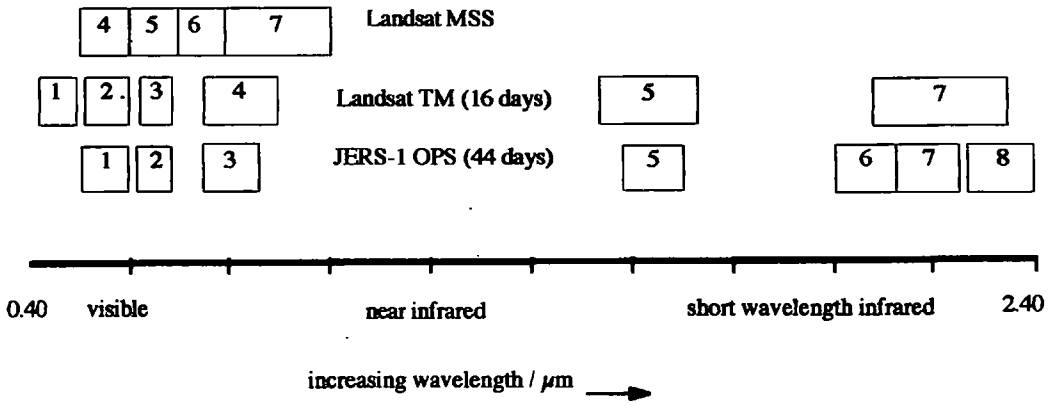

Figure 1.1 Schematic comparison of the location of the imaging channels on Landsat MSS, TM and JERS-1 OPS. OPS 4 occupies the same wavelength range as OPS 3. (TM 6, 10.4-12.5 μm is not shown). Repeat frequencies JERS-1 aand Landsat TM shown in brackets, radiometric resolution quoted in Tables 2.4 (JERS-1) and 2.9 (TM).

Numerous geological studies have been conducted around the world over various terrains using TM data. Examples include: Sultan *et al.* (1987); Abrams *et al.* (1988); Kaufmann (1988); Qari (1989); Crosta and Moore (1989); and Davis and Berlin (1989). All of these reported a significant increase in the amount of geologically useful data that was extractable from TM compared with MSS. As a result Landsat TM data have become very widely used in geological mapping projects.

It was envisaged that this would change with the launch of JERS-1 in February 1992, by the National Aeronautical Space Development Agency (NASDA) of Japan. Unlike previous satellites, JERS-1 was designed primarily for geological applications. It carried a Synthetic Aperture Radar (SAR) and an Optical Scanner (OPS) (NASDA, 1990), a combination of sensors capable of producing geologically useful information for almost all of the Earth's surface. The optical sensor of JERS-1 differs from the TM in a number of ways;

- it records 8 channels of data between 0.52 - 2.40 μm, although it has no channels equivalent to TM 1 or TM 6 (see Figure 1.1);
- the 2.01 - 2.40 μm wavelength range is subdivided into three narrow channels, OPS 6, 7 and 8 (see Figure 1.1);
- it has along-track stereoscopic capabilities;
- small 18 m x 18 m pixel size (resampled);

- data recorded at 6-bit resolution; and a;
- repeat frequency of 44 days.

(A full description of all of these differences can be found in chapter 2).

Key differences, such as the subdivision of the SWIR and the smaller pixel size, should mean that JERS-1 is capable of acquiring satellite data especially suited to geological applications. The increased spectral resolution in the SWIR should allow absorption features associated with Al-OH, Mg-OH and carbonates (Yamaguchi, 1987, Akiyama *et al.*, 1989) to be recorded in individual channels as opposed to being recorded together in the broad band of TM 7. This, combined with the smaller pixel size, should result in a significant improvement in lithological discrimination. The advance in geological remote sensing ought to be equivalent to that achieved with the advent of TM.

1.2.2 Volcano monitoring

As remote sensing technology has developed, so have the associated applications of these data. One such application is that of 'monitoring' volcanoes. Many of the world's volcanoes are in geographically remote regions and ground-based monitoring techniques can be very difficult to implement, especially if local infrastructure is poor. Because of the dangerous nature of volcanoes, it is essential that they are monitored so that any signs of a potential future eruption are detected as early as possible. Remote sensing is, therefore, a valuable technique, which is contributing increasingly towards monitoring volcanoes.

Currently, volcano monitoring tends to rely on low spatial resolution data, such as those acquired by the Advanced Very High Resolution Radiometer (AVHRR). These data are available from satellites which have short revisit frequencies of a few hours, instead of a few weeks, and the data cost is comparatively low. However, satellite data of a high spatial resolution are still of considerable importance to the volcanologist, as they can provide detailed information about the volcano and its environs. Landsat TM data have been used in a number of studies to provide detailed mapping information of pre-existing lava flows as well as information on the structure of thermal anomalies associated with an active volcano (Rothery *et al.*, 1988; Pieri *et al.*, 1990; Abrams *et al.*, 1991; Oppenheimer and Rothery, 1991).

Detailed thermal information can be derived from remotely sensed imagery (providing the data can be calibrated), using Planck's distribution law which expresses radiated power output as a function of temperature and wavelength (Oppenheimer, 1991). It can be used as a two-waveband (dual-band) algorithm to estimate temperatures and the sizes of sub-pixel thermal features (Rothery *et al.*, 1988). The peak in spectral radiance from a surface at magmatic temperatures (800-1250°C) corresponds to wavelengths between 1.5 and 3.0 μm, therefore the 2.0 - 2.5 μm atmospheric window is of great importance in volcano monitoring. Only one channel of high resolution satellite data was available at these wavelengths prior to the OPS sensor, which has three channels in this region. The increased spectral resolution of the OPS, combined with its smaller pixel size, should constrain thermal anomalies at volcanic targets more effectively. Allowing more accurate quantitative information relating to the size and temperature of these anomolies to be determined from remotely sensed images.

1.3 Rationale of the thesis

Chapter 2 of this thesis provides a detailed introduction to the JERS-1 system. This is provided because literature on the satellite is not widespread. A possible reason for this is that the data obtained by the Optical Sensor (OPS) onboard JERS-1 is of a highly variable nature. The majority of data, in particular the SWIR channels, are of a very poor quality. As a result very little OPS data has been released to users other than the initial Principal Investigators. Only a limited number of evaluation studies (approximately 250 for both SAR and OPS data) have been conducted globally, with only a small percentage of these concentrating on geological applications. Chapter 2 describes the highly variable quality of the OPS data and details the complex noise structures that affect all channels of data to varying degrees. It also considers the implications of data quality for the anticipated geological advances expected from JERS-1, especially as the channels most severely affected by noise are OPS 6 and 7, two of the new SWIR channels.

Various techniques for the removal or suppression of the noise structures associated with OPS data are discussed in chapter 3. Both spatial domain and frequency domain noise removal techniques are described. Emphasis is given to frequency domain processing as these techniques prove capable of isolating the noise component without removing or suppressing any 'real' image detail. A number of techniques are described and assessed on various OPS channels of data. Recommendations are given

on the suitability of each technique. The quality of the 'cleaned' data is also commented on with respect to the initial expectations of the data.

Chapter 4 provides a general introduction to the suitability of Oman for this study, as well as summarising previous remote sensing studies there. The geology of the ophiolite and the associated lithologies are also introduced. Fundamental to this chapter is the measurement of the spectral responses of igneous rock samples collected in the field. These spectra are examined for diagnostic features both before and after they have been convolved to TM and OPS band widths. The convolved spectra form the basis for the remainder of the chapter, being used to determine which spectral features should be identifiable on the OPS and TM data. These spectra are also compared with reflectance spectra extracted directly from TM and OPS data, to see if image spectra have the same ability to discriminate. This is particularly important with regard to the OPS data as it indicates whether or not spectrally important discrimination information has been lost due to the poor quality of the OPS data. Finally, this chapter discusses a number of techniques to determine which bands of data to combine in a false colour composite, in order to maximise lithological information. Techniques to further enhance these band combinations are also discussed.

Chapter 5 takes the suggested band composites and enhancements determined in the previous chapter and applies them to three test regions within the ophiolite, giving special emphasis to the Maqsad region. This region was being extensively mapped by Isma Amri and Georges Ceuleneer (Université Paul Sabatier, Toulouse) during the time of this study, therefore detailed ground verification information is available. The processed TM imagery for each region is then compared to the known geology to determine the level of discrimination possible using previously tested techniques (Rothery, 1987; Abrams *et al.*, 1988) The processed OPS imagery is then compared directly to the known geology and to the TM imagery to determine if any additional geological information can be discerned. The geological significance of any new features distinguished on the OPS data is also discussed. The chapter concludes by summarising the suitability of OPS data for lithological discrimination in the Oman ophiolite.

The potential of OPS data for volcano monitoring is briefly introduced in chapter 6 in the form of two papers; Denniss *et al.*, (1996) and Denniss *et al.*, (in press). These concentrate on lithological mapping of lava flows and thermal anomaly detection at Lascar volcano, Chile. The chapter concentrates primarily on the temporal information

derived from a series of OPS images of the pyroclastic flows emplaced during Lascar's largest historic eruption in April 1993 (GVN, 1993). The potential of multichannel SWIR data is also considered with respect to the extraction of temperature information from thermal anomalies, although temperature extraction is not attempted with the available OPS data due to its poor quality. The chapter summarises what additional volcanological information can be extracted from existing OPS data, despite its quality.

Chapter 7 summarises the usefulness of JERS-1 OPS data for lithological mapping and volcano monitoring, despite the associated data quality problems. This chapter also describes future high spatial and spectral resolution sensors which are due to be launched over the next few years. The potential of these new sensor are discussed with respect to lithological mapping and volcano monitoring. The chapter concludes by looking forward towards geological remote sensing in the 21st Century.

1.4 Collaboration

The work in this thesis is approximately 90% my own. However, having been part of a large and active research group I inevitably benefited from collaborating with my colleagues. These are listed in the acknowledgements. In particular, noise suppression techniques discussed in chapter 3 were developed jointly with a fellow student Carlos Roberto De Souza (De Souza 1995, De Souza *et al.*, 1996). Chapter 6 is derived from a collaborative study of Lascar, in which I was responsible for the JERS-1 work and a colleague Andy Harris was responsible for the AVHRR work.

1.5 Project origins

This Ph.D. project is the direct result of two Principal Investigatorships (PIs) on JERS-1 OPS data awarded to Dr. Dave Rothery. These were project numbers J-0107 using JERS-1 OPS data for lithological mapping and project J-0101 PI using JERS-1 OPS data for volcano monitoring.

2.0 Satellite sensor characteristics and data quality

2.1 Introduction to the remotely sensed data used in this study

This study primarily uses optical data from the Japanese Earth Resources Satellite (JERS-1). JERS-1 is a new satellite platform, which carries sensors designed for geological applications. After initial data delivery delays a total of 19 scenes of optical (OPS) data became available during this study (Table 2.1a); 6 scenes supplied as part of the Principal Investigator (PI) project; J-0107, and 13 additional scenes supplied directly by the Earth Remote Sensing Data Analysis Centre (ERSDAC). These scenes provide examples of Level 0, 2 and 5 pre-processing, see section 2.2.4.

Landsat Thematic Mapper (TM) data were also available (Table 2.1b) for some of the regions covered by the JERS-1 scenes. These data were used primarily to provide reference images to which the JERS-1 OPS data could be compared. TM data were used because of their proven capabilities in distinguishing lithological variations (Rothery 1987). Black and white and colour air photographs at scales of 1:50,000 and 1:20,000 respectively, were also available for some of the study areas. These photographs were used to evaluate the spatial resolution of the JERS-1 OPS data.

Landsat Thematic Mapper data have been used in geological projects for a number of years, and as a result the satellite and sensor characteristics of Landsat TM are fairly well known. In comparison JERS-1 data are not commonplace, due partly to the sensors relatively short history, and partly to the limited distribution of the data. Therefore the major design and operational characteristics of JERS-1 are described here.

No	Path - Row	Date	Level	Channels	Gain	Country	Latitude / Longitude	Supplier
1	207 - 261	24 / 06 / 92	L 2	All OPS	Normal	Oman	23° 13' - 23° 53' N / 58° 18' - 59° 10' E	PI J1-107
2	208 - 261	25 / 06 / 92	L 2	All OPS	Normal	Oman	23° 13' - 23° 53' N / 57° 44' - 58° 37' E	PI J1-107
3	208 - 262	25 / 06 / 92	L 2	All OPS	Normal	Oman	22° 37' - 23° 17' N / 57° 36' - 58° 28' E	PI J1-107
4	208 - 262	09 / 10 / 94	L 5	VNIR	Normal	Oman	22° 37' - 23° 17' N / 57° 36' - 58° 28' E	ERSDAC
5	210 - 261	27 / 06 / 92	L 2	All OPS	Normal	Oman	23° 13' - 23° 53' N / 56° 38' - 57° 30' E	PI J1-107
6	210 - 262	27 / 06 / 92	L 2	All OPS	Normal	Oman	22° 37' - 23° 17' N / 56° 29' - 57° 21' E	PI J1-107
7	211 - 260	28 / 06 / 92	L 2	All OPS	Normal	Oman	23° 49' - 24° 28' N / 56° 56' - 57° 05' E	PI J1-107
8	212 - 259	25 / 09 / 92	L 2	All OPS	High	Oman	24° 24' - 25° 04' N / 55° 50' - 56° 42' E	ERSDAC
9	212 - 259	04 / 02 / 93	L 2	All OPS	Normal	Oman	24° 24' - 25° 04' N / 55° 44' - 56° 37' E	ERSDAC
10	212 - 260	25 / 09 / 92	L 2	All OPS	High	Oman	23° 49' - 24° 29' N / 55° 42' - 56° 34' E	ERSDAC
11	212 - 260	04 / 02 / 93	L 2	All OPS	Normal	Oman	23° 49' - 24° 29' N / 55° 42' - 56° 34' E	ERSDAC
12	421 - 340	11 / 12 / 92	L 0	All OPS	Normal	Chile	23° 21' - 24° 01' S / 68° 29' - 67° 46' W	ERSDAC
13	421 - 340	11 / 12 / 92	L 2	All OPS	Normal	Chile	23° 21' - 24° 01' S / 68° 29' - 67° 46' W	ERSDAC
14	421 - 340	22 / 04 / 93	L 0	All OPS	Normal	Chile	23° 21' - 24° 01' S / 68° 29' - 67° 46' W	ERSDAC
15	421 - 340	22 / 04 / 93	L 2	All OPS	Normal	Chile	23° 21' - 24° 01' S / 68° 29' - 67° 46' W	ERSDAC
16	421 - 340	19 / 07 / 93	L 0	All OPS	Normal	Chile	23° 21' - 24° 01' S / 68° 32' - 67° 49' W	ERSDAC
17	421 - 340	19 / 07 / 93	L 2	All OPS	Normal	Chile	23° 21' - 24° 01' S / 68° 32' - 67° 49' W	ERSDAC
18	421 - 340	15 / 10 / 93	L 0	All OPS	Normal	Chile	23° 21' - 24° 01' S / 68° 29' - 67° 46' W	ERSDAC
19	421 - 340	15 / 10 / 93	L 2	All OPS	Normal	Chile	23° 21' - 24° 01' S / 68° 29' - 67° 46' W	ERSDAC

Table 2.1a JERS-1 OPS imagery available for this project

1	158 - 044	31 / 03 / 85	-	All	Normal	Oman	23° 58' - 22° 13' N / 57° 11' - 58° 59' E	-
2	158-043	23 / 02 / 86	-	All	Normal	Oman	25° 25' - 23° 40' N / 57° 49' - 57° 26' E	-

Table 2.1b Landsat TM data available for this project

2.2 Characteristics of the Japanese Earth Resources Satellite-1

The first Japanese Earth Resources Satellite (JERS-1) was launched on February 11, 1992 by a H-1 launch vehicle from the Tanegashima Space Centre, Japan. After the launch the satellite was renamed 'Fuyo-1' (Nishidai, 1993); however this name has not been widely adopted by the remote sensing community.

JERS-1 is the first Earth observing satellite to carry both a passive OPtical Sensor (OPS) and an active Synthetic Aperture Radar (SAR) on the same platform (Figure 2.1).

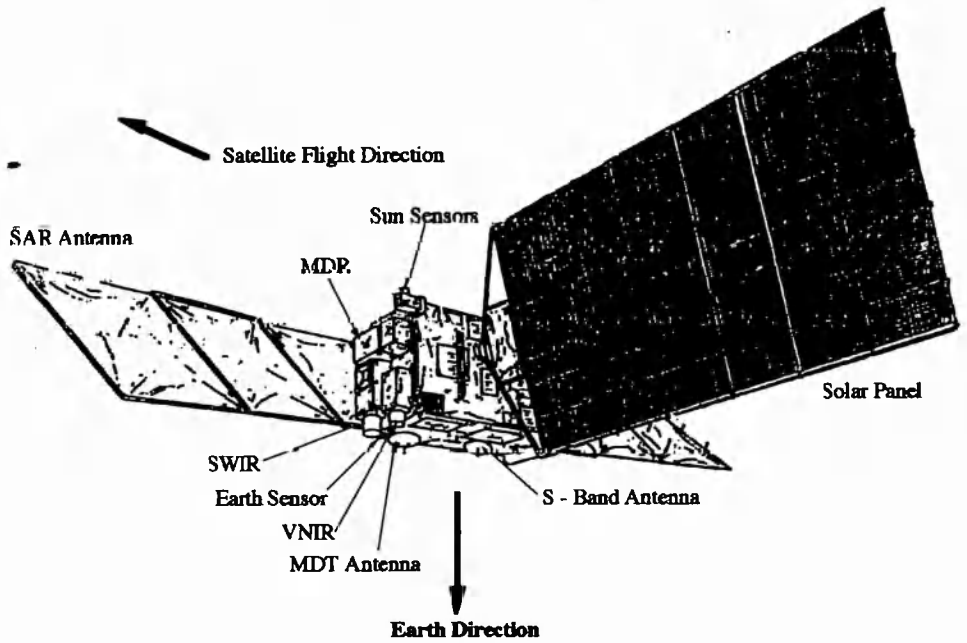

Figure 2.1 Schematic diagram of JERS-1 (After NASDA 1990). See text for abbreviations.

2.2.1 Satellite Orbit

JERS-1 is in a near circular sun-synchronous, polar orbit at an altitude of 568 km above the equator (Figure 2.2). Each orbit takes 96 minutes and the satellite completes fifteen orbits per day, covering the entire Earth (except polar regions) in 44 days. JERS-1 crosses the equator from north to south on a descending orbital node between 10.30 and 11.00 a.m., local solar time (NASDA, 1994). The main orbit characteristics of JERS-1 are summarised in Table 2.2.

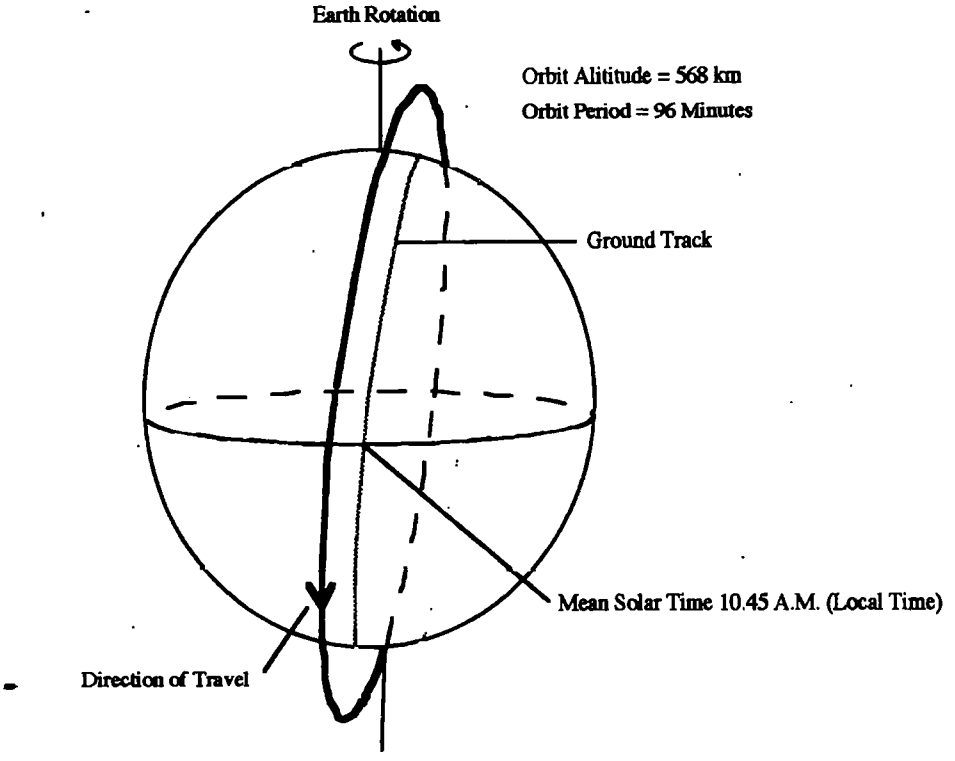

Figure 2.2 Schematic diagram of JERS-1 orbit (After Nishidai, 1993).

Orbit Parameter	Value	Comment
Satellite Altitude	568.023 km	Above equator
Orbit Period	96.146 minutes	
Orbit Inclination	97.67°	
Orbit Type	Sun-synchronous	Moving westwards
Revisit Period	44 Days	659 revolutions
Revolutions per Day	15 revolutions	
Local Solar Time	10.30 to 11.00 a.m.	Descending orbit
Distance to adjacent ground trace	60.7 km	Above equator

Table 2.2 JERS-1 orbit parameters (After NASDA, 1994).

2.2.2 Satellite equipment and data acquisition

Equipment on board JERS-1 can be broadly divided into four major subsystems: (1) Synthetic Aperture Radar (SAR); (2) Optical Sensor (OPS); (3) Mission Data Recorder (MDR); and (4) Mission Data Transmitter (MDT). Additional minor subsystems control orbit, attitude and thermal parameters (NASDA, 1994).

1) Synthetic Aperture Radar (SAR)

Only a very brief description of the SAR system will be given here as this project concentrates on the use of JERS-1 optical (OPS) data. Detailed information on JERS-1 SAR can be found in Chapman *et al.*, (1995), Zink (1995) and Raggam *et al.*, (1995).

JERS-1 SAR transmits up to 1600 pulses per second towards the Earth from its 11.9 m x 2.2 m antenna, which is positioned at 35° off-nadir on the right hand side of the satellite. JERS-1 therefore provides SAR illumination from east to west in a descending orbit. The SAR frequency is 1275 MHz (L Band) and has a HH (Horizontal transmit, Horizontal receive) polarisation. Ground resolution is 18 meters. Table 2.3 lists the major characteristics of the JERS-1 SAR.

SAR Parameter	Specification	Remarks
Observation Frequency	1275 MHz	
Bandwidth	15 MHz	
Polarisation	H-H	(Transmit and receive)
Off Nadir Angle	35°	Nominal value
Range Resolution	18 meters	At swath centre
Azimuth Resolution	18 meters	3 Looks
Transmitting Power	1100 - 1500 Watts	
Antenna Gain	33.5 dB or more	At antenna beam centre
Back-Scattering Coefficient	-20.5 dB	Equivalent to noise
S / A	14 dB or more	
Quantization Bit Number	3	

Table 2.3 Characteristics of the JERS-1 SAR (After NASDA, 1994).

The SAR on JERS-1 is constructed around three major subsystems, the Antenna Subsystem, the Transmit and Receive Subsystem, and the Signal Processing Subsystem (NASDA, 1994).

The Antenna Subsystem consists of an antenna comprised of eight 2.2 m x 1.5 m antenna panels (total size 11.9 m x 2.2 m), a deployment mechanism and thermal control devices. The Transmit and Receive Subsystem consists of a signal generator, a transmitter and a receiver, branching filters and a control device. The Signal Processing Subsystem consists of the signal processing unit, an operational control unit and a power supply. This subsystem is responsible for digitising the signal received by the 'receiver' subsystem, it then adds relevant observation information required for ground based processing and finally sends the data to the MDR prior to transmission to Earth.

2) Optical Sensor (OPS)

The OPS on board JERS-1 comprises a Radiometric Subsystem and an Electronic Circuit Subsystem (NASDA, 1994). The Radiometric Subsystem contains the pushbroom optical sensors, an electrical power supply unit and a thermal control unit. Onboard optical calibration procedures are also controlled by this system. The Radiometric Subsystem is divided between two sensors, a visible and near-infrared radiometer (VNIR) and a short wavelength infrared radiometer (SWIR). This division of the sensor into VNIR and SWIR components is one factor contributing to the channel-to-channel spatial misregistration, that will be discussed in section 2.5.3. A total of eight images are acquired through atmospheric windows within the 0.52 - 2.40 μm range covered by these two sensors. Table 2.4 lists the major characteristics of the OPS.

The VNIR radiometer (Figure 2.3a) uses an optical prism to split reflected solar radiation into four discrete channels, ranging from visible to near infrared wavelengths; OPS 1; 0.52 - 0.60 μm, OPS 2; 0.63 - 0.69 μm, OPS 3 and OPS 4; 0.76 - 0.86 μm (Figure 2.3b). Three of these bands OPS 1, OPS 2 and OPS 3 are incident from directly beneath the satellite whilst OPS 4 is incident from 15.33° in front of the satellite (Figure 2.4). OPS 4 provides JERS-1 with along-track stereoscopic capabilities.

Parameter	Specification	Dynamic Range
Observation Wavelengths	OPS 1 0.52 - 0.60 μm	0 - 324 W / (m^2.str.μm)
	OPS 2 0.63 - 0.69 μm	0 - 250 W / (m^2.str.μm)
	OPS 3 0.76 - 0.86 μm	0 - 248 W / (m^2.str.μm)
	OPS 4 0.76 - 0.86 μm	0 - 23.9 W / (m^2.str.μm)
	OPS 5 1.60 - 1.71 μm	0 - 33.3 W / (m^2.str.μm)
	OPS 6 2.01 - 2.12 μm	0 - 17.8 W / (m^2.str.μm)
	OPS 7 2.13 - 2.25 μm	0 - 13.7 W / (m^2.str.μm)
	OPS 8 2.27 - 2.40 μm	0 - 10.8 W / (m^2.str.μm)
Instantaneous View Angle	32.2 μrad	
View Angle	7.55°	
Stereoscopic View Angle	15.33° Alongtrack (B / H = 0.3)	
Imaging Period	3.46 msec	
Ground Resolution	18.3 m x 24.2 m (Across & Along -Track)	
Number of Pixels	4096 per line	
Swath Width	75 km	
Output Data Rate	30 Mbps x 2 channels	
Quantization Level	64 (6 bits)	

Table 2.4 Specifications of the OPS (After NASDA, 1994).

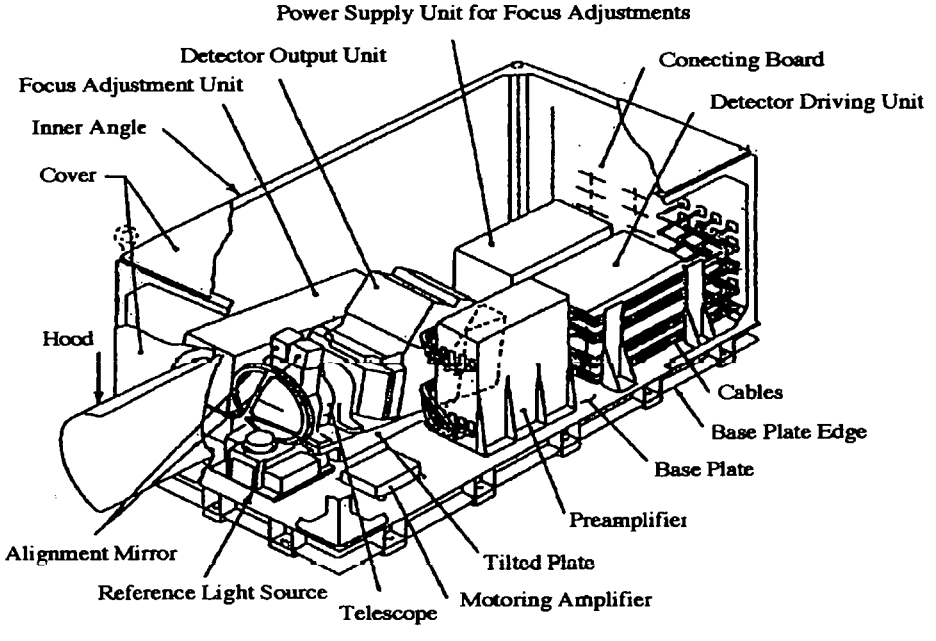

Figure 2.3a Schematic of JERS-1 VNIR, Approx. size 1 m x 1.8 m x 3.1 m, weight 1.4 tons (NASDA 1994).

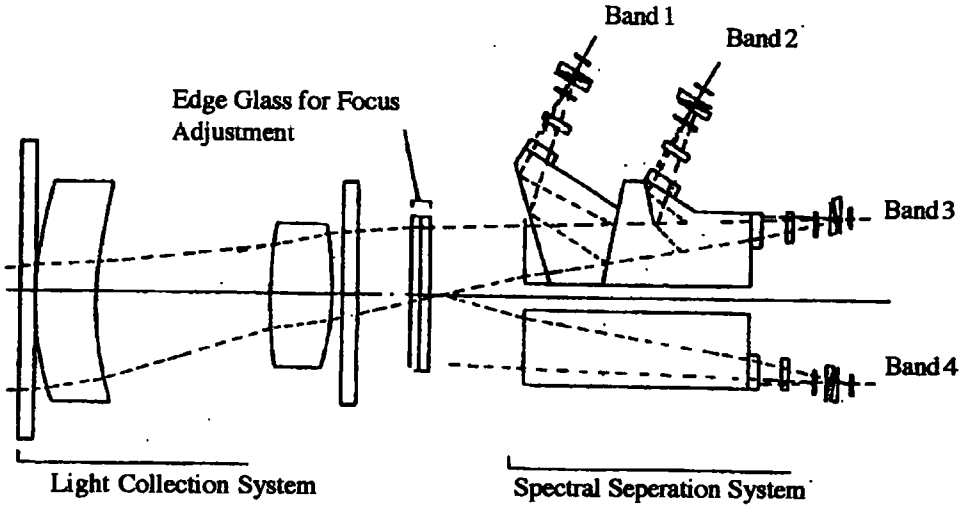

Figure 2.3b Schematic of VNIR telescope design (NASDA, 1994).

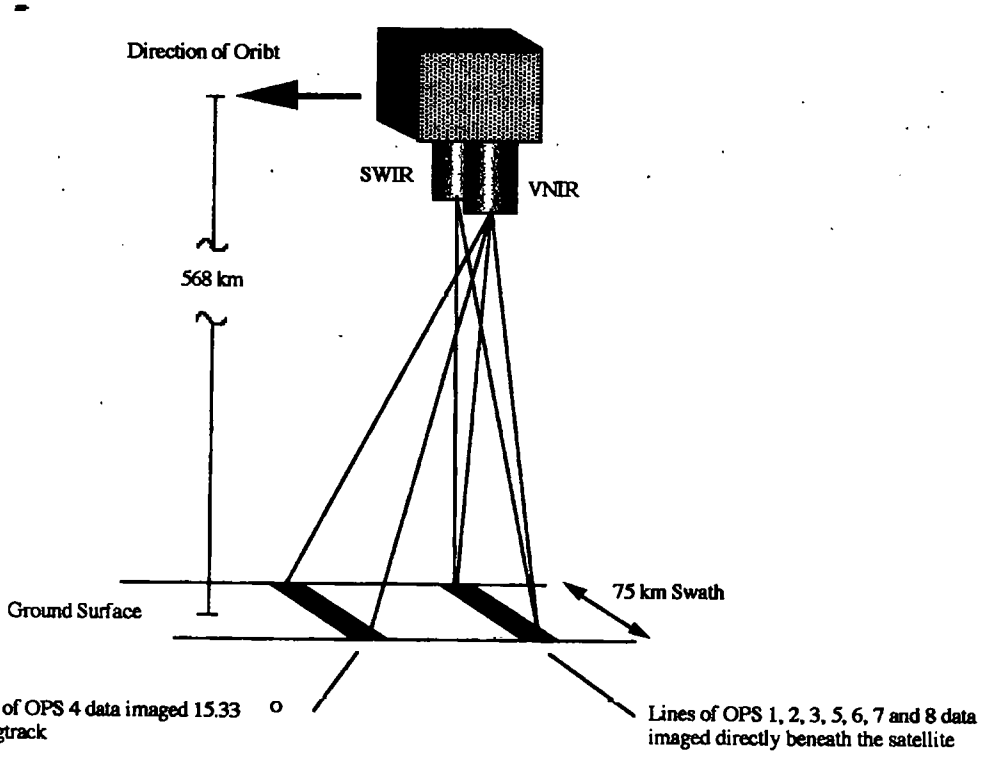

Figure 2.4 Configuration of stereoscopic OPS 4 viewing.

Radiance from all of these channels is focused and directed to the appropriate Charge Coupled Devices (CCD), where the radiance measurements are converted to electrical signals and output to the Electronic Circuit Subsystem. The major components and functions of the VNIR subsystem are summarised in Table 2.5.

In the SWIR radiometer (Figure 2.5a) radiation is separated using a filter set in front of the CCD's into four discrete spectral bands; OPS 5; 1.6 -1.71 μm, OPS 6; 2.01 - 2.12 μm, OPS 7; 2.13 - 2.25 μm and OPS 8; 2.27 -2.40 μm. Radiance from all of these channels is then focused and directed to the appropriate CCDs where the radiance measurements are converted to electrical signals and output to the Electronic Circuit Subsystem. Table 2.6 lists the major components and their functions of the SWIR subsystem. One major difference between the SWIR and the VNIR is the cooling unit. Because reflected light energy is very low at SWIR wavelengths it is necessary to reduce noise by cryogenically cooling (Figure 2.5b) the detector to a temperature range between 77 and 82 K.

Data from all channels, both VNIR and SWIR, has an initial pixel size of 18.3 m x 24.2 m. Image acquisition time is determined by the data storage rate; 3.46 msec per scene.

Component	Function
Telescope Unit	Uses an aspheric lens to focus images with a wide range of visible wavelengths. Stereoscopic view (OPS 4) captured by forward viewing.
Reference Light Source Unit	Emits calibration light inside the telescope during ground eclipse to check the radiometric performance of the radiometer
Focus Adjusting Mechanism	Compensates for thermal expansion / shrinkage of the telescope unit
Detector	Four CCDs (one for each channel) with 4096 elements each, converts incident light to electrical signals
Detector Driving Unit	Converts the timing signals to drive the detector
Preamplifier	Amplifies the detector image signal and transmits it to the Analogue Signal Processor (ASP)
Focus Adjustment Control Unit	Drives the focus adjustment motor

Table 2.5 Components and functions of the VNIR subsystem (After NASDA, 1994).

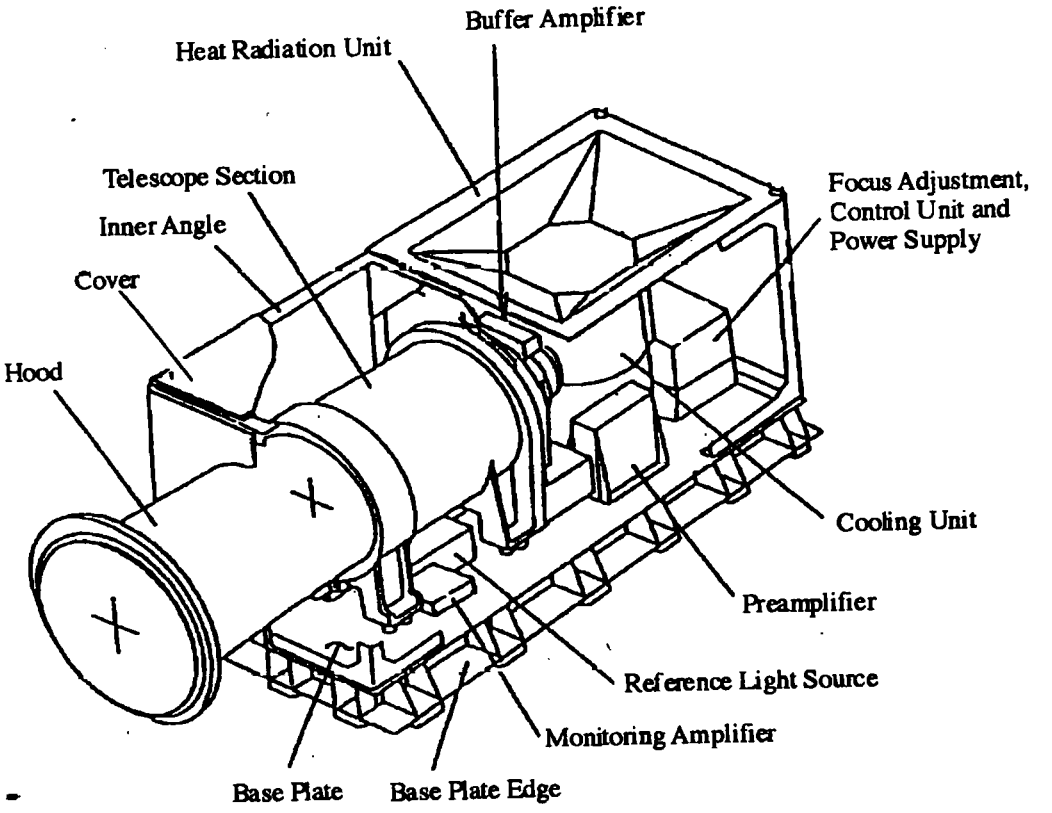

Figure 2.5a Schematic diagram of the SWIR Optical Sensor (OPS) (NASDA 1994).

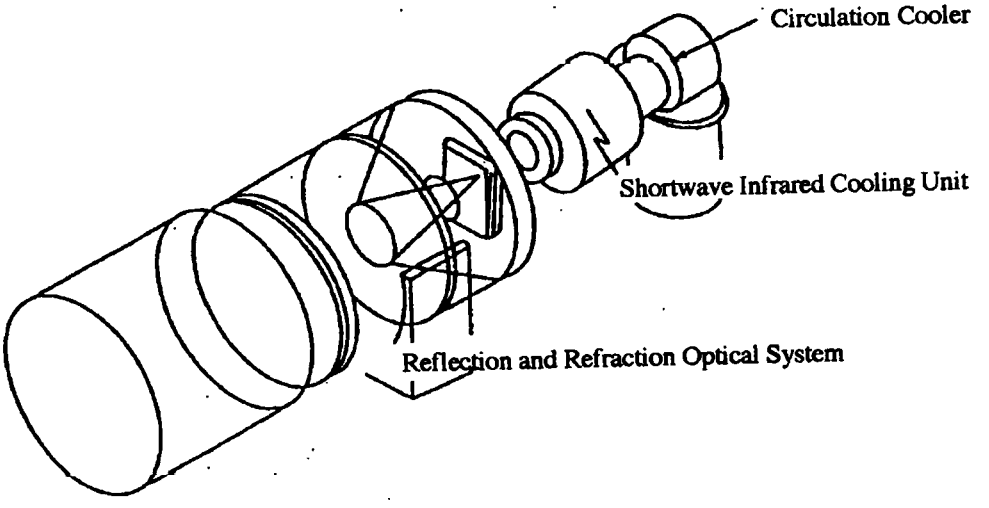

Figure 2.5b Schematic of SWIR telescope (NASDA, 1994).

Component		Function
Telescope		Reflection and refraction optical systems used to focus images over wide range of wavelengths with the least distortion
Reference Light Source		Emits calibration light inside the telescope to check its radiometric performance
Cooling Unit	Cooler	Integrated He cooler cools the short-wave detector to 77 - 82 K
	Detector	4096 element CCDs
Detector Driving Unit		Generates driving pulses for detector and temperature telemetry signals
Preamplifier		A feed back amplifier circuit

Table 2.6 Components of the SWIR sensor (After NASDA, 1994).

The Electronic Circuit Subsystem digitises and formats the analogue output signals from the optical radiometric subsystems. These formatted signals are then divided into two channels, one containing VNIR data the other SWIR, and are output to the Mission Data Recorder (MDR). The majority of data are recorded using the 'normal' gain setting but for scenes acquired over spectrally dark terrains the 'high' gain setting is used.

Additional to the VNIR and SWIR radiometers are the Thermal Control unit (TC), Analogue Signal Processing unit (ASP) and the Digital Signal Processing unit (DSP). The Thermal Control unit uses three platinum sensors in the VNIR and SWIR to measure temperature. Measured temperatures from the sensors of channels 1 to 6, are compared with pre-set temperature settings and are used to control the onboard heater. The Digital Signal Processing unit takes the output (8 channels of 6 bit digital data) from the ASP, edits and processes it, adds synchronising and telemetry signals and feeds the output to the MDR as two signals.

3) Mission Data Recorder (MDR)

The Mission Data Recorder is a multitrack tape recorder equipped with separate magnetic heads for recording and reproduction (NASDA, 1994). Data are written from the Beginning of Tape (BOT) to the End of Tape (EOT), but are read in the opposite direction (EOT to BOT). This has the advantage that recorded data which have not been read cannot be written over. It also minimises wear and tear on the tape and recording / reproduction heads as rapid tape forwarding and rewinding operations are not performed.

The MDR consists of the Transport Unit (TU), which houses the magnetic tape and its driving mechanisms in a closed container, filled with inert gases. The tape used is 9,200 feet long and has a recordable length of 8,900 feet between the primary BOT and EOT markers. Table 2.7 lists the main functions of the MDR.

Specification	Performance	Remarks
Recording Time	20 minutes or more	
Reproduction Time	20 minutes or more	
Number of Channels	Input: 2 channels (I and Q) Output: 2 channels (I and Q)	
Data Rate	Recording: 60 Mbps Reproduction: 60 Mbps	Total values for both channels
Recording Capacity	7.2 x 104 Mbit or more	Total for both channels
Number of Tracks	40 tracks: 16 x 2 data tracks 2 x 2 parity tracks 1 x 2 spare tracks 2 synchronising tracks	
Tape Speed	87 inches per second	
Tape Length	9200 feet x 1 inch	Effective recording length 8900 feet
Reel Structure	14 inch tandem coaxial reel vertically mounted	Two reels, upper and lower
Tape Guidance	Active guidance system	
Tape Running Time	2300 hours	Total recordable time
Number of Tape Starts / Stops	20000	Maximum

Table 2.7 Functions of the MDR (After NASDA, 1994).

4) Mission Data Transmitter (MDT)

The Mission Data Transmitter is used to downlink data to ground receiving stations. It consists of a switching device, a modulator, an amplifier, a synthesiser and an antenna (NASDA, 1994).

The MDT can either transmit real time SAR and OPS data to the Earth at a frequency of 8.15 GHz or it can transfer the data to the MDR, where it awaits downlinking to a Type-2 ground station (see section 2.2.3). Data temporarily recorded on the MDR are transmitted at a frequency of 8.35 GHz.

2.2.3 Satellite operation and data reception

Operational control and data reception for JERS-1 is divided between the Earth Observation Centre (EOC), the Tracking And Control Centre (TACC), and Type-1 and Type-2 Foreign stations (NASDA, 1994).

EOC (Saitama, Japan) is responsible for monitoring mission equipment, data acquisition, pre-processing, distribution, and data archiving. EOC also routinely monitors all OPS and SAR images for data quality.

The TACC is primarily responsible for maintaining the stable orbit of JERS-1. Any orbit variations are notified to EOC so that image acquisition timing utilises the most accurate orbit information.

A total of 15 world-wide receiving stations (Figure 2.6) are used to down load JERS-1 data. Thirteen of these stations are classified as Foreign Type-2, whilst two are Type-1 stations. Type-2 stations are capable only of receiving real-time SAR or OPS data, within the station coverage area. On the other hand, Type-1 stations Fairbanks (Alaska) and EOC are capable of receiving both recorded MDR data and real time data.

2.2.4 Data products

1) Ground Reference System

The Ground Reference System (GRS) identifies the location of the images acquired by the OPS and SAR systems onboard JERS-1. The GRS is defined by a lattice of points fixed on the Earth's surface. This lattice of points forms a common coordinate system for both sensors, despite the two systems imaging different geographical areas from the same orbit position. Once acquired, data are catalogued with a Path and Row value. Further details of the GRS can be found in NASDA (1994).

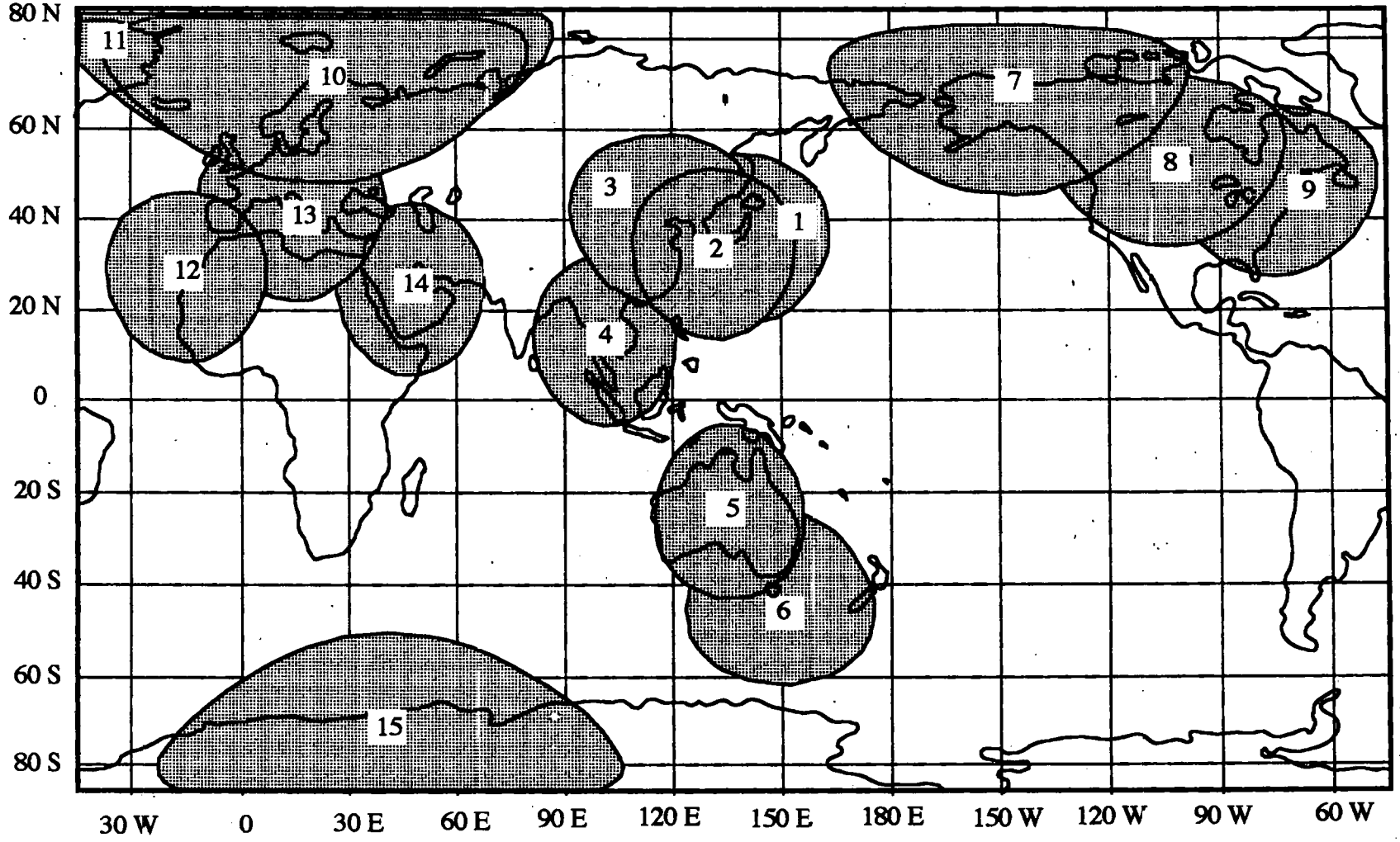

Figure 2.6 Reception coverage by JERS-1 direct reception ground stations (after NASDA, 1994). (1) EOC, (2) Tokyo Univ., (3) Beijing, (4) Bangkok, (5) Alice Springs, (6) Hobart, (7) Fairbanks, (8) Prince Albert, (9) Galineau, (10) Tromso, (11) Kiruna, (12) Maspalomas, (13) Fucino, (14) Riyadh and (15) Syowa.

2) Output data products

The Earth Observation Centre (EOC) outputs data from both sensors in either digital or hard copy format. OPS data, both normal and high gain, can be output to any of six levels, Level 0 to Level 5. The OPS pre-processing levels are (NASDA, 1994);

- **Level 0 - Unprocessed Signal Data Product**
  This level contains the raw data for all channels with no radiometric or geometric corrections applied.

- **Level 1 - Radiometric Corrected Image Product**
  A radiometric correction for element sensitivity deviation has been applied to all channels. No geometric corrections applied.

- **Level 2 - System Corrected Image Product / Standard Processed Products**
  - This is the standard product as it contains all OPS channels except OPS 4. A radiometric correction has been applied (as per Level 1) and a geometric correction. Output image data are transformed to either a Universal Transverse Mercator (UTM), Space Oblique Mercator (SOM) or Polar Stereo (PS) projection.

- **Level 3 - Precision Corrected Image Product**
  In addition to Level 2 pre-processing, Level 3 data have a more accurate geometrical correction applied using Ground Control Points (GCP).

- **Level 4 - Registration Corrected Image Product**
  In addition to Level 2 pre-processing the data are registered to a standard geometric image.

- **Level 5 - Stereo Image Product**
  This level contains only data recorded by channels OPS 3 and 4; pre-processing is as per Level 2

Geometrically corrected OPS data (Levels 2 to 5) are resampled using a nearest neighbour technique, resulting in an output pixel size of 18 m x 18 m and a nominal scene size of 75 x 75 km. Digital Level 2 images are 4680 samples by 4201 lines (138 Mb), whilst Level 0 images are 4096 samples by 4001 lines (117 Mb).

2.3 Comparison of Landsat Thematic Mapper (TM) and JERS-1 OPS sensor characteristics

Compared with JERS-1 the Landsat series of satellites has had a long history and is well tested, since the launch of the first Multispectral Scanner (MSS) in 1972. Landsat 4, launched on 16 July 1982, was the first to carry the Thematic Mapper (TM) sensor. Landsat 5 followed shortly afterwards on 1 March 1984. Comprehensive descriptions of the Landsat satellites can be found in the literature, such as Pierce (1979), Engel and Weinstein (1983), and Markham and Barker (1985). Only the major differences between Landsat TM and JERS-1 are described here. Landsat TM data used in this project were acquired by Landsat 5.

2.3.1 Orbit differences

Landsat 5 is in a circular polar sun synchronous orbit, similar to that of JERS-1, except that it is 135.5 km higher, at an altitude of 705.3 km above the equator. Spacing between adjacent ground tracks is 172 km, as opposed to 60.7 km for JERS-1. This is to allow for the wider imaging swath width of TM (185 km) than JERS-1 (75 km). Landsat makes a total of 14 $^{9}/_{16}$ orbits a day, resulting in a repeat frequency of 16 days, 28 days quicker than JERS-1. The initial equatorial crossing time of Landsat 5 was 9.45 a.m. (±15 minutes), but due to orbit degradations which have not been rectified this has now changed to 9.15 a.m. The major orbit parameters are summarised in Table 2.8.

Orbit Parameter	Value	Comment
Satellite Altitude	705.3 km	Above equator
Orbit Period	99 minutes	
Orbit Inclination	98.2°	
Orbit Type	Sun-synchronous	Moving westwards
Revisit Period	16 Days	659 revolutions
Revolutions per Day	14 $^{9}/_{16}$	
Local Solar Time	9.45 a.m. ± 15 minutes	Original
Distance to adjacent ground trace	172 km	Above equator

Table 2.8 Landsat 5 orbit parameters.

2.3.2 Sensor Differences

Landsat 5 carries only an optical sensor, the Thematic Mapper (TM), which is a line scanner as opposed to the OPS pushbroom design. It has no SAR capabilities. The TM sensor collects radiometric data in seven bands between 0.45 μm and 12.5 μm. Four bands are in the visible and near infrared: TM 1 (0.4 - 0.45 μm); TM 2 (0.52 - 0.60 μm); TM 3 (0.63 - 0.69 μm); and TM 4 (0.76 - 0.90 μm). Two bands are in the SWIR: TM 5 (1.55 - 1.75); and TM 7 (2.08 - 2.35). One band, TM 6, is in the Thermal Infrared (10.4 - 12.5 μm) (Engel and Weinstein, 1983). All bands except TM 6 have a pixel size of 30 m x 30 m, whilst TM 6 has a pixel size of 120 m x 120 m. All TM data are recorded from radiation incident from directly beneath the satellite, Landsat TM does not have any along- or across-track sensing capabilities. All TM data are recorded at the higher quantization rate of 8 bits, as opposed to the 6 bit rate for JERS-1.

In effect there are three major differences between the spectral capabilities of JERS-1 OPS and Landsat TM. The first difference is that the OPS does not have a blue-green channel equivalent to TM 1. Secondly OPS channels 3 and 5 have significantly smaller bandwidths than the equivalent TM bands 4 and 5. The most important difference occurs in the 2.0 - 2.4 μm region of the SWIR. In this geologically important part of the spectrum (see section 2.4.2) the broad band of TM7 has been sub-divided into three narrow OPS channels (OPS 6, 7 and 8). These three channels in combination occupy a slightly wider spectral region than TM 7. It is this sub-division of the SWIR part of the spectrum which makes the spectral discrimination capabilities of JERS-1 significantly different from those of TM. Table 2.9 summarises the major characteristics of the TM sensor.

2.4 Geological potential of OPS data compared with TM data

Thematic Mapper data have already proved to be very useful in numerous geological applications, ranging from mineral exploration (Abrams *et al.*, 1983), hydrocarbon microseepage (Segal and Merin, 1989), and structural tectonics (Drury and Berhe, 1993) to lithological mapping (Rothery, 1987, Sultan *et al.*, 1987 and Qari, 1989). All of these studies have utilised the synoptic viewing capabilities (185 km^2), and the high spatial and spectral resolutions of TM data. In comparison, OPS data offer significantly higher spatial and spectral resolution, increases which should allow considerably more geologically useful information to be extracted from the imagery.

Parameter	Specification	Dynamic Range
Observation Wavelengths	TM 1 0.40 - 0.45 μm	0 - 324 W / (m^2.str.μm)
	TM 2 0.52 - 0.60 μm	0 - 250 W / (m^2.str.μm)
	TM 3 0.63 - 0.69 μm	0 - 248 W / (m^2.str.μm)
	TM 4 0.76 - 0.90 μm	0 - 239 W / (m^2.str.μm)
	TM 5 1.55 - 1.75 μm	0 - 33.3 W / (m^2.str.μm)
	TM 7 2.08 - 2.35 μm	0 - 17.8 W / (m^2.str.μm)
	TM 6 10.4 - 12.5 μm	0 - 13.7 W / (m^2.str.μm)
Instantaneous View Angle	42.5 μrad	
View Angle	approximately normal to ground track	
Imaging Period	3.46 msec	
IFOV	30 m x 30 m	
Number of Pixels	6320 per line	
Swath Width	185 km	
Output Data Rate	84.903 Mbps	
Quantization Level	256 (8 bits)	

Table 2.9 Specifications of the TM (After Engel and Wienstein, 1983)

2.4.1 Spatial Resolution

The quoted higher spatial resolution of OPS data will be advantageous in geological applications as it will offer the potential to identify smaller scale features such as layering, dykes and small intrusive bodies. Features which are not discernible on lower resolution TM data. Increased spatial detail is important not only for image interpretation, but also during field validation checks. Increased image detail can help determine the location of field features more accurately, a task which is often difficult without the aid of high resolution air photographs or a Global Positioning System (GPS). Reducing locational errors results in an overall improvement in field validation accuracy.

Plates 2.1 and 2.2 are 512 x 512 pixel subscenes of OPS 5 and TM 5 data from the Maqsad region, Oman. These two images look very different primarily because of seasonal illumination differences, topographic detail is far greater on the TM imagery due to low-angle winter sun illumination. The OPS data does show more spatial detail compared to the TM imgery, but the resolution is not as good as expected from 18 metre data. This is due to the OPS data having an original resolution of 24 metres in the along-track direction which is resampled to 18 metres. Despite the data being

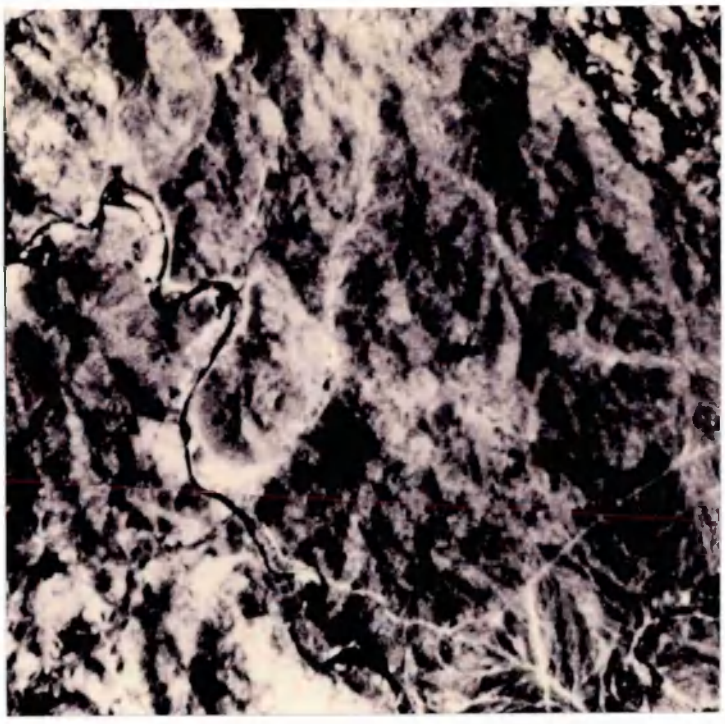

Plate 2.1 Example of high resolution OPS data, 512 x 512 pixel subscene of OPS 5, 208-262, Maqsad, Oman. The 18 m pixel size of OPS data enhances the spatial detail of small scale features such as the wadi flowing across the image from top left to bottom right. This higher resolution means that OPS data are capable of identifying smaller important geological features such as layering, dykes and intrusives.

Plate 2.2 Example of TM data centred on the wadi seen in Plate 2.1. This 512 x 512 pixel subscene of TM 5 (158-044) covers a larger area than the OPS data, because of the larger pixel size. This image shows greater topographic detail due to the image being illuminated with a low winter sun, compared with the high summer sun illumination of the OPS data. The larger 30 m pixel size means that the TM sensor is not capable of recording the same degree of detail as the OPS. This is evident when comparing the wadi detail in both images.

resampled OPS images are of a slightly higher resolution, this can be seen when comparing the major wadi which crosses both images from top left to bottom right. Variations in the width and course of the wadi within its erosional channel can be easily seen on the OPS data, features which are not so clear on the TM data. Further examples of the higher spatial resolution of OPS data are given in chapter 5. A disadvantage of the slightly higher resolution OPS data is that it only covers approximately a quarter of the area of the TM subscene. A disadvantage for regional studies as OPS data do not offer the synoptic overview of TM, unless a number of scenes are mosaiced together, which can be a time consuming and expensive task.

Another advantage of the smaller pixel size of OPS data means that they can be enlarged to a scale of 1:50,000 without the pixels becoming prominent, which occurs when TM data are enlarged to this scale. TM data are best enlarged to a maximum scale of 1:75,000. Being able to enlarge OPS data to a larger scale means that they can be more easily compared or integrated with other high resolution data sets, such as airborne data.

2.4.2 Spectral resolution

Compared with TM data, OPS data offer increased spectral resolution because of the increased number of channels in the 2.0 - 2.4 μm atmospheric window, and because of the narrower bandwidths of OPS 3 and 5. A schematic representation of the spectral resolution of the OPS and TM sensors is shown in Figure 2.7. Note that the three OPS SWIR channels (OPS 6, 7 and 8) occupy a slightly larger window (2.01 - 2.40 μm) than the broad band of TM 7 (2.08 - 2.35 μm).

The 2.0 - 2.4 μm atmospheric window is of great importance in geological remote sensing because it includes wavelengths with mineralogically diagnostic absorption features, caused by either electronic or vibrational processes (Hunt, 1977). Electronic processes produce broad absorption features associated with ferric iron (Fe^{3+}) at 0.65 μm and 0.87 μm, although the presence of ferrous iron (Fe^{2+}) can produce an absorption feature at 2.2 - 2.3 μm (Blom *et al* 1980). Vibrational processes, including bending and stretching of molecules, results in absorptions caused by Al-OH and Mg-OH associated with clays, micas, amphiboles and serpentine (Blom *et al.*, 1980). Al-OH produces absorption bands near 2.2 μm, whereas Mg-OH produces features near 2.3 μm, both of which are contained within the broad band of TM 7 (Figure 2.8a & c). In contrast the Al-OH feature is contained in OPS 7 (Figure 2.8b) and the Mg-OH feature contained in OPS 8 (Figure. 2.8d).

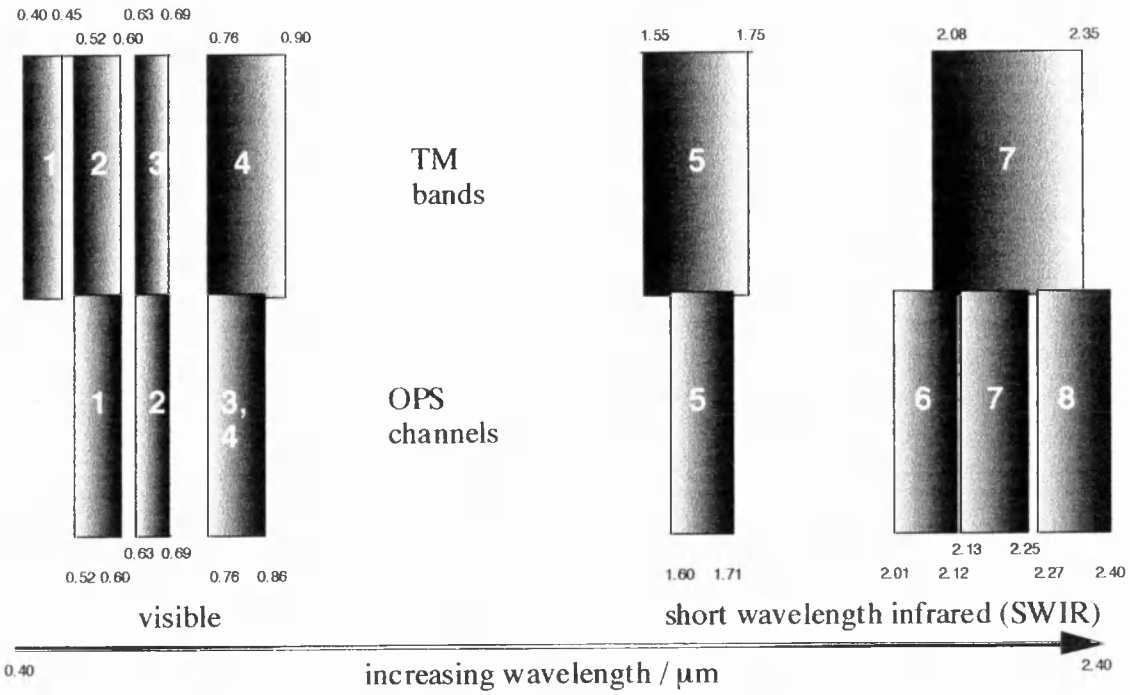

Figure 2.7 Schematic diagram showing the location of JERS-1 OPS channels compared with Landsat TM bands (TM 6 not shown).

The carbonate ion (CO_3^{2-}) results in an absorption feature around 2.35 μm, which is towards the upper edge of TM 7 (Figure 2.8e), but in the centre of OPS 8 (Figure 2.8f). Because TM 7 is affected by Al-OH, Mg-OH and CO_3 absorptions it almost impossible to discriminate between these absorptions using TM data. Differentiating between these on OPS data is easier because the absorptions are contained within independent narrow SWIR channels. Increased discrimination between these absorption features should help to distinguish numerous lithologies.

2.4.3 Stereoscopic capabilities

Another advantage of JERS-1 over Landsat TM is its capability to acquire along-track stereoscopic data. The acquisition of stereoscopic data means that OPS data can be used to derive topographic information for regions imaged by the other OPS channels. The small pixel size of JERS-1 should result in accurate Digital Elevation Models (DEM), although the poor base to height ratio of 0.3 may cause some accuracy problems. JERS-1 has the advantage that it acquires along-track stereoscopic data, which means that temporal variations, for example, cloud cover, are kept to a minimum between stereoscopic channels (in contrast to SPOT, which collects stereo data across-track from different orbits).

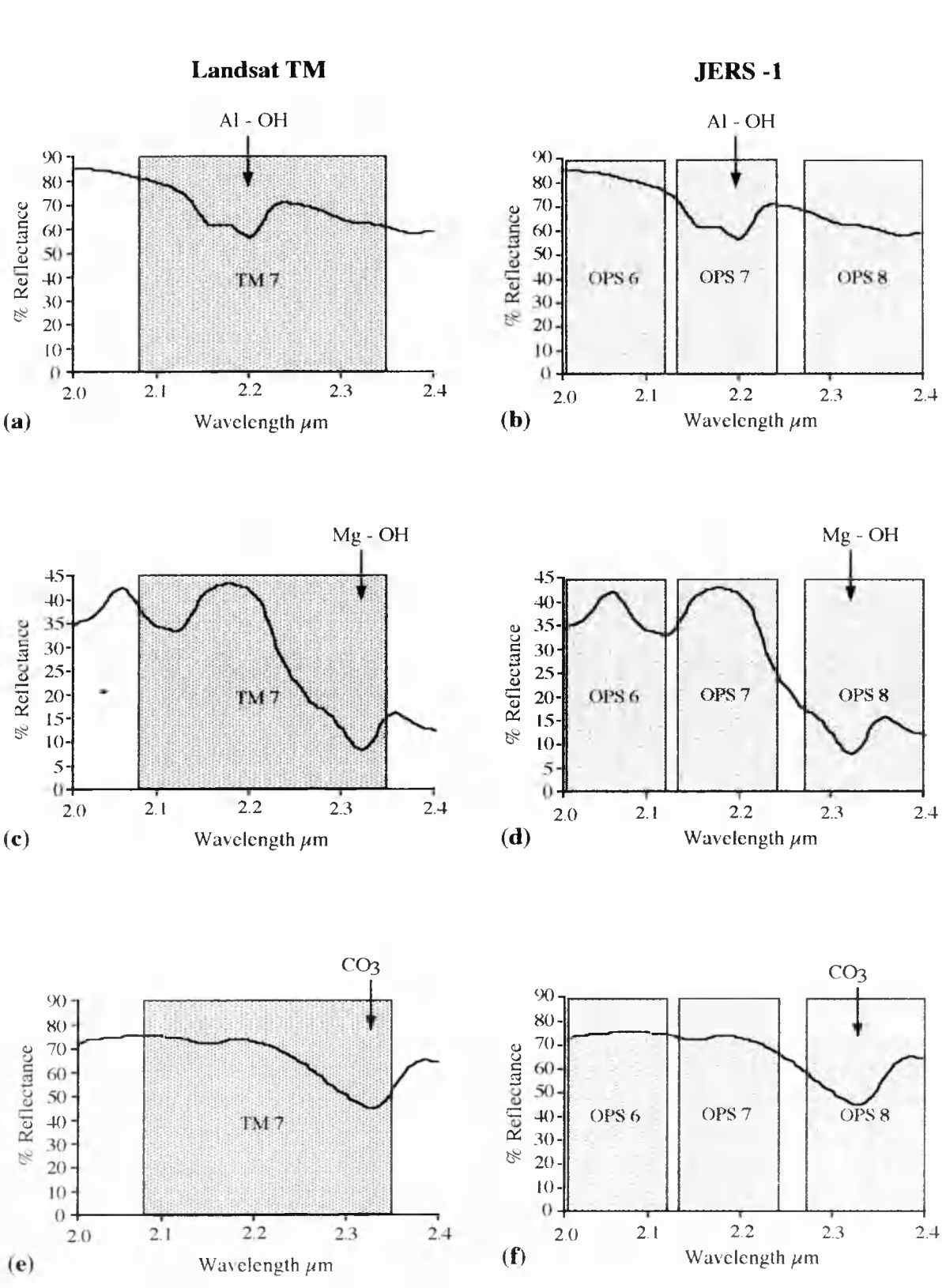

Figure 2.8 Comparison of the spectral resolution of Landsat TM 7 and JERS-1 OPS 6, OPS 7 and OPS 8 when considering (a) and (b) Al-OH (kaolinite); (c) and (d) Mg-OH (serpentine); (e) and (f) CO_3 (calcite) absorption features. This figure clearly shows that the increased spectral resolution of OPS is capable of recording absorption features previously contained within the broadband of TM 7 in individual narrow SWIR channels. Mineral spectra from Grove *et al.*, 1992.

2.5 JERS-1 mission status, data availability and quality

2.5.1 JERS-1 mission status

After initial mission checks the OPS sensor onboard JERS-1 started observations on 12 March 1992. Unfortunately the shortwave infrared radiometer ceased operation on 7 December 1993. This was due to the failure of the cooling system, believed to have been caused by dust in the bearings chamber of the SWIR cooler (Takata, 1995). Since December 1993 only visible data have been acquired by the OPS. As of September 1994 OPS operation time totaled 187 hours, 12 % of the 1500 hour design limit (Takata, 1995), whilst MDR (Missions Data Recorder) and MDT (Mission Data Transmitter) operations totaled 58 % and 41 % of their life design values, respectively. On 10 February 1994 JERS-1 officially finished its two year design life. Since that date JERS-1 has been operating in an extended life mode. As of December 1994 JERS-1 had sufficient fuel (90 kg) to support a further seven years in extended life mode, hopefully extending JERS-1 operations until the year 2001 (Matsui, 1995). All other systems, including the solar arrays are believed to be able to withstand this extended mission life.

2.5.2 Data availability

Between March 1992 and October 1994 a total of 65,987 OPS scenes were acquired, of which 30,868 contain less than 30 % cloud cover (Nishidai, 1995). In comparison 110,754 SAR scenes were acquired in the shorter period September 1992 to October 1994. OPS data acquisition is behind schedule due to the severity of cloud cover encountered over target areas.

The majority of JERS-1 data distributed outside of Japan has been via Principal Investigator (PI) projects. A total of 243 PI projects were established (86 Japanese, 157 non-Japanese), resulting in 809 suitable images being distributed since 9 November 1992 (Shimada, 1995). Users outside of the PI scheme had to wait until 15 October 1993 before JERS-1 data became available commercially. Initial commercial prices, as of May 1994, were JPY 120,000 (approx. £670) for OPS or SAR data, but data for research purposes were available at a reduced rate of JPY 8,800 (approx. £50) for either SAR, VNIR or SWIR data (personal communication Nishidai).

2.5.3 Data quality

All data, both OPS and SAR, acquired by JERS-1 since its launch, have been of variable quality due to numerous noise artifacts appearing on imagery. All OPS channels are affected to varying degrees, although in practice the data recorded by the SWIR tend to be the most severely affected. The severity of the various noise structures encountered varies depending on gain settings and on pre-processing procedures applied. A description of common noise structures seen on OPS data follows:

1) Dynamic range

All OPS normal gain channels have a poor dynamic range. Figure 2.9 illustrates the Level 0 and Level 2 histograms for each channel of scene 421 - 340. This scene covers an area of varied geological terrain with lithologies ranging from spectrally bright sediments to dark basalts. Despite this the dynamic range of Level 0 data can be seen to be exceptionally poor, ranging from a minimum of 12 DN (OPS 8) to a maximum of 54 DN (OPS 5). Pre-processing the data to Level 2 (section 2.2.4) transforms the data distribution to an 8 bit range. Details of the transformation algorithm used to scale the data from 6 to 8 bit have not been published. It is believed that this is a non-linear scaling (personal communication, Shimada), which would explain why the histogram shape appears slightly modified on the Level 2 data. Low dynamic range images cause a loss of both textural and spectral information resulting in large regions of terrain appearing fairly uniform. Poor sensor sensitivity significantly reduces spectral contrast between lithologies. It can also cause some minor spectral variations, particularly those within a fairly homogeneous lithology to be missed. This results in lithologies appearing more homogeneous than they actually are.

2) Saturation

An offset and gain (x3) is applied to radiance values in high gain mode (Nishidai *et al.*, 1995), which results in severe saturation problems. High gain mode slightly improves the dynamic range of VNIR channels over dark terrains, however bright regions within these images are easily saturated. An example of high gain OPS 2 data is shown in Plate 2.3. Reasonable levels of spectral variation are evident over the dark mafic lithologies but the spectrally bright sedimentary lithologies are saturated. SWIR channels are also severely saturated in high gain mode, as illustrated by OPS 8 data in Plate 2.4.

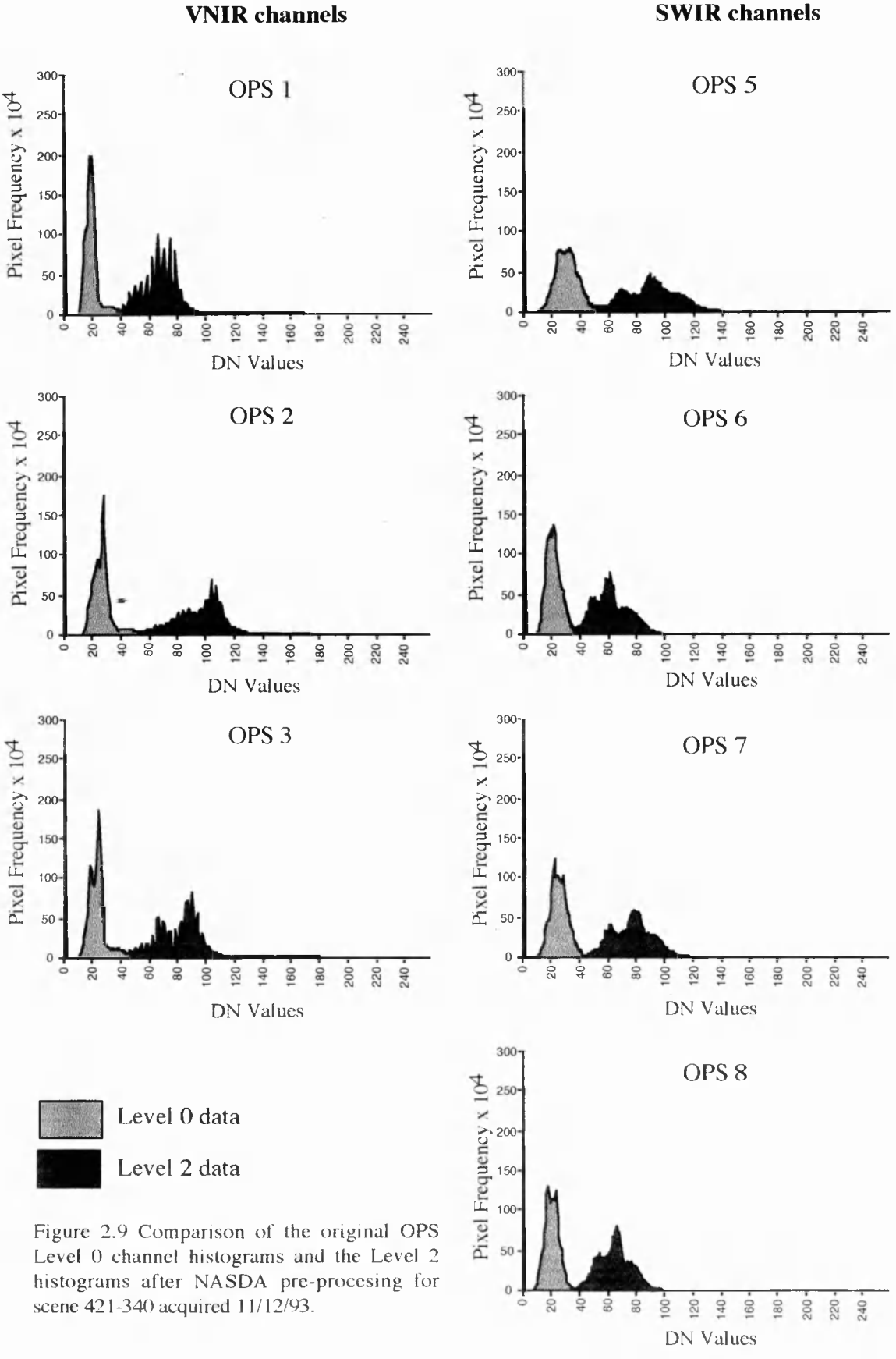

Figure 2.9 Comparison of the original OPS Level 0 channel histograms and the Level 2 histograms after NASDA pre-processing for scene 421-340 acquired 11/12/93.

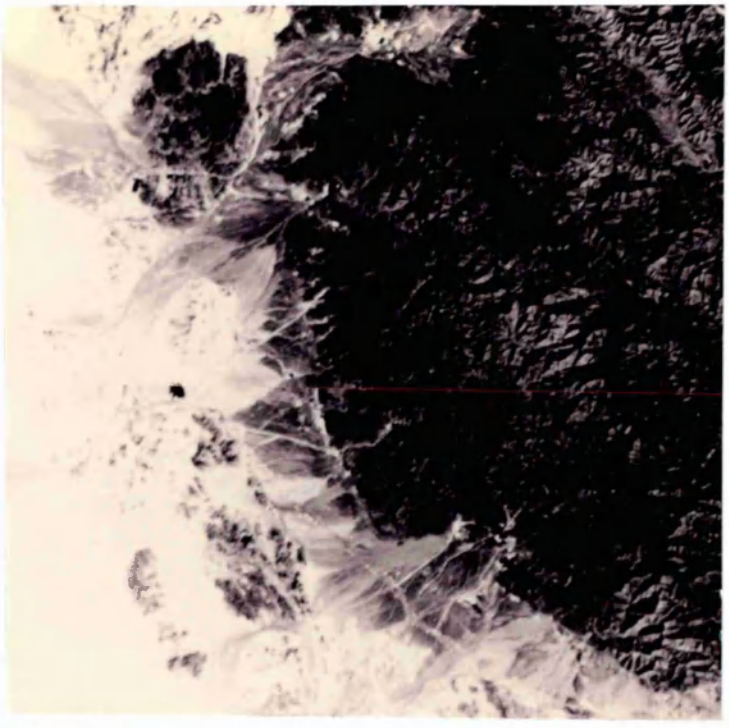

Plate 2.3 A 2048 x 2048 pixel subscene of Level 2 OPS 2 high gain data, from scene 212-260, Oman. The high gain setting has resulted in moderate spectral variation within the dark mafic lithologies and saturation of the spectrally bright sediments.

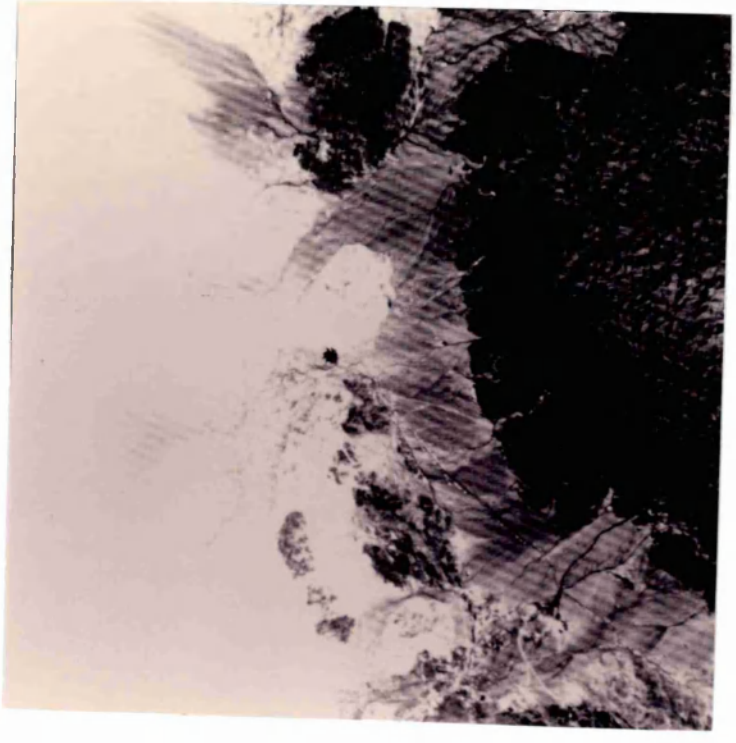

Plate 2.4 A 2048 x 2048 pixel subscene of Level 2 OPS 8 high gain data, from scene 212-260, Oman. OPS 8 shows some spectral variation within the dark mafic lithologies but the majority of the scene is severely saturated.

Figure 2.10 shows the channel histograms for the high gain scene illustrated in Plates 2.3 and 2.4. The histograms of each of these high gain channels differs significantly from those seen in Figure 2.9, which represents normal gain data. All of the VNIR channels in Figure 2.10 show similar distributions with relatively small numbers of pixels occupying the range of values between 100 and 240 DN, with a peak in data between 240 and 255 DN. This peak represents the saturated image data. The histograms of the high gain SWIR data are slightly more varied. OPS 5 and OPS 7 are the most severely saturated as almost all of the pixels have values between 220 and 255 DN. Very few DN values outside of this range have been recorded. The histograms of OPS 6 and OPS 8 show that these channels contain some information (e.g. Plate 2.3b) as there is a reasonable data distribution between 130 and 230 DN. However the peak at 255 DN in both histograms indicates that a large amount of data is saturated.

These histograms not only illustrate sensitivity differences between the VNIR and SWIR radiometers, but also differences within the SWIR radiometer. The SWIR histograms in Figure 2.10 suggest that channels OPS 5 and OPS 7 have similar sensitivities, as do OPS 6 and OPS 8. This inter-channel response variation may represent a feature of the SWIR system design and / or electronics.

3) Random noise spikes

Occasionally severe noise spikes occur, which affect only a few isolated pixels within a scene. When these spikes occur they tend to be concentrated in a group of 5 to 6 spikes, each separated by 10 to 20 samples across-track. Because of the severity of these spikes (±75 DN) they usually affect four lines of data, two lines for a centre spike and a line either side for a halo. The halo modulates image DN by a negative amount if the centre spike is positive and vice versa. These noise spikes have been seen in all channels of Level 0 and Level 2 data; their occurrence is random. Intermittent noise spikes like these are probably caused by fluctuations in the sensor power supply.

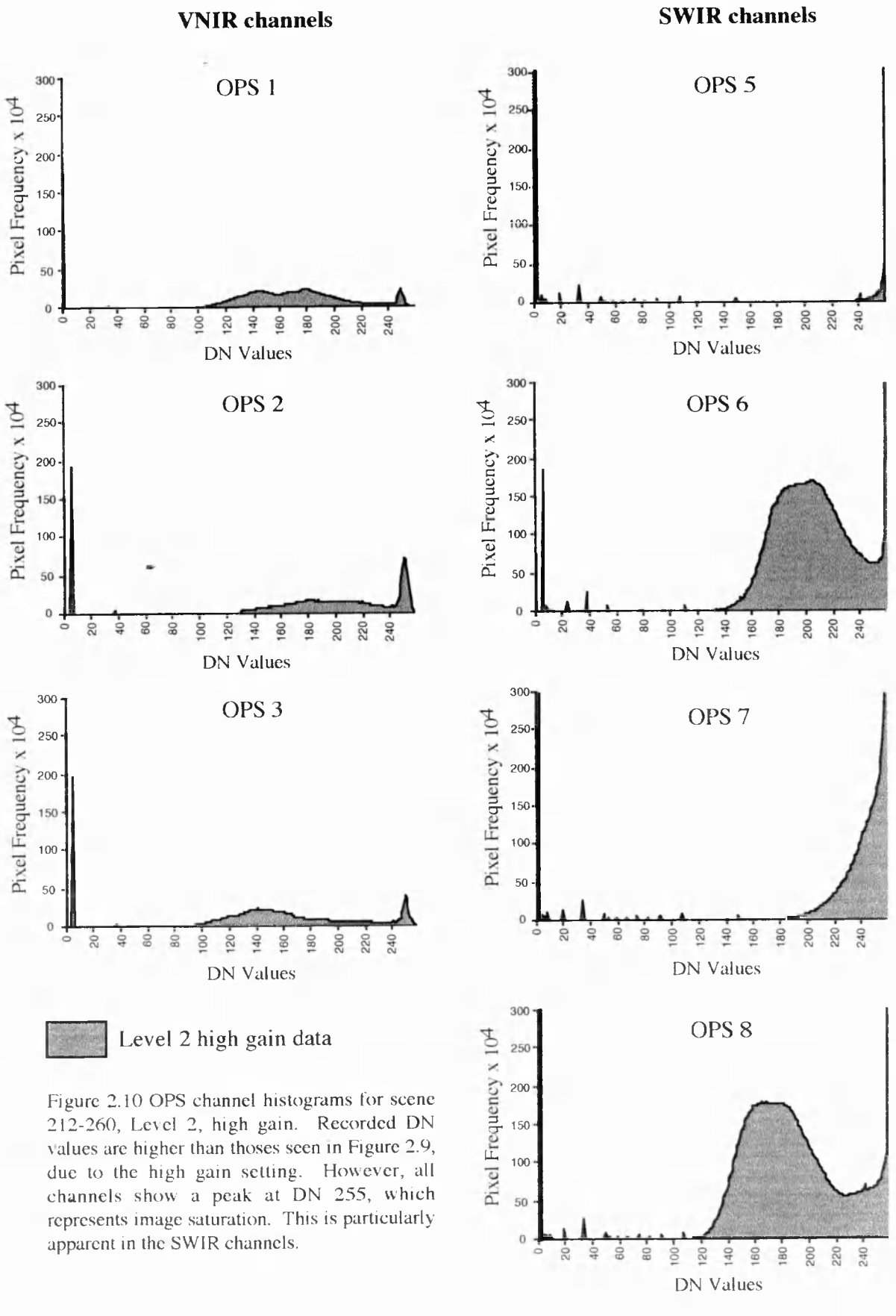

Figure 2.10 OPS channel histograms for scene 212-260, Level 2, high gain. Recorded DN values are higher than thoses seen in Figure 2.9, due to the high gain setting. However, all channels show a peak at DN 255, which represents image saturation. This is particularly apparent in the SWIR channels.

4) Across-track striping

VNIR channels (OPS 1, 2, 3 and 4) are affected by quite significant horizontal across-track striping (Plate 2.5). Stripes extend across entire scene widths, although they vary in frequency throughout a scene. On Level 0 data (Figure 2.11) stripes are very clear as the majority have a fairly consistent repeat frequency of 3 lines. Occasionally, severe noisy zones are encountered where two out of every three lines of data are affected. Across-track stripes in these zones are more fragmented in appearance, due to along-track striping being the predominant noise structure (section 2.5.3(5)). Over areas of homogeneous terrain these stripes can be seen to modulate scene DN values by up to ±2 DN.

Less severe across-track striping is sometimes apparent on SWIR channels, the worst affected channel being OPS 8. SWIR striping is similar to VNIR striping except that the frequency alternates between zones of 3 to 4 lines and zones of 7 to 8 lines. Level 2 data are also affected by across-track striping, although the frequency of these structures is not always apparent as they are severely fragmented by along-track striping (see section 2.5.3(5)). Nishidai (1995) suggests that across-track striping has been introduced by electronic crosstalk somewhere in the VNIR circuit; this may also be true for the SWIR circuit. In the future NASDA hopes to be able to remove across-track striping as a part of the routine pre-processing procedure.

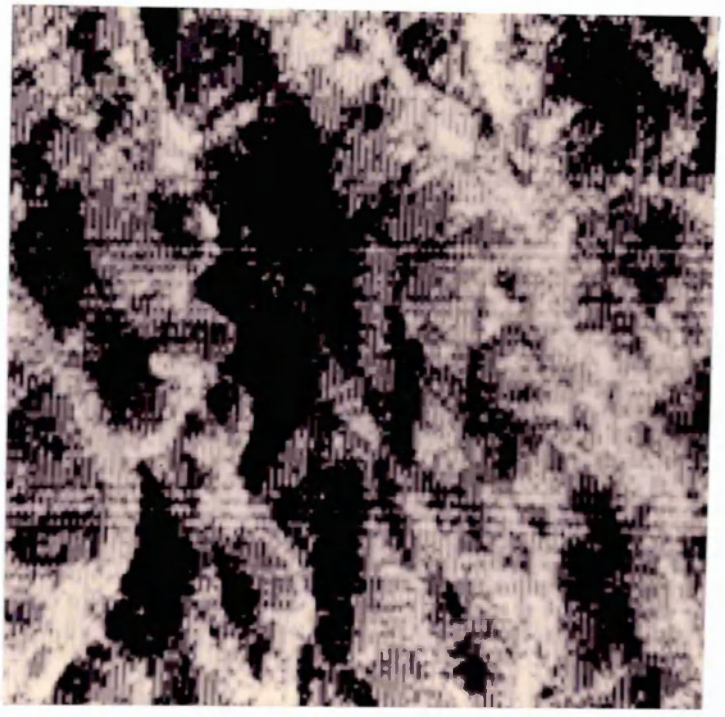

Plate 2.5 A 200 x 200 pixel subscene of Level 2 OPS 2 data clearly showing across-track striping. This plate illustrates the intermittent nature of across-track striping which tends to occur within blocks of data.

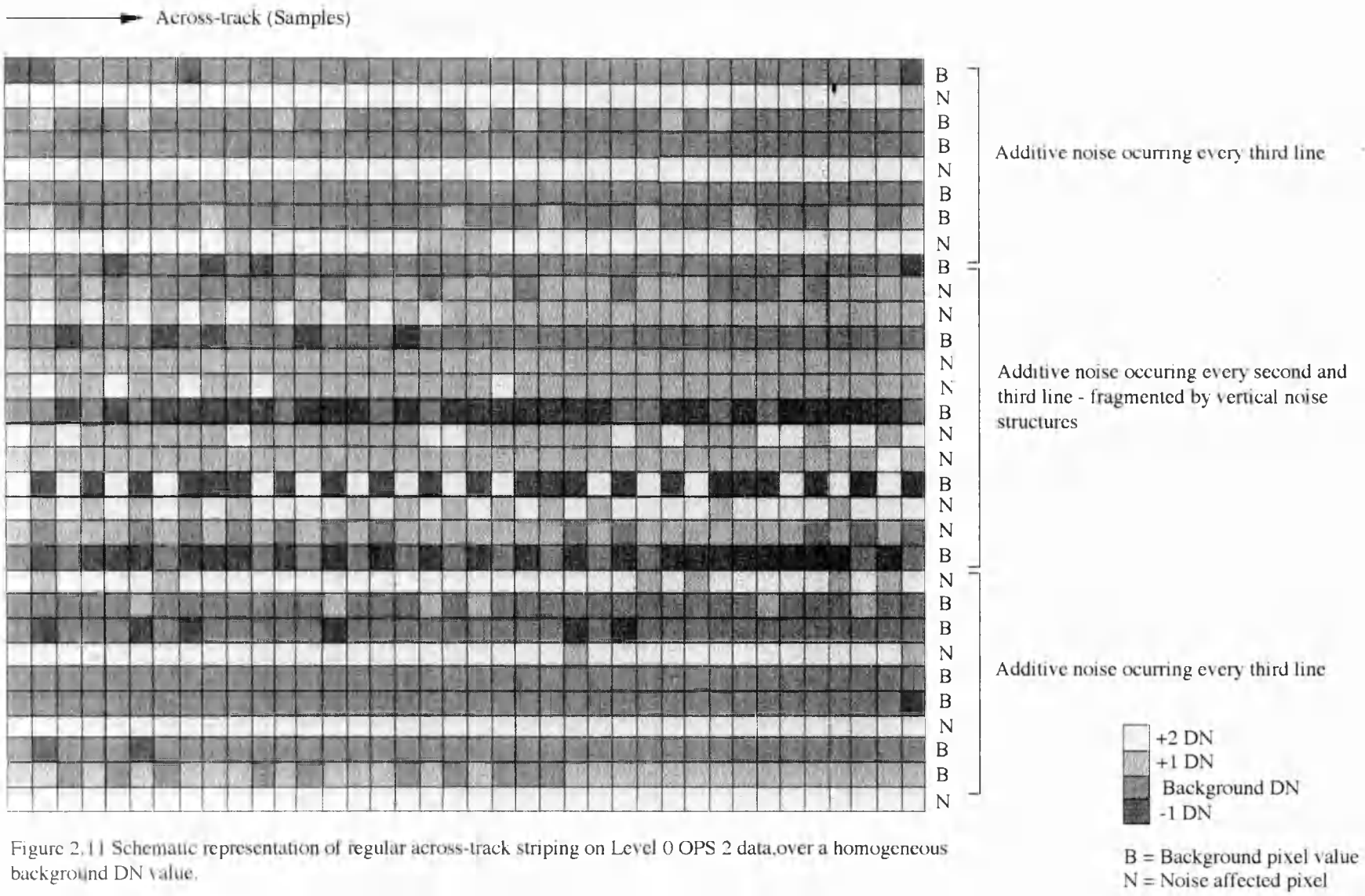

Figure 2.11 Schematic representation of regular across-track striping on Level 0 OPS 2 data,over a homogeneous background DN value.

5) Along-track striping

Along-track striping is very apparent in all channels of OPS data, although the complex nature of this noise varies greatly between channels. On Level 0 data along-track noise artifacts have quite a simple structure affecting alternate one pixel wide columns. Typically this noise is continuous on SWIR channels (Plate 2.6) and fragmented into short lengths on VNIR channels. Figures 2.12a and 2.12b represent these variations schematically. In both cases the noise structures modulate image DN by approximately ±1 DN.

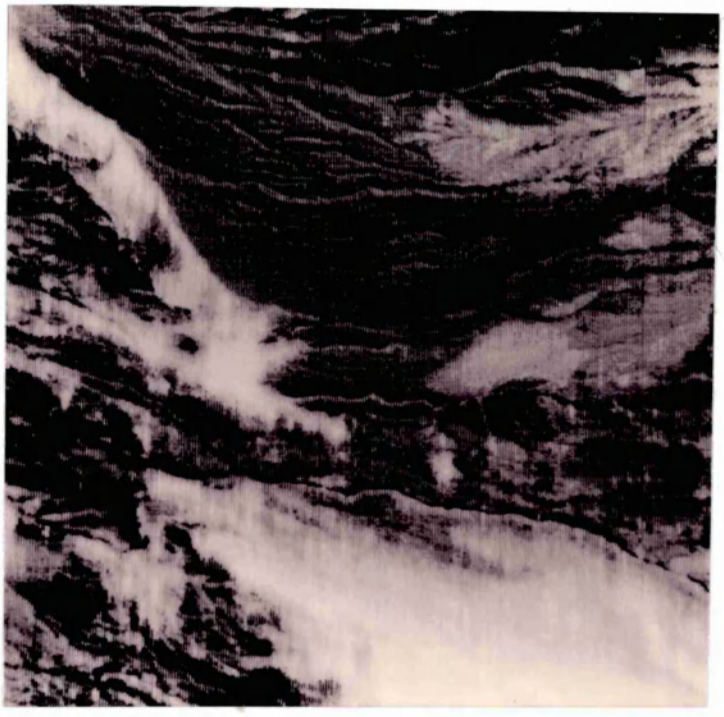

Plate 2.6 A 1024 x 1024 pixel subscene of Level 0 OPS 6 data (Scene 421-340). This scene clearly shows the continuous nature of along-track noise which affects alternate columns of data. It also shows the slow response of the sensor CCDs when changing from high to low (or vice versa) radiance levels, see section 2.5.3(6).

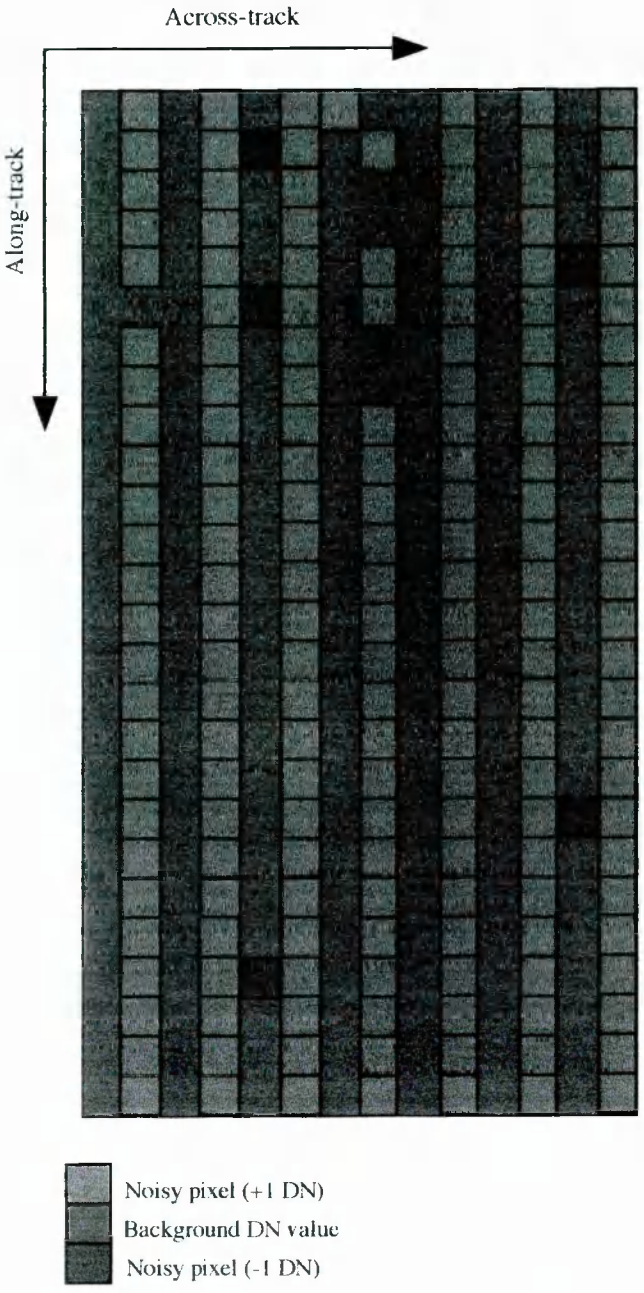

Figure 2.12a Schematic representation of the simple alternate column nature of Level 0 OPS 6 along-track noise (Scene 420-341), over a homogeneous background DN value

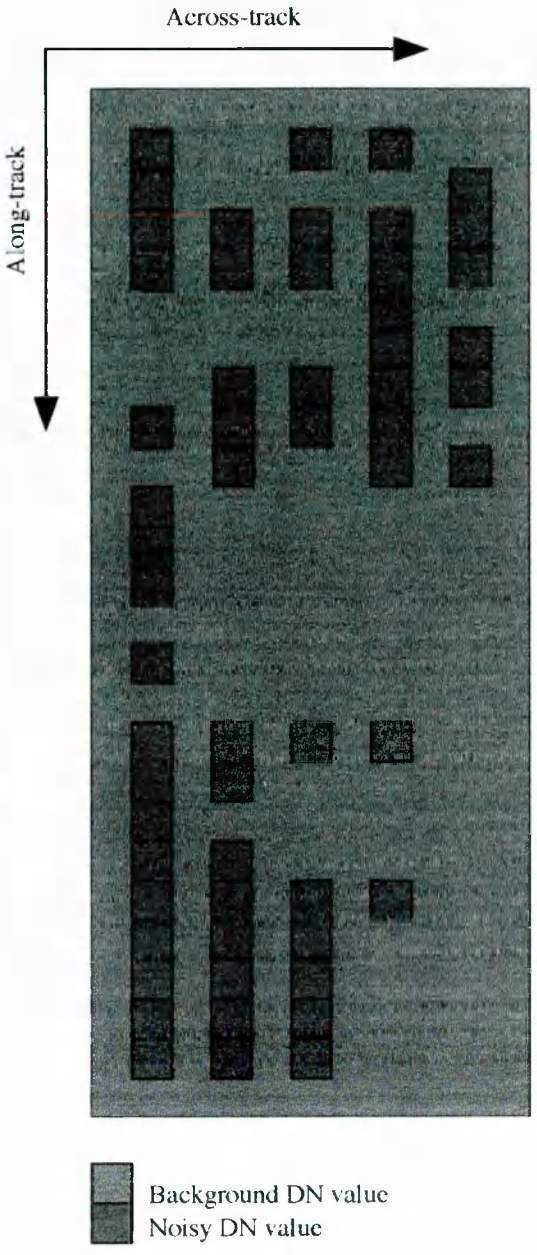

Figure 2.12b Schematic representaion of Level 0 OPS 2 along-track noise, consisiting of fragmented alternate noisy columns.

Along-track striping on Level 2 data looks very different (Plate 2.7) to that of Level 0 data (Plate 2.6). This is due to the geometric transformation applied during the pre-processing procedure. The continuous vertical noise, seen in the Level 0 data (Figure 2.12a) has been transformed so that it is slightly inclined to the vertical (Figure 2.13). This means that along-track noise is no longer confined to alternate columns, but now repeatedly affects short lengths of all columns. The amount by which the noise modulates the image varies along these lengths from +6 DN to -3 DN. This increased range of noise intensities is probably as a result of the 6 bit to 8 bit conversion, applied as a part of Level 2 pre-processing. This increased range of intensities has the effect of producing a repetitive transition from light to dark, which produces a broad diagonal noise structure inclined at approximately 40° to the horizontal (Figure 2.13). This noise structure is particularly apparent when an enlarged image is viewed (Plate 2.8).

Along-track noise (±4 DN) on OPS 8 occurs frequently over very short lengths, giving the image an almost speckled appearance (Plate 2.9). These short lengths are partly due to the occurrence of across-track striping (Figure 2.14).

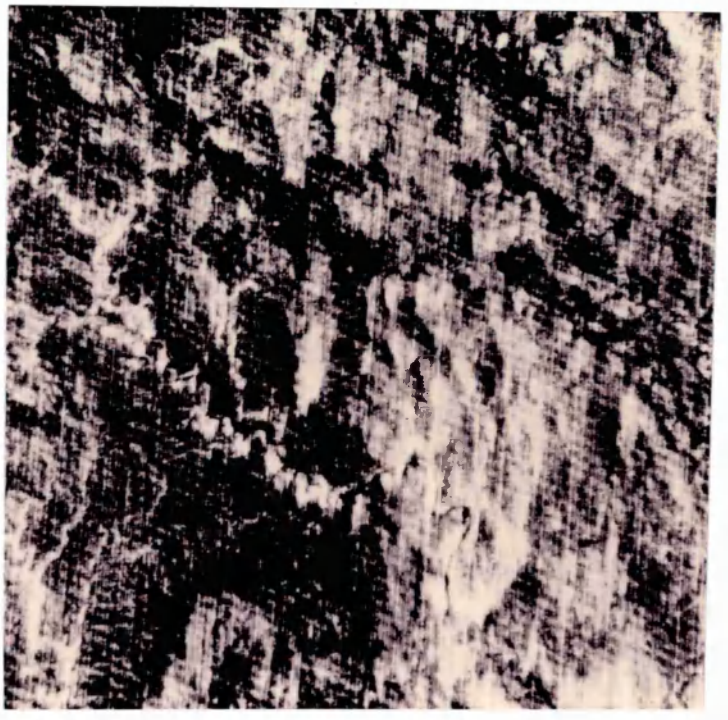

Plate 2.7 A 1024 x 1024 pixel subscene of Level 2 OPS 6 data (Scene 262-208). The geometric transformation applied as a part of NASDAs pre-processing has transformed the vertical along-track striping into an off vertical noise artifact. This image also shows a secondary striping feature which occurs at approximately 40° to the horizontal, see Figure 2.12 for explanation. Note image has been stretched to clearly show noise structures.

Plate 2.8 256 x 256 pixel subscene of Level 2 OPS 6 (scene 208-262). At this scale the off vertical along-track noise is clearly visible. It can be seen that this is noise is composed of short lengths of noisy pixels affecting all columns. The offset nature of these blocks of pixels create the broad noise pattern at 40° to the horizontal.

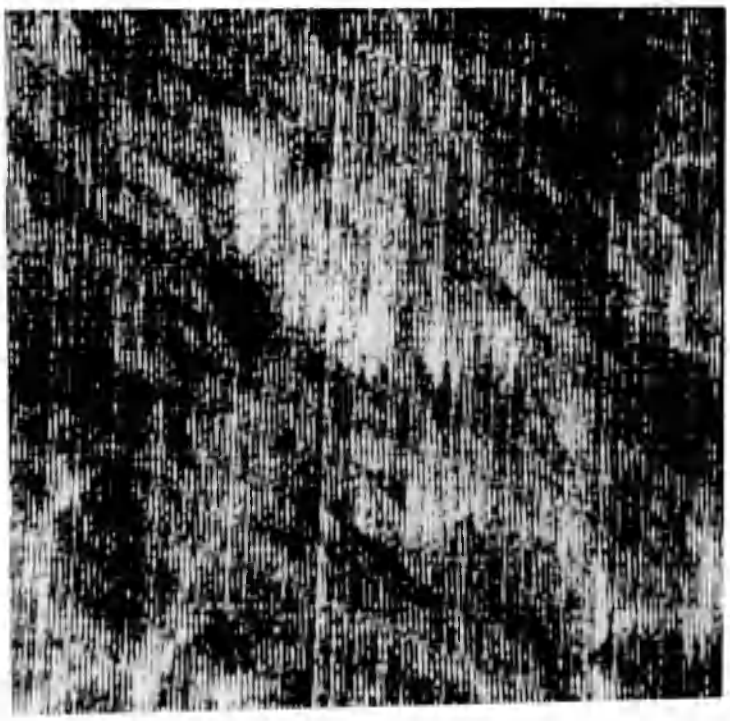

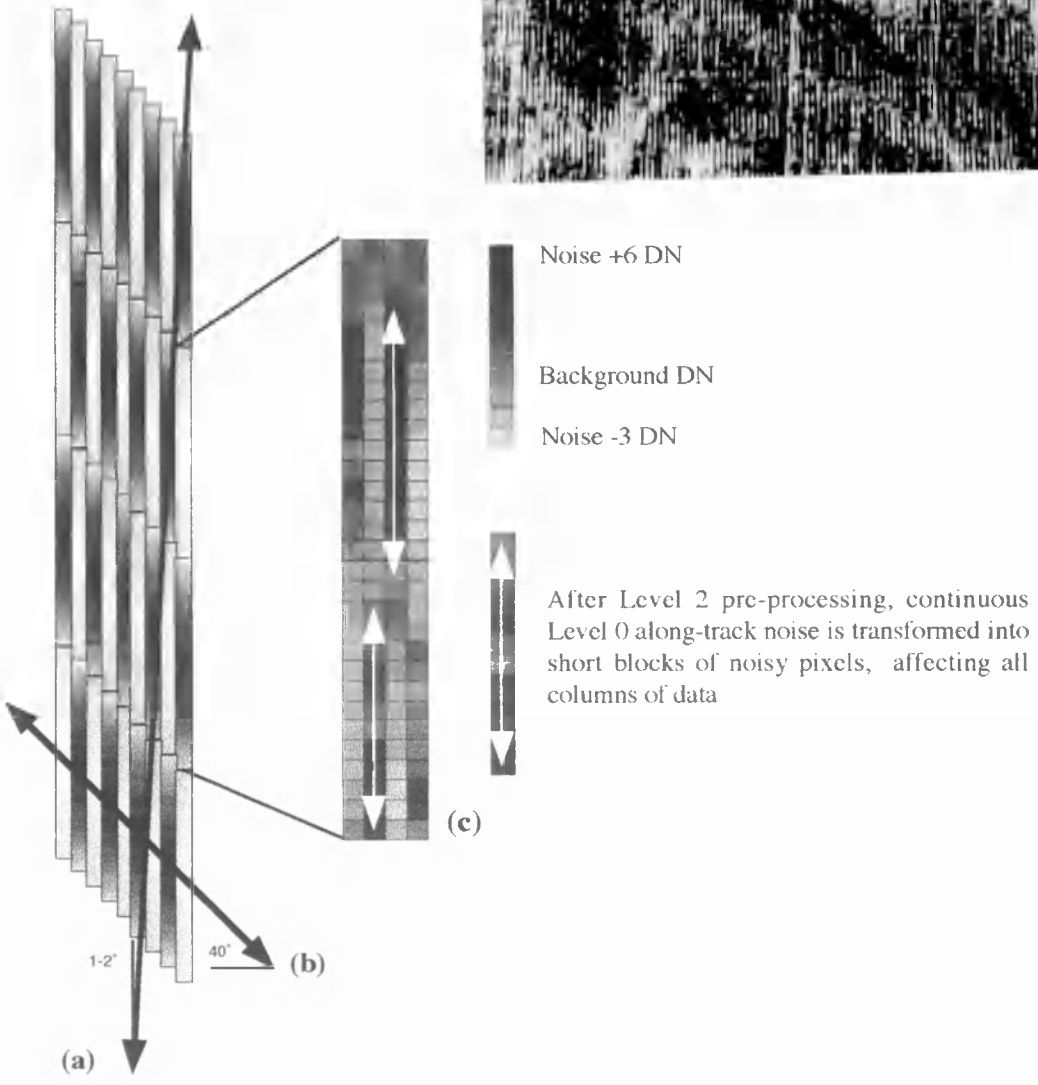

Figure 2.13 Schematic representation of Level 2 OPS 6 along-track noise. (a) The geometric correction applied as a part of the pre-processing of Level 2 data has resulted in the along-track noise being rotated so that it is slightly inclined (1-2°) to the vertical. This rotation has resulted in the noise being broken down into short lengths affecting all columns of data, instead of only alternate colums as per Level 0 (Figure 2.12). (b) This gives the appearance of a broad noise pattern at 40° to the horizontal. (c) This noise pattern is further exaggerated as the intensity of the noisy pixels have been increased by the 6 bit to 8 bit transformation.

Shimada (1993) suggests that the striping in the SWIR channels is caused by instability of the power supply. Nishidai (1995) suggests that the striping in all channels is the result of different responses of the individual CCD elements, combined with variations in the two series of signal processing circuits used for odd and even detector elements. Whatever causes the striping varies with time as the severity of the stripes, both along- and across-track, vary from scene to scene.

6) Image blur

All SWIR channels are affected to some degree by image blur. Image blur occurs either when a surface topographic feature, for example a river, trends across-track, or when a sharp change in incident radiance occurs, for example at a water edge (Figure 2.15a). When these abrupt boundaries are encountered individual CCDs fail to respond immediately to the changed radiance level. This results in the previous radiance level being smeared along-track for a number of lines, before the new radiance level is detected. The amount of along-track smearing varies depending on the channel and on whether the transition is from high to low radiance values or vice versa. High to low transitions tend to be smeared for a greater number of lines (e.g. 8 lines on OPS 5, Figure 2.15b) whilst low to high transitions are smeared for less (e.g. 4 lines on OPS 5, Figure 2.15c). OPS 6 and 7 exhibit the worst smearing with almost all boundary features being spread over 25 lines or more. This smearing effect is exaggerated in SWIR channels by the differing response functions of the odd and even detectors (as suggested by Nishidai, 1995). Differing response functions result in sharp boundaries being displaced along-track between odd and even detectors, resulting in a jagged appearance of linear features (Figure 2.15d). If smearing occurs often enough throughout an image it gives the impression of image blur parallel to the satellite flight direction. VNIR channels are not affected by these problems, although they still appear slightly blurred due to their poor dynamic range resulting in a lack of contrast at definable boundaries.

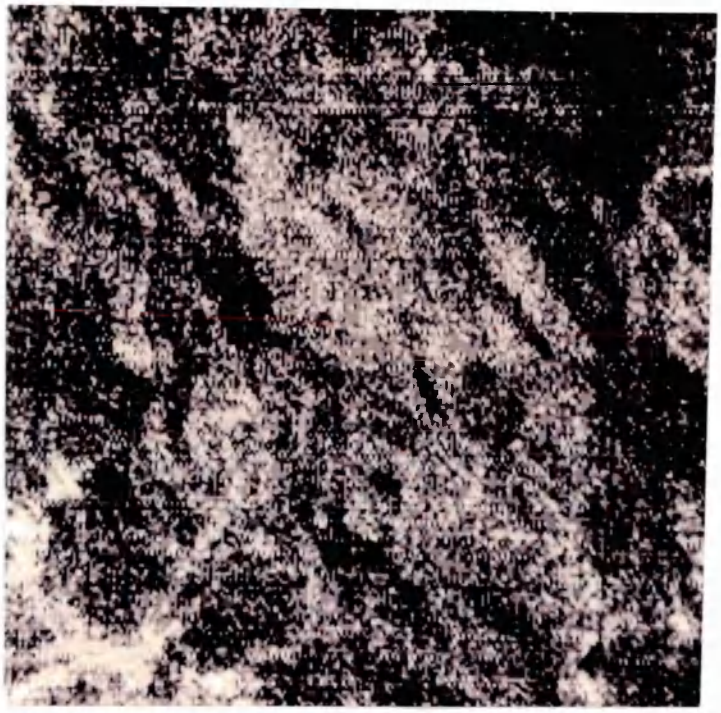

Plate 2.9 Level 2 OPS 8 data showing speckled appearance due to a mixture of along- and across-track noise.

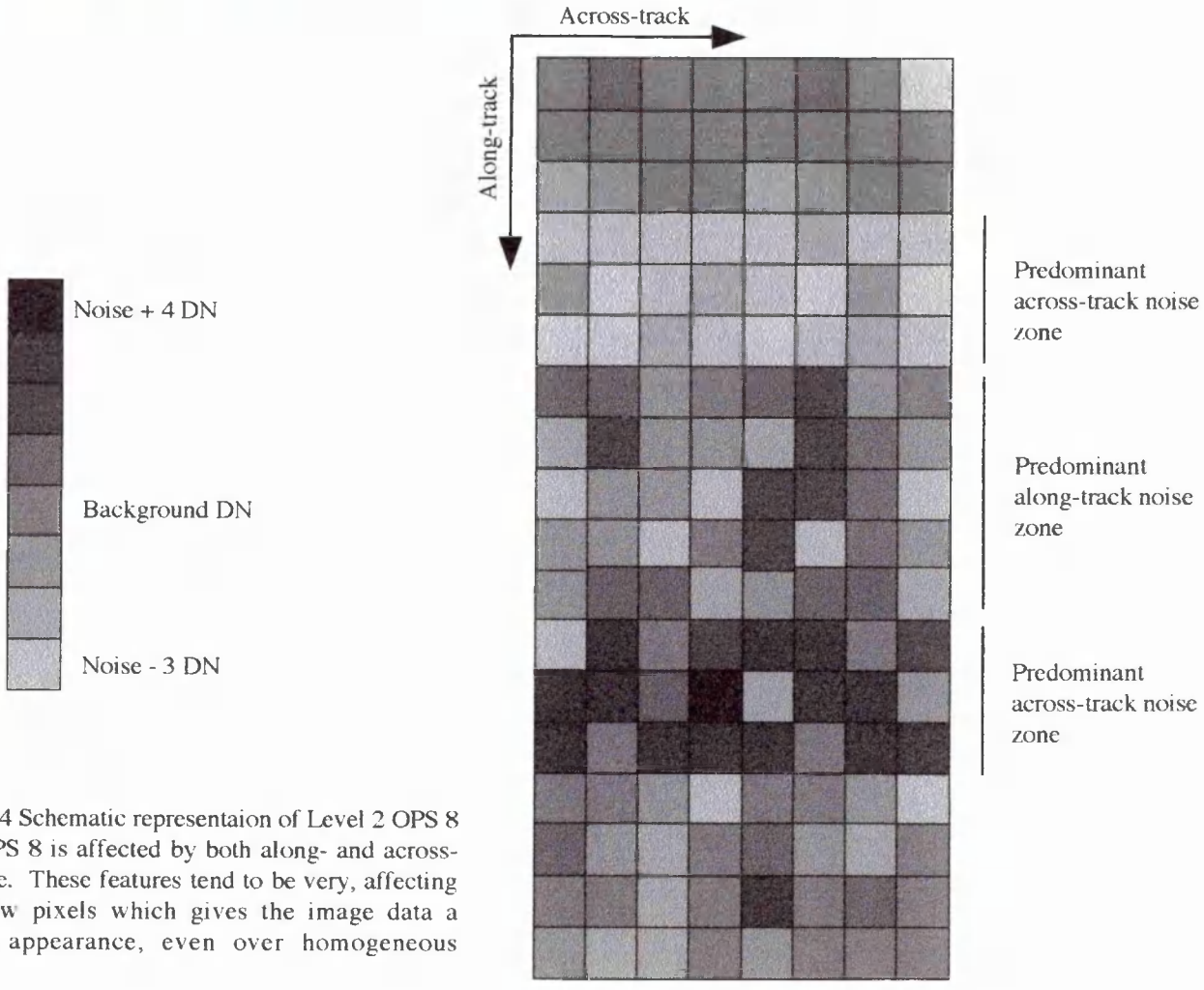

Figure 2.14 Schematic representaion of Level 2 OPS 8 noise. OPS 8 is affected by both along- and across-track noise. These features tend to be very, affecting only a few pixels which gives the image data a speckled appearance, even over homogeneous regions.

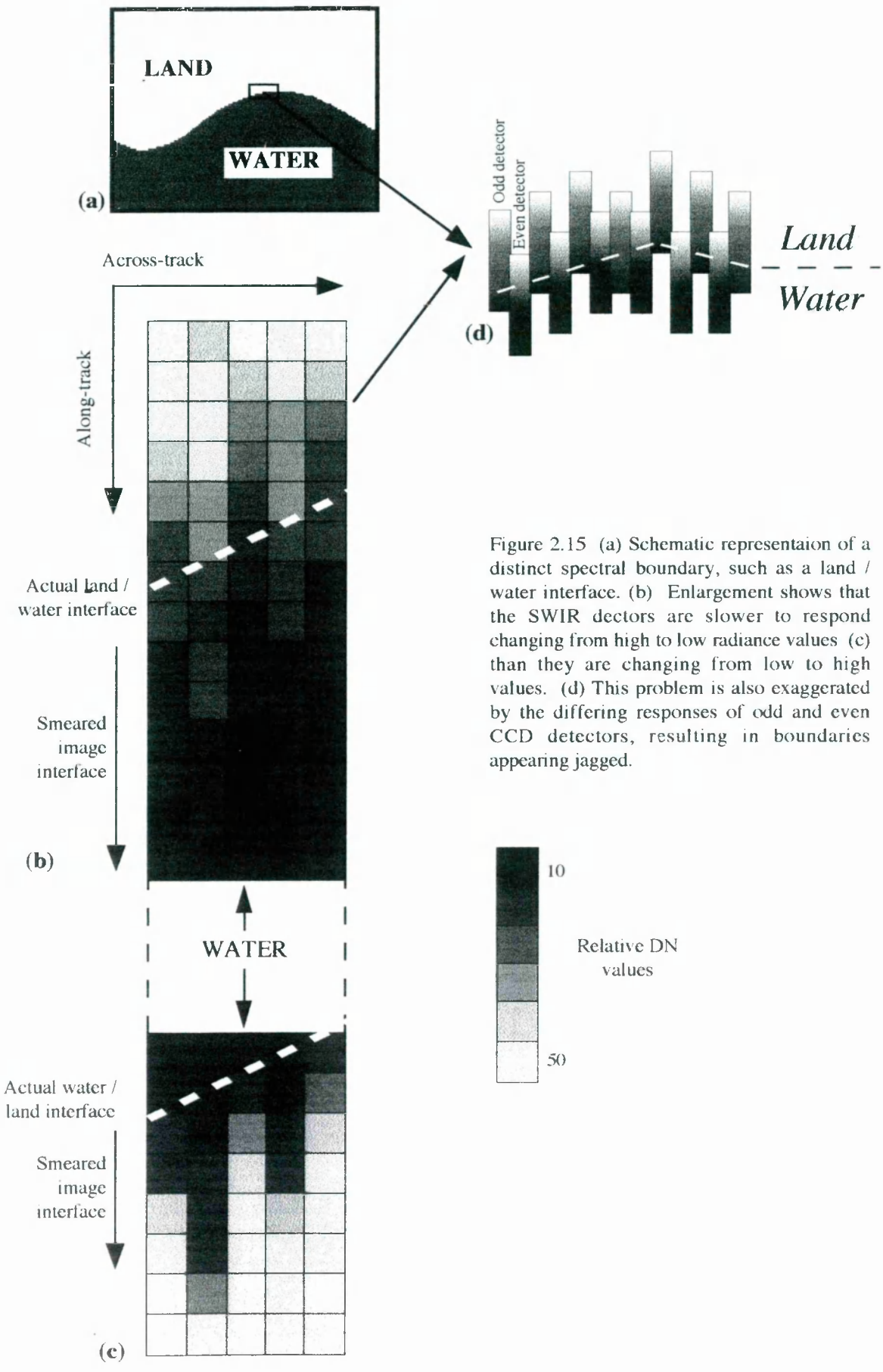

Figure 2.15 (a) Schematic representaion of a distinct spectral boundary, such as a land / water interface. (b) Enlargement shows that the SWIR dectors are slower to respond changing from high to low radiance values (c) than they are changing from low to high values. (d) This problem is also exaggerated by the differing responses of odd and even CCD detectors, resulting in boundaries appearing jagged.

7) Mis-registration

Two-fold mis-registration occurs between all channels of OPS data. Individual channels of data recorded by either the VNIR or SWIR radiometer subsystems are mis-registered with the other channels recorded by the same subsystem. Data from both of these subsystems are then mis-registered with each other. Mis-registration is extremely variable from scene to scene and is not consistent, except that SWIR mis-registration is always more severe than that of the VNIR. Figure 2.16 illustrates the most severe Level 0 mis-registration seen on the available data. The VNIR channels on scene 421 - 340 (11 December 1992) are mis-registered by relatively small amounts, ±2 samples and ±17 lines, whilst the SWIR channels are mis-registered by large amounts, ±25 samples and ±290 lines. Mis-registration between the SWIR and VNIR radiometers is also quite considerable; ±15 samples and ±135 lines. Mis-registration errors appear to be consistent across an entire scene, although Nishidai (1995) suggests that errors vary across a scene depending on their location within the scene.

In theory all channels of Level 2 data should be registered as they have been geometrically corrected during the pre-processing procedure. However, in practice this is not the case as all channels show registration errors. Figure 2.17a illustrates the registration errors for the Level 2 data product seen in Figure 2.16. Pre-processing has greatly reduced registration errors, but it has not eliminated them completely. The worst channels are still mis-registered by up to ± 2 samples and ± 19 lines. Figure 2.17b-d illustrate that similar registration errors occur for this scene on three subsequent acquisition dates. This undermines the claim by NASDA (Shimada, 1993) that all Level 2 data should have a maximum registration error of ± 0.057 pixels for the worst channel (OPS 1).

Another problem affecting registration which sometimes occurs on Level 2 data is a 'wrap around' of image data. Often the last 350 - 750 samples from each line appear at the beginning of the same line. This has the effect of translating the right-hand side of the image to the left-hand side. Occasionally a similar problem affects the last few lines of data, moving them from the bottom to the top of the image. This problem is caused by an error in the data archiving routine.

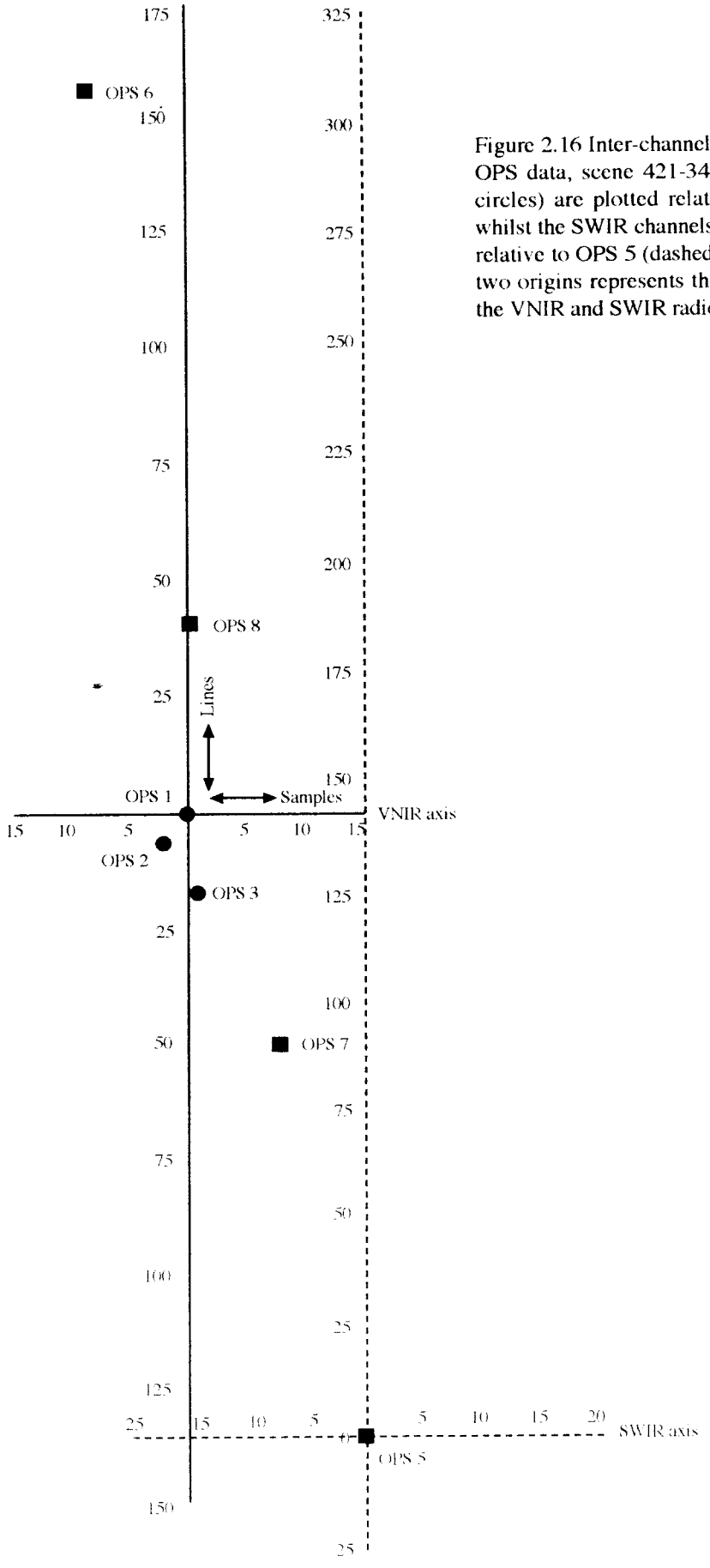

Figure 2.16 Inter-channel misregistration of Level 0 OPS data, scene 421-340. VNIR channels (solid circles) are plotted relative to OPS 1 (solid axis) whilst the SWIR channels (solid squares) are plotted relative to OPS 5 (dashed axis). Offset between the two origins represents the mis-registration between the VNIR and SWIR radiometers.

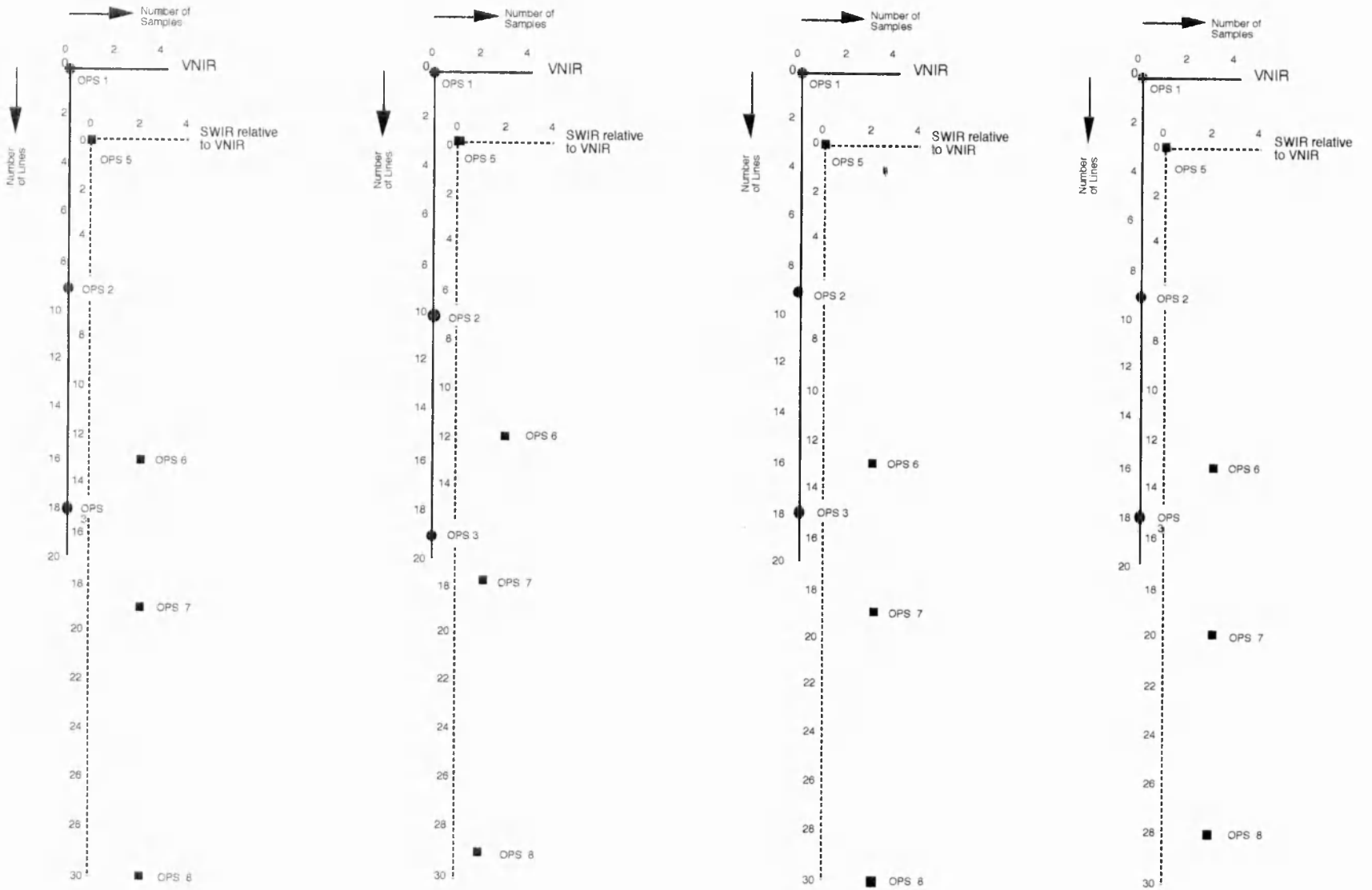

(a) 11 December 1992 (b) 22 April 1993 (c)19 July 1993 (d) 15 October 1993

Figure 2.17 Inter-channel misregistration of Level 2 data, scene 421-340 , on four acquistion dates. VNIR channels (solid circles) are plotted relative to OPS 1 (solid axis) whilst the SWIR channels (solid squares) are plotted relative to OPS 5 (dashed) axis. The offset between the origins corresponds to the misregistration between the VNIR and SWIR radiometers.

2.6 Implications of data quality for geological applications

Anticipated geological improvements from the higher spatial and spectral resolution JERS-1 OPS data (section 2.4) will be greatly diminished because of the severity of the noise problems described in section 2.5.3.

Dynamic range problems were initially anticipated because of the 6 bit nature of the data, the actual dynamic range problems encountered are far worse than expected. Poor dynamic ranges greatly reduce image detail as subtle spectral variations are often not recorded. The loss of spectral information reduces class separability, which hinders the discrimination of similar lithological units. It also means that subtle spectral variations within a lithology may not be visible. Spatial resolution is also reduced by poor dynamic ranges as images appear quantitised and lack contrast. The lack of contrast results in the loss of textural information, which is geologically important. Lithologies often have distinct image textures associated with them, aiding discrimination between spectrally similar lithologies. Dynamic ranges are slightly improved on high gain data. However, this is at the expense of spectrally bright terrains which are completely saturated. Saturation is so severe that most high gain data can be regarded as useless, unless it has been acquired over extremely dark terrains. Even then OPS 5 has a tendency to saturate. Image interpretation is also made difficult due to inter-channel mis-registration. Unless all channels are carefully registered, localised spectral variations are lost and false features are generated due to mis-registration fringes.

Additive noise structures such as random noise, across- and along-track striping and image blur, are all very severe on JERS-1 OPS data. This is especially true of Level 2 data where some noise structures have been further complicated by the geometric transformations applied as a part of pre-processing. Any one of these noise structures has the potential to severely reduce image information content, whilst the combined effect has the potential to make entire channels of data useless. Unfortunately it is the SWIR channels, OPS 6 and OPS 7 (two OPS channels with the potential to provide geologically important data not currently available from any other satellite platform), which are most severely affected by these combined noise structures. These noise artifacts are further exaggerated when simple image processing techniques are performed, such as combining three channels of data to produce a False Colour Composite (FCC).

Initially the geological potential of JERS-1 OPS data looked to be very high because of the increased spectral and spatial resolution it offered over Landsat TM data. However the exceptionally low quality of OPS data greatly reduces the potential advantages, especially as the most important geological channels, OPS 6, 7 and 8, are the most severely affected. The geological information content of any OPS scene therefore depends on the severity of the noise artifacts affecting it, and not on the sensor resolution. The extraction of useful geological information will depend on the utilisation of noise removal techniques to minimise the intrusive effect of noise structures. This task is made difficult by the highly variable nature of the noise structures, both from channel to channel and from scene to scene. This variability means that each scene has to be assessed on an individual basis for data quality.

The geological potential of JERS-1 OPS data were further reduced in December 1993 when the SWIR sensor failed completely. This was reportedly due to the failure of the SWIR cooling sub-system (Takata 1995). Since December 1993 JERS-1 has only acquired VNIR data. This means that there is only a limited supply of OPS SWIR data acquired between February 1992 and December 1993. SWIR data acquired during this time covers only a small percentage of the desired coverage planned during the lifespan of JERS-1 (Takata 1995).

3.0 Restoration of noise-corrupted JERS-1 Optical data

Some of the Frequency Domain noise removal techniques described in this chapter (Section 3.3.4 (3)), were developed jointly with C.R. De Souza. These techniques are described fully in the paper; 'Restoration of Noise Corrupted Optical Fuyo-1 (JERS-1) Data Using Frequency Domain Techniques', De Souza et al, 1996, Photogrammetrical Engineering and Remote Sensing, Vol. 62, No.9, pp. 1037-1047.

3.1 Introduction to noise removal

The image data collected by both the VNIR and SWIR sensors on JERS-1 OPS are affected by severe noise structures, as described in Chapter 2, Section 2.5.3. To maximise the information content of OPS images, especially those of the narrow SWIR channels, noise removal techniques have to be applied at an early stage. Techniques to remove noise or to suppress its affects within an image can be applied either in the spatial domain or in the frequency domain. Both approaches as applied to JERS-1 OPS images are described here.

3.2 Spatial domain techniques

3.2.1 Algebraic methods

One of the simplest techniques to remove noise from images is that of image averaging (Castleman, 1979). This technique relies on the production of a cleaned output image by averaging N input channels. This is a simple technique which is best used to remove random noise and cannot be implemented on data where noise structures may be correlated between channels, for example, OPS across-track striping. Ideally for this technique to work, numerous images over the same wavelength range and geographic region are required, and even then only non-correlated random noise can be reduced. A lack of suitable images prevented this technique from being tested.

3.2.2 Convolution filtering

Convolution filtering is a very common technique applied in the spatial domain to improve image quality (Westin, 1990). It involves multiplying the DN values in an input image by a *box* filter or kernel which contains a matrix of weighted values. The product of this operation is then used to replace the original image DN value at the centre of the matrix. A new output image is produced by moving the matrix over every pixel in the input scene. A full description of the mathematics of convolution filtering can be found in the literature, (for example, Drury (1987)) and only a brief account is given here.

Convolution filtering is very flexible, as both the size and the weightings of the convolution kernel (matrix) can be easily changed. Examples of some filters applied to JERS-1 OPS images can be seen in Table 3.1. Varying these parameters means that the effect of the filter on the output image can be controlled. Convolution filters are used to either enhance or suppress edge information in an image; these are known respectively as high- and low pass filters. Noise removal by convolution tends to utilise low pass filters, as these suppress the visibility of noise artifacts in an image.

Isolated random noise, such as that seen in OPS 8, can be reduced by applying a low pass or mean filter, kernel 1 (Table 3.1). This filter replaces the central DN value with the average DN of the surrounding 8 pixels (assuming a 3 x 3 kernel). This has the effect of suppressing any high frequency variations, i.e. those associated with random noise, within the 3 x 3 image window (Castleman, 1979). Tests on OPS 8 show that this type of filter does suppress some of the random noise, but this is achieved at the expense of suppressing high frequency information (such as topographic and spectral edges), resulting in the output image appearing slightly blurred.

An alternative to the mean filter is the median filter which replaces the central image DN value with the median value derived from the surrounding 8 pixels. Tests on OPS 8 show that the median filter is able to remove isolated random noise without introducing such severe image blur. This technique can be slightly improved by the introduction of an algorithm which decides whether a pixel requires replacing or not, depending on its deviation from the surrounding pixel values. If a pixel deviates more than a given threshold value it is replaced, otherwise it remains unchanged. Using an algorithm such as this ensures that only the minimal number of image pixels are

changed, thereby helping to preserve image detail. An example of such an algorithm is given by Schowengerdt (1983);

DN_1	DN_2	DN_3
DN_4	DN_5	DN_6
DN_7	DN_8	DN_9

$AVE_1 = (DN_1+DN_3+DN_7+DN_9) / 4$

$AVE_2 = (DN_2+DN_4+DN_6+DN_8) / 4$

$DIFF = |AVE_1-AVE_2|$

IF $|DN_5-AVE_1|$ OR $|DN_5-AVE_2|>DIFF$

THEN $DN_5' = AVE_2$ OTHERWISE $DN_5' = DN_5$

This technique can be modified to remove bad lines of data;

DN_1	DN_2	DN_3
DN_4	DN_5	DN_6
DN_7	DN_8	DN_9

$AVE_1 = (DN_1+DN_2+DN_3) / 3$

$AVE_2 = (DN_7+DN_8+DN_9) / 3$

$DIFF = |AVE_1-AVE_2|$

IF $|DN_5-AVE_1|$ OR $|DN_5-AVE_2|>DIFF$

THEN $DN_5' = (DN_2+DN_8) / 2$ OTHERWISE $DN_5' = DN_5$

or bad columns of data;

DN_1	DN_2	DN_3
DN_4	DN_5	DN_6
DN_7	DN_8	DN_9

$AVE_1 = (DN_1+DN_4+DN_7) / 3$

$AVE_2 = (DN_3+DN_6+DN_9) / 3$

$DIFF = |AVE_1-AVE_2|$

IF $|DN_5-AVE_1|$ OR $|DN_5-AVE_2|>DIFF$

THEN $DN_5' = (DN_4+DN_6) / 2$ OTHERWISE $DN_5' = DN_5$

The problem with these techniques is that they rely on the assumption that the pixels surrounding a noisy pixel are themselves unaffected by noise. Unfortunately this is often not the case with OPS data as the across- and along-track noise structures tend to affect contiguous pixels. This means that these techniques cannot be satisfactorily applied to OPS data.

Convolution filtering offers great flexibility which means that numerous kernels can be developed to try to reduce OPS noise artifacts. In practice filter design can be very time consuming, before optimum filter parameters are found. Examples of some kernels applied to OPS data and their results are summarised in Table 3.1.

Kernel 1 1 1 1 1 1 1 1 1 1	Mean Filter - this kernel slightly supresses VNIR noise, but has little effect on SWIR noise. Slight image blur introduced in VNIR, considerable blur of SWIR channels.
Kernel 2 1 1 1 1 4 1 1 1 1	Crippen (1994) -This kernel doesn't introduce as much image blur as Kernel 1, although it does leave more noise visible in the final images. Preserves some SWIR texture information.
Kernel 3 1 4 1 4 12 4 1 4 1	Gaussian Profile Kernel - VNIR noise is quite well suppressed, whilst SWIR is moderately suppressed. Only slight image blur introduced.
Kernel 4 1 2 3 2 1 2 7 11 7 2 3 11 17 11 3 2 7 11 7 2 1 2 3 2 1	Gaussian Profile Kernel - VNIR and SWIR noise suppressed although image blur is very severe, especially in SWIR channels.
Kernel 5 0 1 2 3 2 1 0 1 3 4 7 4 3 1 2 4 9 16 9 4 2 3 7 16 48 16 7 3 2 4 9 16 9 4 2 1 3 4 7 4 3 1	Gaussian Profile Kernel - Across-track noise in VNIR completely removed, SWIR noise slightly suppressed. Image blur is very severe, spectral boundaries appear diffuse.
Kernel 6 5 5 5 -1 -1 -1 5 5 5	Directional Kernel - Across-track noise in VNIR channels almost completely removed, slight blur introduced. Removes across-track component from SWIR but along-track component is still evident.
Kernel 7 5 5 -1 5 -1 5 -1 5 5	Directional Kernel - Reduces the Level 2 SWIR off vertical along-track noise, does not remove any of the across-track noise structures. Introduces some image blur.

Table 3.1 Examples of convolution kernels applied to OPS data to try to remove or reduce noise artifacts.

Tests of these and other filters have shown that the noise structures associated with OPS data are very difficult to suppress using convolution filters. Some filters (kernel 3) are capable of reducing the simple across-track noise in the VNIR channels without introducing too much image blur (Plate 3.1). Other filters such as kernel 2 (Crippen, 1994) remove more of the across-track noise but start to introduce significant image blur (Plate 3.2). Filters, such as kernel 6 are capable of removing almost entirely the across-track noise, but this is done at the expense of substantial image blur (Plate 3.3). None of the filters tested was capable of suppressing the complex noise structures associated with the SWIR channels. Filtering by convolution tends to be a compromise between removing noise whilst preserving image detail. This is because convolution kernels are not selective, they affect noise and image detail equally. Filters which adequately suppress noise will simultaneously suppress image detail. As a result convolution kernels are not capable of removing OPS noise structures; they are only able to reduce its visibility in some channels.

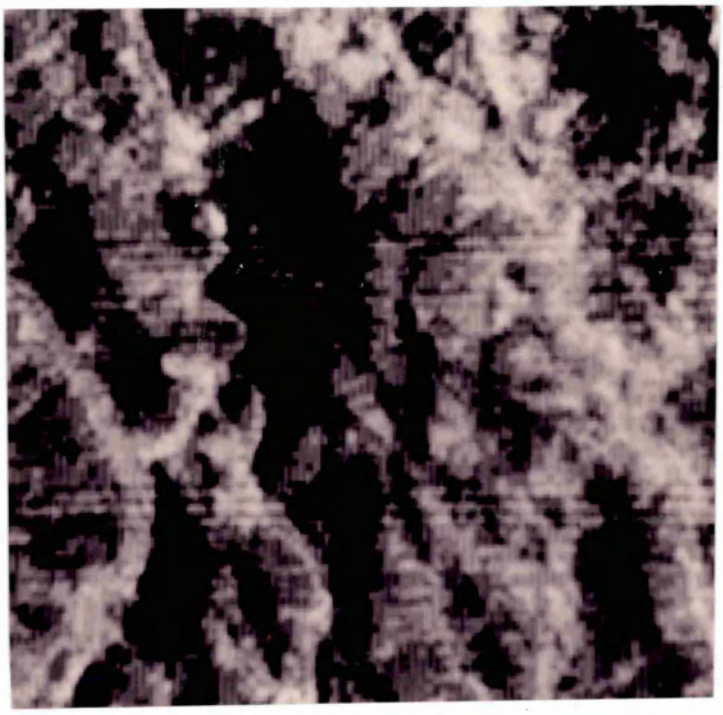

Plate 3.1 Convolution kernel 3 applied to a 200 x 200 pixel subscene of Level 0 OPS 2, as per Plate 2.5. This filter preserves the image detail reasonably sharply but it does not greatly reduce the across-track noise.

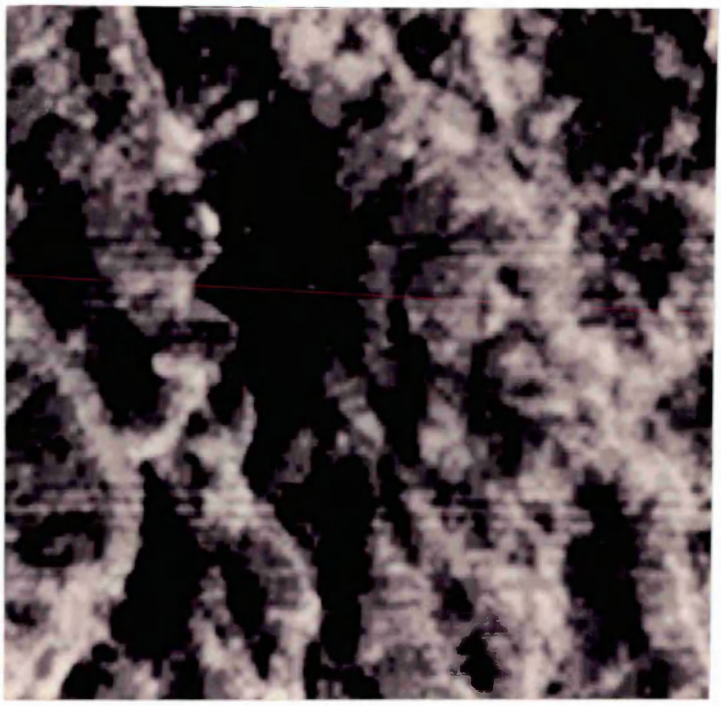

Plate 3.2 Kernel 2 (Crippen, 1994) is an intermediate filter as it reduces the across-track noise fairly well but it also starts to blur significantly the image detail.

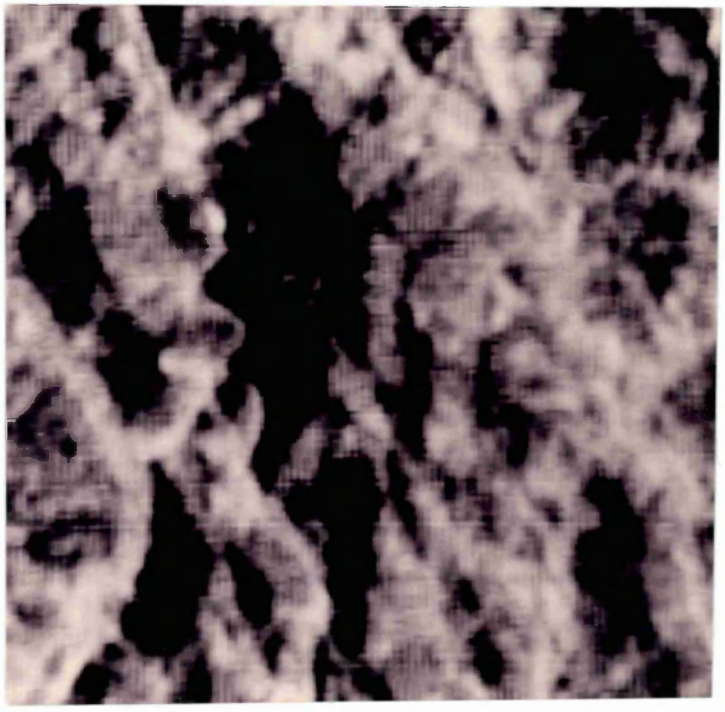

Plate 3.3 Kernel 6 almost completely removes across-track noise but this is at the expense of the image detail which is extremely blurred. This demonstrates that convolution kernels are not a good way of suppressing noise, because they also suppress image detail.

3.2.3 Principal Component Analysis (PCA)

Principal Component Analysis is a mathematical co-ordinate transformation which produces new mutually perpendicular and uncorrelated variables, called principal components (PCs), from originally highly correlated variables. Performing this transformation does not result in the loss or addition of data only the reorganisation of existing data (Davis, 1973). Full descriptions of this technique can be found in the literature, for example Schowengerdt (1983), Rees (1990) and will not be repeated here.

The application of PCA on multichannel data results in the first PC (PC 1) containing the maximum proportion of variance from the original data. Higher order PCs account for progressively smaller amounts of variance, resulting in the higher order PCs having lower signal-to-noise ratios (SNR). This reduces data dimensionality (Schowengerdt, 1983) because only the lower order PCs contain useful scene derived variance, higher PCs contain sensor derived variance (i.e., noise). This means that prior to interpretation or inverse transformation the higher order PCs can be disregarded as they contain unwanted information. Performing the inverse transformation using only the lower order PCs will reproduce data which is almost identical to the original with the exception that sensor induced variance has been removed, as demonstrated by Rothery and Hunt (1990). This results in an improvement in data quality.

In theory this is quite a simple procedure which should allow significant amounts of noise to be easily and quickly removed from all OPS channels, with minimal processing requirements. However, in practice this technique has only a limited success when applied to JERS-1 OPS images, because individual noise components affecting OPS images tend to be poorly correlated across all channels (although they may be highly correlated between pairs of channels). This results in only a limited portion of the noise being isolated in the higher order PCs whilst significant amounts of noise are transformed into the lower order components, similar results are reported by De Souza *et al.*, (1995) and Okada *et al.*, (1995). This can be seen when the eigenvector matrix of a 1024 x 1024 pixel subscene of a land target is examined (Table 3.2a).

PC	OPS 1	OPS 2	OPS 3	OPS 5	OPS 6	OPS 7	OPS 8
PC 1	+0.262	+0.416	+0.376	+0.592	+0.291	+0.382	+0.185
PC 2	-0.530	-0.512	-0.274	+0.444	+0.342	+0.255	-0.022
PC 3	+0.163	-0.032	-0.169	-0.600	+0.497	+0.496	+0.298
PC 4	-0.267	-0.0143	+0.050	+0.030	-0.285	-0.120	+0.910
PC 5	-0.406	+0.088	+0.553	-0.205	+0.535	-0.436	-0.031
PC 6	-0.408	-0.0109	+0.479	-0.218	-0.426	+0.579	-0.196
PC 7	+0.467	-0.744	+0.465	+0.030	-0.019	+0.041	+0.087

Eigenvalues	(%)
1508.58	96.18
29.94	1.91
15.43	0.98
5.13	0.33
3.82	0.24
3.23	0.21
2.37	0.15

Table 3.2a Eigenvector matrix and eigenvalues for a 1024 x 1024 pixel subscene (207-261) over a mixed land target. Refer to text for a full description.

PC	Noise structures
PC 1	Slight across-track noise, very slight along-track noise
PC 2	Moderate across-track noise and strong along-track noise
PC 3	Very slight across-track noise, stong along-track noise, moderate speckle
PC 4	Very slight along-track and across-track noise, high speckle and isolated spikes
PC 5	Very stong along-track noise dominates, moderate across-track noise
PC 6	Strong along-track noise dominates, moderate across-track and slight speckle
PC 7	Moderate across-track noise, slight along-track noise

Table 3.2b Summary of the noise structures visible in the PCs created from the eigenvector matirx in Table 3.2a.

The eigenvector matrix shown in Table 3.2a illustrates the linear weights applied to each OPS channel to produce each PC. Examination of these weights (or eigenvectors) gives an idea of which original features are being mapped into which PC. The sign of each eigenvector indicates whether these features will be represented as bright pixels (positive eigenvectors) or dark pixels (negative eigenvectors) in the PC image. Considering PC 1 it can be seen that this is comprised of roughly equal magnitude positive eigenvectors from all seven OPS channels. This is because the most correlated feature across all channels (scene brightness or albedo), has been mapped into PC 1. Examining the eigenvectors a little more closely indicates that OPS 5 and OPS 2 contribute slightly more to PC 1 than the other OPS channels. This results in PC 1 having a very high image quality with only slight along- and across track noise structures. This reflects the original data quality of OPS 5 and OPS 2 which is very high compared with the other channels. The eigenvalue for PC 1 indicates that 96.18 % of the original image variance is contained within it, leaving only 3.82 % to be distributed over the other 6 PCs.

The eigenvectors of PC 2 separate the VNIR and SWIR contributions into dark pixels (negative weightings) and bright pixels (positive weightings, with the exception of OPS 8 which is almost zero) respectively. The VNIR channels OPS 1 and OPS 2 contribute across-track noise whilst the SWIR channels OPS 5, OPS 6 and OPS 7 contribute along-track noise. The along-track noise will be more apparent in the PC image because of the positive eigenvectors (i.e., bright pixels) associated with the SWIR channels. PC 3 (Plate 3.4) has low eigenvectors across all of the VNIR channels so across-track noise will minimal, however the moderate eigenvectors of OPS 6 and OPS 7 mean that along-track noise will be strong. The PC image will also have the speckled appearance characteristic of OPS 8 as this channel contributes a moderate amount. PC 4 will be severely speckled as the eigenvectors are dominated by OPS 8. PC 5 and PC 6 have very similar eigenvectors so will be similar in appearance. The only major difference between the two is the variation of OPS 6 and OPS 7, both in terms of magnitude and sign. Reasonably high eigenvectors from OPS 1, OPS 3, OPS 6 and OPS 7 means that both of these PCs contain strong across- and along-track noise (Plate 3.5). The final PC is dominated by the VNIR channels with negligible contribution from the SWIR channels, resulting in severe across-track noise. Visual examination of the PC images created from the above eigenvector matrix confirmed the presence of noise in all of the PCs. Table 3.2b summarises the severity of the visible noise structures.

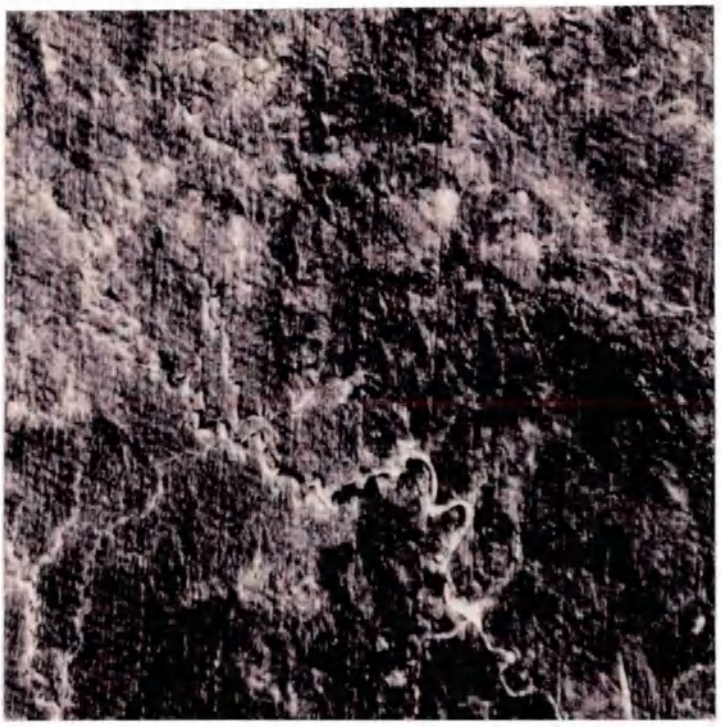

Plate 3.4 PC 3 exhibiting minor across-track noise but quite severe along-track noise and random speckle. See text for a full description.

Plate 3.5 PC 6 exhibiting moderate across-track noise and strong along-track noise. Note that despite this being a high order PC the noise content of this image is not much worse than that of the low order PC in Plate 3.4. Refer to text for a full description.

A water subscene was chosen for the second study to see if PCA could isolate noise structures when the natural scene variance (with the exception of OPS 1 and OPS 2) was at a minimum. The resulting eigenvector matrix (Table 3.3a) and PC images were quite similar to those seen in the first study. The original spectral information contained in OPS 1 was transformed almost entirely into PC 1. Whilst noise structures were redistributed with various weights throughout all of the PCs, including PC 1. This is indicated by the eigenvalues which show that only 52.59 % of the original scene variance was transformed into PC 1. This leaves 47.41 % of noise derived variance to be redistributed throughout the other PC's. A summary of the noise structures visible in each PC can be found in Table 3.3b.

Some of the resulting PC images from the second study did appear to contain only noise structures. This was because the original scene spectral variance was so low it was primarily transformed into one PC (PC 1). Both of these tests demonstrate that PCA is not capable of isolating the complex noise structures associated with OPS imagery from good image data. This is due to the poor correlation of OPS noise structures between channels, despite their similar appearance. An alternative technique such as the Maximum Noise Fraction (MNF) transformation, as developed by Green *et al.*, (1988), which orders the new components to maximise the signal-to-noise ratio, instead of maximising variance, might be more successful. This technique was not tested as I felt that PCA had demonstrated that spatial domain techniques are not capable of isolating complex OPS noise structures from image data.

3.2.4 Summary of spatial domain techniques

Spatial domain noise removal techniques are fairly quick and easy to implement. However, due to the complex nature of the noise structures associated with OPS channels they have little success. Techniques like convolution filtering cannot remove OPS noise structures; they can only suppress the visibility of these features in some channels, namely those of the VNIR sensor. Noise structures in the SWIR channels cannot be adequately suppressed by these techniques without the loss of large amounts of image detail.

Spatial domain processes associated with noise removal, such as PCA, are not capable of isolating the complex inter-channel noise structures associated with OPS data. As a result little benefit is gained by removing the higher order PCs prior to performing the inverse transformation. Lower order PCs still contain sufficient noise to produce output channels of a similar quality to the original data.

PC	OPS 1	OPS 2	OPS 3	OPS 5	OPS 6	OPS 7	OPS 8
PC 1	+0.503	-0.108	-0.142	-0.500	+0.680	+0.02	+0.016
PC 2	+0.512	-0.073	-0.035	-0.263	-0.564	-0.539	+0.227
PC 3	+0.342	-0.134	+0.896	+0.192	+0.047	+0.145	+0.007
PC 4	+0.317	-0.114	-0.166	+0.110	-0.234	+0.149	+0.876
PC 5	+0.304	+0.937	-0.019	+0.112	-0.001	+0.120	+0.026
PC 6	+0.340	-0.241	-0.313	+0.210	-0.220	+0.679	+0.415
PC 7	+0.237	-0.118	-0.219	+0.757	+0.336	-0.433	+0.075

Eigenvalues	(%)
11.85	52.59
3.36	14.92
1.89	8.39
1.56	6.93
1.46	6.48
1.32	5.85
1.09	4.84

Table 3.3a Eigenvector matrix and eigenvalues for a 1024 x 1024 pixel subscene (207-261) over a mixed water target. Refer to text for a full description.

PC	Noise structures
PC 1	Moderate across- and along-track noise
PC 2	Moderate across-track noise, very strong along-track noise
PC 3	Very strong across-track noise
PC 4	Moderate along- and acrosstrack noise, high speckle and isolated spikes
PC 5	Very stong across-track noise dominates
PC 6	Moderate across- and along-track noise, moderate speckle
PC 7	Moderate along- and across-track noise, isolated spectral boundaries visible

Table 3.3b Summary of the noise structures visible in the PCs created from the eigenvector matirx in Table 3.3a.

3.3 Frequency domain techniques

3.3.1 Introduction to the frequency domain

An alternative approach to noise removal is to consider the noise components associated with JERS-1 OPS images in the frequency domain. Images are transformed into the frequency domain using the Fast Fourier Transform (FFT). Once transformed into the frequency domain, the magnitude component of the FFT can be used to help visualise the spatial frequency attributes of complex noise artifacts. Filters can then be applied in the frequency domain to remove noise artifacts, before performing an Inverse Fourier Transform (IFT), to return the filtered image back to the spatial domain (Figure 3.1). The advantage of filtering in the frequency domain is that results can be achieved which would otherwise be very difficult or impossible to achieve using spatial domain techniques. This is because the frequency domain allows the noise component of an image to be identified and removed, without affecting any of the real image information. This is impossible in the spatial domain, because of the difficulty of separating noise artifacts from image detail It is possible in the frequency domain because noise structures have a high frequency and regular periodic nature, compared with geological variations which are much lower in frequency and less periodic in nature. Previous studies using Advanced Very High Resolution Radiometer (AVHRR) data (Simpson and Yhan, 1994); Thermal Infrared Multispectral Scanner (TIMS) data (Hummer-Miller, 1990) and Airborne Visual Infrared Imaging Spectrometer (AVIRIS) data (Rose, 1989) have all demonstrated the versatility of noise removal in the frequency domain.

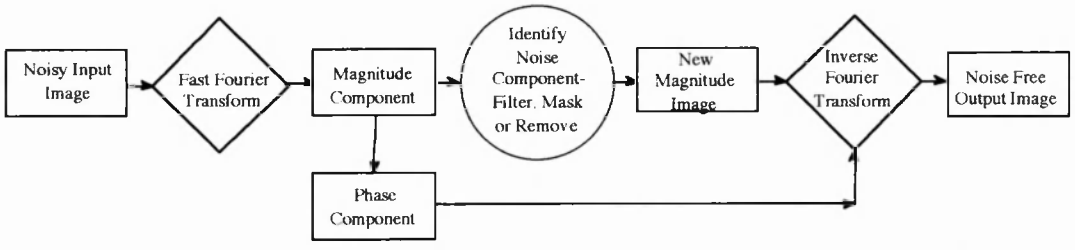

Figure 3.1 Flow diagram to illustrate the processing concept for noise removal in the frequency domain.

3.3.2 The Fourier Transform

A line of image data can be regarded as a periodic function, which in turn can be broken down into fundamental pieces, i.e. the sum of a series of superimposed sine and cosine functions with different amplitudes, frequencies and phases. This representation of a periodic function is termed its Fourier series (Schowengerdt,

1983). For non-periodic continuous functions the 1-Dimensional Fourier transformation is defined by;

$$F(\nu_x) = \int_{-\infty}^{+\infty} f(x) e^{-i2\pi\nu_x x} dx \qquad [3.1]$$

where

$$e^{-i2\pi\nu_x x} = \cos(2\pi\nu_x x) - \sin(2\pi\nu_x x)$$

However, an image is comprised of many lines of data and has to be regarded as a discrete 2-Dimensional input, therefore the Fourier transform is defined by;

$$F(\nu_x, \nu_y) = \int_{-\infty}^{+\infty}\int f(x, y) e^{-i2\pi(\nu_x x + \nu_y y)} dxdy \qquad [3.2]$$

where f(x,y) is an image and $F(\nu_x, \nu_y)$ is the image spatial spectrum as a function of the spatial frequency coordinates, ν_x and ν_y (Schowengerdt, 1983). The units of spatial frequency are cycles / unit length, e.g. cycles / mm at image scales or cycles / km at ground scales. The Inverse Fourier Transform (IFT) can be derived by simply interchanging f(x,y) and $F(\nu_x, \nu_y)$, changing the variable of integration, and changing the sign of the exponent in equation [3.2], to give;

$$f(x, y) = \int_{-\infty}^{+\infty}\int F(\nu_x, \nu_y) e^{+i2\pi(\nu_x x + \nu_y y)} d\nu_x d\nu_y \qquad [3.3]$$

The complex mathematics of Fourier Transforms are well documented in a number of texts, including; Schowengerdt (1983), Gonzalez and Wintz (1977), Andrews and Hunt (1977) and Castleman (1979).

3.3.3 Description of JERS-1 OPS noise structures in the frequency domain

1) Introduction to magnitude plots

An image in the spatial domain represents variations in radiance levels over geographic space whilst the Fourier transform of this image represents these radiance levels with regard to variations in frequency. These frequency variations can be viewed either via a Fourier spectrum, or more usefully in image form by looking at the intensity values in the magnitude plot produced by the FFT. Prior to viewing, magnitude plots have to

be scaled using either a gaussian or a logarithmic function, otherwise the high frequency information tends to be obscured by the low frequency terms, which have higher intensity values. It is important that the high frequency terms are visible on the magnitude plot as these terms often represent noise. Intensity or brightness in the magnitude plot is proportional to the amplitude of the original input periodic function.

A magnitude plot displays spatial frequency variations radially from a central origin of zero frequency. High spatial frequencies correspond to points furthest away from the origin whilst low spatial frequencies correspond to points closest to the origin (Figure 3.2). The normal image detail occupies a broad zone, centred about the zero frequency point or origin (centre of Figure 3.2). The shape and extent of this zone will vary on all magnitude plots as it depends directly on the distribution of spatial frequencies in the real image. For example, an image of a relatively homogeneous region with few edges (either spectral or topographic) would have a small central zone which would plot close to the magnitude origin at low frequencies, whilst an inhomogeneous region with numerous edges would plot over a larger zone further away from the origin at higher frequencies. Features with a regular period, for example, across-track striping caused by noise would plot as bright spots concentrated at specific frequencies. Figure 3.2 shows a series of bright spots (high intensities) caused by periodic along-track noise structures at different frequencies (i.e., different pixel spacings in the image data).

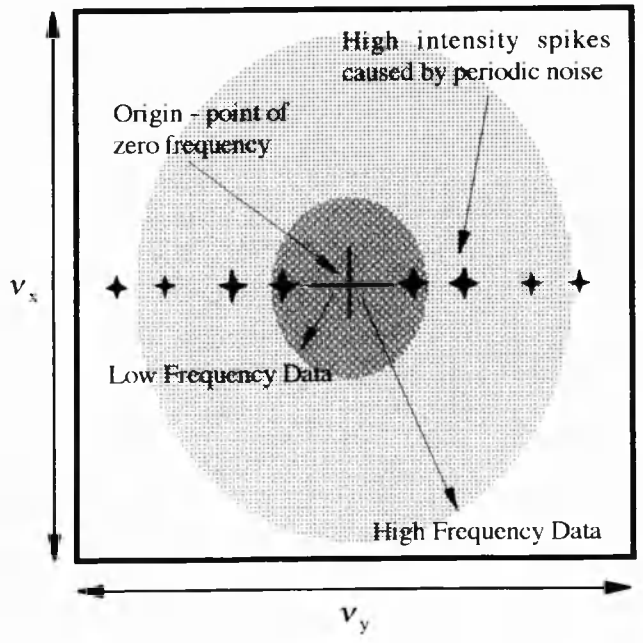

Figure 3.2 A schematic representation of image data as seen on a magnitude plot. Note that the axes of the magnitude plots shown in this thesis are the opposite way round when compared with some examples in the literature, for example in Gonzalez and Wintz (1977). This is a computational attribute of the TerraMar IDIMS v4.6 image processing software used for this study.

A circular shape to this central zone represents a random distribution of edge information in the original image. An elongated shape about the central origin suggests a preferred orientation or alignment of features in the original image data.

A regular periodic structure in an image, such as noise (Figure 3.3a), will have a Fourier transform were all the energy is constrained in a well defined bright spot (or spots) in the magnitude plot (Figure 3.3b). Figure 3.3a shows a schematic representation of a low frequency sinusoidal function superimposed on an image to produce across-track noise. In image terms this low frequency noise comprises long run lengths of pixels representing the noise, with unaffected regions of image data in-between. Figure 3.3b shows that this periodic noise produces two spikes in the magnitude plot. These are located relatively close to the origin of the magnitude plot because of the low frequency of the original periodic noise. The superimposition of a high frequency sinusoidal noise function (Figure 3.3c) also produces across-track noise, although this time it is represented on the image by short run lengths of pixels, with only short unaffected regions of image data in-between. On the schematic magnitude plot (Figure 3.3d) this noise is represented by two smaller spikes located further away from the image origin at higher frequencies.

These spikes are smaller, i.e. lower in intensity, because the amplitude of the original sinusoidal function is less than that of the low frequency noise in Figure 3.3a. Introducing a periodic noise component simultaneously in both the x and y directions has the combined affect of producing a diagonal superimposed periodic noise structure at an angle ø to the image axis (Figure 3.4a). This results in the noise spikes in the magnitude plot being rotated off axis by the equivalent angle (Figure 3.4b). The distance of these spikes away from the origin is determined by the original frequency of the periodic function.

Combining two different periodic functions together, for example those seen in Figures 3.3a and 3.4a, produces a complex noise pattern on the image data (Figure 3.4c). It also makes the magnitude plot (Figure 3.4d) more complex as it introduces four spikes, two for each periodic function. Spikes A and A' represent the low frequency noise equivalent to that of Figure 3.3a whilst spikes B and B' represent the slightly higher frequency noise equivalent to that of Figure 3.4a. Note that A and A' have a higher intensity than B and B' because of the higher amplitude of their original input function. These simple schematic examples (Figures 3.3 and 3.4) show how image noise can be regarded as the superimposition of different sinusoidal functions, with different amplitudes and frequencies, parallel to one or both image axes.

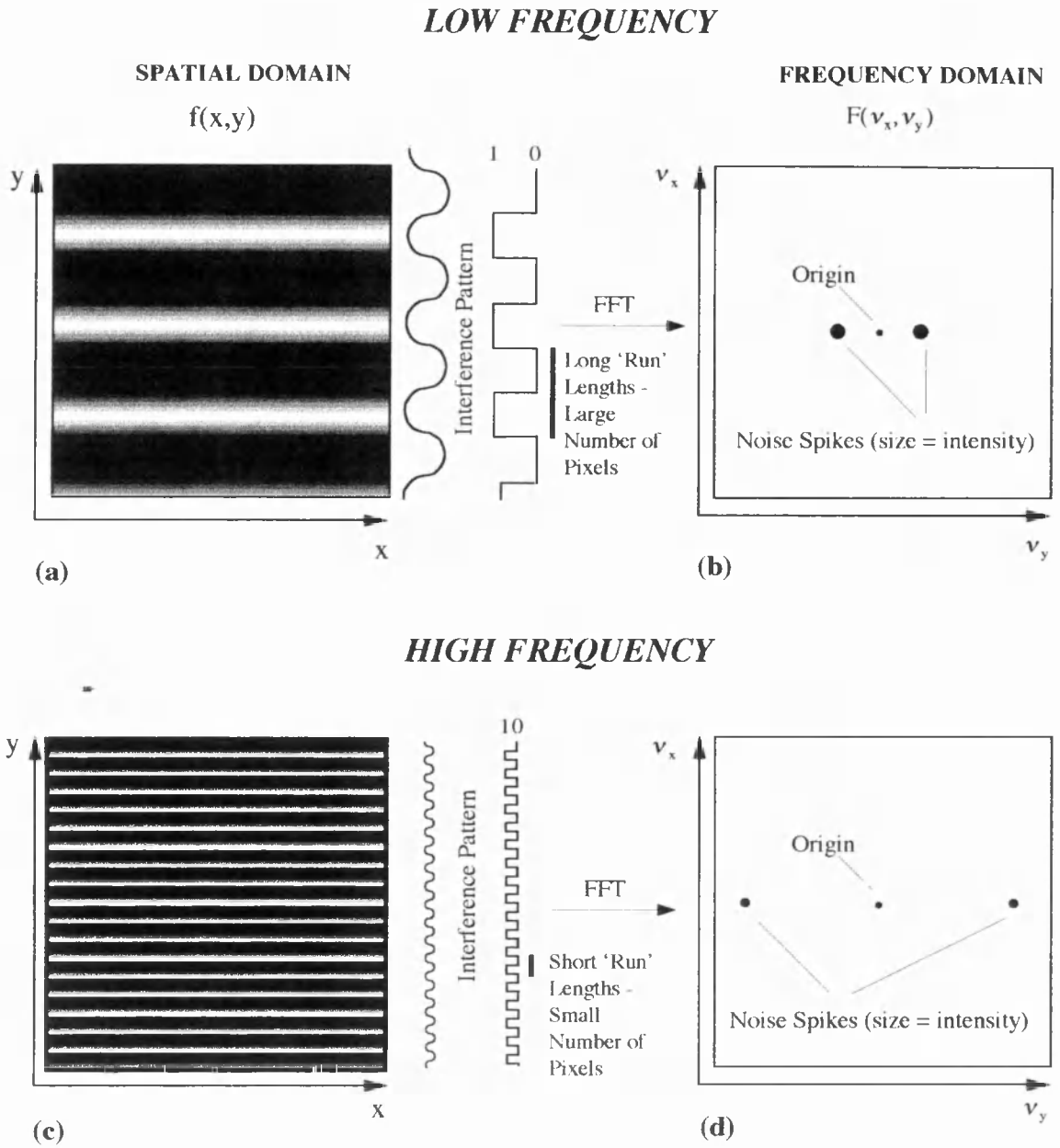

Figure 3.3 Schematic representation of simple periodic noise structures and their associated magnitude plots. a) and b) low frequency across-track noise, c) and d) High frequency across-track noise. Note that ν_x is plotted parallel to y and ν_y parallel to x, to correspond with the convolution used in the IDIMS software. Some authors, e.g. Gonzalez and Wintz (1977) prefer the convention where ν_x is plotted parallel to x.

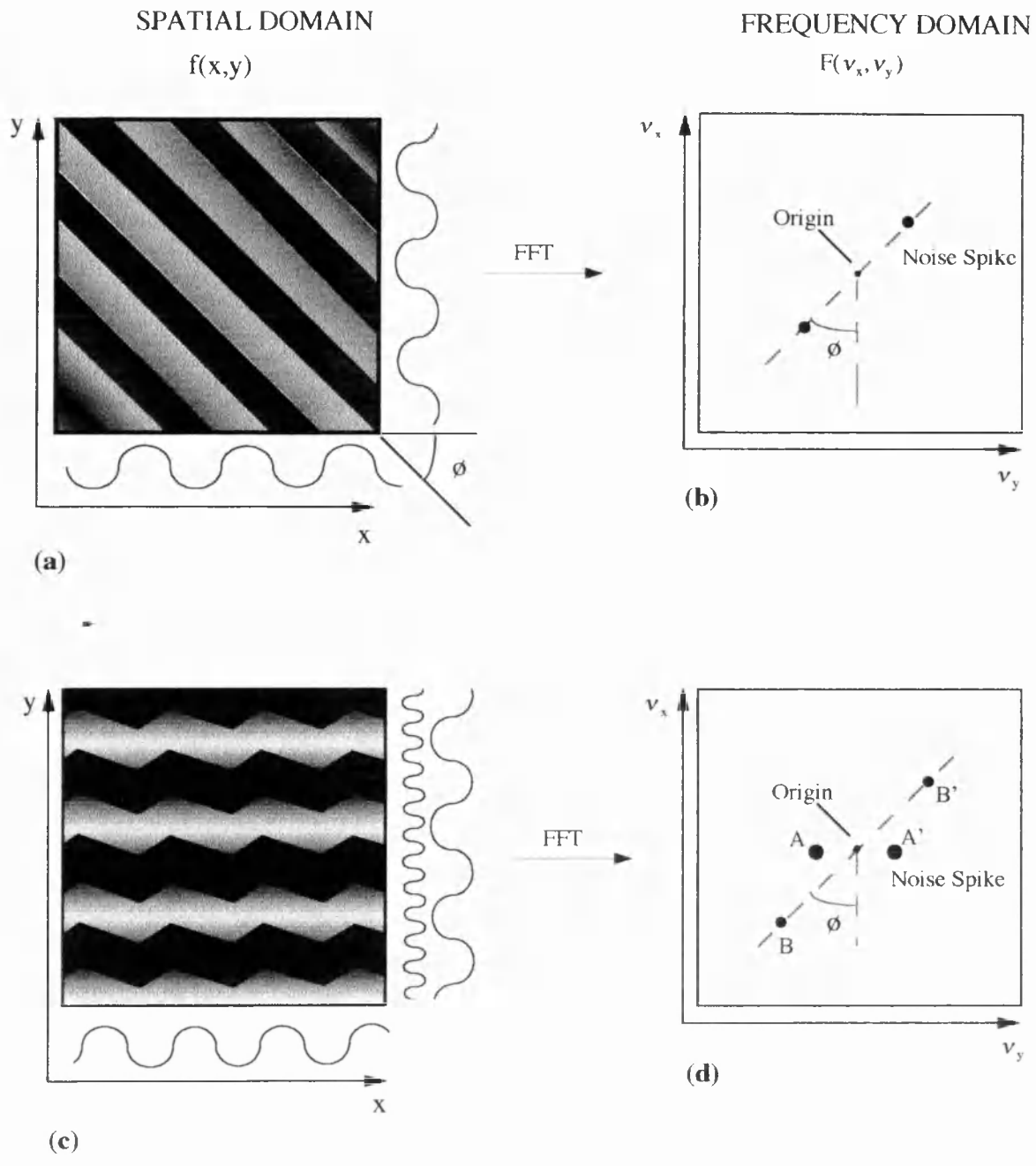

Figure 3.4 Schematic representation of complex periodic noise structures in the spatial domain and in the frequency domain. (a) and (b) low periodic across-track noise rotated by ø , (c) and (d) Combined low frequency across-track noise with high frequency along-track noise.

Varying any one of these components results in a distinct noise structure. These examples also demonstrate how variations in the sinusoidal function are represented as variations in the frequency domain. Considering these simple examples helps to clarify the complex structures found in real OPS image data. However, without a thorough knowledge of all of the processes that have affected OPS image data from the time of acquisition, through pre-processing to final product distribution, it is impossible to explain all of the features seen in a magnitude plot. However, the majority of noise artifacts associated with JERS-1 OPS data produce features in the frequency domain, which can be recognised as being distinct from the image data. Magnitude plots of noisy OPS Level 0 and Level 2 data are described below.

2) OPS Level 0 noisy magnitude plot

A 1024 x 1024 subscene of Level 0 SWIR OPS 6 data from scene 341-420 was used as the input channel, as this exhibited characteristic noise artifacts. These noise artifacts are primarily along- and across-track striping as illustrated in Figure 3.5. The important feature to note is that the along- and across-track stripes are perpendicular to each other in the raw Level 0 data.

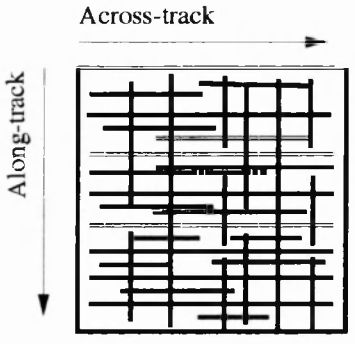

Figure 3.5 Schematic diagram illustrating Level 0 across- and along-track noise structures. Note that these features are perpendicular to each other.

These noise structures produce distinct features, clearly visible in the frequency domain magnitude plot. The magnitude plot of this channel (Plate 3.6) shows a zone around the central origin which represents real image detail. This zone is quite large because the image is of a fairly varied region with numerous edges and therefore has a moderately large spatial frequency range. This zone is elongated across the plot because this is the primary direction of the structure in the imagery. Two smaller zones at the top and bottom of the plot represent high frequencies information, such as edges.

Level 0 OPS data

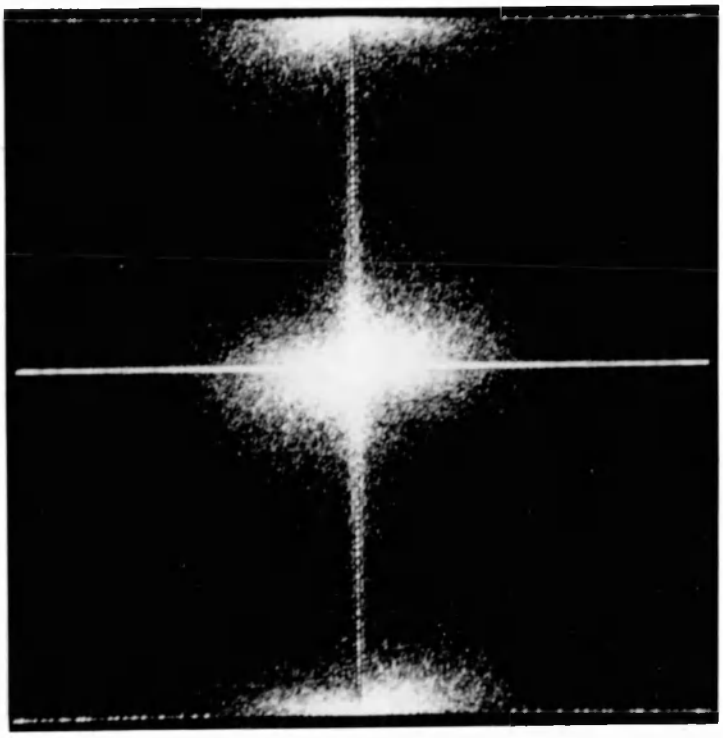

Plate 3.6 Magnitude plot of a 512 x 512 pixel subscene of Level 0 OPS 6 data, scene 421-340. See Figure 3.6 for an explanantion of this plate.

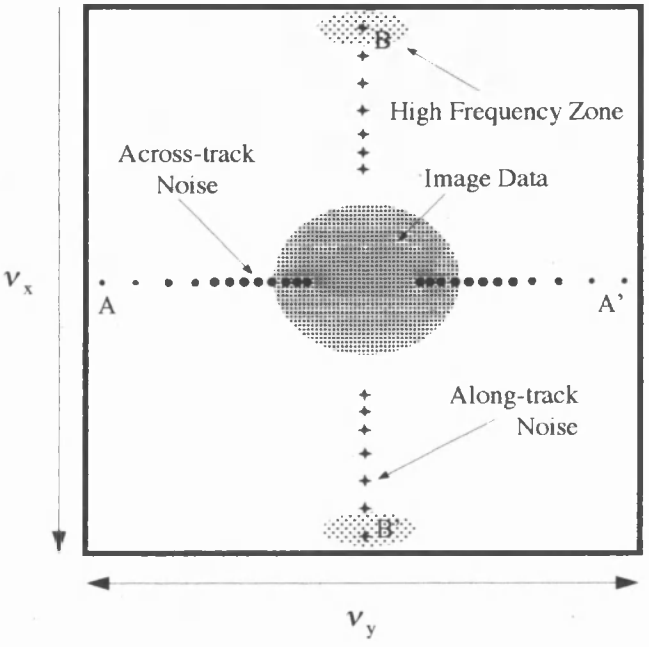

Figure 3.6 Schematic diagram of a Level 0 OPS 6 magnitude plot as seen in Plate 3.6. The magnitude plot is comprised of four main components; a central zone of image data; a high intensity line (A-A') representing across-track noise; a perpendicular high intensity line (B-B') representing along-track noise and two high frequency zones comprised of both image and noise data. Refer to text for a full description.

The remainder of the features are probably best explained with the aid of a schematic representation of the magnitude plot, Figure 3.6. Across-track noise is represented by the strong horizontal lines, A-A'. This line is comprised of a series of closely spaced high intensity spikes which together give the appearance of a line. Each of these spikes represents an along-track noise structure with a constant periodicity. The frequency of these noise structures vary from low to high. The intensity (or amplitude) of these spikes also varies with frequency. Along-track noise is represented by the line B-B' and is similar to line A-A' in that it is comprised of individual high intensity spikes, however, these spikes are not as well defined as those on line A-A'. The frequency of this noise also varies from low to high.

3) OPS Level 2 noisy magnitude plot

A 1024 x 1024 pixel subscene of Level 2 SWIR OPS 6 data from scene 208-262 was used as the input channel, as this exhibits noise artifacts. These noise artifacts are primarily along- and across-track striping as illustrated in Figure 3.7. Unlike the Level 0 data these noise structures are no-longer perpendicular to each other.

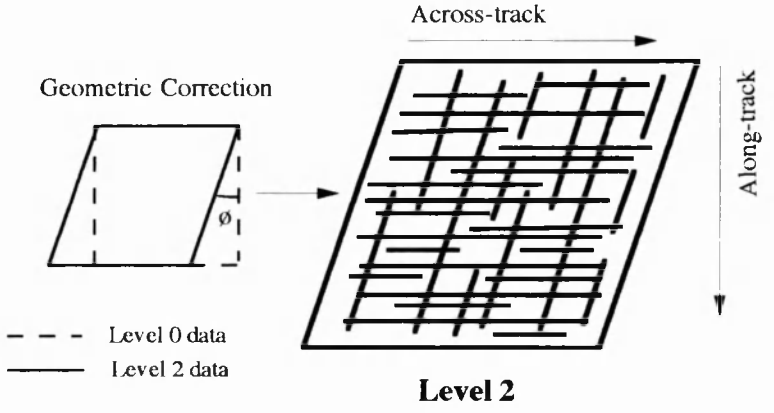

Figure 3.7 Schematic diagram showing how the pre-processing applied by NASDA rotates the Level 0 along-track noise by an angle ø. This results in the across- and along-track noise being inclined to each other in Level 2 data.

These rotated noise structures produce distinct features clearly visible in the frequency domain magnitude plot. The magnitude plot of this channel (Plate 3.7) shows a small zone around the central origin which represents the real image detail. This zone is quite small compared to that in Plate 3.7, because this image is of a fairly homogenous region with comparatively few edges and therefore has a low spatial frequency range.

Level 2 OPS data

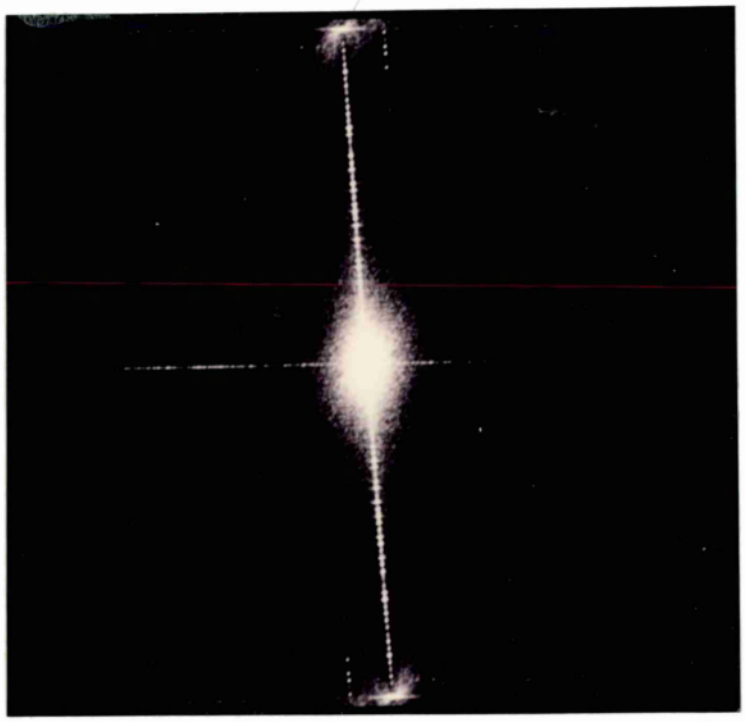

Plate 3.7 Magnitude plot of a 512 x 512 pixel subscene of Level 2 OPS 6 data, scene 208-262. See Figure 3.8 for an explanantion of this plate.

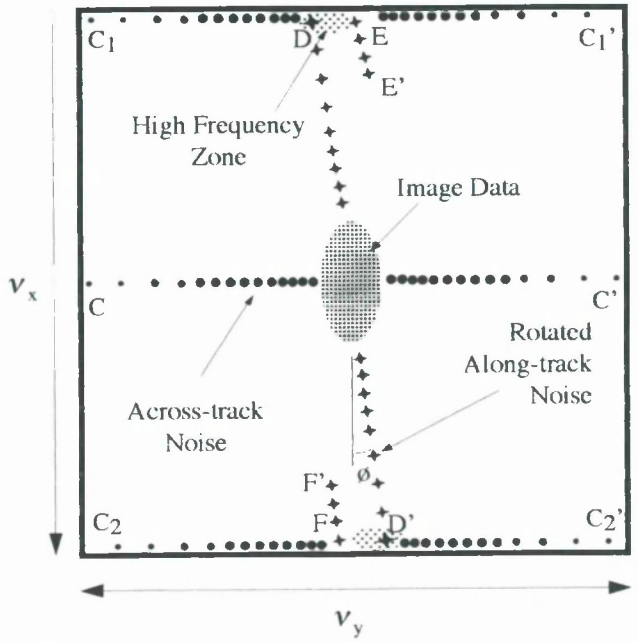

Figure 3.8 Schematic diagram of a Level 2 OPS 6 magnitude plot as seen in Plate 3.8. This Level 2 magnitude plot is rather more complex than the Level 0 one seen in Figure 3.6. This plot is comprised of six main components; a central zone of image data; a high intensity line (C-C') representing across-track noise; two additional lines at high frequencies (C_1-C_1' and C_2-C_2') also represent across-track noise. Along-track noise is no longer represented by a perpendicular high intensity line, but is now represented by an off vertical line (D-D'); which has been replicated at high frequencies and forms two additional lines (E-E' and F-F'). Two small high frequency zones comprised of both image and noise data are also visible. Refer to the text for a full description.

This is also indicated by the high frequency data zones at the top and bottom of the image which are much smaller than those in Plate 3.6. Numerous additional features are visible in this magnitude plot which are not visible in Plate 3.6. These have been introduced by the geometric transformation applied by NASDA. This transformation not only increases the complexity of the noise structures in the spatial domain (section 2.5.3 (5)), it also increases their complexity in the frequency domain.

These complex features are best explained using Figure 3.8 which is a schematic representation of the Level 2 magnitude plot. The across-track noise in the Level 2 data is still represented by a horizontal line, C-C', of high intensity spikes of consistent periodicity. This is because this noise structure has only been translated in the across-track direction and has not been rotated by the pre-processing procedure. Suggesting that the Level 2 geometric pre-processing consists of botha translational and rotational component. However, the across-track noise is also now represented by a symmetrical pair of lines, C_1-C_1' and C_2-C_2', which have been introduced at extremely high frequencies. Along-track noise is no longer represented by a vertical line of spikes, as in the Level 0 data (Figure 3.6), but by a line, D-D', (Figure 3.8) of enlarged spikes at an angle ø to the vertical axis. These spikes are more diffuse than the spikes seen in the Level 0 data, suggesting that they contain some real image information as well. The higher frequency end of this line of spikes has been duplicated into two short lines, of slightly lower intensity spikes, represented by E-E' and F-F'. These lines are strange features only visible on magnitude plots of Level 2 SWIR channels. Plate 3.7 illustrates that performing even a relatively simple geometric transformation on the original data complicates the existing noise artifacts and results in the production of new complex interference noise patterns.

3.3.4 Noise removal in the frequency domain

The major advantage of transforming images into the frequency domain is that the noise component of an image can be distinguished independently from real image data. This means that processing in the frequency domain can be used either to suppress or remove noise artifacts. Removal of noise is accomplished by filtering the magnitude plot before performing the Inverse Fourier Transformation to return the data back to the spatial domain (as summarised in Figure 3.1).

Although this may sound simple it is in fact quite a difficult task to perform. This is because the noise component can be masked or removed by numerous techniques and the suitability of any one technique will depend on the nature of the noise being removed. Care has to be taken when processing in the frequency domain to ensure

component. This is best ensured by not attempting to remove 100% of the image noise, as this approach will undoubtedly remove some image information as well. It is better to leave some noise in the final image, rather than risk losing any real image data. Five approaches to noise removal in the frequency domain are discussed and demonstrated here, with regard to OPS data.

1) Notch filters

The simplest processing technique available to remove noise from magnitude plots is that of notch or wedge filtering (Peli and Verly, 1983). This technique relies on the insertion of a zero-weighted mask over any feature in a magnitude plot which represents a noise artifact (Figure 3.8). These masks should ideally be the exact size of the feature they are masking to ensure that no real image data are removed. This is quite easy to accomplish for noise of a consistent periodicity which produces a well defined high intensity spike in the magnitude plot, but it is not very easy to accomplish for features which do not have a consistent periodicity and therefore produce broad spikes in the magnitude plot. Masking these to zero may result in the loss of some image detail, which is contained within their broad 'skirts' (Gonzalez and Wintz, 1977). Problems also occur when trying to mask even a well defined spike which occurs at fairly low frequencies as it may be contained within the central zone of image data. Even perfect delineation of such a point will result in the loss of some image detail, as the spike will be partially comprised of real image data as well as a noise. One way of reducing the loss of image detail in such circumstances is to mask the point with a non zero value. A suitable value can be determined by interpolation from noise free regions from the surrounding magnitude plot (Schowengerdt 1983).

Notch filtering is a very simple technique which is best used to remove only well defined periodic features seen in a magnitude plot. It is best applied to Level 0 data, specifically VNIR channels, which exhibit the simplest noise structures in the frequency domain. Notch filters are capable of removing the across-track noise seen in the VNIR channels of Level 2 data (Plate 3.8), however their application to more complex Level 2 noise structures such as those associated with the SWIR channels are limited.

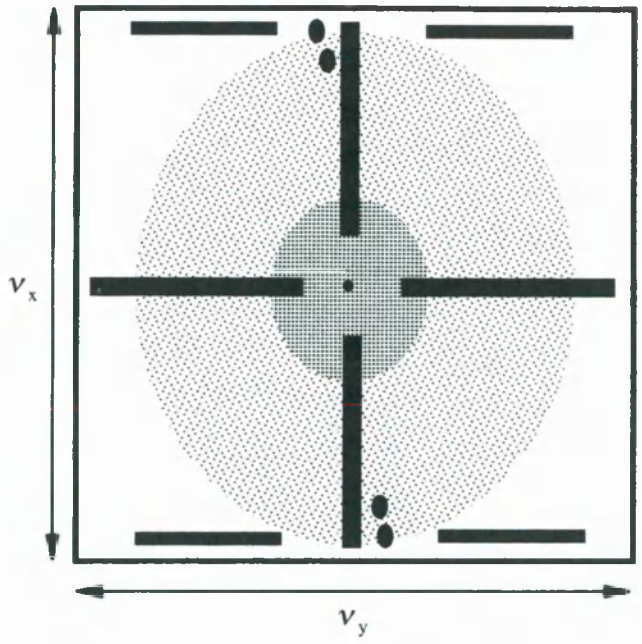

Figure 3.9 A simple schematic representation of Notch filters inserted into a magnitude plot. The Notch filters have a DN value of zero so that they mask the noise component.

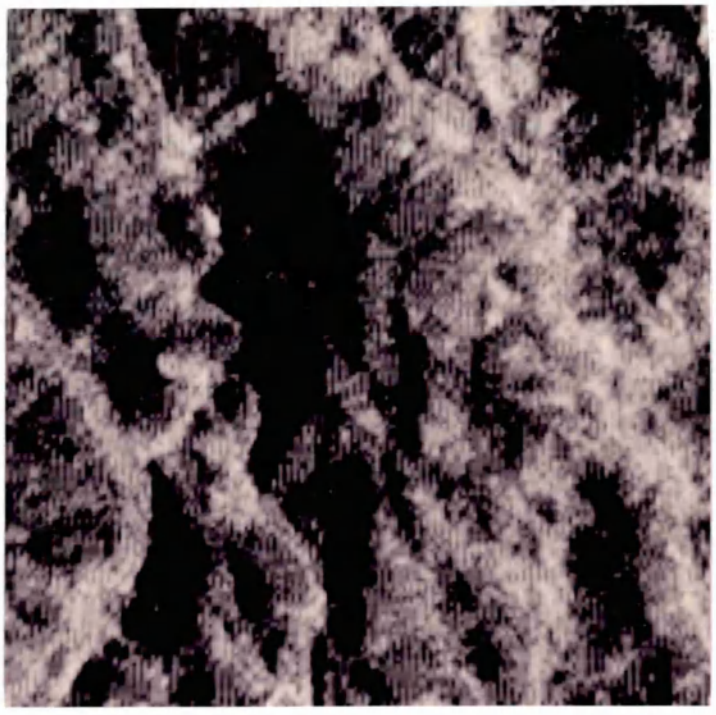

Plate 3.8 An example of Level 2 OPS 2 data cleaned by the Notch filtering technique (Plate 2.5 shows the original noisy image). The Notch filters have managed to remove the majority of the across-track noise component without introducing significant image blur. Compare this result with the original (Plate 2.5) and the results of convolution filtering (Plates 3.1, 3.2 and 3.3).

The major disadvantage of notch filtering, apart from that of its limited success, is that of time. This process is extremely slow to implement as the magnitude plot of each channel has to be examined visually, and appropriate notch filters created. The process can be speeded up slightly by inserting the zero-weighted notches into a constant image with a background DN value of one. This creates a binary mask which can be used to multiply any magnitude plot by mapping 'notched' areas to zero whilst leaving the rest of the image unaffected. The problem with this approach is that it relies on the assumption that the locations of well defined periodic spikes do not move from one magnitude plot to the next. Unfortunately this is not always the case. A further problem associated with notch filtering is that the sharp edges in the filter may introduce spurious unwanted patterns in the spatial domain, such as ringing (Ballard and Brown, 1982).

2) High Frequency Cut-Off Masks

Another approach to noise removal is to combine a magnitude plot multiplicatively with a large filter centred at low frequencies. These filters are usually circular or elliptical in shape and are weighted from one DN at their centre to zero DN at their edge (Figure 3.9). This weighting can either be a straight forward linear gradient or it can be controlled by a predetermined function, such as a gaussian or logarithmic profile. These filters are located so that during multiplication their centres correspond with the zero frequency origin of the magnitude plot. They have the affect of removing the high frequency component of the magnitude plot whilst preserving the lower frequencies. The amount of original data preserved depends both on the shape of the filter and on the weighting profile.

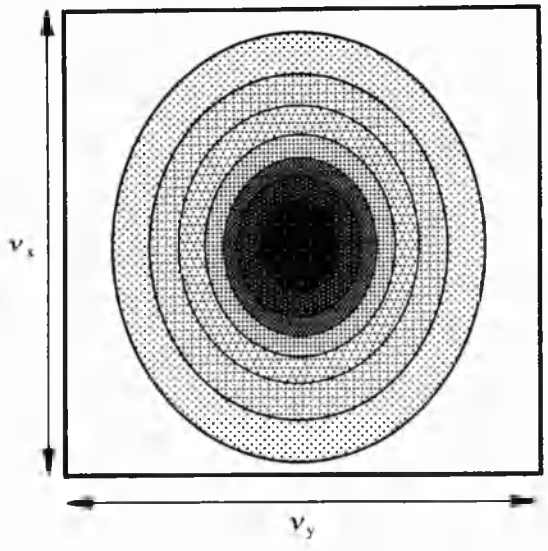

Figure 3.10 Schematic representation of an elliptical high frequency cut off mask.

This technique tends to eliminate the majority of high frequency noise structures although any noise at low frequencies tends to be preserved along with the image detail. Conversely, any high frequency image detail, such as edge information, is lost along with the noise component. This results in the filtered images, once transformed back into the spatial domain, having a slightly blurred appearance, similar to the results of low pass filtering in the spatial domain.

The advantage of this technique is that it is very quick to implement compared to notch filtering. However, it removes artifacts at the expense of real image data. Tests of this technique show that it works reasonably well on both Level 0 and Level 2 VNIR data, as it is capable of removing across-track noise (Plate 3.9), although this has been at the expense of the high frequency image detail. Problems arise with the SWIR channels, as these contain significant noise structures at low frequencies (especially for Level 2 data). Removal of these features using this technique means that a very small filter has to be used, which results in only minimal image detail being preserved. This produces a cleaned output image with very little textural information preserved. This is not acceptable, considering the initial textural information content of channels OPS 6 and 7 is already extremely low.

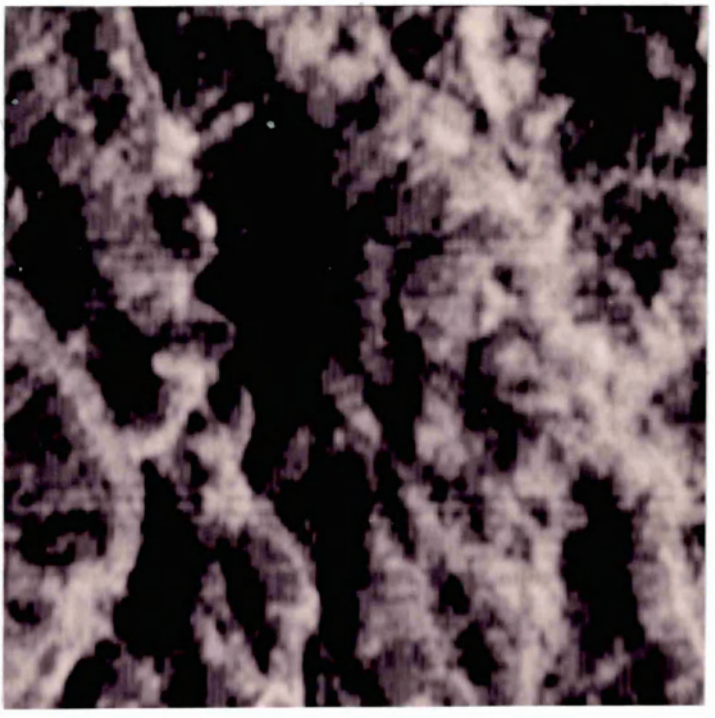

Plate 3.9 Example of Level 2 OPS 2 data cleaned using a high frequency cut off mask. This technique has reduced the severity of the across-track noise, but it has introduced significant image blur. This is because this technique removes high frequency information from the imagery. Compare this result with the original (Plate 2.5) and the results of convolution filtering (Plates 3.1, 3.2 and 3.3).

A variation of this technique is to combine these gradient filters with isolated notch filters. This combined approach means that the gradient filter can be large, which helps to preserve the maximum amount of high frequency textural information, whilst isolated notch filters ensure that specific high or low frequency noise spikes are removed. The problem with this approach is that it is slow to implement, as ideally individual filters need to be produced for each OPS channel. Tests of this combined approach have however produced some favourable results for both Level 0 and Level 2 data noise removal.

3) Zonal Notch Filters (ZNF)

This technique for noise removal relies on having two input channels with correlated noise structures, at similar frequencies, whilst having poorly correlated spectral information. The choice of input channels will be scene dependent, although in practice OPS 5 and 6 usually satisfy these criteria. Despite OPS 5 appearing to be of a higher quality than the other OPS channels, the magnitude plot shows characteristic noise spikes associated with across- and along-track noise. Once two channels have been chosen the frequency domain mask can be constructed. This is accomplished by transforming both images into the frequency domain and producing gaussian stretched magnitude plots. The magnitude plot which shows the noise structures most clearly is then subtracted from the other. The resulting difference image, once scaled back to byte format, can then be used to isolate noise and produce a scene dependent filter. This is accomplished by manually examining the difference image to determine a threshold value which separates the noise component from the real image data. This value is best determined by utilising an interactive pseudo-colouring routine to highlight DN values representing noise. Once a threshold value has been established this is used as a binary mask to map all of the magnitude plot components representing noise to zero, whilst mapping the remainder of the image to one. This mask is known as a Zonal Notch Filter or ZNF (De Souza *et al.*, 1996). Figure 3.10 summarises this procedure, while Plate 3.11 illustrates a typical ZNF. When initially creating a ZNF the task of establishing a threshold value may need to be repeated until a suitable value has been determined. This is because it is not always possible to determine the optimum noise / image cut off value on the first attempt. The choice of an inappropriate value will be immediately apparent when the mask is used to clean an image; if the threshold value is set too low it will leave a significant amount of noise in the cleaned image, whilst if it set too high it will remove a lot of real image detail. Either of these results will require that the threshold value is made larger or smaller as appropriate.

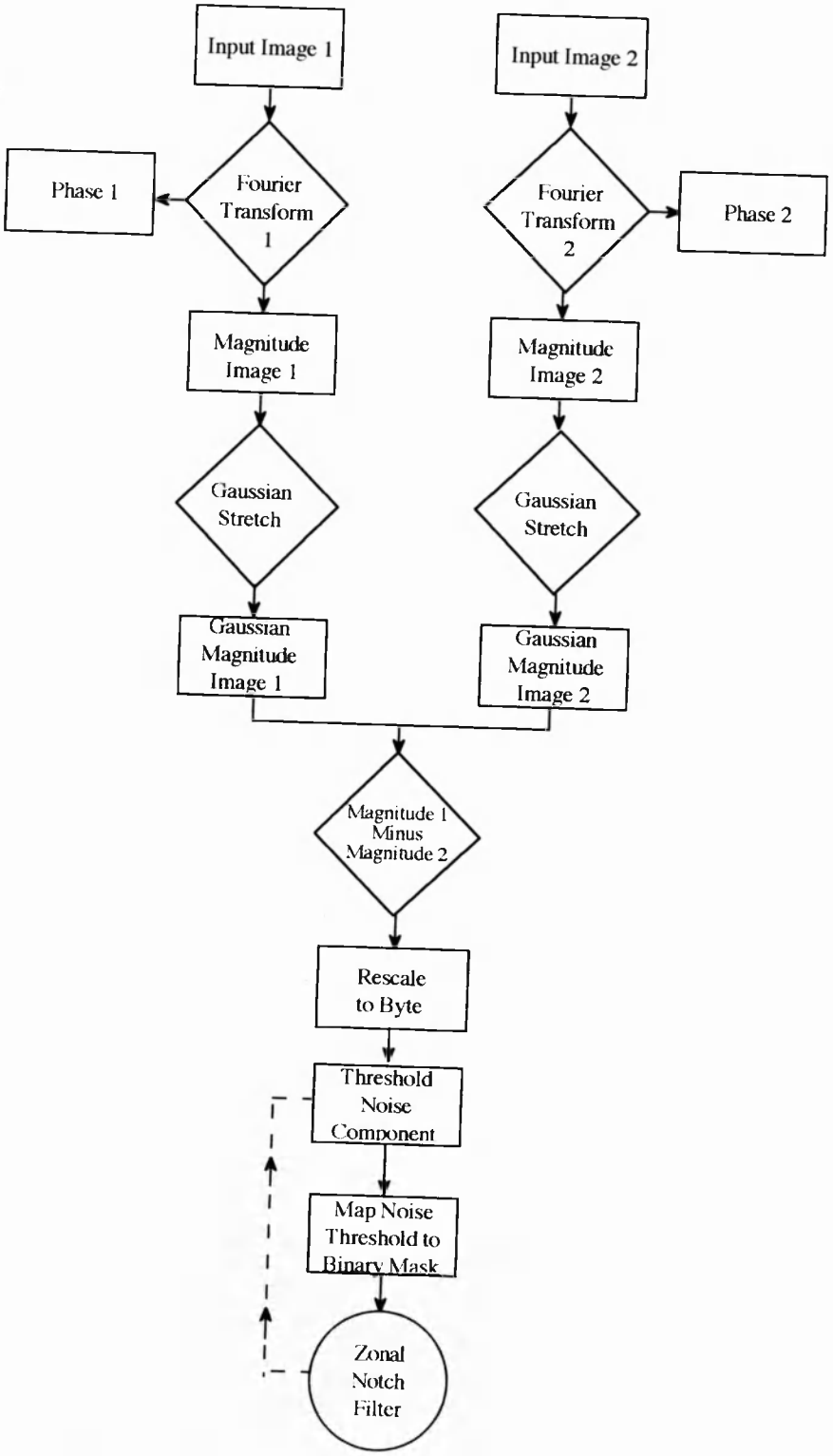

Figure 3.11 A flow chart showing the production of a ZNF filter from two input channels. Dotted line indicates the stages which may need to be repeated until a satisfactory threshold value for the mask is determined.

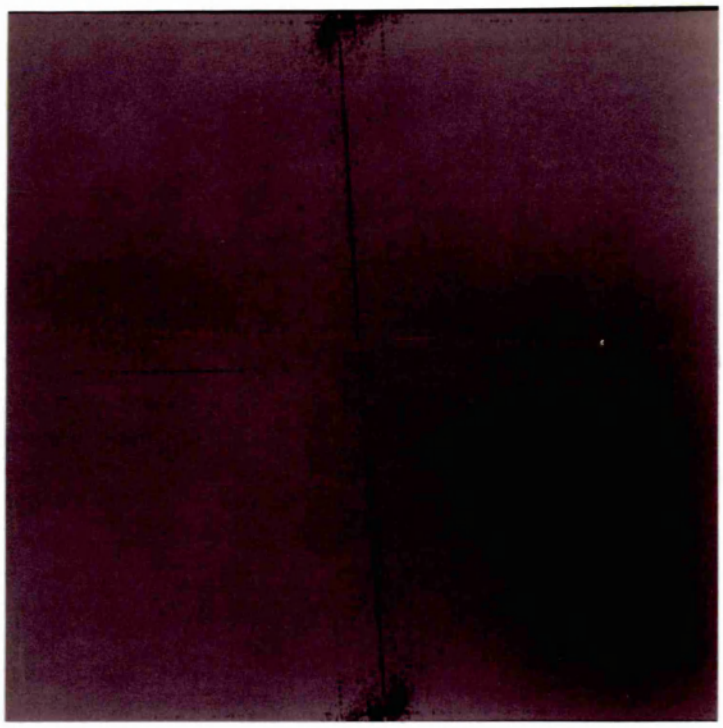

Plate 3.10 A typical ZNF produced from the input channels OPS 5 and OPS 6, this image has been scaled for display purposes as it contains only the DN values one and zero.

Once a ZNF has been produced the process of using it to clean an input image is quite simple as outlined in Figure 3.11. Initially the input image has to be transformed into the frequency domain. The magnitude component is then multiplied by the binary ZNF to produce a new magnitude plot which has had the frequencies associated with noise masked to zero. This new magnitude component is then combined with the original phase component via an Inverse Fourier Transform. Once transformed back into the spatial domain the new output image will be almost noise free, providing that the threshold value for the ZNF has been determined correctly. Because this technique masks out only those frequencies associated with noise the majority of the image detail is preserved. Image detail will only be lost if its frequency coincides with that of a noise artifact being masked out. There is a slight possibility of this occurring at high frequencies, which might result in the loss of some edge information in the image.

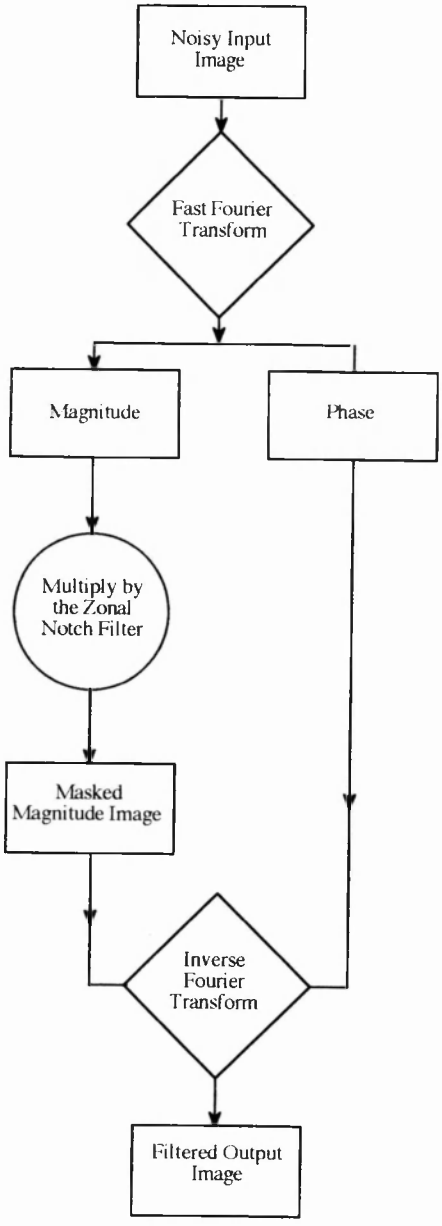

Figure 3.12 A flow diagram showing how a ZNF is used to clean a noisy input channel of OPS data.

The ZNF seen in Plate 3.10 was produced from scene 208-262 using subscenes of OPS 5 and OPS 6. This filter was then applied to the original subscene of OPS 6 (as per Plate 2.7) the resultant cleaned output image can be seen in Plate 3.11. Note how the majority of the noise structures seen in the original image, in particular the across- and along-track striping have been removed by this filtering technique, whilst the real image detail has been preserved. The slightly blurred nature of the output image reflects the original data quality and is not an artifact of the ZNF filter.

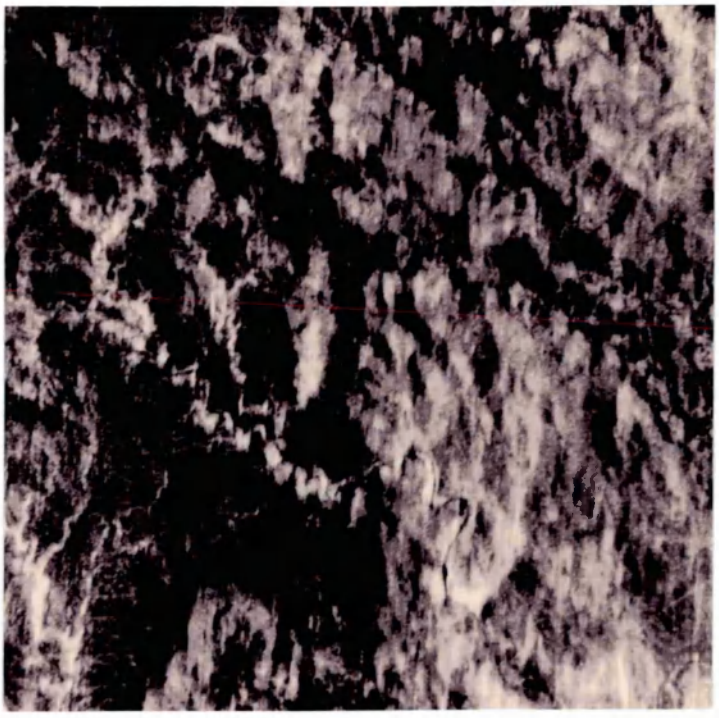

Plate 3.11 Level 2 OPS 6 cleaned using a ZNF. This technique has removed the across- and along-track noise seen in the original (Plate 2.7).

used to remove noise from all channels of data despite the noise structures being slightly different in each original image channel. This is because the ZNF defines the location of noise spikes so precisely it removes (masks) only minimal information from the magnitude image. If the ZNF does not coincide with a noise spike in the magnitude image it will remove only a small amount of real image information.

Since the initial development of this filter technique I have made two modifications. The first of these introduces a third image at the subtraction stage of the production of the ZNF; this image tends to be OPS 8. The reason for this is that OPS 8 exhibits slightly different noise structures which are not totally encompassed by OPS 5 and 6. Whilst a ZNF produced from OPS 5 and 6 removes the majority of noise structures from all channels it does not adequately remove the noise artifacts from OPS 8. The introduction of OPS 8 into the subtraction routine ensures that the resulting ZNF is capable of cleaning this channel as well. The inclusion of this channel does not affect the capabilities of the filter to clean other channels. Figure 3.12 shows the modified production procedure for the ZNF using three input images.

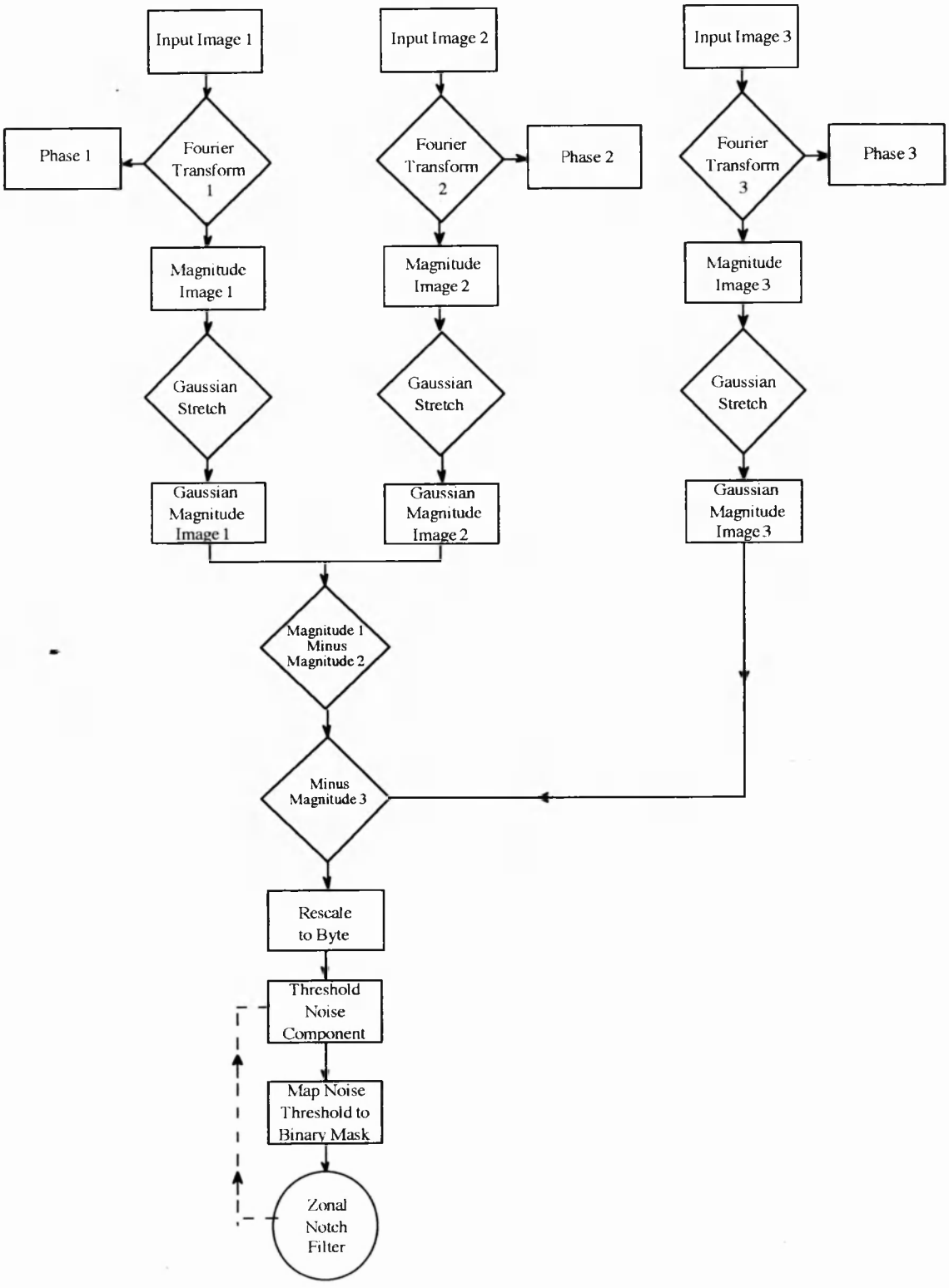

Figure 3.13 Flow chart showing the processing procedure for the production of a ZNF using three input images.

I introduced a second modification to try to reduce 'ringing' which is sometimes apparent at the edges of the cleaned images. Ringing can be reduced by introducing a gradual transition from zero to one in the mask image, as opposed to an abrupt boundary (Hummer-Miller, 1990). This is accomplished by determining a threshold range of values, for example 5 DN, rather than a single value, to represent the breakpoint between the noise and image detail (Figure 3.13). The width of the threshold range will determine the gradient of the mask.

	Noise		Image	
Threshold Values	0	39	40	255
Mask Values	0	0	1	1

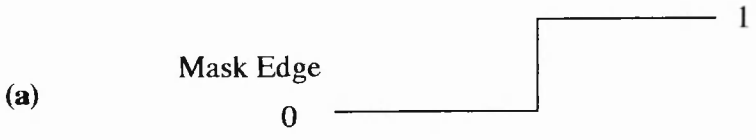

	Noise			Image	
Threshold Values	0	34	35.....39	40	255
Mask Values	0	0	0.01.....0.99	1	1

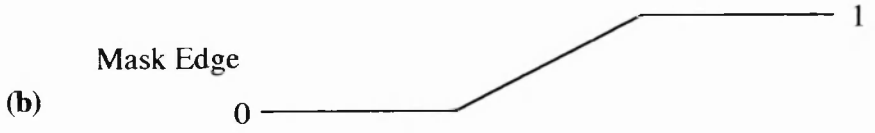

Figure 3.14 Schematic representation of the edge of a ZNF; (a) a binary mask or (b) a real mask were the transition from 0 to 1 DN in the mask has been mapped over a range of 5 DN in the original input image.

Producing a gradational mask with real values can be quite a difficult task as most image processing systems (including TerraMar IDIMS v4.6) only allow integer values to be mapped. One way of producing a mask with a range of real values between 0 and 1 involves initially mapping the threshold range from 99 DN to 1 DN, and then dividing the output mask by 100. This will produce an output mask which has a threshold range mapped between 0.99 and 0.01. Multiplication of a magnitude plot by this 'real' mask will result in the minor modification of some of the magnitude values as it is no longer a binary mask. Care must be taken that the values modified represent noise artifacts and not real image data. This is accomplished by ensuring that the threshold range is chosen on the noise side of the break point value and not on the

image side. In practice, providing the width of the gradational boundary is kept fairly small, it does not produce any noticeable image changes, except the desired reduction of ringing.

4) Principal component noise isolation mask

Instead of using a raw image channel as the initial input to the Fourier transform a different approach to noise removal is to transform a processed channel of data into the frequency domain. The idea is that noise structures can be partially separated from the image data by pre-processing in the spatial domain. An ideal process to perform prior to Fourier transform is Principal Component Analysis (PCA). As discussed in section 3.2.3 PCA does not completely decorrelate all of the noise components from the image data. However, it does produce some PCs which have considerably greater noise components than image data. PC 2 (Plate 3.12), for example, demonstrates little image detail other than moderate across-track and strong along-track striping (see Table 3.2). This provides an ideal base image to transform into the frequency domain, because the task of discriminating the noise component from that of image detail is already half complete. Note that PC 2 will not always be the best input channel as the redistribution of the noise artifacts throughout the PCs is scene dependent. As a result this technique requires that the PC images are initially viewed to determine a suitable input channel.

The magnitude plot of PC 2 (Plate 3.13) is dominated by the very strong noise features which are apparent at both high and low frequencies, as some high intensity noise spikes are located very close to the central origin. Real image detail occupy only a very small central zone. An identical technique to that described in section 3.4.3(3) can now be used to determine a threshold value representing the break point between the noise and image components. The only difference is that the noise component in the magnitude plot will be represented by high DN values as opposed to the low ones, generated by the subtraction operation in the ZNF production process. Once a threshold value or a range of values has been established a binary mask can be produced which maps the noise artifacts to zero. This mask can then be used to multiply the magnitude plot of any input channel, although once again independent masks have to be created for Level 0 and Level 2 data. Production of the PC mask is summarised in Figure 3.13.

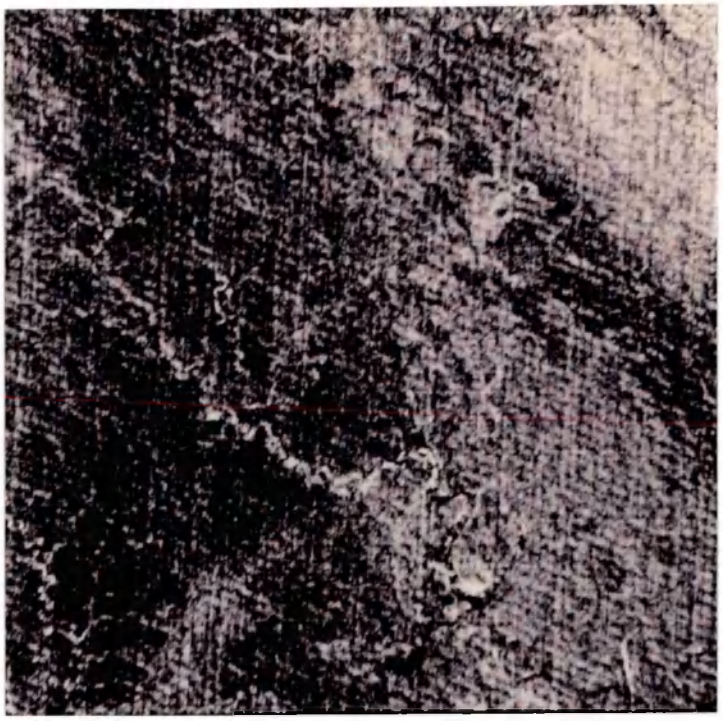

Plate 3.12 PC 2 derived from performing PCA on all seven OPS channels. This channel was chosen as the input into the Principal Component Noise Isolation Mask because it clearly shows across- and along-track noise, whilst having minimal spectral information.

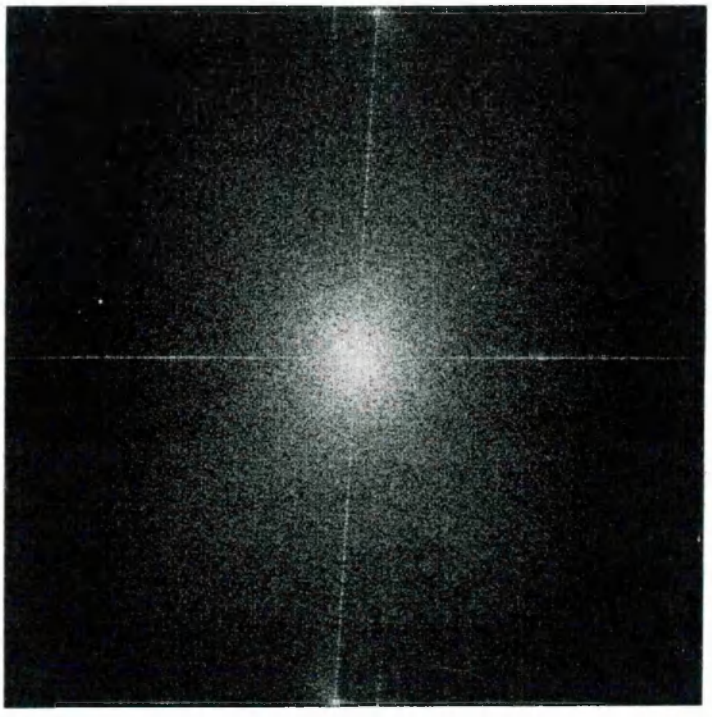

Plate 3.13 Magnitude plot of PC 2 (as per Plate 3.12), note how the noise structures are very clear, even at low frequencies. This is due to the dominance of the noise structures in the input channel, compared with the spectral information.

Tests of this technique on JERS-1 OPS data show that it removes noise artifacts from all OPS channels without significant loss of image detail, although like the ZNF it may take a couple of attempts to derive the optimum threshold value for the mask. Plate 3.14 illustrates this technique applied to OPS 6. Like the ZNF most of the original noise evident in the original OPS 6 (Plate 2.7) has been removed by this filtering technique. This technique can be further improved by repeating the process with a second PC as an input channel, for example PC 4, which highlights slightly lower frequency along-track noise (i.e., longer pixel run lengths). Once a mask has been produced for PC 4 a final combined mask can be derived by multiplying the two intermediate masks together, and then rescaling the output to a binary DN range.

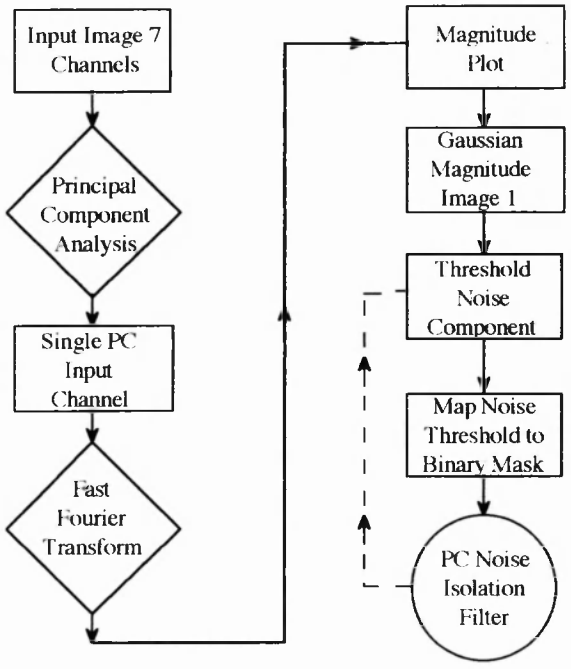

Figure 3.15 Flow diagram illustrating the processing steps to produce a PC noise isolation filter for use in the frequency domain. Dotted line indicates the stages which may need to be repeated until a satisfactory threshold value for the mask is determined.

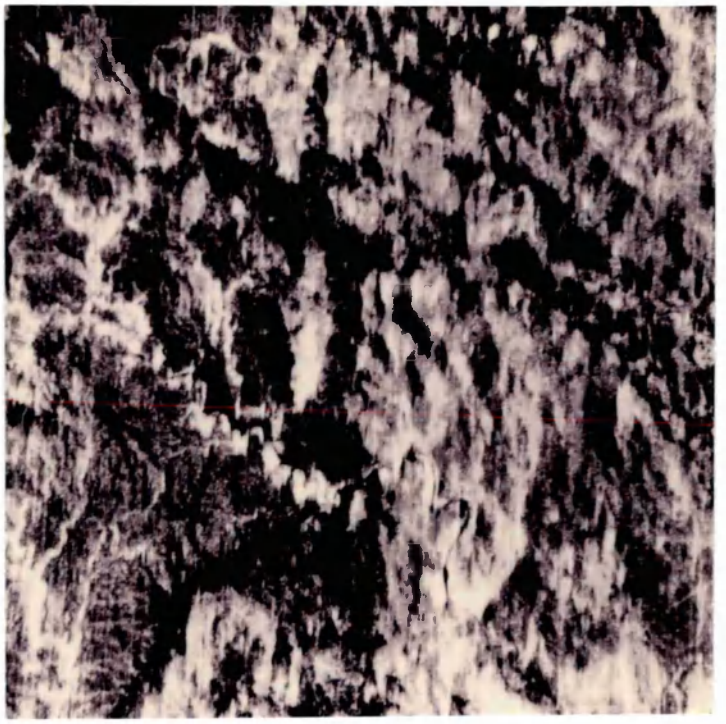

Plate 3.14 Level 2 OPS 6 cleaned using a PC 2 derived noise isolation mask. Compare this cleaned image with the original (Plate 2.7) and the ZNF output image (Plate 3.11).

5) Gradient filter noise isolation mask

Another technique which relies on some preprocessing of the original image prior to transformation into the frequency domain is that of the Gradient Filter Noise Isolation Mask. This technique requires one input OPS channel which clearly shows severe noise structures, i.e. OPS 6 (as seen in Plate 2.7). This single input channel is then used to produce a Gradient Filter (GF) using the following algorithm;

$$GF = (I (x, y) - I (x + 1, y)) + ((I (x, y) - I (x , y + 1)) \qquad [3.4]$$

where I is the input image (Castleman, 1979).

This algorithm will produce an output image which has high DN values in regions of high contrast, i.e. at edges, and has low DN values over homogeneous regions. The GF therefore enhances edges and produces an output image similar in appearance to that of an image convolved with a high pass filter. Figure 3.15 summarises the processing steps required to produce a GF image. If the input channel is chosen so that it contains minimum spectral or topographic edges the predominant enhancement seen in the GF will be that of the noise (Plate 3.15). The lack of textural information in OPS 6 due to the severe along-track image blur, makes this an ideal input channel.

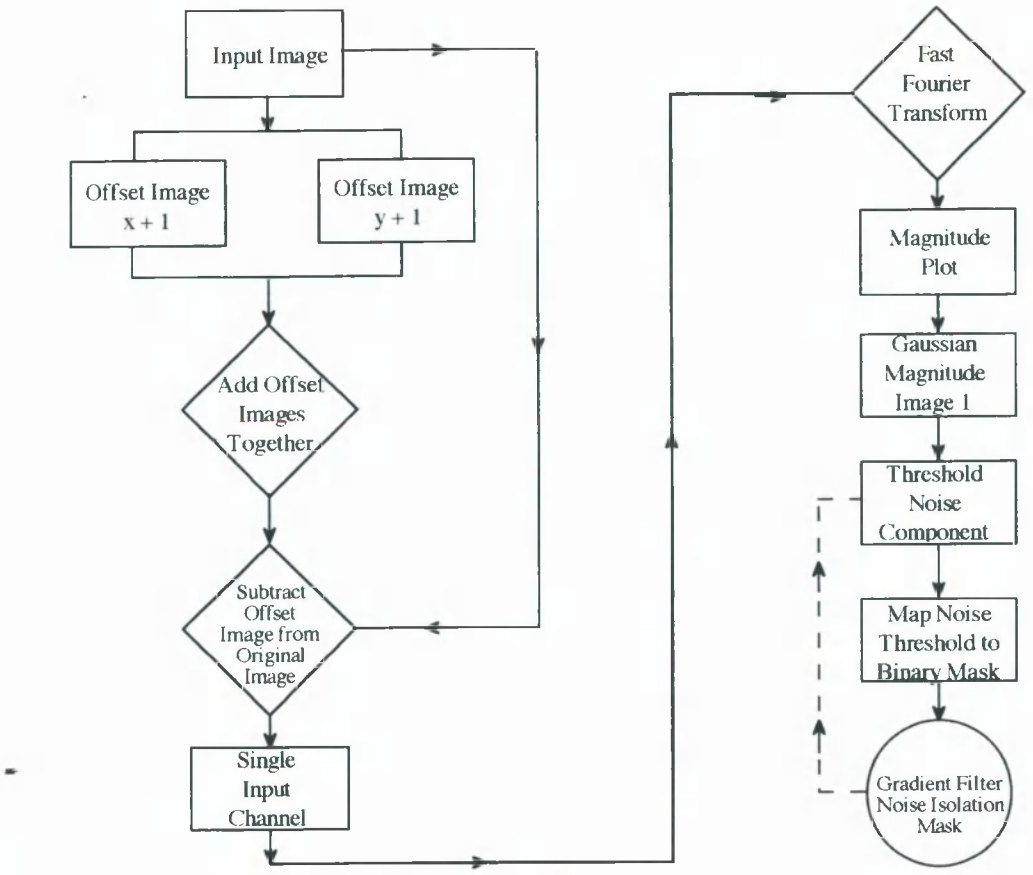

Figure 3.16 Flow diagram summarising the processing steps required to produce a Gradient Filter, from a single input channel, where x equals lines and y equals samples. Dotted line indicates the stages which may need to be repeated until a satisfactory threshold value for the mask is determined.

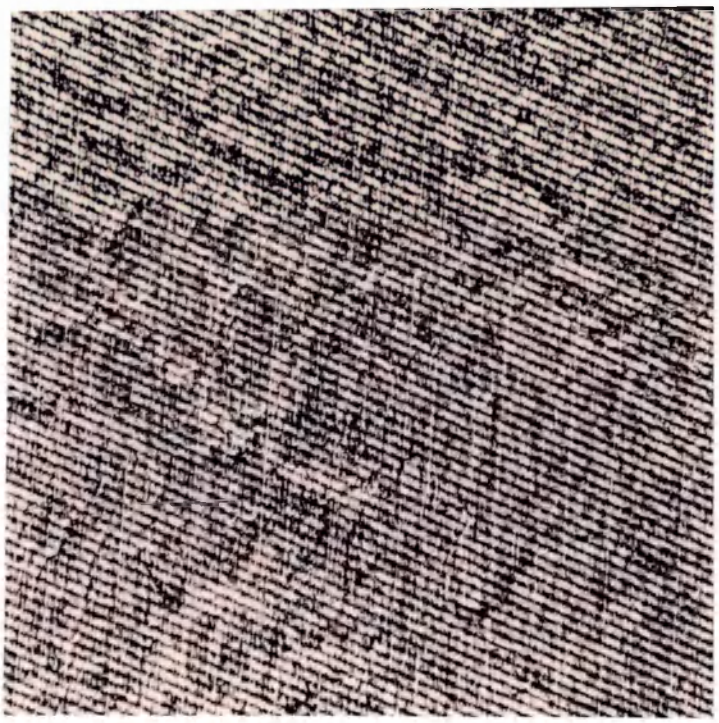

Plate 13.15 GF produced from the Level 2 OPS 6 input channel, note how the edges of noise structures are dominant over spectral or topographic boundaries.

Once the GF has been produced this can be used as the input image to be transformed into the frequency domain. The magnitude plot for this image (Plate 3.16) is very distinct as both the across- and along-track noise artifacts in the original input image have produced very clear high intensity spikes. The low frequency zone representing image data is almost non-existent. The primary noise components can now be identified in this image using the same technique as described in section 3.3.4(3). The offset nature of the GF also enhances the edge of the image data, which results in strong horizontal and vertical lines in the magnitude plot. Neither of these lines results in the loss of any real image data when they are incorporated into the mask. Once a threshold value has been determined it can be used to produce a binary mask image, which can then be used to multiply all OPS channels.

This technique reliably removes noise from all OPS channels of both Level 0 and Level 2 data. Plate 3.18 illustrates the results of this technique on Level 2 OPS 6. The most important criterion for this technique is that the region chosen in the original input image to be used to produce the GF has minimal topographic or spectral edge information. If the input image contains sufficient edges with an almost constant periodicity a spike may be produced in the magnitude plot which is difficult to distinguish from a noise spike. A possible geological context where this may occur would be within a sedimentary environment where the image shows well bedded sediments of an almost constant thickness.

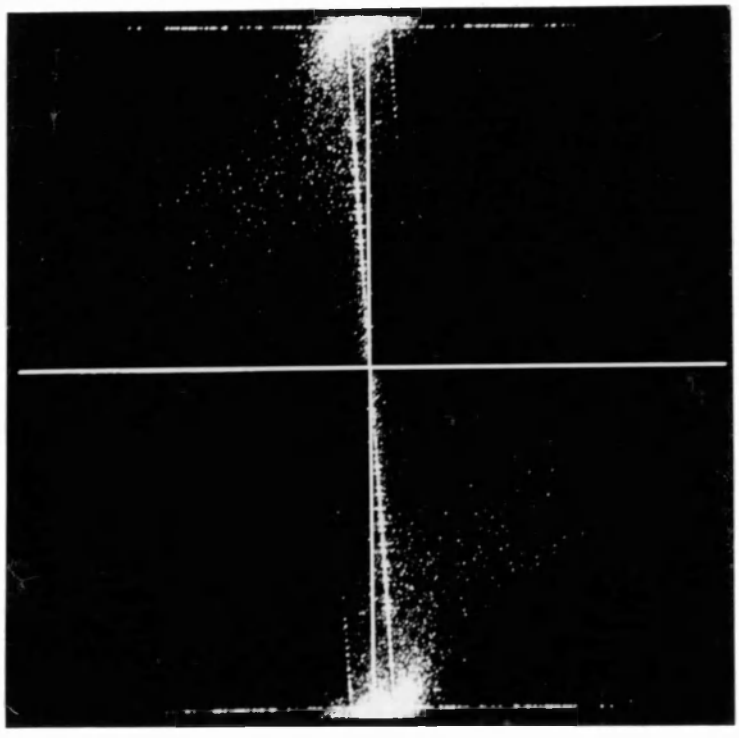

Plate 3.16 A magnitude plot of the GF, noise structures are shown very clearly at both high and low frequencies, real image data around the plot origin is very minimal. Refer to text for full description.

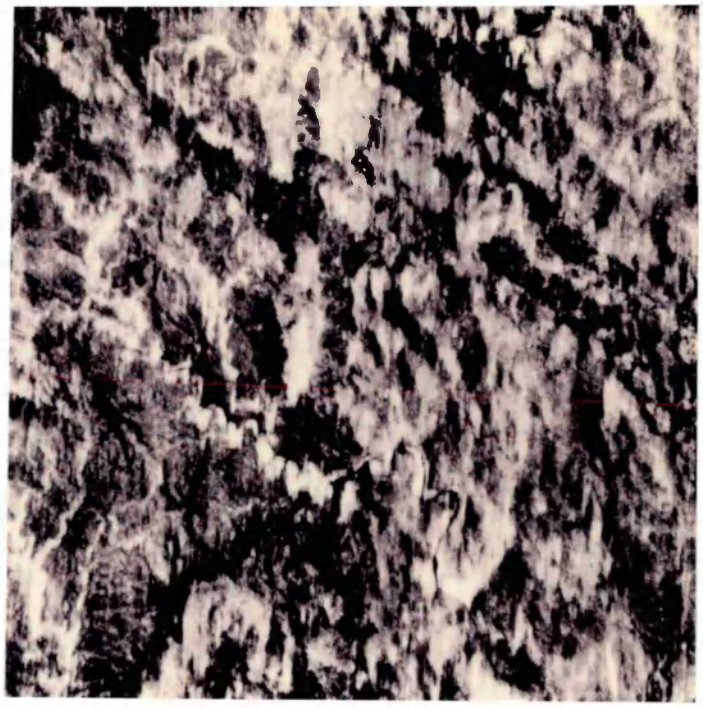

Plate 3.19 Level 2 OPS 6 cleaned using a GF mask, compare with the original (Plate 2.7), the ZNF output image (Plate 3.11) and the PC noise isolation mask image (Plate 3.14).

3.3.5 Noise removal in the frequency domain, special cases

Some of the techniques discussed in section 3.3.4 can be further refined if the available imagery covers an area of deep homogeneous water. If such imagery is available a subscene comprised entirely of water can be used to refine the masks produced by the Principal Component Noise Isolation and Gradient Filter techniques. However, these refinements should be regarded as special cases, as suitable areas of water may not always be available within a given data set. The lack of spectral information in a water subscene (compared to a land subscene) means that noise artifacts can be discriminated even more clearly, prior to the transformation into the frequency domain. Examples of a water based PC 2 image can be seen in Plate 3.18 and the corresponding magnitude image is shown in Plate 3.19. Similarly a water based OPS 6 GF is shown in Plate 3.20 and Plate 3.21 shows the corresponding magnitude image.

Both of the water derived input images (Plates 3.18 and 3.20) show very little spectral information, the most dominant features are the across- and along-track noise structures which are extremely clear. This results in magnitude plots (Plates 3.19 and 3.20) where nearly all of the high intensity spikes are noise related. Compared with the magnitude images from the land derived Principal Component Noise Isolation Filter (Plate 3.13) and the Gradient Filter (Plate 3.16) these new magnitude images

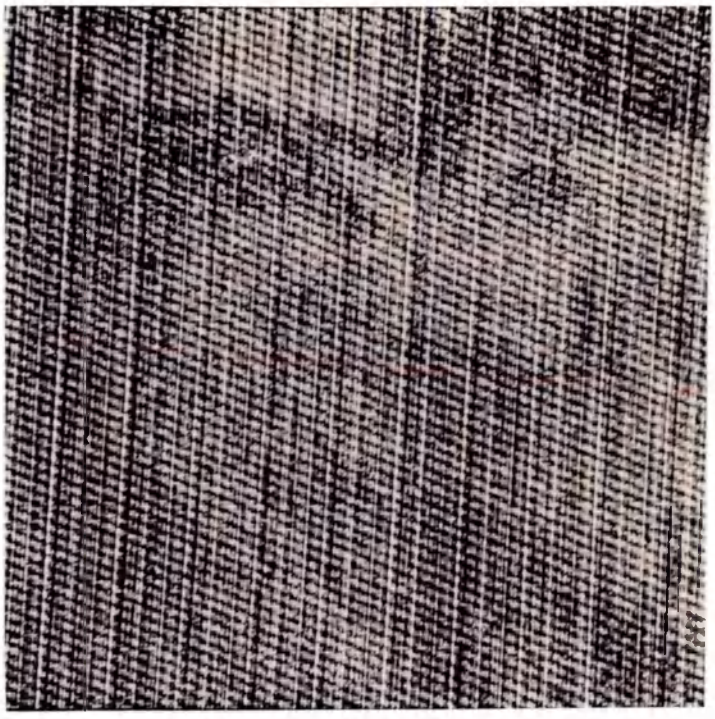

Plate 3.18 Water derived PC 2 image. This image shows predominantly across- and along-track noise structures, real image spectral variation is at a minimum.

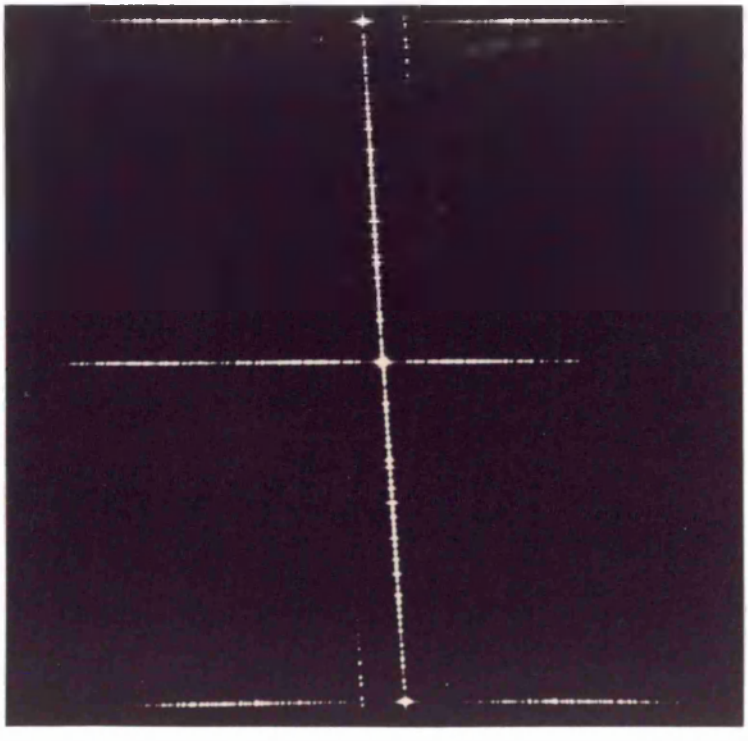

Plate 3.19 Magnitude plot derived from a water based PC 2 input channel (Plate 3.19). Compared with the equivalent land based magnitude image (Plate 3.14) all of the high intensity spikes visible are associated with spatial domain noise structures.

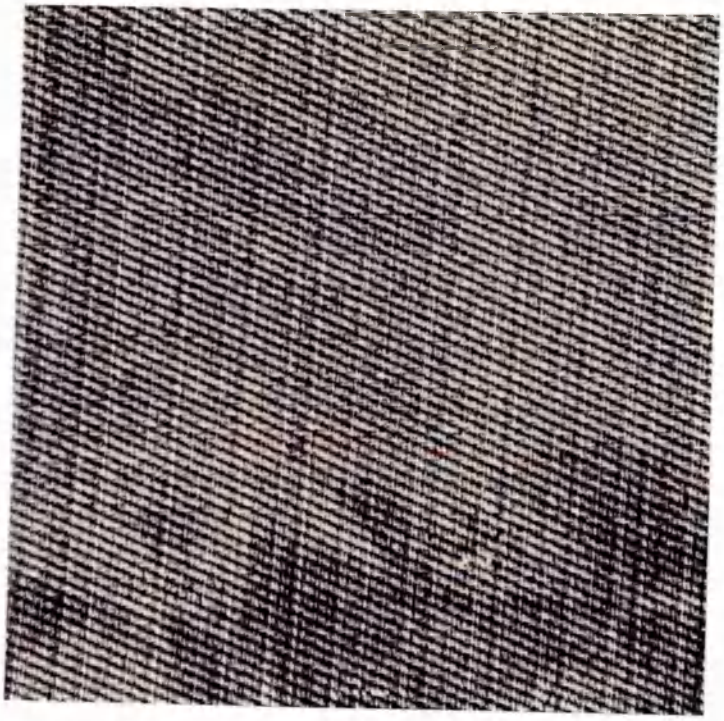

Plate 3.20 Water derived OPS 6 GF. This image shows predominantly across- and along-track noise structures, real image spectral variation is at a minimum.

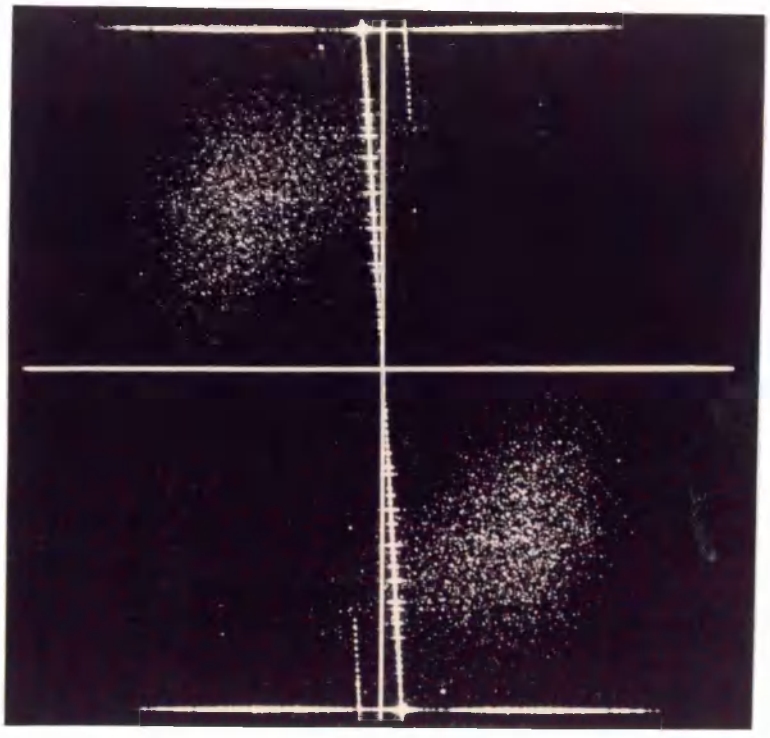

Plate 3.21 Magnitude plot derived from a water based OPS 6 GF input channel (Plate 3.20). Compared with the equivalent land based magnitude image (Plate 3.16) the majority of the high intensity spikes visible are associated with spatial domain noise structures. The high frequency zone seen on Plate 3.16, which is associated with spectral edges has been removed. However, a more diffuse zone at lower frequencies has been introduced. This zone may represent isolated random noise or speckle. Note how the water GF has also highlighted the image edges as seen in Plate 3.16.

contain no low frequency data zones associated with real image data. This means that these water based magnitude images can be used to produce more accurate noise masks.

Masks produced from water input images isolate noise spikes in the frequency domain so precisely that they can be used to clean any land subscene without fear of removing image detail. This is illustrated in Plate 3.22 which is a land region of OPS 6 (as per Plate 2.7) which has been filtered using a GF produced from a water input image. This filter has removed all of the spatial domain noise artifacts whilst preserving the real image data. A similar result would have been achieved if the water derived Principal Component Noise Isolation Mask had been used, as this is almost identical to the water derived GF.

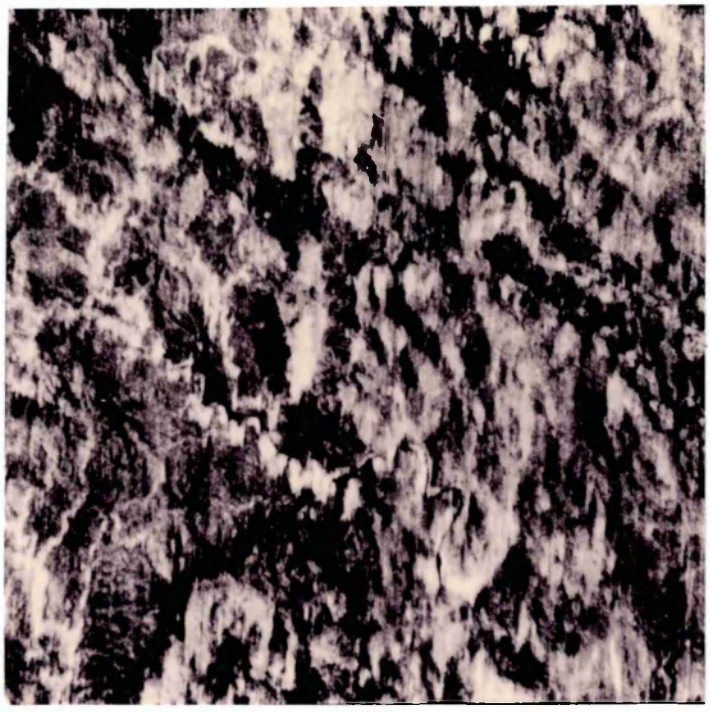

Plate 3.22 An example of Level 2 OPS 6 land data (as per Plate 2.7) which has been cleaned using a water derived noise isolation GF. All of the noise structures have been removed from this image, whilst the real image data have been preserved.

3.4 Summary of noise removal techniques

The complex inter-relationship of image data and superimposed noise structures means that processing in the frequency domain is required to remove OPS noise structures. The implementation of any frequency domain technique is quite time consuming and computationally demanding compared to spatial domain processing. However, the increased effort is rewarded by output images which are of a far greater quality. Frequency domain processing is able to remove noise artifacts whilst preserving real image data, whereas spatial domain techniques are only able to suppress the visibility of the noise component. Unfortunately this suppression usually results in the image detail you are interested in being suppressed by the same amount. When considering JERS-1 data, the loss of any real image detail is unacceptable as some OPS channels contain very little spectral or topographic information originally.

Once a user is familiar both with the frequency domain and with the representation of noise artifacts on magnitude plots, processing techniques can be tailored to produce optimum quality output images. All of the techniques described in section 3.3.4 can help to remove noise artifacts, although the best results are obtained by implementing either a Zonal Notch Filter (see 3.3.4 (3)), a Principal Component Noise Isolation Mask (see 3.3.4.(4)) or a Gradient Filter Noise Isolation Mask (see 3.3.4.(5)). In this study I found that the Gradient Filter Noise Isolation Mask produced some of the best results when applied to either Level 0 or Level 2 OPS channels.

It should be remembered that the noise removal techniques described here are far from exhaustive; many more are described in texts such as; Andrews and Hunt (1977), Castleman (1979), Gonzalez and Wintz (1977), Jain (1989), Niblack (1986), Pratt (1978) and Schowengerdt (1983). De Souza (1995) has also demonstrated that similar improvements to frequency domain masks can be achieved if the input image is first filtered using a high pass filter to enhance noise structures.

3.5 Brightness saturation

JERS-1 OPS images not only suffer from periodic and random noise structures, but also from brightness saturation. All OPS scenes have very small dynamic ranges, as a result of the data being quantised to only 6 bits (Ogasawara, 1995). This means that scenes of data, even those over arid regions which range from spectrally bright to dark, are only represented by a maximum of 64 DN values. This results in information being lost in extremely bright or dark regions. Gonzalez and Wintz

(1977) suggest that an image can be considered as being comprised of two components; (1) the amount of source light incident on the scene (illumination) and (2) the amount of light reflected from objects within the scene (reflectance). Illumination will vary only slightly over an image whilst reflectance will vary considerably, particularly at the junction of two different objects. Variations in illumination contribute towards the dynamic range of an image whilst reflectance variations contribute to image contrast. In the frequency domain, illumination is represented by low frequencies whilst reflectance is represented by high frequencies. This means that by applying a multiplicative filter in the frequency domain with weights greater or less than 1 DN (H_1 and H_2, Figure 3.17), the relationship of these two components can be changed, thereby changing the dynamic range and contrast of the image when transformed back into the spatial domain. This technique is known as Homomorphic filtering (Gonzalez and Wintz, 1977). Figure 3.17 shows a schematic representation of a homomorphic filter function which could be applied to a magnitude plot. This filter would tend to amplify the low frequencies whilst reducing the high frequencies, resulting in an extension of the dynamic range, whilst simultaneously reducing contrast.

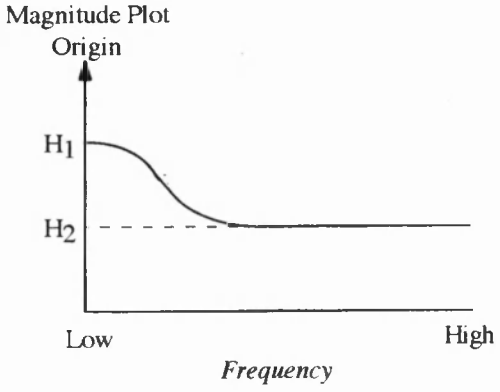

Figure 3.17 Schematic cross section of a Homomorphic Filter function.

De Souza *et al.*, (1996) suggest a similar approach to correcting brightness saturation, by utilising a gaussian mapping function to re-distribute the intensity values in the magnitude plot. This mapping improves the dynamic range, whilst slightly reducing contrast information. It is also simple to implement. Plate 3.23 shows an original Level 2 OPS 8 input channel (scene 208-262) complete with noise. A manually determined linear stretch has been applied to optimise image detail, although information is lost in both spectrally bright and dark regions. Plate 3.24 shows the same subscene after it has been processed in the frequency domain.

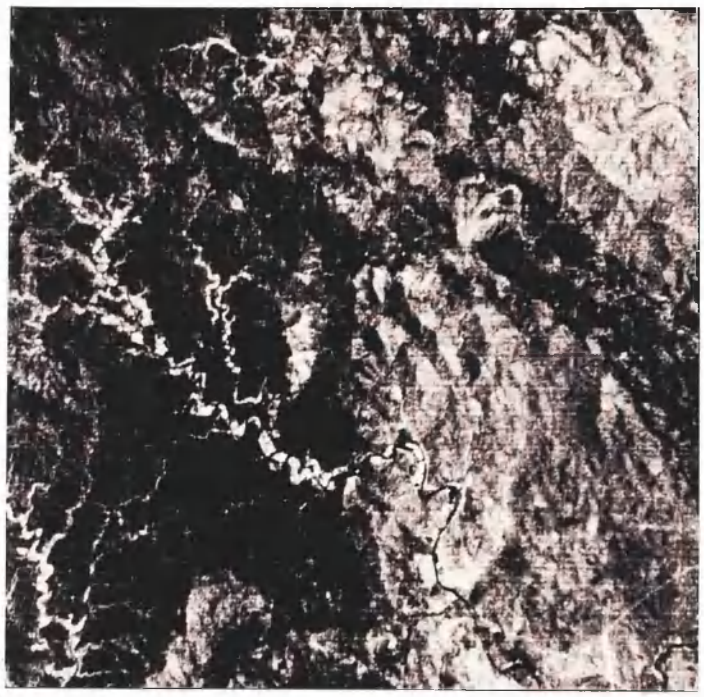

Plate 3.23 1024 x 1024 pixel subscene of Level 2 OPS 8 data. Note the noise content and the lack of image information in both spectrally bright and dark regions, despite the application of a linear stretch.

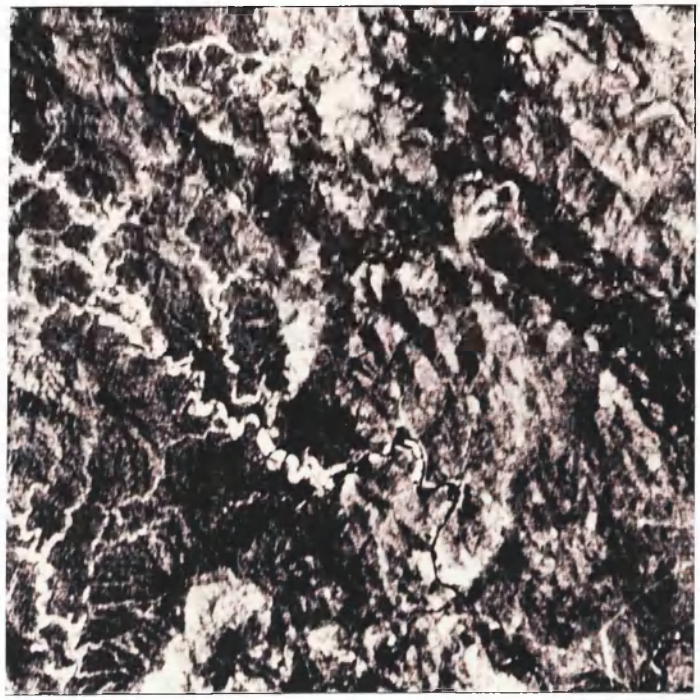

Plate 3.24 The same Level 2 OPS 8 subscene seen in Plate 3.23 after it has been processed in the frequency domain. Frequency domain processing has included the application of a GF to remove the noise and the application of a gaussian stretch to the magnitude component to redistribute the intensity values. This processing has removed the noise structures and the problem of brightness saturation. After the application of a linear stretch in the spatial domain spectral information is now visible in both spectrally bright and dark regions of the image.

Processing in the frequency domain has removed the noise structures by applying a GF mask. It has also removed the problem of brightness saturation by applying a gaussian stretch to the magnitude component, this has had the effect of redistributing the intensity values over a larger frequency range. Once the image is transformed back into the spatial domain, the application of a linear stretch results in information being visible in both spectrally bright and dark regions. This procedure modifies the original histogram (Figure 3.18a) so that the input DN values are redistributed over a larger DN range (Figure 3.18b). This technique is best applied only to scenes that exhibit a near normal distribution of intensities. Application of this technique to a bi-modal data distribution would result in the loss of some data. Note that this technique only improves the brightness and contrast of the dynamic range recorded by the sensor. Therefore if the sensor values are saturated at the time of data acquistion this technique will not improve the spectral information of saturated pixels, these pixels will remain saturated.

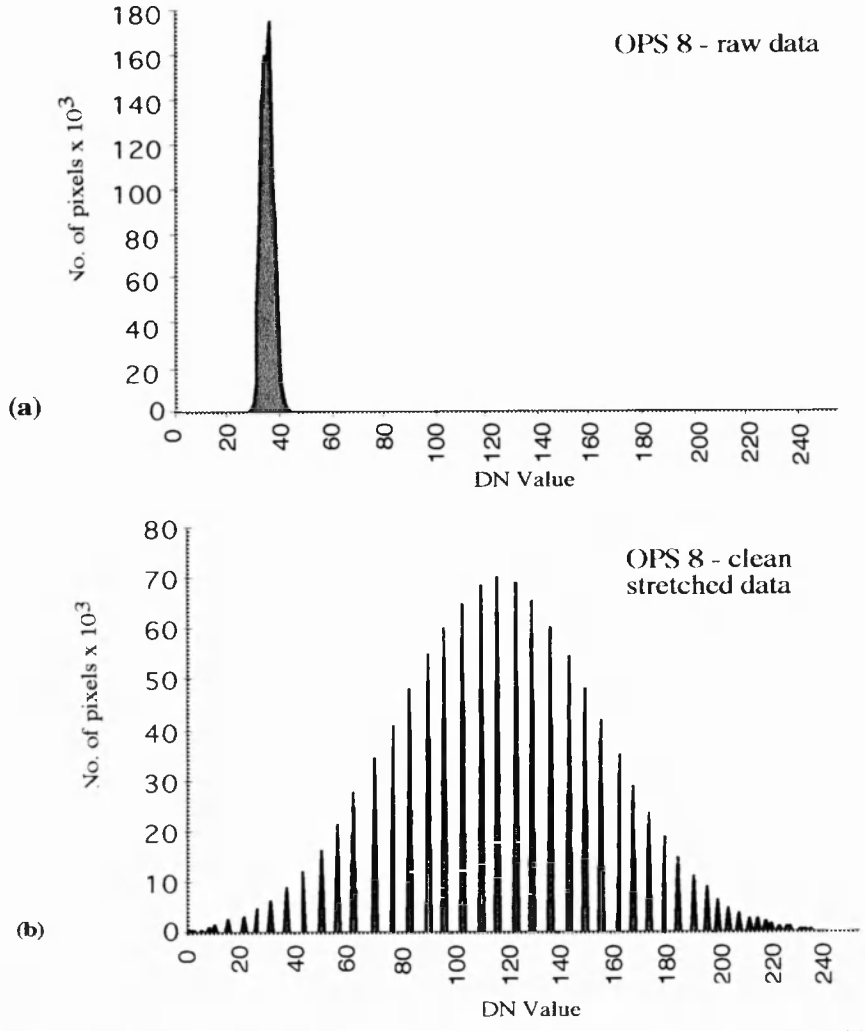

Figure 3.18 (a) Input histogram of a subscene of raw Level 2 OPS 8 data. (b) Output histogram of the same scene after it has been cleaned and has had a gaussian stretch applied to the intensities in the magnitude component. This has resulted in the redistribution of the original DN values over a larger range. Refer to text for a full description.

3.6 Quality of restored OPS images

This chapter has described a number of noise removal techniques which are capable of completely removing, or suppressing the majority of the noise artifacts associated with all channels of both Level 0 and Level 2 OPS data. Frequency domain techniques used in conjunction with brightness saturation filters can greatly improve the visible quality of the data. However, it must be remembered that these techniques only improve image quality by removing noise structures, they do not improve the quality of the real image data. In some cases even a perfectly cleaned OPS 6 image will contain very little useful spectral or topographic information. This is illustrated in Plate 3.25 which shows a subscene of FFT cleaned Level 2 OPS 7 imagery. Despite the FFT processing removing the vast majority of the noise structures associated with this channel the resultant image is still of a very poor quality. This is because the quality of the original data is extremely low due to major sensor defects. Therefore even after successful noise removal the image contains little spectral information. OPS noise artifacts such as low dynamic ranges and image blur induced by the differing responses of odd and even CCDs cannot be overcome by noise removal techniques. Yamaguchi *et al.*, (1995) suggest that image blur can be reduced by the application of a simple algorithm which models CCD response delays, however this is a very time consuming process which has to be applied independently to every scene.

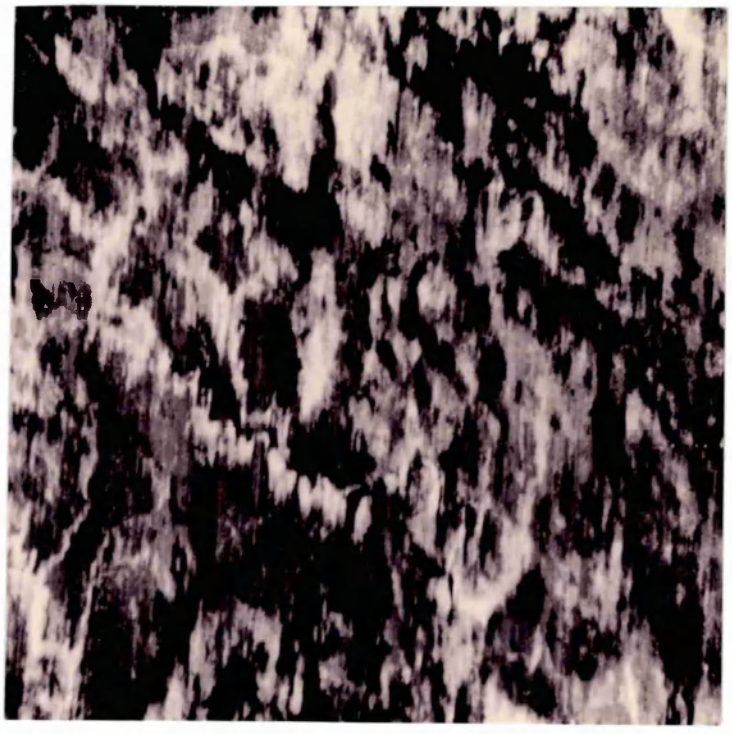

Plate 3.25 Example of Level 2 OPS 7 imagery after it has been cleaned using FFT techniques. The majority of the noise associated with this channel has been removed, however the resultant image is still of a very low quality due to the severity of the original noise problems.

The application of the noise removal techniques described in this chapter prior to image interpretation will significantly improve the amount of useful geological information that is extractable from OPS 1, 2, 3, 5 and 8. The application of these techniques to OPS 6 and OPS 7 will improve their quality, but the resultant imagery will be of an extremely poor 'spectral' quality due to the lack of real image data in the original imagery.

4.0 - The potential of TM and OPS data to discriminate Oman igneous rocks based on their spectral responses

4.1 Introduction

4.1.1 Introduction to the Oman Mountains

The Oman Mountains, also known as the Hajar or Eastern Hajar (Lippard *et al.*, 1986) lie at the eastern extremity of the Arabian sub-continent, and form a broad arc parallel to the Gulf of Oman (Figure 4.1, inset). They extend for approximately 800 km north-south (26° N - 22.5° N) and have an average width of 75 km, increasing to 130 km at their widest central part. They form a very rugged terrain mostly between 500 m and 1500 m, although heights of 3000 m can be found on Jebel Akhdar.

The Oman Mountains are geologically distinct from the rest of the Arabian Peninsula as they form a part of the Alpine-Himalayan fold belt that extends from the Western Mediterranean to the Far East (Lippard *et al.*, 1986). The geology of the mountains is dominated by the Semail Nappe, which is a very large thrust sheet of mid-Cretaceous ophiolitic rocks.

4.1.2 Introduction to the Oman ophiolite

The Oman, or Semail ophiolite is the largest example of intact ocean floor rocks exposed on land, covering approximately 20,000 km^2. Formed by sea floor spreading about 95 Ma ago it was emplaced over the Arabian continental margin by about 70 Ma (Welland and Mitchell, 1977). Today the Semail Nappe has been broken up, as a result of syn- and post emplacement deformation, into twelve tectonic 'blocks' between 600 and 7000 km^2, see Figure 4.1.

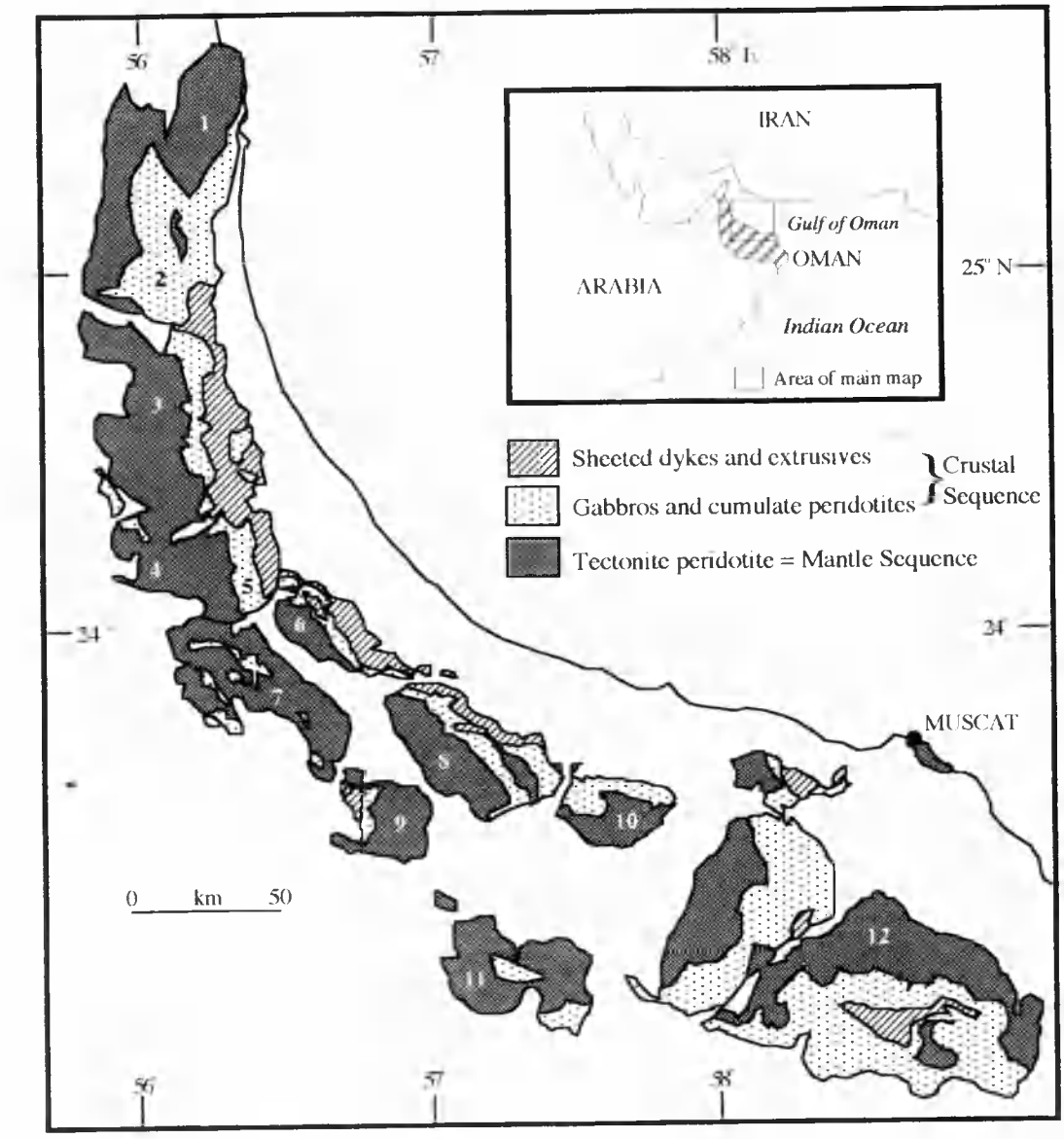

Figure 4.1 (Inset) Location map showing Oman. (Main) Schematic diagram after Lippard *et al.* (1986) showing the distribution of the ophiolite along the Gulf of Oman coastline. The numbers refer to the main ophiolite blocks, these are; (1) Khor Fakkan (870 km^2), (2) Aswad (1700 km^2), (3) Fizh (2610 km^2), (4) West Jizi (590 km^2), (5) Salahi (940 km^2), (6) Sarami (560 km^2), (7) Wuqbah (1470 km^2), (8) Haylayn (1380 km^2), (9) Muqniyat (680 km^2), (10) Rustaq (600 km^2), (11) Bahlah (810 km^2) and (12) Ibra (6740 km^2).

Within each of these blocks the original internal stratigraphy of the ophiolite is more or less intact. However, internal low angle thrust faults have led to tectonic repetition of the ophiolite sequences and in some instances overturning (Coleman, 1977). Ophiolite stratigraphy can be broadly divided about the Petrological Moho into two major units;

1) A lower 'Mantle Sequence' believed to represent the upper part of the sub oceanic mantle (Lippard *et al.*, 1986). This is comprised of variably serpentinised peridotites, mainly tectonized harzburgites with associated lherzolites and dunites.

2) An upper 'Crustal Sequence' consisting of an assemblage of magmatic cumulate peridotites and gabbros (the Layered Series) overlain by non-layered plutonic rocks (High Level Intrusives), a Sheeted Dyke Complex and an extrusive sequence of lavas interbedded with and overlain by sediments. These units (except for the sediments) are cut late-stage plutonic and hypabyssal rocks termed Late Intrusive Complexes.

The complex relationships between these units are illustrated in Figure 4.2.

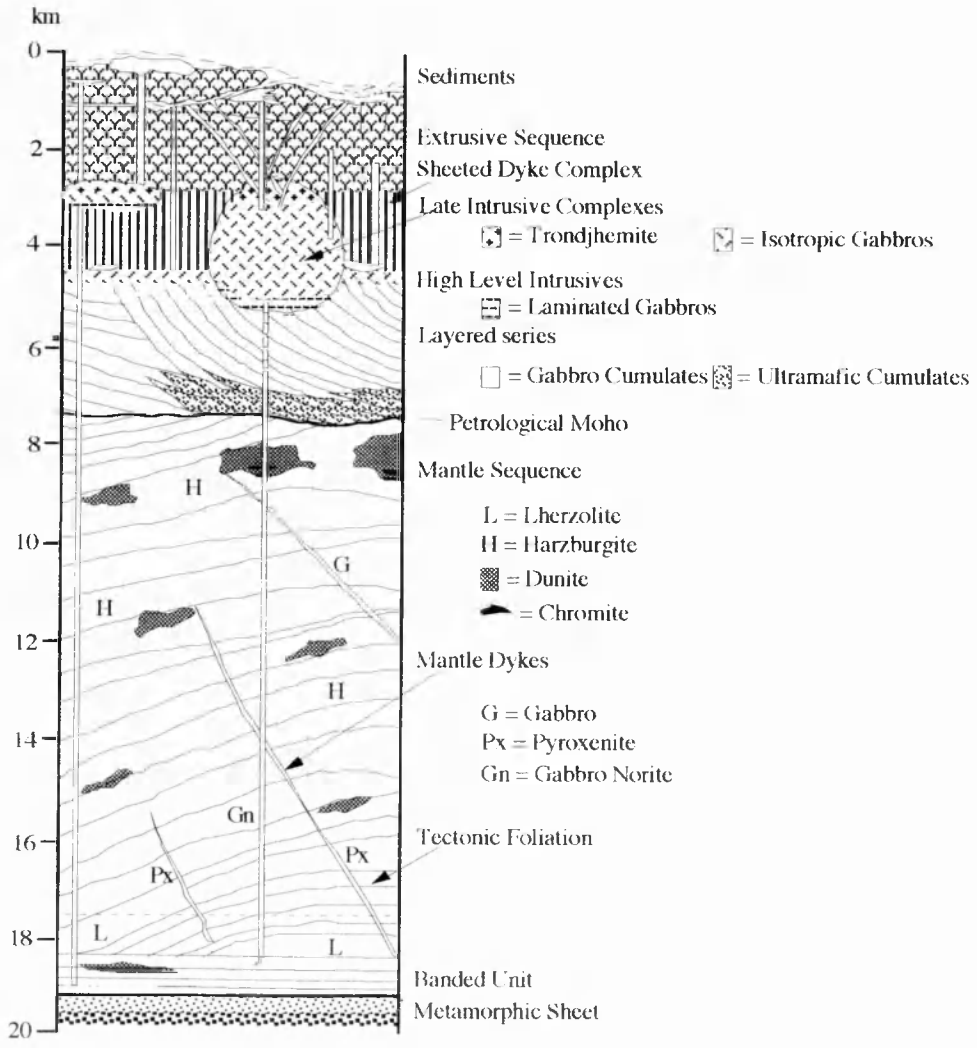

Figure 4.2 Generalised cross section through the Oman ophiolite after Lippard *et al.* (1986), see text for a complete description of the lithologies.

The base of the section is marked by a major thrust which separates the ophiolite and its basal metamorphic sheet from the underlying rocks. The lower part of the mantle sequence is then marked by up to 500 m of mylonitised harzburgites, lherzolites and dunites. These units are highly deformed and are often markedly banded and are hence known as the Banded Unit (Lippard *et al.*, 1986). The remainder of the mantle sequence consists of variably serpentinised tectonised peridotites, predominantly harzburgites, which grade locally into lherzolite and which contain numerous bodies of dunite. The whole sequence in turn is cut by numerous dykes, veins and pods of ultramafic and mafic rock types.

The harzburgites form a very distinct mountainous terrain ranging to 1500 m, which is deeply dissected by numerous steep gullies feeding into larger wadis. Fresh exposures of harzburgite are pale green-grey, but the majority of surfaces are very dark green-grey-brown due to surface weathering. The mantle sequence is comprised of approximately 85-95% harzburgite (with local gradations into lherzolite) and 5-15% dunite (Lippard *et al.*, 1986). Olivine dominates the mineralogy with the harzburgites containing 75-85% medium to coarse grained olivine, with 15-25% orthopyroxene, although clinopyroxene can sometimes account for up to 5%. Chrome spinel (chromite) is often present as an accessory mineral, as well as the alteration products of serpentine, which can sometimes account for as much as 80% of the rock mineralogy (Coleman, 1977). Lherzolite is an orthopyroxene-rich harzburgite which is associated with the base or lower edge (1 - 2 km) of the mantle, typical examples may contain as much as 20-25% orthopyroxene. Dunite bodies vary considerably in their shape and size and in their distribution throughout the mantle sequence. In outcrop they can be distinguished from harzburgites as they weather to a paler brown colour, whilst in thin section they can recognised by their very high olivine content >98%, although like harzburgites they are often severely serpentinised. Chromite occurs locally within the dunite in layers, pods and lenses, where it can form 100% of the mineralogy. In some regions it occurs in bodies large enough to be economically significant. All of these mantle lithologies are cut by small (1 cm to 1m thick) ultramafic and mafic dykes. Despite the large number of these dykes they represent only a very small percentage of the volume of the mantle sequence.

The lower part of the crustal sequence is dominated by the Layered Series which consists of a complex association of gabbros (75% outcrop) with interbedded layered peridotites (25% outcrop, dunites, wehrlites and pyroxenites). The layered series rests unconformably on the mantle sequence along the Petrological Moho, and grades upwards into the High Level Intrusives. The Layered Series forms significant hills of equivalent height to those of the mantle sequence, although the topography has a more

'rounded' appearance. Lower slopes are often covered with large locally derived boulders, which tend to weather to a very dark red-brown. Elsewhere outcrops weather to a light beige-red-brown. The primary minerals within the layered series are plagioclase, clinopyroxene, olivine, chrome spinel, orthopyroxene, hornblende and titanomagnetite (Lippard *et al.*, 1986). The relative percentages of these minerals tends to vary over layers ranging from 0.5cm to 2m thick resulting in layers of olivine-rich gabbro, gabbro norite and troctolite, interspersed with ultramafic rich layers of dunite, wehrlite and pyroxenite. These layers are laterally extensive and large scale (tens to hundreds of metres thick) cyclic units alternating between ultramafic and mafic lithologies can be traced vertically, until the non-layered isotropic gabbros are encountered at the top of the sequence (Hopson and Pallister, 1980).

The isotropic gabbros form a thin discontinuous unit between the Layered Series and the overlying Sheeted Dyke Complex. These gabbros can be differentiated from those of the Layered Series as they tend to be finer grained and they lack well defined igneous layering. Mineralogically they differ by containing significantly less olivine whilst having more hornblende and alteration minerals such as actinolite. The top of this unit is marked by the increased occurrence of plagiogranites (quartz diorites, tonalites and trondhjemites) which can locally coalesce to form a thin sheet. Lithologies such as trondhjemites can be easily recognised in fresh outcrop because of their very bright white-beige colour. Mineralogically these units are distinct because of their high plagioclase (50-90%) and quartz contents.

The Late Intrusive Complexes comprise peridotites, gabbros, diorites and plagiogranites and are mineralogically very similar to the units composing the high level intrusive sequence. However, they can be distinguished by their location in the crustal sequence and by the nature of their cross cutting intrusive contacts. The location of intrusive bodies, for example, wehrlite within crustal gabbros, can be very important as they are often indicative of the mantle-crust transitions zone (Benn *et al.*, 1988).

The sheeted dyke complex lies between the underlying plutonic complex and the overlying extrusive sequence. In prime localities the sheeted dyke complex can be seen to be made up of 100% near vertical dykes, ranging in width from 10cm to 4.5m (Lippard *et al.*, 1986). These produce a very distinct terrain of jagged ridges, elongated parallel to the trend of the dykes. Mineralogically the dykes consist of very fine grained plagioclase, clinopyroxene, titanomagnetite and alteration products such as actinolite, epidote and chlorite. Overlying the sheeted dyke complex are basaltic pillow lavas with some andesite to rhyolite extrusives, which are in turn overlain by

deep water sediments. In places the lavas may contain small massive sulphide deposits formed by sea-floor oxidation of sulphides (Fleet and Robertson, 1980).

The units described above tend to be fairly uniform throughout the twelve ophiolite blocks although the amount each unit is exposed varies between blocks. For this reason satellite imagery and field data are considered in this study for two additional regions (Salahi and Fizh) outside of the main Maqsad study region, see Figure 4.3.

4.1.3 Suitability of Oman for remote sensing studies

The Oman ophiolite is an excellent region to use to evaluate JERS-1 OPS data. Its arid climate means that vegetation and soil cover are minimal, resulting in excellent exposure of bedrock, although some small areas can be obscured by the accumulation of locally derived scree. Surface weathering is not too much of a problem in this region as a severe iron manganese-rich desert varnish does not form (Pontual, 1990), unlike some arid regions of the world.

The very rugged nature of the terrain makes consistent ground based mapping very difficult. Mapping is mostly confined to water worn wadi courses as traverses beyond these are very time consuming. Remotely sensed imagery can therefore provide valuable geological information for poorly accessible regions. Satellite imagery provides both a synoptic view and a data set which can be enhanced to a consistent standard for large areas. This has been demonstrated by previous remote sensing studies of Oman, which have used Gemini IV photography (Wilson, 1969), and imagery from Nimbus III High Resolution Infrared Radiometer (HRIR) and Nimbus IV Temperature Humidity Infrared Radiometer (THIR) (Pohn *et al.*, 1974), Landsat MSS (Moody, 1974; Carlson and Stoibier, 1977; Rothery, 1982), Landsat TM (Abrams *et al.*, 1986, Rothery *et al.*, 1987, Pontual, 1990) and SPOT (Chevrel, *et al.*, 1991). Aerial photography at various scales has also been widely used.

Moody (1974) was the first to publish an MSS scene covering an area of the Oman mountains, although Carlson and Stoibier (1977) were the first to produce a geological map (scale 1:250,000) for parts of the Jizi, Fizh and Salahi blocks from classified MSS imagery. Rothery (1982) used MSS imagery to map the Wuqbah block in considerable detail, relying on both the visual interpretation of processed data and on image classification based on user-defined training sets. This combination of techniques allowed the major ophiolite lithologies to be discriminated over entire MSS scenes.

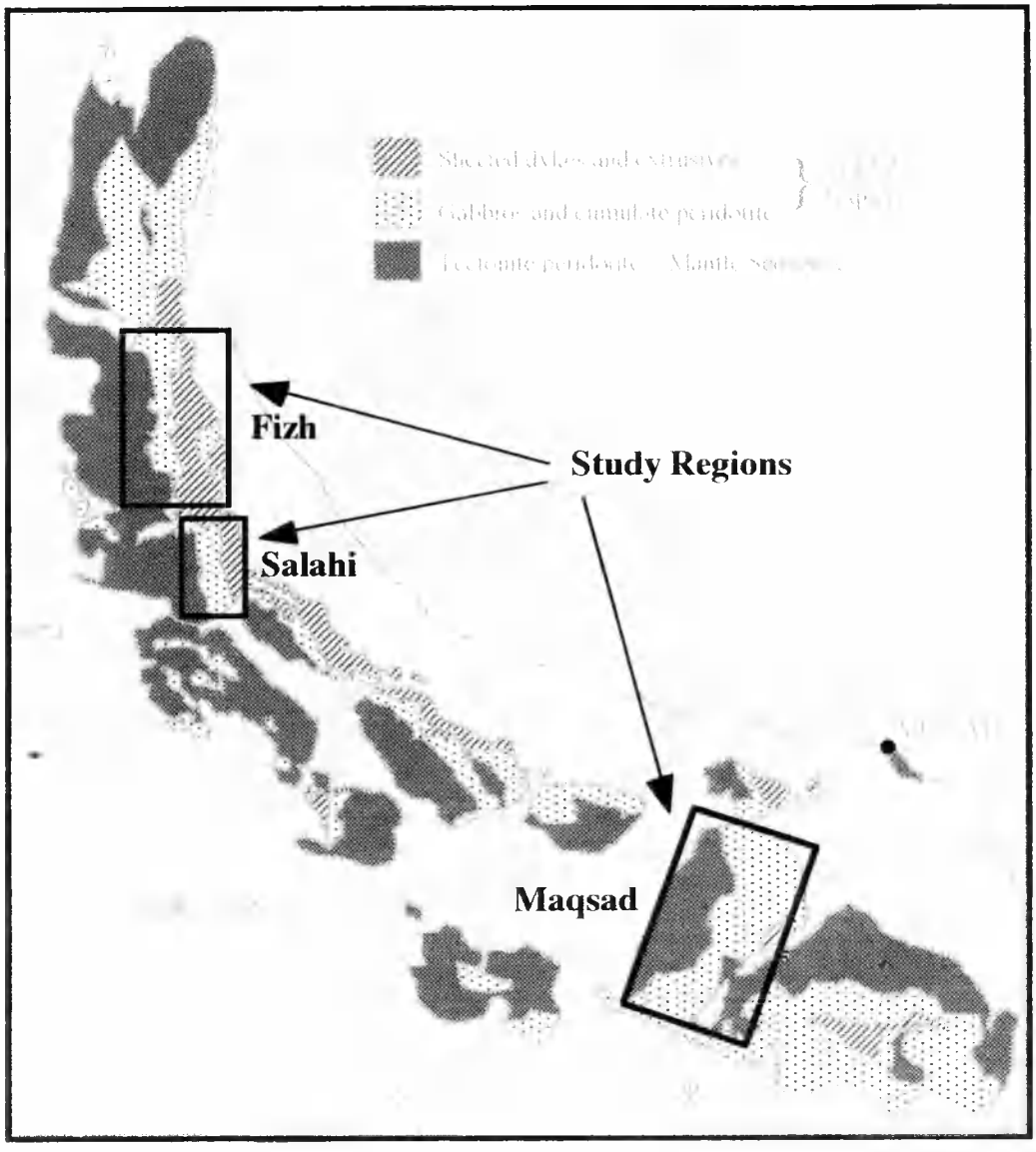

Figure 4.3 Approximate limits of the study regions used in this project, see chapter 5 for a full description.

4.2 Spectral responses of Oman igneous rocks

To acquire the maximum lithological information from remotely sensed imagery it is important that the spectral responses of the rocks in the target areas are known as this allows distinguishing features to be determined.

4.2.1 Principles of spectral absorption

Rock forming minerals have characteristic and often distinct spectral signatures in the 0.4 - 2.5 μm part of the spectrum, due to absorption features caused by electronic and vibrational processes.

Electronic processes consist of crystal field effects, conduction bands and charge transfer effects. Conduction bands and charge transfer effects cause a pronounced decrease in reflectivity at wavelengths < 0.6 μm (Blom *et al.*, 1980), whilst specific absorption features at these wavelengths tend to be due to the charge transfer in the Fe-O bond. Crystal field effects associated with transition metal ions cause several absorption features, whose locations vary depending on the metal involved, the charge and the crystal co-ordination. Ferrous ions can produce absorption features centred at 0.65 μm, 1.0 - 1.1 μm and 1.8 - 1.9 μm or 2.2 - 2.3 μm depending on the crystal structure, whilst ferric ions produce absorptions at 0.65 μm and 0.87 μm. Absorption due to crystal field effects can also occur at wavelengths < 0.6 μm but these are weak features which tend to be obscured by those associated with conduction bands and charge transfer. Vibrational processes tend to be associated with OH stretching and Mg-OH, Al-OH bending modes. Al-OH produces absorption features at 2.2 μm whilst Mg-OH produces absorption bands at 2.3 μm. These absorptions often occur together although one absorption will usually be stronger than the other, i.e. if a strong 2.2 μm (Al-OH) absorption is present a weak 2.3 μm (Mg-OH) absorption may be present, and vice versa (Blom *et al.*, 1980). Al-OH and Mg-OH absorptions tend to be associated with clays, micas and amphiboles. The carbonate ion CO_3^{2-} produces a vibrational absorption feature at 2.35 μm (Hunt and Salisbury, 1971). Absorptions produced by electronic processes tend to be broad and can be distinguished from vibrational features which are relatively sharp and narrow. A very comprehensive description of electronic and vibrational processes for common rock forming minerals can be found in Hunt and Salisbury (1970).

Whole rock spectra are more complex than those of individual minerals. Rock spectra are characterised by the minerals which compose the rock, and by alteration products, impurities and surface weathering. Small variations in any of these components can result in notable changes in the overall spectral signature. Spectral signatures at outcrop scale can also vary greatly due to the mixing of more than one lithology.

4.2.2 Sample collection and spectral measurement

Unfortunately a field portable spectroradiometer was not available during the period of this study so no *in situ* spectral measurements of the ophiolite lithologies where taken. Instead a total of 125 hand samples representing the ophiolite lithologies were collected during two field seasons, for lab based measurements. These samples were collected from numerous locations within the Maqsad, Fizh and Salahi regions (see Figure 4.3).

Preliminary analysis of the processed TM data was used to guide sample collection on the first trip as OPS data were not available at this time. On the second trip sample collection was targeted at specific spectral differences seen on the OPS data. Care was taken that all the samples collected were located away from wadi courses (used as lines of traverse), so that they had not been adversely weathered by seasonal water flow. Care was also taken to try to collect samples which best represented the lithology with regard to variations of mineralogy and weathering at outcrop scale.

Lab based spectral measurements were made using a GER IRIS Mk IV spectroradiometer. This instrument was supplied by the Natural Environmental Research Council Equipment Pool for Field Spectroscopy (NERC-EPFS). The GER IRIS Mk IV has a spectral range of 0.35 - 3.0 μm with a spectral bandwidth of 2nm over the range 0.35 - 1.0 μm, 4nm over the range 1.0 - 1.8 μm and 5nm over the range 1.8 - 3.0 μm. Its field of view is a rectangular area 6° x 1.5°. Simultaneous measurements of a target and a reference panel are acquired, allowing measured spectra to be easily converted to absolute reflectance values. Illumination for lab based measurements was provided by a stabilised 1000W halogen lamp. Figure 4.4 shows the configuration of the IRIS Mk IV lab set up.

A minimum of four spectral measurements were taken for each sample on both weathered and fresh surfaces. The average of these measurements was then calculated to produce a representative fresh and weathered spectrum for each sample.

4.2.3 Measured reflectance spectra

During the course of this study approximately 1800 spectral measurements (including repeat measurements) were made. Emphasis was given to collecting representative spectra of weathered surfaces as these are the surfaces which dominate the reflectance values recorded by satellite platforms. The approximate location of the Maqsad sample localities are shown in Appendix 3.

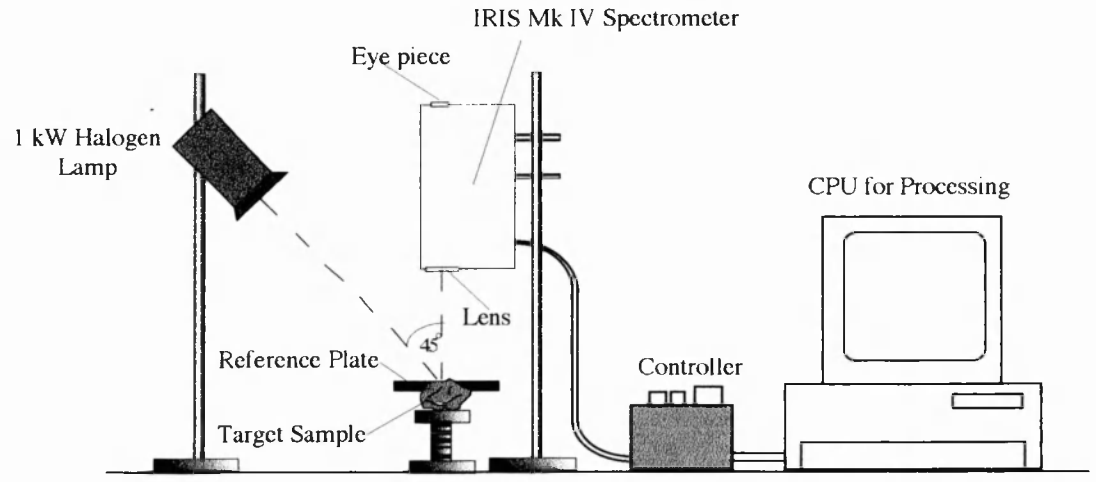

Figure 4.4 Schematic figure showing the IRIS Mk IV spectroradiometer set up in a lab environment to measure the spectral reflectance from a rock sample.

Many of the ultramafic and mafic lithologies in Oman develop a dark red weathered surface, caused by the presence of ferric iron in the rock surface. Despite the often very dark nature of this surface previous spectral studies of Oman igneous rocks (Pontual, 1990) have shown that it does not greatly affect the broad overall spectral response of these lithologies. The greatest differences tend to occur in the visible to NIR part of the spectrum, where the weathered spectra is dominated by a strong drop-off in reflectance at wavelengths less than 0.60 μm, caused by an intense Fe^{3+}-O charge transfer in the ferric oxide on the weathered surface (Pontual, 1990). Spectra of weathered surfaces also tend to exhibit higher overall reflectance values at wavelengths greater than 1.0 μm, than those of fresh surfaces. Pontual (1990) concluded that the majority of 'whole' rock spectral absorption features are preserved, despite the dark nature of the Oman surface weathering, with the exception of the darkest weathered surfaces where absorption features at wavelengths less than 1.40 μm tend to be either lost or significantly quenched.

Illustrated in this section are sample reflectance spectra representing the range of lithologies associated with the Oman ophiolite in the areas of interest. The aim of this section is to introduce the spectral responses of the common ophiolite lithologies and to try to explain some of the characteristic absorption features visible in terms of their mineralogy. The spectra are divided into either mantle or crustal lithologies. The next section (4.2.4) considers how representative these example spectra are with regard to spectral variation within lithologies. Finally section 4.2.5 summarises diagnostic spectral features associated with the common ophiolite lithologies.

1) Mantle lithologies

Mantle lithologies are dominated by ultramafic rocks such as periodites (lherzolites, harzburgites and dunites), serpentinites, cumulate peridotites and late peridotites, all of which tend to be altered to some degree by either low or high temperature serpentinisation.

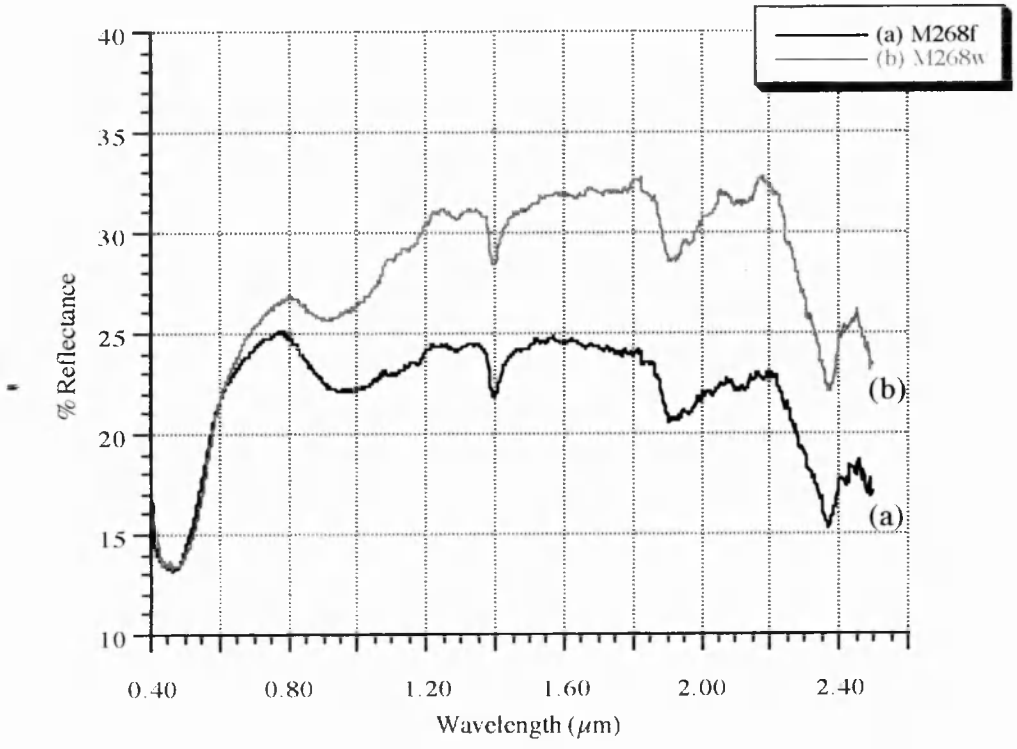

Figure 4.5 Lab reflectance spectra of a sample of lherzolite; (a) fresh surface M268f and (b) weathered surface M268w. Refer to text for a full description.

Lherzolite sample (M268) collected from the Maqsad region. The thin section shows that this sample is approximately 70% olivine, 15% orthopyproxene, 4% clinopyroxene and 11% serpentine, contained mainly in thin veins and cracks. The spectrum of a relatively fresh sample (Figure 4.5 (a)) shows a number of pronounced absorption features. A strong ferrous iron absorption associated with olivine is centred at 1.0 μm, with a weak side band at 1.3 μm (Hunt *et al.*, 1973). The associated olivine side band at 0.82 μm is not visible. A strong ferrous absorption feature occurs at 0.4 - 0.5 μm. Strong serpentine absorption features in the form of molecular water bands can be seen at 1.4 μm and 1.9 μm along with a much weaker feature at 2.1 μm. Mg-OH features indicating the alteration of olivines to serpentine are visible between 2.3 - 2.4 μm. A weak ferric ion feature associated with serpentine

alteration of olivine or pyroxene is visible at 0.7 μm. Small ferrous ion absorptions are visible at 0.63 μm and 1.85 μm. The 1.85 μm absorption and an inflexion at longer wavelengths (2.3 μm) may be a result of ferrous iron in the pyroxenes. The spectrum shows quite a broad peak in reflectance between 1.45 μm and 1.80 μm, which is probably due to the combined reflectance maximum of orthopyroxene (1.4 μm), clinopyroxene (1.6 μm), olivine (1.7 μm) and serpentine (1.7 μm).

The weathered spectrum for the same sample (Figure 4.5 (b)) shows slightly higher overall reflectance values. Absorption features are not as pronounced as those on the fresh sample. A strong ferrous ion absorption associated with olivine is evident, but this has shifted from 1.0 μm to 0.9 μm. This is due to orthopyroxene which tends to broaden this feature towards shorter wavelengths. The weak 1.3 μm side band feature associated with olivine is visible, but the accompanying feature at 0.82 μm is not. The strongest ferrous absorption occurs at 0.4 - 0.5 μm. Serpentine hydroxyl bands occur at 1.4 and 1.9 μm, although these are not as pronounced as those seen on the fresh spectrum. Other weak serpentine absorption features are evident at 2.1 μm and 2.3 - 2.4 μm. The weak ferric features seen in Figure 4.5 (a) at 0.63 μm and 0.7 μm are no longer visible.

Harzburgite spectra can vary greatly due to changes in primary mineralogy, localised segregation of olivine and orthopyroxene into sub-parallel bands, and the degree of weathering and serpentinisation. It is therefore very difficult to collect hand specimens which are representative of the harzburgite over large areas. Figure 4.6 (a) shows the spectrum of a reasonably fresh sample of harzburgite (M056f) which contains only 10-15% serpentine, 75-80% olivine and 5% orthopyroxene. The spectrum shows some very clear absorption features, although it is slightly noisy due to the low variations in reflectance percentage (<6%). The largest absorption feature at 0.4 - 0.5 μm is a ferrous absorption. Another pronounced ferrous absorption feature due to olivine is visible at 1.0 μm, along with one of the characteristic side bands at 1.3 μm. The maximum reflectance near 1.7 μm (excluding the noise induced peak at 1.81 μm) is indicative of a high olivine content. Weak molecular water bands at 1.4 μm and 1.9 μm indicate a low serpentine content, this is supported by a weak ferric feature at 0.7 μm and small features between 1.9 - 2.4 μm.

Weathered harzbugite spectra show a number of distinct spectral features depending primarily on the mineralogy of the sample. Figure 4.6 (b) shows the weathered surface spectrum. It shows predominantly the same features as described above, except that the spectrum seems to be influenced slightly more by the pyroxene content of the sample. This is evident in the broadening of the 1.0 μm feature towards shorter

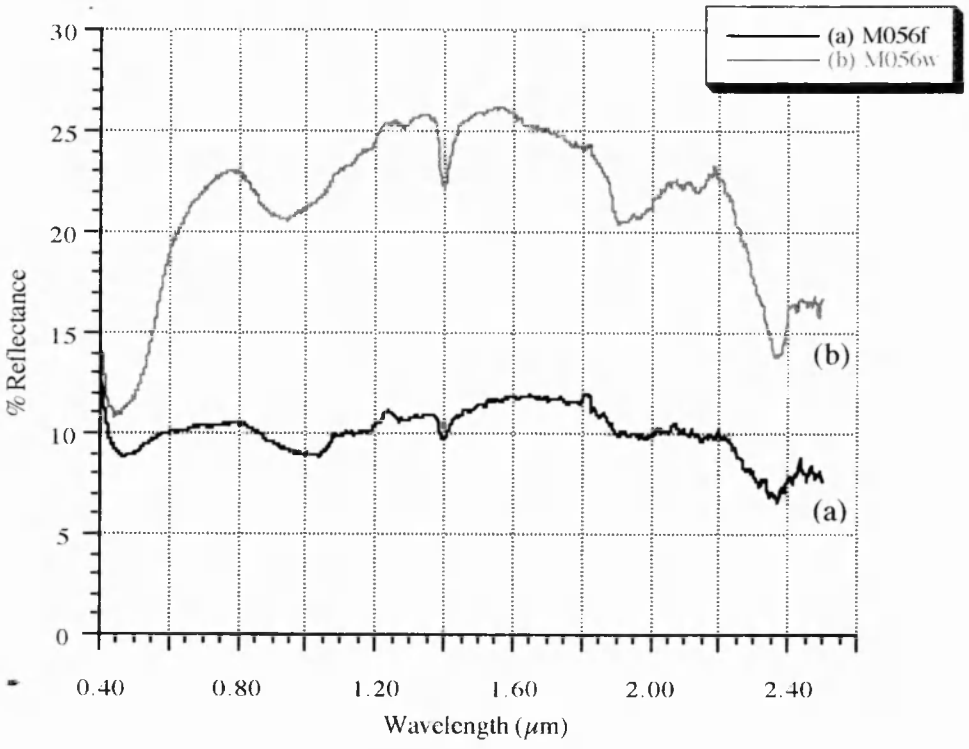

Figure 4.6 Lab reflectance spectra of a harzburgite sample; (a) fresh surface M056f and (b) weathered surface M056w. Refer to text for a full description.

wavelengths, away from the 1.7 μm maximum associated with olivine. Hydroxyl features associated with serpentine at 1.4 μm, 1.9 μm and 2.3 μm are also more pronounced on the weathered spectrum.

Intentionally left blank

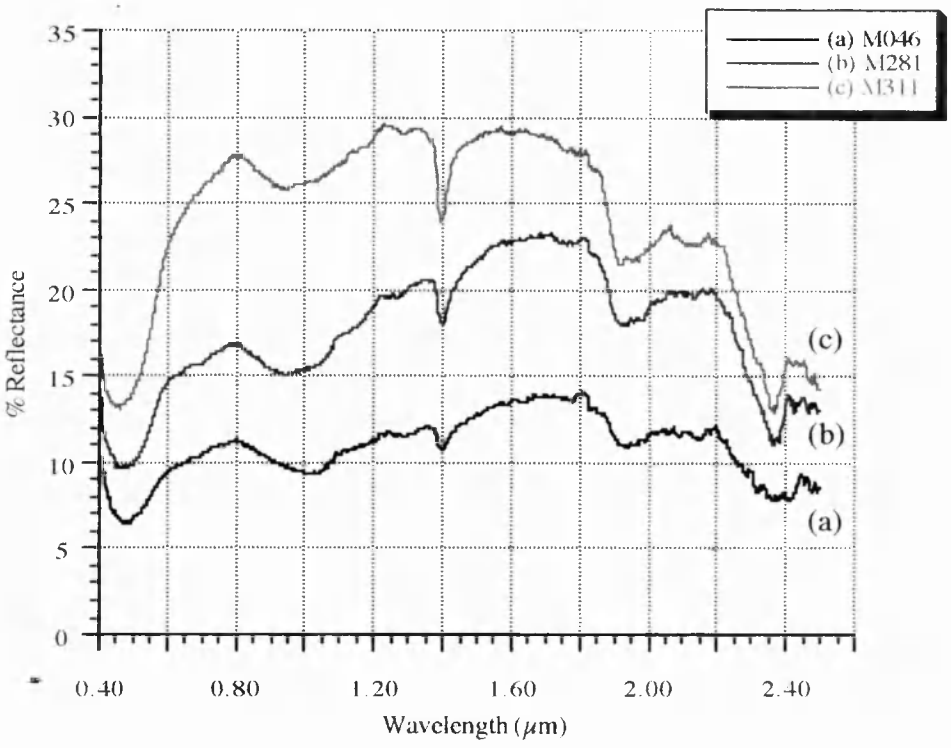

Figure 4.7 Lab reflectance spectra of three weathered harzburgite samples with increasing percentages of orthopyroxene (opx); (a) approximately 5% opx, (b) approximately 15-20% opx and (c) approximately 20% opx. Refer to text for a full description.

Figure 4.7 shows the spectra of three weathered harzburgites with increasing amounts of orthopyroxene, note that all spectra show a small noise spike at 1.81 μm. Sample M046 (a) is very olivine-rich (90%) and contains only 5% orthopyroxene and 5% serpentine alteration. Sample M281 (b) is intermediate with 75-80% olivine, 15-20% orthopyroxene and 5% serpentine. Sample M311 (c) is orthopyroxene-rich (20%) and contains only 60-65% olivine, along with 15% serpentine. The effect of the increasing orthopyroxene content can be seen in that the 1.0 μm ferrous feature associated with olivine and the side bands at 0.82 μm and 1.3 μm are quite pronounced in (a), but not so in (b) and (c). This is because the increasing orthopyroxene content broadens this feature and moves it to shorter wavelengths, so that it is centred at approximately 0.91 μm in (c). The increasing orthopyroxene content can also be seen to move the reflectance maximum from around 1.7 μm in (a) (olivine reflectance maximum) towards 1.4 μm in (c), which is the orthopyroxene maximum. Possibly the 1.4 μm peak in reflectance for orthopyroxene is masked by the 1.4 μm molecular water feature associated with the increased serpentine in this sample. Increased serpentine has also introduced stronger features at 1.9 μm and between 2.3 - 2.4 μm, along with a weak feature at 2.1 μm. The orthopyroxene-rich sample has a reflectance maximum which

is double that of the olivine-rich sample and as a result the ferrous feature between 0.4 - 0.5 μm is stronger, producing a steep drop off in reflectance between 0.5 - 0.8 μm. These three samples show how even small variations in mineral percentages result in some quite pronounced spectral variations.

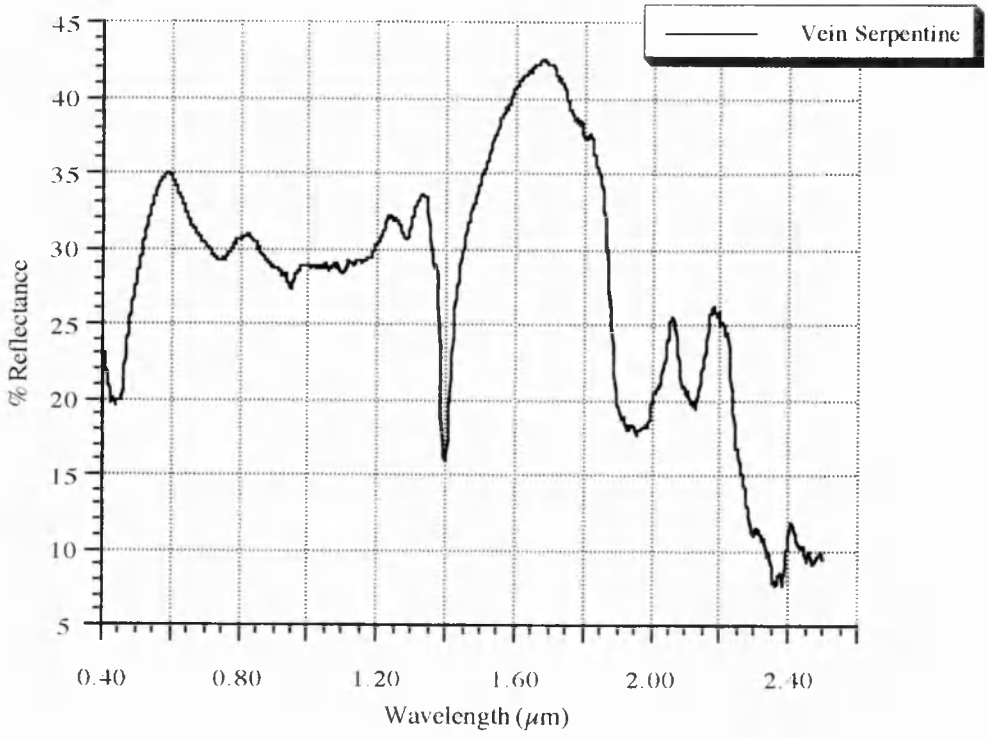

Figure 4.8 Lab spectrum of a sample of slightly weathered vein serpentine. See text for a full description.

Some outcrops of harzburgite have a very high serpentine content due to the precipitation at low temperatures of serpentine from meteoric waters along numerous cross cutting veins and cracks. An example of the spectral response of a weathered piece of fibrous serpentine from a vein is shown in Figure 4.8. This spectrum clearly shows all of the absorption features associated with serpentine. Very strong molecular water absorptions are visible at 1.4 μm and 1.9 μm, whilst other hydroxyl features are visible at 2.1 μm, 2.3 μm and 2.4 μm. Weaker ferrous and ferric absorptions occur near 0.73 μm, 0.90 μm, 1.0 μm and 1.12 μm. Ferric iron also causes a peak at short wavelengths around 0.5 μm, although this occurs nearer 0.6 μm for this sample. Maximum reflectance occurs near 1.7 μm.

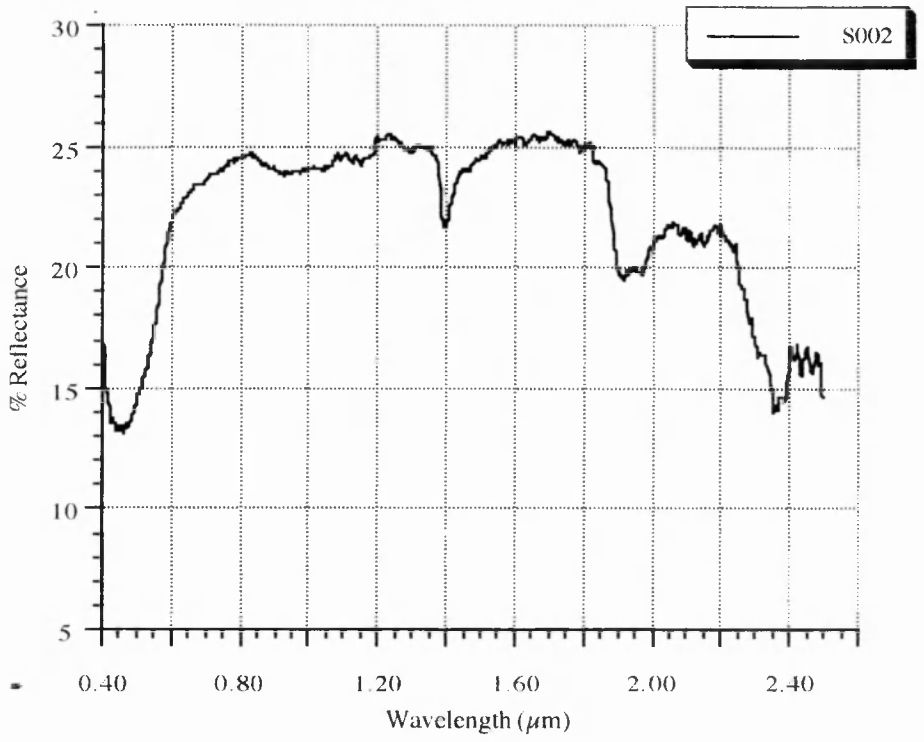

Figure 4.9 Lab spectrum of a very weathered piece of basal serpentinite. See main text for a full description.

Similar spectral features can be seen in Figure 4.9, which is the spectrum of a weathered piece of basal serpentinite. This unit represents regions of mantle material which were serpentinised during emplacement and enclose metamorphic rocks of non-ophiolite lithology (Lippard 1986). Typical products of such alteration in Oman are lizardite cross cut by veins of chrysotile which contain magnetite (Pontual, 1990). Overall reflectance values for basal serpentinite are low corresponding to the dark grey-green colour of the lithology in outcrop. The spectrum is dominated by ferric and ferrous features at 0.92 μm, 1.12 μm and sharp hydroxyl features at 1.4 μm, 1.9 μm and between 2.1 - 2.4 μm. Some outcrops of harzburgite are cut by numerous veins of magnesite. Magnesite is a carbonate mineral ($MgCO_3$) which is often found in altered veins of serpentine, and which is very obvious in the field. It is bright white on a fresh surface and weathers to an off white-beige colour. Its very hard nature tends to make it prominent on weathered surfaces. In some areas magnesite veins along with localised magnesite scree can account for 20-30% of the outcrop exposure. However its localised occurrence may affect only isolated pixels, making it difficult to see at OPS or TM resolution. Figure 4.10 shows the very distinct spectral response of fresh vein magnesite (a) and weathered magnesite (b).

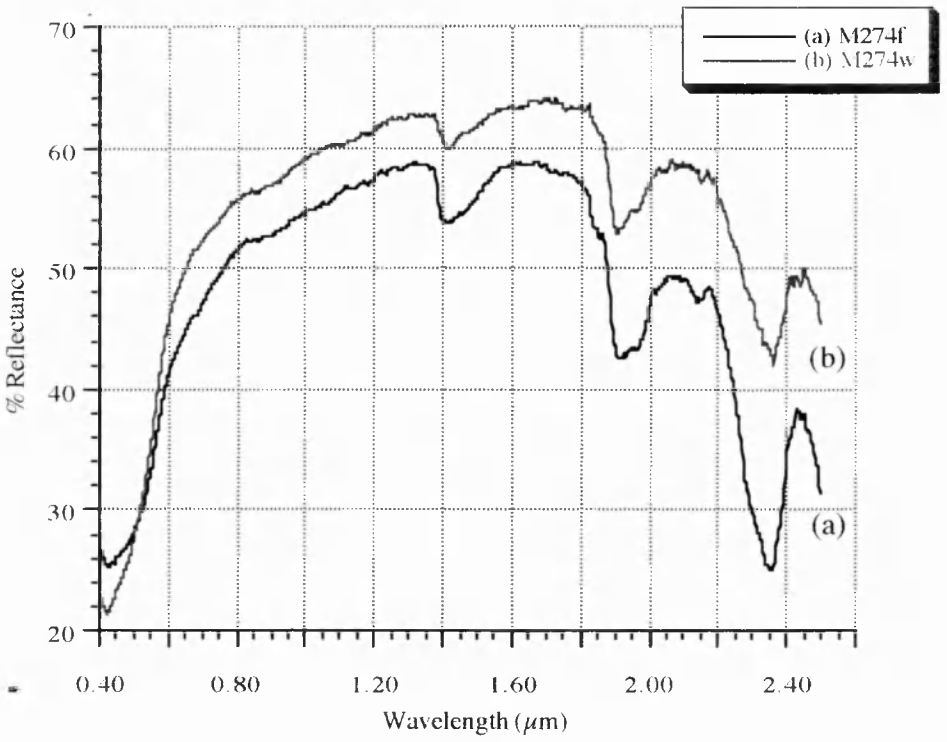

Figure 4.10 (a) Lab reflectance spectra of a sample of fresh vein magnesite, (b) spectra of a weathered sample of vein magnesite. Refer to text for a full description.

Both spectra show water absorption features at 1.4 μm and 1.9 μm suggesting that these samples are in part made up of hydromagnesite (Hunt and Salisbury, 1971) as pure magnesite does not exhibit any water bands. Other absorption features at 1.85 μm, 2.15 μm and 2.35 μm are vibrational in origin and are overtones of the carbonate ion. The 2.35 μm carbonate absorption is particularly strong on the fresh sample (a).

The occurrence of serpentine and magnesite in sufficient proportions can greatly change the spectral profile of a fresh harzbugite. Figure 4.11 illustrates how the spectrum of fresh harzburgite (a) changes with the introduction of 25% serpentine ((b) - Mix 1), 25% magnesite ((c) - Mix 2), and both together ((d) - Mix 3). Note that all 'mixed' spectra in this thesis have been approximated by the linear addition of the component minerals. In reality mixed spectra may have complex non-linear relationships. The original spectrum (a) contains a small percentage (5%) of serpentine and as a result absorption features due to water are visible at 1.4 μm and 1.9 μm. The addition of 25% serpentine enhances these features along with the hydroxyl features between 2.1-2.4 μm. Overall reflectance values are increased by 4-5% and the point of maximum reflectance moves to slightly longer wavelengths,

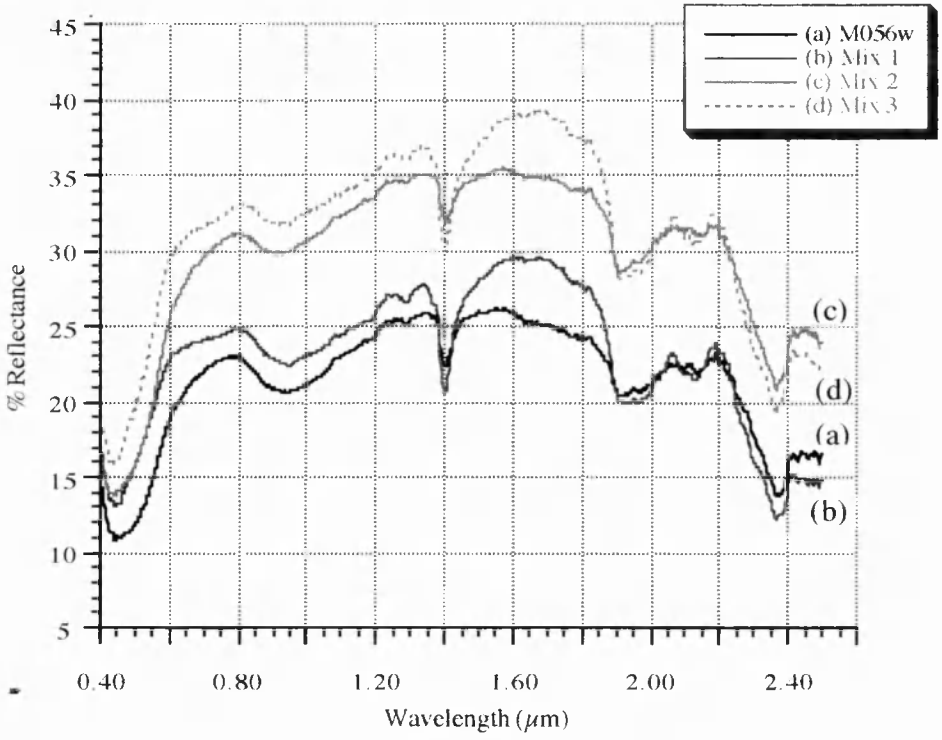

Figure 4.11 Lab reflectance spectra of; (a) weathered harzburgite (M056), (b) with 25% serpentine added (Mix 1), (c) with 25 % magnesite added (Mix 2), (d) with both 25% serpentine and 25% magnesite added (Mix 3).

from 1.6 μm to 1.65 μm. Slight flattening of the spectra occurs between 0.6-0.8 μm, resulting in the steep drop off of reflectance in the visible part of the spectrum. The addition of 25% magnesite increases reflectance at all wavelengths by about 10%, although the overall shape of the original harzburgite spectrum is maintained, except for a slight increase in the 2.35 μm absorption. The introduction of 25% serpentine and 25% magnesite (d) results in an overall increase in reflectance of about 15%, it also moves the maximum reflectance nearer to 1.7 μm. Absorption features at 1.3 μm, 1.4 μm, 1.9 μm, 2.1 μm and 2.35 μm as well as the inflexion near 0.7 μm are more pronounced in this spectrum than in the original harzburgite spectra (a).

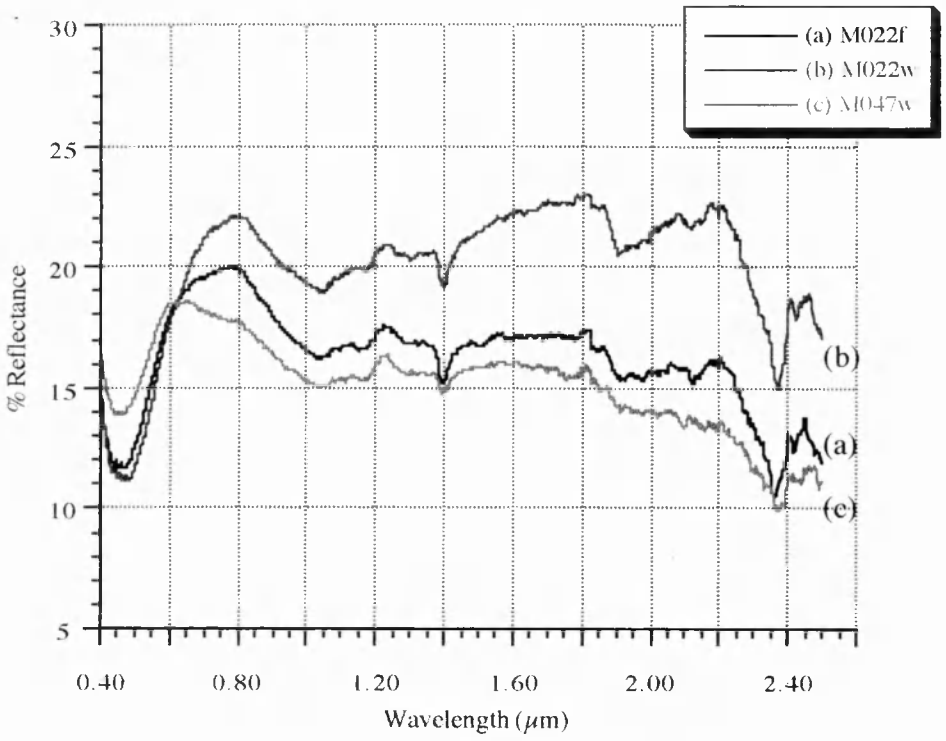

Figure 4.12 Lab reflectance spectra of two dunite samples; (a) fresh sample of M022; (b) weathered sample of M022 and (c) weathered sample of M047. Refer to text for a full description.

Figure 4.12 shows the spectra of two samples of dunite. M022 (a) is relatively fresh with only 10% of the olivines being altered to serpentine compared with about 30% in M022 (b). This increase in serpentine is evident as a shift in the reflectance peak from 1.60 μm to 1.7 μm, along with an increase in depth of the 2.4 μm absorption. Sample (c) from M047 is relatively free of serpentine and exhibits only weak serpentine absorption features. All of the spectra show characteristic olivine spectral features, primarily a broad asymmetric ferrous absorption centred at approximately 1.0 μm, with a secondary side absorption at 1.3 μm and a peak in reflectance near 1.7 μm. Both of the M022 samples show a pronounced peak in reflectance centred at 0.8 μm, a similar peak is visible in M047 but located at 0.7 μm. All spectra show a sharp fall off in reflectance values at wavelengths < 0.7 μm due to the ferric charge transfer in the weathered surface, along with a strong absorption feature between 0.4 - 0.5 μm due to ferrous ion. With the exception of the 0.7 μm to 0.8 μm reflectance peak the rest of the spectral profile is quite similar to that of harzburgite.

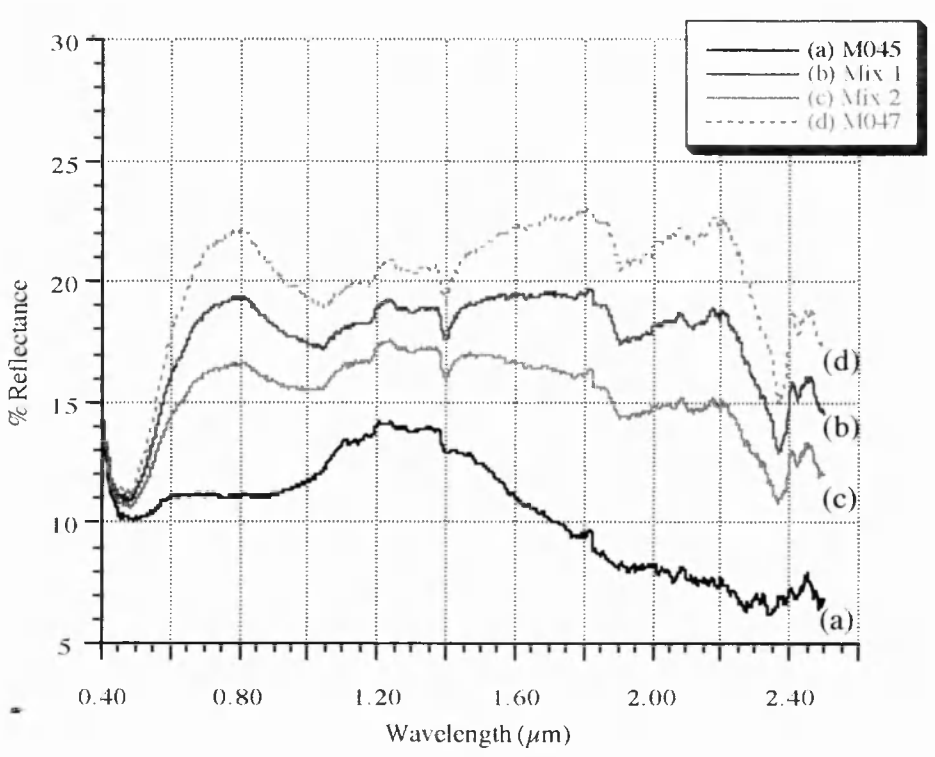

Figure 4.13 Lab reflectance spectra of (a) 100% chromite (M045); (b) 75% dunite and 25% chromite (Mix 1); (c) 50% dunite and 50% chromite (Mix 2) and (d) 100% dunite (M047).

Chrome spinel or chromite is a common accessory mineral associated with dunites. The spectrum for chromite, Figure 4.13 (a) is fairly featureless, except for weak absorption features near 1.15 μm and 1.3 μm, and a broad peak in reflectance between 1.1 and 1.5 μm. However these features can influence the spectrum of dunites if sufficient chromite is present. Figure 4.13 (b) shows a dunite spectrum which contains 75% chromite (Mix 1), whilst (c) shows a spectrum with 50% chromite (Mix 2). Both of these spectra exhibit absorption features associated with olivine as per the original dunite spectrum (d), although they also show some characteristics of the chromite spectrum. In particular the addition of chromite has caused an increase in reflectance over 1.2 μm to 1.4 μm, whilst causing a reduction in the 0.7 μm to 0.8 μm and 1.5 μm to 1.6 μm reflectance peaks of the original dunite spectrum.

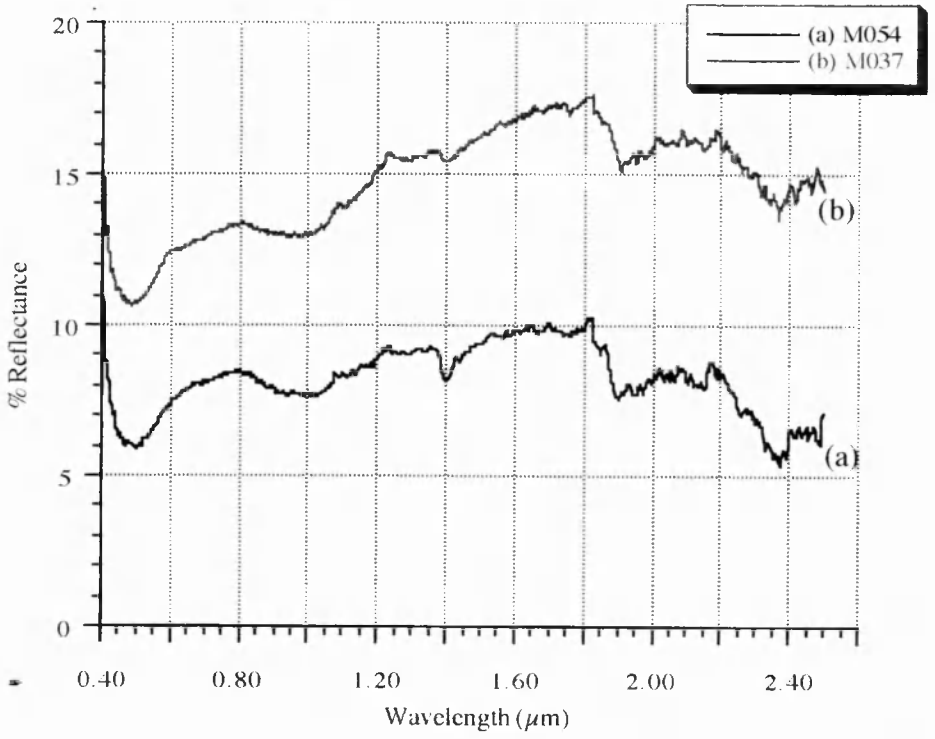

Figure 4.14 Lab reflectance spectra of two weathered wehrlite samples; (a) M054 and (b) M037. Refer to text for a full description.

Wehrlite consists primarily of olivine (60-80%) and phenocrysts (5-10 mm in size) of clinopyroxene. It is a very dark rock which tends to weather quite considerably where it has been severely altered by serpentine. Because of its dark nature, overall reflectance values are low and the spectrum appears noisy. Despite this, the reflectance spectra of two wehrlite samples (Figure 4.14 (a) and (b)) show quite pronounced spectral features associated with their primary mineralogy. Sample M054 (a) is composed of 45% olivine, 25% clinopyroxene, 5% opaques and 25% serpentine alteration. Whilst M037 (b) is composed of 55% olivine, 35% clinopyroxene, 5% opaques and 15% serpentine. Olivine absorption features can be seen in both spectra at 0.45 μm, 1.3 μm (very weak) and 1.0 μm, although the 1.0 μm feature has been broadened towards shorter wavelengths due to the pyroxene content. Other major absorptions are hydroxyl features at 1.4 μm, 1.9 μm and 2.3 μm. Both spectra show reflectance maximum near 1.7 μm corresponding with the high olivine content (the small peak at 1.8 μm is a noise artefact).

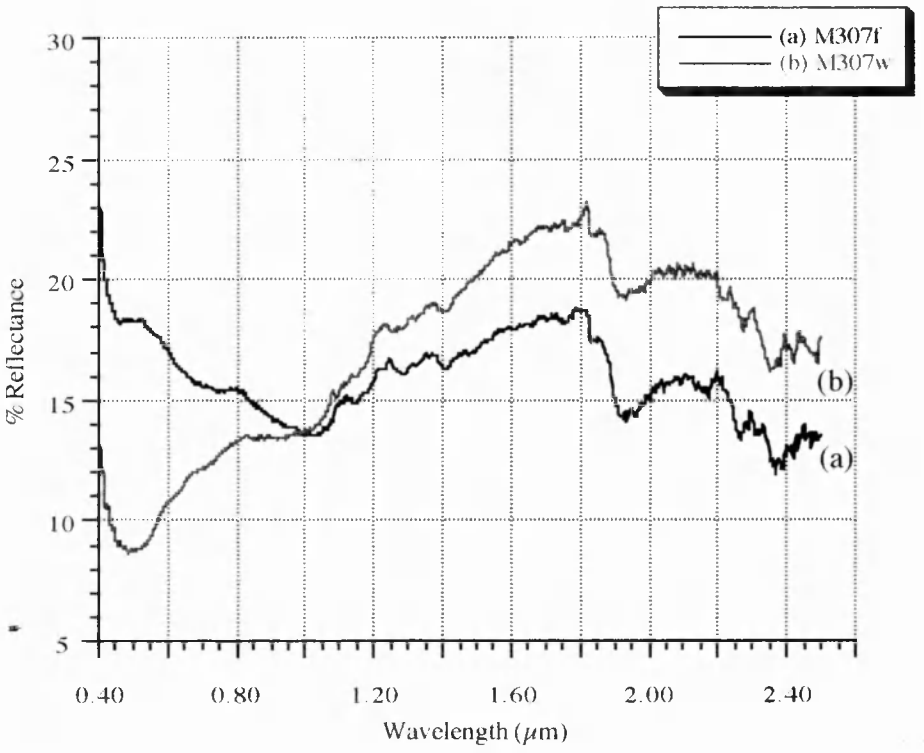

Figure 4.15 Lab reflectance spectra of a sample of cumulate gabbro; (a) fresh spectra (M307f), (b) weathered spectra (M307w).

Figure 4.15 shows the fresh and weathered spectra of a layered or cumulate gabbro which contains, 30% olivine, 45-50% plagioclase, 10% clinopyroxene, 5% amphibole. The thin section of this sample shows that the large (up to 2mm in diameter) olivine crystals tend to be altered at their edges. This alteration is possibly a fine grained mixture of serpentine and chlorite. In places the thin section exhibits an orthocumulate texture with large clinopyroxenes enclosing both olivine and plagioclase crystals. The spectra differ greatly at shorter wavelengths because the fresh sample (a) does not show the characteristic fall off in reflectance at visible wavelengths, caused by the charge transfer in the ferric hydroxide material in the weathered surface. At longer wavelengths the two spectra are fairly similar. The spectra exhibit the characteristic absorption features associated with olivine, primarily the broad absorption around 1.0 μm with side bands at 0.82 μm (visible only on the fresh spectrum as a slight inflexion) and 1.3 μm (visible on both). Maximum reflectance values near 1.7 μm also indicate a high olivine content, although this peak is slightly displaced to 1.8 μm due to the amphibole content (the sharp peak at this wavelength is a noise artefact). Weak hydroxyl features occur at 1.4 μm and 1.9 μm due to

molecular water in both serpentine and plagioclase. Absorption features between 1.9 μm and 2.4 μm are due to serpentine and chlorite.

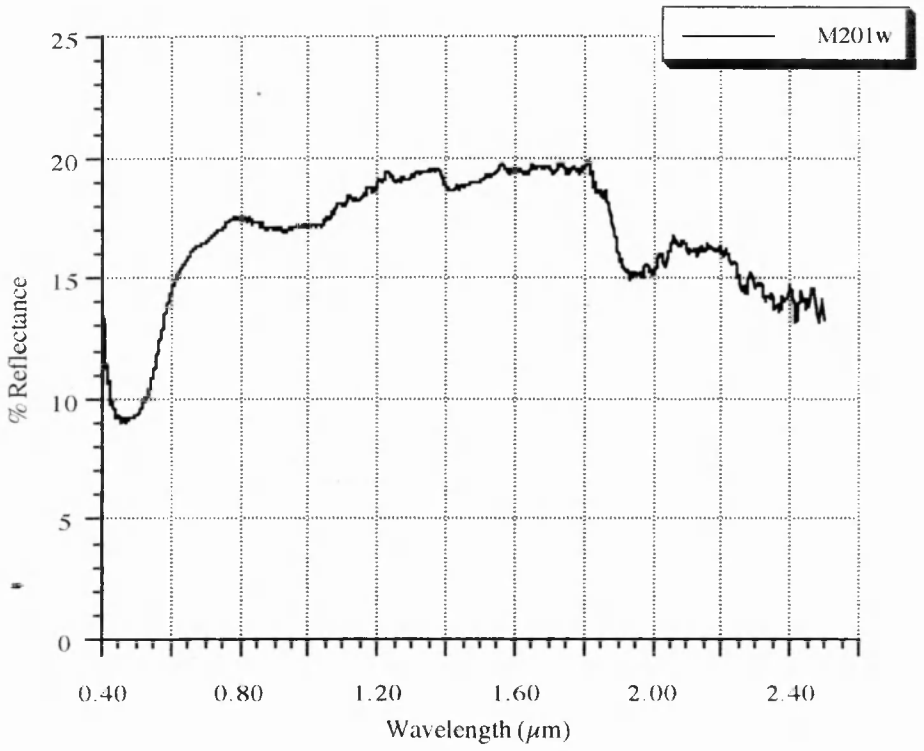

Figure 4.16 Lab reflectance spectrum of a weathered sample of medium grained cumulate gabbro.

Figure 4.16 shows the spectral signature for a medium grained cumulate gabbro which has almost equal proportions of olivine (15%), orthopyroxene (10%) and amphibole (10%), the remainder of the rock is plagioclase (60%) and serpentine (5%). The almost equal proportions of olivine, orthopyroxene and amphibole means that there is no obvious peak in reflectance, instead the spectrum is consistently high between 1.4 - 1.8 μm. Water absorption features at 1.4 μm and 1.9 μm are prominent along with a broad olivine-orthopyroxene absorption feature centred at approximately 0.91 μm. Weak secondary features associated with olivine and orthopyroxenes are visible at 1.3 μm and 1.85 μm respectively. Hydroxyl features between 2.0 μm and 2.4 μm are not particularly clear as the spectrum is quite noisy at these wavelengths.

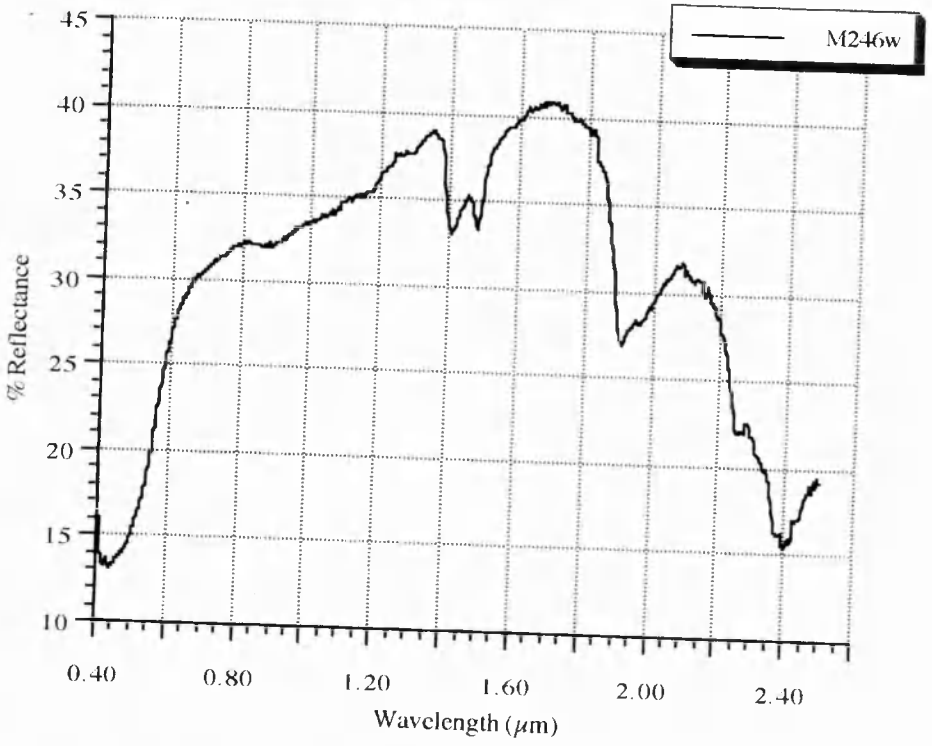

Figure 4.17 Lab reflectance spectrum of a weathered sample of coarse grained cumulate gabbro. Refer to text for a full description.

Figure 4.17 shows the spectrum of a weathered medium coarse grained cumulate gabbro which is composed of 35 % clinopyroxene, 25% olivine, 35% plagioclase and 5% opaques. Despite the high olivine content the spectra shows only a weak absorption feature near 1.0 μm, although a characteristic side band absorption at 1.3 μm is visible. Hydroxyl features dominate at 1.4 μm and 1.9 μm. The peak in reflectance is between 1.6 μm and 1.7 μm due to the high percentages of both olivine and clinopyroxene. Absorption features near 1.54 μm, 2.25 μm and 2.34 μm suggest that the sample may contain some epidote, possibly as the result of alteration of the clinopyroxenes.

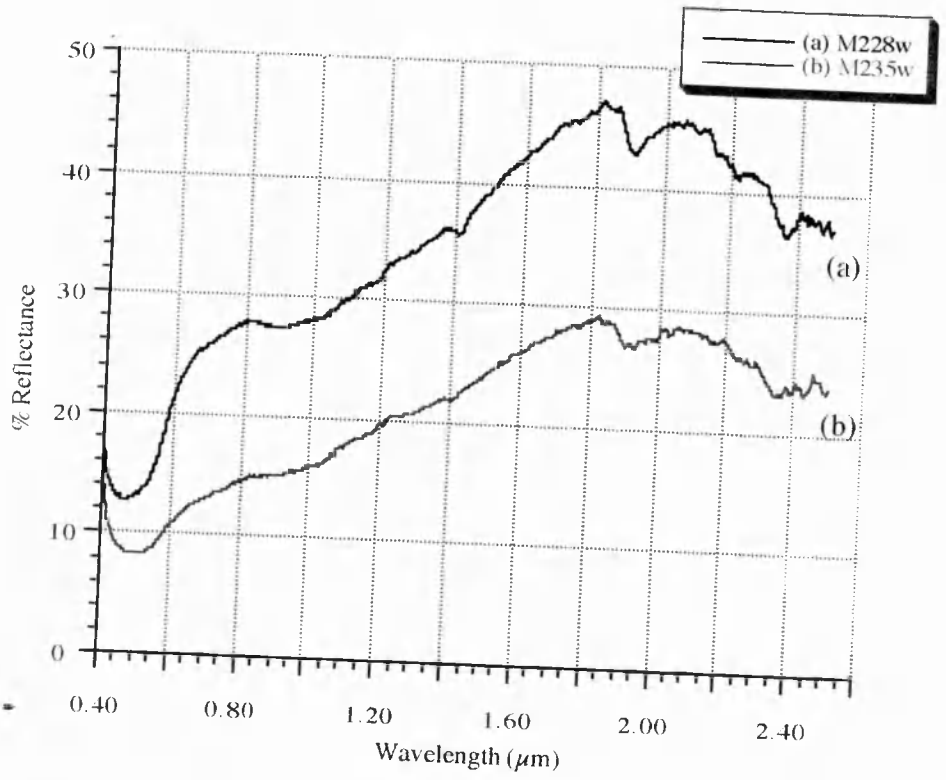

Figure 4.18 Lab reflectance spectra of two weathered samples of isotropic gabbro; (a) M228w and (b) M235w. Refer to text for a full description.

The spectra of two weathered samples of 'high-level' or isotropic gabbro are shown in Figure 4.18 (a) and (b). Both of these are fine grained amphibole-rich gabbros with an approximate mineralogy of 50% hornblende, 48% plagioclase and 2% opaques. Both samples have quite high overall reflectance, peaking around 1.8 μm, the amphibole maximum. The spectra tend to be dominated by weak ferrous features associated with amphibole at 1.0 μm and 2.3 μm. The 2.3 μm feature is accompanied by two side features at 2.25 μm and 2.40 μm. Ferrous and ferric bands are responsible for the drop off in reflectance between 0.4 μm and 0.5 μm. Both spectra show weak hydroxyl features at 1.4 μm and 1.9 μm, which are due to water in both the plagioclase and the amphibole.

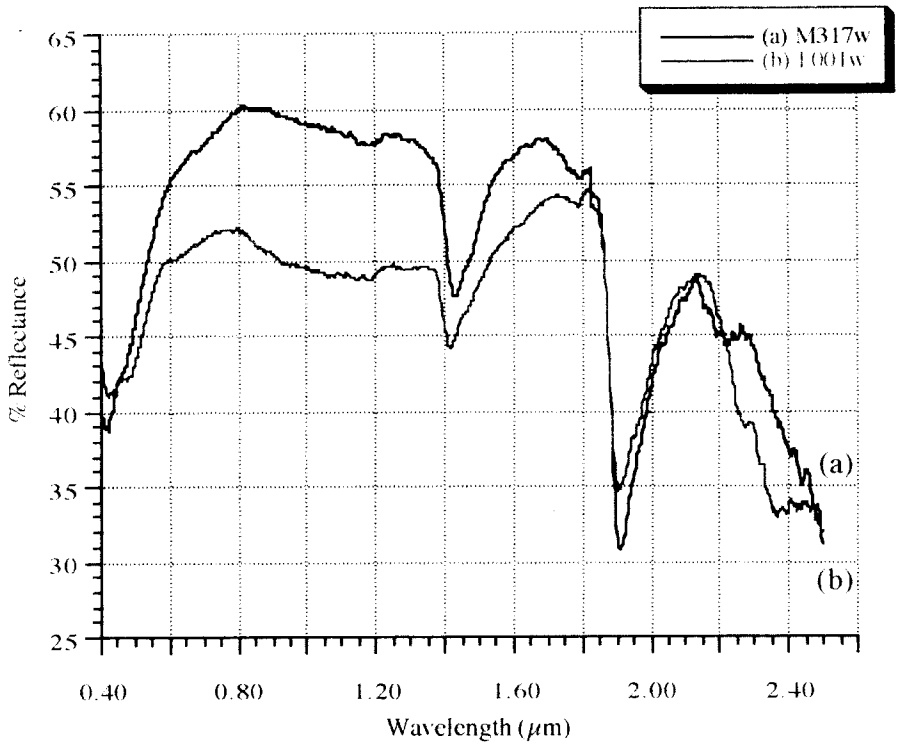

Figure 4.19 Lab reflectance spectra of two weathered trondjhemite samples; (a) M317w and (b) F001w. Refer to text for a full description.

Figure 4.19 shows the spectra of two weathered trondhjemite samples which are mineralogically very similar. Both samples are coarse to medium grained and contain 70 - 8% plagioclase, 10 - 15% quartz (intergrown with the plagioclase), 5% amphibole and < 5% opaques. The major spectral absorption features at 1.4 μm and 1.9 μm (molecular water) are due to the alteration of the feldspars, along with the weaker feature at 2.2 μm. The weak feature at 1.2 μm is characteristic of plagioclase. Neither sample displays features associated with amphibole. The sharp features near 1.8 μm are noise. Note how the high plagioclase content results in this lithology having high reflectance values, making it spectrally 'brighter' than all of the other ophiolite lithologies.

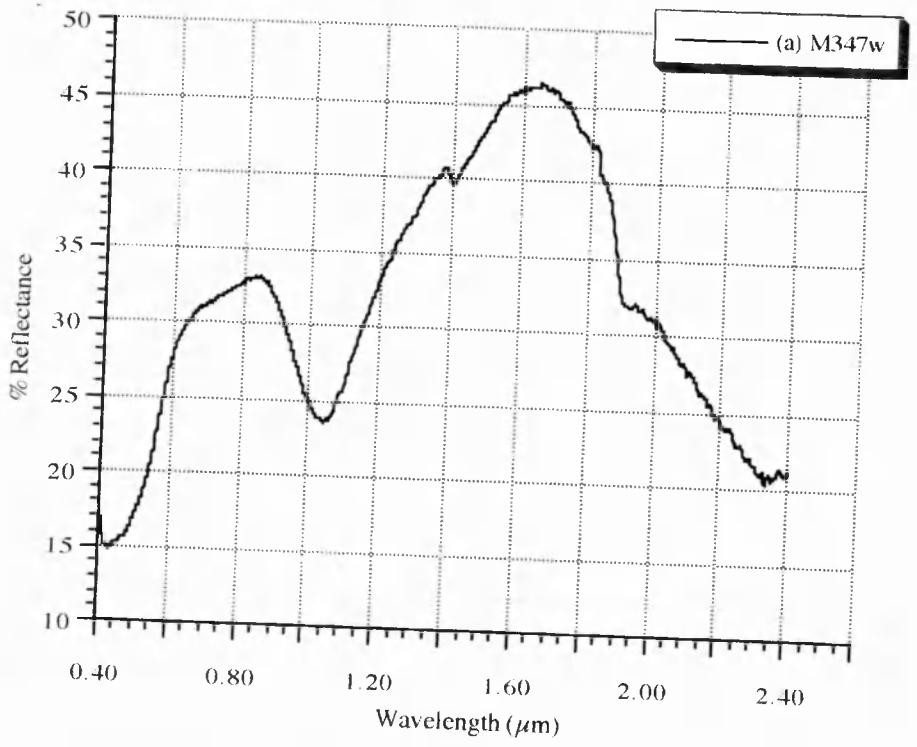

Figure 4.20 Lab reflectance spectrum of a weathered sample of pyroxenite. Refer to text for a full description. (Spectral data > 2.4 μm not recorded).

The spectral signature of a pyroxenite is shown in Figure 4.20. This is a very good spectrum as the sample is composed almost entirely of clinopyroxene (approximately 90%), with some olivine and trace serpentine. The spectrum is dominated by a very well defined ferrous absorption feature between 1.0 - 1.1 μm and a peak in reflectance near 1.6 μm. The shift of both of these features to slightly longer wavelengths may be due to the olivine. Weaker ferrous features associated with pyroxene are visible at 1.85 μm and 2.35 μm. Weak molecular water features associated with the serpentine are visible at 1.4 μm and 1.9 μm.

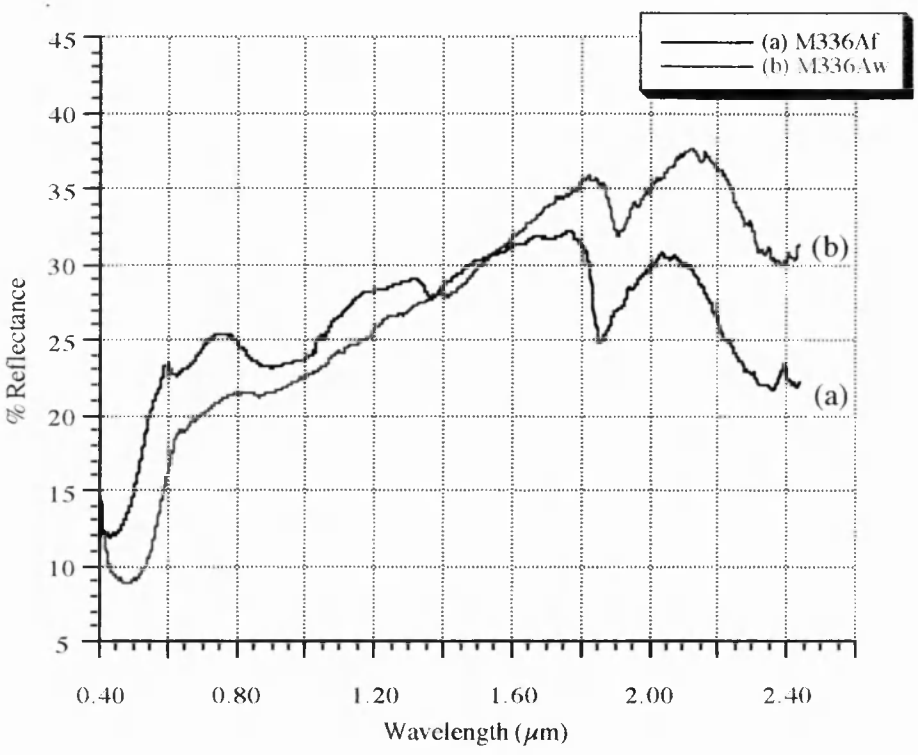

Figure 4.21 Lab reflectance spectra of a sample of Maqsad sheeted dyke material (M336A), (a) fresh spectrum, (b) weathered spectrum. Refer to text for a full description.

Figure 4.21 (a) and (b) show the fresh and weathered spectra of a sample from the Maqsad sheeted dyke complex, which tends to be more poorly exposed than in other regions of the ophiolite. The sample is a very fined grained dyke which is basaltic in texture, comprised primarily of 55% plagioclase laths, 25 % clinopyroxene (possible augite), 15 % quartz, with accessory opaques and possibly some epidote alteration (<1%).

The spectrum of the fresh surface (a) shows absorption features associated with plagioclase 1.4 μm and 1.9 μm (water bands) and clinopyroxene, namely the broad ferrous feature near 1.0 μm and the inflexion near 0.7 μm (ferric ion), the 2.3 - 2.4 μm region of the spectrum exhibits weak hydroxyl features. A very weak inflexion near 1.5 μm may represent the characteristic 1.54 μm hydroxyl feature associated with epidote. The overall high average reflectance of this sample is due to the high plagioclase content. The spectrum of the weathered surface (b) is very similar except that some of the features at shorter wavelengths are not so clearly visible. Note that the well-defined peak in reflectance seen in the fresh spectrum at 0.62 μm but not in the weathered spectrum is a noise artefact. (This is a known problem with the spectrometer used to make the measurements (*pers. com* NERC-EPFS)).

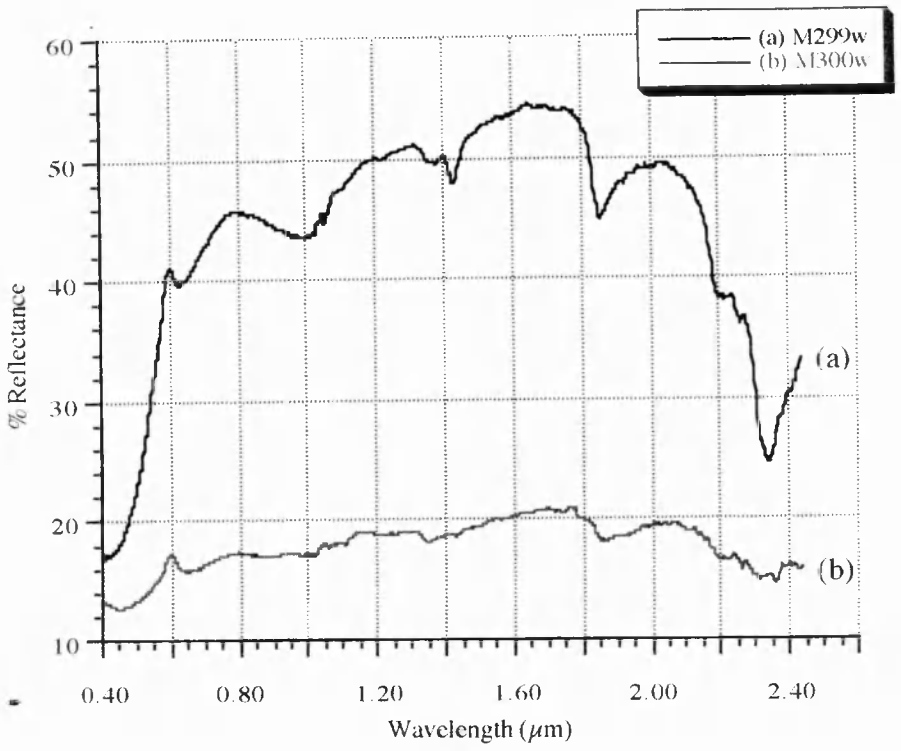

Figure 4.22 Lab reflectance spectra of two extrusive pillow lavas from the Maqsad region. Small spectral peak at 0.65μm in both spectra is a noise artefact. Data beyond 2.45 μm not recorded. Refer to text for a full description.

Both samples M299 and M300 are examples of extrusive pillow lava from the Maqsad region. Figure 4.22 (a) shows the spectrum of weathered pale green fine grained basalt, which is comprised of 35% plagioclase, 15% epidote, 15% chlorite, 10% clinopyroxene, 10% quartz and 10% opaques. This spectrum is dominated by absorptions associated with chlorite at 0.70 μm, 1.05 μm, 1.47 μm and between 2.2-2.4 μm. Small epidote features also occur in this region at 2.34 μm and 2.25 μm. The distinctive epidote hydroxyl feature at 1.54 μm appears to have slightly broadened the chlorite 1.47 μm feature. Figure 4.22 (b) is the spectrum of a weathered dark brown-purple fine grained basalt, comprised of 70% plagioclase, 15% opaques, 10% quartz, 3% clinopyroxene and 2% undistinguished accessory minerals. The dark nature of this sample results in the spectrum having low overall reflectance values compared with M299. M299 is the dominant extrusive lithology encountered in the Maqsad region, although this in turn represents the smallest (in terms of area) lithology exposed.

4.2.4 Spectral variability of lithologies

The previous section used individual spectra to illustrate the common reflectance characteristics associated with each of the ophiolite lithologies. These spectra were chosen as being representative of each lithology after comparing all of the recorded spectral measurements. This selection had to be performed as it is impractical to consider all of the spectra on an individual basis. The representative nature of these spectra can be seen when they are compared with other spectra of the same lithologies collected from all three study regions, Figure 4.23 and Figure 4.24.

Figure 4.23 (a) and (b) illustrate a number of harzburgite and lherzolite reflectance spectra recorded from samples collected from all three study regions. These lithologies show the most spectral variation, therefore I have used a number of spectra in the previous section to illustrate their characteristics. These spectra can be broadly divided into two groups; those which exhibit strong spectral features (a), in particular a strong 1.0 μm olivine absorption, and those which exhibit weak features (b). This variation is caused by differences in mineralogical composition, sample freshness and crystal size. Samples in (a) tend to be fresh despite having a strongly weathered surface, whilst those in (b) are more heavily weathered throughout the sample. Figure 4.23 (c) shows how harzburgite spectra are modified with the occurrence of increasing serpentine, typically indicated by a shift in the reflectance peak towards 1.8 μm and the increasing depth of absorptions at 1.9 μm, 2.1 μm and 2.4 μm. Dunite spectra (d) are all very similar with the major variation being the depth of the weathering absorption at visible wavelengths. Other variations centre around the depth of the 1.0 μm olivine feature and the 1.4 μm and 1.9 μm water features associated with serpentine. All of these dunite spectra exhibit a characteristic reflectance peak in the visible at about 1.2 μm. The characteristically dark nature of wehrlite means that its spectra (e) are all very similar, exhibiting only minor reflectance peaks and absorptions. These spectra are relatively flat compared with those of the other lithologies.

Figure 4.24 illustrates spectral variation for the main crustal lithologies. Cumulate gabbros (a) tend to be the most spectrally varied, primarily because of their wide ranging mineralogy, but also due to variations in crystal size and weathering. Crystal size in cumulate gabbros ranges from fine to very coarse, which in turn causes variations in overall reflectance levels or 'brightness'. To account for this variation a number of cumulate gabbro spectra were described in the previous section. Isotropic gabbro (b) spectra are more consistent, particularly with respect to the long positive increase in reflectance between 0.6 μm and 1.8 μm. The strength of Fe-O absorptions (at wavelengths < 0.6 μm) associated with weathered surfaces causes distinct

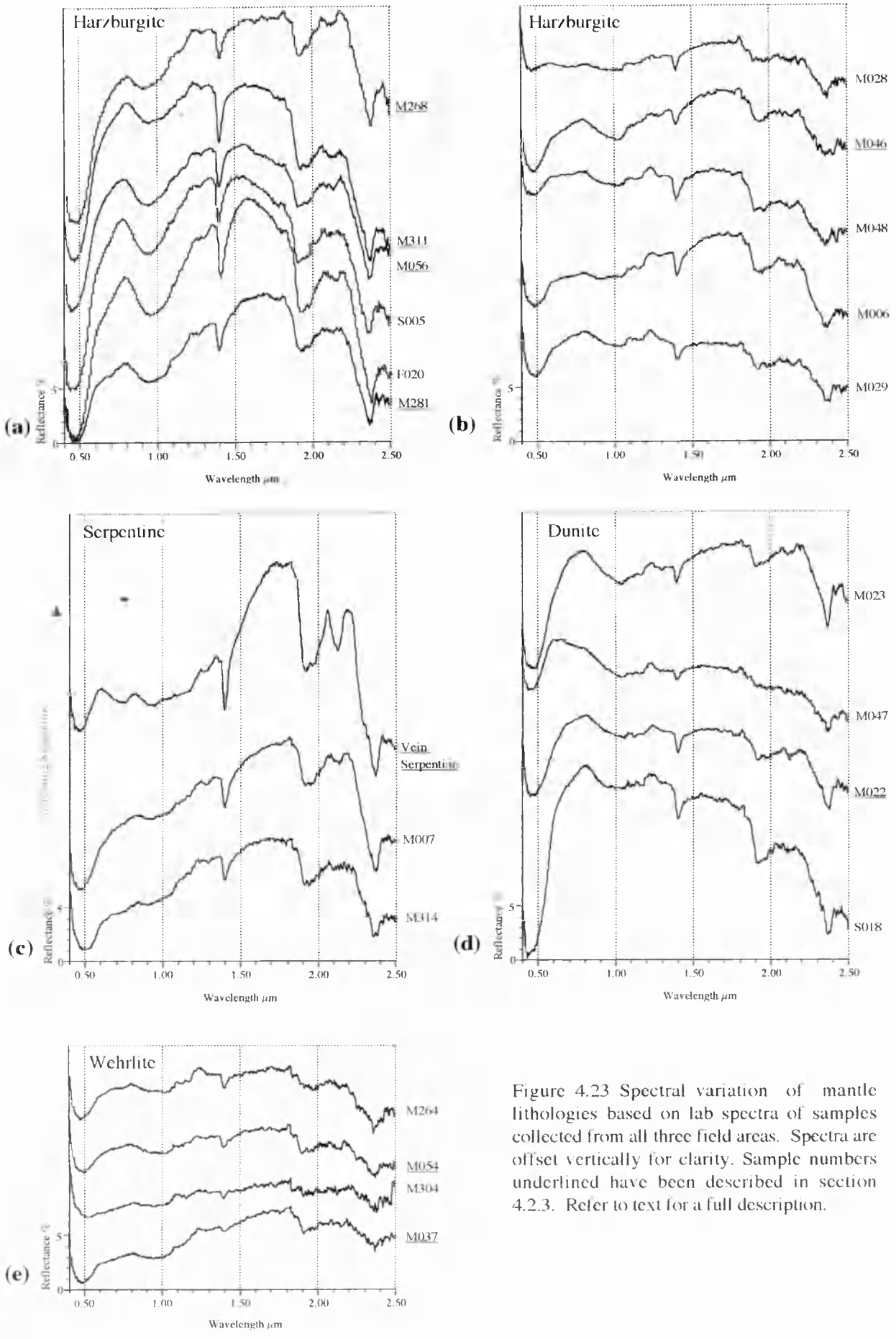

Figure 4.23 Spectral variation of mantle lithologies based on lab spectra of samples collected from all three field areas. Spectra are offset vertically for clarity. Sample numbers underlined have been described in section 4.2.3. Refer to text for a full description.

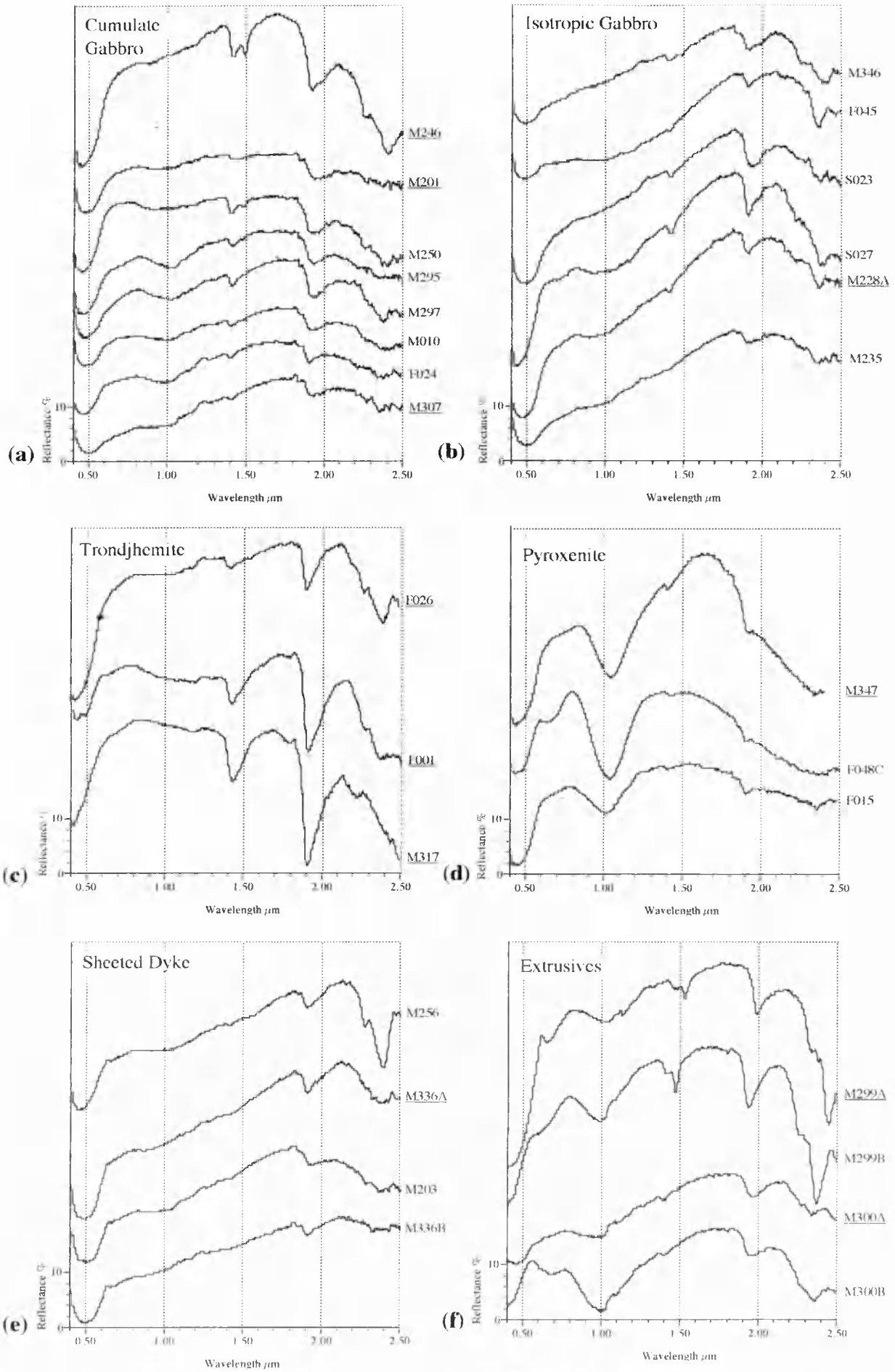

Figure 4.24 Spectral variation within each of the crustal lithologies based on lab spectra of samples collected from all three field areas. Spectra are offset vertically for clarity. Sample numbers underlined have been described in section 4.2.3. Refer to text for a full description.

spectral variations in all gabbro samples. Trondjhemite (c) and pyroxenite (d) spectra are fairly consistent, due to their relatively pure mineralogy.. Spectral variation in these lithologies occurs as a result of the inclusion of accessory minerals or differential weathering. Sheeted dykes (e) are also fairly consistent although once again variations in crystal size along with differential weathering results in some spectral variation. The pillow lavas appear to be quite varied although this may in part be as a result of the limited outcrop available for sampling. Available samples indicate two distinct spectral profiles controlled primarily by mineralogy and weathering.

Examination of numerous spectra confirm that the example spectra used in section 4.2.3 are indicative of the major spectral characteristics of the main ophiolite lithologies encountered in the study regions. Extraction of individual example spectra allows inter-lithology spectral comparisons to be made. However, it has to be accepted that these spectra are only representative and that the comparison of numerous spectra of the same lithology will result in additional spectral variations being detected. The aim of section 4.2.3 is therefore to highlight spectra which can be regarded as representative of each lithology (or sub-lithology) from the samples collected. These spectra can then be used as a basis for assessing lithological discrimination at the spectral resolution of Landsat TM and JERS-1 OPS, see Section 4.3.

4.2.5 Summary of diagnostic spectral features

A number of ophiolite spectra are broadly similar in their shape, however variations in overall reflectance levels combined with the location, depth and width of individual absorption features make discrimination between these lithologies possible when considering the continuous 0.4 μm to 2.4 μm range. These discriminating features are directly related to the absorption and reflectance properties of the major rock forming minerals along with those of secondary accessory, or alteration minerals associated with weathering. Variations in composition or quantity of these secondary minerals aids discrimination between similar lithologies, and allows the subdivision of lithologies to occur. Figure 4.25 summarises both the major and minor absorption features associated with weathered surfaces of the main ophiolite lithologies in the 0.4 μm to 2.4 μm range as detected from the analysis of the example spectra seen in Section 4.2.3. Absorption features have been shaded according to their strength; strong absorptions are dark grey, moderate absorptions are mid-grey and weak absorptions are pale grey. All of the lithologies exhibit strong absorptions in the 0.4 μm to 0.6 μm range. These are Fe-O absorptions associated with weathered surfaces.

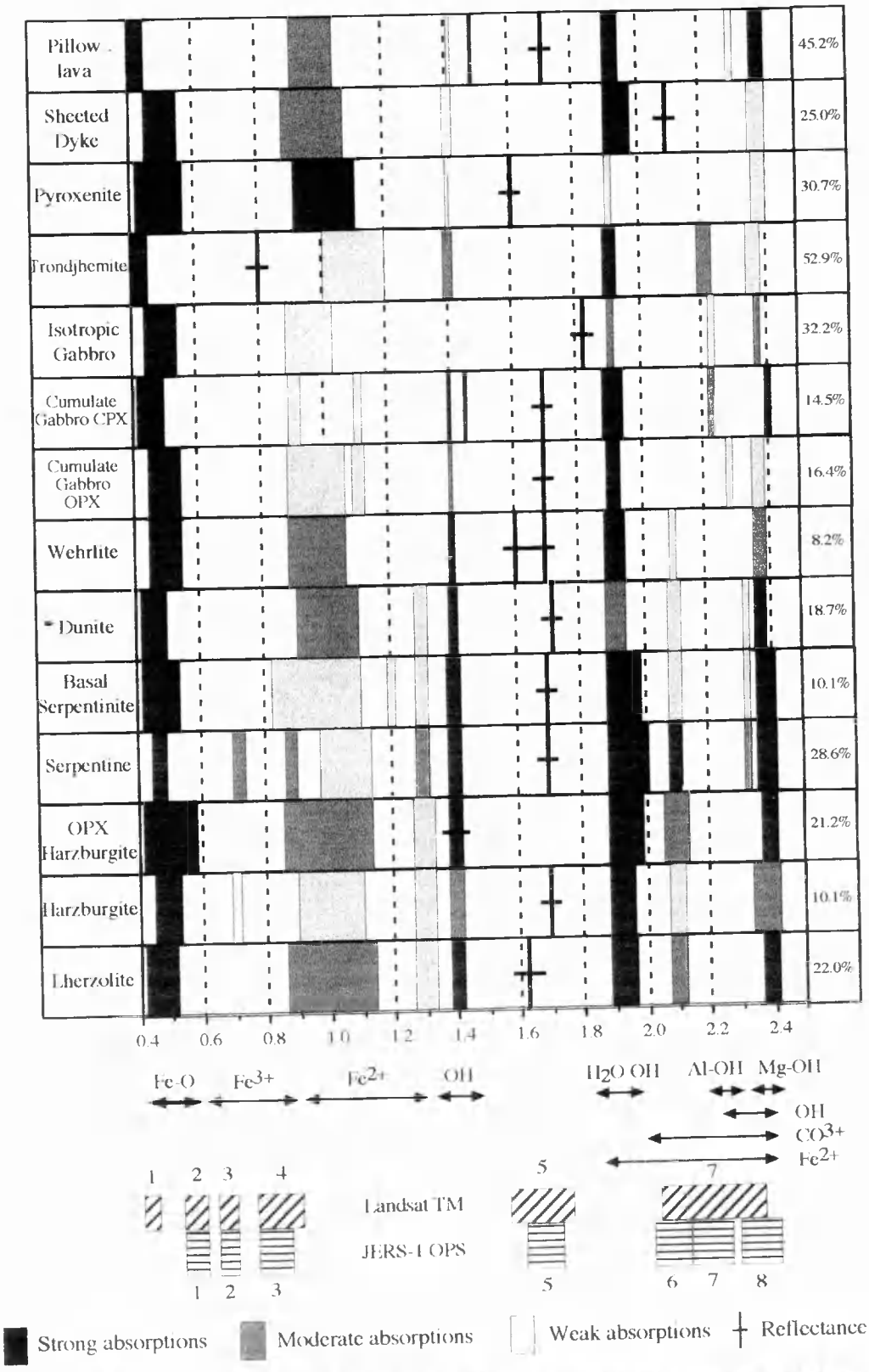

Figure 4.25 Summary diagram of the major spectral absorption features associated with the main ophiolite lithologies encountered in the three study regions. Refer to text (section 4.2.3) for a full description of the spectral absorption features summarised here. Average reflectance percentages for each lithology over the entire 0.4 to 2.4 wavelength range are given in the right-hand column. Approximate location of both TM and OPS channels are also shown.

The next major absorptions are associated with Fe^{2+} between 0.8 μm and 1.2 μm, although a couple of minor Fe^{3+} absorptions occur near 0.7 μm. The majority of the Fe^{2+} absorptions are weak to moderate in strength, although pyroxenite exhibits a strong feature. Weak absorptions at these wavelengths are usually broad shallow features. Some lithologies (primarily mantle ones) exhibit secondary Fe^{2+} absorptions at longer wavelengths around 1.3 μm. These features are very weak. Mantle lithologies also show stronger OH absorptions at 1.4 μm compared with those of the crustal lithologies. OH absorptions in crustal lithologies tend to be very narrow and very weak. However they do exhibit some distinct features such as the secondary features at 1.46 μm in clinopyroxenne cumulate gabbro and 1.48 μm in pillow lavas.

Once into the SWIR part of the spectrum absorption features become more varied between the different lithologies. Molecular water produces strong sharp absorption features at 1.9 μm in the majority of the lithologies. Mantle lithologies also show weaker secondary water features centred around 2.1 μm. Moderate strength absorption features associated with Al-OH occur at 2.2 μm in a few of the crustal lithologies. These absorption features result in only weak Mg-OH absorptions being visible at 2.3 μm. Lithologies not showing Al-OH absorptions exhibit strong to weak Mg-OH absorptions at 2.3 μm to 2.4 μm. The strongest Mg-OH absorptions are associated with mantle lithologies. A number of lithologies also exhibit weak water features around 2.3 μm.

Figure 4.25 illustrates that both mantle and crustal lithologies exhibit fairly similar absorption features at visible wavelengths and that the major variations in spectral absorption occur at longer wavelengths, in particular between 2.2 μm and 2.4 μm. It also clearly shows how the majority of the mantle lithologies are affected to varying degrees by secondary serpentine absorptions features. Increased spectral variability at SWIR wavelengths indicates the importance of having multi-channel satellite data recorded from this part of the EM spectrum, i.e. JERS-1 OPS data. Figure 4.25 also gives an indication of reflectance levels (in percentage) averaged over the entire wavelength range. This value is intended as an approximate guide to determine the spectral 'brightness' of each lithology. These values show how the majority of the crustal lithologies tend to be brighter than the mantle lithologies.

4.3 Spectral responses of Oman igneous rocks convolved with OPS and TM bandpasses

4.3.1 Introduction

When considering rock spectra over the continuous spectral range 0.4 - 2.5 μm (as illustrated in section 4.2.3), the majority of the ophiolite lithologies can be distinguished from each other with reasonable confidence. However, this becomes more difficult when spectral reflectance information is only available from isolated wavelength ranges, such as that provided from satellite sensors. Reflectance spectra produced from Landsat TM or JERS-1 OPS are very crude in comparison, because they consist of only 6 or 7 (TM and OPS respectively) values across the equivalent wavelength range. As a result TM and OPS reflectance spectra are very basic, with only broad overall spectral profiles being determinable. Figure 4.26 illustrates the degree to which a complex mineral spectrum, such as that of calcite, is simplified once sampled at either the resolution of Landsat TM (a) or JERS-1 OPS (b). The discrete nature of multichannel satellite data means that important spectral information is often lost. This can be as a result of the lack of satellite channels located at wavelength ranges which coincide with absorption features. This can be illustrated in (a) and (b) by the hydroxyl absorption features at 1.4 μm and 1.9 μm. These absorption features do not affect the satellite spectra because they occur at wavelengths where neither sensor has channels. These absorptions show how the discrete sampling nature of a satellite sensor can completely miss large absorption features. (Note that the 1.4 μm and 1.9 μm absorptions were only used to illustrate this point and that satellite channels would not be located at these wavelengths due to severe atmospheric absorptions).

The broad nature of some satellite channels, for example TM7, can also result in the loss of spectral information. Because satellite sensors record an average reflectance value determined over the entire wavelength range of each channel, narrow absorption features centred in a broad channel may not be evident as they only affect a small percentage of the entire channel width. This can be seen in Figure 4.26 (a) where the strength of the absorption feature at 2.3 μm is partially lost due to the broad nature of TM 7, within which it occurs. This is not the case in (b) where the SWIR part of the spectrum is divided into three channels, now the 2.3 μm absorption feature is located within one narrow channel, OPS 8.

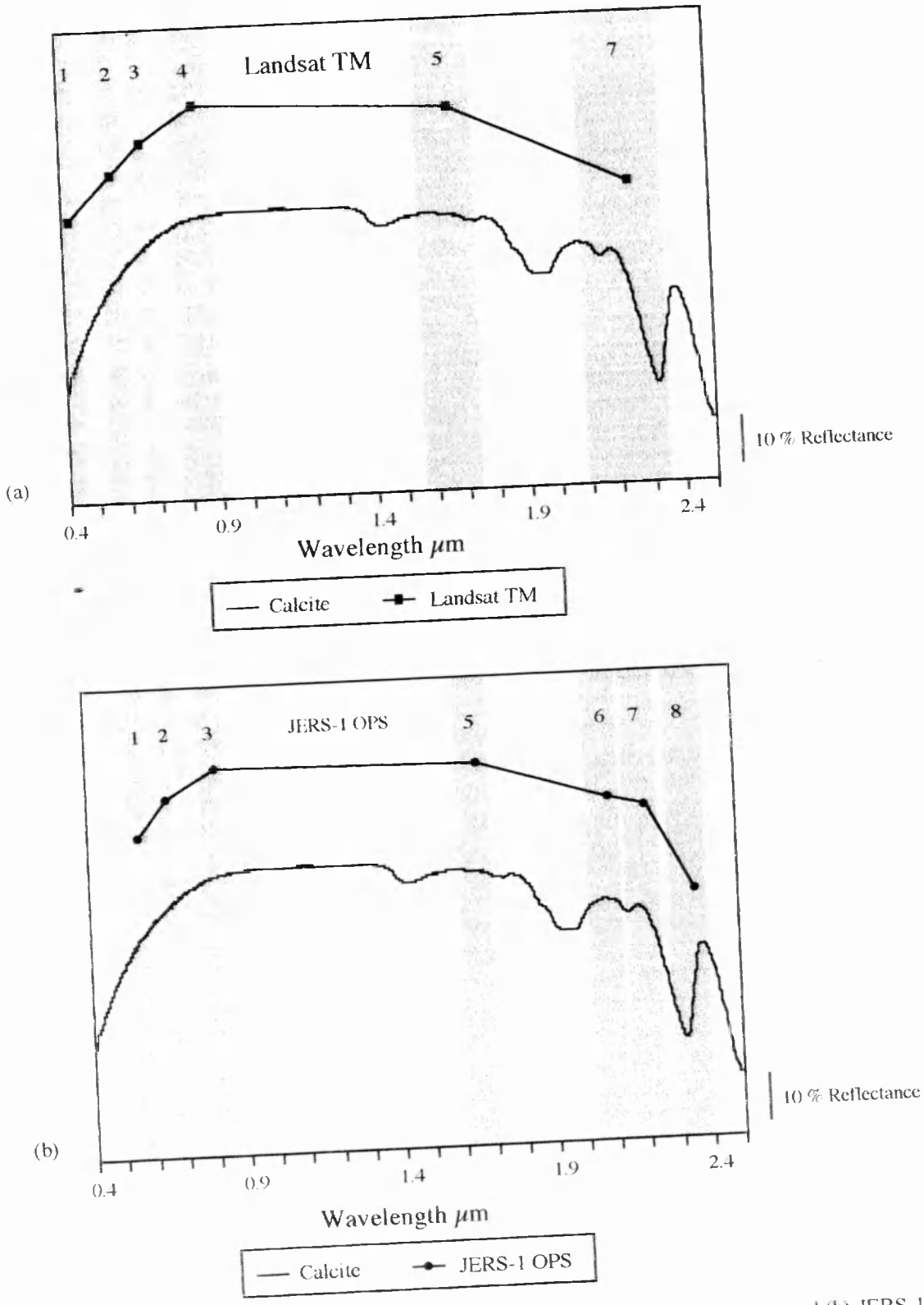

Figure 4.26 Calcite spectrum (Grove *et al.*, 1992) convolved with (a) TM bandpasses and (b) JERS-1 OPS bandpasses. **Note** that the original spectrum is a continuous data series from 0.4 to 2.4 μm, but the convolved 'satellite-resolution' spectrum consists of only 6 (TM) or 7 (OPS) spectral values. Data does not exist between these points, therefore the lines drawn between these points are illustrative only and are used to aid spectral comparison between the different resolutions.

As a result the strength of this absorption feature is fully recorded by OPS 8 which shows considerably lower reflectance values than TM 7. Narrow satellite channels are required to distinguish sharp specific features, otherwise absorption features have to be broad to significantly affect an entire channel bandwidth.

The location and width of satellite channels within the 0.4 - 2.5 μm spectral range is very important, as even a limited number of discrete narrow channels centred at appropriate wavelengths can record valuable diagnostic spectral information. This can be illustrated by comparing the amount of spectral information preserved when pure mineral spectra are convolved with TM and OPS bandpasses.

4.3.2 Comparison of pure mineral spectra convolved with OPS and TM bandpasses

Intially pure mineral spectra will be used to examine the spectral resolution of the TM and OPS sensors before examining complex (multi-mineral) lithological spectra. The pure mineral spectra used in this section were selected from the NASA digital mineral archive (Grove *et al.*, 1992). They were convolved by multiplying the recorded mineral reflectance by the average sensor response function for each channel's wavelength range. The average response function for each of the sensors in a channel is used. The response functions for JERS-1 OPS sensors are illustrated in Figure 4.27. The response functions for Landsat TM can be found in the literature (Markham and Barker, 1985) and are not reproduced here.

It can be seen from the plots in Figure 4.27 that the OPS sensors are not uniform in their sensitivity across an entire channel bandpass, instead they each show an approximately 'normal' distribution. This means that very little information is recorded at the beginning and end wavelengths of each channel, where the response function is very low. To compensate for this the channels are sensitive to a small percentage of energy at wavelengths outside of the quoted channel bandpasses (overlain in grey on Figure 4.27). This bandpass extension is very low for channels OPS 1, OPS 2 and OPS 5, but is slightly larger on the other channels. This bandpass extension is particularly noticeable on the shorter wavelength edge of each channel, for example OPS 7 appears to be sensitive from 2.07 μm as opposed to the quoted 2.12 μm, whilst OPS 8 is sensitive from 2.22 μm as opposed to 2.27 μm. These extended bandpasses result in slight channel overlap between OPS 7 and OPS 8 over the wavelength range 2.22 - 2.28 μm. However, low response function values over these extended regions means that little extra spectral information is added from outside of the quoted channel bandpasses.

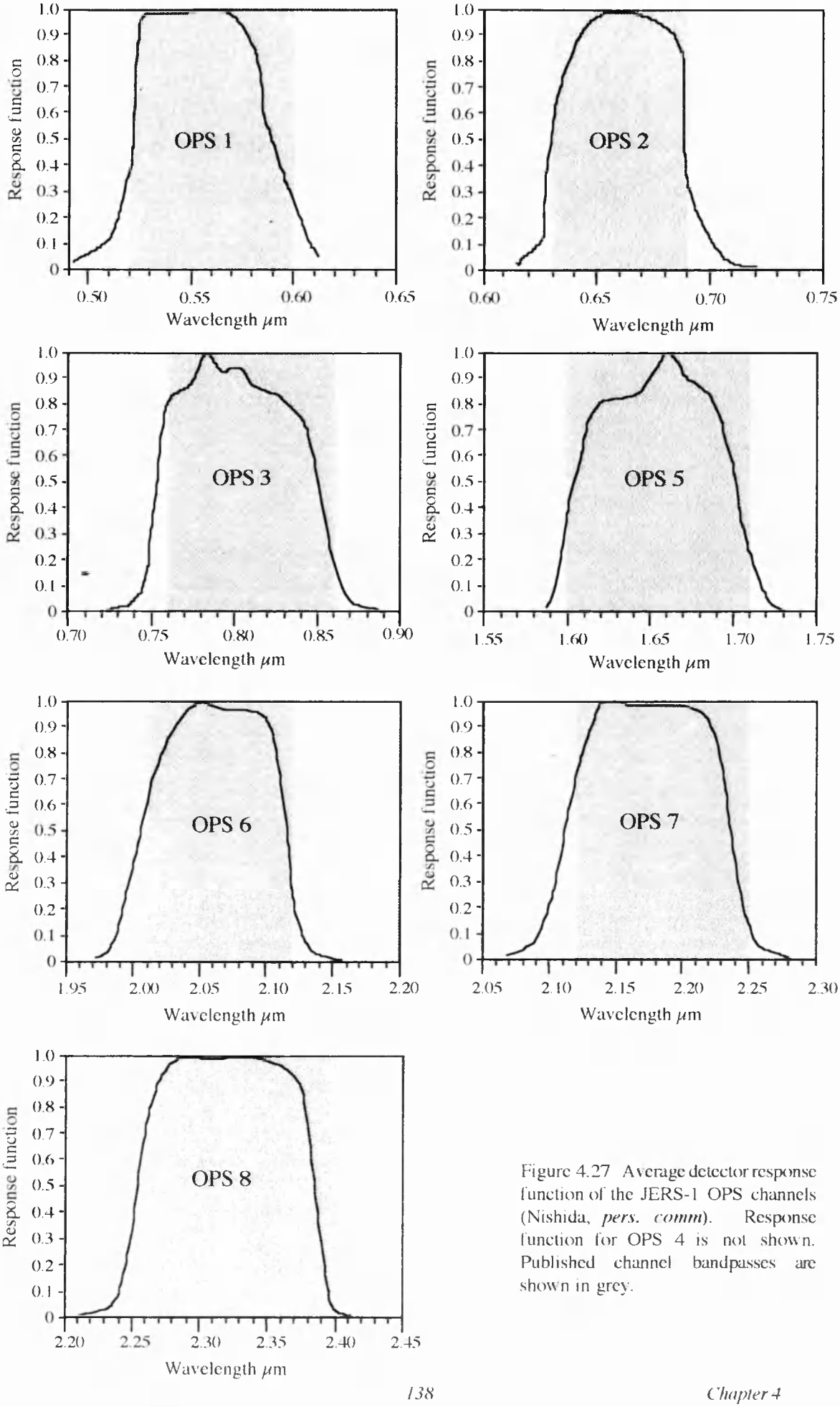

Figure 4.27 Average detector response function of the JERS-1 OPS channels (Nishida, *pers. comm*). Response function for OPS 4 is not shown. Published channel bandpasses are shown in grey.

Figure 4.28 (a) shows the continuous reflectance spectra for six common minerals over the 0.4 - 2.5 μm range, all of these spectra show well defined absorption features which allow the minerals to be distinguished. However, distinguishing between these spectra is not so easy when they have been resampled to satellite resolution, Figure 4.28 (b) and (c). The TM spectra (b) replicate the real mineral spectra quite well at visible and NIR wavelengths, because of the availability of four channels of data. However the complex SWIR spectral features are missed because of the availability of only two channels of data at these wavelengths. TM spectra show only the broadest trends relating to increasing or decreasing reflectance values at SWIR wavelengths. None of the complex SWIR absorption features seen in the original spectra is evident at TM resolution, making discrimination between some spectra, for example; muscovite and serpentine, quite difficult. JERS-1 OPS spectra 4.28 (c) show considerably more spectral information at these wavelengths, because reflectance values are available for four channels instead of two. These additional channels mean that minerals such as muscovite and serpentine can now be distinguished between, because the OPS sensor reveals the characteristic Mg-OH (2.3 μm) absorption feature associated with serpentine as an independent feature in channel OPS 8. The sharp decrease in reflectance between OPS 7 and OPS 8, allows the serpentine spectrum to be distinguished from the muscovite spectrum which does not have an Mg-OH feature. The talc spectrum also shows a sharp Mg-OH feature on the OPS spectrum which is not visible on the TM spectrum. The same can also be seen for Al-OH (2.2 μm) absorption features which are isolated in OPS 7. The OPS spectrum for kaolinite shows a sharp drop in reflectance in OPS 7 due to an Al-OH absorption, a feature which is not apparent on the TM spectra.

The additional information in the SWIR part of the spectrum on the OPS data comes at the expense of one visible channel equivalent to TM 1. This means that the TM spectra exhibit some features at these wavelengths which the OPS spectra do not, for example the absorption feature in chlorite at 0.4 μm. The loss of this visible channel is not vital as absorption features at these wavelengths are not as diagnostic of mineralogy as those at longer wavelengths. Moreover, features in the visible region are more easily masked by absorptions caused by surface weathering. When considering pure mineral spectra it is apparent that OPS data have significantly more discrimination potential than TM data primarily due to the isolation of Al-OH and Mg-OH absorption features into individual channels.

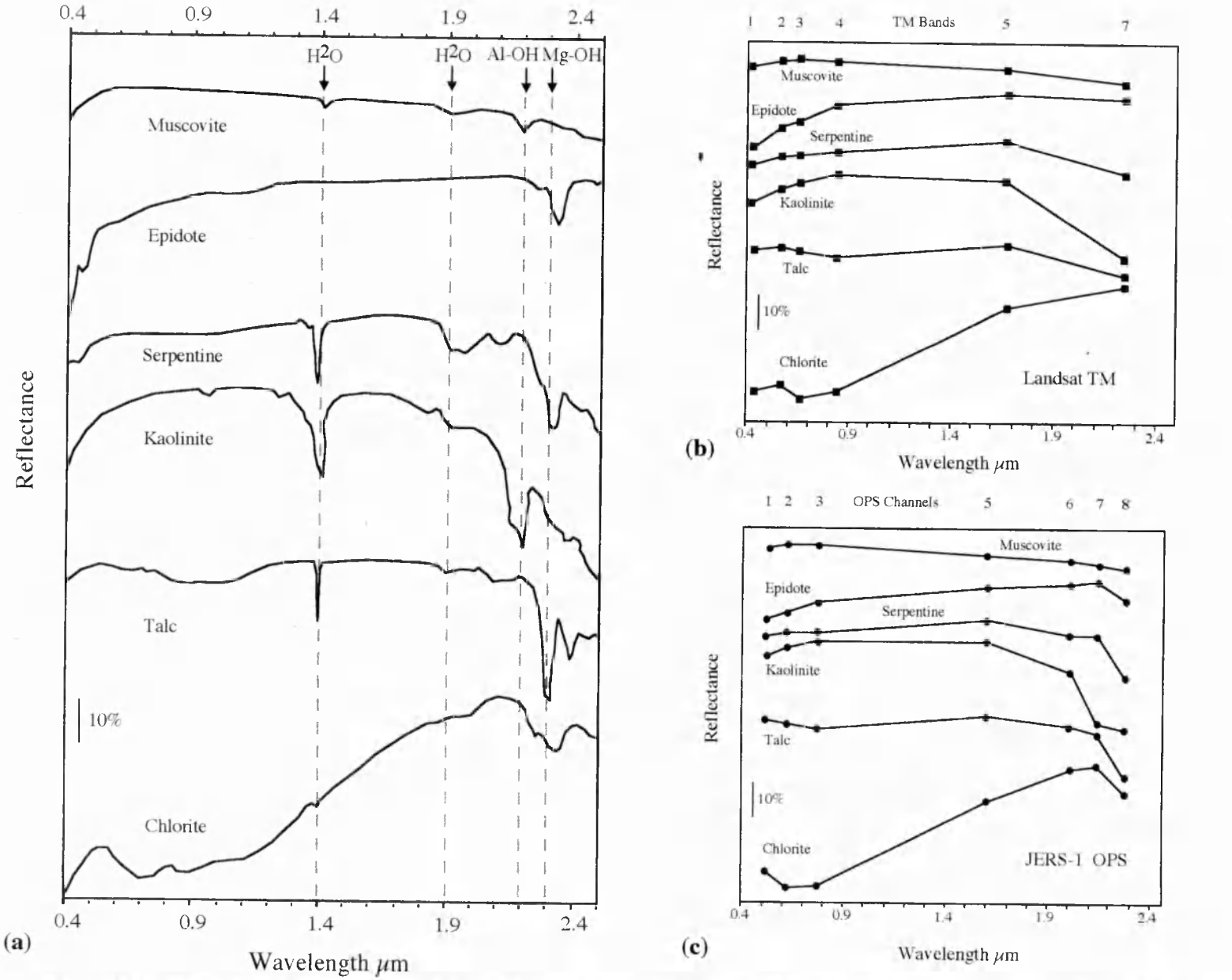

Figure 4.28 (a) Pure mineral spectra (Grove *et al.*, 1992) (b) spectra convolved over TM bandpasses,(c) spectra convolved over OPS bandpasses.

4.3.3 Comparison of ophiolite lithology spectra convolved over OPS and TM bandpasses

This section aims to see if OPS data offer the same discrimination advantages over TM data when considering whole rock reflectance spectra, as opposed to those of pure minerals. The spectra of the weathered ophiolite lithologies seen in section 4.2.3 have been convolved over TM and OPS bandpasses and are displayed here in Figures 4.29, 4.30 and 4.31. As in section 4.2.3 the lithologies have been divided into mantle and crustal lithologies.

1) Mantle lithologies

Figure 4.29 (a) shows the mantle lithologies convolved over TM bandpasses and Figure 4.29 (b) shows them convolved over OPS bandpasses. Considering the TM spectra first, all of the lithologies can be seen to be quite similar in appearance (with the exception of the serpentine spectrum). Overall reflectance values are low peaking in TM 5 at around 30%. All lithologies show very low reflectance values in bands TM 1 and TM 2, due mainly to the ferric oxide charge transfer on the weathered surface. Reflectance in TM 3 and TM 4 tends to be slightly higher for some lithologies (dunite, altered harzbugites and lherzolite), corresponding to the higher reflectance seen on the continuous spectra (Section 4.23) at 0.6-0.8 μm. The orthopyroxene-rich harzburgite (M311) shows very high reflectance values in TM 2 and TM 3 compared with those of the orthopyroxene-poor harzburgite (M046). The high in TM 2 is echoed in the lherzolite spectra. The addition of 25% magnesite to harzburgite (altered harzburgites Mix 2) causes a considerable increase in reflectance in these channels, whilst the addition of 25% serpentine (Mix 1) tends to increase reflectance mainly in TM 5, because of the location (1.7 μm) of the peak in serpentine reflectance. Both together (Mix 3) cause the spectra to resemble that of lherzolite (M268) except for the decreasing reflectance in TM 7. Decreasing reflectance in TM 7 is influenced by the severity of hydroxyl absorptions occurring between 2.1 and 2.4 μm associated with serpentine. Wehrlite (M037 and M054) displays fairly uniform low reflectance levels across all channels, corresponding to the characteristically dark nature of this lithology. Dunite spectra are also fairly featureless with almost uniform reflectance levels across TM 4, TM 5 and TM 7.

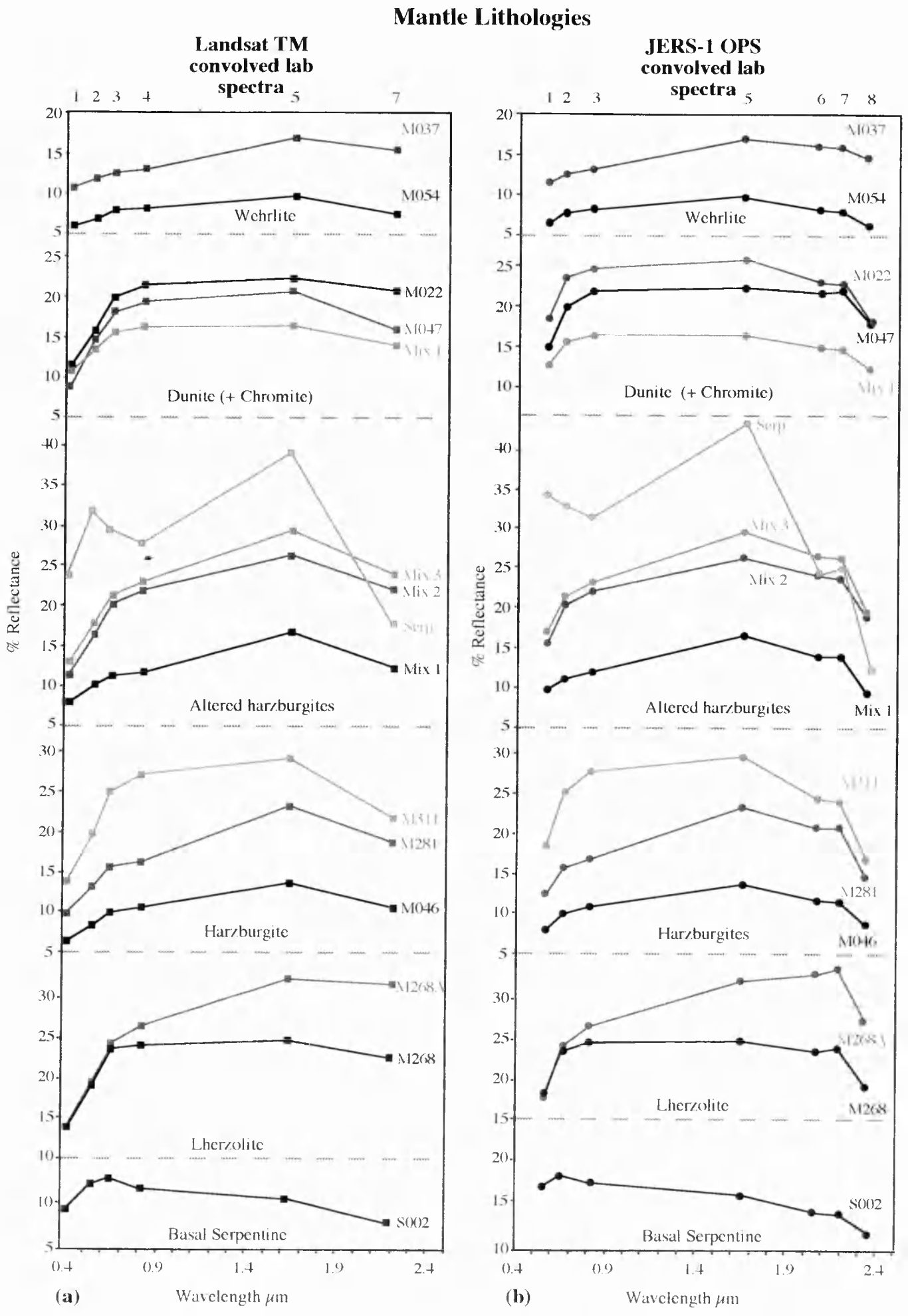

Figure 4.29 Lab spectra of Oman ophiolite rock samples convolved over (a) TM and (b) OPS bandpasses.

Variations between the OPS convolved spectra, Figure 4.29 (b) are greater than those seen on the TM spectra because of the extra SWIR data. Overall reflectance values are still low with the maximum around 30%. Like the TM spectra OPS 1 (which is equivalent to TM 2) has predominantly low reflectance values for all lithologies due to ferric oxide absorptions on weathered surfaces. All spectra (except chromite; M045) show an increase in reflectance values between OPS 2 and OPS 3, comparable to those seen between TM 3 and TM 4. Reflectance values for OPS 5 are fairly similar to those of TM 5, although in some cases they are marginally higher. The major variations are at wavelengths greater than 2.0 μm, where considerably more spectral detail is provided by OPS 6, OPS 7 and OPS 8. With the exception of dunite (M022) and lherzolite (M268) all of the lithologies show a flattening of the spectra between OPS 6 and OPS 7, prior to a sharp drop off in OPS 8. The peak in reflectance for lherzolite (M268) has moved to longer wavelengths to OPS 7. Absorption in OPS 8 is dominated by Mg-OH features associated with serpentine, as a result the lherzolite (M268) and harzburgite (M311) samples containing the most serpentine show the strongest absorptions.

2) Crustal lithologies

Figure 4.30 (a) shows the crustal lithologies convolved over TM bandpasses whilst Figure 4.30 (b) shows them convolved over OPS bandpasses. Compared with the mantle lithologies, the crustal spectra are more varied, corresponding to the more diverse mineralogy of the crustal lithologies. Overall reflectance values are considerably higher, up to 60 % for trondhjemite, whilst the peak in reflectance varies between TM 4, TM 5 and TM 7. Most of the lithologies show low reflectance in TM 1 due to the intense ferric absorptions associated with weathered surfaces. Cumulate and isotropic gabbros (with the exception of M246) also show low reflectance in TM 2, which may be as a result of these samples having a very dark weathered surface, which is often common on exposed gabbro surfaces. The trondhjemite samples (M317 and F001) do not develop this weathered surface and therefore show high reflectance values in TM 1 which rapidly increase through the visible and NIR channels. Pyroxenite and the clinopyroxene-rich cumulate gabbro (M246) show steadily increasing reflectance values up to a peak in TM 5, and then drops off rapidly in TM 7. The other gabbro samples show a flattening of the spectra between TM 5 and TM 7 as both channels show very similar reflectance levels. All trondhjemite samples show decreasing reflectance in TM 7.

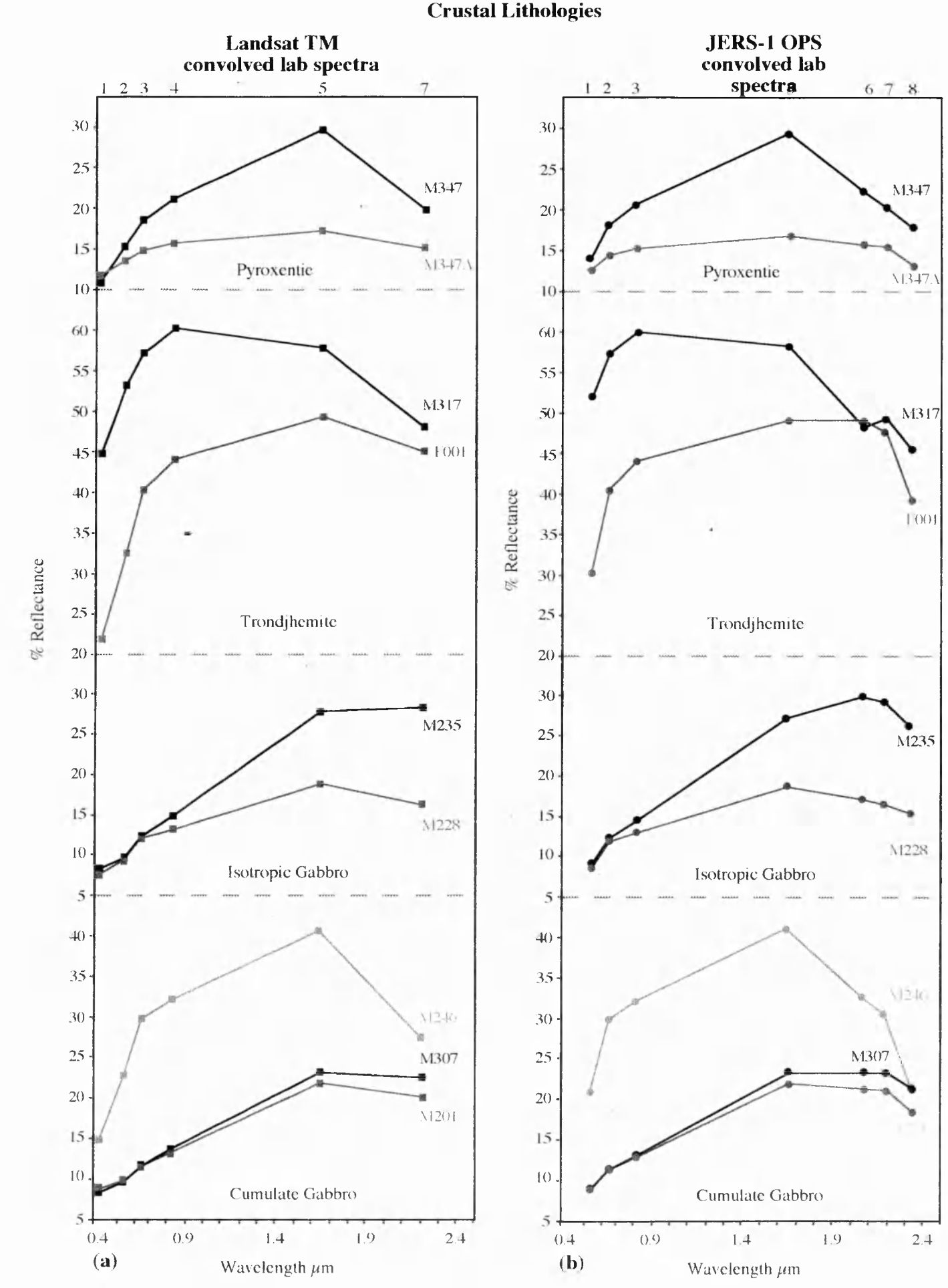

Figure 4.30 Lab spectra of Oman ophiolite rock samples convolved over (a) TM and (b) OPS bandpasses.

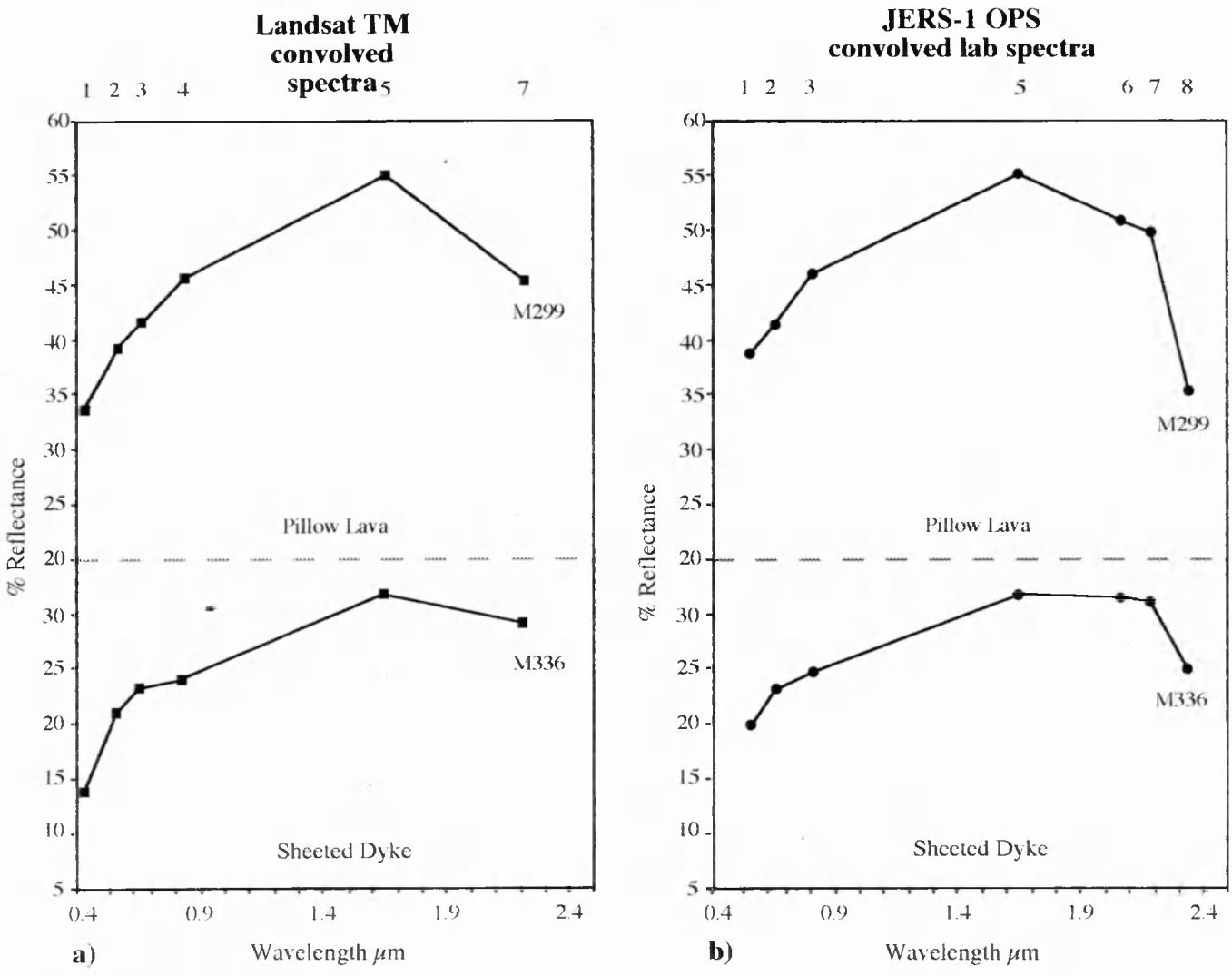

Figure 4.31 Lab spectra of Oman ophiolite rock samples convolved over (a) TM and (b) OPS bandpasses.

The sheeted dyke and pillow lava samples both show distinct spectra, Figure 4.30 (a). Reflectance values increase rapidly for both lithologies across TM 1 to TM 3. The sheeted dyke spectrum then flattens off between TM 3 and TM 4 before rising sharply towards TM 5, eventually decreasing in TM 7. The pillow lava spectrum continues to rise very steeply between TM 3 and TM 4 until it reaches a very pronounced peak in TM 5, reflectance then decreases very sharply in TM 7.

The OPS spectra (b) look quite different to the TM spectra due to the extra SWIR information. With the exception of the isotropic gabbro spectra (M235 and M228) all the OPS spectra show similar profiles across the visible and NIR channels. The only spectral information missing is the change of slope which occurs between TM 1 and TM 2 on the isotropic gabbro spectra. This is not apparent on the OPS spectra because of the lack of a channel equivalent to TM 1. Reflectance maxima occur in OPS 3, OPS 5 and OPS 6. The cumulate gabbro spectra M307 and M201 show only a very slight decrease in reflectance values between OPS 5 and OPS 6, with the spectra being almost flat between OPS 6 and OPS 7, before a notable decrease in OPS 8. The clinopyroxene-rich cumulate gabbro (M246) shows a pronounced decrease in reflectance between OPS 5 and OPS 8, with the steepest drop off occurring between OPS 6 and OPS 7. This feature does not occur on the pyroxenite spectra (M347) allowing these two lithologies to be distinguished between, despite having almost identical TM spectra. The isotropic gabbro show a more pronounced reduction in reflectance at SWIR wavelengths than on the TM spectra. At SWIR wavelengths, the OPS trondhjemite spectra are very different to the TM spectra. Sample M317 shows a strong absorption in OPS 6, followed by a small peak in reflectance in OPS 7, prior to a very sharp drop in reflectance in OPS 8. The slight absorption in OPS 6 is a remnant of the very broad 1.9 μm molecular water absorption that these two samples exhibit, caused by the alteration of feldspar. Sample F001 shows an overall peak in reflectance in OPS 6 before a very sharp fall in reflectance in OPS 8 caused by a strong Mg-OH absorption. Both of the OPS pyroxenite spectra show very similar responses to those of the TM sensor, except for a stronger SWIR absorption feature occurring in OPS 8. The OPS spectra for the sheeted dyke and extrusive samples are very similar to the TM spectra at visible and NIR wavelengths. They differ slightly in the SWIR as the sheeted dyke spectrum is almost flat between OPS 5 to OPS 7 before decreasing in OPS 8, whilst the pillow lava spectrum decreases slowly between OPS 5 and OPS 7 before decreasing very rapidly in OPS 8.

4.3.4 Summary of discrimination potential based on convolved spectra

The best way to summarise the potential discrimination of ophiolite lithologies on either TM or OPS data is to consider the spectra of all of the major mantle and crustal lithologies together.

1) Mantle lithologies

Figure 4.32 shows the major mantle lithologies convolved over TM bandpasses plotted together for comparison. Lherzolite (M268) and the orthopyroxene-rich harzburgite (M311) have very similar spectra at short wavelengths making discrimination between these lithologies in TM 1, TM 2 and TM 3 very difficult. Spectral discrimination is best in TM 4 and TM 5 where the orthopyroxene-rich harzburgite has slightly higher overall reflectance values. The other harzburgite spectra (M281 and M046) are considerably different from both the lherzolite and the orthopyroxene-rich spectra. M046 which contains approximately 5% orthopyroxene can be distinguished from the other harzburgites as it has fairly low overall reflectance values. The moderately orthopyroxene-rich harzburgite (M281) can be distinguished by its intermediate reflectance levels, which show a significant peak in TM 5, compared with the other channels. The shape of the dunite spectrum (M022) closely resembles that of harzburgite and lherzolite (M268) except that it shows slightly lower overall reflectance values. A small identifying feature is that the curve between TM 3 and TM 4 is steeper than that on the lherzolite spectrum. Discrimination of dunite from harzburgite and lherzolite will be difficult at TM resolution. Wehrlite (M054) also has a fairly similar spectral profile to harzburgite, but it can be distinguished by its relatively flat spectrum which shows the lowest reflectance values in all bands.

Figure 4.33 shows the major mantle lithologies convolved over OPS bandpasses plotted together for comparison. Lherzolite (M268) and the orthopyroxene-rich harzburgite (M311) once again have similar spectra at short wavelengths making discrimination between these lithologies in OPS 1 and OPS 2 difficult. Like the TM spectra, the lherzolite spectrum is fairly flat across OPS 3, and OPS 5, whilst the orthopyroxene-rich harzburgite shows increasing reflectance in these channels. Both spectra are very similar in OPS 6 and OPS 7 although there is a slight difference as the lherzolite shows slightly increasing reflectance values between OPS 6 and OPS 7, whilst the harzbugite spectra is flat across these two channels. The other harzburgites

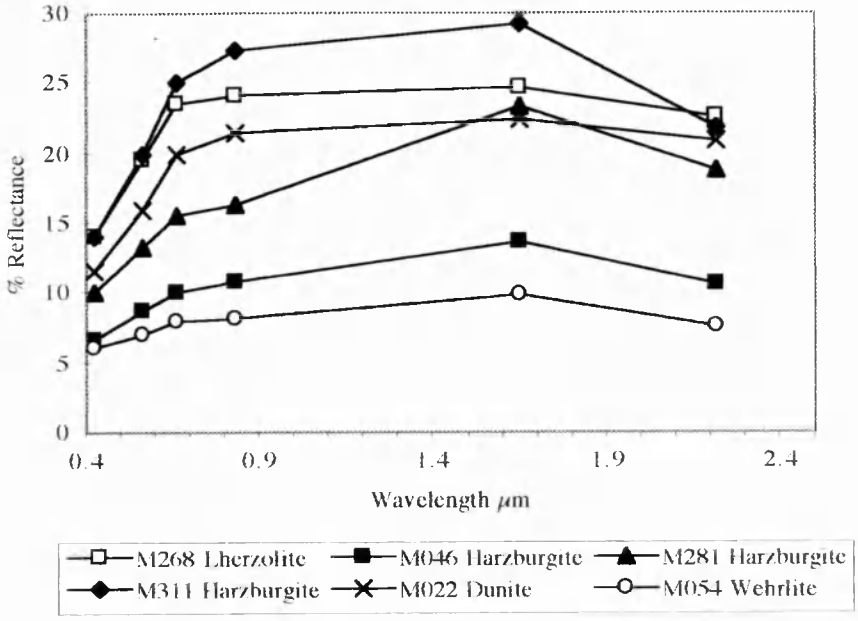

Figure 4.32 Spectral discrimination between the main mantle lithologies when convolved over TM bandpasses.

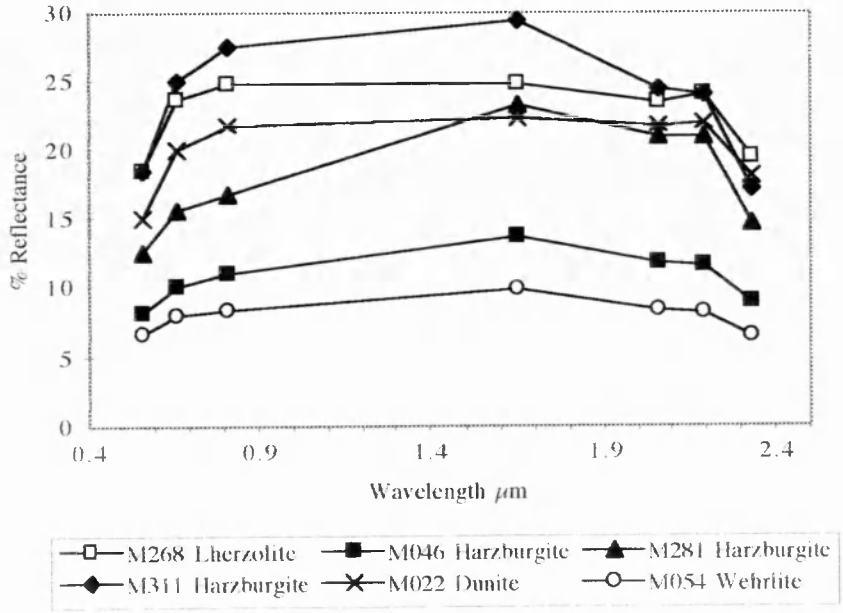

Figure 4.33 Spectral discrimination between the main mantle lithologies when convolved over OPS bandpasses.

lherzolite shows slightly increasing reflectance values between OPS 6 and OPS 7, whilst the harzbugite spectra is flat across these two channels. The other harzburgites (M046 and M281) show very similar spectral features to those seen on the TM spectra and can be easily distinguished. Note that both of these samples show decreasing reflectance values between OPS 5 and OPS 6 and between OPS 7 and OPS 8, but show a flat spectrum between OPS 6 and OPS 7. The OPS spectra of dunite and wehrlite are very similar to the TM spectra. The additional SWIR channels OPS 6 and OPS 7 do not add much additional discrimination information for these lithologies, but the narrow channel of OPS 8 gives additional information regarding the strength of Mg-OH absorptions.

2) Crustal lithologies

Figure 4.34 shows the major crustal lithologies convolved with TM bandpasses plotted together for comparison. Discrimination between cumulate (M307) and isotropic gabbro (M235) may be a problem as the two spectra are very similar, especially in the visible and NIR bands (TM 1 to TM 4), due mainly to surface weathering. Potential discrimination may lie in the fact that the isotropic gabbro has higher reflectance values in the SWIR channels TM 5 and TM 7.

Problems will also arise distinguishing pyroxene-rich cumulate gabbro (M246) from pyroxentite (M347) as these two lithologies have very similar spectral profiles. Both of these pyroxene-rich lithologies have distinct spectra compared with the other crustal lithologies as they show rapidly increasing reflectance values across TM 1 to TM 4, with a distinctive peak in TM 5. This peak causes reflectance to increase very rapidly between TM 4 and TM 5, whilst decreasing even more sharply between TM 5 and TM 7. The problem is distinguishing between pyroxenite and pyroxene-rich cumulate gabbro which also shows these features. The sheeted dyke spectrum (M336) has quite a similar profile to the cumulate gabbro spectrum except that it has higher reflectance in all bands, especially in bands TM 1 to TM 4. Both trondhjemite (M317) and the extrusives (M299) are distinct because they are spectrally very bright. They can be distinguished from each other because trondhjemite has a reflectance maximum in TM 3 or TM 4 whilst the pillow lavas have maximum reflectance in TM 5. TM data should be able to distinguish between most of these lithologies, although some problems may arise distinguishing between various gabbros if they are severely effected by surface weathering.

Figure 4.35 illustrates the spectral discrimination between the main crustal lithologies when convolved with OPS bandpasses. Like the TM spectra (Figure 4.32) the majority of the lithologies appear to have quite distinct spectral profiles allowing

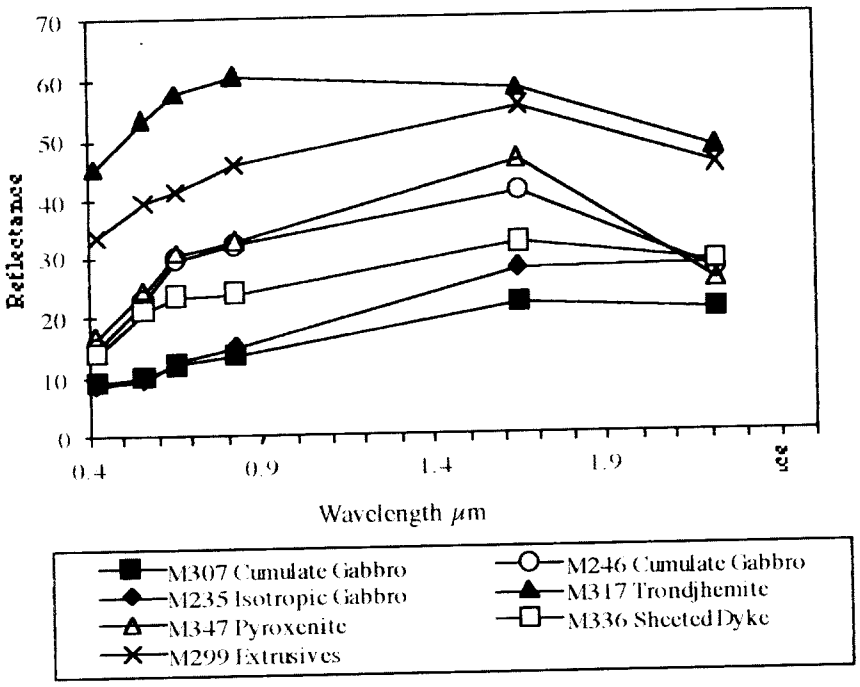

Figure 4.34 Spectral discrimination between the main crustal lithologies when convolved over TM bandpasses.

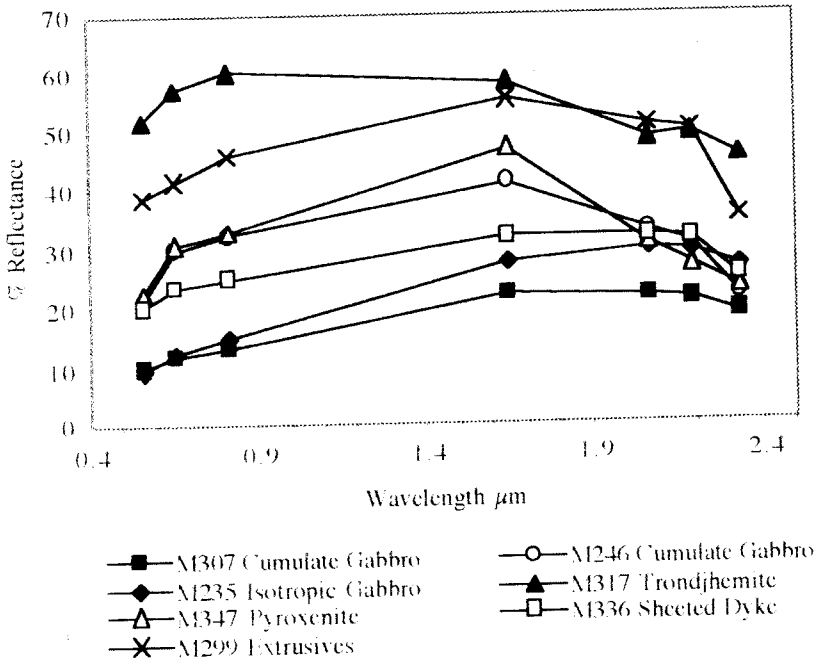

Figure 4.35 Spectral discrimination between the main crustal lithologies when convolved over OPS bandpasses.

them to be distinguished. The isotropic gabbro spectrum (M235) shows a slightlymore pronounced decrease in reflectance in OPS 8 than that of the cumulate gabbro (M307), a feature which may aid discrimination between these two lithologies. The additional SWIR channels also help to separate the pyroxene-rich gabbro spectrum (M246) from that of the pyroxenite (M347). The pyroxenite has a strong decrease in reflectance between OPS 6 and OPS 7 whilst the gabbro has a strong decrease between OPS 7 and OPS 8, resulting in the separation of these spectra when compared to the TM profiles. The sheeted dyke spectrum (M336) shows a very similar response across the SWIR channels to that of the pyroxene-rich gabbro (M246), but can be distinguished because of its distinct reflectance values across OPS 1 to OPS 3. Trondhjemite (M317) and pillow lavas (M299) are distinct from the other lithologies because of their high reflectance values. The pillow lavas show similar reflectance levels in OPS 6 and OPS 7 with a sharp fall-off in OPS 8, whilst trondhjemite shows a slight increase in reflectance between OPS 6 and OPS 7 followed by a small decrease in OPS 8.

Comparing lab measured spectra convolved with TM and OPS bandpasses suggests that the OPS data ought to be able to distinguish more conclusively between some lithologies. Primarily due to the sub-division of the 2.0-2.4 region of the EM spectrum into three narrow channels. However problems will still arise discriminating between mantle lithologies due to their similar mineralogical composition. Discriminating between harzburgites is made all the more difficult due to their highly variable nature. Despite the increased spectral resolution in the SWIR the additional channels OPS 6 and OPS 7 add very little spectral information with respect to discriminating between mantle lithologies, although in some cases OPS 6 can be distinguished from OPS 7 by the occurrence of a weak hydroxyl absorption. Figure 4.35 shows that in practice the reflectance values in OPS 6 and OPS 7 are highly correlated for crustal lithologies. Additional spectral information is provided by OPS 7 for some crustal lithologies (Figure 4.35). This is because OPS 7 contains weak but distinct Al-OH absorptions. The narrow SWIR channel OPS 8 which is dominated by the Mg-OH absorption provides the vast majority of the additional spectral information for both mantle and crustal lithologies. This is particularly true of mantle lithologies which tend to be dominated at these wavelengths by absorptions related to serpentine.

Table 4.1 summarises potential discrimination of the major ophiolite lithologies based upon the qualitative analysis of lab spectra convolved with TM and OPS bandpasses. This initial analysis suggests that discrimination potential of five lithologies will be low to medium on TM imagery whilst five will be medium to high. On OPS imagery discrimination potential for only two lithologies will be low to medium whilst it will be medium to high for the remaining eight.

Lithology	TM Convolved Spectra		OPS Convolved Spectra	
	Discrimination Potential	Distinguishing Factor	Discrimination Potential	Distinguishing Factor
Lherzolite	Low - Medium	Near constant reflectance, TM 3, 4, 5 and 7	Low - Medium	Higher reflectance in OPS 7 than OPS 6
Harzburgite	Medium	TM 5 very variable depending on mineralogy	Medium	OPS 5 variable, OPS 6 and 7 very similar, OPS 8 absorption
Dunite	Low	Near constant reflectance	Medium	Constant reflectance OPS 3, 5, 6 and 7
Wehrlite	High	Very low reflectance all channels	High	Very low reflectance all channels
Cumulate Gabbro	Low - Medium	Reflectance peak TM 5, TM 7 very similar	Medium	Reflectance peak in OPS 5
Isotropic Gabbro	Low - Medium	Reflectance peak in TM 7	Medium - High	Peak in OPS 6 and OPS 7
Trondhjemite	High	Very high reflectance all channels	High	Peak OPS 3, very high reflectance
Pyroxenite	Medium	Higher TM 5 than TM 7	Medium - High	OPS 5 higher than OPS 3 or OPS 6
Sheeted Dyke	Low	TM 3 and 4 very similar reflectance	Medium	Similar reflectance OPS 6 and 7, absorption in OPS 8
Pillow Lava	Medium - High	Quite high reflectance TM 2 and 3 very similar	Low - Medium	Quite high reflectance, very strong absorption OPS 8

Table 4.1 Summary of discrimination potential of ophiolite lithologies at TM and OPS resolution, based upon the qualitative comparison of convolved lab spectra of representative lithology samples.

4.4 Comparison of convolved lab spectra with image spectra

The previous section compared the potential lithological discrimination of the Oman ophiolite lithologies based on convolved lab spectra. Actual discrimination can now be tested by comparing the convolved lab spectra with spectra derived from both TM and OPS image data. Note that the OPS data were not cleaned prior to the extraction of pixel DN values, however the data have been resampled as a part of Level 2 pre-processing.

4.4.1 Pre-processing of image data

Prior to the extraction of DN values from either the TM or OPS image data the effects of atmospheric attenuation have to be considered. Attenuation by the atmosphere is caused by electromagnetic radiation being both absorbed and scattered. Atmospheric scattering, particularly at visible wavelengths, is a major problem as significant amounts of EMR are redirected back towards the satellite sensor. This causes an additive effect resulting in image data having increased reflectance values. Appendix 1 describes this process in more detail and explains how offset DN values can be established which represent the additive scatter component of each channel. Once these offset values have been determined a simple correction can be applied to the image data, known as the 'dark object subtraction' technique (Chavez 1988).

Once a correction has been applied to compensate for atmospheric scattering, the modified DN values can be extracted from the imagery and converted to semi-calibrated reflectance values. This is a two part procedure which first converts DN values to spectral radiance and then to reflectance by normalising for solar irradiance. This procedure is described in full in Appendix 2. Sensor gain and offset values for both TM and OPS can also be found in Appendix 2.

Once these procedures have been applied lithological reflectance information can be extracted from the image data for comparison with the convolved lab spectra. The image spectra for each lithology represents the average spectra for a minimum of ten sample locations. All sampling points where chosen from areas representing fairly homogeneous lithologies or areas of known lithological mixes. All sample points where chosen from sunlit slopes to avoid inducing variations in spectra caused by differing illumination levels. Figure 4.36 (a) illustrates ten image spectra extracted from TM data representing an area of fairly homogeneous harzburgite. These reflectance spectra show the typical levels of variation between different sampling

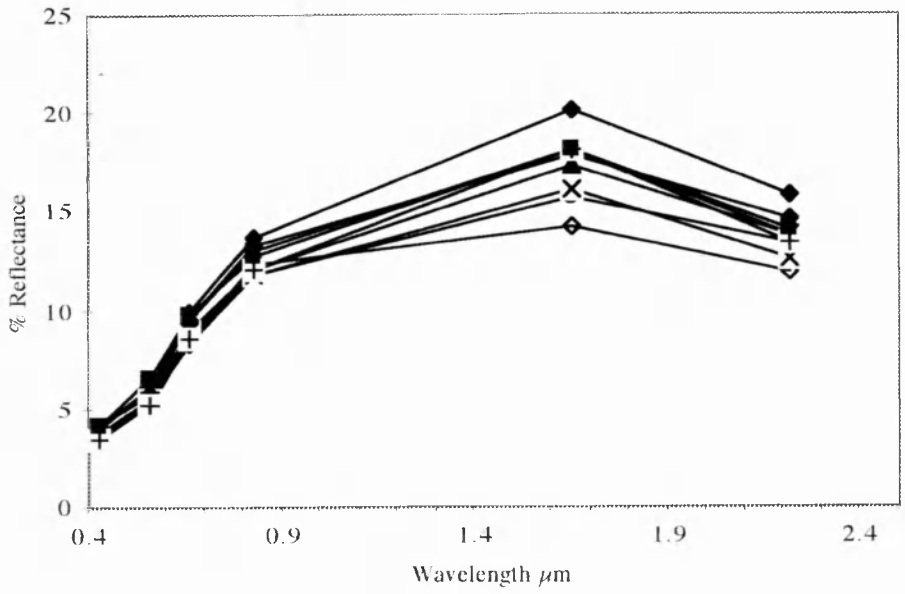

Figure 4.36 (a) Plot showing the variation in TM image reflectance spectra for harzburgite extracted from 10 neighbouring pixel locations.

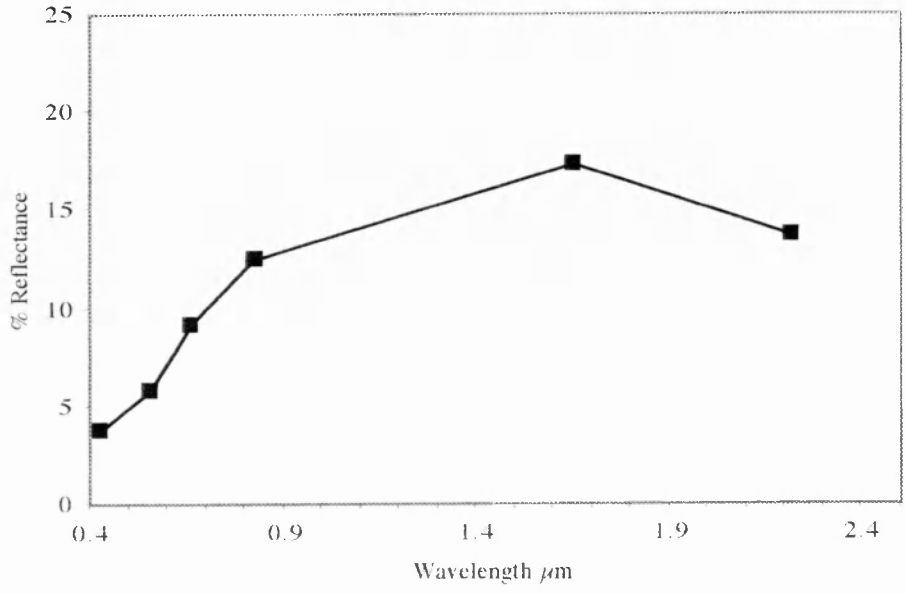

Figure 4.36 (b) Plot showing the average TM image reflectance spectrum for harzburgite derived from the spectra in Figure 4.36 (a).

points for a given lithology. Reflectance values are fairly consistent in bands TM 1 to TM 4, varying by only 1-2%. TM 7 shows increased variability with reflectance levels ranging between 12-16%, whilst TM 5 shows the maximum variability with reflectance levels varying between 13-20%. Increased variability in TM 5 and TM 7 is not unexpected as these bands will respond to mineralogical changes associated with olivine and orthopyroxene (TM 5) and serpentine (TM 7). Figure 4.36 (b) illustrates the average TM harzburgite spectra derived from the sample locations.

Figure 4.37 (a) illustrates ten image spectra extracted from OPS data from the same homogeneous harzburgite as that sampled in the TM imagery. Reflectance values in OPS 1 are almost consistent, whilst OPS 2 and OPS 3 vary over about 4% reflectance. A maximum variation of 6% is seen in OPS 5, which is approximately equal to the maximum seen in TM 5. Variations in OPS 6 and OPS 8 are 2% and 3% respectively, whilst OPS 7 varies by approximately 1%. Figure 4.37 (b) illustrates the average OPS image spectrum derived from these sample locations.

Intentionally left blank

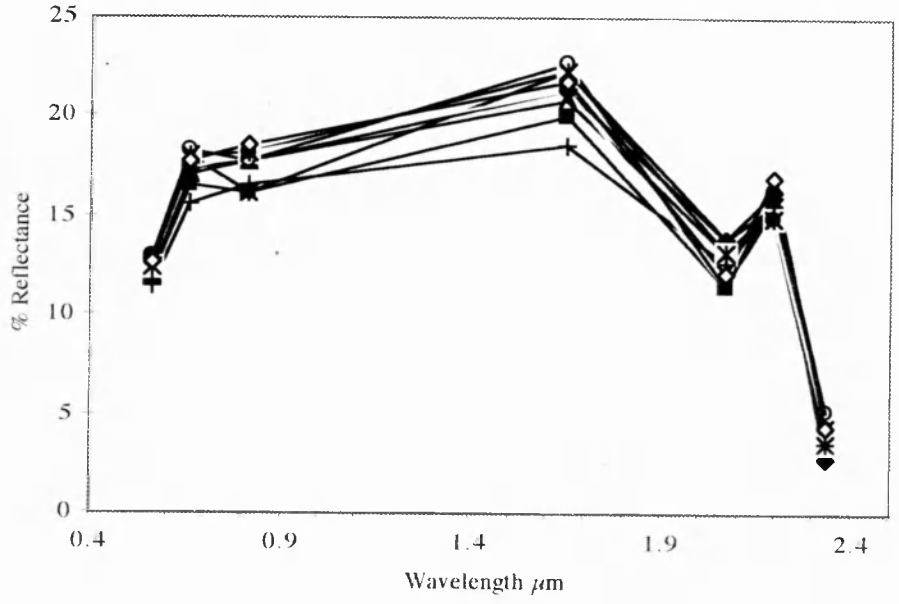

Figure 4.37 (a) Plot showing 10 OPS image spectra of harzbugite extracted from 10 neighbouring pixel locations.

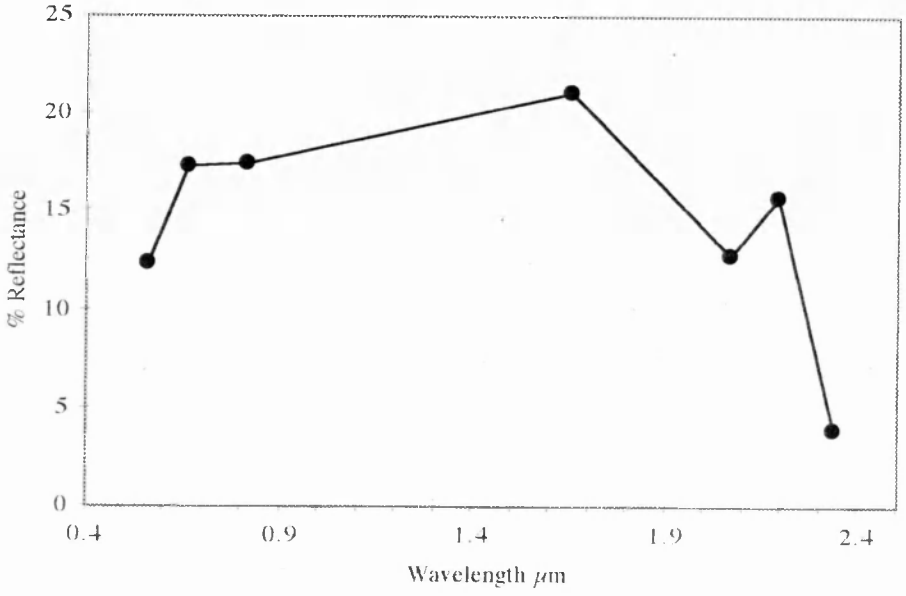

Figure 4.37 (b) Plot showing the average OPS harzbugite spectrum derived from the spectra shown above.

Spectral profiles extracted from image data will never perfectly match those of the convolved spectra for a number of reasons:

1) Approximations in atmospheric correction and reflectance conversion

It is recognised that the dark object subtraction technique used to correct for atmospheric scatter (Appendix 1) is quite a simple approximation to the complex atmospheric processes affecting the image data. As a result this technique may slightly over or under compensate for atmospheric scatter. The DN to reflectance conversion process (Appendix 2) is also an approximation as it does not take into account complex parameters such as local slope geometry. Both of these 'simplified' techniques will slightly modify image spectra.

2) Mixed pixels

Each TM pixel represents the average reflectance over an area of 900 m^2 whilst an OPS pixel represents that over an area of 324 m^2. Both of these are quite large areas over which numerous parameters, both geological and non-geological can change. Geological variations can be quite large, for example, the occurrence of two mineralogically distinct lithologies within one pixel, or they can be quite minor, representing only localised mineralogical variations e.g., increased accessory or alteration minerals. Often a pixel will be comprised of a mixture of two or more of the lithologies described in Section 4.1.2 in varying proportions. As a result the lab spectra measured in Section 4.2.3 for each lithology should be considered as 'end members' between which any mixture of lithologies can occur. It should also be remembered that the spectra described in section 4.2.3 have been derived from a limited number of hand samples. It is therefore possible that these spectra are not fully representative of all of the lithological variations present on the imagery.

Small geological variations can also be introduced by variations in weathering across an outcrop, for example, increased localised weathering may be caused by the action of water within a wadi channel. The localised build up of scree deposits may dominate the spectral response of some pixels (or parts thereof).

3) Data quality

The extremely variable quality of OPS data, as described in Chapter 2, will also induce some 'spectral' variation. Because of the complex nature of the noise structures

affecting all OPS channels it is extremely doubtful (when considering 'non-cleaned' OPS data) that the pixel locations used to extract pixel information will be noise-free. Sampling a pixel which has an additive noise component will result in a slightly higher than expected reflectance spectrum. Different levels of noise modulation between channels will introduce more variability into the entire spectra. Some of these effects will be removed by sampling DN values from a number of locations and averaging the results, thereby removing isolated noise features. However, if a noise feature is consistent in any one channel across all sample points it will modify the derived average spectrum.

4.4.2 TM and OPS image spectra

Variations between convolved TM spectra of mantle lithologies and averaged TM image spectra (as per Section 4.4.1) can be seen in Figure 4.38 (a) and (b). Despite the problems outlined above the majority of the image spectra correspond to the predicted (i.e. convolved) spectra very well. Image reflectance values for all lithologies increase more rapidly than predicted across bands TM 1 to TM 4. Reflectance values across TM 3 and TM 4, and in turn the steepness of the spectral curve between them, is controlled by absorption features near 0.7 μm, 0.9 μm and 1.0-1.1 μm, i.e., minerals such as chlorite, epidote, orthopyroxene, serpentine and amphibole. The presence of these minerals will result in absorption features which lower the reflectance in these two bands and produces a gentle positive spectral slope between TM 3 and TM 4. The steeper image spectra at these wavelengths suggests that the TM sensor is not as sensitive to these absorption features as the lab based spectroradiometer. Reflectance values in TM 5 and TM 7 correspond very well to those of the convolved spectra. Reflectance maxima on the image spectra are approximately 5% lower than those of the convolved spectra.

Figures 4.38 and 4.39 show TM convolved spectra (a) and image spectra (b) for the main crustal lithologies. Once again the overall spectral profiles correspond quite well, although there are some notable differences. The image spectra for cumulate gabbro have only a slight positive slope between TM 4 and TM 5, whereas convolved spectra (M201 and M307) have very steep slopes. This may be due to the convolved spectra of these samples being strongly influenced by dark surface weathering. The isotropic

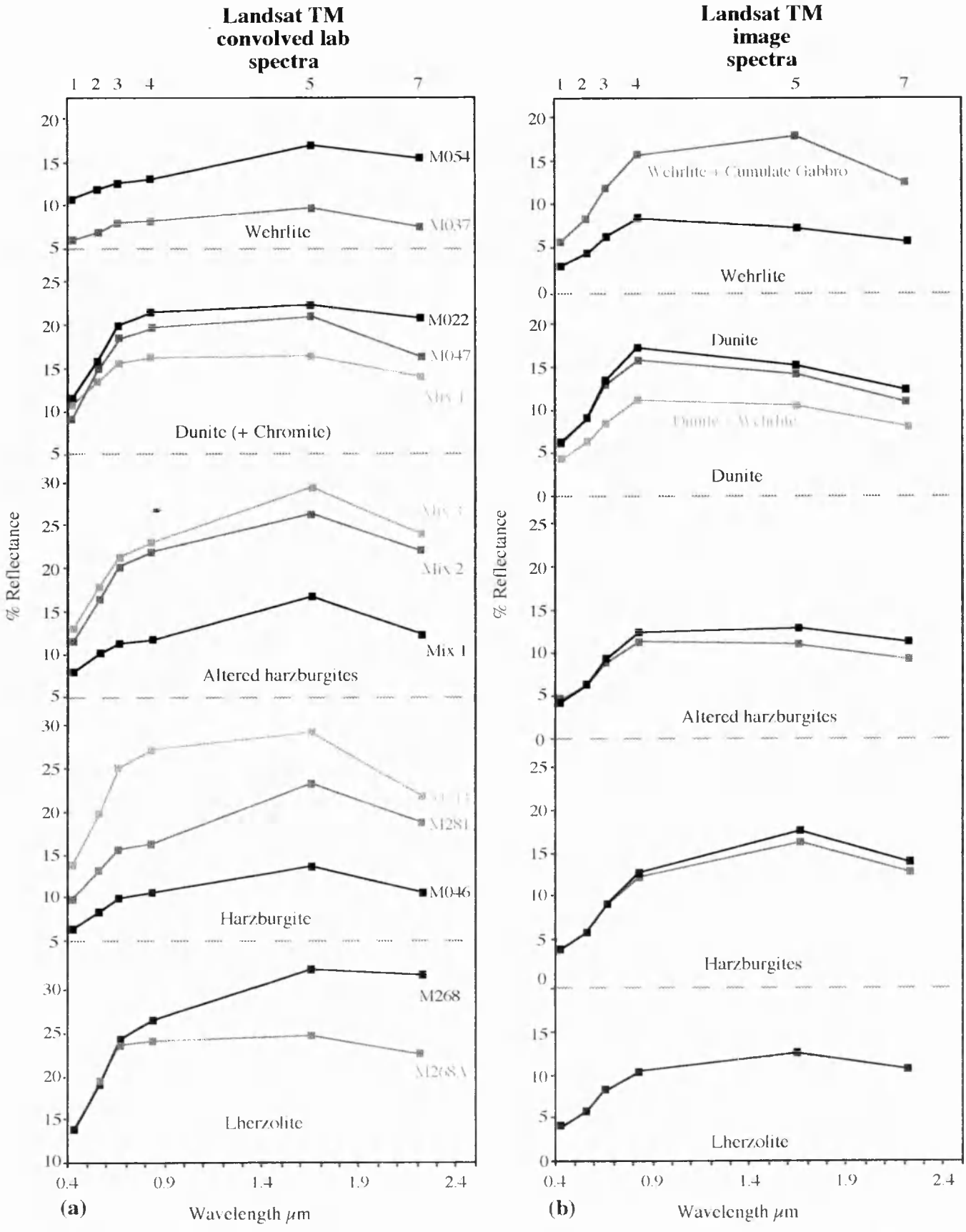

Figure 4.38 Comparison of (a) lab spectra convolved over TM bandpasses and (b) image spectra extracted from TM data (average spectra from 10 pixels), for mantle lithologies. Image spectra are also shown for some lithological mixes.

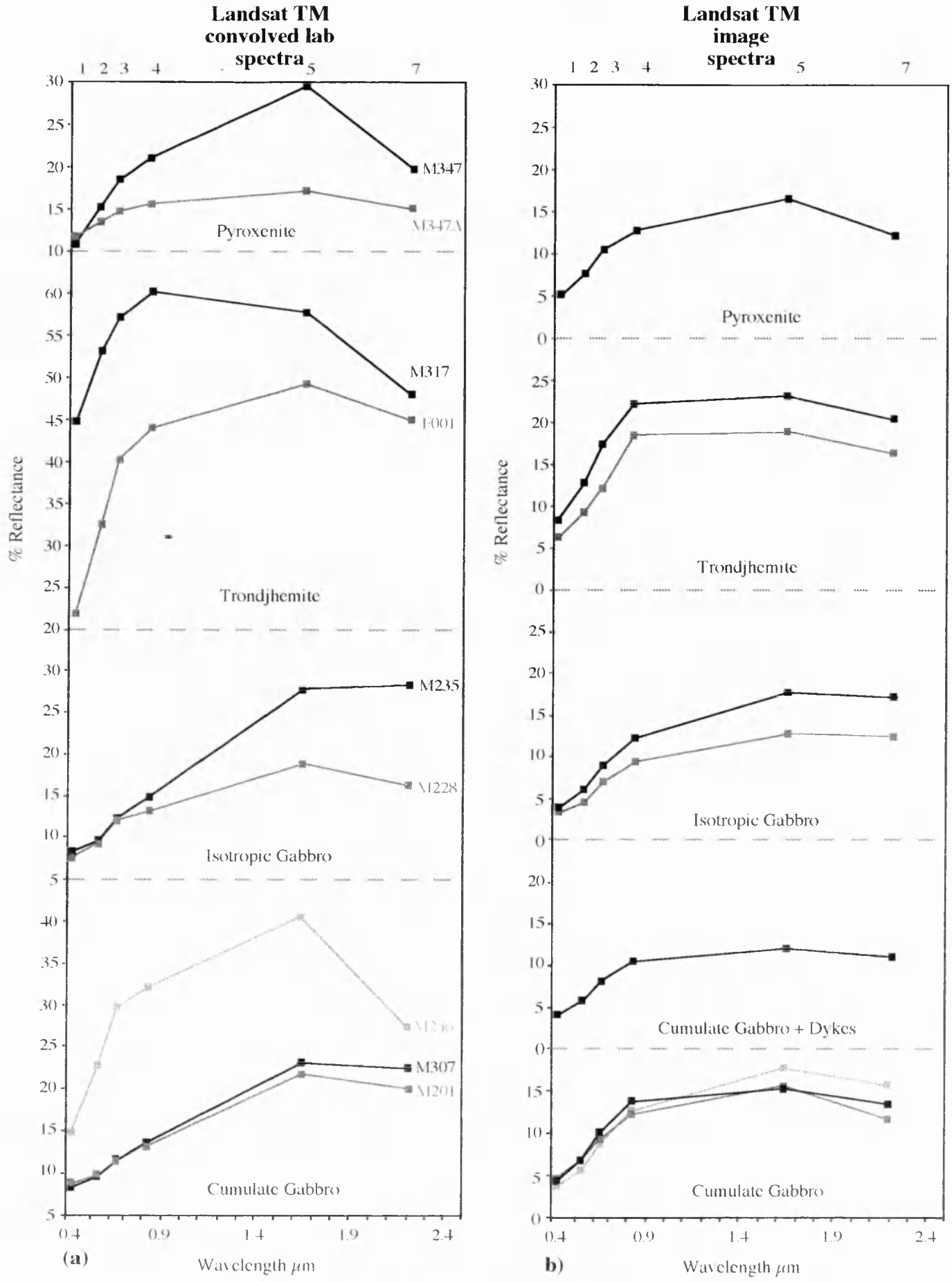

Figure 4.39 Comparison of (a) lab spectra convolved over TM bandpasses and (b) image spectra extracted from TM data (average spectrum from 10 neighbouring pixels) for crustal lithologies.

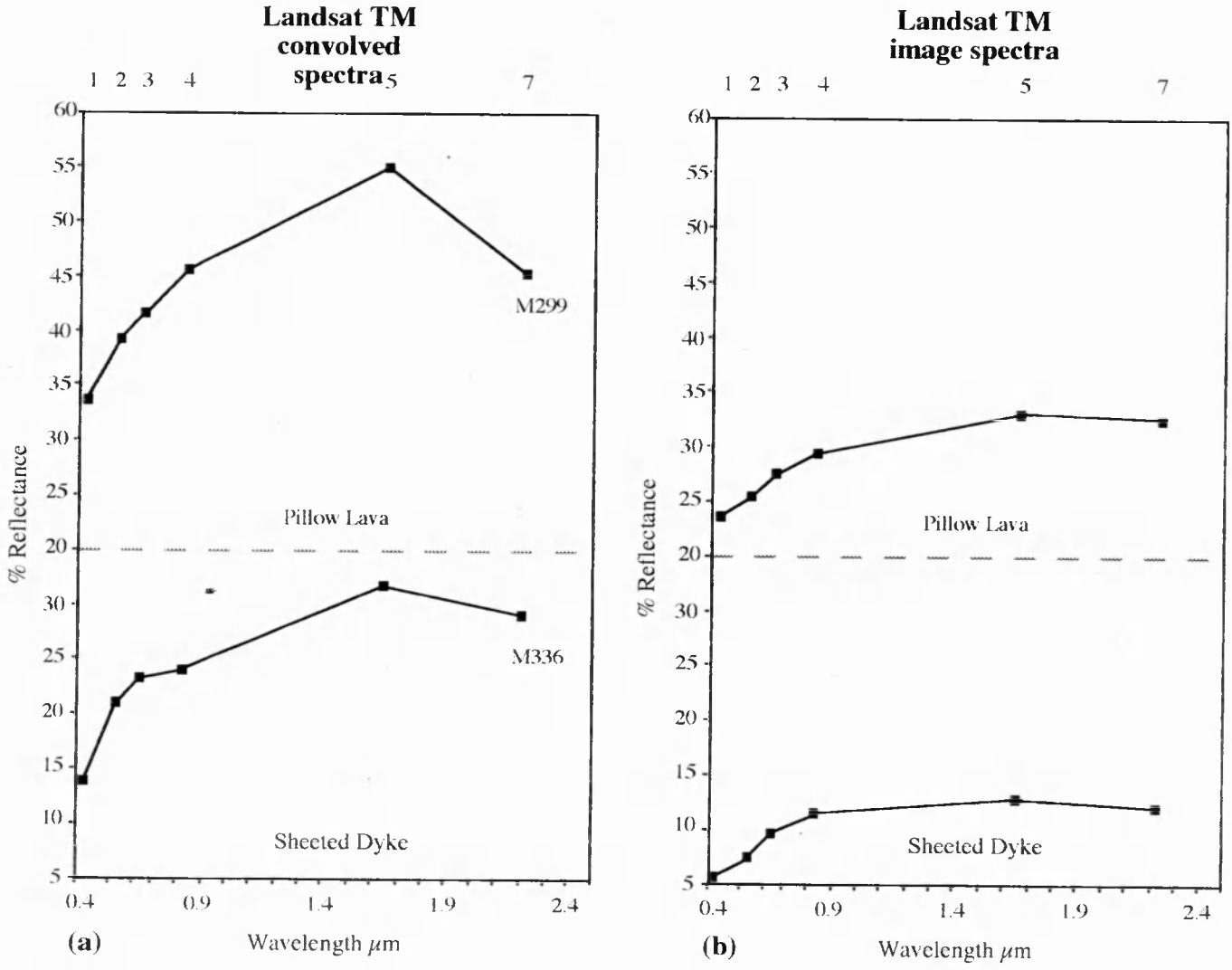

Figure 4.39 (continued) Comparison of (a) lab spectra convolved over TM bandpasses and (b) image spectra extracted from TM data (average spectrum from 10 neighbouring pixels) for crustal lithologies.

gabbro image spectra match the convolved ones very well, although the increase in reflectance between TM 4 and TM 5 is not as great as expected. The trondhjemite image spectra are very similar to the convolved spectra except that they show more consistent reflectance levels between TM 4 and TM 5. The pyroxenite spectra are also a good match except for the peak in TM 5 being slightly subdued. The image spectra of sheeted dyke and pillow lava, Figure 4.39 (b), are quite different to the convolved spectra. The convolved sheeted dyke spectrum, Figure 4.39 (a), increases rapidly between TM 1 and TM 2, whereas the image spectrum (b) is comparatively flat over this region. The convolved spectrum (a) has a pronounced peak in reflectance in TM 5 which is not evident in the image spectrum. This is also true for pillow lava although there is a slight increase in reflectance in TM 5 on the image data (b). Reflectance levels across the visible channels also increase less sharply on the image spectrum (b) compared with the lab spectrum of pillow lava. Overall the convolved TM spectra are a reasonable approximation to the actual spectral response of the TM sensor with respect to these sample lithologies.

The OPS image spectra for mantle lithologies, Figure 4.40 (b) are quite different from the convolved spectra (a) with significant differences occurring at all wavelengths. Reflectance values for OPS 1 are as expected but those of OPS 2 tend to be lower than expected, this is particularly evident on the dunite and lherzolite spectra. Reflectance values for OPS 3 and OPS 5 are as expected but those of OPS 6, OPS 7 and OPS 8 are noticeably different. OPS 6 shows much lower than expected reflectance values resulting in a sharp drop-off in the spectra between OPS 5 and OPS 6. Whilst OPS 7 shows higher than expected values producing a steep positive slope between OPS 6 and OPS 7. Convolved spectra indicate that reflectance across both of these channels should be fairly constant. In fact the reflectance values for OPS 6 and OPS 7 are almost consistent for all lithologies (including crustal ones) suggesting that the image derived reflectance values are not representing mineralogical variations. Instead these reflectance values are controlled by data quality as OPS 6 and OPS 7 have extremely poor dynamic ranges. As a result spectral detail in OPS 6 and OPS 7 should be disregarded when comparing the image spectra to the convolved spectra. OPS 8 also exhibits lower reflectance values than expected, as a result of data quality. However the problem is not as severe as that of OPS 6 and OPS 7, as OPS 8 responds to some mineralogical variations.

Ignoring the reflectance data from OPS 6 and OPS 7 the image spectra of mantle lithologies match the convolved ones reasonably well although there are some distinct differences. The lherzolite image spectra correspond quite well with the convolved

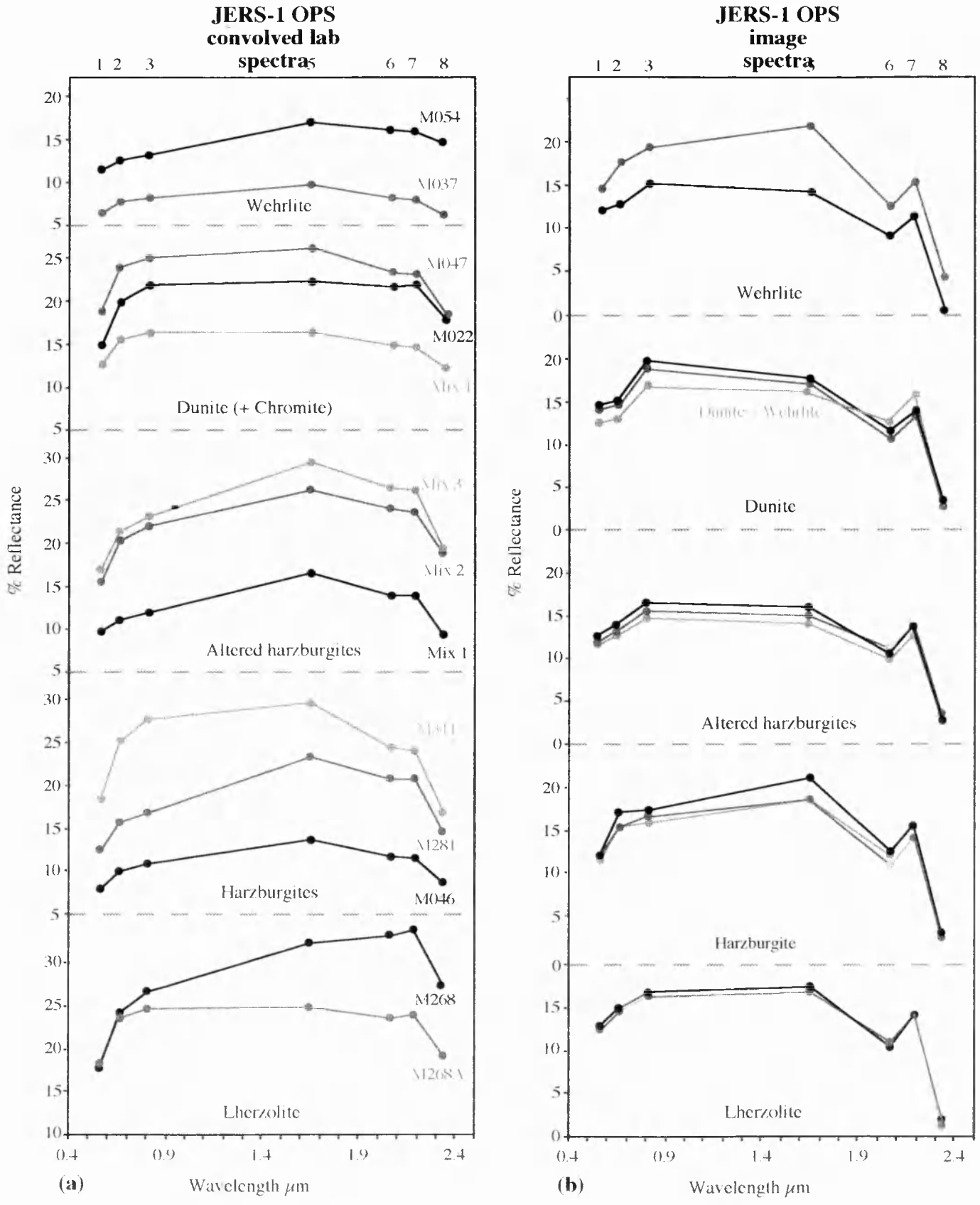

Figure 4.40 Comparison of (a) lab spectra convolved over OPS bandpasses and (b) image spectra extracted from OPS data (average spectrum from 10 neighbouring pixels)for mantle lithologies.

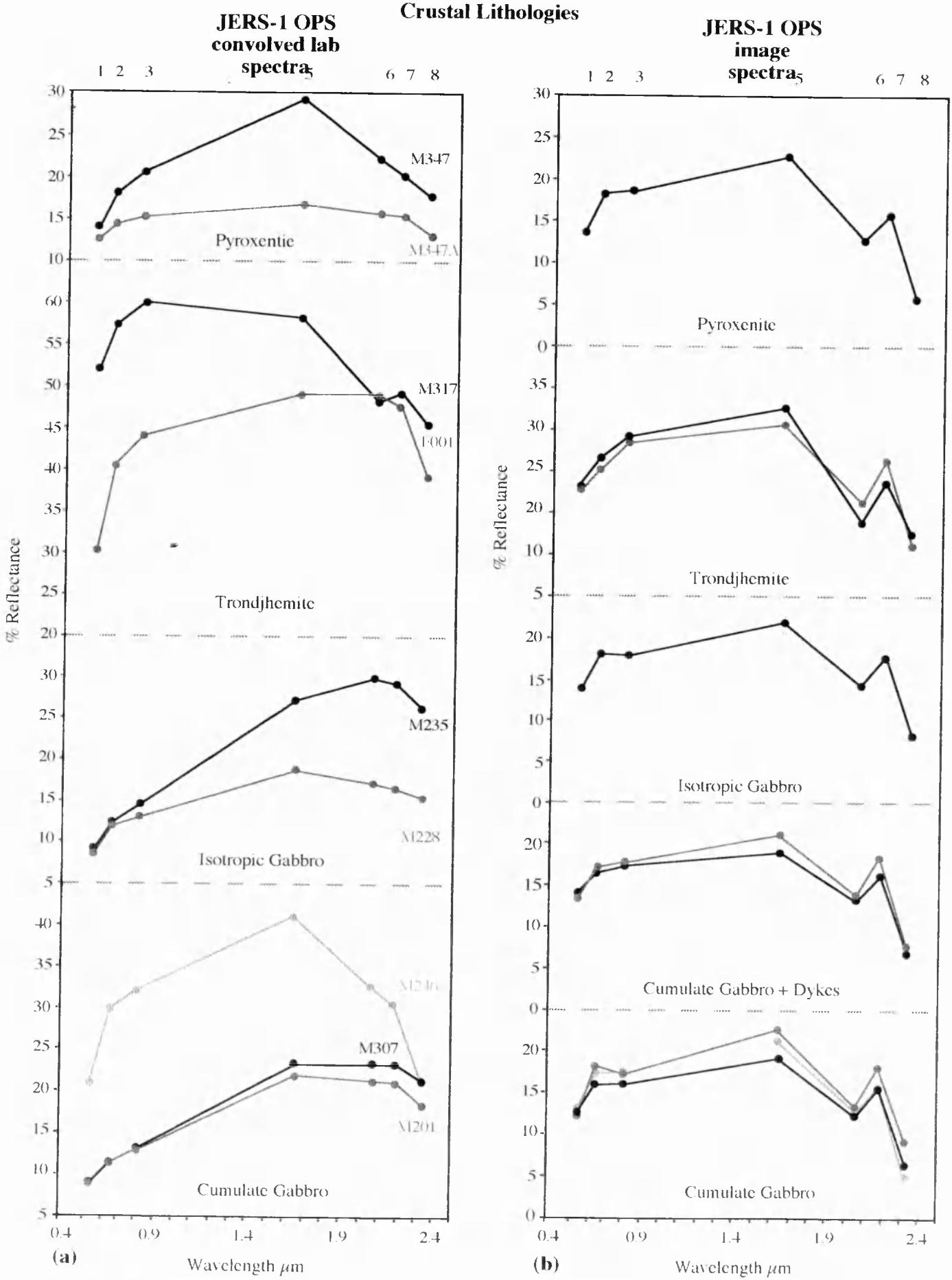

Figure 4.41 Comparison of (a) lab spectra convolved over OPS bandpasses and (b) image spectra extracted from OPS data (average spectrum from 10 neighbouring pixels) for crustal lithologies.

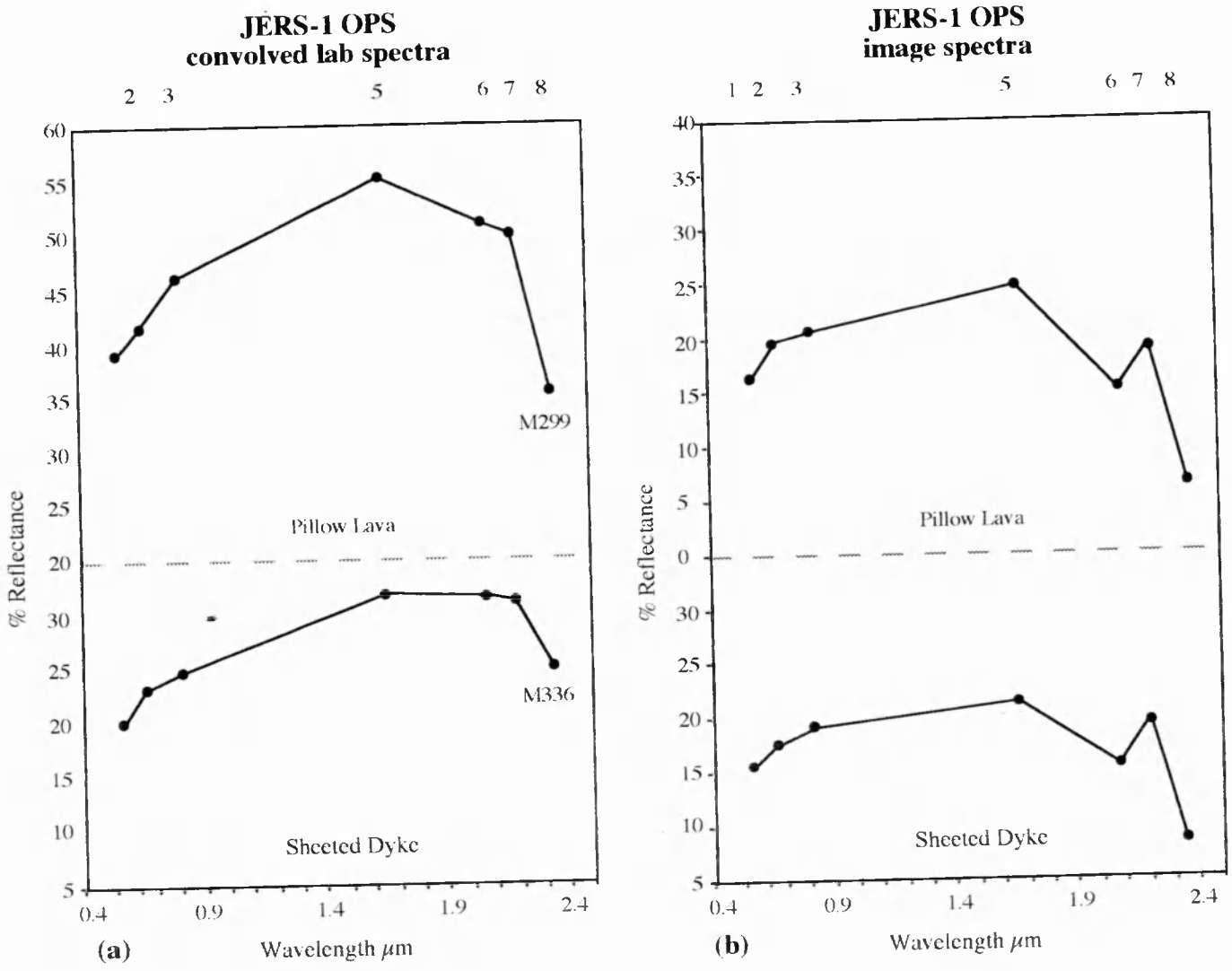

Figure 4.42 Comparison of (a) lab spectra convolved over OPS bandpassess and (b) image spectra extracted from OPS data (average spectrum from 10 neighbouring pixels) for crustal lithologies.

lab spectra, although differences in reflectance levels across OPS 1 and OPS 2 are not as great as expected. Harzburgite image spectra are also similar to the convolved ones with the exception that reflectance levels across OPS 2 and OPS 3 tend to be quite uniform, whereas OPS 3 is usually higher than OPS 2 on the convolved data. The dunite image spectra is noticeably different from the convolved one at visible wavelengths. The convolved spectra shows a steady increase in reflectance over OPS 1, OPS 2 and OPS 3, whilst the image spectra show fairly uniform reflectance levels over OPS 1 and OPS 2 with a major increase in reflectance in OPS 3. This increase in OPS 3 corresponds to the high at visible wavelengths seen in the original lab spectra (Figure 4.12). Wehrlite image spectra appear to be slightly brighter than the convolved spectra suggest.

OPS image spectra for crustal lithologies, Figure 4.41 (b), also look very different in the SWIR from the convolved spectra, Figure 4.41 (a), due to the reasons described above. The gabbro image spectra (both isotropic and cumulate) differ quite a bit from the convolved spectra. The image spectra do not show the rapid drop off in reflectance from OPS 5 to OPS 1 as per the convolved spectra. This difference is probably due to the fact that the convolved spectra have been influenced by the spectral characteristics of surface weathering on the samples. Surface weathering causes a strong drop in reflectance at visible wavelengths which is not as apparent on the image spectra. The trondhjemite spectra are quite similar, although once again the variation in reflectance levels between OPS 1 and OPS 2 on the image spectra is not as great as that on the convolved spectra. The pyroxenite spectra is very similar to that of the convolved spectra. Sheeted dyke and pillow lava image spectra (Figure 4.42 (b)) are very similar to the convolved lab spectra, more so than the TM spectra.

4.4.3 Summary of discrimination potential based on image spectra

The best way to summarise the discrimination of ophiolite lithologies based on TM and OPS image data is to consider the spectra of the major mantle and crustal lithologies together.

1) Mantle lithologies

Figure 4.43 shows spectra for the major mantle lithologies extracted from TM image data, plotted together for comparison. The lherzolite, harzburgite and wehrlite spectra are all very similar in shape, especially at visible and NIR wavelengths.

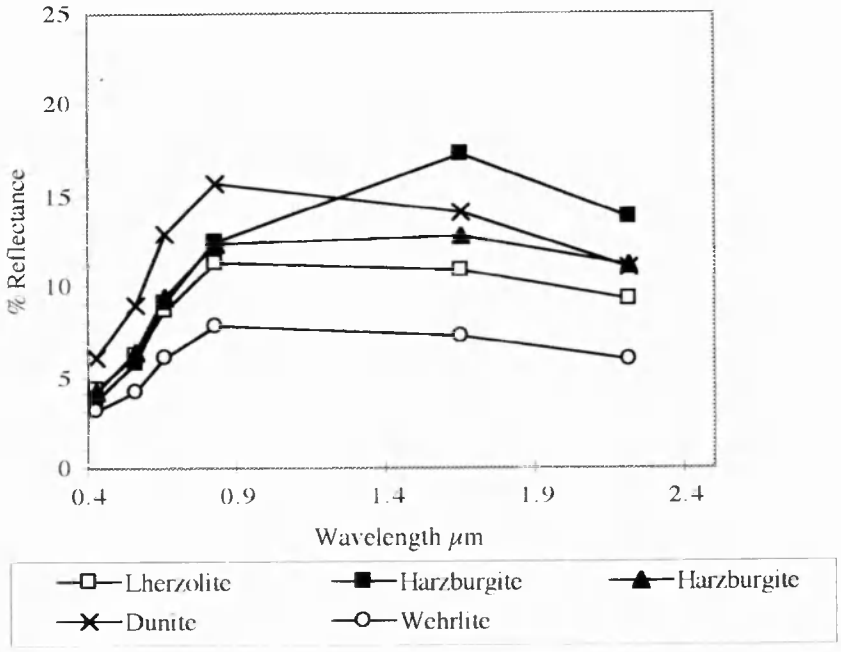

Figure 4.43 TM image spectra of major mantle lithologies plotted together for comparison.

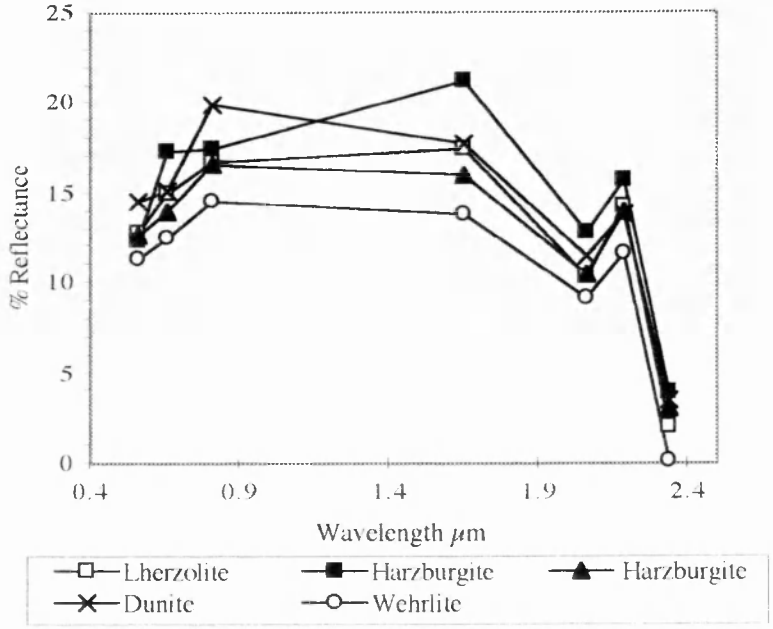

Figure 4.44 OPS image spectra of the major mantle lithologies plotted together for comparison.

Despite the similar profiles wehrlite can be distinguished by characteristically low reflectance levels (3-8%) in all bands. Harzburgites and lherzolites have higher reflectance values than wehrlite, although distinguishing between these two lithologies is difficult. Reflectance variations in TM 5 and TM 7 may allow some limited discrimination between these lithologies. Dunite is clearly distinguishable because of its higher visible and NIR reflectance values which peak in TM 4, resulting in a negative spectral slope between TM 4, TM 5 and TM 7.

Figure 4.44 shows spectra for the major mantle lithologies extracted from OPS image data. When these spectra are plotted together the extremely high correlation in the SWIR channels (OPS 6, OPS 7 and OPS 8) is obvious. Reflectance values in OPS 6 and OPS 7 are mainly controlled by noise artefacts in the image data. Image noise also strongly influences OPS 8 although this channel does respond to some mineralogical features. Ignoring the reflectance data from OPS 6 and OPS 7 the spectral curves for lherzolite, harzburgite and wehrlite are all very similar, as for the TM data. Wehrlite can be distinguished by characteristic low reflectance values. Mineralogical variations in harzburgite cause reflectance variations in OPS 5 and OPS 3, but discrimination between harzburgite and lherzolite is still difficult. High reflectance in OPS 3 distinguishes dunite from the other lithologies.

2) Crustal Lithologies

Figure 4.45 shows the TM image spectra for the major crustal lithologies plotted together for comparison. Crustal lithologies can be distinguished from mantle lithologies as they have higher overall reflectance levels, especially at SWIR wavelengths. The other major difference is that crustal lithologies have a positive spectral slope between TM 4 and TM 5, and a flat to negative slope between TM 5 and TM 7. Whereas mantle lithologies have a negative slope across channels TM 4, TM 5 and TM 7.

Discriminating between different crustal lithologies may be difficult as all of the lithologies have quite similar spectral responses, except for trondhjemite which exhibits higher reflectance across all wavelengths. Cumulate gabbro and isotropic gabbro have very similar profiles across TM 1 to TM 5, the major difference between these two lithologies occurs in TM 7 where cumulate gabbro shows a pronounced absorption feature. This is also true for pyroxenite which shows an even stronger decrease in reflectance between TM 5 and TM 7. Pillow lava, sheeted dykes and cumulate gabbro with dykes are the hardest lithologies to discriminate between as all of these exhibit very similar spectral profiles.

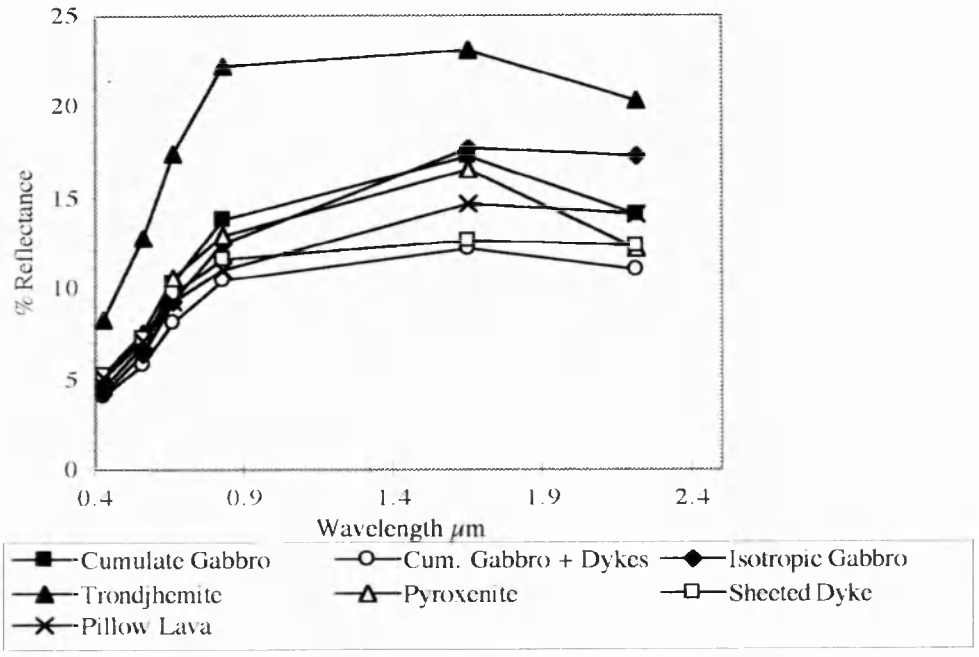

Figure 4.45 TM image spectra of the major crustal lithologies plotted together for comparison.

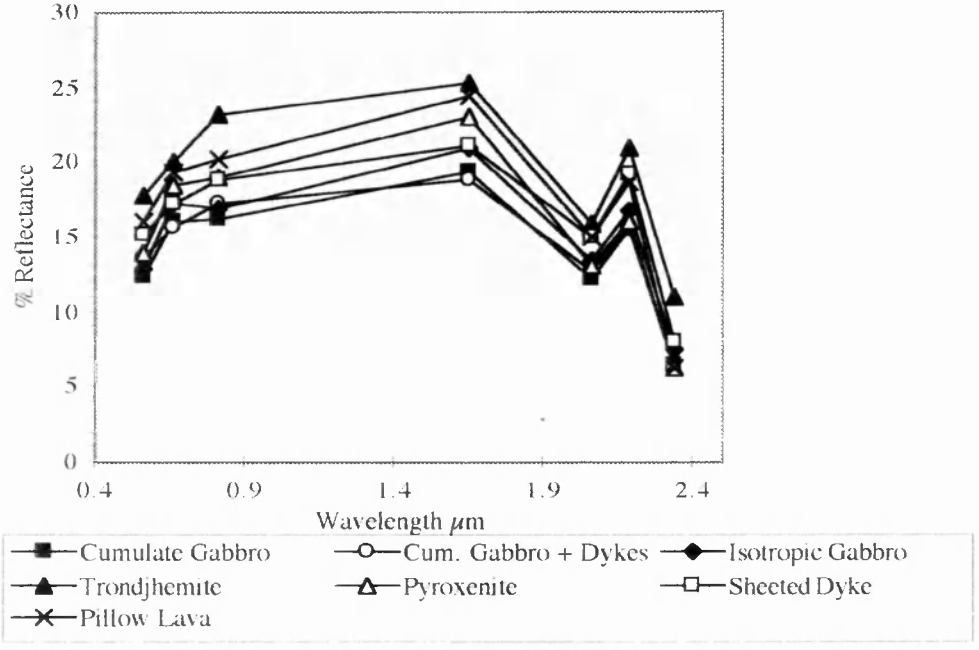

Figure 4.46 OPS image spectra of the major crustal lithologies plotted together for comparison.

OPS image spectra of crustal lithologies are shown in Figure 4.46. All of the lithologies have extremely similar spectral responses at visible and SWIR wavelengths. The only lithology easily distinguished is that of trondhjemite which exhibits high reflectance values. The other lithologies are very difficult to distinguish. Similarities in the SWIR are due to poor image quality of channels OPS 6, 7 and 8. Low dynamic range may also account for the high spectral correlation at visible wavelengths. Spectral separation only occurs in OPS 3 and OPS 5 and then it is very limited. Discrimination between the majority of crustal lithologies is very difficult due to the lack of spectrally distinct features.

Comparing image derived spectra for both mantle and crustal lithologies it is apparent that discrimination between some lithologies may not be as easy as predicted, based on the analysis of convolved lab spectra. Tables 4.2 and 4.3 provide a qualitative summary of the expected TM and OPS discrimination based on convolved spectra (Table 4.1) against anticipated discrimination based on image derived spectra. For mantle lithologies (Table 4.2) discrimination based on TM image derived spectra is approximately the same as that anticipated by convolved lab spectra. OPS image spectra also appear to discriminate mantle lithologies as well as expected. Discrimination levels appear to be good for crustal lithologies when comparing TM convolved spectra with image spectra. This is not true of OPS data where discrimination levels for the majority of the crustal lithologies are worse than anticipated from the analysis of convolved spectra.

Image quality is the reason why OPS data have a lower discrimination potential than anticipated. Analysis of convolved lab spectra indicated that OPS 6 and OPS 7 would provide useful additional spectral information for some lithologies compared with the broad band of TM 7. However OPS image-derived spectra have shown that OPS 6 and OPS 7 are highly correlated as a result of being dominated by image noise. The new spectral information expected from these channels is not apparent, making their addition almost pointless. However OPS 8 does add new spectral information, compared with TM 7 absorption features are stronger (i.e., deeper) in OPS 8. If OPS 6 and OPS 7 are removed the increased depth of the OPS 8 absorption significantly changes the shape of OPS resolution spectra compared with TM resolution spectra. The comparison of image and lab spectra has also indicated that there is a higher than expected correlation between the OPS visible and NIR channels. This is because these channels (OPS 1, OPS 2 and OPS 3) are strongly controlled by low dynamic ranges. It is obvious from this spectral comparison that, despite OPS data having more channels located at geologically significant parts of the spectrum, discrimination of ophiolite lithologies on OPS imagery is far worse than the anticipated discrimination.

Lithology	*TM Convolved Spectra*		*OPS Convolved Spectra*	
	TM Image Spectra		**OPS Image Spectra**	
	Discrimination Potential	Distinguishing Factor	Discrimination Potential	Distinguishing Factor
Lherzolite	*Low - Medium*	*Near constant reflectance, TM 3, 4, 5 and 7*	*Low - Medium*	*Higher reflectance in OPS 7 than OPS 6*
	Low - Medium	TM 4 higher reflectance than TM 3, decreasing in TM 5 and 7	Low	Reflectance in OPS 6 and OPS 7 noise related.
Harzburgite	*Medium*	*TM 5 very variable depending on mineralogy*	*Medium*	*OPS 5 variable, OPS 6 and 7 very similar, OPS 8 absorption*
	Medium	TM 5 and TM 7 variable depending on mineralogy	Medium	OPS 5 and OPS 2 variable, strong absorption in OPS 8
Dunite	*Low*	*Near constant reflectance*	*Medium*	*Constant reflectance OPS 3, 5, 6 and 7*
	Medium - High	High reflectance in TM 3 and TM 4	High	High reflectance in OPS 3
Wehrlite	*High*	*Very low reflectance all channels*	*High*	*Very low reflectance all channels*
	High	Very low reflectance all channels	High	Very low reflectance all channels

Table 4.2 Comparison of lithological discrimination potential of mantle lithologies based on convolved lab spectra (*italics*) and extracted image spectra (non-italics).

Lithology	*TM Convolved Spectra*		*OPS Convolved Spectra*	
	TM Image Spectra		**OPS Image Spectra**	
	Discrimination Potential	Distinguishing Factor	Discrimination Potential	Distinguishing Factor
Cumulate Gabbro	*Low - Medium*	*Reflectance peak TM 5, TM 7 very similar*	*Medium*	*Reflectance peak in OPS 5*
	Low - Medium	Reflectance peak TM 5, absorption in TM 7	Low	Slight peak in OPS 5, OPS 2 and OPS 3 very similar
Isotropic Gabbro	*Low - Medium*	*Reflectance peak in TM 7*	*Medium - High*	*Peak in OPS 6 and OPS 7*
	Low - Medium	TM 5 and TM 7 reflectance very similar	Low	Slight peak in OPS 5
Trondhjemite	*High*	*Very high reflectance all channels*	*High*	*Peak OPS 3, very high reflectance*
	High	Very high reflectance in all channels	High	Highest reflectance especially in OPS 3
Pyroxenite	*Medium*	*Higher TM 5 than TM 7*	*Medium - High*	*OPS 5 higher than OPS 3 or OPS 6*
	Medium	Peak in TM 5	Low - Medium	Peak OPS 5, OPS 2 and OPS 3 similar reflectance
Sheeted Dyke	*Low*	*TM 3 and 4 very similar reflectance*	*Medium*	*Similar reflectance OPS 6 and 7, absorption in OPS 8*
	Low - Medium	TM4, 5 and 7 very similar reflectance	Low	No distinct features
Pillow Lava	*Medium - High*	*Quite high reflectance, TM 2 and 3 very similar*	*Low - Medium*	*Quite high reflectance, very strong absorption OPS 8*
	Low - Medium	*TM 5 and 7 very similar*	*Low - Medium*	*Quite high reflectance in OPS 2, 3 and 5*

Table 4.3 Comparison of lithological discrimination potential of crustal lithologies based on convolved lab spectra (*italics*) and extracted image spectra (non-italics).

4.5 Selection of OPS and TM band combinations based on lab and image spectral data

The process of selecting and combining three bands of image data from an original *n* bands of data is a difficult task. Numerous techniques exist to subset data ranging from interactive-operator analysis through to complex statistical techniques. The effectiveness of these techniques will depend on the quality of the original data and on the output product required. No one three-band output image will contain all of the scene information, usually a range of composite images is required for final analysis. In this section I will discuss various techniques for determining band combinations and enhancements capable of 'maximising' lithological discrimination.

It is obvious from the previous section that selecting 'best' band combinations from OPS image data will be difficult because of data quality. Where appropriate, convolved lab spectra at OPS resolution will be used to guide band selection. Comparison of TM lab and image spectra (Section 4.4.2) has shown that the reflectance characteristics of the convolved spectra approximate image data fairly well. It can therefore be assumed that the convolved OPS spectra approximate a 'noise-free' OPS sensor. Differences seen in this study between OPS image and lab spectra are a direct result of the poor quality of both the VNIR and SWIR subsystems onboard JERS-1. Using the reflectance characteristics of lab convolved spectra to determine the best OPS image composites and enhancements will give a true insight into the potential discrimination capabilities of a noise-free OPS sensor. However, validating these results will be difficult without good image data, although by applying the same techniques to TM data an indication of their success will be determined. Remembering that the available OPS data are restricted by serious noise artefacts, recommendations will be made on how to maximise the spectral information in the available good channels.

This section outlines possible band combinations and enhancements applicable to both TM and OPS data. Discussion of the results of these recommendations can be found in Chapter 5.

4.5.1 Colour composites

It is possible to produce 20 different (no band repetition) TM three-band composites from an original 6 bands of data (excluding TM 6) and 35 composites from 7 channels of OPS data. Because these are quite small numbers it is feasible to create and analyse all of these

combinations interactively. This will not always be possible with the development of hyperspectral satellite platforms in the near future will vastly increase the dimensionality of multispectral data sets. Such an increase would mean that automated or semi-automated band selection techniques would have to be developed, because as an example a 200 channel sensor is capable of producing 1,313,400 three band composites. In anticipation of such multi-dimensional data sets, various techniques for pre-determining image composites will be discussed and tested on both TM and OPS data.

The analysis of lab spectra of sample lithologies from a study area can be used to guide the selection of band composites. The spectra can be used to determine which TM or OPS channels will coincide with the most spectral variation for the target lithologies. Combining channels with large spectral variations (i.e., large variations in reflectance percentages within a channel) will produce the most informative band composites (Hunt *et al.*, 1986), providing that the variations seen in the convolved lab spectra are significant enough to be detected by the satellite sensor. Considering the convolved TM and OPS spectral plots for mantle and crustal lithologies (Figures 4.29 to 4.31) the following orders of spectral variation were determined (Tables 4.4 and 4.5), by comparing the range of reflectance percentages within each channel to those of the other channels.

Lithology	**Spectral Variation**					
	Maximum ←					→ Minimum
Mantle	TM 5	TM 4	TM 3	TM 7	TM 2	TM 1
Crust	TM 5	TM 4	TM 7	TM 3	TM 2	TM 1

Table 4.4 Predicted spectral variation on TM data over ophiolite lithologies (trondhjemite was excluded from this analysis because of its distinct high reflectance in the visible channels) based on qualitative analysis of convolved lab spectra.

Lithology	Spectral Variation						
	Maximum ← → Minimum						
Mantle	OPS 5	OPS 3	OPS 2	OPS 6	OPS7	OPS 8	OPS 1
Crust	OPS 5	OPS 3	OPS 2	OPS 1	OPS 6	OPS 7	OPS 8

Table 4.5 Predicted spectral variation on OPS data over ophiolite lithologies (Trondhjemite was excluded from this analysis because of its distinct high reflectance in the visible channels) based on qualitative analysis of convolved lab spectra.

Analysing average convolved spectra in this way suggests that a band combination of TM 543 would show the maximum spectral variation for mantle lithologies whilst TM 547 would be best for crustal lithologies. Composites of OPS 532 would be best for both mantle and crustal lithologies.

A more quantitative analysis of the interchannel variation of spectral reflectance considers the correlation coefficient(R) between pairs of channels. Figure 4.47 (a) and (b) illustrate interchannel correlation for TM data, whilst Figures 4.48 (a), (b) and (c) illustrate interchannel correlation for OPS data. These scattergrams are based on approximately 120 convolved lab spectral measurements representing the range of ophiolite lithologies.

TM 3 and TM 4 are the most highly correlated pair of bands (R=0.976) closely followed by TM 2 and TM 3 (R=0.955) and TM 1 and TM 2 (R=0.928). The least correlated channels are TM 1 and TM 7 (R=0.386), TM 2 and TM 7 (R=0.499) and TM 1 and TM 5 (R=0.519). This can be seen on the scatterplot by the diffuse spread of points away from the line of maximum correlation. Figure 4.48 (a), (b) and (c) illustrate interchannel correlation for OPS data based on the analysis of convolved lab spectra. OPS 6 and OPS 7 are almost perfectly correlated (R=0.992) along with OPS 2 and OPS 3 (R=0.984) and OPS 1 and OPS 2 (R=0.983). The least correlated pairs of channels are those comprising OPS 1 and one of the SWIR channels OPS 6 (R=0.481), OPS 7 (R=0.484) or OPS 8 (R=0.411). These results differ slightly from those of the previous section because this analysis was based on a large sub-set of spectra as opposed to average spectra.

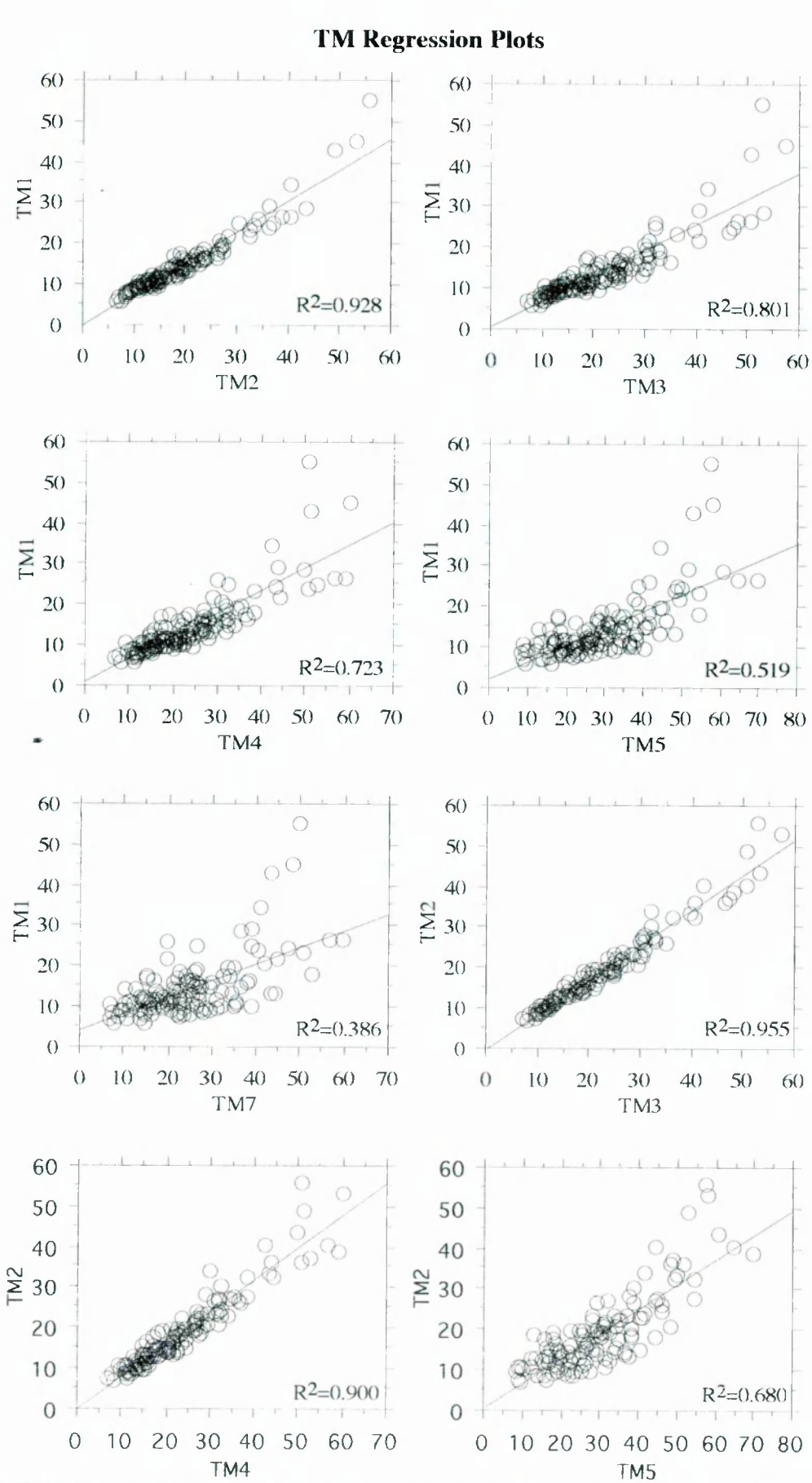

Figure 4.47 (a) Inter-channel scattergrams showing the degree of spectral correlation between TM channels based on 120 convolved lab spectra, representing the range of ophiolite lithologies. Refer to text for a full description.

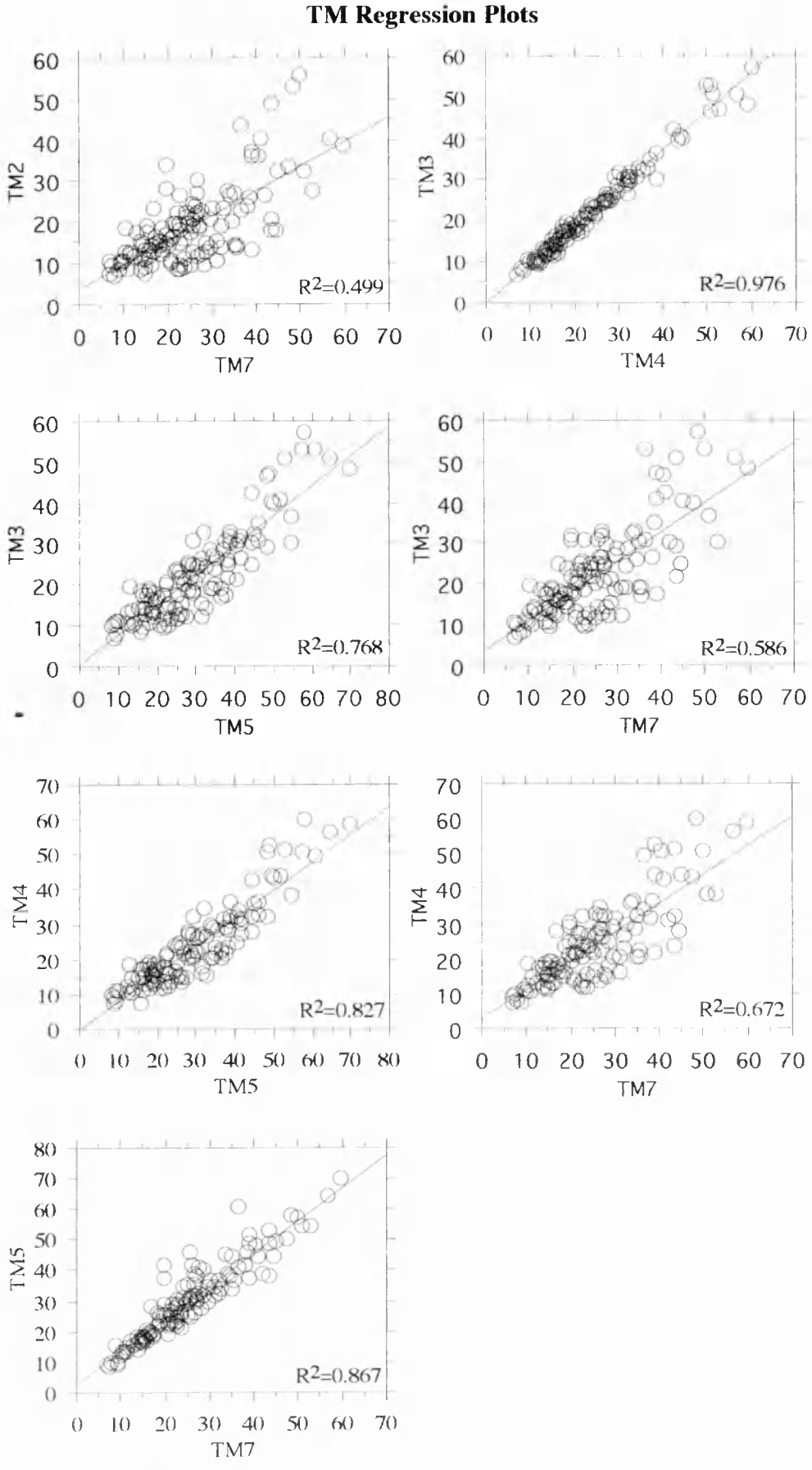

Figure 4.47 (b) Continuation of Figure 4.47 (a).

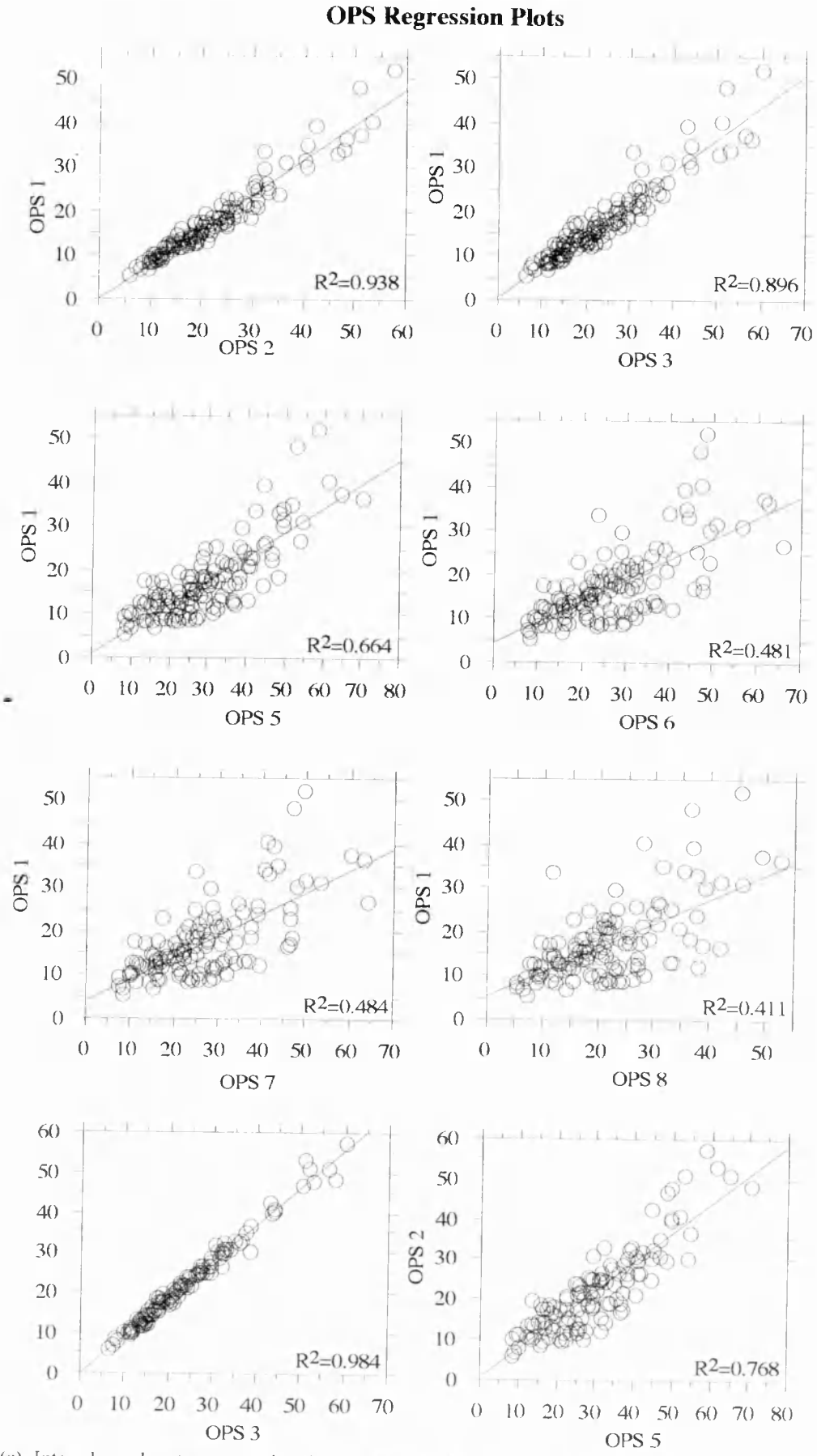

Figure 4.48 (a) Inter-channel scattergrams showing the degree of spectral correlation between OPS channels based on 120 convolved lab spectra, representing the range of ophiolite lithologies. Refer to text for a full description.

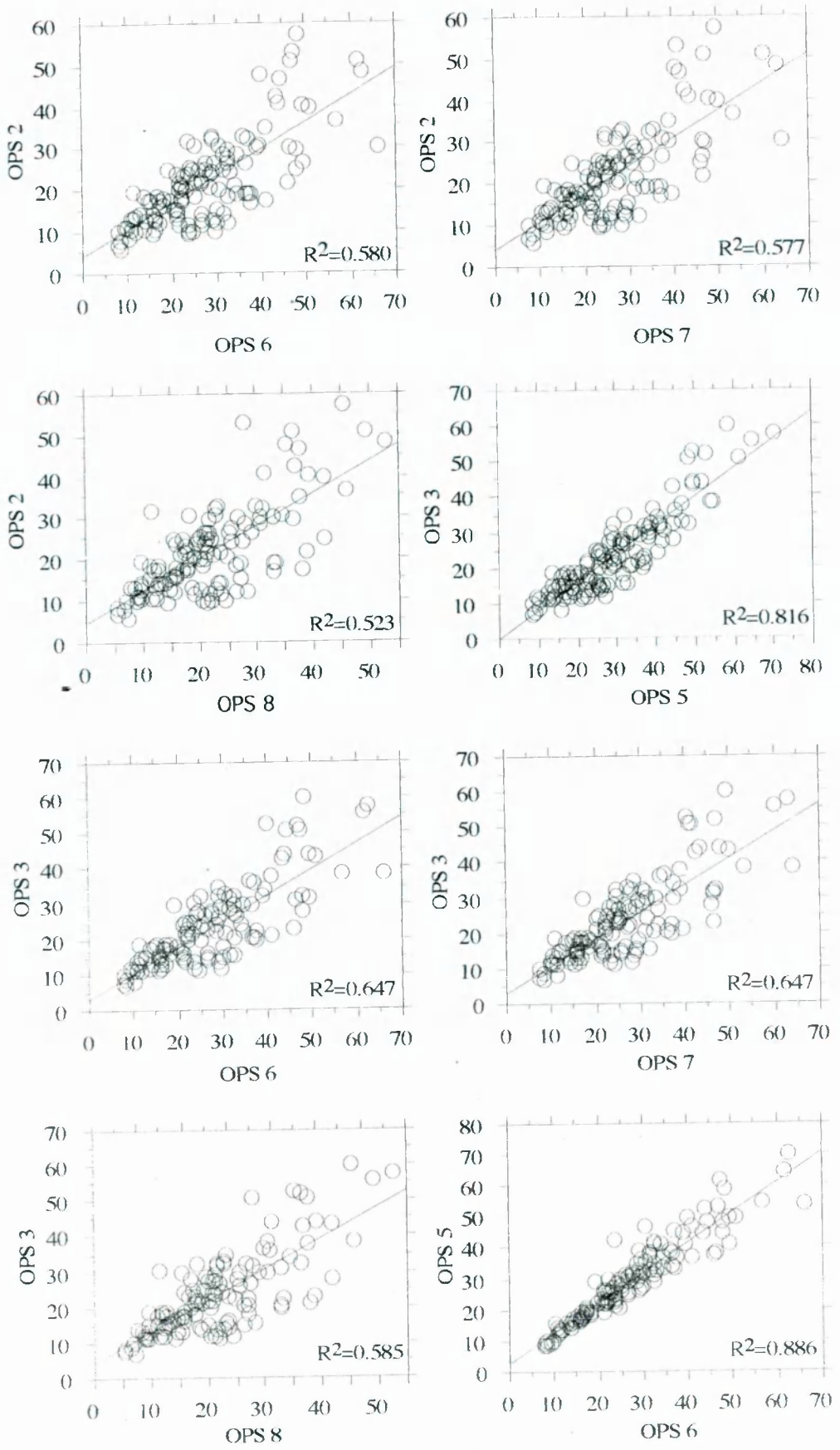

Figure 4.48 (b) Continuation of Figure 4.48 (a).

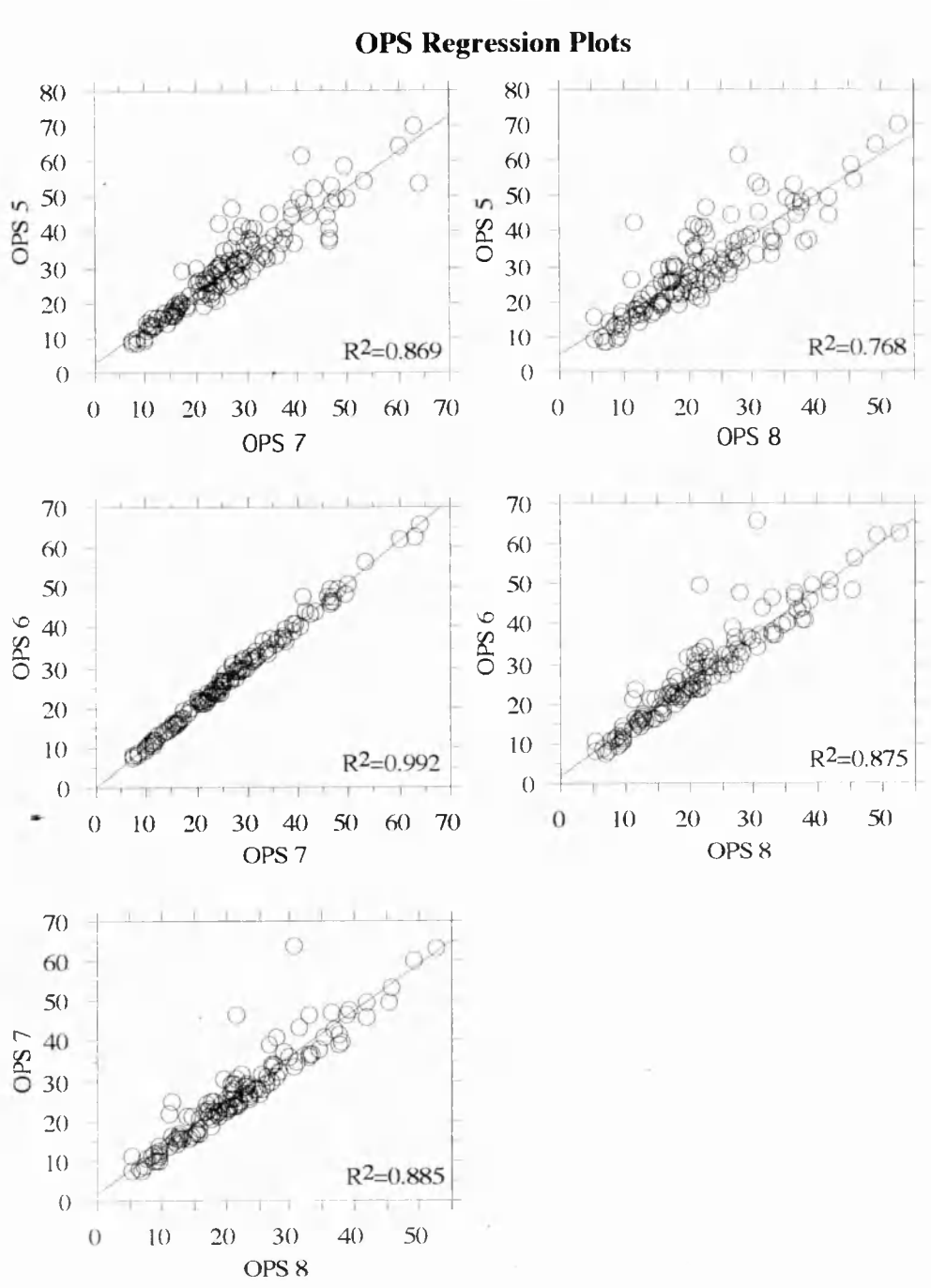

Figure 4.48 (c) Continuation of Figure 4.48 (a).

To obtain the maximum spectral variation over ophiolite lithologies in either a TM or OPS false colour composite, at least one band at visible wavelengths and one at SWIR wavelengths should be combined. Combinations including any of the highly correlated bands shown in Figures 4.47 and 4.48 should be avoided.

Interchannel scatterplots and correlation coefficients can also be calculated directly from image data. However spectral correlation based on lab spectra convolved to OPS and TM sensor resolution is more informative. This is because this approach considers only spectral data from the lithologies you want to discriminate between. Correlation values are therefore a true indication of the degree of variation between lithologies based on mineralogical reflectance properties. Spectral correlation of ophiolite lithologies based directly on image data will differ from those based on lab spectra, because of; (1) the affects of atmospheric scattering, which may still be apparent even after atmospheric correction, (2) the inclusion of other spectral components in the image data, e.g., roads, buildings, water, vegetation and other non-ophiolite lithologies, (3) data quality.

Interchannel correlation is also an important factor in a number of statistical approaches to determine the best false colour composite.

4.5.2 Statistical Analysis

A more quantitative approach to determining the best bands to combine in a false colour composite is to consider image statistics. Numerous statistical techniques have been adapted for the analysis of remotely sensed data. Here I will consider three such techniques; the Optimum Index Factor (Chavez 1982); Ellipsoid of Maximum Volume (Sheffield 1985) and the Three-dimensional Index (Crippen, 1989).

1) Optimum Index Factor

The Optimum Index Factor (OIF) is a statistical technique developed to derive the best composites of ratio images based upon the variance and correlation among different band ratios. However the technique can also be applied to individual bands of data as opposed to ratio images (Chavez 1982). The OIF weights the variance of individual bands by using their standard deviation and the correlation between bands, determined by correlation coefficients. An OIF value is calculated for every possible band combination by dividing the sum of the standard deviation for each of three band components by the sum of the absolute value of the correlation coefficients, calculated for the same three bands taken two at a time (Chavez 1982).

$$OIF = \sum_{i=1}^{3} SDi \,/\, \sum_{j=1}^{3} |CCj| \qquad (4.1)$$

where;

SDi = standard deviation for band i

$|CCj|$ = absolute value of the correlation coefficient between any two of the three bands

The larger the calculated OIF value for a three band combination the better (statistically) the band combination.

2) *Ellipsoid of Maximum Volume*

The Ellipsoid of Maximum Volume (EMV) technique considers the three-dimensional ellipsoid space defined by the variance-covariance matrix for any particular band triplet, chosen from a parent set of *n* bands (Sheffield, 1985). Where *n* is the total number of images channels, i.e., 6 for Landsat TM (ignoring TM 6) and 7 for OPS data. This technique differs from that of PCA because it selects band triplets based on the volume of the ellipsoid defined by the principal axes a, b and c. Whereas PCA selects band triplets based on the largest sum of the squares of the principal axes a, b and c. The EMV technique is favourable when considering data which may be highly correlated.

$$EMV = n/2 + n/2 \ln(2\pi) + 1/2 \ln|m| \qquad (4.2)$$

where;

n = total number of bands

m = n by n covariance matrix

In practise the EMV is equal to the determinant of the 3 by 3 variance-covariance submatrix of the original *m* by *m* parent matrix (Sheffield 1985).

3) Three-dimensional Index

The Three-dimensional Index (TI) is based on channel correlation and subjective considerations of image noise. The determinant of the correlation matrix for three channels provides an index that measures the degree to which the channels are three-dimensional and non-redundant (Crippen 1989).

$$TI = \sqrt{1 + 2abc - a^2 - b^2 - c^2} \qquad (4.3)$$

where a, b and c are the pairwise channel correlation coefficients. TI can equal;

1.0 = perfectly three-dimensional

0.0 = not at all three-dimensional

Band combinations with a TI value equal to or near to one are best.

The above three techniques were applied to test scenes of TM and OPS data. OPS test scenes measuring 1024 lines by 1024 samples where extracted, TM scenes covering the equivalent area were also extracted but because of the larger pixel size these measured only 615 lines by 615 samples. The location of this test area was carefully chosen to ensure that it covered a region exhibiting the majority of the ophiolite lithologies. However it is not possible to choose a region which contains only the spectral response of the features you are interested in discriminating, i.e., ophiolite lithologies. It was possible to choose a scene which contained no sedimentary rocks and had an extremely low amount of vegetation, thereby avoiding unwanted channel correlation associated with these features. The only non-ophiolite features which could not be avoided in this region were wadi channels and the associated gravels and scree deposits. The inclusion of these features will have minimal influence on the correlation statistics because (a) they occupy a relatively small percentage of the scene area and (b) the material within the wadis is primarily derived from ophiolite source rocks. The statistical analyses were applied initially to the raw TM and OPS data and then repeated on atmospherically corrected data (Appendix 1) and on cleaned OPS data. Table 4.6 summarises the results of the statistical analysis on TM and OPS image data.

TM and OPS Image Statistical Analysis															
	TM raw data			TM atmos.correct			OPS raw data			OPS atmos. correct			OPS cleaned data		
Rank	A	B	C	A	B	C	A	B	C	A	B	C	A	B	C
1	537	541	741	534	541	741	526	526	167	526	237	167	673	673	671
2	534	531	541	537	531	541	536	523	168	536	238	168	671	675	672
3	531	534	742	531	534	742	516	536	367	516	317	367	672	671	673
4	547	571	371	574	571	712	236	516	267	236	231	267	675	672	678
5	541	537	712	571	537	371	316	531	187	316	318	187	678	678	675
20/35	412	312	231	412	312	321	687	687	231	687	687	231	128	128	312
Overall	541			541			516 / 526			526			673		

Table 4.6 Summary of the statistical analysis techniques (A= OIF, B=EMV and C=TI) applied to TM and OPS image data. All band combinations are ranked from 1 (highest) to 20 lowest TM combination or 35 lowest OPS combination (intermediate ranked combinations not shown). Combination with the highest total rank from all three techniques is listed as the 'overall' best combination. For convenience the bands are combined in order of decreasing band variance; the best order to display them in red, green and blue depends on visual perception, which cannot be established by statistical techniques.

Table 4.7 lists the first five band combinations suggested by each technique (A=OIF, B=EMV and C=TI) and the last band combination, rank 20 for TM data and rank 35 for OPS. Considering the raw TM data each of the three techniques suggests a different band combinations (TM 537, TM 541 and TM 741) as being the best composite. Between the three techniques 5 of the original 6 TM bands are included in rank 1 band combinations, only TM 2 is excluded. All three techniques include TM 1 and TM 2 in the lowest ranked combination. When considering the overall ranking for each band combination from all three techniques the best band combination is TM 541 Applying these techniques to atmospherically corrected TM data resulted in the same overall band combination being defined (TM 541).

Applying these techniques to raw OPS data resulted in band combinations of 516 and 526 having the highest overall rank. Both the OIF and the EMV techniques ranked band combinations including OPS channels 2, 3, 5 and 6 quite highly, whilst the TI technique ranked combinations of 1, 6, 7 and 8 highly. The OIF and EMV techniques also agreed on OPS 678 as the lowest ranking combination whilst the TI technique highlighted 231 as the lowest. Applying an atmospheric correction to the OPS data did not affect the OIF or TI band rankings, but it did change those of the EMV. With an atmospheric correction applied the EMV technique tended to replace OPS 5 with either OPS 7 or OPS 8. The best and worse overall band rankings were not changed from those of the non-corrected data.

Cleaning the OPS data using frequency domain techniques described in chapter 2 significantly changed the results of all three statistical techniques. Band combinations comprising OPS 6 and 7 plus one visible channel (OPS 1, 2 or 3) now occupy the majority of the top five ranked positions for each technique, whereas combinations of OPS 1, 2, 3 and 8 occupy the lowest ranked positions. These results are almost the exact opposite to those of the previous two OPS data sets. This is because the frequency domain noise removal techniques have significantly altered the image statistics.

The major problem with applying statistical techniques to the OPS data is that these techniques cannot discriminate between image variance and/or correlation caused by genuine spectral variations and those caused by noise artefacts. This results in the nosiest OPS channels (OPS 6 and OPS 7) being included in some of the composites. Another problem when applying these techniques to image data is that of scene dependency. The statistical analysis of a sub-set of a scene may not produce the same statistical results as those from the entire scene. If statistical analysis is going to be performed on a subset image it is important that it is representative of all of the lithologies to be discriminated. As a result a more genuine band selection may be determined by applying these statistical techniques directly to convolved spectral data.

The results of the above three statistical techniques applied to convolved spectral data are summarised in Tables 4.7 and 4.8. These techniques were first applied to a spectral data set representative of all ophiolite lithologies and then to spectra of individual lithologies. Considering the TM spectral analysis first (Table 4.7), the band combinations of either TM 571 or 471 are ranked the highest for discriminating all lithologies in one composite, whilst TM 321 and 432 are the lowest combinations.

Band combinations of TM 571 are ranked statistically the best for discriminating harzburgite and trondhjemite, whilst combinations of TM 537 are best for wehrlite and gabbro. Dunite and pyroxenite are best distinguished using TM 541 and 547 respectively. Dykes (TM 423) are the only lithology to be distinguished without using either of the

TM Spectral Analysis																								
	All lithologies			Harzburgite			Dunite			Wehrlite			Gabbro			Pyroxenite			Dykes			Trond		
	A	B	C	A	B	C	A	B	C	A	B	C	A	B	C	A	B	C	A	B	C	A	B	C
1	571	471	471	571	573	741	574	542	541	543	537	471	347	357	571	547	572	571	423	423	375	571	571	571
2	572	572	731	572	574	731	573	541	741	537	541	371	327	527	371	543	547	572	421	427	315	521	415	537
3	573	571	571	574	572	541	572	531	531	532	471	531	357	547	471	572	537	537	425	275	415	15	371	371
4	547	573	541	573	571	531	543	742	731	542	531	541	427	571	357	537	571	547	427	437	431	31	471	471
5	471	731	573	541	541	571	571	741	542	437	527	537	527	371	527	542	543	471	431	237	425	1	275	275
20	321	321	432	321	432	432	321	321	432	321	321	432	321	321	321	321	421	432	172	471	231	3	321	321
Overall	571 or 471			571			541			537			357			547			423			571		

Table 4.7 TM channel combinations determined by statistical techniques (A=OIF, B=EMV and C=TI) applied to convolved OPS lab spectra.

OPS Spectral Analysis																							
	All lithologies			Harzburgite			Dunite			Wehrlite			Gabbro			Pyroxenite			Dykes			Trond		
	A	B	C	A	B	C	A	B	C	A	B	C	A	B	C	A	B	C	A	B	C	A	B	C
1	672	381	581	571	381	581	672	538	538	352	318	518	681	528	581	537	538	581	678	681	673	127	138	387
2	562	528	681	671	582	538	562	528	528	326	528	358	628	538	538	538	537	571	671	671	683	123	186	367
3	671	682	781	561	538	582	572	381	631	526	518	528	781	581	528	536	581	538	675	651	783	128	187	385
4	561	581	538	573	581	571	563	631	381	327	358	318	728	628	681	532	571	537	681	675	851	137	137	386
5	563	538	682	563	572	681	673	731	581	527	527	618	528	638	638	561	536	561	781	851	521	138	127	157
35	321	321	321	321	321	567	321	678	567	678	678	678	321	321	678	678	678	567	321	821	672	867	567	167
Overall	581			571			528			518			528			538			681			127		

Table 4.8 OPS channel combinations determined by statistical techniques (A=OIF, B=EMV and C=TI) applied to convolved OPS lab spectra.

SWIR bands. In fact this is the only lithology to include SWIR channels in the lowest ranked positions, as opposed to TM 1, 2, 3 or 4 which dominate the other lowest ranked combinations. Considering only the first ranked combination from each of the three techniques a total of 9 band composites are defined; TM 571, 471, 573, 574, 542, 543, 347, 572 and 423. Only trondhjemite has the same band combination (TM 157) ranked top by all three statistical techniques.

Considering the OPS spectral analysis (Table 4.8) the band combination of OPS 581 has the overall highest ranking for discriminating all lithologies, whilst OPS 321 has the lowest ranking. OPS 581 also has the highest ranking for wehrlite, whilst OPS 582 is dominant for dunite and gabbro and OPS 571 is defined for harzburgite. Overall combinations for dykes and trondhjemite are slightly different as the first combines two SWIR channels (OPS 681) and the later combines two visible channels (OPS 127). With the exception of trondhjemite and dykes the majority of the OPS combinations tend to be comparable in terms of wavelength with the TM band combinations. However this is not the case for the lowest ranked positions as these often contain OPS SWIR channels, whereas the TM combinations were restricted to visible and VNIR bands. The OPS data also show more variation when considering the first ranked combinations from each of the statistical techniques, in total 15 different band combinations are defined; OPS 672, 381, 581, 571, 538, 352, 681, 528, 537, 678, 681, 673, 127, 138 and 387.

4.5.2 Ratio images

Selective ratios of pairs of channels are often very good for discriminating distinct spectral features, such as the TM 5/7 for clay, TM 3/1 for iron. Excluding TM 6 there are 15 possible TM ratios (assuming the ratios 1/2 and 2/1 etc. are the inverse of each other) and 21 OPS ratios. Resulting in 455 TM three band ratio composites and 1330 OPS ratio composites.

A systematic approach to determine which ratios have potential to discriminate specific lithologies is to ratio the convolved spectral data for each lithology. Such an approach saves time as only selected image ratios have to be produced. Figure 4.49 graphically illustrates the spectral ratios of mantle lithologies for TM and OPS bandpasses. The calculated ratio value for each channel is plotted as an offset value from an axis value of 1, equivalent to zero discrimination. Large offset values, either greater than or less than 1 represent inter-channel spectral differences which have been highlighted by the ratio. The output range of ratio values is a product of performing the operation on reflectance data, image data would be rescaled to an appropriate DN range, with values greater than 1 typically appearing bright in the image and values less than 1 appearing dark.

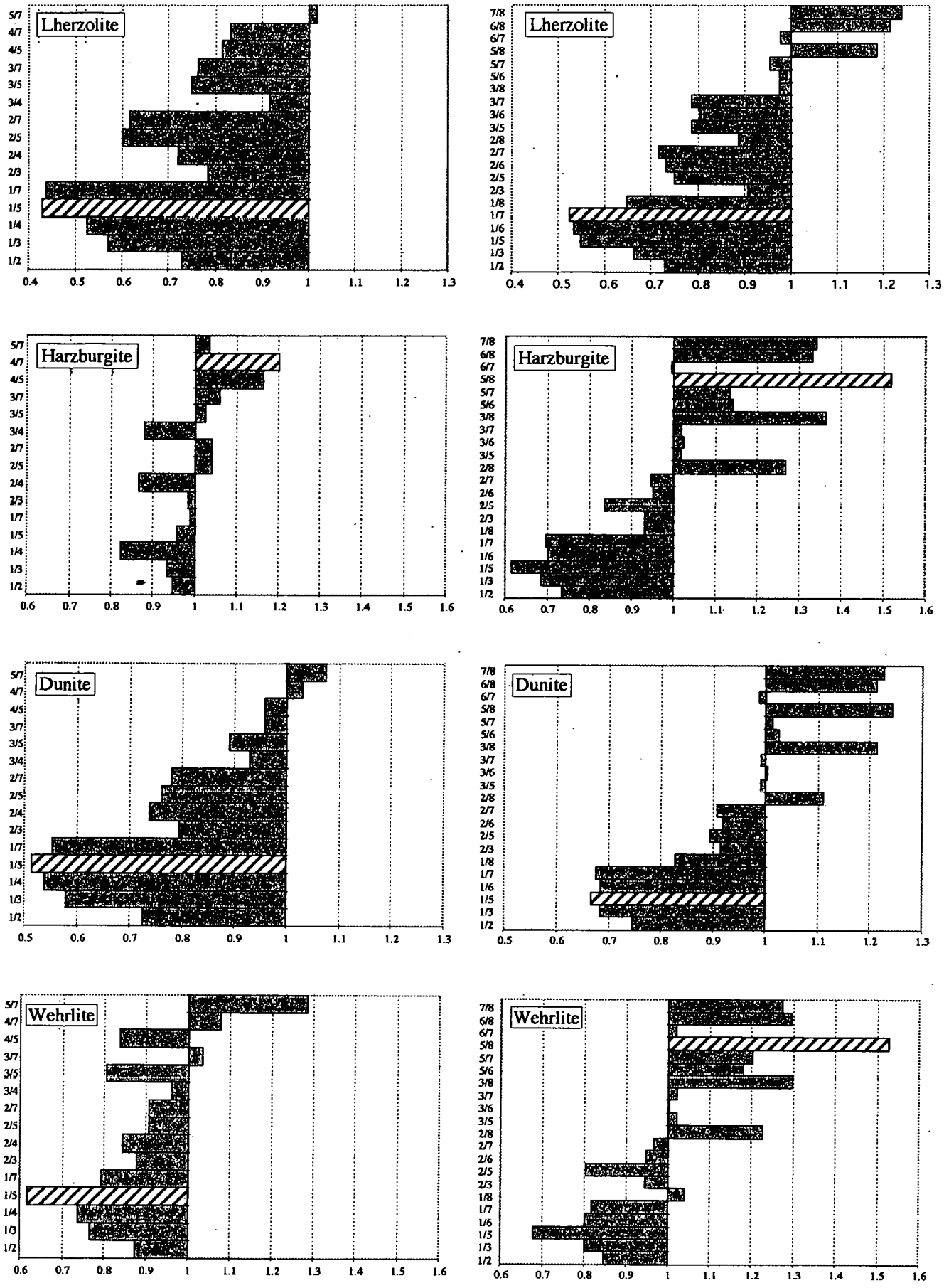

Figure 4.49 TM and OPS band ratios for mantle lithologies calculated on convolved lab spectra.

Based on spectral analysis the TM ratio of bands 1/5 (or 5/1) would offer the maximum discrimination of lherzolite, dunite and wehrlite whilst 4/7 would be better for harzburgite. More varied results are seen on the OPS data with ratios 1/7 (lherzolite), 5/8 (harzburgite and wehrlite) and 1/5 (dunite) being distinguished. As a result OPS ratios may be able to discriminate between individual mantle lithologies. Considering crustal lithologies, Figures 4.50 (a) and (b), predicted TM ratios include 1/5 (cumulate gabbro, sheeted dyke and pillow lava), 1/7 (isotropic gabbro), 4/7 (trondhjemite) and 5/7 (pyroxenite). OPS ratios include 1/5 (cumulate gabbro and sheeted dyke), 1/6 (isotropic gabbro), 3/8 (trondhjemite) and 5/8 (pillow lava and pyroxenite). The majority of the TM ratios with a high discrimination potential consist of one visible channel (usually TM 1) and one SWIR channel (TM 5 or 7), thereby maximising brightness differences between these two spectrally distinct parts of the spectrum. This is also true of OPS data. The occurrence of TM 1 in a number of the ratios suggests that the OPS data may be disadvantaged by not having a visible channel covering the equivalent wavelength range. It must be remembered that an OPS ratio of 1/7 is in fact equivalent to a TM ratio of 2/7. And it can be seen from Figures 4.49 and 4.50 that TM ratios of 2/7 have considerably lower discrimination potential than ratios of TM 1/7. The OPS sub-division of the SWIR does appear to be important, as ratios vary between OPS 6 and OPS 8. Variability between OPS 6 and OPS 8 suggests that these two ratios are discriminating Al-OH and Mg-OH features respectively. Although for ophiolite lithologies OPS 8 tends to be the predominant channel. Note how the ratios of 6/7, 6/8 and 7/8 do not appear to offer significant discrimination suggesting that both the mantle and crustal lithologies are highly correlated across these three channels. It would appear that any spectral variations contained in OPS 6 and OPS 7 are very minimal and are not significant enough to be enhanced by ratio operations.

Intentionally left blank

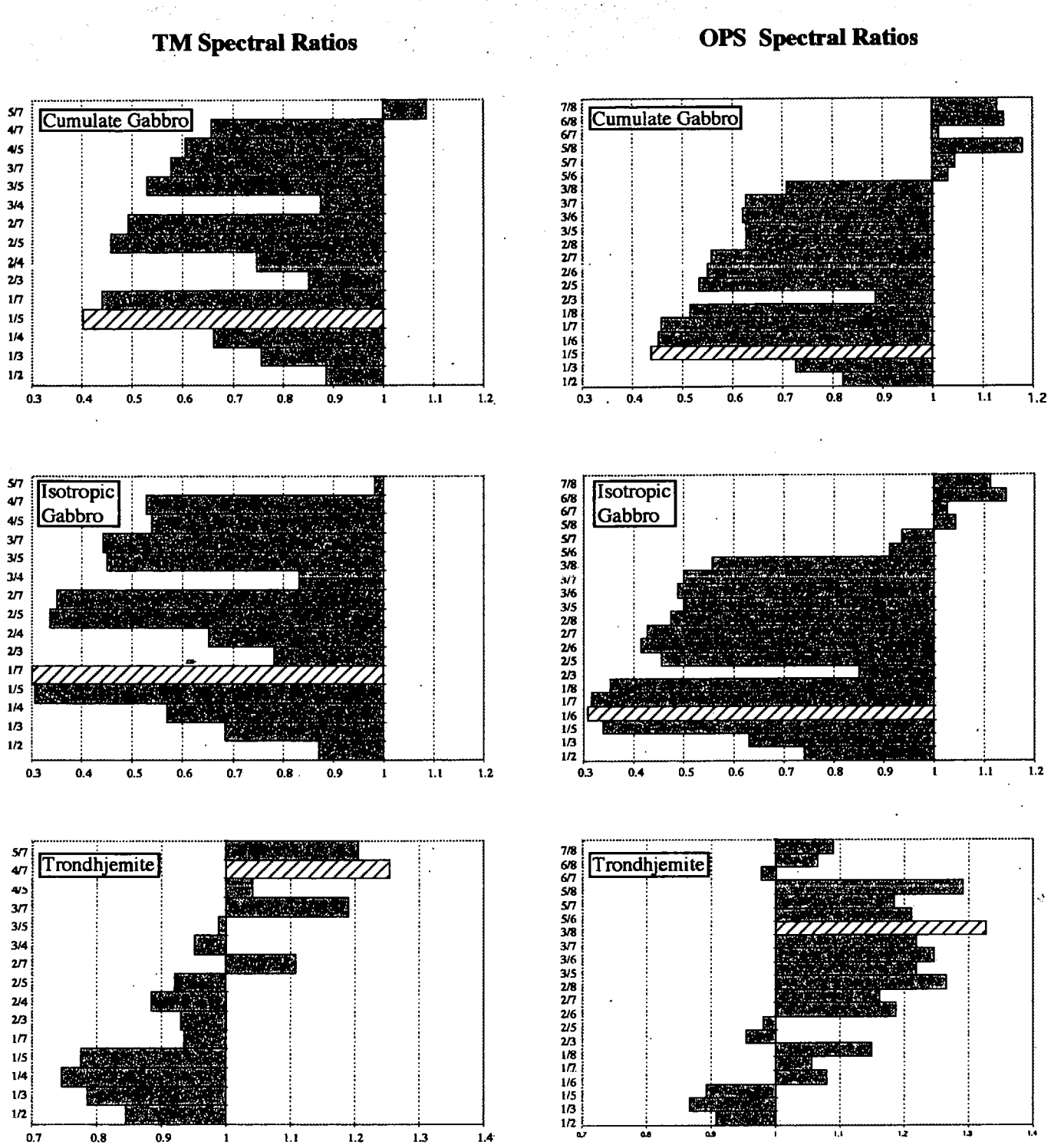

Figure 4.50 (a) TM and OPS band ratios for crustal lithologies calculated on convolved lab spectra

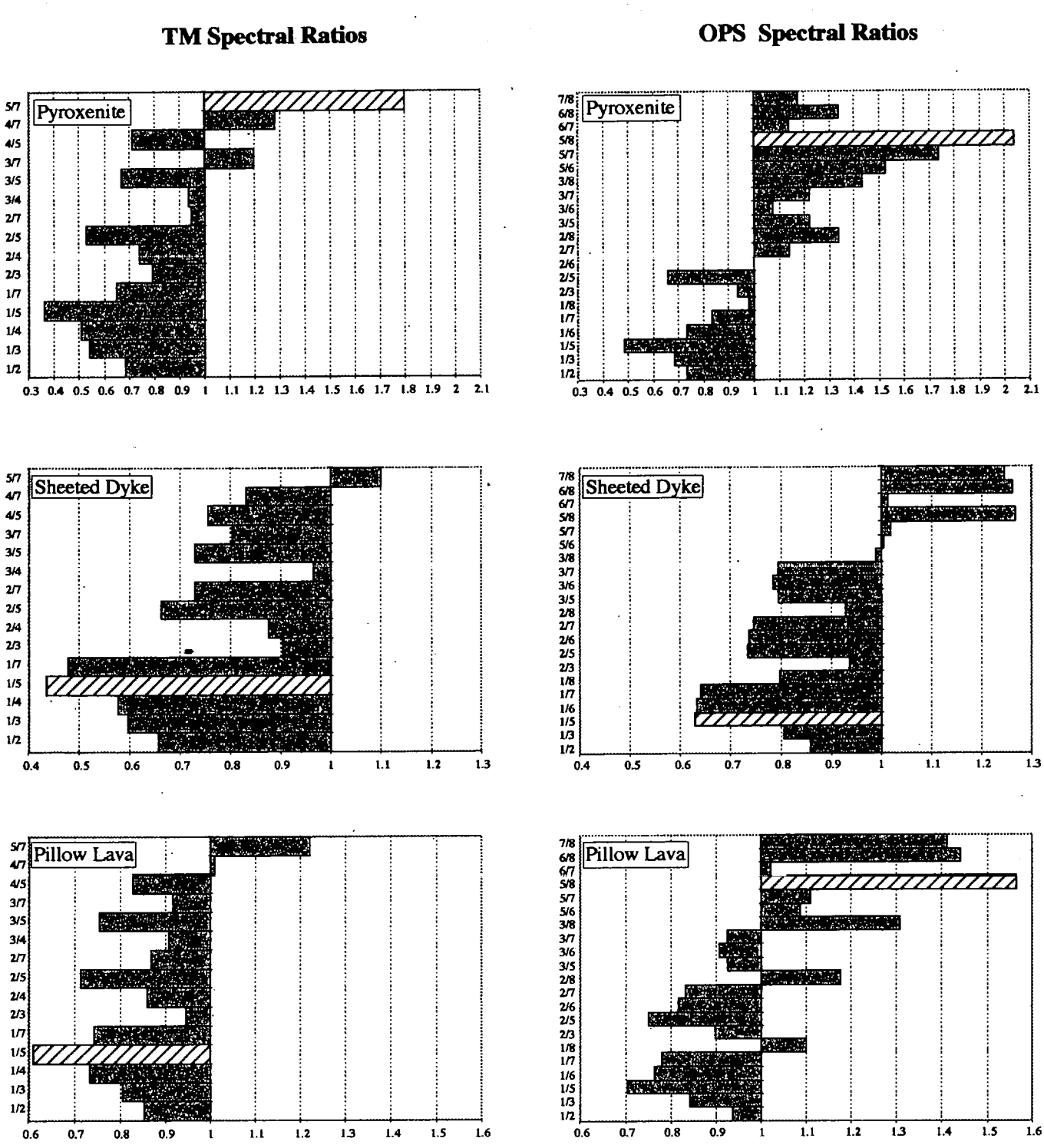

Figure 4.50 (b) TM and OPS band ratios for crustal lithologies calculated on convolved lab spectra, continued from Figure 4.50 (a)

4.5.4 Spectral Indices

Principal Component Analysis and Decorrelation Stretching are two techniques often used to help discriminate between features in multi-dimensional data sets (see section 4.5.5). A rather less common technique is that of Spectral Indices (SI). Spectral Indices tend to be used to identify specific features within a multi-dimensional data set, for example Kauth and Thomas (1975) and Jackson (1983) developed SIs to identify vegetation on Landsat MSS data. Techniques later adapted for TM data by Crist and Cicone (1984).

Discriminating vegetation is not a major problem in this study as it is almost non-existent. However the techniques initially defined for vegetation discrimination have since been modified to discriminate geologically important minerals, for example clay minerals; Elvidge and Lyon (1984) and iron oxide minerals Miller and Elvidge (1985) and Madeira *et al.*, (1996). These discrimination techniques were respectively known as the Mineral Absorption Index (MAI) and the Iron Absorption Index (IAI). Both of these techniques demonstrated that n-dimensional spectral indices could be used to identify geologically important mineralogy from TM data. Therefore it should be possible to develop both these and new indices for the higher spectral resolution OPS data. In fact Yamaguchi (1987) and Yamaguchi (1988) developed alunite and calcite indices from simulated OPS data prior to the launch of JERS-1. Since the launch of JERS-1 Yamaguchi *et al.*, (1995) have demonstrated some success deriving kaolinite, alunite and carbonate spectral indices.

In many ways spectral indices are similar to PCA eigenvectors, as they represent a unit vector where an imaginary line (axis) is projected from a fixed point to a feature of interest (Davis, 1977). Each successive index is established perpendicular to the previous one. The difference between the two techniques is that SI vectors define specific features of interest whilst the PC vectors are constrained by the statistical properties of the data.

The creation of the first SI is very important as this represents a baseline of background values (Jackson, 1983) from which all other indices are created. Ideally this baseline vector is calculated from a feature which is spectrally distinct from the target feature(s). However this is often not possible so an alternative technique is to predict an average baseline using the mean response or brightness of each data channel. Surfaces which are spectrally distinct from the baseline will plot furthest away from it in n-dimensional space, resulting in large vectors or weighting factors. Spectrally similar or correlated features will plot close to the baseline resulting in small vectors and weighting factors.

A basic outline of the processing steps required to produce spectral indices is shown in Figure 4.51. The initial step is to acquire spectral reflectance measurements for the minerals / features you want to distinguish, M_1, M_2 ..... $M_{(f-1)}$ (where f equals the number

of features to distinguish, *f* cannot exceed the number of channels of data; *n*) and to produce a mean spectra at sensor (i.e. TM or OPS) resolution. Next these reflectance spectra are averaged by band (X_1, X_2.....X_n, where n equals the number of sensor channels) and a vector BR is produced by dividing each factor by a normalisation factor B, where;

$$B = \sum (X_{(i)}^{(2)})_{0.5} \qquad (4.4)$$

and the coefficients of brightness are;

$$br_{(1,i)} = X_i / B \qquad (4.5)$$

Brightness can now be expressed as;

$$BR = X_{(1,1)}\, br_{(1)} + X_{(1,2)}\, br_{(2)} + \ldots\ldots\ldots X_{(1,n)}\, br_{(n)} \qquad (4.6)$$

The next stage is to normalise the data by removing overall band brightness this emphasises inter-band spectral variations. This normalisation procedure is fairly similar to that used to produce the unit vector of brightness, the only difference being that M_1 to $M_{(f-1)}$ normalisation factors are produced. These values are then divided a band at a time by the brightness coefficient, producing a matrix which maximises the reflectance of each surface, both within a band and between bands. Orthogonal vectors for each of the surface types can now be produced from this matrix. Finally these vectors are checked for orthogonality by summing the products of any two vectors and ensuring they equal zero. A full description of the mathematics of spectral indices can be found in Jackson (1983).

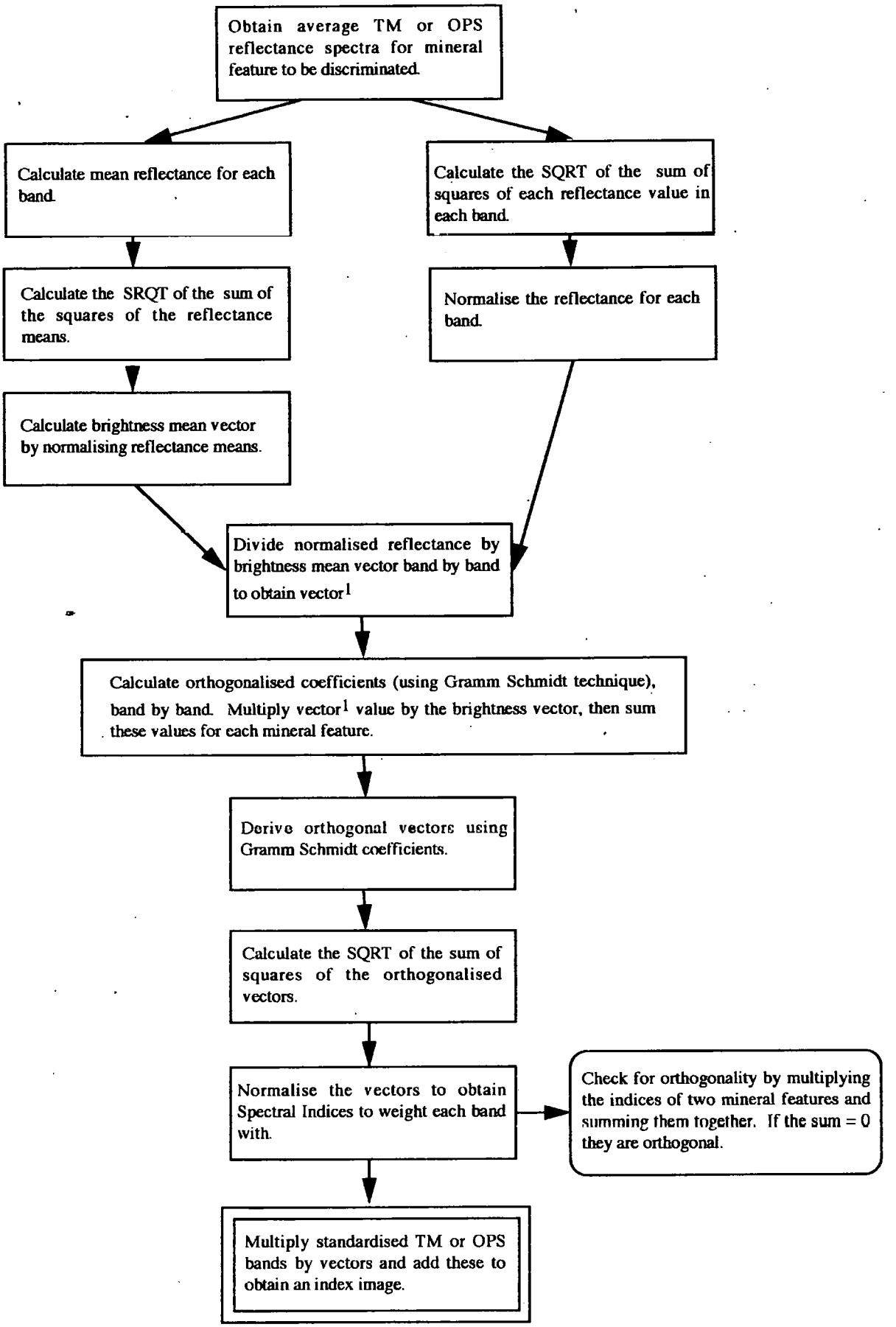

Figure 4.51 Flow chart showing production steps required to produce Spectral Indices.

As an example of this technique the Spectral Indices for clay, goethite, hematite and vegetation, calculated from TM data are shown in Table 4.9.

Index	TM 1	TM 2	TM 3	TM 4	TM 5	TM 7
Clay	0.77	0.39	0.23	-0.04	-0.33	-0.26
Goethite	-0.51	0.42	0.55	-0.11	-0.04	0.18
Hematite	0.26	-0.19	-0.01	-0.67	-0.04	0.66
Vegetation	0.05	0.09	-0.49	0.49	-0.54	0.45

Table 4.9 Example Spectral Indices for mapping clay, vegetation, goethite and hematite. These were produced using the NASA (Grove *et al.*, 1992) mineral spectra (with the exception of vegetation which was reproduced from Lillesand and Keifer, 1994) resampled to TM bandpasses.

Like PC eigenvectors, the SI values can be used to assess which TM bands are contributing to which mineral index. For example the highest component in the clay vector is from TM 1, with the lowest (most negative) values coming from TM 5 and TM 7. These values relate directly to the original spectral reflectance of clays, i.e. high reflectance values in visible channels and low reflectance in the SWIR channels. The same can be seen on the vegetation index as TM 4, the peak in vegetation reflectance contributes the largest factor to the index. Applying these indices by using them to weight atmospherically corrected TM bands should produce an image which enhances the discrimination of these four spectrally distinct features.

The above indices were derived from the lab spectra of pure minerals or surfaces. A more complex task is to try to apply this technique to rock spectra, which are a complex mixture of rock forming minerals. Here I shall try to produce spectral indices which are representative of some of the major ophiolite lithologies. Hopefully such indices will increase the spectral discrimination of mantle and crustal lithologies on both TM and OPS data. Spectral Indices for mantle and crust lithologies calculated from TM and OPS resolution spectra are shown in Figures 4.52 and 4.53.

In both Figures 4.52 and 4.53 the calculated index values are listed in (a) and (c), although these are best visualised in the graphs (b) and (d). Enhancement of the mantle lithologies on the TM imagery is going to be very limited as the spectral indices, Figure 4.52 (a) and (b), are almost identical, except for wehrlite which differs slightly in TM 3, 4 and 5. The OPS indices, Figure 4.52 (c) and (d), show slightly more variation as wehrlite, dunite and serpentine all differ slightly from the general trend, but not by much. The similarity of these indices is a direct result of the limited mineralogical variation of these lithologies. TM

TM Mantle Spectral Indices

	TM1	TM2	TM3	TM4	TM5	TM7
Lherzolite	0.73	0.41	0.14	-0.04	-0.44	-0.30
Harzburgite	0.71	0.39	0.16	0.03	-0.46	-0.33
Dunite	0.70	0.33	0.14	0.03	-0.61	-0.09
Wehrlite	0.82	0.38	-0.04	-0.21	-0.35	-0.10
Serpentine	0.63	0.40	0.21	0.09	-0.55	-0.30
Magnesite	0.74	0.28	0.15	0.00	-0.59	-0.08

(a)

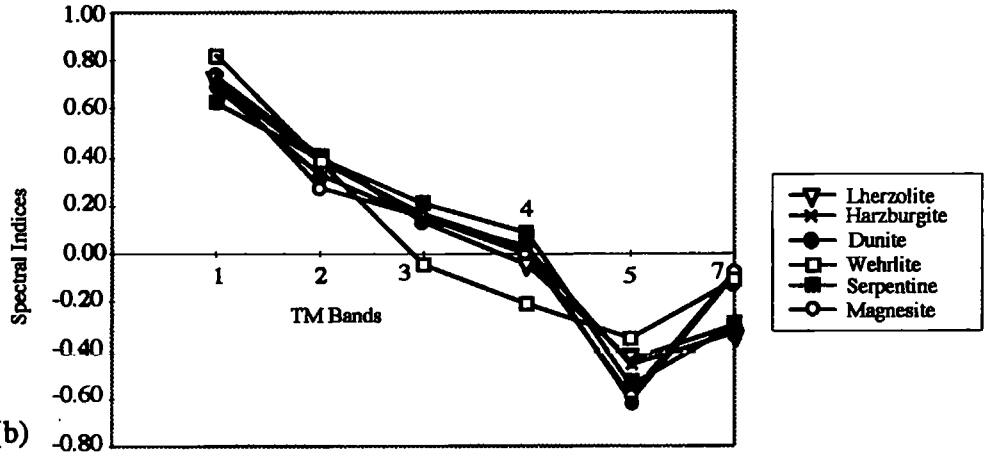

(b)

OPS Mantle Spectral Indices

	OPS 1	OPS 2	OPS 3	OPS 5	OPS 6	OPS 7	OPS 8
Lherzolite	0.55	0.12	-0.02	-0.59	-0.17	-0.08	0.55
Harzburgite	0.60	0.07	-0.06	-0.51	-0.17	-0.14	0.57
Dunite	0.42	-0.22	-0.08	-0.50	0.04	-0.06	0.71
Wehrlite	0.74	0.24	0.09	-0.42	-0.27	-0.28	0.26
Serpentine	0.88	0.21	-0.06	-0.07	-0.29	-0.23	-0.19
Magnesite	0.47	0.09	0.02	-0.56	-0.14	-0.17	0.64

(c)

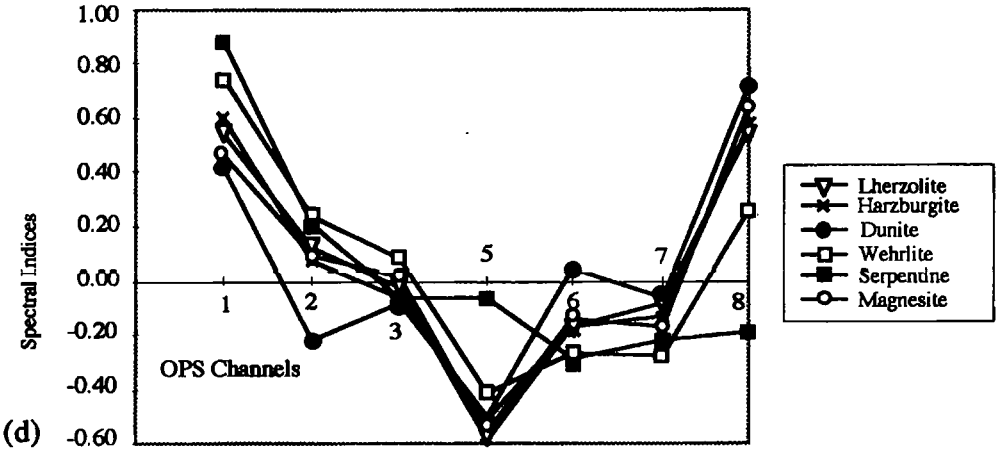

(d)

Figure 4.52 Spectral indices for mantle lithologies calculated for TM (a) and (b), and OPS data (c) and (d) from convolved lab spectra.

TM Crustal Spectral Indices

	TM1	TM2	TM3	TM4	TM5	TM7
Cumulate Gabbro	0.60	0.42	0.25	0.02	-0.53	-0.35
Isotropic Gabbro	0.50	0.38	0.32	0.16	-0.57	-0.39
Pyroxenite	0.39	0.28	0.35	0.22	-0.77	-0.08
Trondjhemite	0.64	0.44	0.16	-0.11	-0.58	-0.12
Sheeted Dykes	0.38	0.37	0.37	0.24	-0.65	-0.33
Pillow Lava	0.32	0.18	0.43	0.25	-0.78	-0.05

(a)

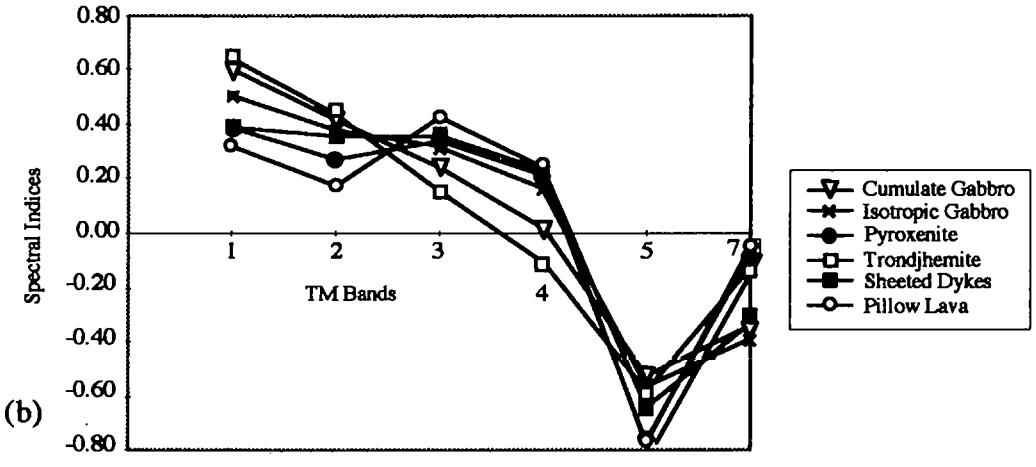

(b)

OPS Crustal Spectral Indices

	OPS1	OPS2	OPS3	OPS5	OPS6	OPS7	OPS8
Cumulate Gabbro	0.42	0.36	0.05	-0.34	-0.39	-0.32	0.57
Isotropic Gabbro	-0.31	-0.34	-0.39	-0.16	0.16	0.22	0.73
Pyroxenite	0.68	0.17	0.26	-0.41	-0.29	-0.32	0.28
Trondjhemite	0.61	0.45	0.24	-0.42	-0.34	-0.26	0.09
Sheeted Dykes	0.71	0.13	-0.10	-0.42	-0.24	-0.17	0.45
Pillow Lava	0.75	0.34	0.23	-0.31	-0.32	-0.23	-0.12

(c)

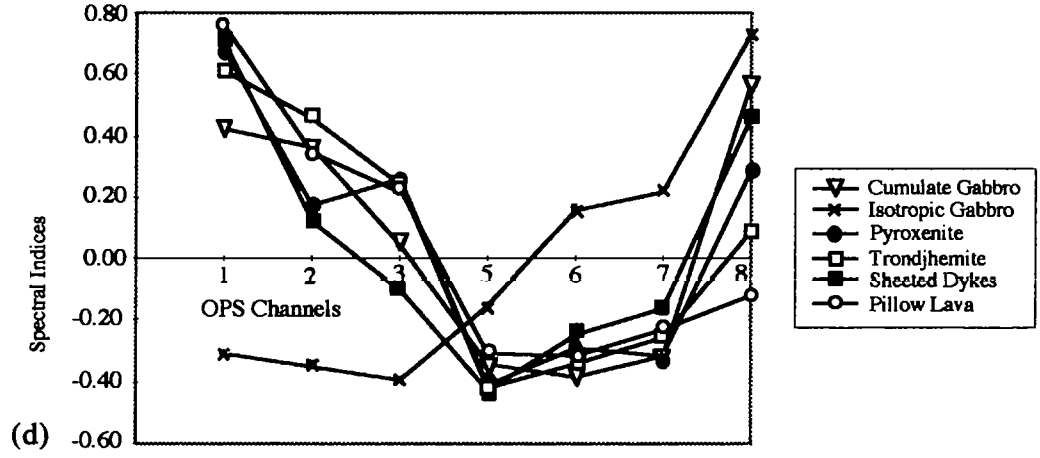

(d)

Figure 4.53 Spectral indices for crustal lithologies calculated for TM data (a) and (b), and OPS data (c) and (d) from convolved lab spectra.

crustal indices, Figure 4.53 (a) and (b), are also fairly similar although the profile of pillow lava is quite distinct from the others. The OPS indices for crustal lithologies, Figure 4.53 (c) and (d), are more varied. Isotropic gabbro is quite distinct across all channels, whilst pyroxenite deviates from the general trend in OPS 3.

By comparing these graphs the importance of the sub-division of the SWIR part of the EM spectrum is once again emphasised. On both of the TM graphs the indices are very similar for all lithologies in TM 7. However on both of the OPS graphs the index values for OPS 8 are significantly more varied, suggesting that these indices are emphasising Mg-OH features detected by OPS 8. Note how the index values for OPS 6 and especially OPS 7 are very similar for all lithologies, with the exception of dunite. This suggests that these two channels have limited discrimination capabilities for ophiolite lithologies. Results of the application of these indices are discussed in chapter 5.

4.5.4 Common image processing enhancements

Common image processing techniques such as Principal Component Analysis (PCA), Decorrelation Stretching (DS), Tasseled Cap (TC) and Intensity, Saturation and Hue (ISH) transforms can be used to help discriminate between features in multi-dimensional data sets. The basics of PCA has already been described in the context of noise removal (chapter 3, section 3.2.3) and will not be repeated here, except to say that this technique can also be used to help uncorrelate spectral information which is highly correlated across satellite channels. The disadvantage of this technique is the lack of textural information in PCs (except PC 1), combined with unusual feature colouring can make image interpretation difficult. This can be eased by analysing the transformation statistics in a similar way to that discussed in section 4.5.3, thereby determining which original spectral features are contributing to each PC. The potential of PCA will be demonstrated in chapter 5.

A similar technique to PCA is that of decorrelation stretching. This technique relies on PCA but produces images which are easier to interpret because the output colours relate to the original spectral responses of the surfaces in the input scene. Textural information is also preserved in all channels. The basic principle of DS is the production of principal components which are then stretched in their decorrelated state before being transformed back so that the data once again lies along the original RGB axes. This results in the data having an improved distribution in colour space which results in more intensely coloured images (as illustrated in chapter 5). A full description of this technique can be found in Gillespie *et al.*, (1986), and Rothery (1987).

Tasseled Cap (TC) transformation is a linear transformation which concentrates the vast majority of data variability into a few component images (Crist and Cicone, 1984). This transformation was developed by Kauth and Thomas (1976) using MSS data to derive four new vegetation component images, but the technique was later expanded to TM data by Crist and Cicone (1984). Tasseled cap analysis of TM data produces three primary components and three secondary components. As described by Crist and Cicone (1984) these are; brightness, which is a weighted sum of all six reflective TM bands; greenness, which is the contrast between the sum of the visible bands and the near infrared bands and wetness, the contrast between the sum of the visible and near infrared bands with the shortwave infrared bands. The three secondary components are less important and represent residual variations not contained in the first three components.

Preliminary work has been undertaken by Malila and Meyers (1995) to develop the TM tasseled cap transformation for application to OPS data. This work has involved applying TM tasseled cap coefficients directly to OPS data and to deriving new OPS coefficients. The overall spectral similarity of TM and OPS means that the TM coefficients can be easily applied to OPS data. With respect to the additional OPS SWIR channels, either an average channel can be used or individual channels can be used. Development of an OPS based tasseled cap transform by Malila and Meyers (1995) has resulted in the development of a fourth primary component; haziness. This fourth component is primarily the contrast between the two visible channels. Both TM and OPS derived tasseled cap coefficients will be tested in chapter 5.

ISH is a slightly different enhancement technique as it relies on the manipulation of colour via intensity, saturation and hue values, as opposed to RGB values. A full description of the transformation from RGB to ISH can be found in Gillespie *et al.*, (1986). ISH colour space occupies either a spherical or conical volume where the intensity component represents the overall brightness of a scene (varying from black to white), saturation represents the purity of a colour and hue represents the dominant wavelength (i.e. colour). An advantage of representing colour variation in this way is that every colour can be described by spherical co-ordinates.

In its simplest form this technique can be used to enhance the intensity of the colours in a three band composite in order to produce a more colourful image. However it can also be used as a technique for combining different data sets, for example, satellite data and geological maps, or satellite data at different resolutions. Data merging is achieved by producing ISH components for both of the data sets. The intensity image from one data set is then combined with the hue and saturation components from the other, prior to performing the inverse transformation (Edwards and Davis 1994). This results in the image detail and resolution in the output image being controlled by the intensity component

whilst the image colours are controlled by the hue and saturation components. An example of an ISH data merge between OPS data and air photography will be shown in chapter 5.

4.5.5 Previously used techniques for ophiolite mapping

A review of recent literature on geological mapping and/or lithological discrimination has highlighted a number of image processing techniques which may be applicable to the Oman ophiolite. A summary of the most appropriate techniques are given here.

Previous remote sensing work mapping the Oman ophiolite (Abrams, 1986; Rothery, 1987a; Rothery, 1987b; Abrams *et al.*, 1988) has highlighted the band combination of TM 754 as a decorrelation stretched image (Gillespie and Kahle, 1986) as being very good for lithological discrimination of ophiolite lithologies. This view was supported by Gnos *et al.* (1991) and Pontual (1990). Pontual (1990) also suggested pseudoratios of TM 5/7, 5/4 and 3/2, equivalent to OPS ratios of 5/8 (or 5/7, 5/6), 5/3 and 2/1. This would be equivalent to a combination of OPS 8,7 or 6 with OPS 5 and OPS 3. Earlier work by Harding and Bird (1984) mapping the Josephine peridotite (USA) suggested combining MSS ratios 5/7 and 6/5 with PC 1, in order to distinguish harzburgite, serpentinite and intrusives. This would be equivalent to TM 2/4 and TM 3/2 or OPS 1/3 and OPS 2/1.

Sultan *et al.*, (1986) demonstrated that a composite image of the TM ratios 5/7, 5/1 and a band 4 ratio (where the band 4 ratio equals a linear interpolation between bands TM 3 and TM 5 divided by TM 4) was capable of discriminating serpentinites from other lithologies. This TM band combination is best approximated with the OPS composite 5/8 (or 5/7, 5/6), 5/2 and a band ratio of OPS 3. Sultan (1988) also suggested serpentinites could be distinguished using the TM band combinations of TM 5/4 x 3/4, 5/1 and 5/7, approximated by OPS 5/3 x 2/3, 5/2? (nearest OPS channel to TM 1) and 5/8 (or 5/7 or 5/6).

The suitability of these techniques for enhancing lithological discrimination in the study areas in this project will be discussed in chapter 5.

4.6 Summary and recommendations

This chapter has introduced the major ophiolite lithologies and their mineralogies. It has also described in great detail the spectral characteristics of these lithologies over the 0.4 μm to 2.4 μm range. Characteristic spectra of each lithology have then been identified and used to compare the discrimination potential of these lithologies at the spectral resolution of Landsat TM and JERS-1 OPS. This analysis has indicated that OPS 8 should provide new

and useful discrimination information for a number of lithologies. The resampled lab spectra have also been compared with image derived spectra. This comparison has shown that the majority of the image spectra are fairly similar to the resampled lab spectra except for the OPS SWIR channels (OPS 6 and OPS 7). Major variations are evident between the expected spectral response across OPS 6 and OPS 7 as determined by the analysis of resampled lab spectra, and the actual spectral response indicated by image data. This comparison has shown that the spectral response of channels OPS 6 and OPS 7 are primarily controlled by sensor quality. The spectral information in OPS 6 and OPS 7 imagery will therefore be a poor representation of ground changes caused by mineralogical variations.

The latter part of this chapter has concentrated on applying various qualitative and quantitative techniques to both the convolved lab spectra and sample image spectra to try to establish a short list of image processing techniques and band combinations which may be capable of discriminating ophiolite lithologies. Wherever possible the convolved lab spectra have been used to try to guide the processing of image data with respect to enhancing specific features. This approach allows good spectral information for OPS 6 and OPS 7 to be included in the analyses, a task which is not possible using image derived spectra. This allows me to ask the question "If OPS 6 and OPS 7 were of a high quality would this additional spectral information aid the discrimination of ophiolite lithologies ?" This approach has shown that for the majority of the lithologies in question in this study, good OPS 6 and OPS 7 image data would be highly correlated. As a result either OPS 6 or OPS 7 would be capable of adding some additional discriminatory information, but the need for both channels is very minimal. This is indicated by the number of OPS band combinations (determined by spectral statistics) and ratios that include one of these channels but not both. The spectral studies have clearly shown that OPS 8 is the truly important channel for discriminating between ophiolite lithologies. This channel is responding to Mg-OH absorptions caused by varying amounts of serpentine, an important mineralogical feature which is not truly recorded by TM 7 because of its broad bandwidth and its failure to extend to the deepest part of the Mg-OH absorption at 2.4 μm. OPS 8 will provide new spectral information which is not available from Landsat TM. This will be the most significant advantage of JERS-1 over Landsat TM with respect to mapping ophiolite lithologies.

Tables 4.10 and 4.11 summarise the results of the different techniques used in sections 4.5.1 to 4.5.5 to determine useful band combinations for false colour composites. The effectiveness of these band combinations and enhancements for discriminating ophiolite lithologies will be discussed in chapter 5.

Band Combination	Lithologies Enhanced	Determined by
TM 543	Mantle	Spectral interpretation
TM 547	Crust	Spectral interpretation
TM 715	All	Correlation coefficients
TM 725	All	Correlation coefficients
TM 541	All	Image statistics
TM 571, 471	All	Spectra statistics
TM 571	Harzburgite	Spectra statistics
TM 541	Dunite	Spectra statistics
TM 537	Wehrlite	Spectra statistics
TM 357	Gabbro	Spectra statistics
TM 547	Pyroxenite	Spectra statistics
TM 423	Sheeted dykes	Spectra statistics
TM 157	Trondjhemite	Spectra statistics
TM 1/5	Lherzolite, dunite, wehrlite	Spectral ratio
TM 4/7	Harzburgite	Spectral ratio
TM 1/5	Cum. gabbro, dykes, lava	Spectral ratio
TM 1/7	Isotropic gabbro	Spectral ratio
TM 4/7	Trondjhemite	Spectral ratio
TM 5/7	Pyroxenite	Spectral ratio
TM 2/4, 3/2, PC 1	Harzburgite, serpentine	Harding and Bird, 1984
TM 754 (decorrelation)	All	Abrams 1986
TM 5/7, 5/1, (3+5)/4	Serpentinites	Sultan *et al.*, 1986
TM 5/4 x 3/4, 5/1, 5/7	Serpentine	Sultan *et al.*, 1986
TM 5/7, 5/4, 3/2	All	Pontual, 1990

Table 4.10 Summary of TM band combinations and ratios highlighted by various techniques as being potentially cabable of discriminating ophiolite lithologies.

Band Combination	Lithologies Enhanced	Determined by
OPS 532	Mantle	Spectral interpretation
OPS 532	Crust	Spectral interpretation
OPS 816	All	Correlation coefficients
OPS 516, 526	All	Image statistics
OPS 581	All	Spectra statistics
OPS 571	Harzburgite	Spectra statistics
OPS 528	Dunite	Spectra statistics
OPS 518	Wehrlite	Spectra statistics
OPS 528	Gabbro	Spectra statistics
OPS 538	Pyroxenite	Spectra statistics
OPS 681	Sheeted dykes	Spectra statistics
OPS 127	Trondjhemite	Spectra statistics
OPS 1/7	Lherzolite	Spectral ratio
OPS 5/8	Harzburgite, wehrlite	Spectral ratio
OPS 1/5	Dunite	Spectral ratio
OPS 1/5	Cum. gabbro , dykes	Spectral ratio
OPS 1/6	Isotropic gabbro	Spectral ratio
OPS 3/8	Trondjhemite	Spectral ratio
OPS 5/8	Pyroxenite, lavas	Spectral ratio
OPS 1/3, 2/1, PC 1	Harzburgite, serpentine	Approximated to Harding
OPS 8 (7) (6) 53	All	Approximated to Abrams
OPS 5/8, 5/2 (2+5)/3	Serpentinites	Approximated to Sultan
OPS 5/3 x 2/3, 5/2, 5/8	Serpentine	Approximated to Sultan
OPS 5/8 5/3, 2/1	All	Approximated to Pontual

Table 4.11 Summary of OPS band combinations and ratios highlighted by various techniques as being potentially cabable of discriminating ophiolite lithologies.

The evaluation of multichannel shortwave infrared (SWIR) optical data from the Japanese Earth Resources Satellite (JERS-1), for geological applications

A thesis presented for the degree of Doctor of Philosophy by

Anthony Maurice Denniss BSc (Hons), MSc

1997

Department of Earth Sciences, The Open University

The evaluation of multichannel shortwave infrared (SWIR) optical data from the Japanese Earth Resources Satellite (JERS-1), for geological applications

Volume 2 of 2

****

Chapter 5 onwards

5.0 Comparison of OPS and TM image data for lithological mapping in the Oman ophiolite

5.1 Introduction

The previous chapter outlined a number of possible band combinations, for both OPS and TM data, which may discriminate all or specific ophiolite lithologies. The effectiveness of the band combinations and ratios summarised in Tables 4.10 and 4.11 and the spectral indices defined in Figures 4.52 and 4.53 will now be tested. General image processing techniques such as those discussed in section 4.5.4 will also be tested. Effective band combinations and enhancements for TM and OPS data will be applied to imagery of all three study regions described in section 4.1.2. TM and OPS composites will then be compared with each other and with the known geology of each region. Finally this chapter will summarise the effectiveness of OPS data compared with TM data for lithological discrimination within the Oman ophiolite.

5.2 Maqsad study region - an introduction

5.2.1 General structure

The Maqsad study area is approximately 70 km long and 40 km wide and lies within the Sumail massif of the Oman ophiolite. The area is in fault contact with sedimentary formations on its western edge (NNE-trending fault along the Sumail Gap) and on its eastern edge (NNE-trending Andam fault), see Figure 5.1. The original high temperature thrust contact with the country rocks is preserved along the northern termination of the massif. In this area the ophiolite lithologies are highly mylonitized and are in contact with a 200-300m thick amphibolitic sole (Ceuleneer *et al.*, 1988). Several hundred metres away from this contact the massif is only weakly affected by emplacement-related deformation, with the exception of a few north-west trending mylonitic shear zones (Nicolas et al., 1988b). The majority of the internal structures visible in the Sumail massif are related to spreading centre processes (Ceuleneer *et al.*, 1988), which are related to a palaeo-spreading ridge, orientated N130°E (Figure 5.1).

The Sumail massif comprises a nearly complete ophiolite sequence from sheeted dyke complex and rare pillow basalts down to mantle periodites. On a regional scale all the lithological contacts dip gently (0° to 15°) to the ESE. This restricts mantle lithologies to the western part of the massif (Sumail Gap area) and the shallow crustal formations to the eastern region (Wadi Andam area). Relatively small outcrops of sheeted dykes and pillow lavas are restricted to the far eastern edge of the crustal region and towards the south of the region. Rugged topography, ranging in elevation between 200 and 1000 metres, combined with sub-horizontal lithological contacts results in a complicated lithological map (see section 5.5.4 and 5.5.5). The Maqsad lithological map is further complicated by numerous NW to NNW trending faults which displace some lithological contacts vertically by a few metres to a few hundreds of metres.

5.2.2 Mantle section

Microstructural studies of non-mylonitized mantle peridotites show a pervasive foliation and lineation imprinted by plastic deformation at very high temperatures (*c.* 1200°C) and low stress conditions, i.e. corresponding to asthenospheric conditions (Nicolas *et al.*, 1993, Ceuleneer *et al.*, 1996). Detailed mapping of these structures by Ceuleneer *et al.*, (1996) has allowed asthenospheric flow patterns to be traced, resulting in the detection of an upwelling zone (palaeo-spreading structure), centred on the Maqsad oasis, referred to by Ceuleneer (1990) as the 'Maqsad diapir'. This diapir is approximately 16 kilometres wide and narrows at Moho level where it is elongated parallel to a NW-SE azimuth (Rabinowicz *et al.*, 1987). Either side of the Maqsad diapir the flow structures become horizontal, indicating consistent south-westward flow on the western side and north-eastward flow on the north-western side (Ceuleneer 1991).

Within the Sumail massif the composition of the mantle peridotites is predominantly harzburgitic. Mineralogical variations of these harzburgites include orthopyroxene which ranges from almost zero (dunitic) to 30%. These harzburgites are also serpentinised to varying degrees. The mantle peridotites also vary compositionally due to the nature and abundance of trapped melt relics (pyroxenitic and gabbroic dykes, chromite ore bodies, etc.). These trapped melt relics are most abundant a few hundred metres below the Palaeo-Moho, where they form a 'field-mappable' transition zone of dunites, wehrlites, troctolites and scattered gabbroic lenses (Benn *et al.*, 1988). The thickness of this zone decreases away from the Maqsad diapir down to tens of metres. Palaeo-upwelling areas are characterised by orthopyroxene-rich harzburgites and a lack of melt relics (Nicolas *et al.*, 1988a).

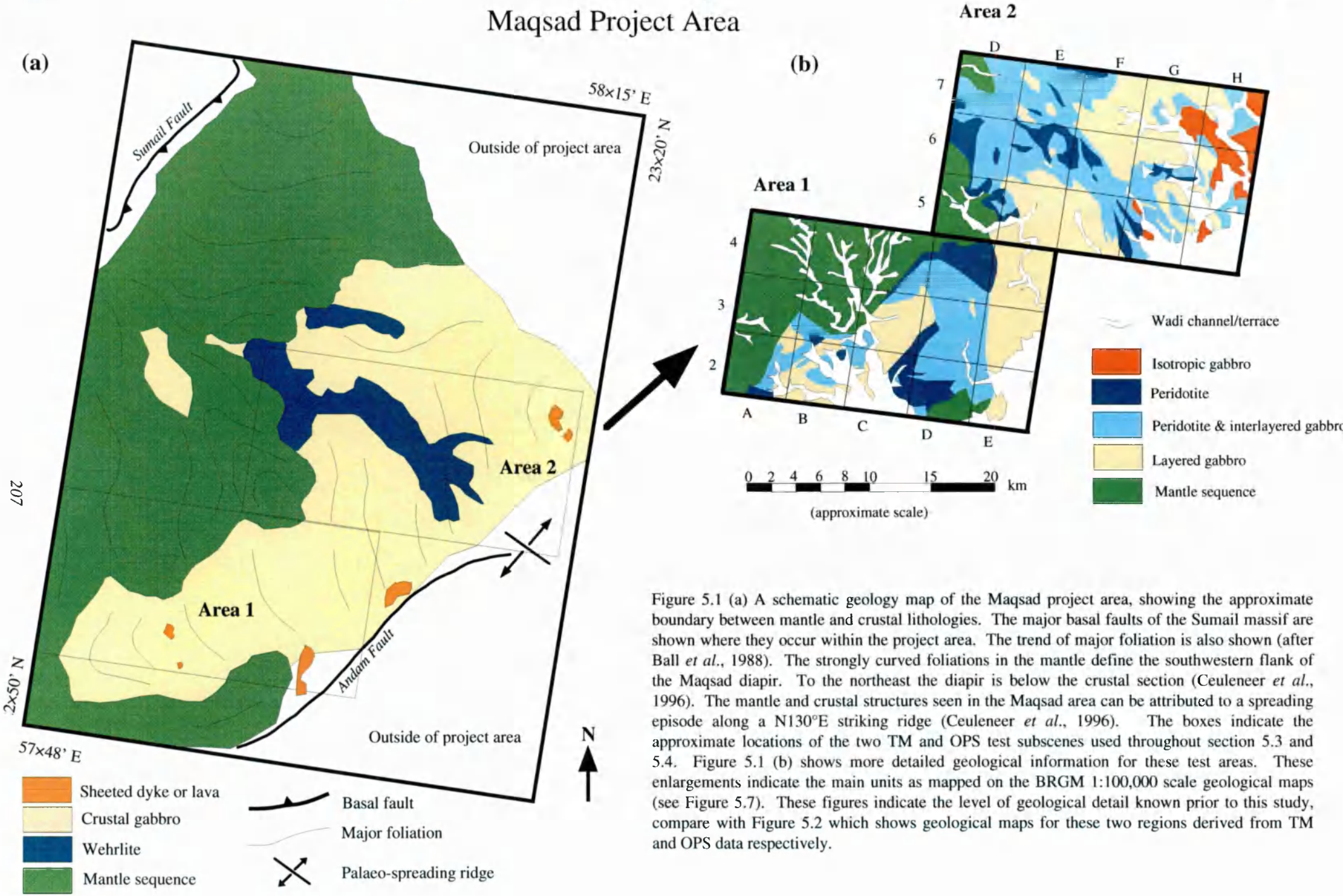

Figure 5.1 (a) A schematic geology map of the Maqsad project area, showing the approximate boundary between mantle and crustal lithologies. The major basal faults of the Sumail massif are shown where they occur within the project area. The trend of major foliation is also shown (after Ball *et al.*, 1988). The strongly curved foliations in the mantle define the southwestern flank of the Maqsad diapir. To the northeast the diapir is below the crustal section (Ceuleneer *et al.*, 1996). The mantle and crustal structures seen in the Maqsad area can be attributed to a spreading episode along a N130°E striking ridge (Ceuleneer *et al.*, 1996). The boxes indicate the approximate locations of the two TM and OPS test subscenes used throughout section 5.3 and 5.4. Figure 5.1 (b) shows more detailed geological information for these test areas. These enlargements indicate the main units as mapped on the BRGM 1:100,000 scale geological maps (see Figure 5.7). These figures indicate the level of geological detail known prior to this study, compare with Figure 5.2 which shows geological maps for these two regions derived from TM and OPS data respectively.

Gabbroic-pyroxenite dykes are virtually absent from the Maqsad diapir although they become progressively more abundant (making a few percent of the outcrop) approximately 3 to 4 km away (Ceuleneer 1990). Further away from the palaeo-spreading axis pyroxentic and gabbro dykes form approximately 20% of the outcrop. Locally they may form mappable intrusive bodies several hundred metres in size.

5.2.3 Crustal section

In comparison the crustal section of the Sumail massif shows a very large diversity of petrological and structural facies. The majority of the crustal section is comprised of cumulate gabbro, however this is dominated by intrusive magmatic bodies up to several kilometres in size. The composition of these bodies varies widely between wehrlite, troctolite, gabbro and trondhjemite. Their distribution appears to be related to the palaeo-spreading structure in the underlying harzburgites (Ceuleneer, 1990 and Benn *et al.*, 1988). Wehrlite and troctolite intrusions are more abundant above the palaeo-spreading axis, whilst isotropic gabbro and trondhjemite intrusions are restricted to an off-axis location (Ceuleneer 1990). These intrusives also vary widely in their dyke content. Dyke densities tend to increase upsection reaching a maximum towards the base of the sheeted dyke complex. Dykes within the sheeted dyke complex strike northwest-southeast, approximately equivalent to the orientation of the palaeo-ridge axis (Ceuleneer 1990).

5.2.4 Test subscenes

The Maqsad study region is very large, so in order to effectively test all of the TM and OPS band combinations described in the previous chapter two test areas were established. The approximate locations of these are shown in Figure 5.1. These test areas have been chosen because all of the major ophiolite lithologies outcrop within them. Detailed geological maps of these regions are shown in Figure 5.2. Maps (a) and (b) have been produced from interpretation of TM data whilst (c) and (d) have been produced from OPS data. These maps are enlargements of sections of the image interpretation maps shown in Figures 5.38 (b) and 5.39 (b). These extracts have been included at this point in the thesis to indicate the location of the ophiolite lithologies within 'Area 1' and 'Area 2', thereby aiding the explanation of the TM and OPS processing in sections 5.3 and 5.4. To ensure that both the TM and OPS subscenes cover the same area they have been registered to the same projection as the published geological maps covering the Maqsad region (see Figure 5.37). A 5 km grid has been superimposed on these subscenes allowing a two letter grid reference to be used

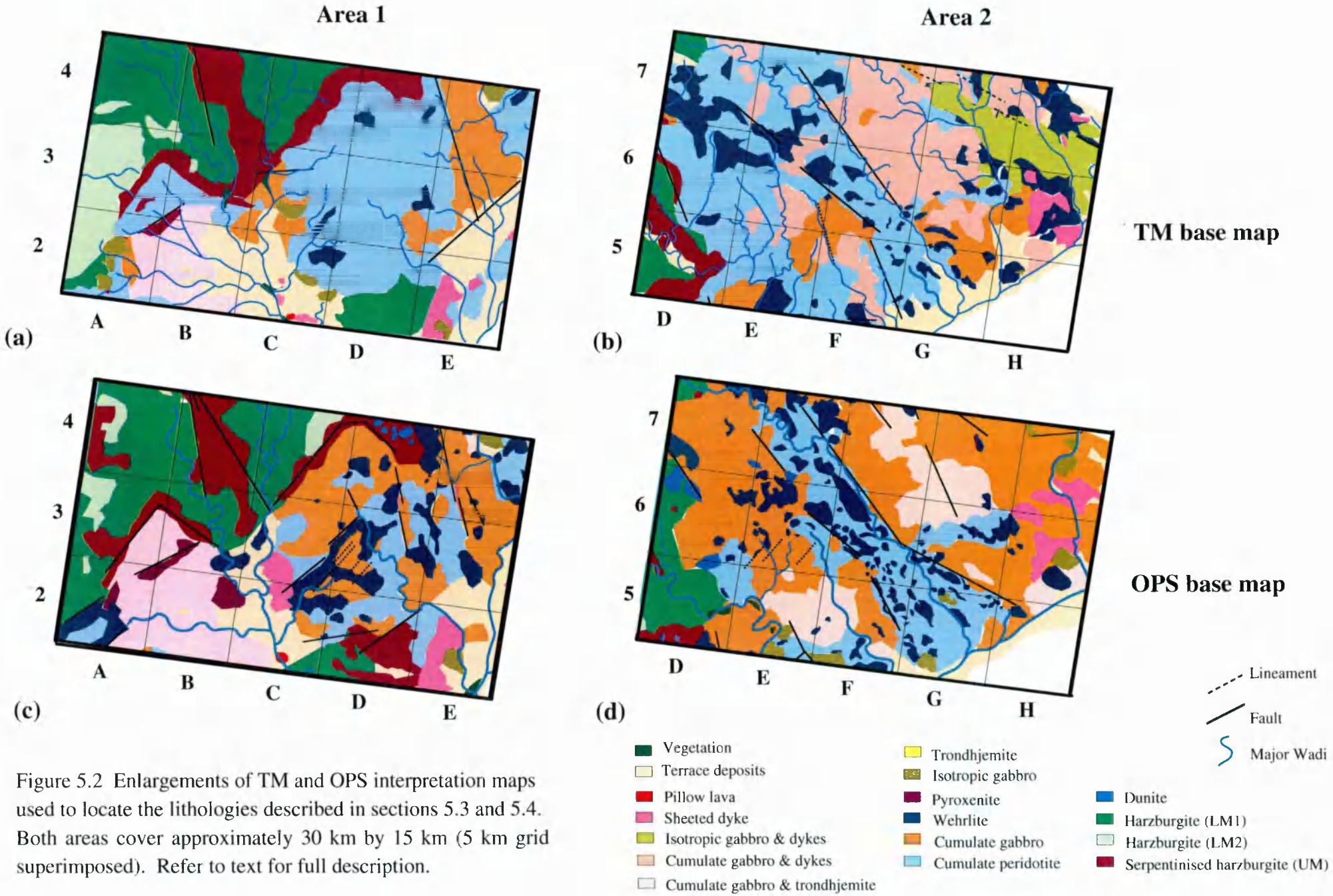

Figure 5.2 Enlargements of TM and OPS interpretation maps used to locate the lithologies described in sections 5.3 and 5.4. Both areas cover approximately 30 km by 15 km (5 km grid superimposed). Refer to text for full description.

to locate features of interest, for example B3. This grid is used to aid the comparison between TM, OPS and map data. All TM band composites use atmospherically corrected data (Appendix 1), and bands are listed in the order of red, green and blue (RGB).

5.3 TM processing

5.3.1 TM composites

Section 4.5.1 discussed various techniques to determine which of the 20 TM band composites (excluding TM 6) would offer the highest levels of lithological discrimination between ophiolite lithologies. Seven composites were chosen from spectral interpretation, correlation coefficients, image statistics and spectra statistics (Table 4.10). The discrimination potential of these composites is summarised in Table 5.1 and Plates 5.1 to 5.3. The levels of discrimination (Low, Medium and High) used in Table 5.1 relate to how easy it is do distinguish each lithology from all other lithologies. This is a qualitative measure of the ease with which a unit can be identified. Obviously discrimination of specific outcrops will vary across a scene depending on locational context, in particular the spectral contrast with surrounding lithologies.

Levels of lithological discrimination varied considerably between the suggested composite images. TM 543 (Plate 5.1 (a) and (b)) composites derived by analysis of the spectra discriminated both dunite in pale blue (lower D5) and trondhjemite in bright white-pink (B3) quite well, although without field knowledge the small dunite and trondhjemite outcrops are difficult to distinguish on the imagery. This composite also discriminated variations in the mantle quite well, with harzburgites exhibiting various red-brown colours (A3). It was however poor at discriminating the different crustal gabbroic lithologies (E6), as well as the sheeted dyke complex (E2) and pillow lavas (C2). These units tended to exhibit colours very similar to those of the wadi terrace deposits, making them difficult to distinguish. The second composite derived by spectral analysis, TM 547, was extremely poor when displayed in the original band order. Re-ordering the bands to TM 754 (Plate 5.1 (c) and (d)), greatly improved lithological discrimination (see Table 5.1). Overall discrimination of mantle lithologies was good with harzburgite ranging from bright green (A3) to dark green (A4) and red-purple towards the upper mantle (D5). Cumulate gabbro is normally yellow-green-brown (F5), although occasionally bright yellow (E4) where outcrops develop a thick iron varnish. Isotropic gabbro appeared a more orange-yellow colour

Lithology	TM 543		TM 754 (547)		TM 751 (715)		TM 752 (725)		TM 541		TM 741 (471)	
	Colour	Dis.	Colour	Dis.	Colour	Dis.	Colour	Dis.	Colour	Dis.	Colour	Dis.
Pillow lavas	green-brown	L	red-pink	H	red-purple	L-M	red-purple	L-M	blue-purple	M	purple-red	L
Sheeted dyke	red-brown	L	orange to purple-red	M	pink-purple	H	ornage-pink	H	pink-brown	L	bright pink-red	H
Isotropic gabbro	pink-red	L-M	orange-yellow	M-H	yellow-brown	M	yellow-brown	M	red-brown	M	orange-red	M
Cumulate gabbro	orange-brown-red	M	yellow-green-brown	M-H	green-yellow	M	green-yellow	M-H	yellow-beige	M	orange-brown	M
Cumulate peridotite	dark brown-red	L-M	cyan-green	L-M	yellow-brown	L-M	green-yellow-brown	M	green-brown	L	green-brown	L-M
Harzburgite	red-brown	M	bright green-dark green, red-purple	M-H	green-yellow, brown-purple	M	brown-red	L-M	brown-red	M	green-brown	L-M
Dunite	light blue	H	blue-pink	L-M	pale purple	L	purple-blue	M	cyan-blue	M	pale blue-green	L
Wehrlite	dark purple-black	L	dark purple-brown	M	dark purple-blue	M	dark purple	L	dark green-brown	L	purple-blue	L-M
Trondhjemite	bright white - pink	H	white-pink	M	white-pink	M	white-pink	M	pink	M	pink	H
Isotropic gabbro + dykes	orange-pink-red	L-M	yellow-orange	M-H	red-brown	M	red-brown	M	orange-red-brown	M	red-brown	M
Cumulate gabbro + dykes	pink-brown-red	L	orange-pink	M-H	yellow-green	M	yellow-green	M	orange-brown	M	ornage-yellow	L-M
Cumulate gabbro + trondhjemite	pink-brown	M	pink-brown	M	beige-brown	L	brown-red	L	ornage-pink	L	orange-pink	L-M
Pyroxenite	red-brown	L	green-blue	L-M	green	M	green-blue	M	beige-brown	L	green-brown	L

Table 5.1 Colours of the main lithologies on TM composites as defined in Table 4.11. Dis. = Discrimination, were L=Low, M=Medium and H=High. Band combinations in brackets denotes original composite order prior to band re-ordering. See text for full description.

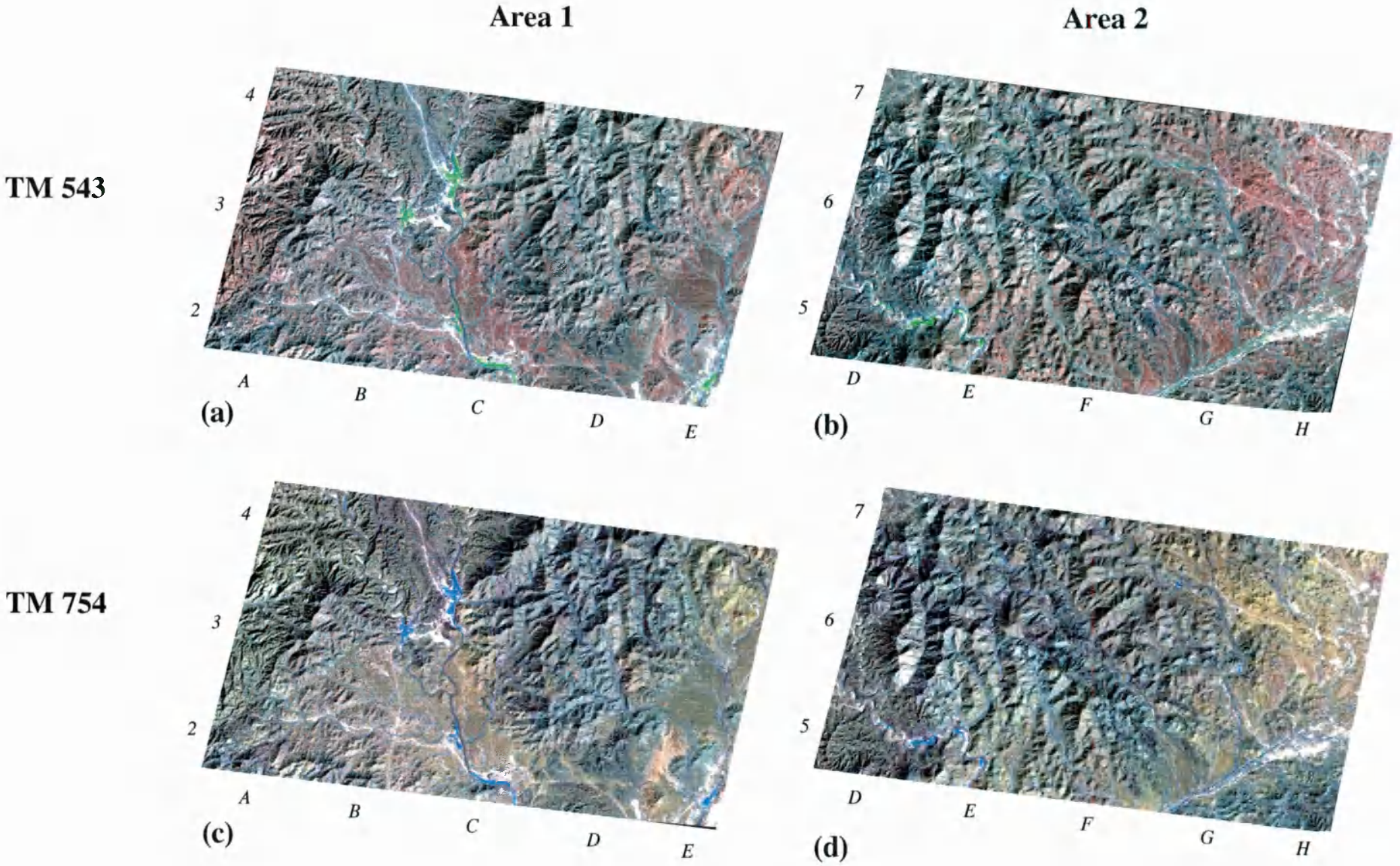

Plate 5.1 Two TM composites of the Maqsad study areas (see Figure 5.1 for location). Refer to text for a full description.

(H6), allowing discrimination between it and cumulate gabbro. Dyke-rich areas of isotropic gabbro are more yellow (G7), whilst dyke-rich cumulate gabbros are orange-pink (F7). Cumulate peridotite is a distinct cyan-green (F6) colour whilst large wehrlite bodies are dark purple-blue colour (F6). Sheeted dykes (orange to purple-red, E2) and trondhjemite (white-pink, B3) are also distinct. The discrimination of dunite (blue-pink, D5), pyroxenite (green-blue, B3) and pillow lavas (red-pink, C2) were all poor.

Discrimination levels on both the composites defined by correlation coefficients (TM 715 and TM 725) were very similar, although both composites had to be re-ordered to TM 751 (Plates 5.2 (a) and (b)) and TM 752 (Plates 5.2 (c) and (d)) to maximise visual discrimination. TM 752 was the slightly better composite as dunite (pale purple-blue, D5) and cumulate peridotite (green-yellow-brown, D3) were easier to distinguish. Discrimination of all other lithologies on these composites was fairly average, with the exception of the sheeted dykes complex which was very distinct (pink, E2). TM 541 (Plate 5.3 (a) and (b)) defined by the analysis of image statistics showed reasonable discrimination of both mantle and crustal lithologies. A fiarly distinct lithology on this composite was that of sheeted dykes (red-purple), whilst the least distinct was cumulate peridotite (D3). Harzburgites also showed less colour variations (brown-red, A4)) than on some of the other composites, making discrimination between upper and lower mantle sections difficult. Analysis of spectra statistics suggested two potentially useful composites, TM 571 and TM 471. TM 571 was very poor and was best re-ordered as TM 751 as described previously (Plate 5.2 (a) and (b)), whilst TM 471 was best re-ordered as TM 741 (Plate 5.3 (c) and (d)). Overall discrimination on TM 741 was reasonable with crustal lithologies ranging in colour from pink-red (sheeted dykes, E2) through orange-red-brown (cumulate, F5, and isotropic gabbros, H7) to dark purple-blue (wehrlite, F6). Mantle lithologies were fairly distinct from crustal lithologies in various green-brown-red (D5) tones. This composite was very similar to those of TM 543 and TM 541.

Considering discrimination of all of the lithologies, the TM 754 composite offered the best overall discrimination with TM 741 and TM 752 coming a close second and third. The selection of TM 754 is supported by previous studies, such as Abrams (1986), Rothery (1987a), Rothery (1987b) and Abrams *et al.* (1988), all of whom used this image as a base for performing a decorrelation transform. Comparison of these predefined band combinations illustrated the importance of combining the chosen bands in the 'best' display order, not just in the order of maximum variance as used in

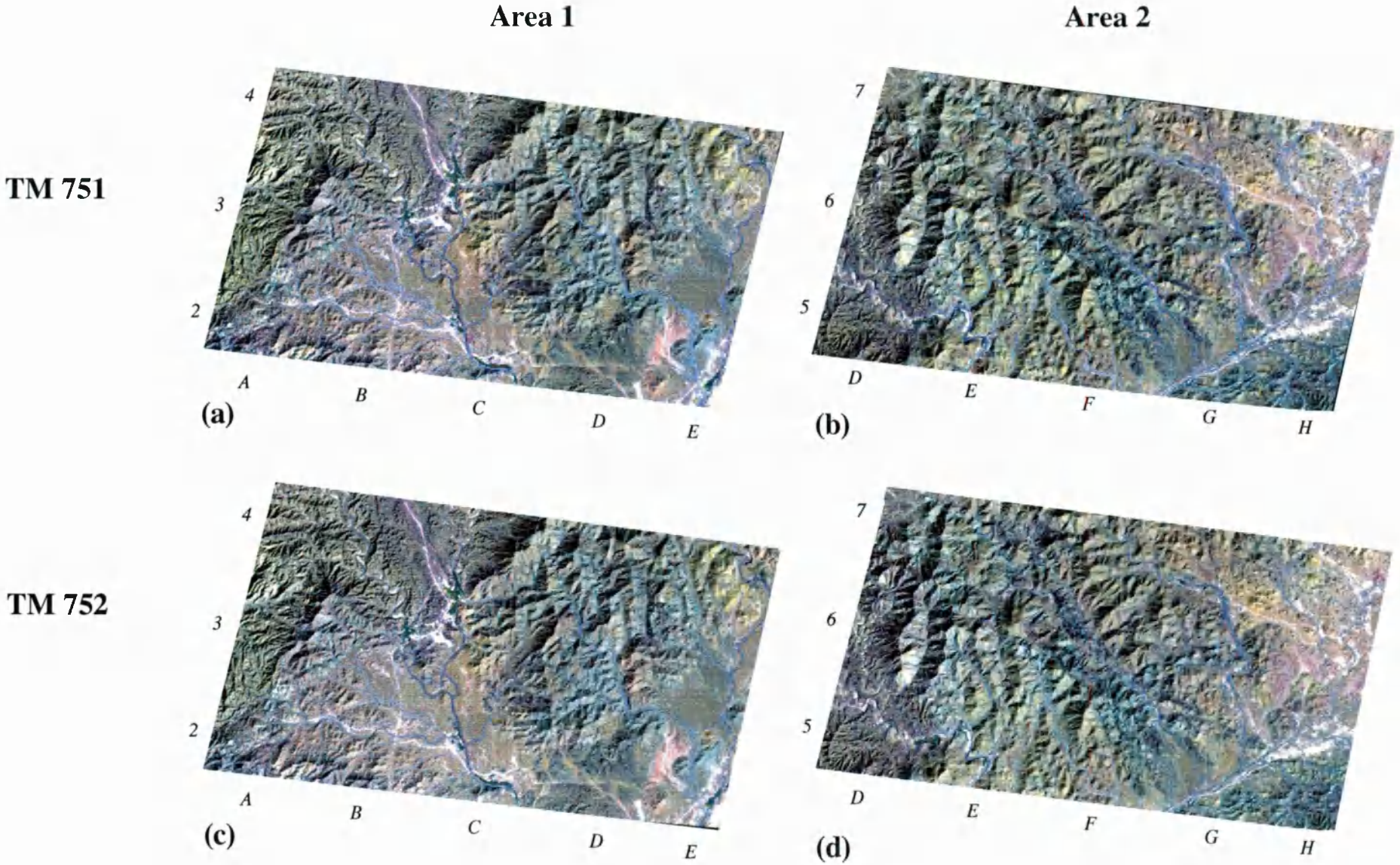

Plate 5.2 Two TM composites of the Maqsad study areas (see Figure 5.1 for location). Refer to text for a full description.

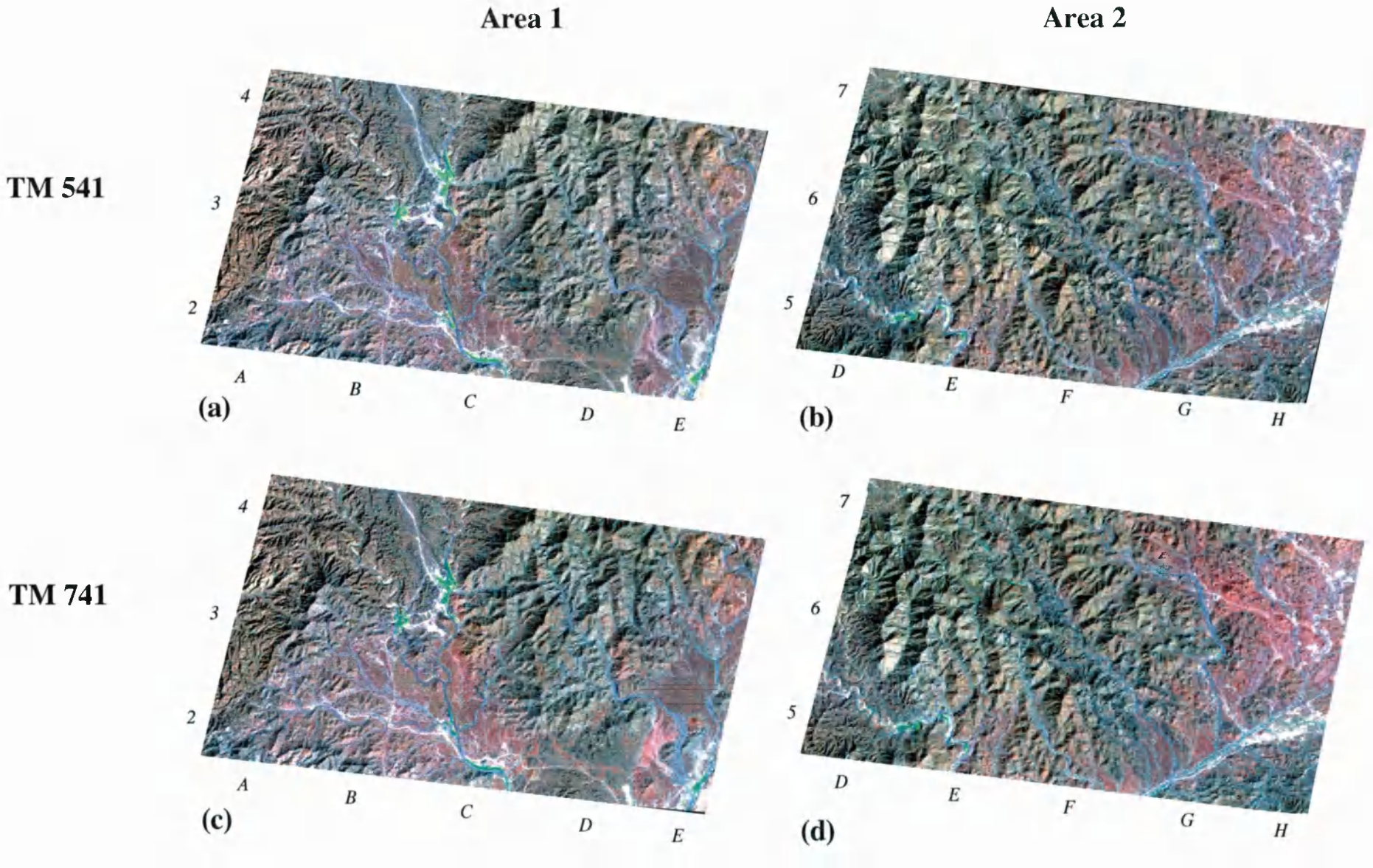

Plate 5.3 Two TM composites of the Maqsad study areas (see Figure 5.1 for location). Refer to text for a full description.

section 4.5.1. The best display order can only be determined visually as it relies on the visual perception of the operator, it may therefore differ between operators.

A further seven three band composites were identified by statistical analysis in section 4.5.2 as potentially discriminating one lithology more than the others. Table 5.2 compares the expected discrimination of each highlighted lithology against the actual discrimination on each composite (Plates 5.4 to 5.7). In this instance all band orders have been left as defined by the statistical techniques. This statistical approach to selecting band composites had mixed results. Between them composites of TM 541 (Plates 5.4 (c) and (d)), TM 357 (Plates 5.5 (c) and (d)), TM 423 (Plates 5.6 (c) and (d)) and TM 157 (Plates 5.7 (a) and (b)) discriminated the predetermined lithologies; dunite (D5), gabbro (E6), sheeted dykes (E2) and trondhjemite (B3) quite well. The other composites, TM 571 (Plates 5.4 (a) and (b)), TM 537 (Plates 5.5 (a) and (b)) and TM 547 (Plates 5.6 (a) and (b)) discriminated the predetermined lithologies; harzburgite (A4), wehrlite (F6) and pyroxenite (B3) to a lesser degree.

Composite	Expected discrimination	Colour on composite	Dis.	Highest discrimination	Colour on composite	Dis.
TM 571	harzburgite	yellow-green-purple	M	cumulate gabbro sheeted dykes	yellow -green green-blue	M-H H
TM 541	dunite	bright cyan-green	M	cumulate gabbro wehrlite.	red-brown dark blue	M M
TM 537	wehrlite	dark green-purple	L-M	isotropic gabbro	purple-pink	M
TM 357	gabbro	cyan-blue (variable)	M-H	dunite sheeted dykes	red-brown blue-purple	M M
TM 547	pyroxenite	beige-brown	L	sheeted dykes	pink-purple	M-H
TM 423	sheeted dykes	green	M-H	vegetation	bright red	H
TM 157	trondhjemite	white-pink	M-H	sheeted dykes pyroxenite	red-pink green	H M

Table 5.2 Comparison of band composites derived by statistical analysis. Each composite was expected to discriminate one lithology more than the others (as per section 4.5.2). Discrimination levels of these 'expected' lithologies are shown against other lithologies also discriminated by the composite. Dis.= Discrimination, L=Low, M=Moderate and H=High.

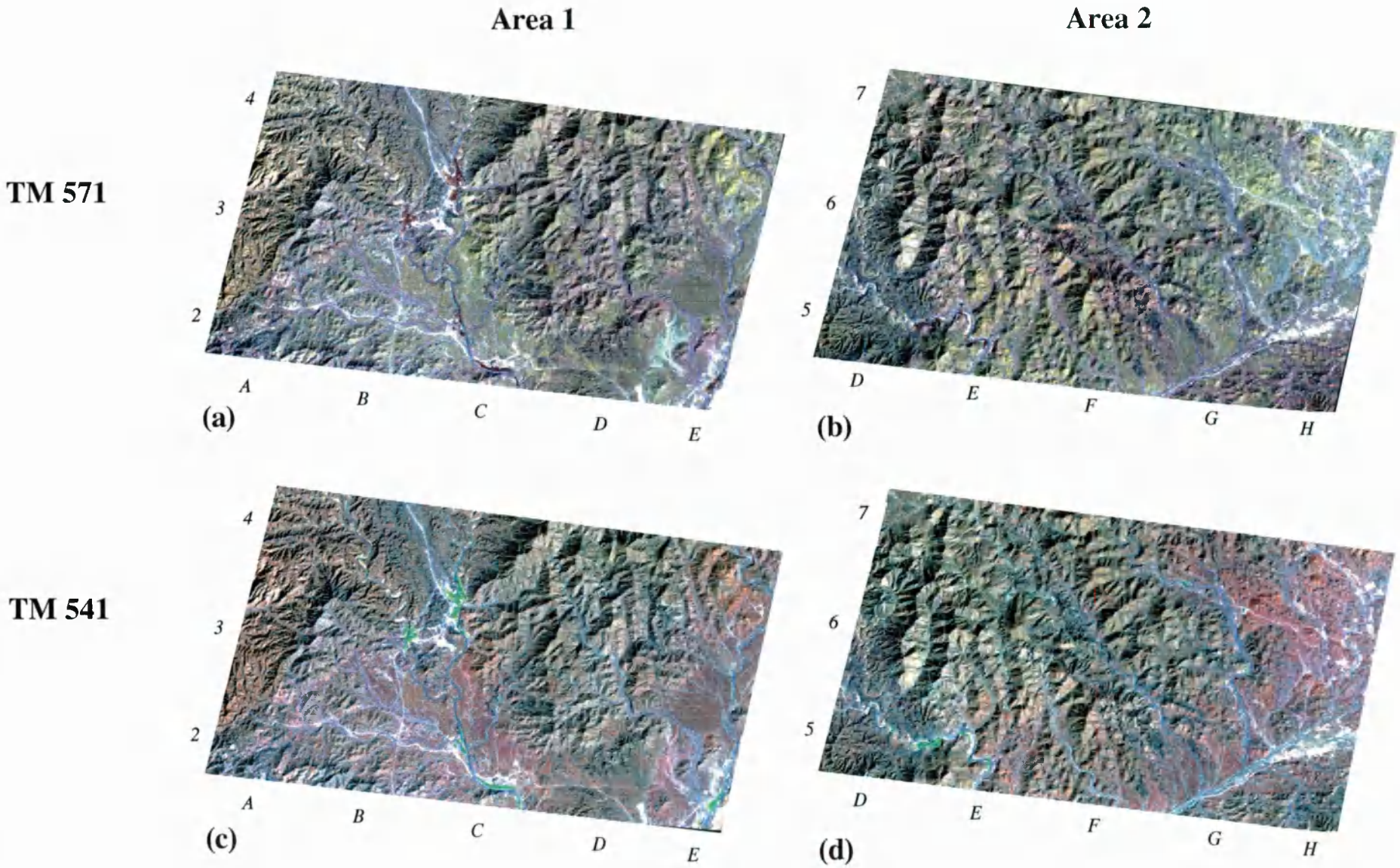

Plate 5.4 Two TM composites of the Maqsad study areas (see Figure 5.1 for location). Refer to text for a full description.

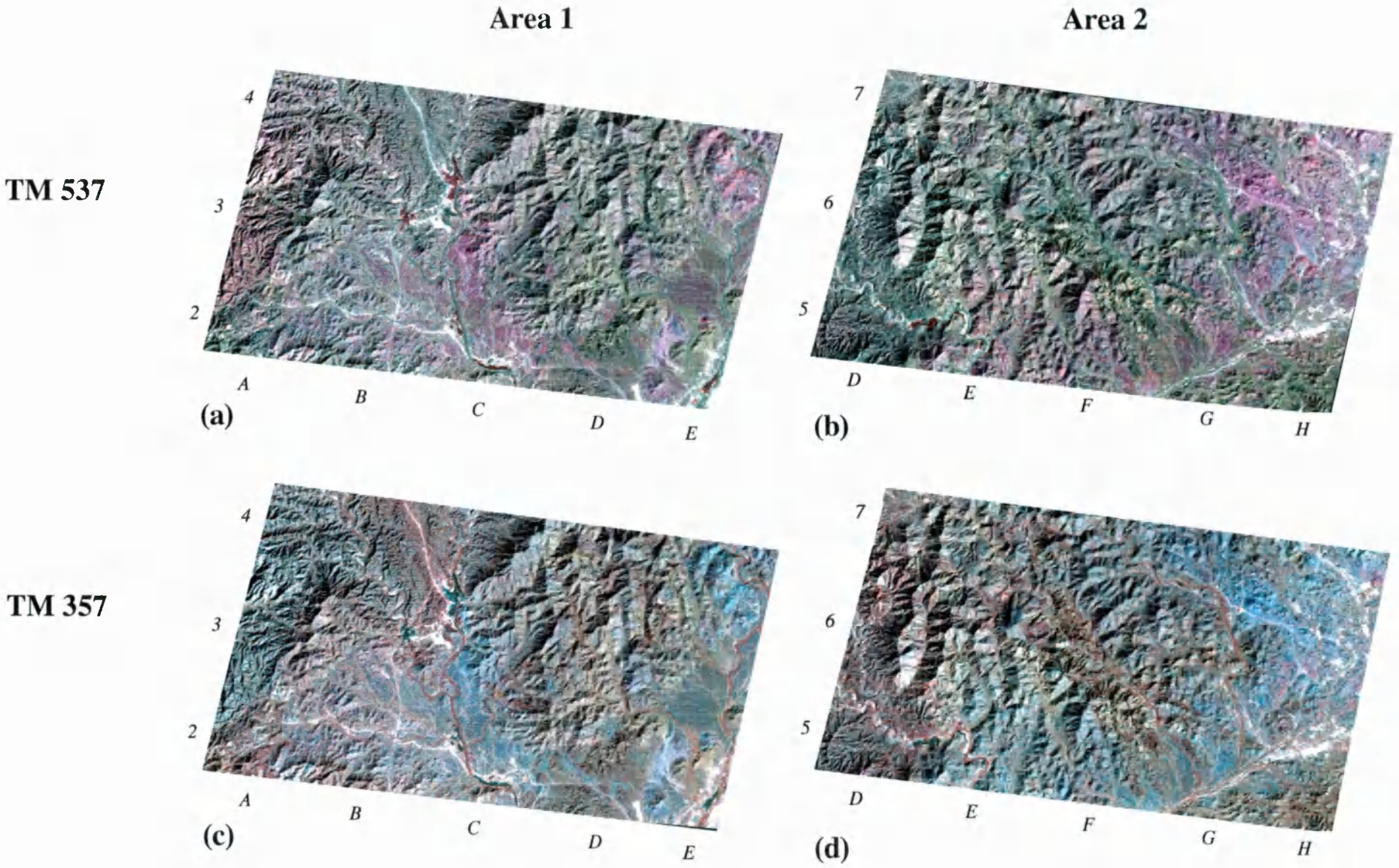

Plate 5.5 Two TM composites of the Maqsad study areas (see Figure 5.1 for location). Refer to text for a full description.

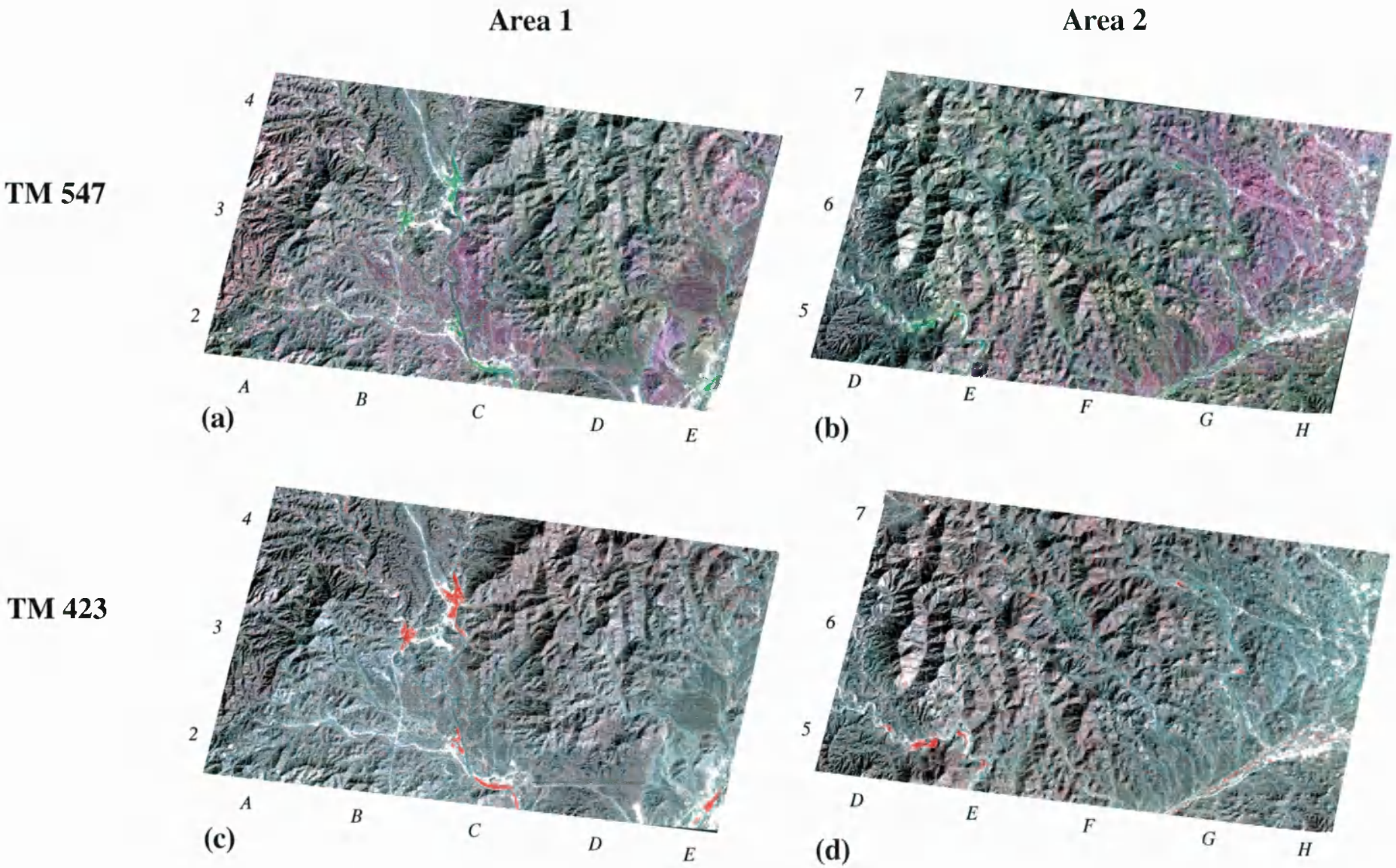

Plate 5.6 Two TM composites of the Maqsad study areas (see Figure 5.1 for location). Refer to text for a full description.

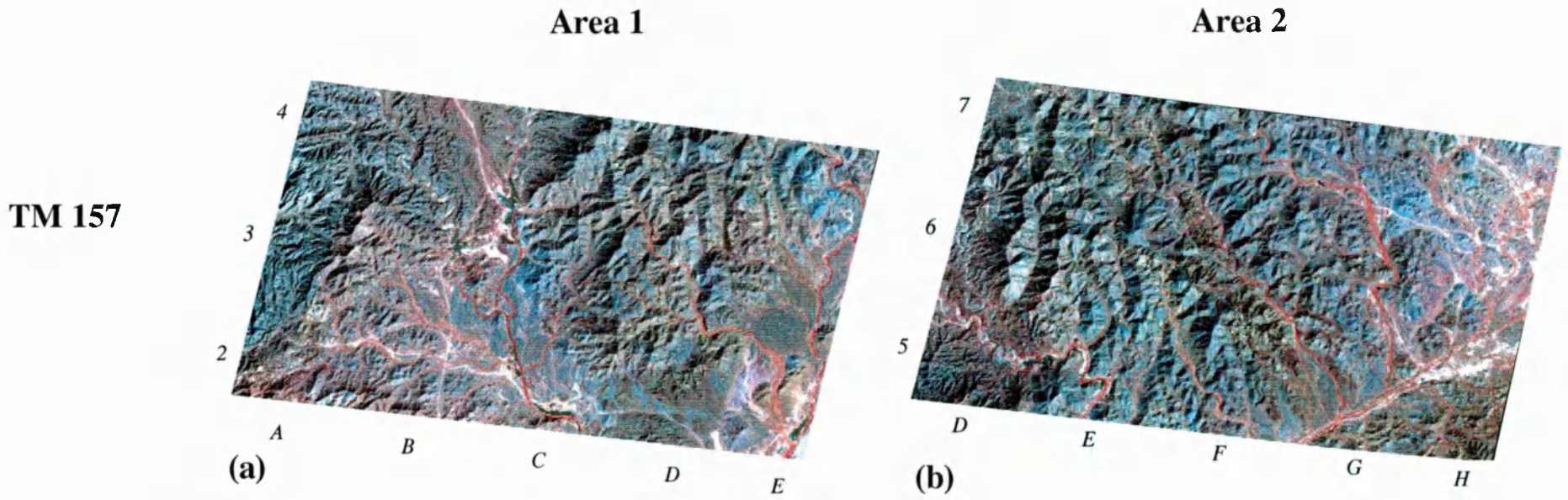

Plate 5.7 One TM composite of the Maqsad study areas (see Figure 5.1 for location). Refer to text for a full description.

However, all the tested band combinations discriminated additional lithologies as well, if not better, than the lithologies predicted by the statistical analysis. For example, TM 571 (Plate 5.4 (a) and (b)), predetermined as discriminating harzburgites, actually discriminated cumulate gabbro in a brighter yellow-green (E5) than the yellow-green of the harzburgites (A4), as well as clearly discriminating the sheeted dyke complex (E2) in green-blue. Table 5.2 lists the additional lithologies discriminated by each composite.

These variations in the discrimination of the anticipated lithologies are not completely unexpected as each band combination will obviously highlight more than just one lithology. This can be seen in Table 4.7 where a composite ranked number 1 for one lithology may also appear highly ranked (rank 2, 3, 4 or 5) for another lithology.

5.3.2 TM ratios

Analysis of the convolved lab spectra in section 4.5.2 highlighted four ratios potentially capable of distinguishing ten of the major ophiolite lithologies. Table 5.3 (and Plates 5.8 to 5.11) summarise the discrimination capabilities of these ratios. The TM 1/5 ratio (Plates 5.8 (a) and (b)) was determined as being able to distinguish six lithologies; harzburgite, dunite, wehrlite, cumulate gabbro, sheeted dykes and pillow lava. Analysis of this ratio image showed that it discriminated sheeted dykes (E2) quite poorly as areas of low intensities as opposed to high intensities. Dunite (D5) was also discriminated in low intensities but was difficult to identify due to the very small size of outcrop. The majority of gabbro (E6) lithologies were discriminated in medium to high intensities, although the highest intensities tend to represent gabbros with very dark weathered surfaces (E4). This ratio also picked out some variation in the harzbugites (A4 and B4), however discrimination of wehrlites (F6) was almost non-existent.

The TM 4/7 (Plate 5.8 (c) and (d)) ratio did not discriminate areas of trondhjemite as expected, however, areas of trondhjemite with gabbro (B3) were distinct. Discrimination of harzburgite on this ratio was not as good as expected as the ratio exhibited almost constant intensities across all areas of harzburgite (A3 to B4). Cumulate gabbro, especially dark weathered surfaces (E4) and dunite (D5) were discriminated by this ratio, as well as isotropic gabbro (H6). The TM 1/7 ratio (Plates 5.9 (a) and (b)) ratio highlighted isotropic gabbro (H6) in lower intensities than expected. Cumulate gabbro (F5) was highlighted in medium-high intensities.

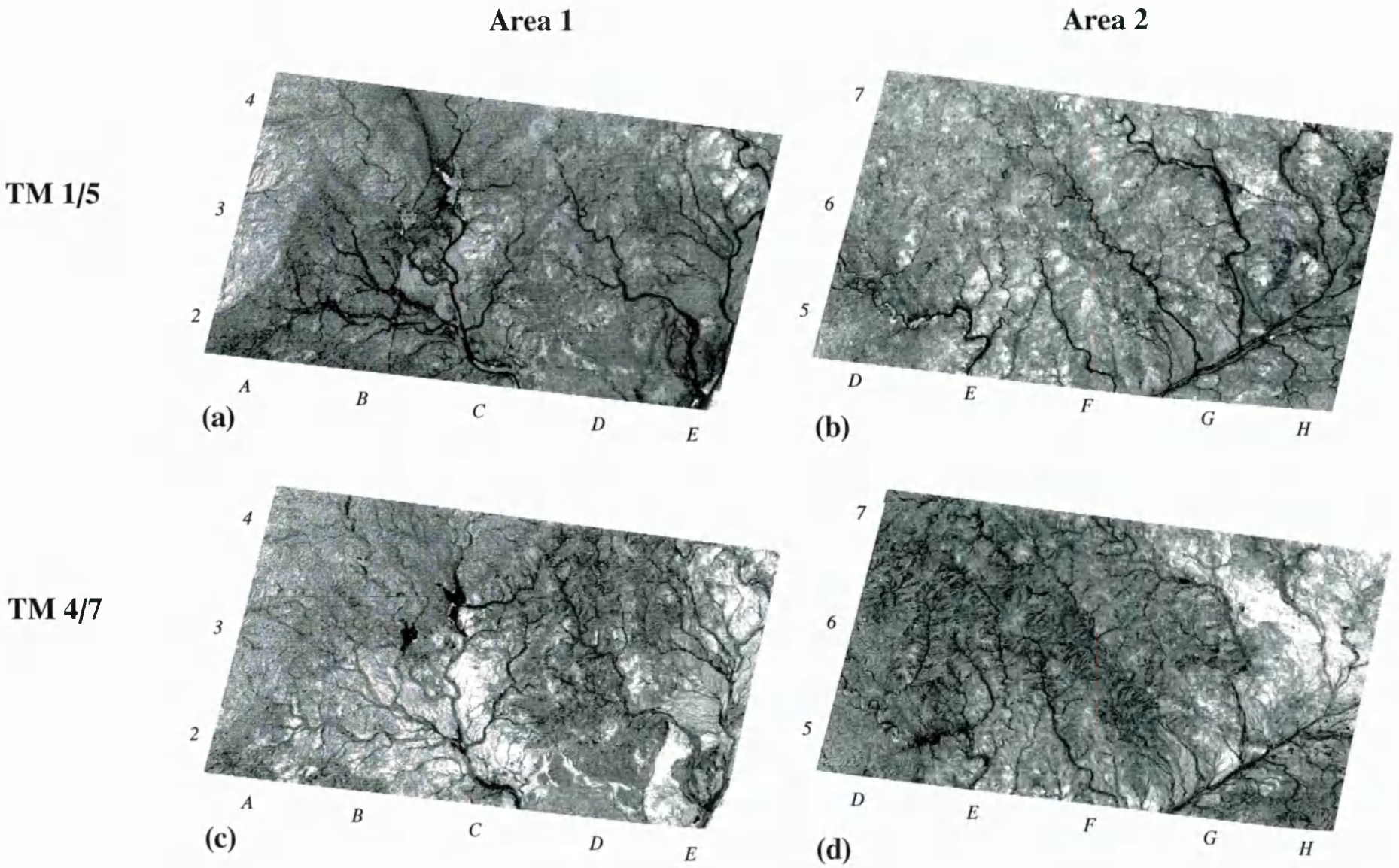

Plate 5.8 Two TM ratio images of the Maqsad study areas (see Figure 5.1 for location). Refer to text for a full description.

Ratio	Predicted discrimination	Predicted image intensities	Actual image intensities	Dis.
TM 1/5	harzburgite	low	medium-high	M
	dunite	medium	medium	M
	wehrlite	medium	low-medium	L
	cumulate gabbro	low -medium	high-medium	M-H
	sheeted dykes	very high	low	L
	pillow lava	low	low	L
TM 4/7	harzburgite	low-medium	medium	M
	trondhjemite	very low	medium	L
Additional discrimination	*cumulate gabbro*	-	*low-medium*	*M-H*
	dunite	-	*low*	*M*
	isotropic gabbro	-	*high*	*H*
TM 1/7	isotropic gabbro	very high	medium	L-M
Additional discrimination	*sheeted dykes*	-	*medium-high*	*M-H*
	cumulate gabbro	-	*medium-high*	*H*
	dunite	-	*low*	*L-M*
	wehrlite	-	*low-medium*	*L-M*
TM 5/7	pyroxenite	high	low	M-H
Additional discrimination	*wehrlite*	-	*low*	*M*
	cumulate gabbro	-	*medium-high*	*M-H*
	sheeted dykes	-	*high*	*H*
	gabbro + trond.	-	*medium-high*	*H*

Table 5.3 Comparison of predicted discrimination capabilities of predefined band ratios against actual discrimination. Dis. = Discrimination were L=Low, M=Medium and H=High. Additional lithologies discriminated are shown in italics.

This ratio also discriminated to varying degrees, sheeted dykes (E2), dunite (D5) and wehrlite (F6). The TM 5/7 (Plates 5.9 (c) and (d)) ratio showed quite good variation within the crustal sequence. Pyroxenite (B3) was discriminated well, although in low intensities not high. Cumulate gabbro (E6), especially dark weathered areas (E4) and wehrlite (F6) were also discriminated by this ratio. The sheeted dyke complex was discriminated in very high intensities, whilst trondhjemite with gabbro was discriminated in moderate to high intensities.

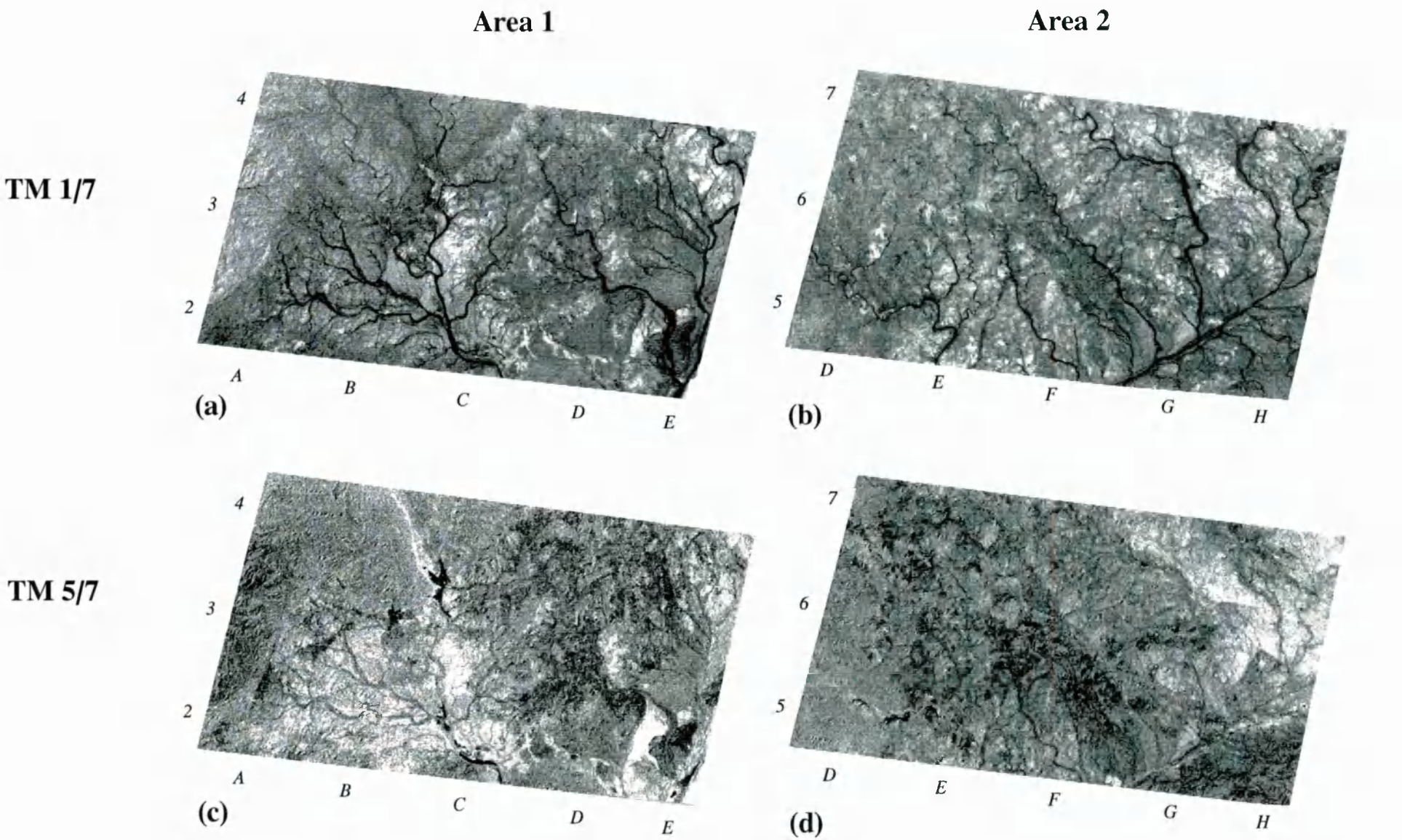

Plate 5.9 Two TM ratio images of the Maqsad study areas (see Figure 5.1 for location). Refer to text for a full description.

Two additional ratios which were not directly recommended by section 4.5.2 were also tested, TM 5/4 and TM 3/1 (Plates 5.10 (a), (b) and (c), (d)). These ratios are known to discriminate ferrous and iron oxides, respectively. As a result they show varying discrimination within the crustal section, in particular differences relating to the surface weathering of the gabbro lithologies. Highly weathered gabbro areas appear in low intensities on the TM 5/4 ratio suggesting ferrous absorptions associated with the dark varnished surface. Wadi terrace deposits which are also heavily weathered exhibit similar low intensitites on the TM 5/4 ratio. The TM 3/1 ratio shows that a couple of these areas also exhibit iron oxide absorptions. These ratios also discriminate sheeted dykes very well. The TM 3/1 ratio highlights sheeted dyke outcrops in high intensities, whilst the TM 5/4 ratio highlights sheeted dykes in low intensities.

To fully appreciate the variations seen on the grey-scale ratio images I have combined the best ratios into two colour composites. Combining greyscale ratio images into colour composites allows more subtle variations to be detected. An example of such a variation can be seen on Plate 5.11 (a), where gabbro with trondhjemite (B3) ranges in colour from cyan blue to pink-blue. These colour variations are related to varying percentages of trondhjemite and gabbro. This ratio composite (Plates 5.11 (a) and (b)) also highlights the sheeted dyke complex (E2) particularly well in light cyan-blue. Crustal gabbros (E6) are discriminated in various shades of red-pink-white, with the brightest areas representing the darkest weathered outcrops (E4). Areas of dyke rich gabbros (H7) are a cyan-green colour. This band combination also discriminates small dunite outcrops (D5) in a dark red-purple colour, however these are difficult to distinguish due to their small size. The second ratio composite (Plates 5.11 (c) and (d)) shows similar levels of lithological discrimination. Cumulate gabbros (E6) are red-magenta, whilst heavily weathered outcrops (E4) are dark blue to magenta. Cumulate gabbros with dykes (F7) are difficult to distinguish from cumulate gabbro because they have a similar dark red-magenta colour. Isotropic gabbros (H6) appear blue-green, similar in colour to terrace deposits. Outcrops of sheeted dyke complex (E2) are also discriminated in similar blue-green colours. Individual dunite outcrops are discriminated on this composite (D5) in red, however these can not be distinguishable from gabbro outcrops without field knowledge. Wehrlite (F6) discrimination is poor on this composite.

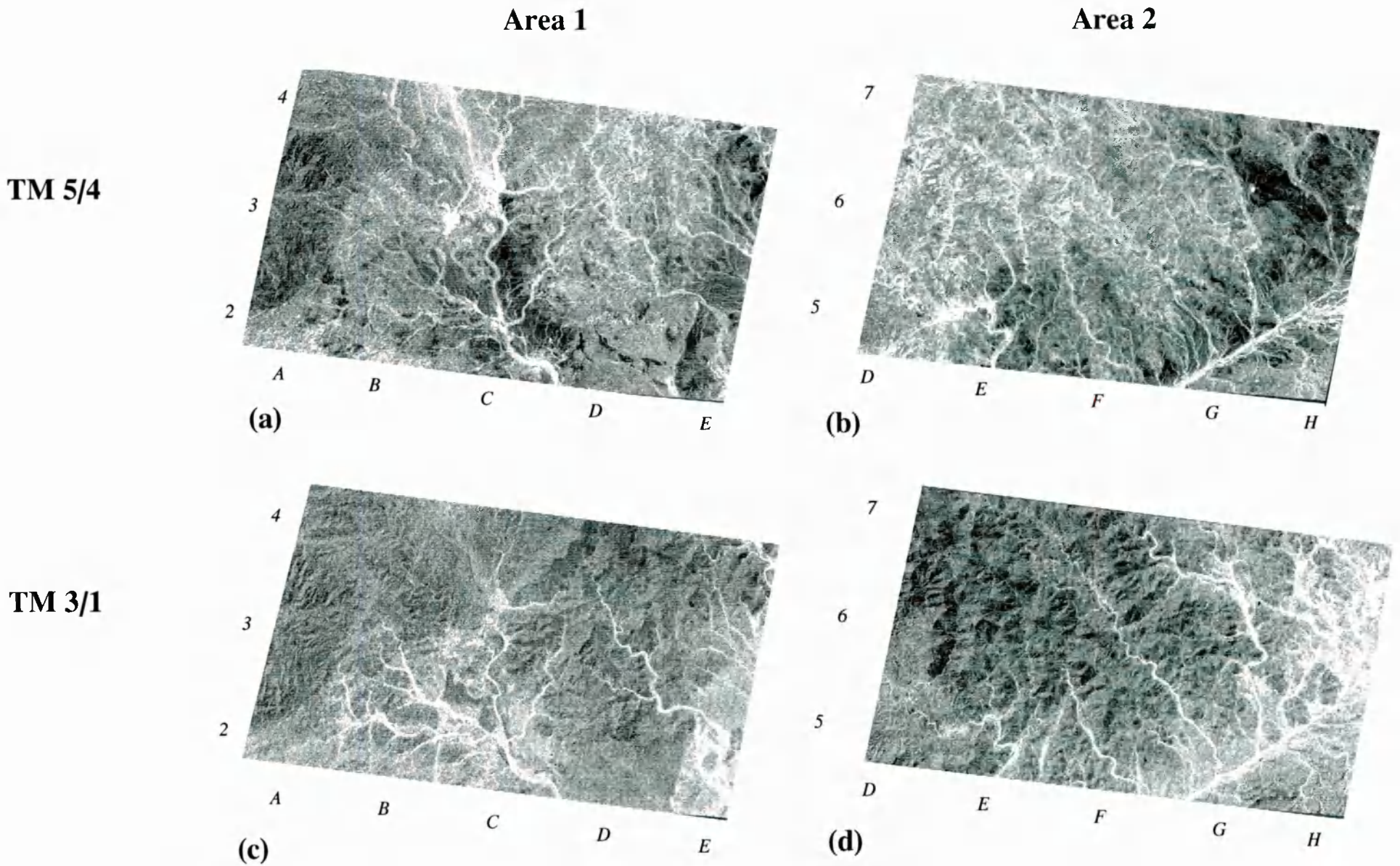

Plate 5.10 Two TM ratio images of the Maqsad study areas (see Figure 5.1 for location). Refer to text for a full description.

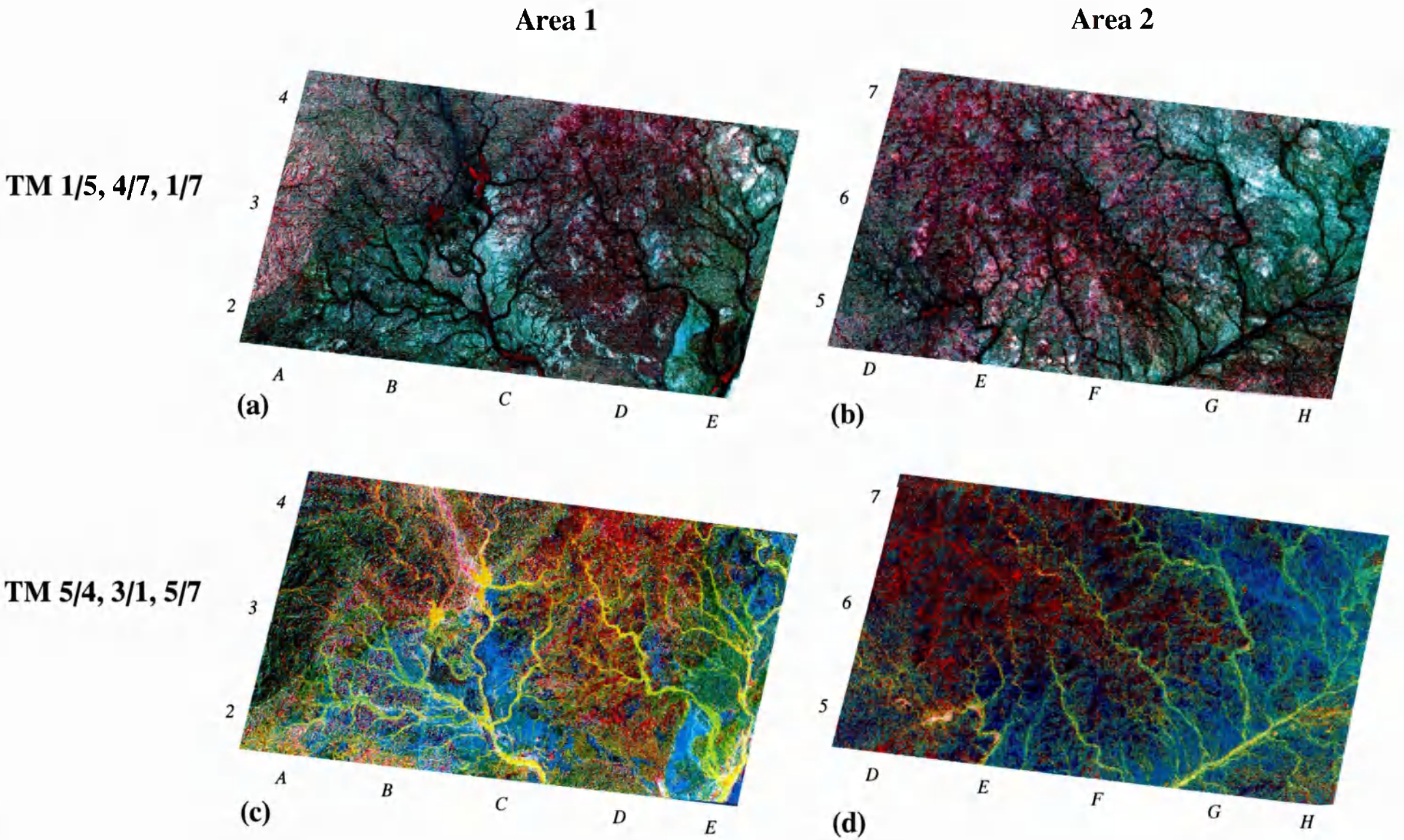

Plate 5.11 Two TM ratio colour composites of the Maqsad study areas (see Figure 5.1 for location). Refer to text for a full description.

Overall the ratios predicted from the analysis of lab based spectra did highlight the lithologies in question, although sometimes discrimination between lithologies was difficult on a single ratio image. This problem is made more difficult due to the lack of topographic information on a ratio image. The discrimination of additional lithologies on some ratio images is not surprising especially when the calculated ratio values in Figures 4.49 and 4.50 are examined, for most lithologies there is little difference between the ratio offering the maximum discrimination and the ratios defined in second and third place.

5.3.3 Specific TM processing

A review of the recent literature on lithological discrimination of ophiolite lithologies using remotely sensed data suggested five specific band combinations (listed in Table 4.10) possibly capable of discriminating ophiolite lithologies. The first was a TM equivalent to an early MSS composite image described by Harding and Bird (1984). Analysis of the derived TM composite (TM 2/4, 3/2 and PC 1) showed that this band combination was extremely poor at discriminating all lithologies. The resulting composite showed mainly noise structures and is not illustrated here.

A band combination recommended by a number of authors is that of a decorrelation stretched composite of TM 754. This combination of TM bands and processing produces a very informative image (Plate 5.12 (a) and (b)) which clearly discriminates a number of ophiolite lithologies. A full description of this composite will be given later in section 5.5.1. A band combination recommended by Pontual (1990) is that of the pseudo-ratio composite of TM 5/7, 5/4 and 3/2 (Plate 5.12 (c) and (d)). Like the ratio images described earlier this image is quite difficult to interpret because of the lack of topographic information, it does however produce a good discriminative image. Discrimination within the mantle (A4) tends to be very poor, compared with that of crustal lithologies. The composite image discriminates gabbros very clearly in various colours from red (dark weathered cumulate gabbros, E4) to light green (cumulate gabbro, E6). Cumulate peridotite (F6) in dark cyan-green is easy to distinguish from cumulate gabbro, but is not easy to distinguish from wehrlite (F6). Dunite rich outcrops (D5) have a distinct bright yellow-green colour. The sheeted dyke complex (E2) exhibits a bright magenta-red colour, identical to both terrace deposits and areas of isotropic gabbro with dykes (G7).

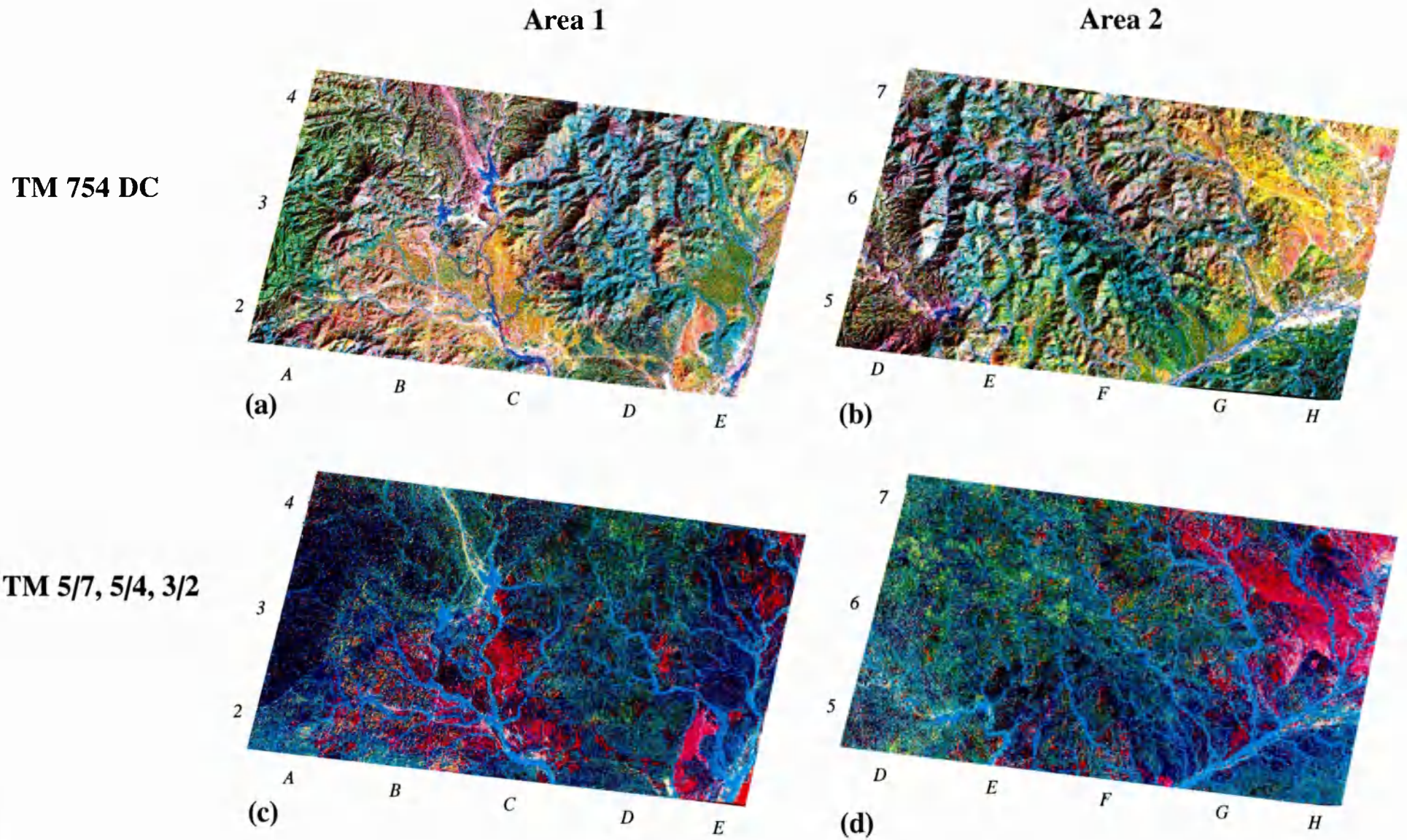

Plate 5.12 Two TM colour composites of the Maqsad study areas (see Figure 5.1 for location). Refer to text for a full description.

A TM 5/7, 5/1 and (3+5)/4 composite (Plate 5.13 (a) and (b)) described by Sultan *et al.*, (1986) has been demonstrated to highlight serpentinites. Tests of this band combination in the Maqsad area produced a reasonably good image, although the lack of serpentinite outcrops made it difficult to test Sultan's discrimination claims. However, this composite does distinguish areas of cumulate peridotite (F6) and wehrlite (F6) reasonably well in dark blue-green colours, although discrimination between these two lithologies is almost impossible. The discrimination of these two lithologies may be associated with the high levels of serpentine often found in wehrlite rich outcrops. Areas devoid of serpentine, for example cumulate gabbro outcrops (F5) appear magenta-red. Tests of the second Sultan *et al.*, (1986) composite, TM 5/7, 5/1 and (5x3)/4 (Plates 5.13 (c) and (d)), produced an image with very similar discrimination capabilities. Like the first composite this image discriminated cumulate peridotite and wehrlite in dark blue-green (F6) and cumulate gabbro in red-magenta (F5). Both of these composites also showed good discrimination between spectrally brighter crustal lithologies, for example, sheeted dyke complex (orange, E2), isotropic gabbro (yellow-orange-red, H6) and gabbro with trondhjemite (orange-pink, B3). Discrimination on the second composite was marginally better than that on the first.

5.3.4 General TM processing

General image processing techniques such as those described in section 4.5.4 (PCA, decorrelation stretching, tasseled cap and hue, saturation and intensity transforms) were also applied to TM imagery of the Maqsad region. Principal component analysis of the TM data produced very good results with a number of lithologies being highlighted in different PCs. Table 5.4 summarises the spectral characteristics of the main ophiolite lithologies when transformed into principal component images.

PC 1 did not really distinguish any one lithology, but represented the albedo information from all of the bands (as expected). PC 2 did show some differential discrimination with cumulate gabbro (medium intensities), sheeted dykes (high intensities) and dunite (low intensities) being distinguished. PC 3 highlighted both sheeted dykes and trondhjemite as very high intensities, although discrimination between these two lithologies was not possible. PC 4 mainly discriminated the sheeted dyke complex (low intensities). Areas of harzburgite and trondhjemite were highlighted in slightly lower intensities, otherwise there was little discrimination. PC 5 clearly distinguished the sheeted dyke complex (high intensities) as well as

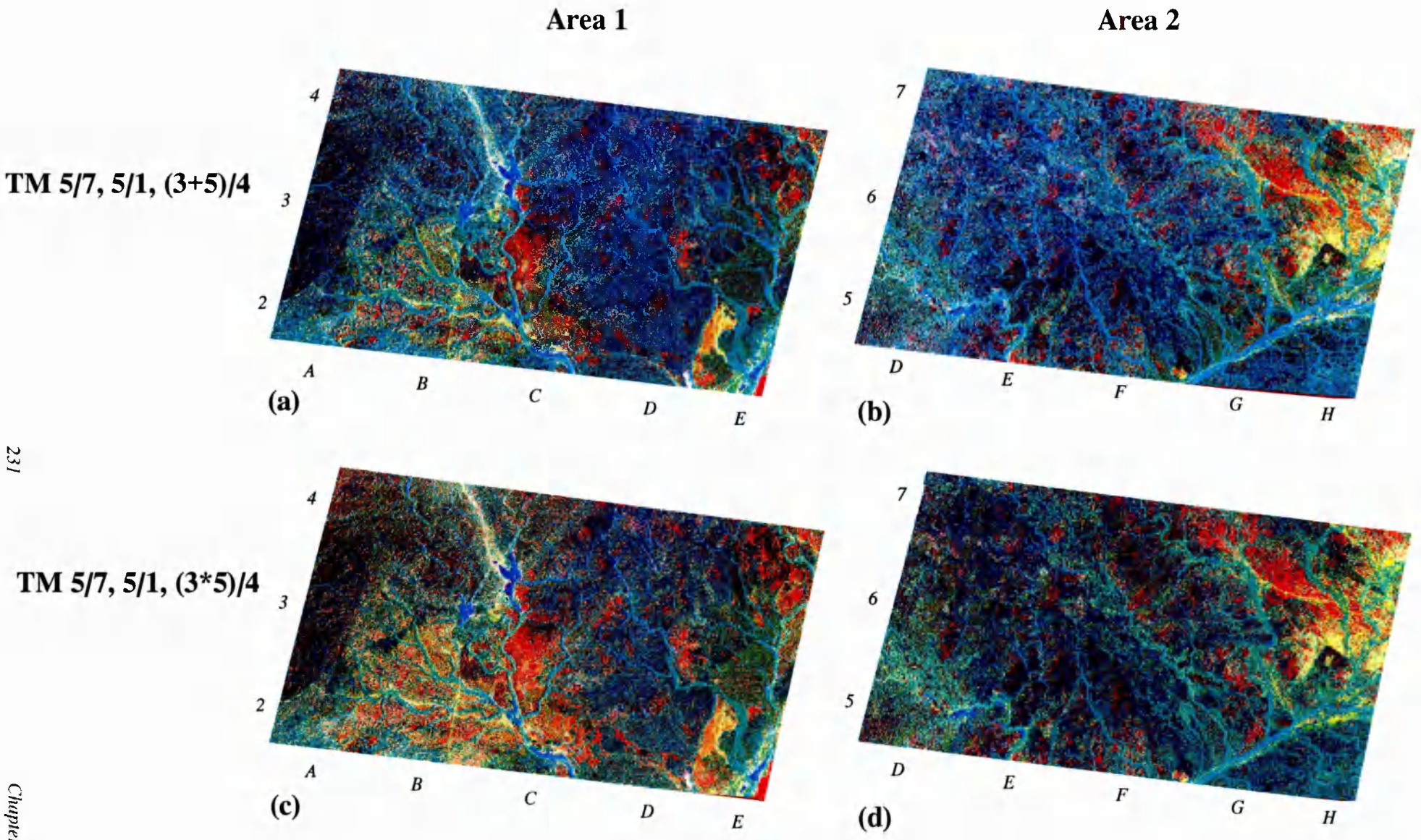

Plate 5.13 Two TM colour composites of the Maqsad study areas (see Figure 5.1 for location). Refer to text for a full description.

Lithology	PC 1		PC 2		PC 3		PC 4		PC 5		PC 6	
	Intensity	Dis.	Intensity	Dis.	Intensity	Dis.	Intensity	Dis.	Intensity	Dis.	Intensity	Dis.
Pillow lavas	medium	L	low-medium	M	medium	M	low	L-M	-	ND	-	ND
Sheeted dyke	medium-high	M-H	high	H	very high	H	low	H	high	H	-	ND
Isotropic gabbro	medium	L-M	medium	M-H	medium-high	L	low-medium	M	-	ND	-	ND
Cumulate gabbro	medium-high	M	medium	H	medium-dark	L	medium-dark	L	-	ND	-	ND
Cumulate peridotite	medium	L	low-medium	L-M	medium	L	medium-dark	M	low-medium	M	-	ND
Harzburgite	medium	M	medium-high	M-H	medium	L-M	low (variable)	M	medium	L	-	ND
Dunite	high	M	very low	H	-	ND	low	L-M	-	ND	-	ND
Wehrlite	low	L	medium	L	-	ND	medium	L	medium	L	-	ND
Trondhjemite	high	M	medium	L-M	very high	H	low	M-H	high	H	-	ND
Isotropic gabbro + dykes	medium	M	medium-high	M	medium-high	M	medium-high	M	-	ND	-	ND
Cumulate gabbro + dykes	medium	M	medium	M-H	medium	M	medium	M	-	ND	-	ND
Cumulate gabbro + trondhjemite	Medium	M	medium	L-M	medium	M	medium-high	M	-	ND	-	ND
Pyroxenite	Medium	L-M	medium-high	L-M	low-medium	L-M	high	M-H	low	L	-	ND

Table 5.4 Description of lithological discrimination of TM six-band PCA. Pixel intensity values described as low (approx. <80 DN), medium(approx. 81-160) and high (approx. >161). Dis.=discrimination level, L=Low, M=medium and H=High, ND=Not Distinct. See text for a full description.

trondhjemite (high intensities) and cumulate peridotite (low intensities). PC 6 showed noise but no lithological information. Overall individual PC images clearly distinguished outcrops of sheeted dykes, trondhjemite and dunite. Harzburgite, cumulate peridotite and wehrlite were distinguished to a lesser degree. The majority of the discrimination information was contained within PCs 2, 3 and 4, Plates 5.14 (a) and (b) show FCC of these three channels. When these three PCs are combined into a composite image they produce a very colourful image which is quite informative, although not all lithologies are discriminated by this band combination. Cumulate gabbro outcrops (F5) are reasonably clear in yellow-green colours, although some areas of harzburgite (A3) appear in quite similar colours. These two lithologies can be distinguished by outcrop texture and locational context. Cumulate peridotites (F6) are distinct from cumulate gabbros which are in a darker green, whilst wehrlite (F6) units are distinguished in a darker green-blue. Dunite rich areas appear a very deep magenta-red (D5). Overall discrimination is quite good on this image although some colour variations are difficult to explain.

The Tasseled Cap (TC) transform (described in section 4.5.4) produced some good results. The transformation was performed using the TM coefficients defined by Crist and Cicone (1984). Discrimination on individual TCs appeared to be poor, but combining one secondary (TC 5) and two primary components (TC 3 and TC 2) into a false colour composite (Plate 5.14 (c) and (d)) produced a useful image. These three bands were chosen because they produced a composite capable of discriminating a number of lithologies. This band combination is particularly good at discriminating cumulate peridotite (dark cyan-green, F6) from wehrlite (dark magenta-purple, F6), allowing numerous small wehrlite bodies to be distinguished. This composite is also very good at discriminating dunite rich (D5) areas in red-pink.

The other two techniques described in section 4.5.4 (decorrelation stretching and ISH) are best applied to a pre-determined colour composite. These techniques are not used to determine useful band combinations, but to improve the interpretation of a colour composite. They do this by enhancing the colour contrast between lithologies, e.g., the TM 754 decorrelation stretched image described earlier. Comparative tests of decorrelation stretching and ISH transforms showed that the decorrelation stretched image was usually the better. ISH images sometimes appeared too colourful due to the saturation component being over stretched. ISH transformations can also be used to integrate different types of data into one composite (Haydn *et al.*, 1982), see section 5.5.7.

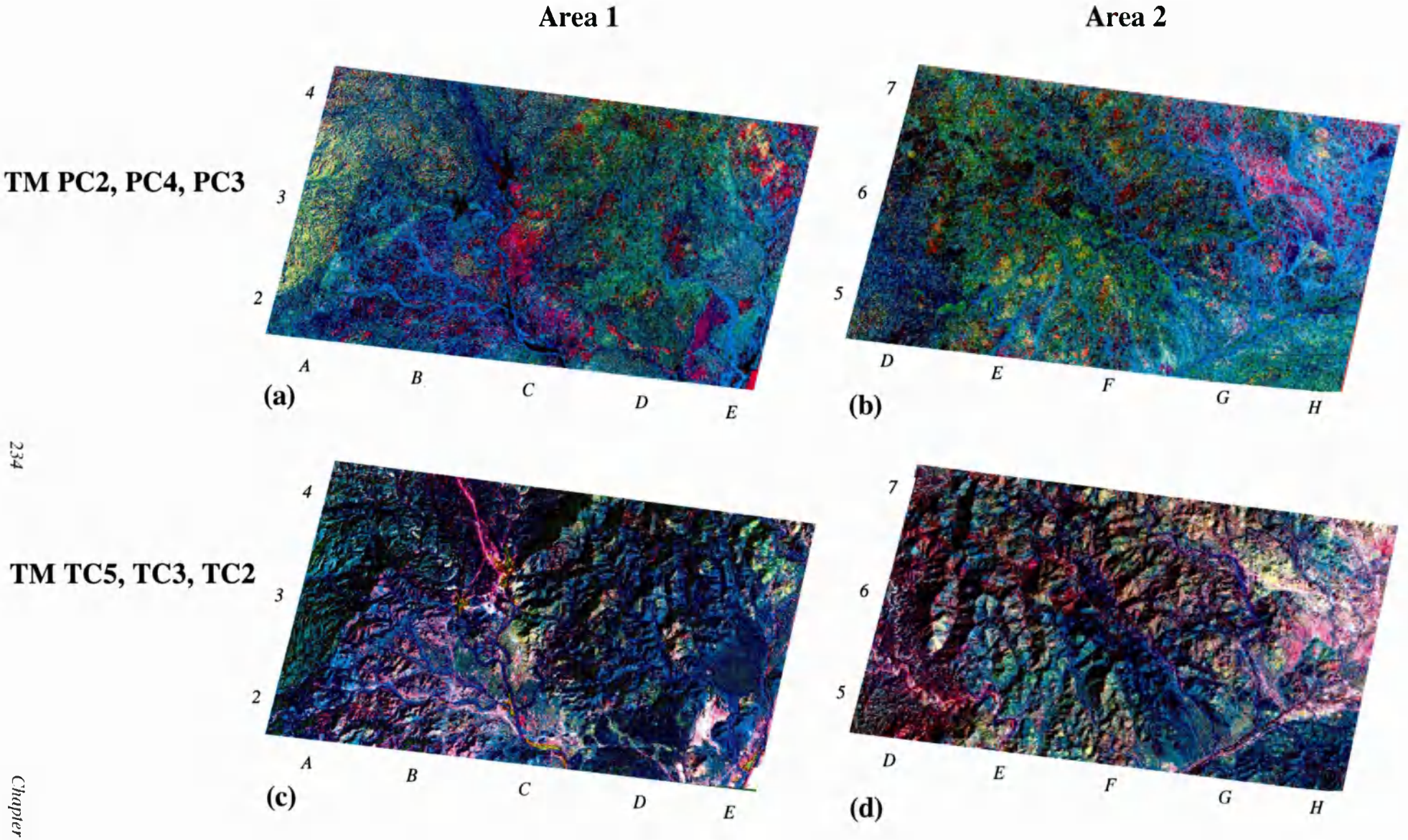

Plate 5.14 Two TM colour composites of the Maqsad study areas (see Figure 5.1 for location). Refer to text for a full description.

5.3.5 TM spectral indices

In Section 4.5.5 spectral indices were calculated for TM data in order to discriminate clay, goethite, hematite and vegetation (Table 4.9). Tests of these SI values applied to TM data produced some quite favourable results. Combining the clay, vegetation and goethite index images in an RGB composite produced a fairly meaningful colour composite. Vegetation was particularly clear as it appeared a very bright green, whilst wadi bottoms and terraces appeared various shades of red, indicating the distribution of clay minerals associated with weathering. However, gabbro outcrops had quite a mixed response ranging from red-pink (weathered clay ?) to blue-green (goethite ?). Some of the gabbro colour changes appeared to be related to illumination variations as opposed to mineralogical variations.

Indices for six mantle and six crustal lithologies were calculated in chapter 4 using resampled lab spectra of the major ophiolite lithologies. Applying these indices to TM data produced extremely poor results. Examples of wehrlite, isotropic gabbro and sheeted dykes spectral indices are shown in Plates 5.15 (a), (b), (c), (d) and Plates 5.16 (a), (b) respectively. All these images are very similar, exhibiting only minor spectral variations between them. Combining these three images into a colour composite (Plates 5.16 (a) and (b)) produces an image with very little colour variation, proving the similarity of the three input channels. Discrimination on this colour composite should show wehrlite in red, isotropic gabbro in green and sheeted dykes in blue. In reality wehrlite is not discriminated at all, isotropic gabbro as well as cumulate gabbro appear in red-brown tones and the sheeted dyke complex appears orange-red. In addition cumulate peridotites and dunite rich areas of mantle appear in pale blue. The only specified lithology distinguished is that of the sheeted dyke complex.

This failure of the SI values to discriminate the individual lithologies is not completely unexpected as the individual weighting values calculated for each TM channel are extremely similar for all lithologies. This is particularly apparent when viewing Figures 4.52 (b) and 4.53 (b). The similarity of these values is a direct result of the spectral and mineralogical similarities of the ophiolite lithologies. These similarities result in the Spectral Index transform calculating unit vectors which are not distinct from the baseline vector, i.e., one vector enhances all similar lithologies as opposed to individual specific lithologies.

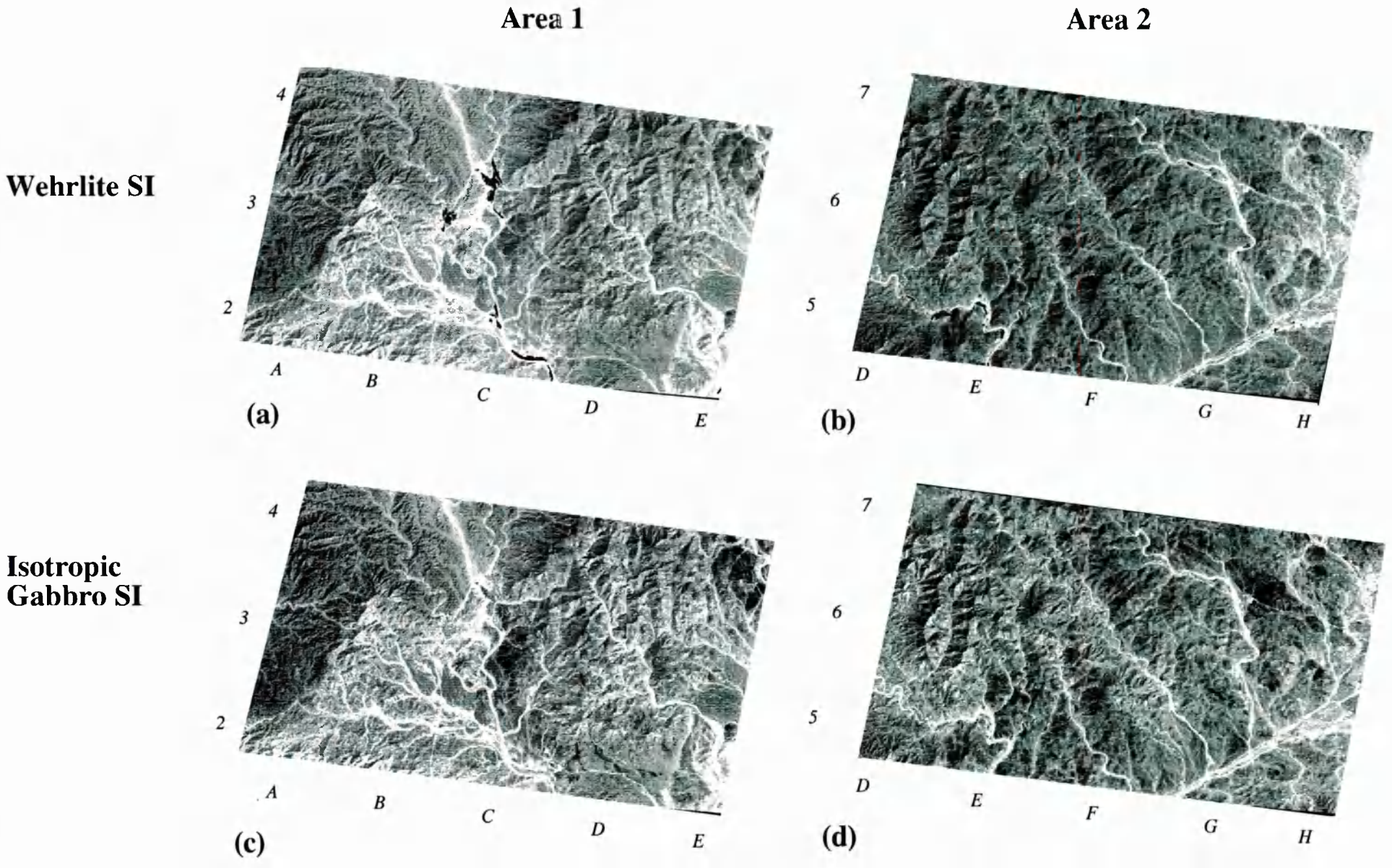

Plate 5.15 TM spectral indices of the Maqsad study areas (see Figure 5.1 for location). Refer to text for a full description.

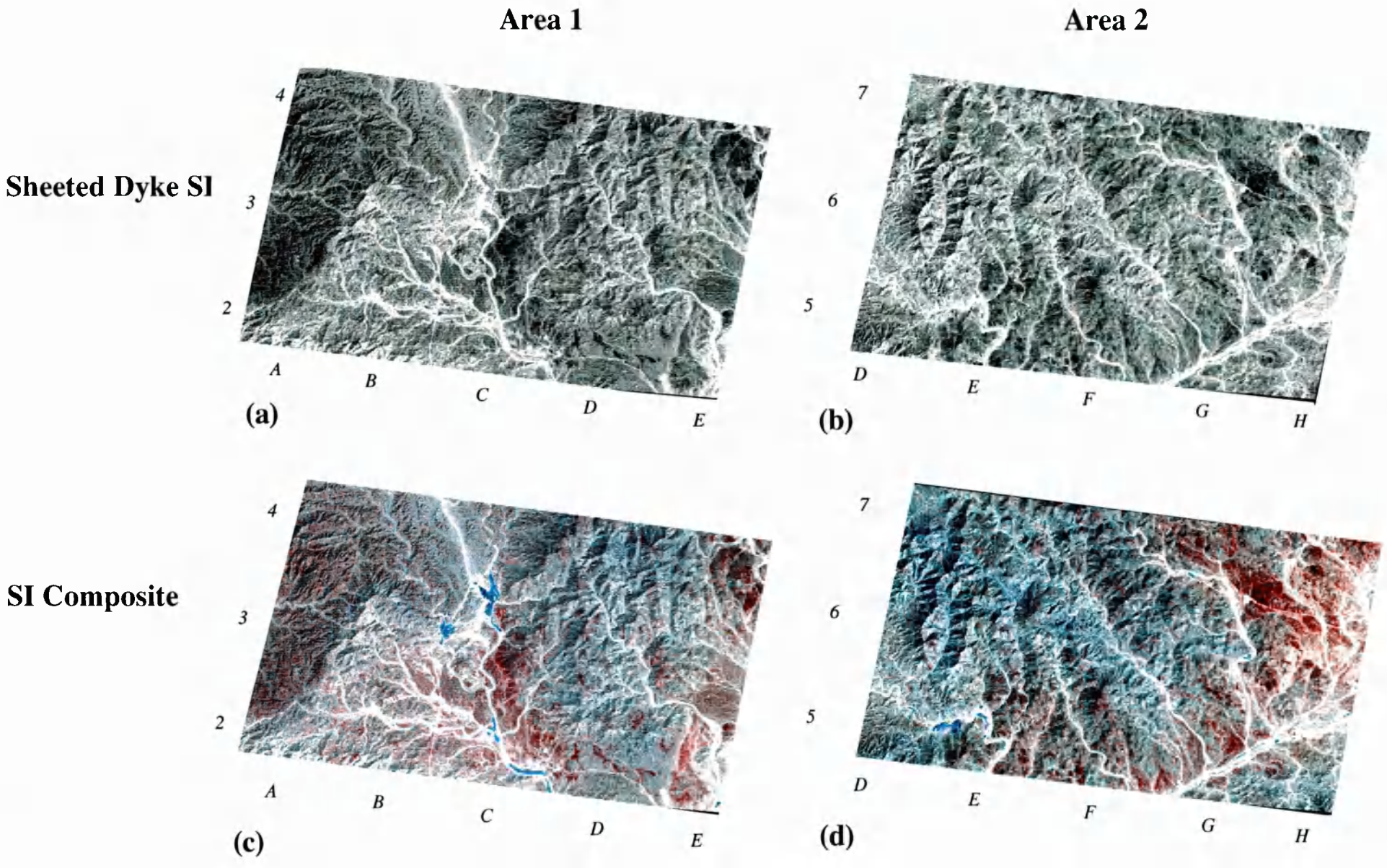

Plate 5.16 TM spectral indices of the Maqsad study areas (see Figure 5.1 for location). Refer to text for a full description.

5.3.6 TM image processing summary

A vast range of image processing techniques and band combinations has been tested in this chapter. These band combinations have been primarily determined from the analysis of resampled lab spectra. The level of discrimination of ophiolite lithologies on the resultant composites varies greatly. Some composites are only capable of distinguishing one or two lithologies whilst others distinguish the vast majority. One such composite which discriminates most lithologies is the TM 754 decorrelation stretched image, as used by numerous authors previously. Tests in the Maqsad region have confirmed the potential of this composite to discriminate the majority of the lithologies. As a result this composite will be used as the base image from which the geological interpretation will be performed (section 5.5.4) However this does not mean that the other composites and image processing techniques will be ignored, instead those techniques which are particularly good at identifying specific lithologies will be used as an aid to image interpretation, for example, TM 543 (trondhjemite), TM 4/7 (cumulate gabbro and gabbro with trondhjemite), TM 1/7 (dunite), TM 5/7 (pyroxenite) as well PC and TC composites.

5.4 OPS processing

5.4.1 OPS composites

Section 4.5.1 discussed various techniques to determine which of the 35 possible OPS band composites, including OPS 6 and OPS 7, would offer the highest levels of lithological discrimination. Five different composites were determined from spectral interpretation, correlation coefficients, image statistics and spectral statistics (Table 4.11). The discrimination potentials of these five composites are summarised in Table 5.5 and Plates 5.17 to 5.19. Each of the OPS band combinations will be tested on two subscenes of data equivalent to the test areas defined in Figure 5.1 and Figure 5.2. All OPS data used in this section have been cleaned using FFT techniques (as described in chapter 3) and have had an atmospheric correction applied (Appendix 1).

Lithological discrimination on the composites described in Table 5.5 varied greatly, both due to the spectral characteristics of the channels used to form the composite and due to the quality of those channels. The first composite OPS 532 (Plates 5.17 (a) and (b)) was chosen by spectral analysis of the lab spectra. It was anticipated that this composite image would discriminate both mantle and crustal lithologies (see Table

Lithology	OPS 532		OPS 861 (816)		OPS 651 (516)		OPS 652 (526)		OPS 851 (581)	
	Colour	Dis.	Colour	Dis.	Colour	Dis.	Colour	Dis.	Colour	Dis.
Pillow lavas	orange-red	L	blue-red	L	red-purple	L	red-purple	L	pink-purple	L
Sheeted dyke	blue-lilac	M	purple-blue	M-H	blue-purple	M-H	blue-purple	M	purple-blue	H
Isotropic gabbro	orange-red-pink	M	yellow-brown	M	orange-yellow-green	M	yellow-orange	M	orange-brown	M
Cumulate gabbro	orange-brown-beige	M	yellow-brown (-red)	M-H	yellow-green	M-H	yellow-brown	M-H	yellow-orange-brown	M-H
Cumulate peridotite	red-brown	M	green-yellow	L-M	cyan-yellow	M	cyan-green	M	cyan-green	M-H
Harzburgite	dark red-magenta	H	green (variable) red-purple	M-H	green-brown red-purple	M-H	green-brown dark purple-red	M	green (variable) purple-blue	M
Dunite	bright cyan -blue	H	blue-purple	L-M	blue-purple	M-H	bright blue purple	M	bright blue	H
Wehrlite	dark blue-black	M	dark blue-black	M-H	dark purple	H	dark purple	H	dark green-brown	M
Trondhjemite	pink-white	M-H	pink	M-H	pale blue	L	pink-blue	L	purple-blue	L
Isotropic gabbro + dykes	red-brown	L-M	red-brown	L-M	pink-yellow-green	L-M	red-brown	L-M	pink-brown	M
Cumulate gabbro + dykes	purple-brown	L-M	purple-brown	L-M	purple-brown-yellow	L	brown-green	M	(yellow) red-pink	M
Cumulate gabbro + trondhjemite	orange-pink-lilac	M	pink-yellow-beige	L	yellow-brown	L	grey-blue	L-M	yellow-green	L-M
Pyroxenite	blue-red	L	dull green	L	mid green	M	grey-green	L	brown	L

Table 5.5 Colours of the main lithologies on OPS composites as defined in Table 4.12. Dis.=discrimination were L=Low, M=Medium and H=High. Band combinations in brackets denotes original composite order prior to band re-ordering. See text for full description.

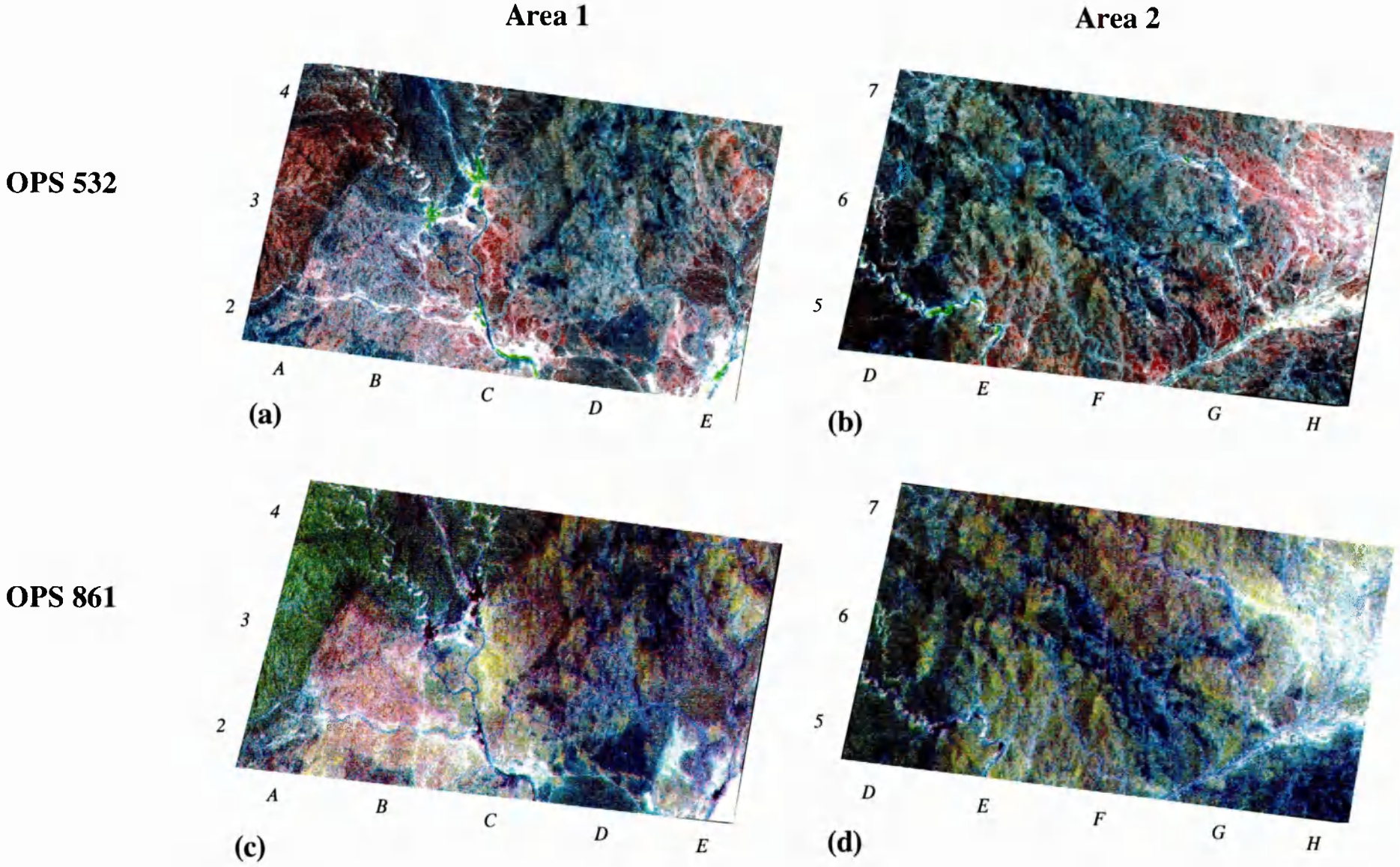

Plate 5.17 Two OPS composites of the Maqsad study areas (see Figure 5.1 for location). Refer to text for a full description.

4.11). Actual discrimination includes; dunite (bright cyan-blue, D5), harzburgite (red-magenta, D5) and trondhjemite (pink-white, B2). Discrimination of gabbro lithologies was fairly good, with cumulate gabbro in brown-red (E5), isotropic gabbro red-pink (H7) and gabbro with dykes red-purple-brown (G7). This band combination also discriminated wehrlite (dark blue, F6) and sheeted dykes (pink, E2). In terms of image quality this composite is fairly good as both OPS 5 and OPS 2 are of a high quality, it is the lower quality OPS 3 which gives the composite a quantised look. The second composite OPS 816 determined by correlation coefficients was best re-ordered as OPS 861 (Plates 5.17 (c) and (d)). This composite shows reasonable discrimination of all lithologies. Gabbro and harzburgite lithologies are more distinct than on the OPS 532 composite. The harzburgite lithologies show good colour variation ranging from bright green (A3) to dull green (B4), changing to dark blue-purple (C4) towards the Moho (upper mantle). A number of other lithologies are also discriminated very well, including, wehrlite (dark blue, F6), trondhjemite (pink, B2), sheeted dykes (pale blue, E2) and cumulate gabbro (yellow-brown, E5). Image quality is reasonable despite OPS 6 being quite severely degraded by noise and OPS 8 and OPS 1 being slightly degraded.

OPS 516 and 526 were both determined by image statistics, these composites were best reordered to OPS 651 (Plates 5.18 (a) and (b)) and OPS 652 (Plates 5.18 (c) and (d)). These two composites are very similar, the only major difference being that OPS 652 discriminates dunite (blue-purple, D5) slightly more clearly than OPS 651, due to the higher response of dunite in OPS 2. Harzburgites range from bright to dull green (A3 to A4), through to dark cyan-green (C4). Wehrlite (dark blue, F6) is very clearly distinguished on both composites, although the associated cumulate peridotite (F6) is not very clear. Both images show reasonable variation in the gabbros allowing cumulate gabbro (yellow-brown-green, E5) to be distinguished from isotropic (yellow-orange, H7). OPS 651 exhibits slightly lower image quality due to the inclusion of two spectrally poor channels, OPS 6 and OPS 1. OPS 518, when re-ordered as OPS 851 (Plates 5.19 (a) and (b)) formed a reasonable composite, especially for discriminating dunite (dark blue, D5), sheeted dykes (pale blue, E2) and cumulate gabbro (yellow-orange, E5) and cumulate peridotite (cyan-green, F6). Discrimination of the other lithologies is moderate, except for trondhjemite (pink-blue, B2) and pyroxenite (green-brown, B3) which are both low. Image quality is reasonable as OPS 5 is of a high quality and OPS 8 and OPS 1 are of an intermediate quality.

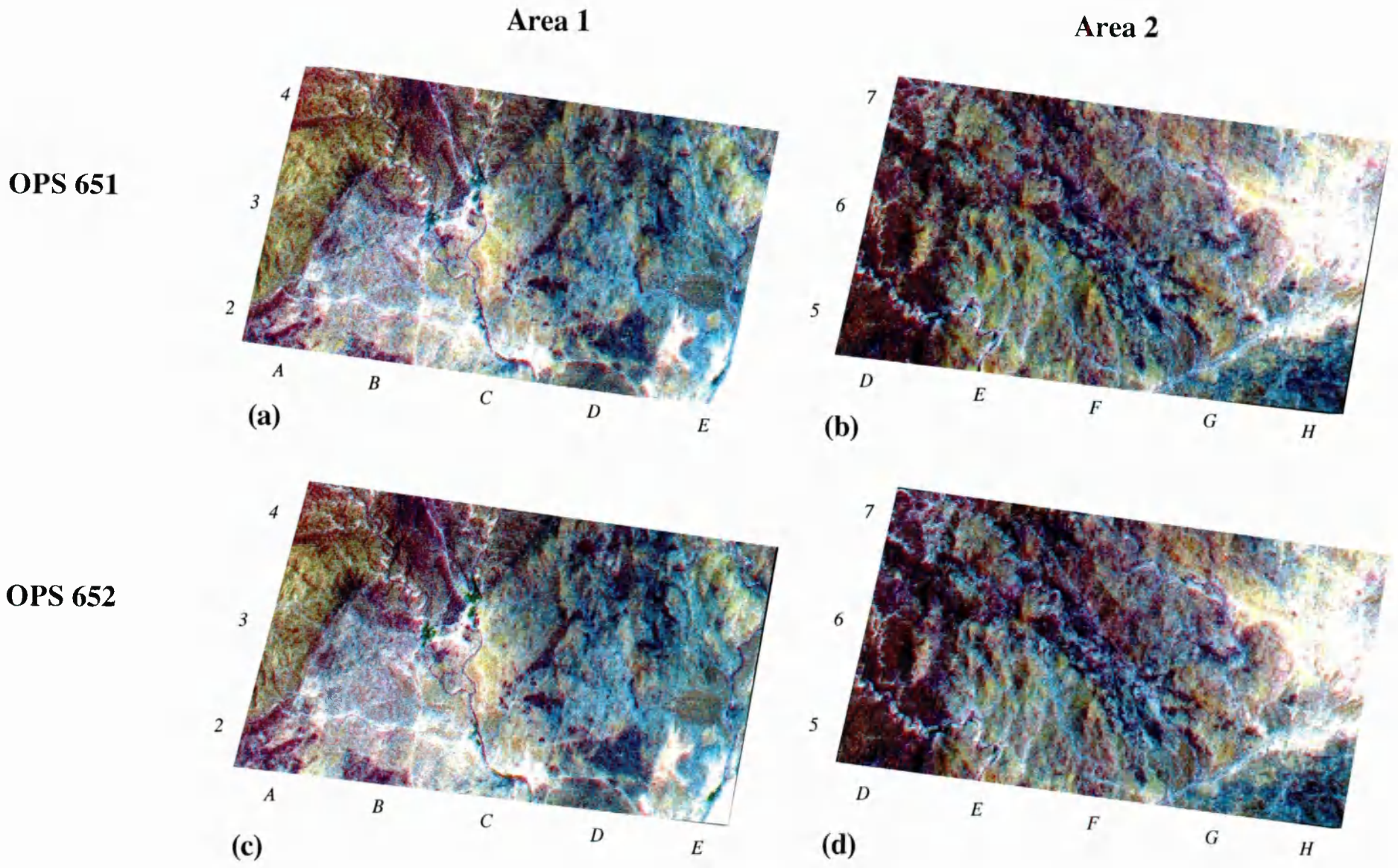

Plate 5.18 Two OPS composites of the Maqsad study areas (see Figure 5.1 for location). Refer to text for a full description.

OPS 851

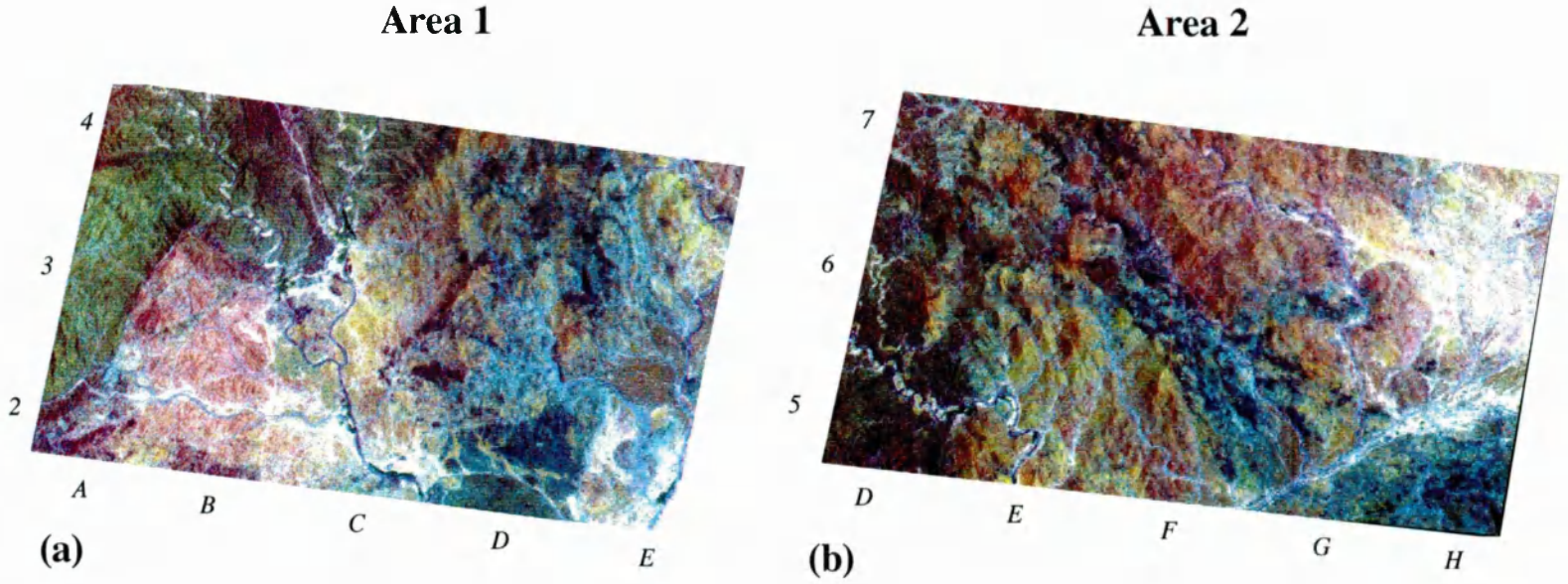

Plate 5.19 OPS composite of the Maqsad study areas (see Figure 5.1 for location). Refer to text for a full description.

An additional five three-band composites were identified in section 4.5.2 as potentially discriminating one lithology more than the others. Table 5.6 (and Plates 5.20 to 5.22) compare the expected discrimination of each of the highlighted lithologies against the actual discrimination of each composite. All band orders have been left as defined by the statistical techniques. Like the TM data the statistical approach of selecting band composites had mixed results. Composites of OPS 528, 681 and 127 (Plates 5.20 (c) and (d), Plates 5.22 (a), (b), (c) and (d) respectively) discriminated the predetermined lithologies (dunite (D5), sheeted dykes (E2) and trondhjemite (B2)) quite well. The other composites OPS 571, 518 and 538 (Plates 5.20 (a) and (b), Plates 5.21 (a), (b), (c) and (d)) discriminated the predetermined lithologies (harzburgite (A3), wehrlite (F6) and pyroxenite (B3)) quite poorly. However all the tested band composites discriminated additional lithologies, at least as well as the lithologies predicted by the statistical analysis. For example, OPS 571 (Plates 5.20 (a) and (b)) actually discriminated wehrlite (blue-purple, F6) and cumulate peridotite (pink-red, F6) as well as the predicted harzburgite (green-brown (A3)). Like the TM data these variations between predicted and actual discrimination are due to the statistical rankings of the additional lithologies being very close to the lithology with the maximum ranking (see Table 4.7).

Composite	Expected discrimination	Colour on composite	Dis.	Highest discrimination	Colour on composite	Dis.
OPS 571	harzburgite	green-brown	M-H	wehrlite cumulate peridotite	blue-purple pink-red	M-H M-H
OPS 528	dunite gabbro	very bright green red-pink	H M-H	harzburgite	red-green and magenta-purple	H
OPS 518	wehrlite	dark green	L-M	gabbro (all) harzburgite	pink-purple orange-red	M M
OPS 538	pyroxenite	yellow-brown	L			
OPS 681	sheeted dykes	bright blue-purple	H	wehrlite	dark blue-purple	M-H
OPS 127	trondhjemite	yellow-green	H	harzburgite	dark blue	M

Table 5.6 Comparison of band composites derived by statistical analysis. Each composite was expected to discriminate one lithology more than the others (as per Section 4.5.2). Discrimination levels of these 'expected' lithologies are shown against other lithologies also discriminated by the composite. Dis.=discrimination were L=Low, M=Medium and H=High.

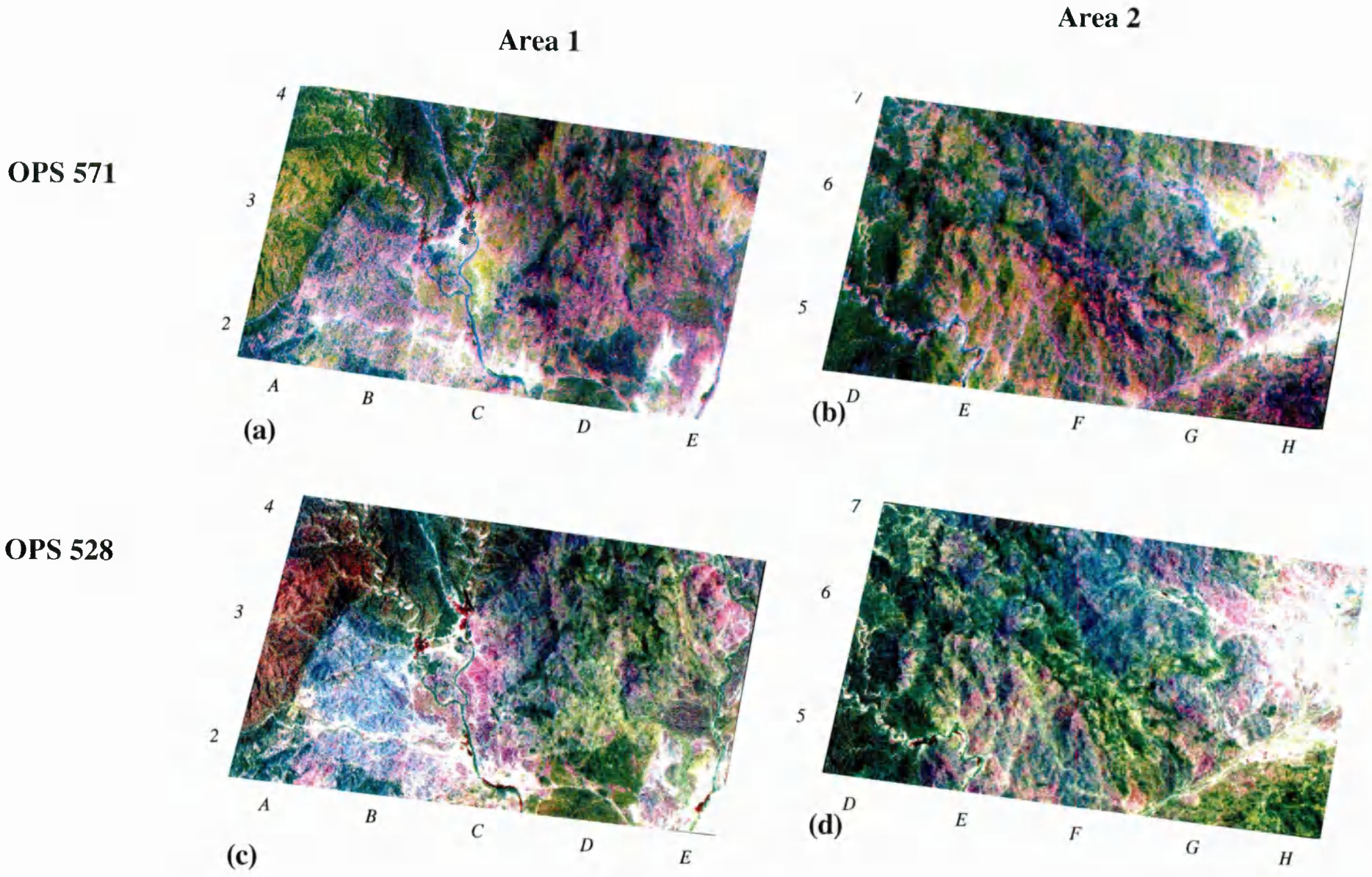

Plate 5.20 Two OPS composites of the Maqsad study areas (see Figure 5.1 for location). Refer to text for a full description.

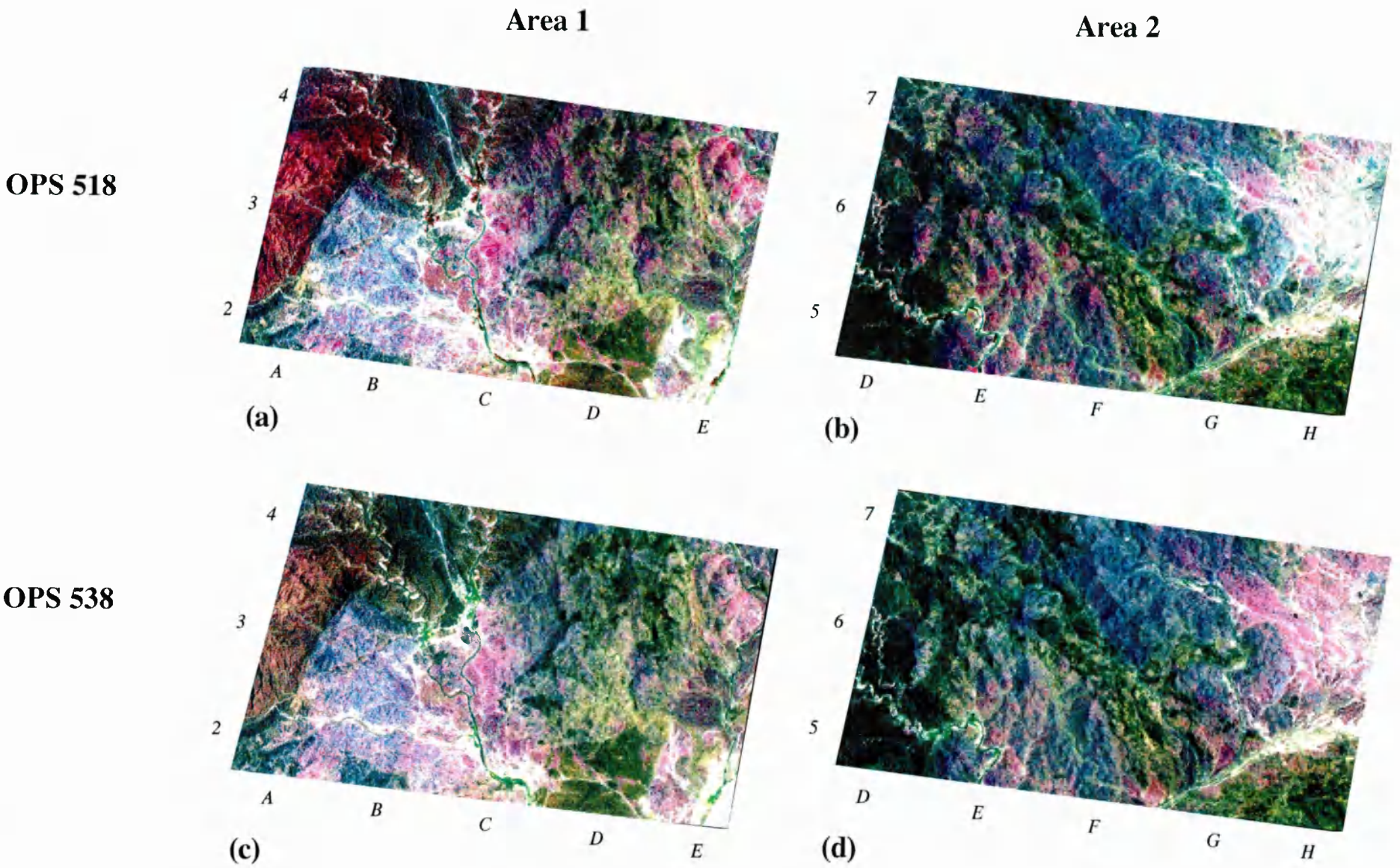

Plate 5.21 Two OPS composites of the Maqsad study areas (see Figure 5.1 for location). Refer to text for a full description.

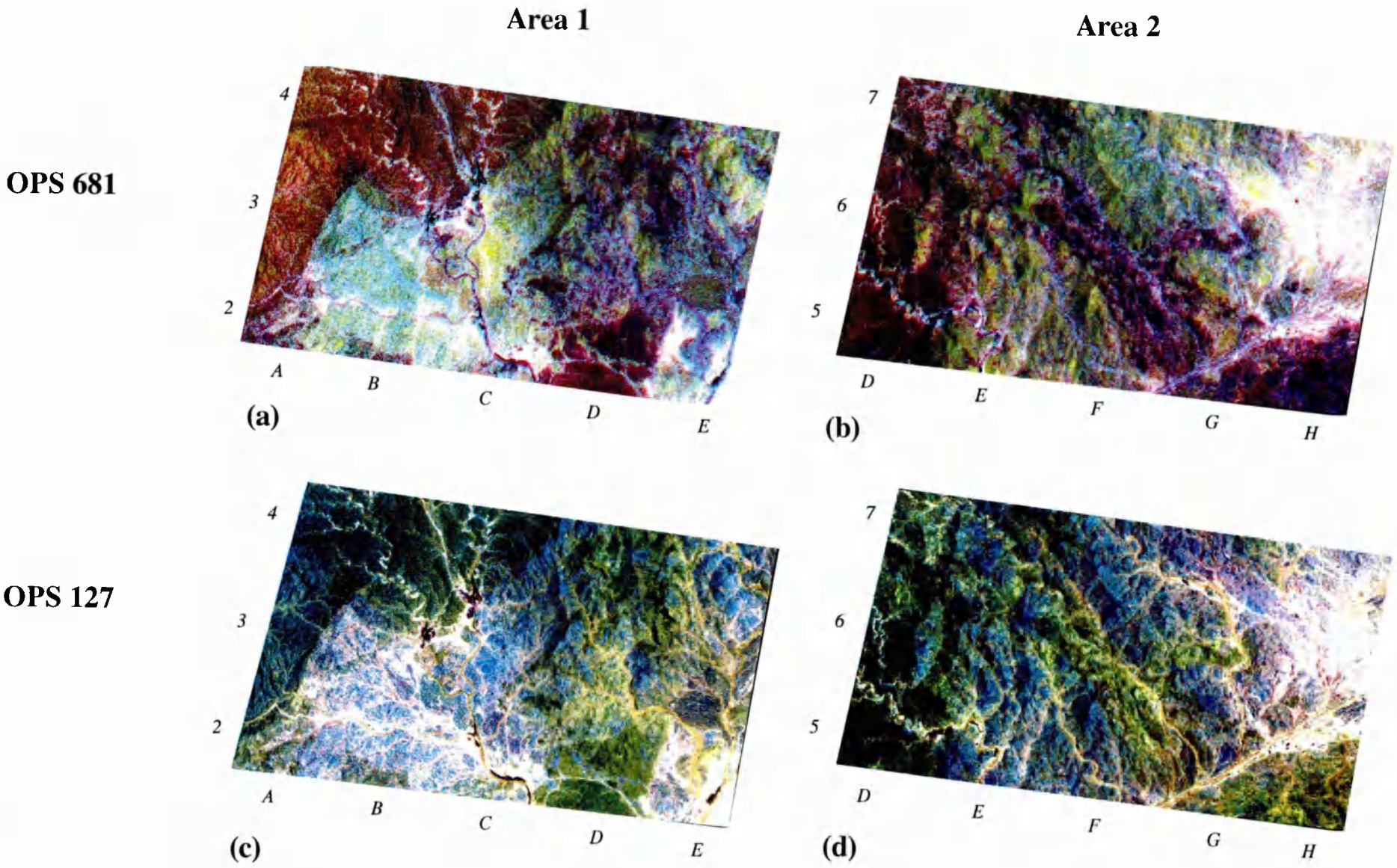

Plate 5.22 Two OPS composites of the Maqsad study areas (see Figure 5.1 for location). Refer to text for a full description.

5.4.2 OPS ratios

Analysis of the convolved lab spectra in section 4.5.2 highlighted five different OPS ratios which may be capable of distinguishing ten different lithologies. Table 5.7 (and Plates 5.23 to 5.26) summarises the discrimination capabilities of these ratios.

Ratio	Predicted discrimination	Predicted image intensities	Actual image intensities	Dis.
OPS 1/7	lherzolite	medium-high	medium-high	L / ND
Additional discrimination	*dunite*	-	*low*	*L-M*
	wehrlite	-	*low*	*M*
	cumulate gabbro	-	*high*	*M*
OPS 5/8	harzburgite	high	low-medium	M-H
	wehrlite	medium-high	low	H
	pyroxenite	high	low-medium	M-H
	pillow lavas	medium-high	medium	L
Additional discrimination	*cumulate peridotite*	-	*low*	*M-H*
	cumulate gabbro	-	*high*	*M*
	cumulate gabbro with trondhjemite	-	*high*	*H*
OPS 1/5	dunite	low	low	H
	cumulate gabbro	medium	medium-high	M-H
	sheeted dykes	low	low	M
Additional discrimination	*wehrlite*	-	*medium-low*	*M*
OPS 1/6	isotropic gabbro	low	high	M-H
Additional discrimination	*cumulate gabbro*	-	*medium-high*	*M*
	dunite	-	*low*	*M*
OPS 3/8	trondhjemite	medium	medium-high	L
Additional discrimination	*dunite*	-	*low*	*M*

Table 5.7 Comparison of predicted discrimination capabilities of predefined band ratios against actual discrimination. Dis.=discrimination were L = Low, M = Medium, H = High and ND = Not Distinct. Additional lithologies discriminated are shown in italics.

The OPS 1/7 ratio (Plates 5.23 (a) and (b)) was determined as discriminating lherzolite. Analysis of the ratio image has shown that this ratio highlights variations within areas of harzburgite (A3 to B4) very well. However it is difficult to tell if these

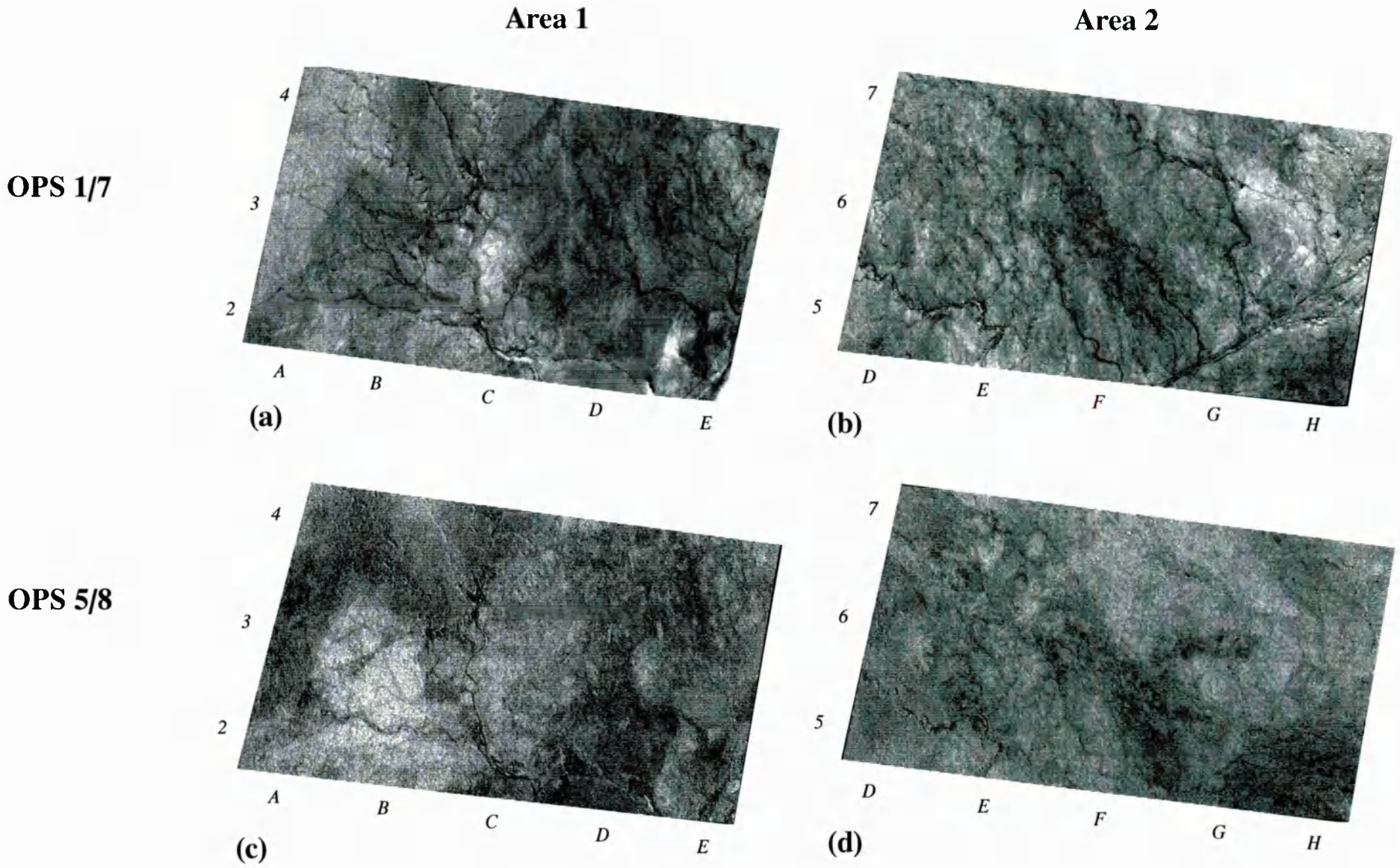

Plate 5.23 Two OPS ratio images of the Maqsad study areas (see Figure 5.1 for location). Refer to text for a full description.

variations relate directly to lherzolite. Additionally this ratio clearly discriminates dunite (low intensities, D5)), wehrlite (low intensities, F6) and cumulate gabbro (moderate to high intensities, E5). Note that this ratio image contains slight topographic information. This is because the poor topographic definition in OPS 7 has not normalised the topography in OPS 1, as usually expected by a ratio operation. The OPS 5/8 ratio (Plates 5.23 (c) and (d)) was predicted to discriminate harzburgite, wehrlite, pyroxenite and pillow lavas. Discrimination of harzburgite (low-medium intensities, A3) and pyroxenite (low-medium, B3) was reasonable, although pyroxenite was only distinct because it was surrounded by much higher intensities (cumulate gabbro with trondhjemite, B3). This ratio highlighted pillow lavas in medium intensities but it was difficult to distinguish this lithology from surrounding lithologies. Discrimination of wehrlite (F6) in low intensities was very good. This ratio also discriminated the additional lithologies of cumulate gabbro (moderate intensities) and cumulate gabbro with trondhjemite (high intensities, B3).

The OPS 1/5 ratio (Plates 5.24 (a) and (b)) is of a higher quality than the other OPS ratios, this reflects the higher quality of the original input channels. This ratio was predicted as discriminating dunite (low intensities, D5), cumulate gabbro (medium intensities, F5) and sheeted dykes (low intensities E2). Dunite and cumulate gabbro were discriminated very clearly on the output ratio, although the discrimination of sheeted dykes was worse than expected. The OPS 1/6 ratio (Plates 5.24 (c) and (d)) was predetermined as discriminating isotropic gabbro (H7) in low intensities. This ratio also discriminated bright areas of cumulate gabbro (E4); i.e., iron-weathered and dunite in low intensities. Note that this ratio appears to be very similar to that of OPS 1/7 (Plates 5.23 (a) and (b)). This is because of the lack of spectral variation in OPS 6 and OPS 7. The final predefined ratio, OPS 3/8 (Plates 5.25 (a) and (b)), highlighted trondhjemite (B3) as expected in medium to high intensities, but discrimination was still low due to the similar discrimination of trondhjemite with gabbro (B3). This ratio also clearly discriminated dunite (D5) in low intensities.

Three additional ratios which were not defined in section 4.5.2 were also tested, OPS 5/3, OPS 3/1 and OPS 8/1 (Plates 5.25 (c), (d) and Plates 5.26 (a) to (d) respectively). OPS 5/3 is the equivalent of the TM 5/4 ratio used to highlight ferrous iron. Tests of the OPS 5/3 ratio (Plates 5.25 (c) and (d)) highlighted outcrops of cumulate gabbro (E4) which have developed particularly strong surface weathering in low intensities. Similarly weathered terrace deposits (C3) are also highlighted on this OPS ratio in low intensities. This ratio also very clearly distinguished dunite (high intensities, D5) and

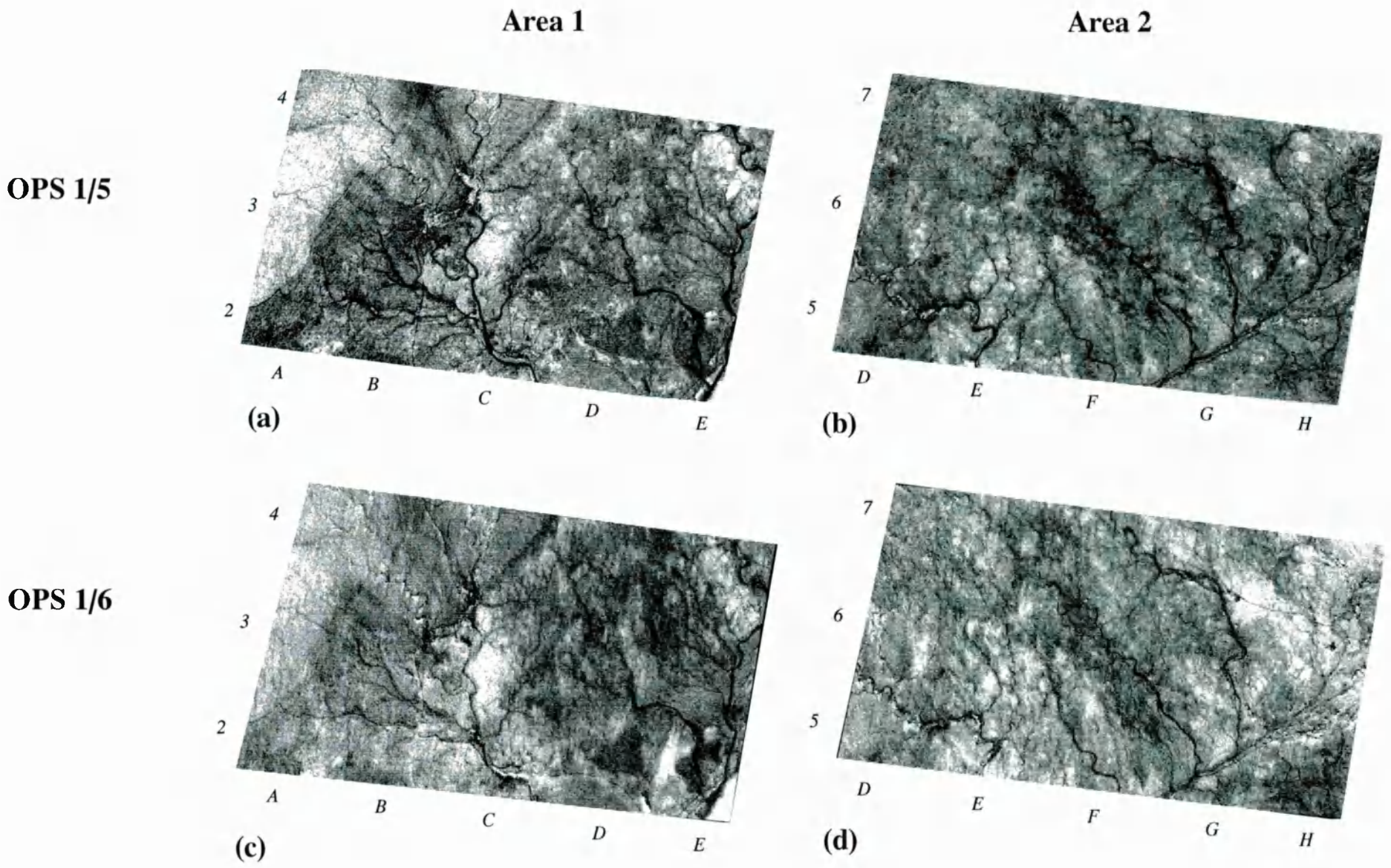

Plate 5.24 Two OPS ratio images of the Maqsad study areas (see Figure 5.1 for location). Refer to text for a full description.

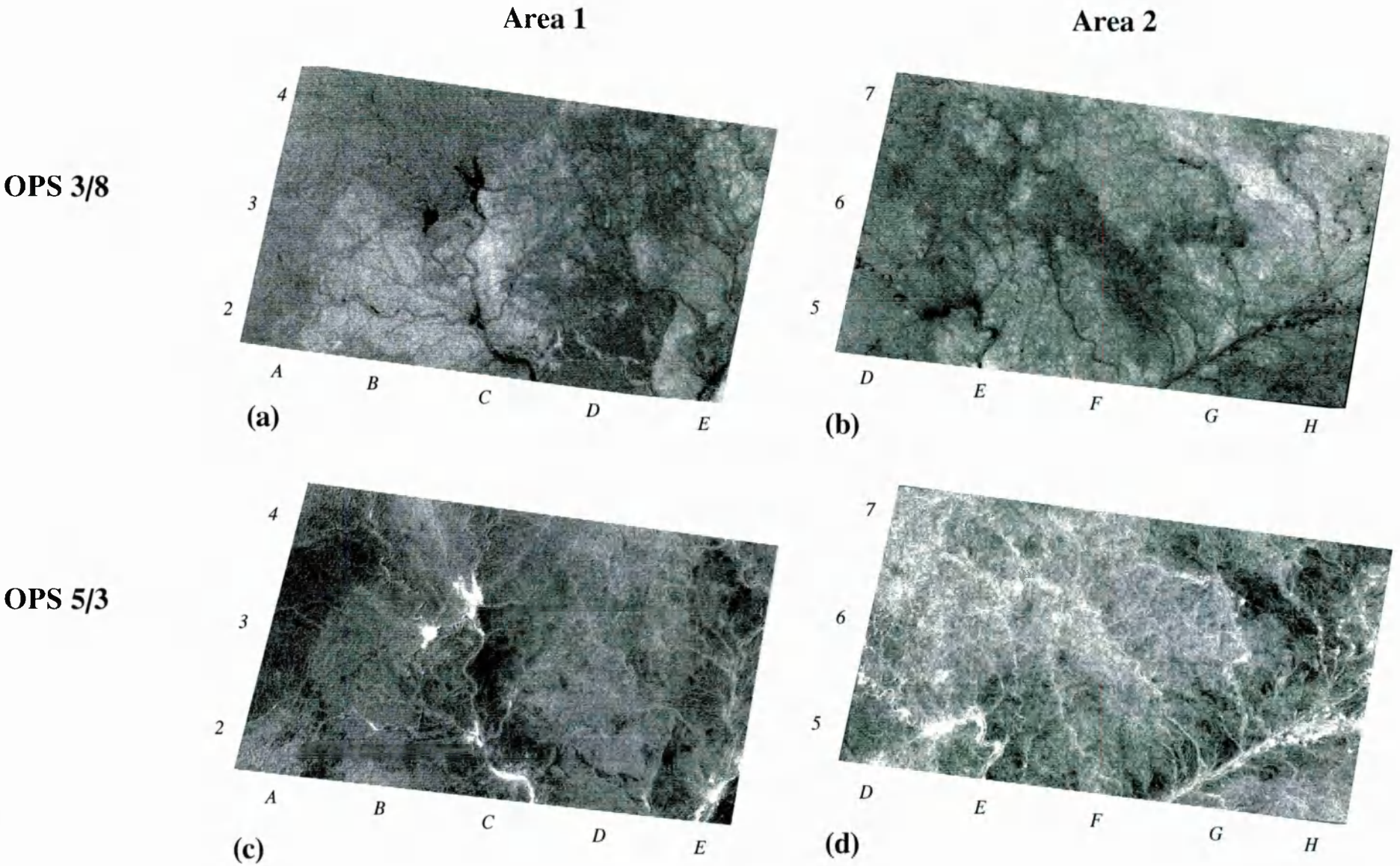

Plate 5.25 Two OPS ratio images of the Maqsad study areas (see Figure 5.1 for location). Refer to text for a full description.

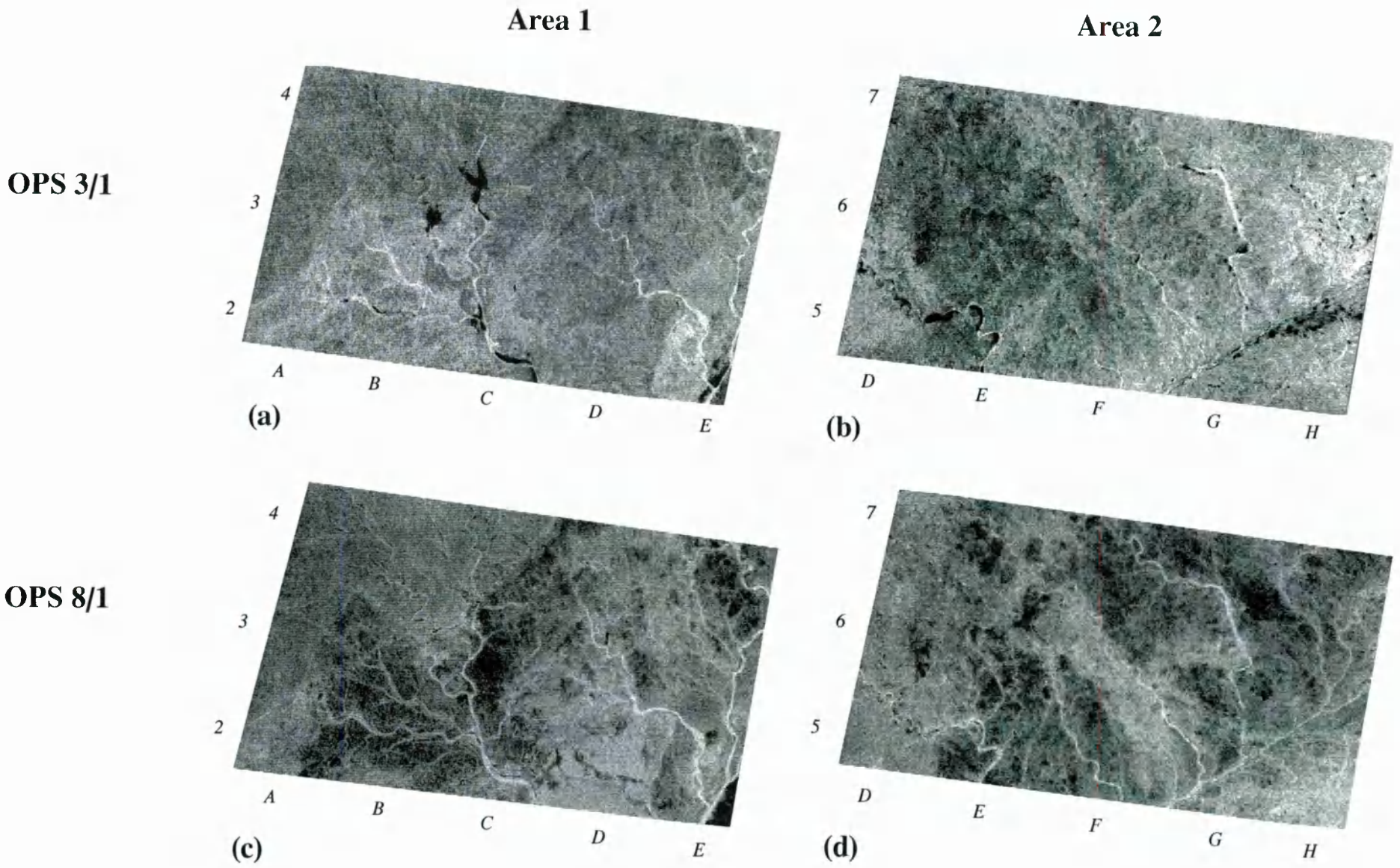

Plate 5.26 Two OPS ratio images of the Maqsad study areas (see Figure 5.1 for location). Refer to text for a full description.

showed good variation within areas of harzburgite (A3). The OPS 3/1 ratio (Plates 5.26 (a) and (b)) was quite poor discriminating only vegetation (low intensities), cumulate gabbro (low-medium intensities) and sheeted dykes (moderate to high intensities, E2). The discrimination of cumulate gabbro is related to surface weathering, Taranik *et al.*, (1995) have demonstrated that an OPS 3/1 ratio discriminates iron oxides. The OPS 8/1 ratio (Plates 5.26 (c) and (d)) very clearly discriminated all areas of gabbro. Spectrally bright outcrops i.e., heavily weathered cumulate gabbro (E4) or isotropic gabbro (H7) are discriminated in very low intensities, whilst other areas of cumulate gabbro exhibit mid-level intensities. This ratio discriminated wehrlite (F6) in moderate to high intensities although discrimination between wehrlite and cumulate peridotite is poor in some parts of the image.

To fully appreciate the spectral variations seen on the grey-scale ratio images I have combined some of the best ratios into four colour composites. The first composite combines OPS 1/7, 1/5 and 3/8 (Plates 5.27 (a) and (b)). This composite highlights gabbro-lithologies from green to almost white (E6 and F5), cumulate peridotite in dark green (F6) and dunite in dark red-black (D5). The second composite combines OPS 1/7, 5/8 and 5/3 (Plates 5.27 (b) and (d)). This composite clearly highlights all areas of gabbro in a range of colours from yellow to orange-red (E5 and E4), however harzburgite lithologies are also highlighted in similar red-yellow colours (A4). Cumulate peridotite is fairly distinct on this ratio in dark cyan-green (F6). The third composite which is a combination of OPS 5/8, 1/6 and 5/3 (Plates 5.28 (a) and (b)) is actually very good at discriminating a number of lithologies, including dunite (bright red, D5), wehrlite (dark red-magenta, F6), cumulate gabbro (pale blue-green, E5), cumulate peridotite (cyan-green, F6) and gabbro with trondhjemite (B3). The final ratio composite combines OPS 3/8, 5/3 and 8/1 (Plates 5.28 (c) and (d)) and highlights dunite (D5) and wehrlite (F6) in shades of cyan-blue, cumulate gabbro in orange-red (E5) and harzburgite in magenta-red (A3).

Overall the pre-determined ratios predicted from the analysis of lab spectra did highlight the lithologies they were supposed to do. However, like the TM ratios the OPS ratios also highlighted some additional lithologies. Lithological discrimination was further improved by combining three greyscale ratio images into a colour composite.

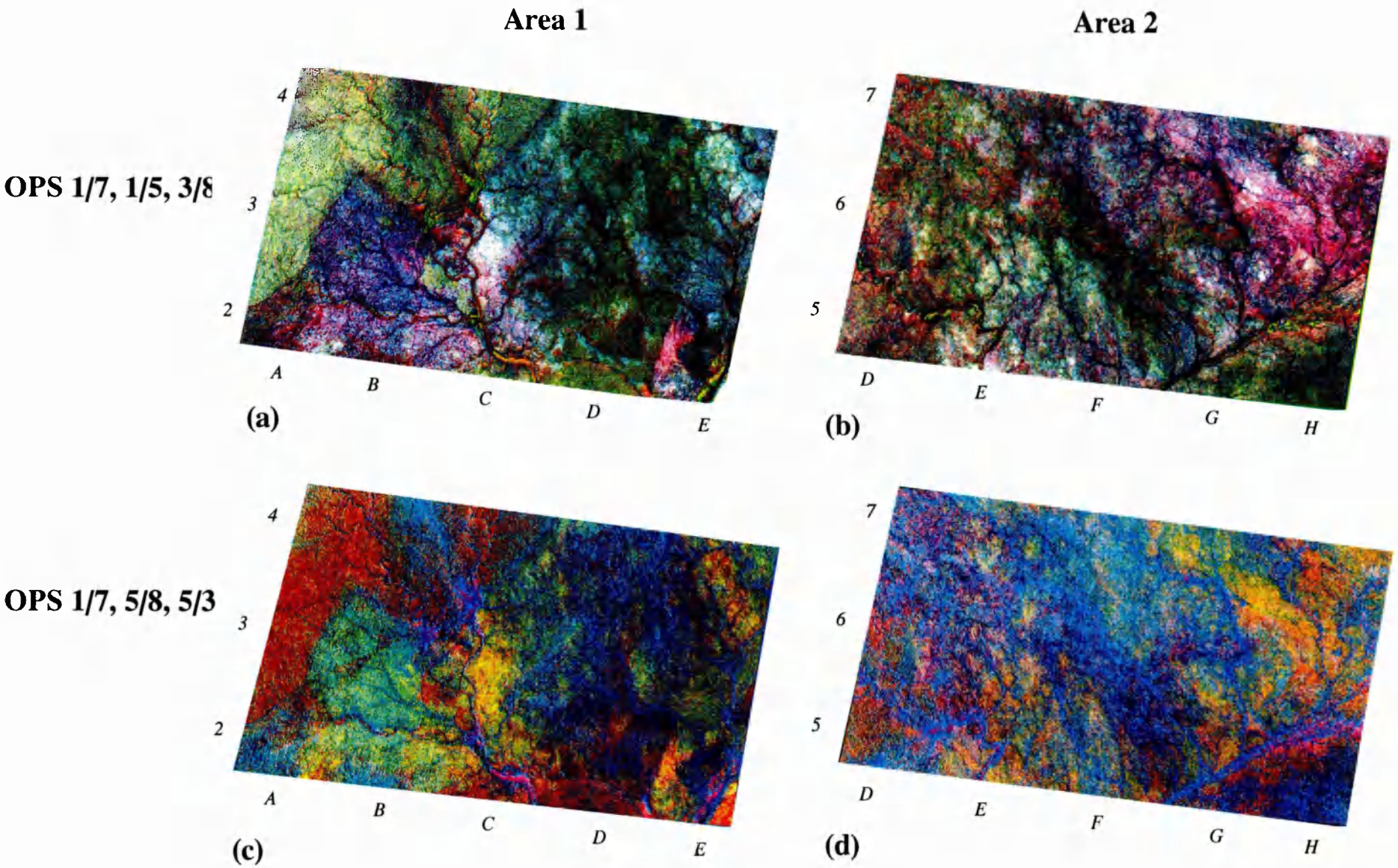

Plate 5.27 Two OPS ratio colour composites of the Maqsad study areas (see Figure 5.1 for location). Refer to text for a full description.

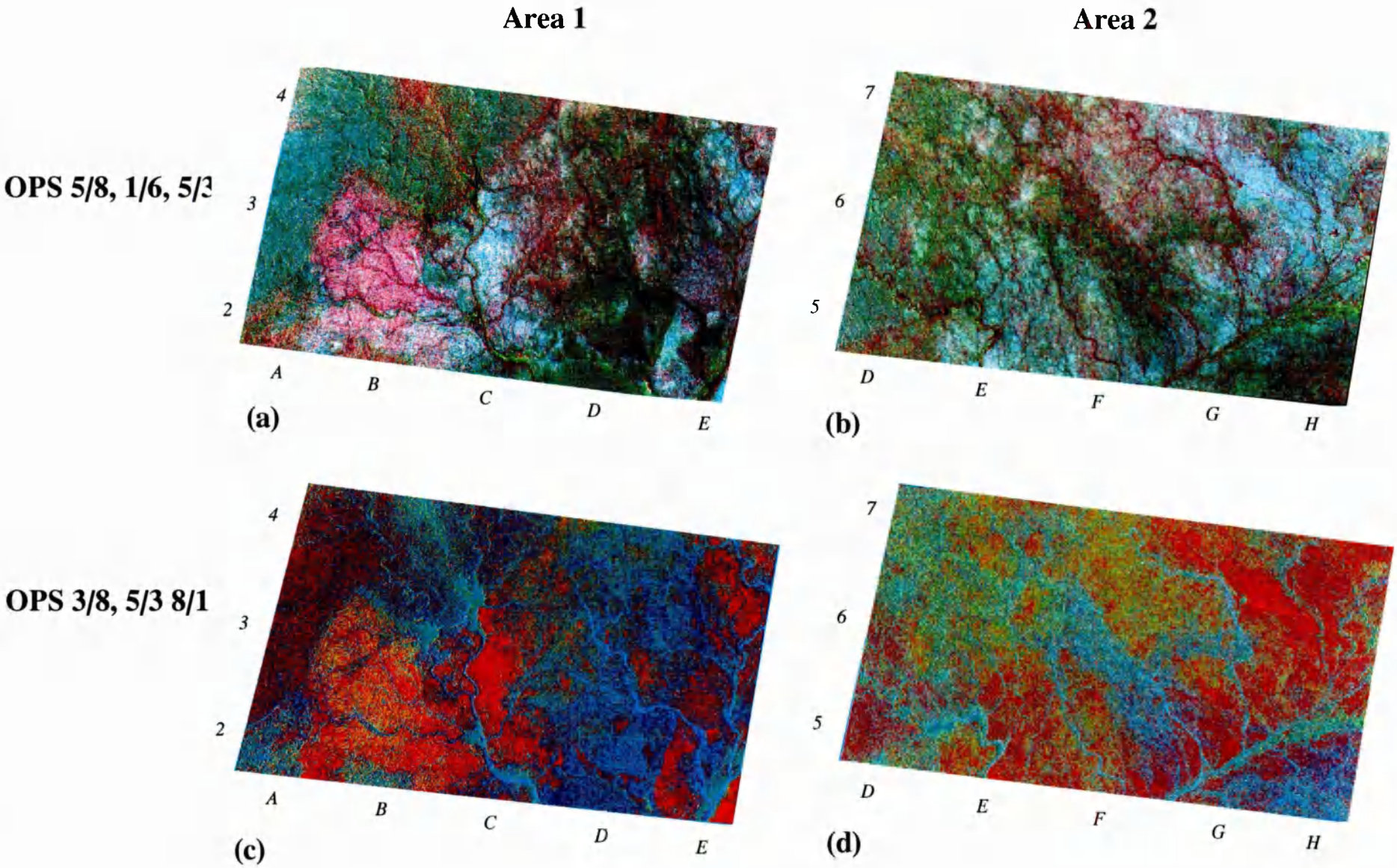

Plate 5.28 Two OPS ratio colour composites of the Maqsad study areas (see Figure 5.1 for location). Refer to text for a full description.

5.4.3 Approximated OPS processing

No predefined band composites exist in the literature for OPS data because of their 'new' nature. However, potentially useful band composites can be inferred by approximating those which have been derived for TM data, in particular those which have been derived specifically for discriminating ophiolite lithologies.

The first to be tested was an approximation to an MSS composite described by Harding and Bird (1984), combining OPS 1/3, 2/1 and PC 1. These bands produced a reasonable image in terms of quality, but spectrally the composite did not discriminate any ophiolite lithologies. The next OPS composite to be tested was the equivalent of the TM 754 decorrelation stretched image recommended by a number of authors. Originally OPS 853 was tested as this is the closest spectral equivalent to TM 754, however the quantised nature of OPS 3 seriously degraded the composite. Therefore OPS 2 was substituted for OPS 3, producing the colour composite OPS 852 (Plates 5.29 (a) and (b)). These channels produced an extremely good colour composite, better than any of the band combinations tested in section 5.4. Despite some of the lithologies in the OPS 852 composite exhibiting similar colours to those seen earlier (e.g., cumulate gabbro on the OPS 851 (Plates 5.19 (a) and (b)), levels of discrimination are far higher on this composite. This is a direct result of the higher quality of these three channels. Compared with the other channels OPS 852 have a far higher dynamic range. It is therefore fortunate that the three OPS channels which have the highest data quality are located at distinct parts of the spectrum where they are able to record diagnostic absorption features. A full description of this composite will be given in section 5.5.5. To further compare the similarity of this composite with the TM 754 decorrelation stretched composite a decorrelation stretched OPS 852 image was produced (Plates 5.29 (c) and (d)). Unlike the TM decorrelation stretched image the OPS decorrelation stretched image offers no improvement over the original OPS 852 composite. Colour saturation is better on the OPS 852 decorrelation stretched images (c) and (d), however this is at the expense of image quality. Both the decorrelation stretched images appear noisy compared with the original composites (a) and (b). Applying a decorrelation stretch emphasised the underlying poor OPS data quality, despite these channels being cleaned using FFT techniques. Closer analysis of the decorrelation stretched composites suggests that some subtle spectral variations may be lost (e.g, colour variation in D3), making the straightforward colour composite best for interpretation.

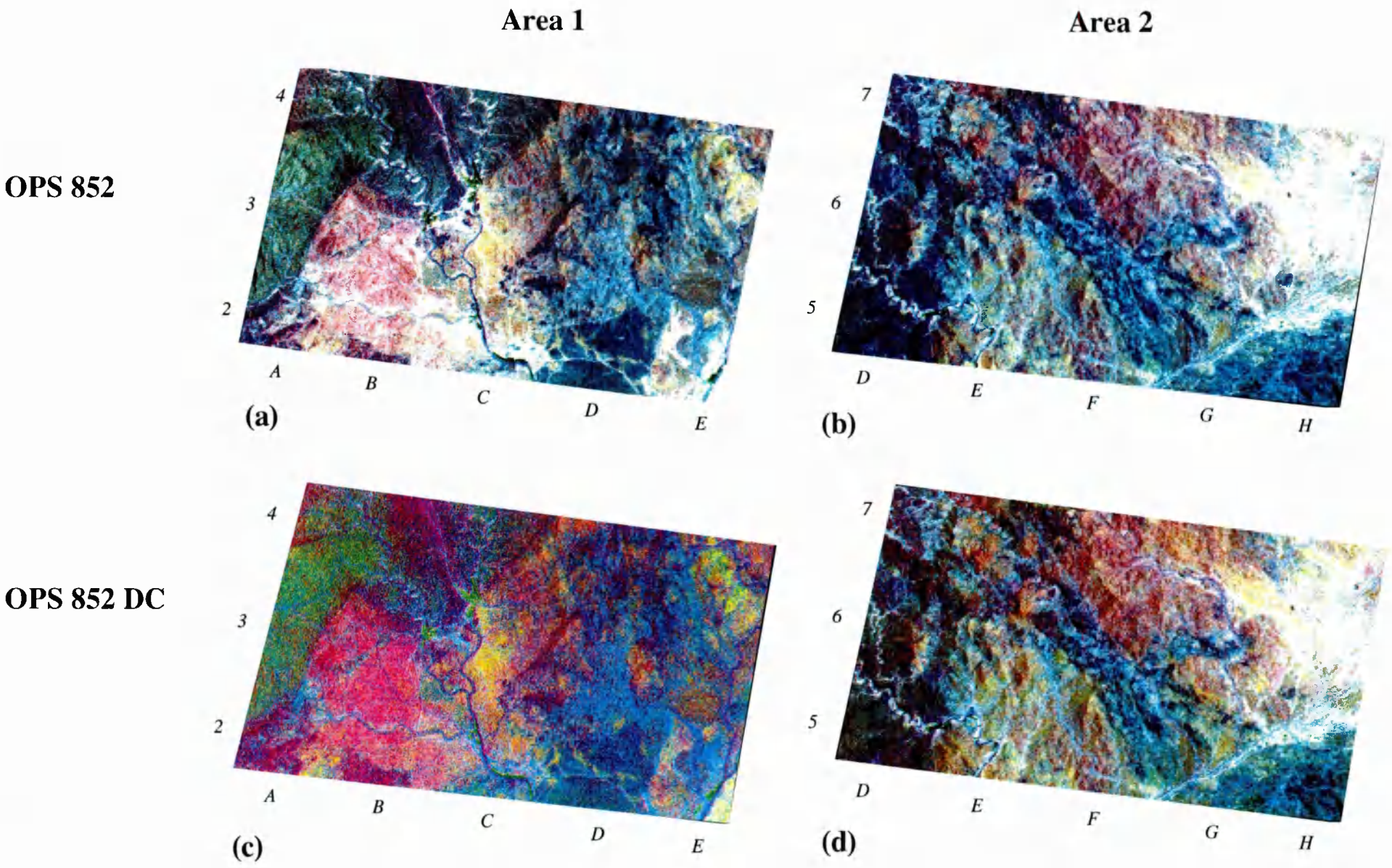

Plate 5.29 Two OPS composites of the Maqsad study areas (see Figure 5.1 for location). Refer to text for a full description.

OPS approximations to both of the Sultan *et al.*, (1986) band combinations are shown in Plates 5.30 (a), (b) and (c), (d). Discrimination on both of these composites is very similar. The first composite (OPS 5/8, 5/1 and (2+5)/3, Plates 5.30 (a) and (b)) discriminates dunite rich areas in red (D5) and wehrlite (F6) rich areas in red-magenta. Cumulate gabbros are distinct in green (E5) whilst cumulate peridotite is yellow-green (F6). Some areas of harzburgite are a similar yellow-green colour (D5), however these two units can be distinguished due to their locational context. The second composite (OPS (5*2)/3, 5/1 and 5/8, Plates 5.30 (c) and (d)) discriminates the same lithologies slightly better. The OPS equivalent to Pontual (1990) produces an image (Plates 5.31 (a) and (b)) which is fairly similar, both in terms of colour and discrimination levels to that produced by the TM data (Plates 5.13 (a) to (d)). Dunite rich areas are clearly discriminated in bright yellow-green (D5) whilst cumulate peridotite is distinguished in a darker green (F6). All gabbro lithologies are discriminated in various shades of red, as per the TM composite, making it difficult to distinguish between cumulate (E5) and isotropic gabbro (H7). This composite also discriminates gabbro with trondhjemite clearly in pink-red (B3). Examining this region at screen resolution indicates some discrimination between gabbro rich areas (red) and trondhjemite rich areas (yellow-pink).

5.4.4 General OPS processing

General image processing techniques such as those applied to TM data in section 5.3.5 can also be applied to OPS data. Applying a principal component transform to subscenes of OPS data produced very good results with some lithologies being clearly highlighted in specific PCs. Table 5.8 summarises the spectral characteristics of the main ophiolite lithologies when transformed into principal component images.

Reviewing Table 5.8 it can be seen that PC 1 represents the albedo information and as such helps to discriminate those lithologies which are either spectrally bright (cumulate gabbro, trondhjemite) or spectrally dark (wehrlite). PC 2 discriminates harzburgite, cumulate gabbro and cumulate peridotite in mid to high intensities, and dunite in low intensities. PC 3 highlights sheeted dykes (low intensities) as well as cumulate and isotropic gabbro (medium-high intensities). PC 4 mainly discriminates the sheeted dykes complex (low-medium intensities). PC 5 discriminates both harzburgite (medium-high intensities) and cumulate gabbro with trondhjemite intrusions (low intensities). PC 6 discriminates cumulate peridotite (low intensities) above all of the

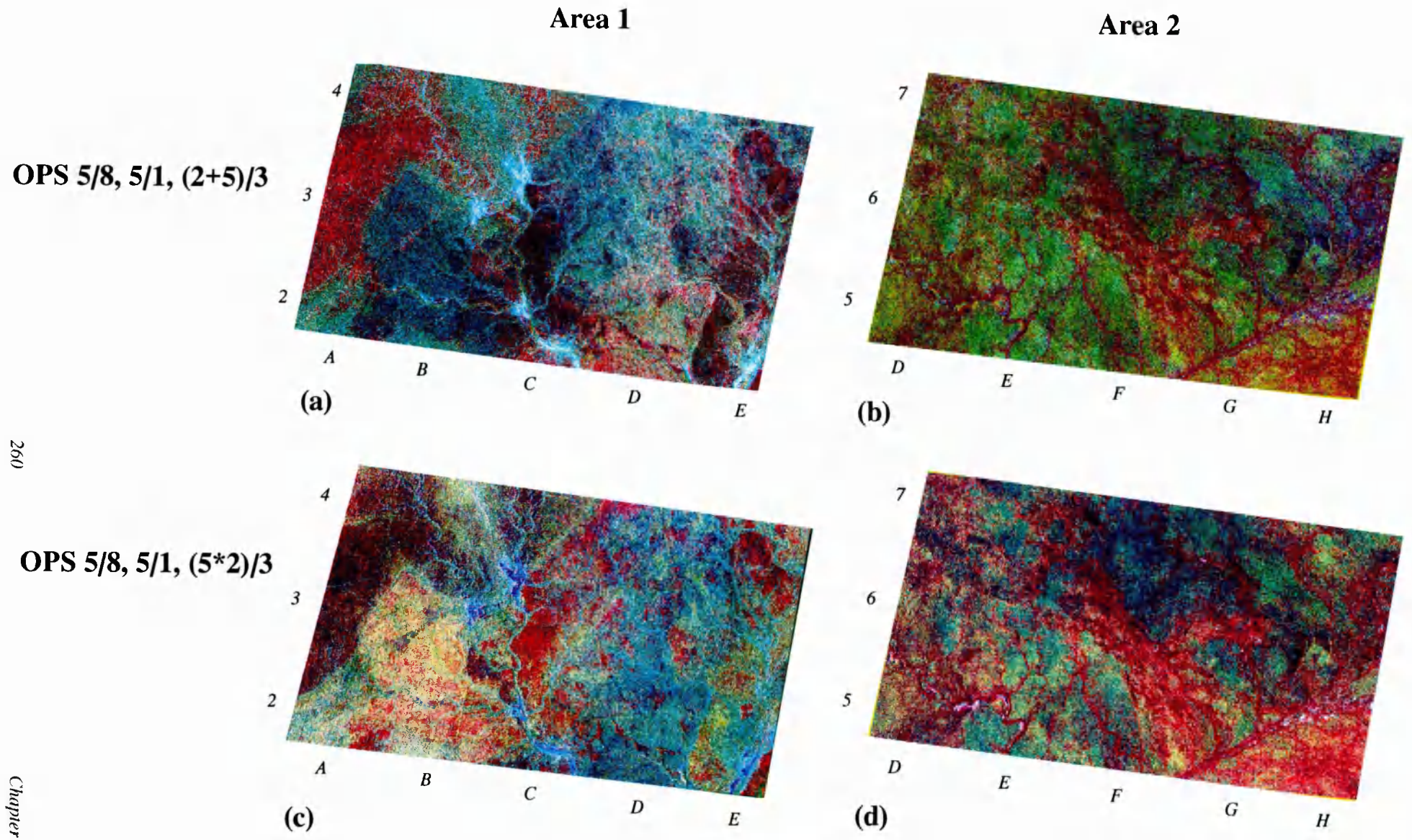

Plate 5.30 Two OPS composites of the Maqsad study areas (see Figure 5.1 for location). Refer to text for a full description.

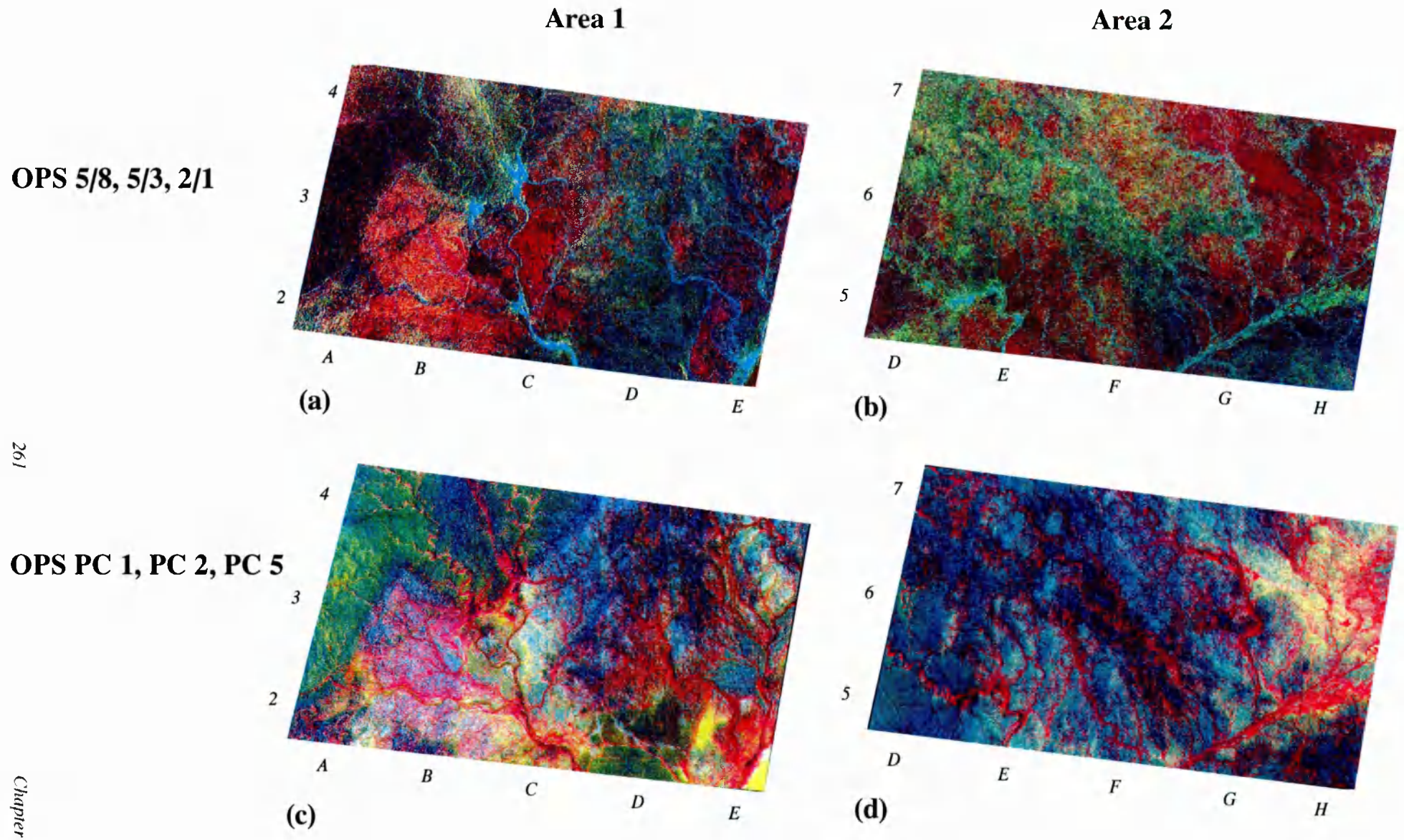

Plate 5.31 Two OPS composites of the Maqsad study areas (see Figure 5.1 for location). Refer to text for a full description.

Lithology	PC 1		PC 2		PC 3		PC 4		PC 5		PC 6		PC 7	
	Intensity	Dis.	Intensity	Dis.	Intensity	Dis.	Intensity	Dis.	Intensity	Dis.	Intensity	Dis.	Intensity	Dis.
Pillow lavas	medium	L	medium	L	low	M	medium	L	high	M	-	ND	-	
Sheeted dyke	medium	L	low-medium	L-M	very low	H	low-medium	H	low	M	medium	L	-	ND
Isotropic gabbro	medium	L	medium-high	L-M	medium-high	M-H	medium-high	L-M	medium	L-M	medium-high	M	-	ND
Cumulate gabbro	medium-high	L-M	medium-high	M	meddium-high	M-H	medium-high	L	medium	L	medium-high	L-M	-	ND
Cumulate peridotite	medium	L	low-medium	M	medium	L-M	very high	M	medium	L	low	M-H	-	ND
Harzburgite	very low	M	high	M	medium-high	L-M	high	M	medium-high	M-H	medium	L-M	-	ND
Dunite	high	L-M	low	M	very low	H	medium	L	medium	L	medium	L	l-ow	M
Wehrlite	very low	M	medium	L	medium	L	medium	L	medium	L	medium	L-M	-	ND
Trondhjemite	medium-high	M	medium	L	medium	L	medium	L	medium-high	L	-	-	-	
Isotropic gabbro + dykes	medium	L	medium	L	medium	L	medium	L	medium	L	medium	L-M	-	ND
Cumulate gabbro + dykes	medium	L	medium	L	medium	L	low-medium	M	medium-high	L-M	medium	L-M	-	ND
Cumulate gabbro + trondhjemite	medium	M	medium-high	M	medium	L	medium	L	low	H	medium-high	L	low-medium	L
Pyroxenite	medium	L	-	ND	low-medium	M	low-medium	M	-	ND	low	L	-	ND

Table 5.8 Description of lithological discrimination of OPS seven-band PCA. Pixel intensity values described as low (approx. <80DN), medium (approx. 81-160 DN) and high (approx. >161 DN). Dis.=discrimination level, were L=Low, M=Medium and H=High. See text for a full description.

other lithologies, whilst PC 7 only discriminated dunite (low intensities) and cumulate gabbro with trondhjemite intrusions (low-medium intensities).

Overall the PC images clearly distinguished cumulate gabbro, cumulate peridotite, isotropic gabbro, dunite, sheeted dykes, harzburgite and cumulate gabbro with trondhjemite. The majority of the spectral information was contained in PCs 1, 2, 3, 4, 5 and 6. Unlike the TM PCs the OPS PCs do not show such a gradual drop off in quality towards the higher ordered components, although OPS PC 7 is by far the noisiest. To maximise the spectral information contained in these grey-scale PC images, OPS PC 1, PC 2 and PC 5 were combined to form a colour composite (Plates 5.31 (c) and (d)). This composite is quite informative as it highlights dunite in dark magenta-red (D5) although cumulate peridotite is also distinguished in a similar dark magenta (F6). This composite also highlights cumulate gabbro (E5) and harzburgite (D5), but once again these are difficult to distinguish because they have a similar cyan-blue colour. This composite image also highlights sheeted dykes very well in bright yellow (E2) and there is good variation in the trondhjemite rich region around B3.

Applying a Tasseled Cap transform to the OPS data produced some very interesting results. The TC transform was performed using both the TM coefficients defined by Crist and Cicone (1984) and the OPS coefficients defined by Malila and Meyers (1995). Overall the TCs produced from the TM coefficients produced the most informative component images. TC 1 was quite similar in appearance to PC 1 as it represented mainly topography, discriminating only spectrally dark and spectrally bright material. TC 2 was a very interesting image as it discriminated only the very brightest of surfaces, primarily the wadi courses and outcrops of dunite. TC 3 was quite a flat image with little spectral contrast, except for highlighting bright gabbro areas (low intensities) and dark wehrlite bodies (high intensities). TC 4 did not really discriminate any one lithology more than any other, and overall spectral contrast was low. TC 5 discriminated mainly gabbro lithologies, although it also showed reasonable variation within areas of mantle harzburgites. TC 6 discriminated mainly wehrlite bodies in low intensities. Combining TC 2, 5, and 6 together (Plates 5.32 (a) and (b)) produced a very informative image despite its limited colour range. By carefully applying a linear stretch to each band it was possible to produce an image which showed only dunite (D5) and wehrlite in red-magenta (excluding obvious wadi courses), serpentinised harzburgite (upper mantle, D5)) in dark blue and crustal gabbro (E5) in various cyan-green colours. Field checks indicate that this composite is correctly defining intrusive dunite bodies, as small as 200-300 metres in diameter and

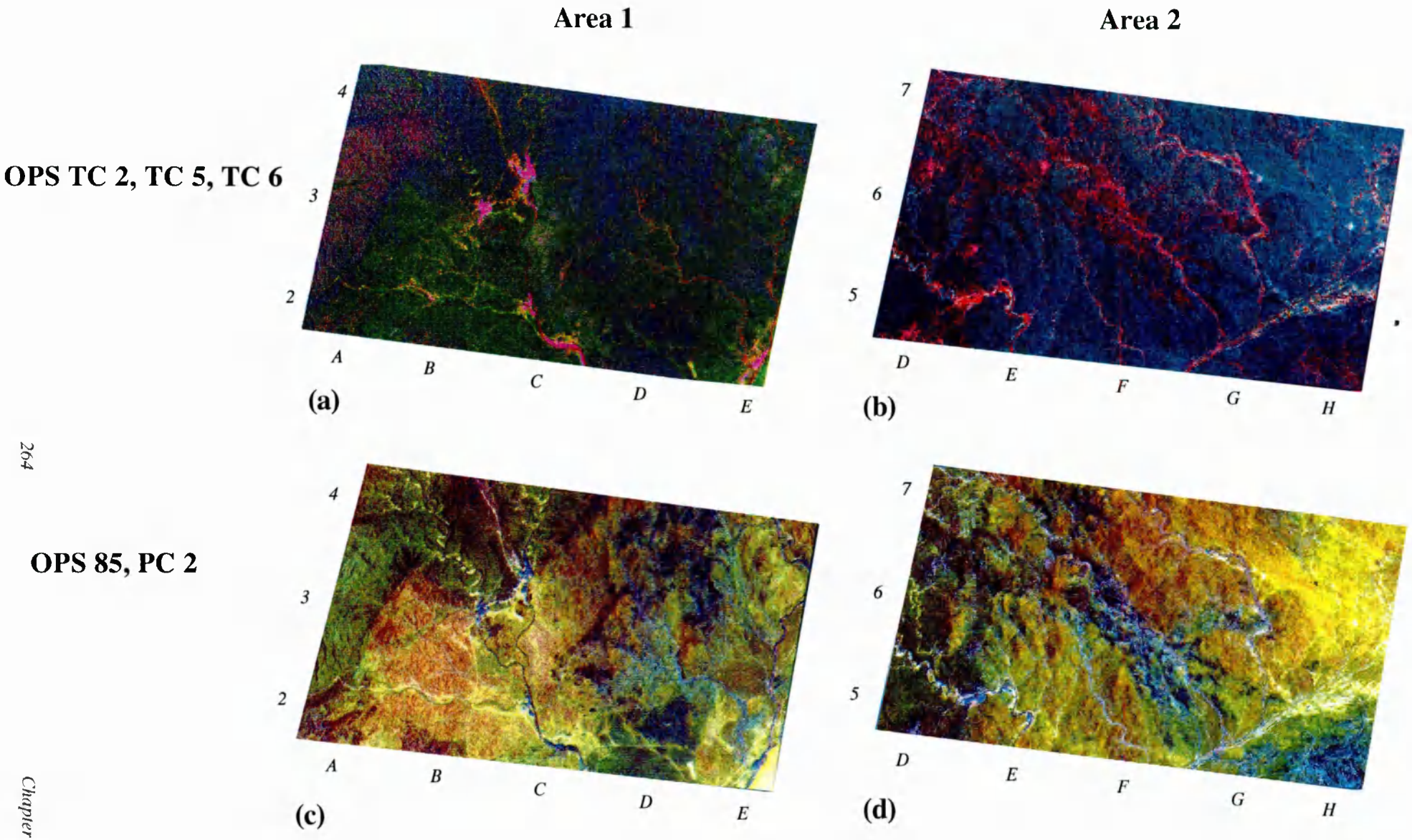

Plate 5.32 Two OPS composites of the Maqsad study areas (see Figure 5.1 for location). Refer to text for a full description.

surrounding dunite rich zones. These features are distinguished on the imagery as bright red targets and duller red zones respectively.

By combining the distinct spectral properties of some of the images described in this section it is possible to derive composites which are particularly good at distinguishing only one or two lithologies. One such composite combines OPS 8, OPS 5 and PC 2 (Plates 5.32 (c) and (d))) to form an image which clearly discriminates dunite (D5), wehrlite (F6) and cumulate peridotite (F6). Dunite is highlighted in purple-blue, wehrlite in mid to dark blue and cumulate peridotite in light cyan-green. Despite the strange colour balance of this image it is possible to clearly distinguish these three units. This image is particularly good for identifying small isolated wehrlite bodies which occur within the cumulate gabbro.

5.4.5 OPS spectral indices

In section 4.5.4 spectral indices for six mantle and six crustal lithologies were calculated from resampled lab spectra. Tests of these spectral indices applied to OPS data were quite poor, giving results similar to those achieved with TM data (section 5.3.5). Examples of wehrlite, isotropic gabbro and sheeted dykes indices are shown in Plates 5.33 (a), (b), (c), (d) and Plates 5.34 (a) and (b), respectively. The sheeted dykes and wehrlite images appear very similar, whilst the isotropic gabbro image is quite different, however this is mainly due to the isotropic gabbro image being inverted. The wehrlite index images (Plates 5.33 (a) and (b)) fail completely to highlight wehrlite (F6), instead it distinguishes dunite (D5) in high intensities (due to the high positive weighting values applied to OPS 1 and 2, see Figure 4.52 (c)) and cumulate gabbro (E6) in low intensities (due to negative weightings applied to OPS 5). The isotropic gabbro index (Plates 5.33 (c) and (d) does highlight isotropic gabbro (H7) in high intensities, however it also highlights spectrally bright outcrops of cumulate gabbro (E4), to a similar degree. The sheeted dykes index images (Plates 5.34 (a) and (b) do not distinguish the sheeted dyke complex. Combining these three images into a composite (Plates 5.34 (c) and (d)) produces a more colourful image than the TM equivalent (Plate 5.16 (c) and (d)). The poor colour balance of these composites confirms that the wehrlite and sheeted dykes indices are almost identical. These colour composite images are not very useful because they do not discriminate the three lithologies in question. These composites should highlight wehrlite in red, isotropic gabbro in green and sheeted dykes in blue. In reality wehrlite (F6) and cumulate peridotite (F6) are shown in pale green, harzburgite in dark green-blue

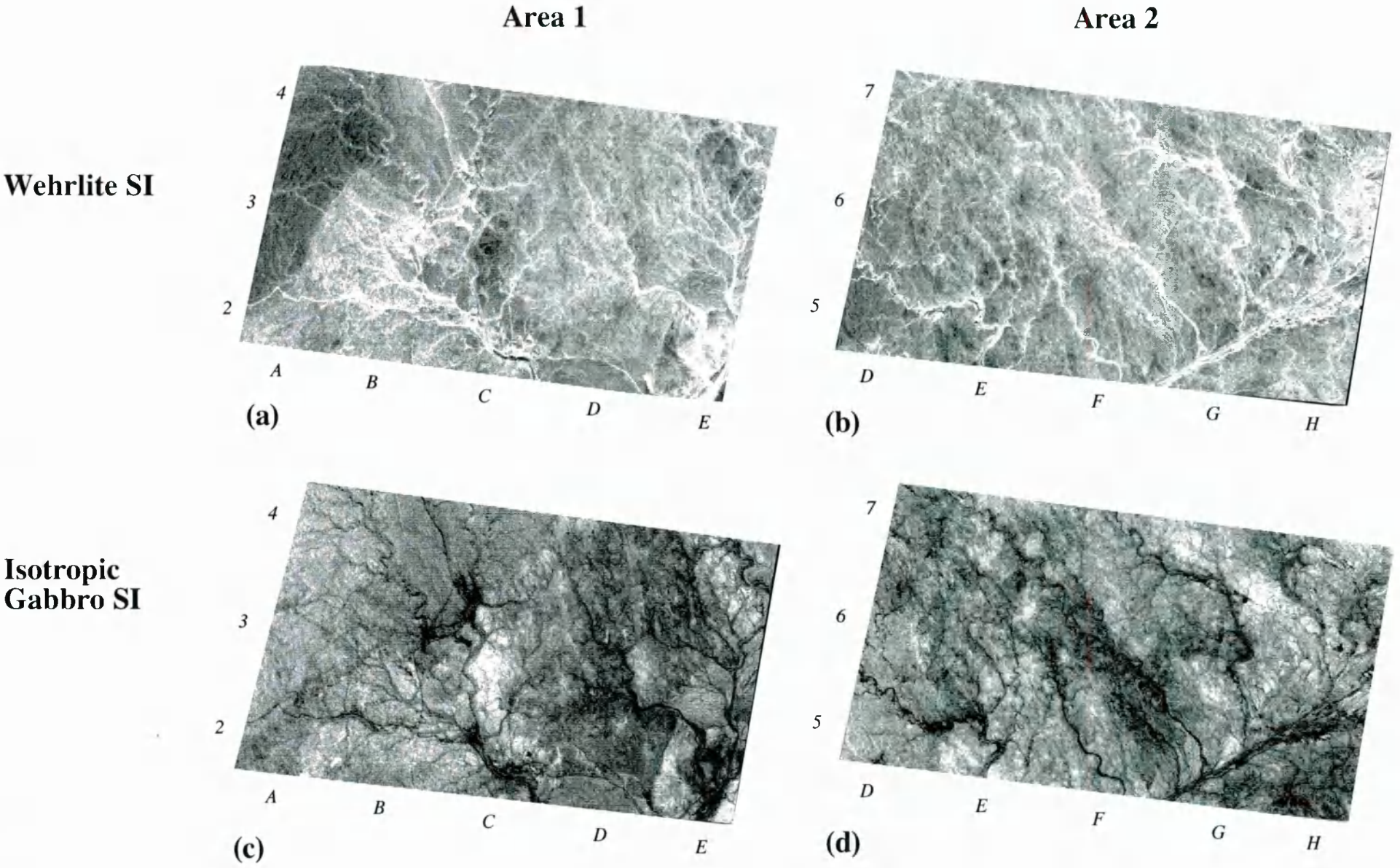

Plate 5.33 OPS spectral indices of the Maqsad study areas (see Figure 5.1 for location). Refer to text for a full description.

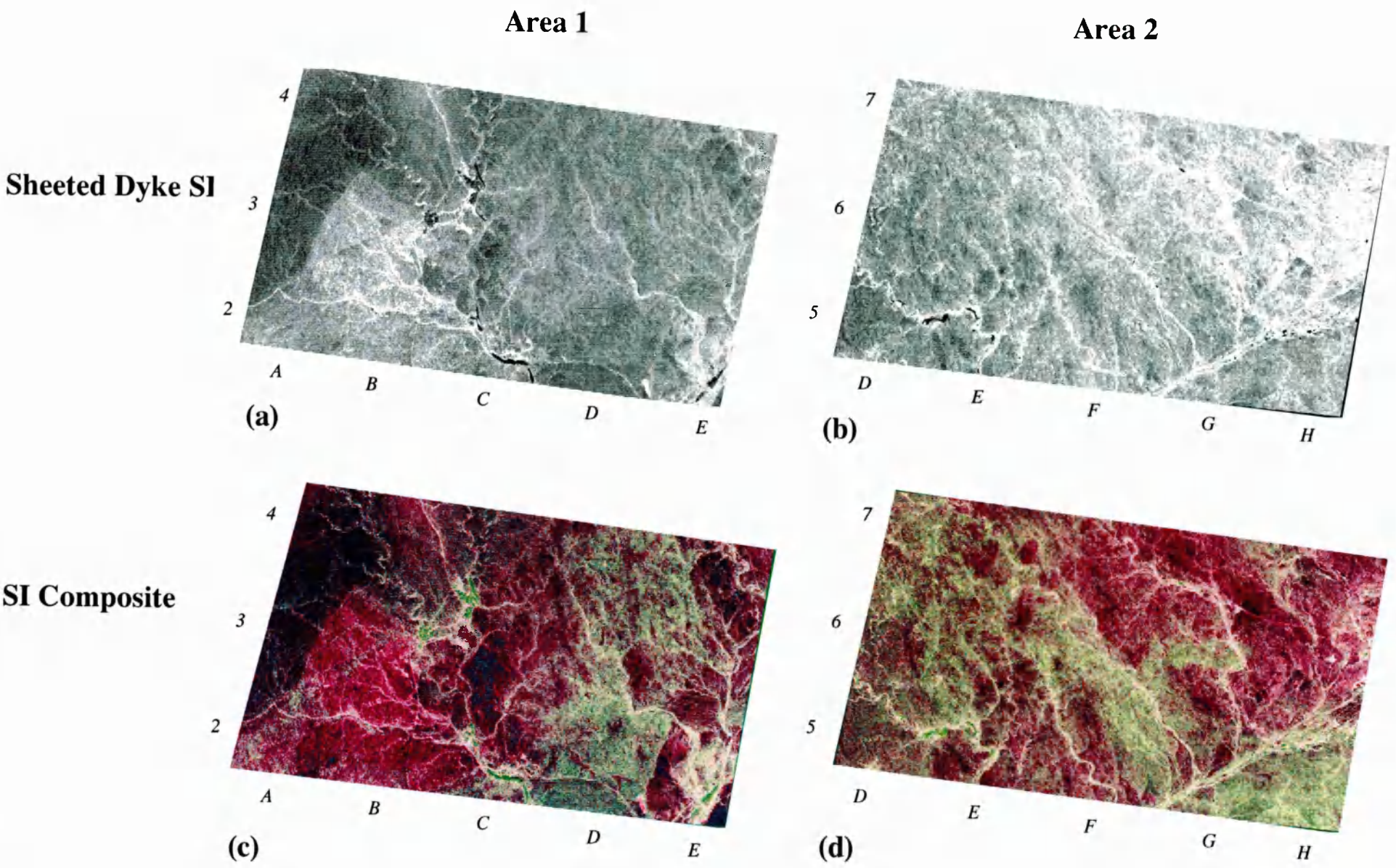

Plate 5.34 OPS spectral indices of the Maqsad study areas (see Figure 5.1 for location). Refer to text for a full description.

and cumulate gabbro in red-magenta (E5). Areas of isotropic gabbro (H7) and sheeted dykes appear in similar red-magenta colours and cannot be distinguished. Overall these spectral index images are very poor.

5.4.6 OPS image processing summary

During the course of this study a vast number of OPS band combinations and image processing techniques have been tried and tested, some of which have been demonstrated here. One of the initial objectives of this thesis was to determine new band combinations and processing techniques for multichannel SWIR data. It has not been possible to fully determine the effectiveness of all of the band combinations, due to the poor quality of the OPS data, in particular the quality of channels OPS 6 and OPS 7.

Despite these problems, this chapter has shown that geologically useful composites, such as, OPS 852, 532 and 861 can be derived. Two of these composites were derived by the analysis of lab based spectra (both at full and resampled resolution), This indicates the potential of using rock reflectance spectra to guide composite selection. Some of the other composites defined by the analysis of reflectance data might have yielded better composites if the image data had been of the quality expected. Despite the lower than expected quality and the restricted composite choice OPS data produce far superior image composites for lithologic discrimination (e.g., OPS 852) than TM data. This is also true of OPS ratios which offer better discrimination relating to specific lithologies, for example; dunite, serpentinised harzburgite, wehrlite and cumulate gabbro. The full potential of ratios such as OPS 1/7 and OPS 1/6 cannot be realised in this study due to data quality.

Overall OPS channels 852 combined as a false colour composite offered the best lithological discrimination. The application of enhanced processing techniques, such as ratios, PCA and decorrelation stretching, produced some reasonable images. However, lithological and mineralogical discrimination on these images was never as good as expected. This was due to the cleaned OPS data not being able to withstand intensive image processing without rapidly degrading. Operations such as those described above very quickly highlight any remaining noise in the image data, which is not visible in a simple false colour composite. These operations are too intensive to apply to channels like OPS 1, 3, 6 and 7 which have small initial dynamic ranges. As a result of this rapid data degradation an OPS 852 composite offers the best lithological discrimination for the Maqsad project area.

5.5 Image interpretation

This section uses the most informative TM and OPS colour composites (as described earlier) to produce lithological distribution maps. These maps have been produced by interpretation of the digital imagery at an enlarged scale. Lithologies have been assigned to 'image colours' based on numerous field checks (see Appendix 3). Lithological assignments inbetween field checks are based on spectral discrimination.

5.5.1 Spectral interpretation of TM 754 decorrelation image

Plate 5.35 shows a TM 754 decorrelation stretched image of the Maqsad study region (surrounding area masked to white). The major lithological units which can be distinguished and mapped on this image are summarised in Table 5.9 and discussed below:

1) Mantle Sequence

The mantle sequence in the Sumail massif appears in two distinct colours; green-yellow and red-purple. The bright green-yellow harzburgites (Plate 5.35 (a)) have a high intensity in TM 5 compared with TM 7 and TM 4. This is due to their spectra being strongly influenced by the olivine maximum at 1.7 μm (see Figure 4.29 (a) - M046 and M281). Some areas of 'green' harzburgite appear a darker green-blue colour (Plate 5.35 (b), these areas have lower intensities in TM 5. This is due to increased orthopyroxene which causes the reflectance maxima to shift from 1.7 μm to 1.6 μm, which results in the spectrum appearing flatter (Figure 4.29 (a) - M268). These spectral features can become quenched if there is sufficient magnetite present. The red-purple harzbugites (Plate 5.35 (b)) show lower reflectance in TM 5 (less input from the olivine maximum at 1.7 μm) and slightly higher in TM 4 and TM 7. This two-tone colouration has been seen before on TM imagery of mantle rocks (Abrams *et al.*, 1988, Pontual 1990). Previous studies have concluded that red-purple harzburgite represents the upper part of the mantle sequence, approximately 1 km below the Moho (Abrams *et al.*, 1988). Studies have shown a general correlation between the purple colouration and sub-seafloor hydrothermal alteration or serpentinisation. This idea is supported by the occurrence of a similar purple colour along late stage fracture lines which have been affected by post-emplacement serpentinisation. These ideas are supported within the Maqsad area as the purple coloured harzburgite occurs mainly along the Moho and along known shear zones. Both red and green harzburgites are extremely difficult to tell apart in the field as there are no obvious differences between the two.

Mappable unit	Typical image colour (754 RGB)	TM band intensities			Spectral slope		Dominant mineralogy controlling spectral response
		4B	5G	7R	TM 4 to 5	TM 5 to 7	
Pillow lavas	magenta-pink	M	L	H	mod. -ve	steep +ve	epidote, chlorite, magnetite, Fe^{2+}, Fe^{3+}
Sheeted dyke	red-orange-purple	M	L	H	steep -ve	steep +ve	chlorite, epidote, amphiboles, Fe^{3+}, plagioclase
Isotropic gabbro	red-orange	L	M	H	steep +ve	steep +ve	plagioclase, amphiboles, OH, Fe^{2+}, Fe^{3+}
Cumulate gabbro	yellow-green-(cyan)	M-H	M	L-M	steep -ve	mod. -ve	plagioclase, cpx, opx, OH, Fe^{2+}
Cumulate peridotite	cyan-green	H	L	L	steep -ve	weak +ve	serpentine, magnetite, opx, cpx, plagioclase
Harzburgite	bright yellow-green	L	H	M	steep +ve	steep -ve	olivine, serpentine, Fe
	dark green-blue	L	M	M	mod. +ve	weak -ve	olivine, opx, serpentine,FE, mafic minerals
	red-purple	M	L	M	steep -ve	mod. +ve	olivine, serpentine, magnetite
Dunite	blue-pink	H	M	L	steep -ve	mod. -ve	olivine, serpentine, chromite, (opx), (cpx)
Wehrlite	dark blue-purple	L	L	L	v.weak -ve	weak -ve	olivine, opx, serpentine, magnetite
Trondhjemite	bright white-pink	H	H	M	weak -ve	mod. -ve	plagioclase, quartz, amphiboles, low Fe, clays?
Isotropic gabbro + dykes	yellow-orange	L	M-H	H	v.steep +ve	mod. +ve	mixture of; plagioclase, amphiboles, OH, Fe^{2+}, Fe^{3+}, epidote, chlorite, cpx
Cumulate gabbro + dykes	orange-pink	H	L	H	steep -ve	steep +ve	mixture of; plagioclase, cpx, OH, Fe^{2+}, epidote, chlorite
Cumulate gabbro + trondhjemite	pink-brown	H	M	L	steep -ve	steep -ve	mixture of; plagioclase, cpx, OH, Fe^{2+}, quartz, amphiboles, clays?
Pyroxenite	green-blue	L	H	L	steep +ve	v.steep -ve	cpx, opx, ol, Fe^{2+}, Fe^{3+}

Table 5.9 Summary of the TM 754 decorrelation stretched image colours of 13 mappable units within the Maqsad study area. Relative band reflectance levels are shown, were L=Low, M=Moderate and H=High. Dominant mineralogy of each lithology also summarised.

Maqsad - TM 754 Decorrelation Stretched

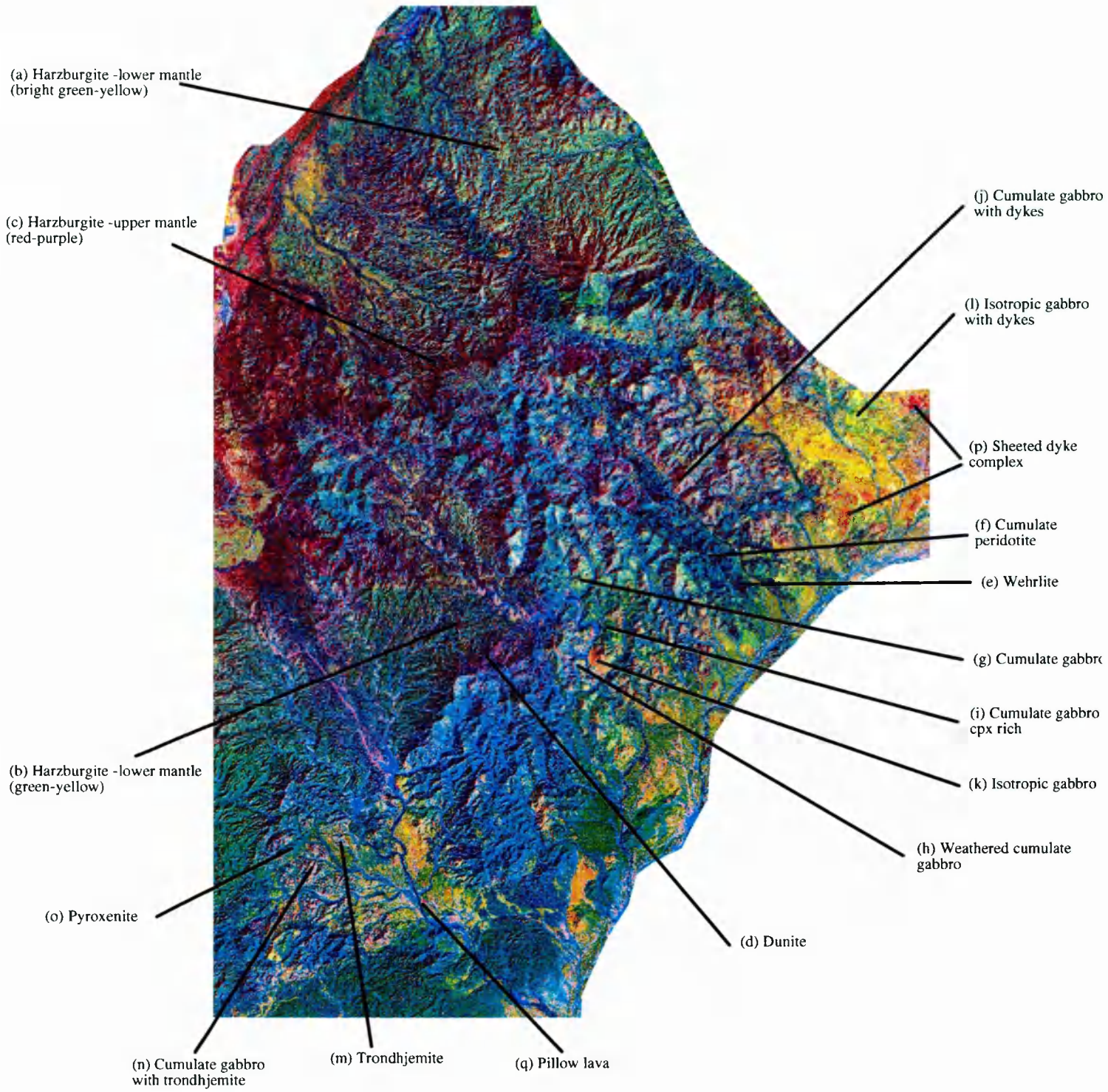

Plate 5.35 TM 754 decorrelation stretched composite of the entire Maqad study area (see Figure 5.1). Labels indicate major lithologies. Refer to text for a full description.

Dunite is just about distinguishable on the TM 754 composite as a blue-pink colour (Plate 5.35 (d)). Spectrally dunite is very similar to harzburgite (Figure 4.29 (a) - M022) because of the similar mineralogy, although the overall albedo of dunite tends to be slightly higher. Increasing serpentine causes the reflectance spectrum to steepen between TM 5 and TM 7 (Figure 4.29 (a) - M047). Wehrlite which occurs as cumulate peridotite or as a late intrusive is reasonably distinct on the TM 754 composite (better at screen resolution, see Plate 5.41) in a very dark blue-purple colour (Plate 5.35 (e)). Wehrlite is mineralogically similar to the serpentinised harzburgites, hence the similar image colour. Wehrlites tend to have a far greater magnetite content, resulting in the lithology having a very low overall albedo making it appear dark on the image. Because of the low albedo the reflectance spectra (Figure 4.29 (a) -M054 and M037) are almost flat, although the spectral influence of serpentine is seen in weak absorptions in TM 7. Whilst the low albedo makes this unit spectrally distinct it can cause some discrimination problems in areas of dark shadow. Areas of cumulate peridotite have a cyan-green colour (Plate 5.35 (f)) due to the mixture of spectrally bright gabbro lithologies and spectrally dark wehrlite.

2) Crustal Sequence

Cumulate gabbro appears yellow-green(-cyan) on the TM754 image (Plate 5.35 (g)). Typically cumulate gabbro shows increasing reflectance from TM 4 to TM 5 to TM 7 (Figure 4.30 (a) -M201). The steepness of the spectrum between TM 4 and TM 5 is controlled by the strength of the ferric iron absorptions, associated with the weathered surface. These affect TM 4 to varying degrees. Very heavily weathered (dark red-brown) surfaces result in very strong absorptions in TM 4, causing the outcrop to appear bright yellow (Plate 5.35 (h)) on the TM 754 composite. Mineralogical variations in the gabbros, primarily those associated with orthopyroxene (opx) and clinopyroxene (cpx) percentages result in variations in the TM 5 reflectance values. Gabbros rich in cpx have a reflectance peak in TM 5 (Figure 4.30 (a) -M246) causing them to appear bright green (Plate 5.35 (i)), whilst opx rich areas have similar reflectance levels across TM 5 and TM 7, making them appear more cyan-green. The high percentages of plagioclase in the gabbros cause the cumulate gabbro units to have a high overall albedo, compared with mantle lithologies. The occurrence of wehrlite within cumulate gabbro reduces this albedo and causes the unit to appear more cyan - blue on the imagery. Areas of cumulate gabbro with a high percentage of dyke material appear an orange-pink (Plate 5.35 (j)) colour, due to relatively high reflectances in TM 4 and TM 7 compared with TM 5. Increased amounts of epidote and chlorite in the dykes cause this variation along with less intense ferric iron absorptions in TM 4.

Isotropic gabbro is fairly distinct in red-orange (Plate 5.35 (k)) although it can be quite similar to some areas of cumulate gabbro, depending on the mineralogy and the intensity of the surface iron absorption affecting TM 4. Typically isotropic gabbros show increasing reflectance from TM 4 to TM 5 to TM 7 (Figure 4.30 (a) -M235). Overall reflectance levels tend to be slightly higher than those associated with cumulate gabbro. Dyke-rich areas of isotropic gabbro are quite hard to identify because they occur in a yellow-green colour (Plate 5.35 (l)), very similar to that of cumulate gabbro. The lithology with the highest albedo is that of felsic trondhjemite. This lithology appears a very bright white-pink colour (Plate 5.35 (m)) due to very high reflectance across all three channels, although there is a slight decline from TM 4 to TM 5 to TM 7 (Figure 4.30 (a) -M317). This lithology is almost completely free from weathering related iron absorptions. Unfortunately the infrequent occurrence and small size of trondhjemite outcrops within the Maqsad area make them very hard to detect on the imagery, despite their distinct colour and spectral response. Areas of cumulate gabbro with a high percentage of trondhjemite can be detected more easily in a pink-brown colour (Plate 5.35 (n)). The occurrence of sufficient trondhjemite intrusions causes the cumulate gabbro to have a higher albedo, resulting in high reflectance in TM 4 decreasing across TM 5 and TM 7. The strength of the absorption in TM 7 is related to hydroxyl features caused by the alteration of plagioclase to clay. Pyroxenite is another intrusive unit which is fairly distinctive due to its high reflectance in TM 5 (Figure 4.30 (a) -M347). Pyroxenite unites appear a bright green (Plate 5.35 (o)) colour, very similar to that of cpx rich cumulate gabbro. Differentiating between these two lithologies can be difficult.

Outcrops of sheeted dykes are quite distinct on the TM 754 composite in shades of red-orange-purple (Plate 5.35 (p)). This lithology has quite low reflectance levels in TM 4 due to large iron absorptions at visible wavelengths. There is usually a steep increase in reflectance between TM 4 and TM 5, whilst TM 5 to TM 7 is variable from flat to moderately negative (Figure 4.31 (a) - M336). This is due to the varying mineralogy; epidote causes TM 7 to be quite high, whilst clay minerals associated with weathering cause absorptions. Pillow lavas due to their similar mineralogy to sheeted dykes appear magenta-pink (Plate 5.35 (q)). They broadly exhibit similar spectral characteristics although the occurrence of magnetite can cause reflectance to be quenched.

Overall the band combination of TM 754 produces an image where the majority of the ophiolite lithologies are distinct. This is due to the three chosen bands being located at

spectrally distinct parts of the spectrum. TM 7 is detecting primarily hydroxyl absorptions, TM 5 variations in the reflectance maximum and TM 4 variations in the strength of iron absorptions. Despite these three channels detecting distinct absorption features the similar mineralogy of some of the ophiolite lithologies causes similarities in colour to occur on the final image. This makes it difficult to distinguish lherzolite from harzburgite, dunite from harzburgite and cumulate peridotite from cumulate gabbro. Lithological discrimination on this composite approximates to that expected of TM data based on the analysis of convolved lab and extracted image spectra, as summarised in Tables 4.2 and 4.3. The only discrepancies are that dunite is harder to discriminate than expected and cumulate gabbro is easier.

5.5.2 Spectral interpretation of OPS 852 image

Plate 5.36 shows a false colour composite of OPS 852 of the Maqsad study region covering exactly the same area as Plate 5.35. The OPS channels comprising this composite have been cleaned using the FFT techniques described in chapter 3. The major lithological units which can be distinguished and mapped on this image are summarised in Table 5.10. The colours associated with each lithology on the OPS composite are broadly similar to those on the TM composite because of the approximately equivalent band combination. The spectral characteristics of each unit are described below :

1) Mantle sequence

The mantle sequence on the OPS composite appears in two distinct colours; green-yellow and red-purple. The green-yellow harzburgite can be further divided into bright and dull green-yellow as on the TM data. The bright green-yellow harzbugites (Plate 5.36 (a)) have a very similar spectral response across OPS 852 as across TM 754. Reflectance is highest in OPS 5 (Figure 4.29 (b) - M046) which is dominated by the olivine peak at 1.7 μm. The duller green-yellow harzburgites (Plate 5.36 (b)) have lower reflectance in OPS 8 than TM 7, suggesting that OPS 8 is responding to variations in serpentine content. Reflectance across OPS 2 and OPS 5 is flatter due to the influence of opx (Figure 4.29 (b) - M268). The spectral response of the red-purple harzburgites (Plate 5.36 (c)) is broadly similar to those on the TM composite, and their distribution corresponds to the upper mantle (as seen on Plate 5.34) A slight difference is that some areas within the red-purple harzburgites appear more blue-red (Plate 5.36 (d)). These regions exhibit higher reflectance in OPS 2 and lower reflectance in OPS 8

Mappable unit	Image colour (852 RGB)	OPS band intensities			Spectral slope		Dominant mineralology controlling spectral response
		2B	5G	8R	OPS 2 to 5	OPS 5to 8	
Pillow lavas	pink-red-brown	H	H	L	weak +ve	steep -ve	epidote, chlorite, magnetite, Fe^{2+}, Fe^{3+}
Sheeted dyke	purple-blue	H	L	M	steep -ve	steep +ve	chlorite, epidote, amphiboles, Fe^{3+}, plagioclase
Isotropic gabbro	orange-brown	L	M	H	steep +ve	steep +ve	plagioclase, amphiboles, OH, Fe^{2+}, Fe^{3+}
Cumulate gabbro	yellow-orange-brown	L	M	H	steep +ve	steep +ve	plagioclase, cpx, opx, OH, Fe^{2+}
	yellow	L	M	H	steep. +ve	steep +ve	
	green	L	H	M	steep +ve	mod. -ve	
Cumulate peridotite	cyan-green	M	H	L	v.weak +ve	steep -ve	serpentine, magnetite, opx, cpx, plagioclase
Harzburgite	yellow-green	L	M	L	steep +ve	v.steep -ve	olivine, serpentine, Fe
	bright yellow-green	L	H	M	v.steep +ve	steep -ve	olivine, opx, serpentine,FE, mafic minerals
	red-purple	H	L	M	steep -ve	mod. +ve	olivine, serpentine, magnetite
	blue-purple	H	L	L	steep -ve	mod. +ve	
Dunite	pink-blue, dark blue	H	M	M-L	steep -ve	steep +ve	olivine, serpentine, chromite, (opx), (cpx)
Wehrlite	dark blue-purple	M	L	L	mod. -ve	weak -ve	olivine, opx, serpentine, magnetite
Trondhjemite	bright pink-white	H	M-H	H	steep -ve	mod. +ve	plagioclase, quartz, amphiboles, low Fe, clays?
Isotropic gabbro + dykes	red-yellow-brown	H	L	H	steep -ve	steep +ve	mixture of; plagioclase, amphiboles, OH, Fe^{2+}, Fe^{3+}, epidote, chlorite, cpx
Cumulate gabbro + dykes	pink-(red)-brown	L	L	H	v.weak +ve	v.steep +ve	mixture of; plagioclase, cpx, OH, Fe^{2+}, epidote, chlorite
Cumulate gabbro + trondhjemite	pink-brown	H	L	M	steep -ve	steep +ve	mixture of; plagioclase, cpx, OH, Fe^{2+}, quartz, amphiboles, clays?
Pyroxenite	green	M	H	L	mod. +ve	mod. -ve	cpx, opx, ol, Fe^{2+}, Fe^{3+}

Table 5.10 Summary of the OPS 852 image colours of 13 mappable units within the Maqsad study area. Relative band reflectance levels are shown, were L=Low, M=Moderate and H=High. Dominant mineralogy of each lithology also summarised.

Maqsad - OPS 852 False Colour Composite

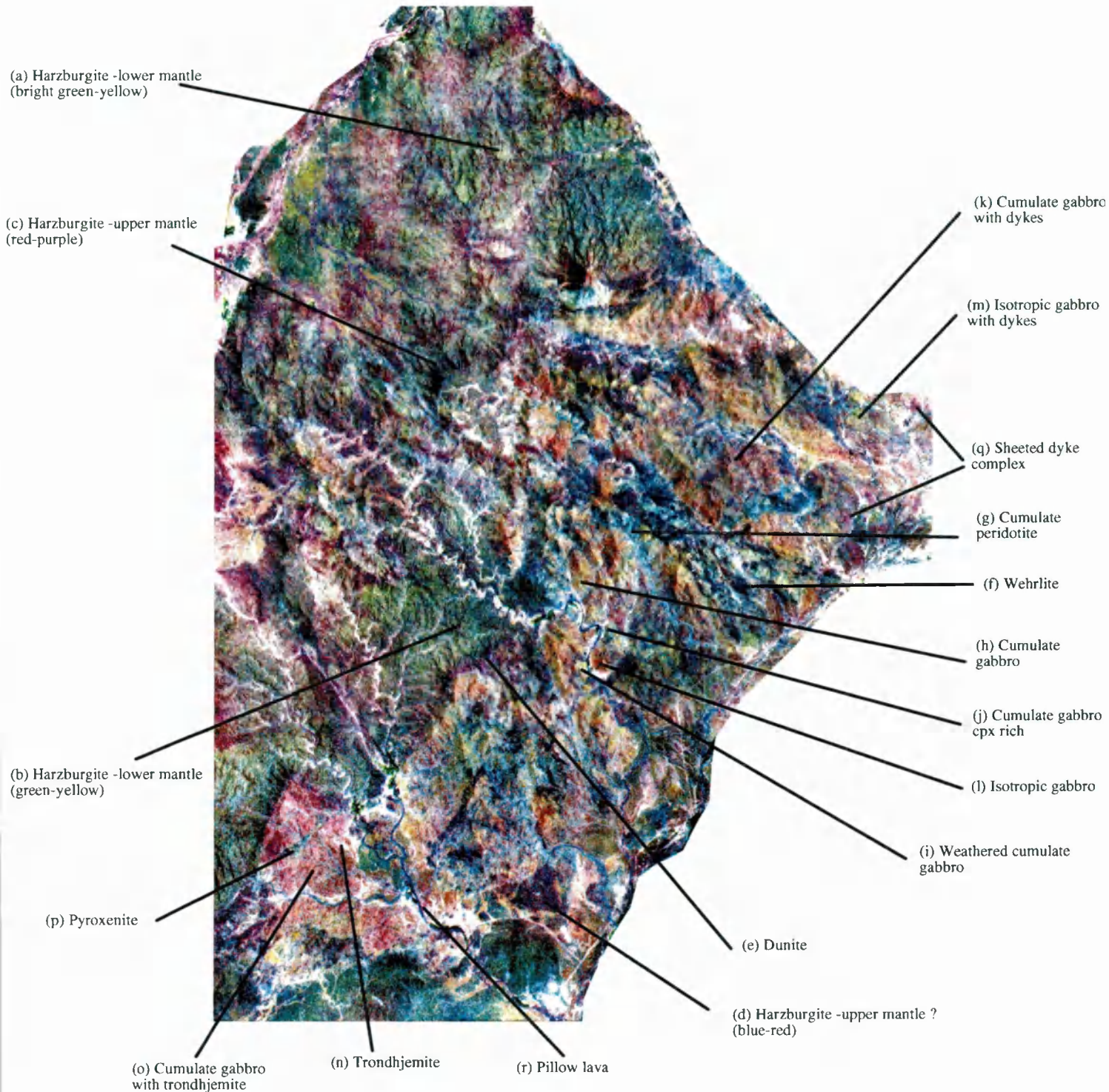

Plate 5.36 OPS 852 colour composite of the entire Maqad study area (see Figure 5.1). Labels indicate major lithologies. Refer to text for a full description.

than the red-purple areas. The low reflectance in OPS 8 is probably due to increased serpentine whilst the higher reflectance in OPS 2 may be caused by increased opx. Field checks have shown that some of the blue-red areas within the harzburgite appear to contain more opx, although this is not always the case.

Compared with the TM composite dunite is spectrally distinct on the OPS 852 composite. The overall spectral shape across OPS 852 is the same as that across TM 754 (low, medium and high reflectance, respectively), but the reflectance in OPS 2 is far higher than that in TM 4. In fact it is higher than that seen in the lab based spectra in Figure 4.29 (b) -M022. Coupled with the lower reflectance values in OPS 8 this causes dunite to appear a very bright blue-lilac colour (Plate 5.36 (e)). At one locality dunite appears a darker blue. This darker colouration may be due to the addition of mafic minerals (e.g., chromite) which have caused the reflectance levels across all the channels to be quenched. The darkest blue tone on the composite relates directly to cumulate and intrusive wehrlite. Wehrlite bodies appear a very dark blue-purple colour on the imagery (plate 5.36 (f)), due to their low reflectance levels across all three channels (Figure 4.29 (b) -M054), although reflectance levels in OPS 2 tend to be slightly higher than those seen in OPS 5 and OPS 8. Wehrlite is very distinct on the OPS composite because of its very dark nature. The higher sun angle on this OPS composite means that shadows are less severe, preventing difficulties distinguishing wehrlite from shadows (as in the TM imagery). Cumulate peridotite is also very distinct on the OPS composite in a light cyan-green colour (Plate 5.36 (g)). This lighter colour is due to the higher reflectance in OPS 2 and OPS 5. Reflectance is still low in OPS 8 as a result of strong serpentine absorptions associated with the wehrlite.

Cumulate gabbro is a very distinct colour on the OPS composite; yellow-orange-brown (Plate 5.36 (h)) as opposed to yellow-green(-cyan) on the TM 754 composite. Areas of cumulate gabbro tend to show a lot of colour variation ranging from golden brown through to a deep red-brown. These colour variations are directly related to the strength of iron absorption features affecting OPS 2. Typical reflectance levels in OPS 2 (low- medium intensity) result in the yellow-brown colour, whilst medium-high intensities cause the more red-brown colours. Very high iron absorptions in OPS 2 (i.e. dark weathered surfaces) result in bright yellow colours (Plate 5.36 (i)) as in the TM imagery. Despite the variations in reflectance in OPS 2, OPS 5 and OPS 8 always show medium to high reflectance levels for cumulate gabbro (as per Figure 4.30 (b) -M307). An advantage of cumulate gabbro appearing this brighter yellow-brown colour is that it can be easily distinguished from areas of cumulate peridotite. Areas of

cpx rich cumulate gabbro are also distinct in green-yellow (Plate %.12 (j)). This is due to these regions having very high reflectance in OPS 5 (due to cpx) compared to OPS 2 and OPS 8. The intrusion of high quantities of dyke material causes the cumulate gabbro to appear pink-brown (Plate 5.36 (k)). The dyke material along with surface iron absorptions cause both OPS 2 and OPS 5 to have low reflectance values compared with those of OPS 8.

A disadvantage of the yellow-orange-brown colour of cumulate gabbro is that it is very difficult to distinguish it from areas of isotropic gabbro. Isotropic gabbros have a very similar spectral profile, i.e., low in OPS 2 and increasing across OPS 5 and OPS 8 (Figure 4.30 (b) -M235). Unfortunately this results in areas of isotropic gabbro having a very similar orange-brown colour (Plate 5.36 (l)). Like cumulate gabbro the colour of isotropic gabbros can vary a little depending on the strength of the iron absorption affecting OPS 2. Dyke-rich areas of isotropic gabbro are a little easier to distinguish as they appear more yellow-(green)-brown (Plate 5.36 (m)), although they can be confused with areas of cumulate gabbro which exhibit strong iron absorptions. Reflectance levels tend to be reasonably high in both OPS 2 and OPS 8, with OPS 5 depending on outcrop composition.

As on the TM composite, the brightest lithology is trondhjemite, caused by its high felsic content and weak iron absorptions. Trondhjemite appears bright pink-white on the OPS composite (Plate 5.36 (n)). Reflectance levels are very high across all three channels (Figure 4.30 (b) - M317). Variations in amphibole content can result in a minor decrease in reflectance in OPS 5, whilst the weathering of plagioclase can produce hydroxyl related absorptions in OPS 8. Areas of cumulate gabbro rich in trondhjemite intrusions are spectrally distinct from normal cumulate gabbro. The bright nature of the trondhjemite increases the overall albedo of the cumulate gabbro, causing it to appear a pink-brown colour (Plate 5.36 (o)). Variations in the amount of trondhjemite cause the colour of the outcrop to range from orange-brown (low percentage trondhjemite) to bright pink-brown (high percentage trondhjemite). Pyroxenite is another intrusive unit which is distinct in a moderately bright green colour (Plate 5.36 (p)). Like the cpx rich cumulate gabbro this colour is due to the high reflectance levels in OPS 5 (Figure 4.30 (b) -M347).

The sheeted dyke complex is reasonably distinct on the OPS composite, appearing a purple-blue(-brown) colour (Plate 5.36 (q)). This lithology has moderate reflectance levels in OPS 2, but these can be lowered by the occurrence of iron absorptions

associated with the surface weathering. Reflectance tends to drop slightly in OPS 5 before increasing in OPS 8. This is a slightly different response to that expected (see Figure 4.31 (b) - M336). Pillow lavas due to their similar mineralogy appear in a similar pink-red-brown colour (Plate 5.36 (r)). The major minerals controlling reflectance levels are epidote (increasing reflectance in OPS 8) and magnetite (overall decrease in albedo).

The combination of OPS 852 produces an image where lithological discrimination of all ophiolite lithologies are moderate to high. All lithologies can be easily distinguished with the exception of isotropic gabbro and pillow lavas which can be confused with cumulate gabbro and sheeted dykes. The spectral discrimination on the OPS 852 composite appears to be slightly better than that expected based on the analysis of convolved lab spectra and extracted image spectra, as summarised in Tables 4.1 and 4.2. Discrimination of both cumulate gabbro and sheeted dykes appears to be higher than originally anticipated. Comparing the OPS spectral characteristics of the main ophiolite lithologies with those of the TM data, indicates that they are easier to identify and distinguish on the OPS data. This increased spectral discrimination is due to the response of OPS 8 being dominated by hydroxyl absorptions (in particular serpentine), OPS 5 responding to reflectance maxima and OPS 2 responding to varying levels of absorptions associated with surface weathering varnishes.

5.5.3 BRGM geological map of Maqsad

The most recently published maps covering the Maqsad region are those published by the Bureau de Recherches Géologiques et Minières (BRGM), France. The Maqsad region was outside of the area mapped by Open University during its Oman ophiolite mapping project. The Maqsad study region lies on the boundary of four 1:100 000 scale sheets; NF40-3E (Rabu *et al.*, 1986); NF40-3F (Villey *et al.*, 1986); NF40-7B (Hutin *et al.*, 1986a) and NF40-7C (Gramont *et al.*, 1986a). Plate 5.37 is a composite image derived from these four map sheets. This map has been masked to the same area as shown on the TM and OPS composites. The extent of the Maqsad region in this thesis is equivalent to that defined by the Ceuleneer and Amri (Toulouse University) during their 1993-94 mapping work. This boundary was adopted as all field checks were carried out in conjunction with Ceuleneer and Amri. Despite the greatly reduced quality of this composite map (due to the large scale reduction factor) it shows the major lithological divisions as mapped by BRGM.

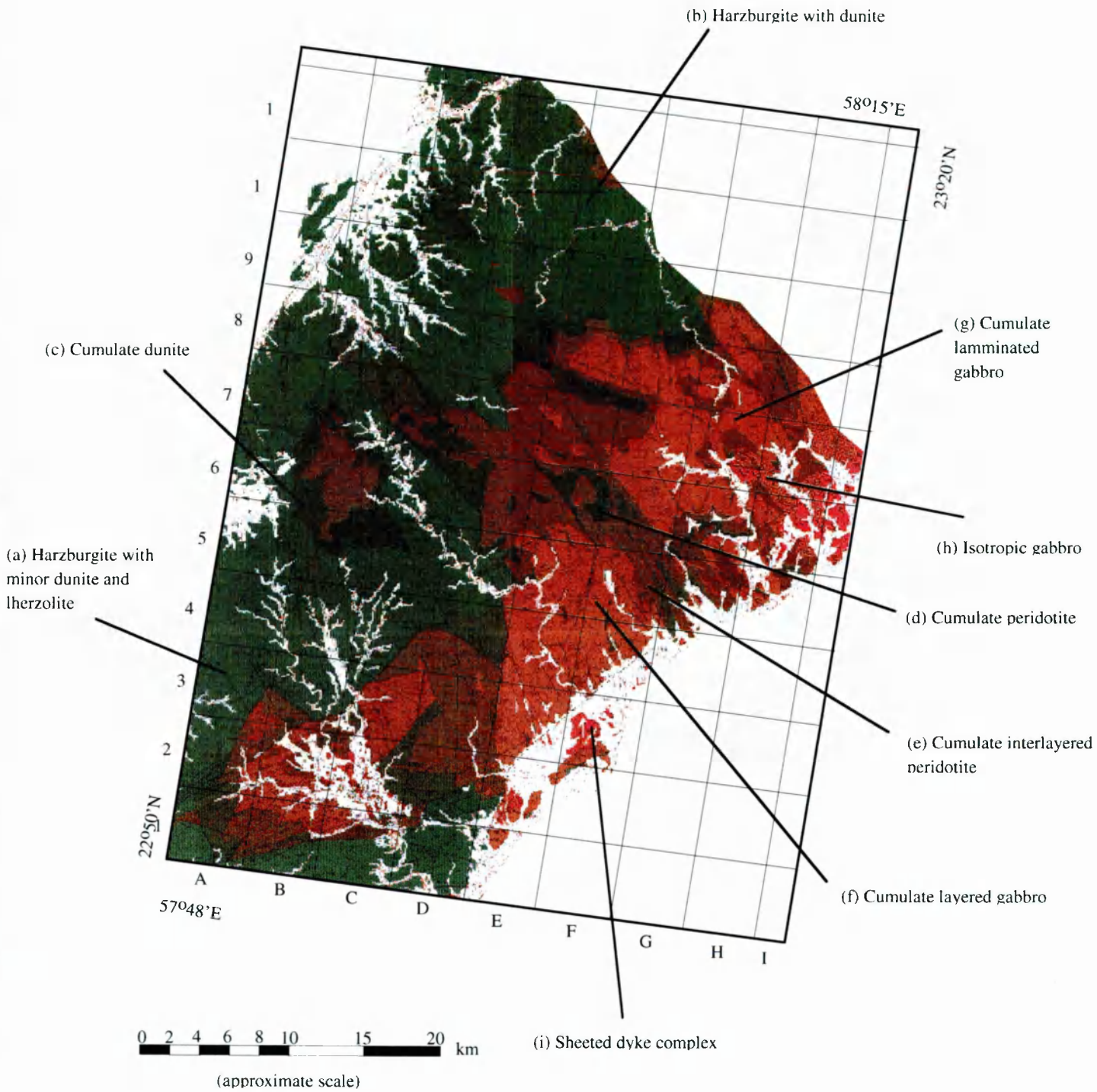

Plate 5.37 Mosaic of four BRGM geological map sheets covering the Maqad study area (see Figure 5.1). Labels indicate major lithologies mapped at 1:100 000 scale. Refer to text for a full description.

Along the western side of the area the mantle harzburgite lithologies are exposed, comprising more than 50% of the project area. This region has been mapped as mainly harzburgite although in places it has been subdivided into harzburgite with minor amounts of dunite and lherzolite (A7) and harzburgite with dunite (E10). Harzburgite with minor dunite and lherzolite (Plate 5.37 (a)) contains small dunite and lherzolite bodies which are too small to map as independent units (Hutin *et al.*, 1986a). This unit is heavily jointed and contains criss-crossing veins of both magnesite and serpentine. At outcrop scale, banding is evident due to alternating 1-3 cm thick opx-rich and dunite-rich layers (Hutin *et.al.*, 1986b). The second unit, harzburgite with dunite (Plate 5.37 (b)), comprises thicker bands of dunite ranging from 1 metre to 10s of metres thick. These dunite pods are usually elongated parallel to the schistosity of the basal part of the nappe (Hutin *et.al.*, 1986a). Field checks have shown that both of these units are very heavily weathered. Some regions on the BRGM map are described as serpentinised harzburgite, these areas relate to the upper mantle and to major fault and fracture zones trending N110°-150° (Gramont *et al.*, 1986b). Interspersed in the harzburgites are discordant dunite bodies up to a 1 km long and several hundreds of metres thick. These units are very distinct in the field because they weather to a very light beige colour and because small (c. 1 metre) caverns form in them. Cumulate sequences from within the crust are exposed mainly in the eastern side of the region, except for cumulate dunite (Plate 5.37 (c)) which occurs extensively in the western and central regions (B5). Cumulate dunite is very similar to that described above. The main cumulate sequence is divided between cumulate peridotite (Plate 5.37 (d)), cumulate peridotite and gabbro (e), cumulate gabbro (f) and cumulate laminated gabbro (g). Cumulate peridotite (primarily dunite and wehrlite) is found throughout the crustal section but tends to directly overlay the mantle sequence. Cumulate peridotite and cumulate dunite have been mapped by BRGM extending through the centre of the Maqsad area (B8 to G5) orientated parallel to the palaeo-spreading ridge (Ceuleneer *et al.*, 1996). Either side of this axis the crustal sequence is dominated by cumulate layered gabbro (e.g., E4 and F7) which grades into cumulate laminated gabbro (G7) towards the top of the sequence (Gramont *et al.*, 1986b). Large isotropic gabbro bodies are also mapped towards the top of the crustal sequence (H7). Finally, Plate 5.37 (i) depicts the sheeted dyke complex along the extreme eastern edge of the region (F3). Pillow lavas are not visible on this reduced version of the map, although the original map shows a small unit located in C2. The original map sheets also show small intrusive bodies such as wehrlite, trondhjemite and dolertic dykes. Despite the greatly reduced quality of Plate 5.37 it serves to indicate the general location of major lithological boundaries known prior to the analysis of the TM and OPS data.

5.5.4 Geological interpretation of TM 754 composite

Geological interpretation was performed directly on a TM 754 decorrelation stretched image (Plate 5.38 (a)), which had been geometrically registered to the BRGM 1:100,000 scale maps. The extent of the imagery is the same as the BRGM map shown in Plate 5.37. The lithological map derived primarily from the interpretation of this image is displayed in Plate 5.38 (b). Some additional images as summarised in section 5.3.6 were also used to refine the identification and discrimination of lithologies difficult to distinguish on the TM 754 (i.e. wehrlite and dunite). However the lithological map will be described with respect to the discrimination seen on the TM 754 composite.

1) Mantle sequence

The mantle sequence is fairly easy to identify on the TM 754 composite as it appears in reasonably distinct colours, although in some places (D1) the green-blue colours of the harzburgites approach those of the cumulate peridotites (D3). Discrimination of the mantle sequence is aided on the TM composite by textural information. The harzburgites tend to be quite heavily eroded which results in a distinct terrain of ridge lines with deeply incised valleys. This texture which is distinct on the TM imagery from that of the crustal sequence which exhibits larger rounded hills. This textural variation between the mantle and crustal lithologies helps to define the boundary between the two, which would be difficult to accomplish in Maqsad using only spectral information.

The mantle sequence on the TM imagery exhibits a wide range of colours. These can be broadly divided into the three primary units as described in section 5.5.2. However placing boundaries between these three units is extremely difficult as spectral changes from one unit to another tend to be gradual. The mantle sequence within Maqsad has been mapped as either lower or upper mantle, with the lower mantle being further subdivided into two units, on the grounds of colour (Table 5.8). These two units are represented on Plate 5.38 (b) as; green (lower mantle 1 - C5) and light green (lower mantle 2 - E10). The third unit (upper mantle - C4) is represented as magenta. This unit occurs on the imagery (Plate 5.38 (a)) as a relatively thin strip (c. 1-1.5 km) along the eastern edge of the mantle sequence, abutting the crustal sequence. Note that the magenta colour associated with the upper mantle has also been used to map areas associated with major fault structures, such as the zone from A6 to B3, relating to the Muqbariah Shear Zone (Ceuleneer 1990). These fault zones are often located away

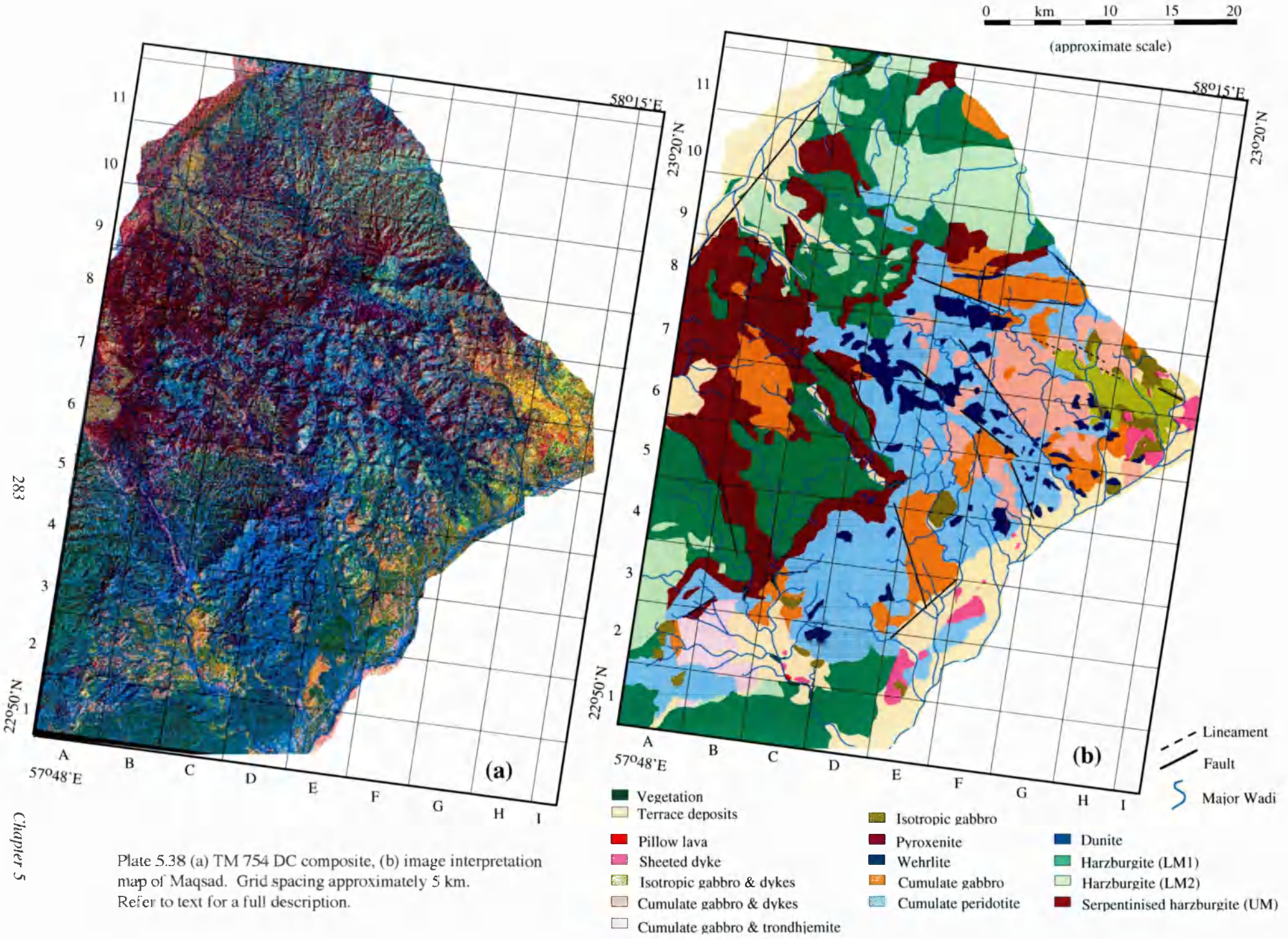

Plate 5.38 (a) TM 754 DC composite, (b) image interpretation map of Maqsad. Grid spacing approximately 5 km. Refer to text for a full description.

from the mantle-crust boundary, but they have a very similar spectral response on the imagery as the upper mantle (Plate 5.38 (a)) due to their similar mineralogy. The lower mantle regions mapped in light green tend to be located towards the north and the south of the region, away from the Maqsad diapir, centred approximately C5-D5, after Ceuleneer *et al.*, 1996.

Comparing the derived mantle map (Plate 5.38 (b)) with the BRGM map (Plate 5.37) the outcrop pattern of the mantle sequence defined by the imagery correlates very highly with that of the BRGM map. The internal structure of the mantle as mapped from the imagery does not correlate so well. This poor correlation is due in part to the fact that the BRGM map does not sub-divide the mantle into upper or lower, instead it is subdivided into harzburgite with minor and major dunite occurrences. Analysis of the original map sheets show a weak correlation between the bright green harzburgite (E10) and the areas mapped as harzburgite with major dunite on the BRGM maps. The BRGM map shows only very small areas equivalent to the upper mantle as defined on the image map (tectonised and serpentinised harzburgites). This may represent an under estimate of the area of the upper mantle on the BRGM map. It is difficult to correlate the boundary defined from the imagery with a boundary on the BRGM map. However, some of the image defined upper mantle areas (Plate 5.38 (b) - C7) do correlate to regions mapped as cumulate dunite (C7) on the BRGM map. This correlation may be due to these regions having increased serpentine associated with the weathering of dunite. This would result in these regions appearing in red on the imagery, as per areas of upper mantle. Dunite is very difficult to distinguish on the TM imagery. Only two small areas have been mapped from the TM 754 composite (D5) and these were located only after they had been initially identified on the OPS imagery (section 5.5.5).

2) Crustal Sequence

The lithological map of the crustal section as defined from the TM imagery (Plate 5.38 (b)) is far more complex than that of the mantle, due mainly to the increased number of units. The largest crustal unit mapped on Plate 5.38 (b) is cumulate peridotite (D3). Cumulate peridotite as mapped from the TM imagery occupies about 60% of the crustal area. This unit tends to correlate with the cumulate peridotite and gabbro unit on the BRGM map (D3), whilst cumulate peridotite on the BRGM map correlates with wehrlite (E6) on the TM map. Comparing the TM map with the BRGM map it would appear that the cumulate peridotite unit mapped from the imagery is too extensive. Despite broadly similar outcrop patterns, cumulate peridotite on the TM map

incorporates some areas mapped as cumulate layered gabbro on the BRGM map, for example F4. This is due partly to the spectral similarities of peridotite and cumulate gabbro on the TM imagery, both units can appear in similar cyan-green colours, resulting in mis-identification. However, field checks in this region have confirmed that the cyan-green colour is caused by numerous wehrlite outcrops, which are not shown on the BRGM map. The locations of the larger wehrlite units mapped on the TM imagery tend to correspond quite well to some of the BRGM cumulate peridotite units, for example E8. However, the correlation is not always as good, i.e., too little wehrlite at D2 and too much at D7. In some places the discrepancies are due to individual wehrlite bodies being mapped on the TM imagery (G5) whilst wehrlite rich zones are shown on the BRGM map (G5).

All areas shown on the TM map as cumulate gabbro (E4) correspond to regions mapped as cumulate layered gabbro on the BRGM map (E4). The TM map shows only about 20% cumulate gabbro whilst the BRGM map shows about 45% , split between cumulate layered and cumulate laminated gabbro. The majority of this difference is due to large areas of cumulate gabbro being wrongly mapped as cumulate peridotite on the image map. This difference can be further reduced if areas mapped on the TM imagery as cumulate gabbro with dykes (F7) are included as these are mapped on the BRGM map as cumulate laminated gabbro.

The region mapped on the TM imagery as cumulate gabbro with trondhjemite (B2) is mapped on the BRGM map as cumulate layered gabbro, although small isolated trondhjemite bodies are also mapped in this region (not visible at scale of map reproduction). Field checks show that there are a few isolated trondhjemite bodies, big enough to be mapped as distinct bodies via field work, but that the majority of the trondhjemite bodies within the cumulate gabbro are too small to be mapped as independent bodies from TM data alone. It is these trondhjemite bodies which give the cumulate gabbro near B2 a distinctive spectral response. I have therefore mapped this area as being distinct from the other areas of cumulate gabbro, although this is not the case on the BRGM map. Some of the isotropic gabbros mapped on the TM imagery are shown on the BRGM map (H7) however others are not (E4-5). Some of these differences are due to isotropic gabbro being mis-identified on the imagery as cumulate gabbro. At location E4-5 field checks confirmed this to be a large outcrop of isotropic gabbro omitted from the BRGM map. The TM map shows a large area of isotropic gabbro with dykes (G7-H7), which was confirmed by field checks, but this area is

wrongly mapped as a mixture of cumulate laminated gabbro, isotropic gabbro and peridotite on the BRGM map.

A small intrusive body of pyroxenite is mapped on both the TM map (B2) and the BRGM map. This unit was initially distinguished on the OPS composite as being unusual, and field checks showed that this area was pyroxenite. The extent of the area was established on the TM imagery using spectral characteristics and additional processing (PCs). A number of small isolated patches of sheeted dyke complex are shown on the TM map (H6), all of these localities correlate very well with those shown on the BRGM map. The only region of dyke complex which was difficult to identify on the TM imagery was that in E2. Originally this was interpreted as isotropic gabbro because of its bright orange response (like the isotropic gabbro in E5), but field checks identified this as an area of heavily weathered dyke complex, with interspersed terrace deposits. One very small area of pillow lava is shown on the TM map (C2). This unit corresponds well to that shown on the BRGM map, although the unit was not distinguished on the imagery until after it had been located in the field.

Overall the TM map is a reasonable approximation to that of the BRGM map, especially with respect to defining the boundary between mantle and crustal sequences. However, some fairly major discrepancies are apparent within the crustal sequence, for example the extent of cumulate gabbro and cumulate peridotite. Some of these differences can be attributed to different subdivisions of lithologies on the two maps, whilst others are due to mis-identification of some units and their boundaries on the TM imagery. Mis-identification can also be caused by some lithologies or mixtures of lithologies having very similar spectral characteristics and hence very similar image colours. However in some cases field checks have shown that spectral variations on the TM image represent features not mapped or wrongly mapped on the BRGM map. These spectral variations represent lithological complexities overlooked on the BRGM map. Analysis of the TM data clearly shows that the crustal section of the Maqsad region is far more complex and inhomogeneous than that shown on the BRGM map. However the spectral and spatial resolution of TM data makes it difficult to determine the exact location of some lithological boundaries without intensive ground checks.

5.5.5 Geological interpretation of OPS 852 composite

Plate 5.39 (a) shows the OPS 852 composite after it has been geometrically registered to the BRGM map sheets, displayed in the same manner as Plate 5.38 (a). The

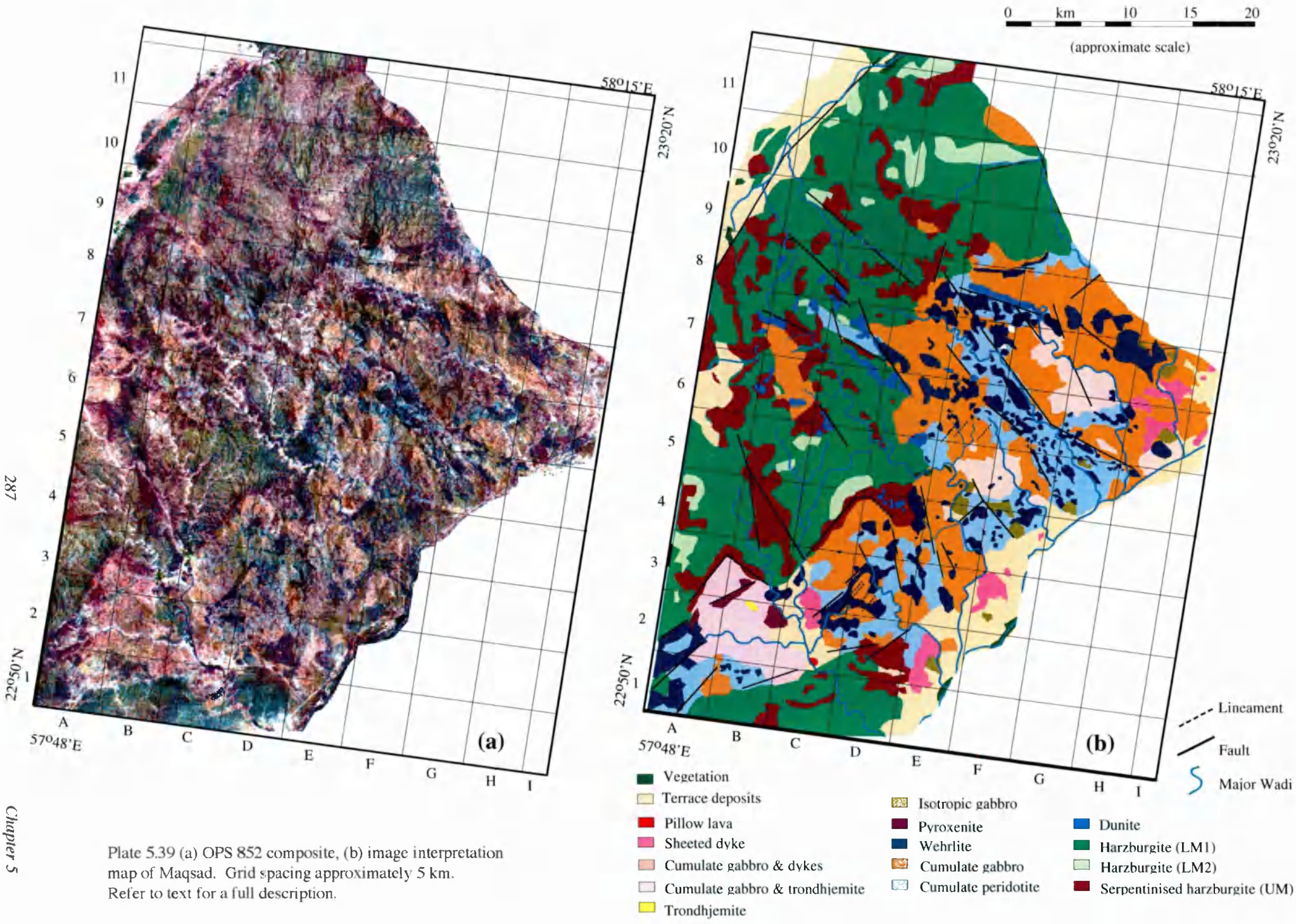

Plate 5.39 (a) OPS 852 composite, (b) image interpretation map of Maqsad. Grid spacing approximately 5 km. Refer to text for a full description.

lithological interpretation map derived from the analysis of the OPS 852 composite is shown in Plate 5.39 (b). Additional OPS composites as discussed in section 5.3.7 were also used to aid the identification of specific lithologies.

1) Mantle sequence

The mantle sequence is reasonably easy to identify on the OPS 852 composite (Plate 5.39 (a)), although some of the colour variations exhibited by mantle lithologies are very similar to colours encountered in the crustal sequence. The distinct texture associated with the mantle lithologies on the TM imagery is not so evident on the OPS composite, and some areas of the mantle sequence even appear entirely without texture (C9) on the OPS composite. This lack of texture is due to; (i) the reduced shadow information caused by the summer acquisition date; (ii) the slightly later local time of image acquisition compared with the TM; (3) initial image quality, in particular dynamic range and image blur and (4) the slight removal of high frequency information during the noise removal operation. This lack of texture means that the boundary between the mantle and crustal sequence is not so obvious in some parts of the OPS composite (C6), as it is on the TM composite.

The overall extent of the mantle sequence as defined from the OPS imagery is almost identical to that of the BRGM map and the TM image map. Like the TM composite the mantle harzbugites have been subdivided into lower mantle units; green (D5) and light green (D10) and the upper mantle; magenta (D9). The majority of the mantle on the OPS map has been mapped in green (D5), equivalent to the BRGM harzburgite with minor dunite and lherzolite. Areas mapped in light green (D10), are possibly equivalent to harzburgite with dunite on the BRGM map, These regions are far less extensive than those mapped on the TM map (Plate 5.38 (b) - D10). This is also true for the areas mapped in magenta (D9) relating to the upper mantle. Purple-red areas within the mantle on the OPS 852 composite (Plate 5.38 (a)) are less extensive and are more isolated, than those seen on the TM. However the location and distribution of these units follow the general trend of those mapped on the TM imagery.

The discrimination of dunite on the OPS 852 composite is far better than on the TM 754 composite. Dunite can be distinguished on the OPS composite as pale blue-lilac areas (C7). The enhanced discrimination of dunite on the OPS composite seems to be due to higher than expected reflectance values in OPS 2. In some instances this spectral response is very discrete and relates directly to small isolated intrusive dunite bodies (D4), whilst on other occasions it relates to zones enriched in cumulate dunite

(C7). Field checks at D4 showed these intrusive dunite bodies to be only a few hundred metres in size. Once these bodies had been identified on the OPS composite, very weak corresponding features at D4 were identified on the TM composite. The correlation between the location of the dunite rich areas identified on the OPS imagery and those mapped on the BRGM map is very good, e.g., C7, although dunite features on the OPS map tend to be more discrete than the continuous cumulate dunite mapped on the BRGM map. One dunite body (D5) was distinguished on the OPS composite in a slightly darker blue, field checks at this locality showed that the outcrop contained isolated pods of chromite, as well as being unusually fresh.

2) Crustal sequence

The OPS lithological map of the crustal section (Plate 5.39 (b)) is far more complex than that defined by the TM imagery. Cumulate gabbro (D7) is the dominant crustal lithology identified on the OPS composite as opposed to cumulate peridotite on the TM composite. This is because it is easier to distinguish cumulate gabbro from cumulate peridotite on the OPS composite. This has resulted in the outcrop pattern for cumulate gabbro correlating much better with that on the BRGM map. However there are still some discrepancies, such as D7 which is cumulate gabbro on OPS map, but cumulate peridotite with gabbro on the BRGM map. Cumulate peridotite is fairly easy to distinguish on the OPS composite (D3) because of its cyan-green colour. However defining the boundary of cumulate peridotite is quite difficult, because localised increases in gabbro content cause the outcrop to appear more orange-brown in colour, it is therefore possible to miss map some areas of cumulate peridotite as cumulate gabbro. In areas of doubt the dominant lithology has been mapped. Overall the outcrop pattern of cumulate peridotite closely matches that of cumulate peridotite with gabbro as shown on the BRGM map, although coverage is not so continuous as that shown on the BRGM map, for example, D3. This is due to the fact that it is very easy to distinguish and map areas of wehrlite on the OPS composite. The wehrlite outcrops (F6) shown on Plate 5.39 (b) can represent either late-stage intrusive bodies or they can represent large outcrops of wehrlite within cumulate peridotite. It is almost impossible to distinguish large cumulate bodies from large intrusive bodies without extensive field checks to establish field relationships. This has resulted in significantly more wehrlite units being identified and mapped on the OPS imagery than on the TM imagery, including some quite small outcrops. Some of the wehrlite bodies mapped on the OPS composite correspond very well to those shown on the BRGM map, e.g., E8 and E6. Overall the BRGM map shows less wehrlite than mapped on the OPS map. Field checks have confirmed the occurrence of both large and small wehrlite units in localities identified on the OPS composite. Despite their large size some

wehrlite outcrops are mapped as cumulate peridotite on the BRGM. The high spatial and spectral resolution of OPS data allows all wehrlite bodies to be mapped as individual features on the OPS map.

Areas of cumulate gabbro with dykes mapped on the OPS composite are less extensive than those on the TM map, they do however occur in the same areas (G7). The corresponding areas on the BRGM map are mapped as either cumulate laminated gabbro or isotropic gabbro. The shape and extent of the area of cumulate gabbro with trondhjemite intrusions (B2) mapped on the OPS is very similar to that defined by the TM composite. Spectral detail within this region is far greater on the OPS image than on the TM and at a larger scale it would be possible to subdivide this region into trondhjemite-rich areas and gabbro-rich areas. The higher spatial resolution of OPS means that one trondhjemite outcrop (B2) is large enough on the OPS composite to be mapped.

Fewer isotropic gabbro (E5) units are shown on the OPS map than on the TM map. This is due to isotropic gabbro on the OPS composite being spectrally similar to cumulate gabbro, therefore making isotropic gabbro units difficult to identify. Correlation of the OPS mapped isotropic gabbros with those shown on the BRGM map is poor. OPS mapped isotropic gabbros appear in the same areas as those on the BRGM map but are not as extensive, e.g., H7. This is a direct result of the spectral characteristic of isotropic gabbro being indistinct from surrounding lithologies. A small area of intrusive pyroxenite is distinct on the OPS composite (B2). This unit corresponds well to that shown on both the TM and BRGM maps. However, this unit is distinct only because it has a high spectral contrast with its background (green against pink-brown). If this unit had occurred elsewhere for example adjacent to harzburgite or cumulate peridotite it may not have been distinguished.

The extent of sheeted dykes mapped on the OPS composite is fairly similar to those on the TM and BRGM map, although in some places the OPS defined outcrops (F3) are more extensive than the TM ones. This is due to it being difficult to distinguish sheeted dykes from associated scree deposits on the OPS imagery. Finally a very small area of pillow lava has been mapped on the OPS composite (C2) as on the TM map. This lithology is very difficult to distinguish on both composites, as a result the boundary as mapped here is mainly based on field knowledge.

5.5.6 Comparison of specific features on TM and OPS composites

In order to give a true indication of the improvement in lithological discrimination offered by an OPS 852 composite compared with a TM 754 decorrelation stretched composite, six enlarged regions from the Maqsad area are examined in Plates 5.40 and 5.41. Each enlarged region represents an area of approximately 7 km square.

Region (a) shows an area of mantle harzburgites ranging in colour on the OPS composite (Plate 5.40) from yellow-green, to dark green to dark magenta. These major colour changes are also visible on the TM composite (Plate 5.41 (a)) with the exception of the light yellow-green zone visible in the centre of the OPS image. Field checks in this area have confirmed that increased serpentine is responsible for the red colouration, but no explanation was found for the light yellow green-zone, visible only on the OPS imagery. Further field work will be carried out by Ceuleneer to try to establish the reason for these spectral variations. The OPS image also clearly discriminates a dunite rich zone in pale blue (lower left corner), a feature not visible on the TM composite. The bright green feature just north of the dunite is a small area of vegetation. Discrimination of the wadi courses is not as easy on the OPS composite despite the higher resolution of OPS data. The BRGM map shows only harzburgite with minor dunite in this region.

Analysis of region (b) on the OPS 852 composite identified an elongated cluster of wehrlite intrusions (dark blue) aligned approximately east-west, within an area of cumulate gabbro (yellow-beige). Field checks confirmed the existence of these features despite them being extremely difficult to distinguish on the TM 754 composite. This area is mapped as cumulate laminated gabbro on the BRGM map. Region (c) on the OPS composite shows a number of large wehrlite bodies (dark blue) located above the palaeo-spreading axis. Some of these wehrlite units appear slightly red-purple, field checks indicate these outcrops to be more serpentine rich. In between these wehrlite bodies the OPS imagery exhibits various shades of pale cyan-blue. These colour variations represent cumulate peridotite with varying amounts of cumulate wehrlite. The darker the blue the higher the percentage of wehrlite. The gradual nature of OPS spectral variations in this region may suggest that there is more of a continuum between wehrlite bodies within cumulate gabbro and later intrusive wehrlite bodies, units previously thought of as distinct. Wehrlite free regions of cumulate gabbro are beige-brown (top right). On the TM composite it is possible to identify the areas of cumulate gabbro (orange-brown) and possibly the serpentine rich

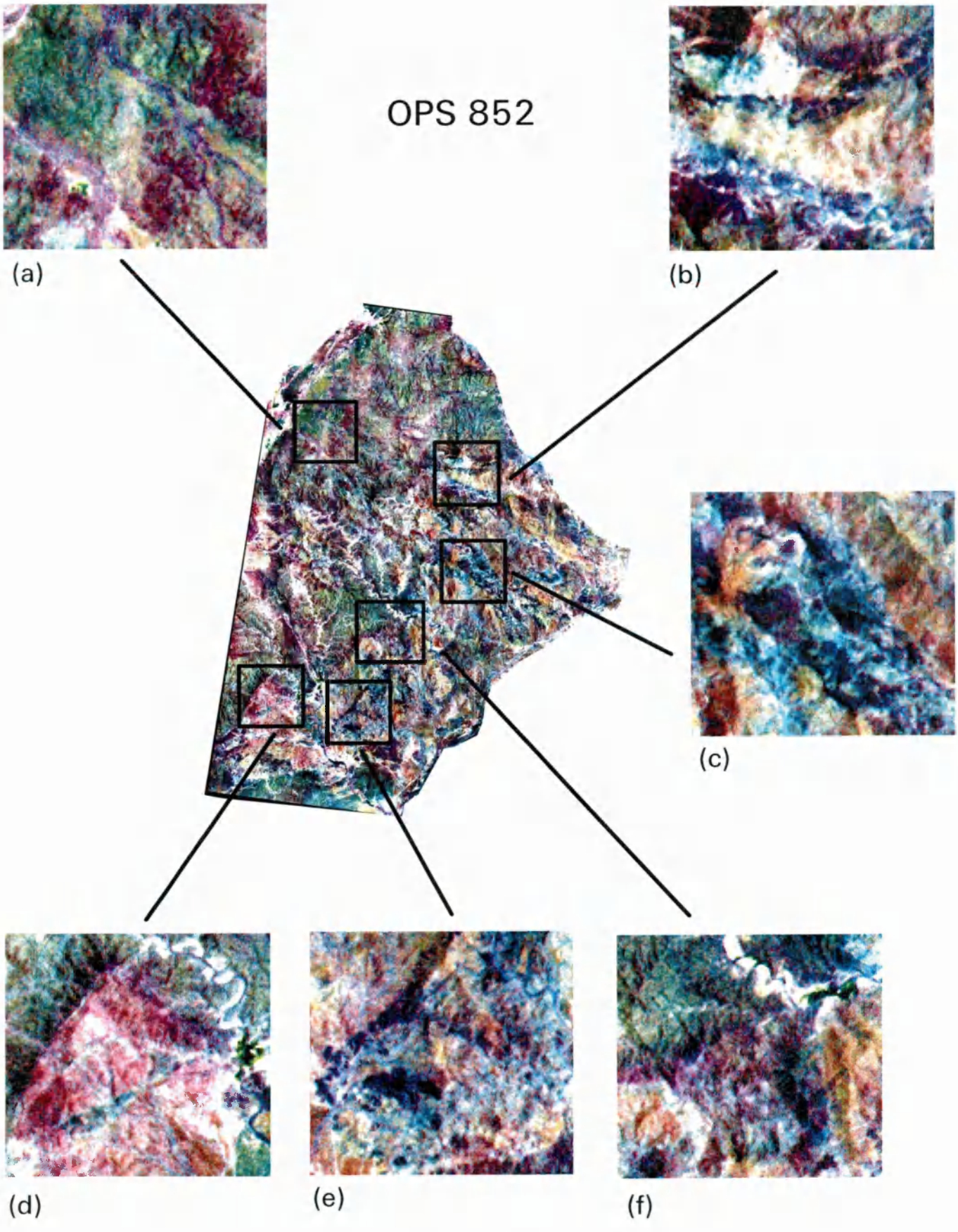

Plate 5.40 Maqsad OPS 852 composite. Enlargements (approximately 8 km square) show specific lithological features. Refer to text for a full description.

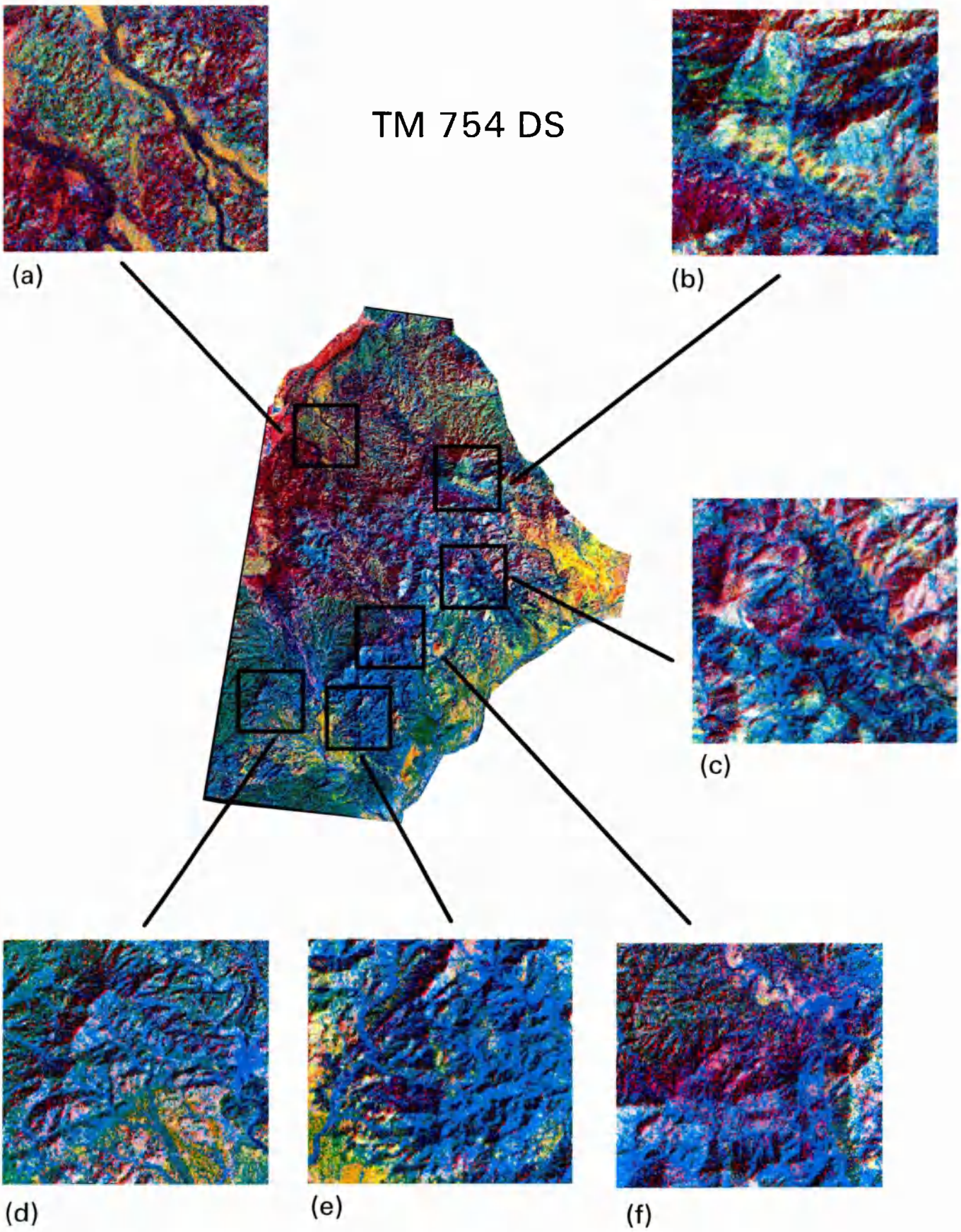

Plate 5.41 Maqsad TM 754 DC composite. Enlargements (approximately 8 km square) show specific lithological features. Refer to text for a full description.

areas of wehrlite (pink-magenta). Cumulate peridotite can be distinguished in dark-cyan blue, but the numerous large wehrlite bodies visible on the OPS composite cannot be distinguished. This region on the BRGM map is shown as predominantly cumulate inter-layered peridotite with outcrops of peridotite. Region (d) on the OPS composite clearly shows the spectrally distinct region of cumulate gabbro with trondhjemite, as mapped on the BRGM map. At this scale spectral variations representing different percentages of cumulate gabbro and trondhjemite are visible. In the centre of this region is a green-blue zone established as an intrusive pyroxenite unit. Discrimination of the equivalent area on the TM composite is extremely poor. On the TM 754 composite it is difficult to establish the extent of the gabbro with trondhjemite unit and almost impossible to identify the pyroxenite unit. This pyroxenite body is mapped on the BRGM map and was confirmed by field checks. Region (f) on the OPS data shows new levels of complexity in this crustal zone not mapped on the BRGM map or visible on the TM data. Increased discrimination on the OPS composite in this region is similar to that seen in (c), mainly the identification of discrete wehrlite units within cumulate gabbro. This area is mapped mainly as cumulate peridotite on the BRGM map, but it can be clearly divided into cumulate gabbro (beige-brown), cumulate peridotite (cyan-blue) and wehrlite (dark blue) on the OPS data. This increased level of discrimination is not possible on the TM imagery.

Finally region (f) illustrates further lithological discrimination on the OPS composite not visible on the TM composite. Region (f) mainly shows the boundary between upper mantle harzburgites (red-purple) and cumulate gabbro (yellow-brown), a boundary which is just about visible on the TM composite. However, within the upper mantle zone the OPS composite clearly shows a number of discrete pale blue-white targets (centre). Field checks confirmed these small spectrally bright targets to be discrete intrusive dunite bodies approximately 300-500 metres in size, within harzburgites. These units are not visible on the TM imagery, although some bright pink anomolies do broadly correlate with the location of these dunite features. The clear identification of dunite is important as it may help to identify new areas of economic importance as chromite deposits are associated with dunite.

5.5.7 Summary of TM and OPS lithological discrimination: Maqsad

Levels of lithological discrimination on the TM 754 decorrelation stretched composite of the Maqsad region, match the levels described for other parts of the Oman ophiolite by Rothery (1987), Abrams *et al.*, (1988) and Pontual (1990). There is also a high

correlation between the colours of the lithologies seen on the Maqsad composite and the ones described by these authors. Overall the TM data provide a reasonable composite, from which a lot of geologically useful information can be derived.

It is very easy to distinguish the mantle sequence from the crustal sequence on the TM imagery, due to distinct variations in texture, as well as spectral variations. The mantle sequence can be divided quite easily into upper and lower units, although the discrimination between these two units is not as clear as it is in some areas of the ophiolite, for example that described by Abrams *et al.* (1988). It appears to be possible to further sub-divide the lower mantle into two spectrally distinct sub-units. However, correlating these units with actual mineralogical variations on the ground has proved difficult. It is generally felt that these variations represent localised changes within the mineralogy and or weathering of the harzbugite.

Lithological identification and discrimination of crustal lithologies is also reasonable, although generally harder than the mantle lithologies. This is due to the similar mineralogy of a number of the crustal units. Similar mineralogy causes different lithologies to appear spectrally similar, making it difficult to distinguish between them at TM resolution. This is a task which is further complicated by weak to moderate surface iron varnishes, affecting gabbroic lithologies. Discrimination between crustal units is also difficult because of the complex distribution and relationships of the lithologies.

Overall it is possible to distinguish and map the majority of ophiolite lithologies within the Maqsad area using a TM 754 decorrelation stretched image. The lithological map produced (Plate 5.38 (b)) broadly corresponds to the existing BRGM map (Plate 5.37). Without reference to this map there is enough spectral information on the TM composite to define the mantle-crust boundary and to map the orientation of a peridotite-rich zone running NW-SE through the crustal lithologies. Problems arise only when trying to locate boundaries between some of the spectrally similar crustal lithologies (i.e., cumulate gabbro and isotropic gabbro). Overall the TM data are capable of producing a reasonable lithological map at a scale of 1:75,000.

Considering the seriousness of the noise structures affecting the OPS data, the OPS 852 composite (Plate 5.39 (a)) used for the lithological interpretation, is of an extremely high quality, due in part to the success of the noise removal techniques applied to the raw data. Spectrally the OPS 852 composite is fairly similar to the TM

754 composite, which explains why some of the lithologies exhibit broadly similar colours. However, the spectral discrimination between lithologies on the OPS 852 composite is generally higher than that seen on the TM composite.

Like the TM data it is possible to distinguish the mantle-crust boundary on the OPS 852 composite reasonably easily, although the reduced textural information on the OPS composite does make it slightly more difficult. Within the mantle sequence it is possible to distinguish upper and lower mantle, although these two units can be further sub-divided. Like the TM data, field checks have proved inconclusive on the reason for these spectral variations. In an attempt to solve this problem Ceuleneer is planning to undertake detailed spectral analysis of the mantle harzburgites using a field portable spectroradiometer. Hopefully this approach used in conjunction with the OPS imagery and lab analyses of samples will help to identify the factor(s) controlling spectral variation.

The crustal map derived from the OPS 852 data (Plate 5.39 (b)) correlates much better with the BRGM map. This is especially true when considering the location and distribution of cumulate peridotite and wehrlite. Because of the ease with which cumulate peridotite and wehrlite can be identified and mapped it has been possible to further refine the extent of the peridotite rich zone related to the palaeo-spreading axis. In fact the ease of discrimination of these lithologies has resulted in significant amounts of wehrlite, in the form of large continuous bodies being mapped off-axis, i.e., D3. Only small amounts of wehrlite are shown in this region on the BRGM map, representing an inaccuracy on the BRGM map.

Dunite is another lithology which is especially easy to distinguish on the OPS composite, but very difficult on the TM composite. This has resulted in a significant zone of dunite extending from the crust into the mantle (B7 to C7) being mapped. This zone corresponds to that mapped by Ceuleneer (1990) as an area of undeformed dunites. Being able to distinguish and map accurately the location of both dunite and wehrlite adds significant amounts of information to the remotely sensed image map. Aside from these lithologies the remainder of the crustal section can be mapped reasonably well on the OPS 852 composite, although like the TM imagery the spectral similarity of some lithologies causes discrimination problems.

Generally the OPS crustal map matches that of the BRGM map. Comparing the TM and OPS derived crustal maps with one produced by Amri (1995) did highlight some

differences. However these differences can be explained by the fact that this map was produced at a much larger scale (1:20,000) by field work and air-photograph interpretation. This allowed Amri to map more lithological sub-units and more structural information than is discernible from satellite imagery. Comparison of the imagery with this map showed that the OPS image was a much better representation of the units mapped by Amri. In fact some boundaries, such as those associated with wehrlite above the spreading axis, matched extremely well. This study showed that it was possible to map lithological boundaries at 1:50,000 scale directly from the OPS imagery, whilst integration with air photography allowed tentative mapping to be made at an equivalent 1:20,000 scale. Plate 5.42 shows an example merge of a 1:20,000 scale air photograph with OPS data. The merge was performed using an ISH transform, to combine the air photography spatial information (intensity component) with the spectral information of OPS 852 (hue and saturation components). Colours on the resultant image are slightly changed from those on the OPS 852 composite, but units such as; cpx rich gabbro, cumulate gabbro with dykes, cumulate gabbro, wehrlite and cumulate peridotite can all be distinguished. Field checks in this area showed that a small wehrlite body (Plate 5.42 - top right corner) discriminated spectrally by the OPS data, covered an outcrop area approximately 60 metres square. This is quite significant because it gives an indication of the true spectral and spatial resolution of the OPS data. If it were possible to check spectral boundaries extensively at this scale a greatly improved lithological map would be derived from OPS data. Integration of OPS spectral data with a DEM derived from the stereo air photographs was also possible. Plate 5.43 shows a perspective OPS drape of the area shown in Plate 5.42, viewed from the northwest corner. This DEM is quite noisy around the edges due to the lack of vertical control at the margins of the stereo overlap region. Despite these noise artefacts this technique provides a good way to correlate OPS spectral features to terrain type and height.

Intentionally left blank

Air photograph and OPS 852 merge

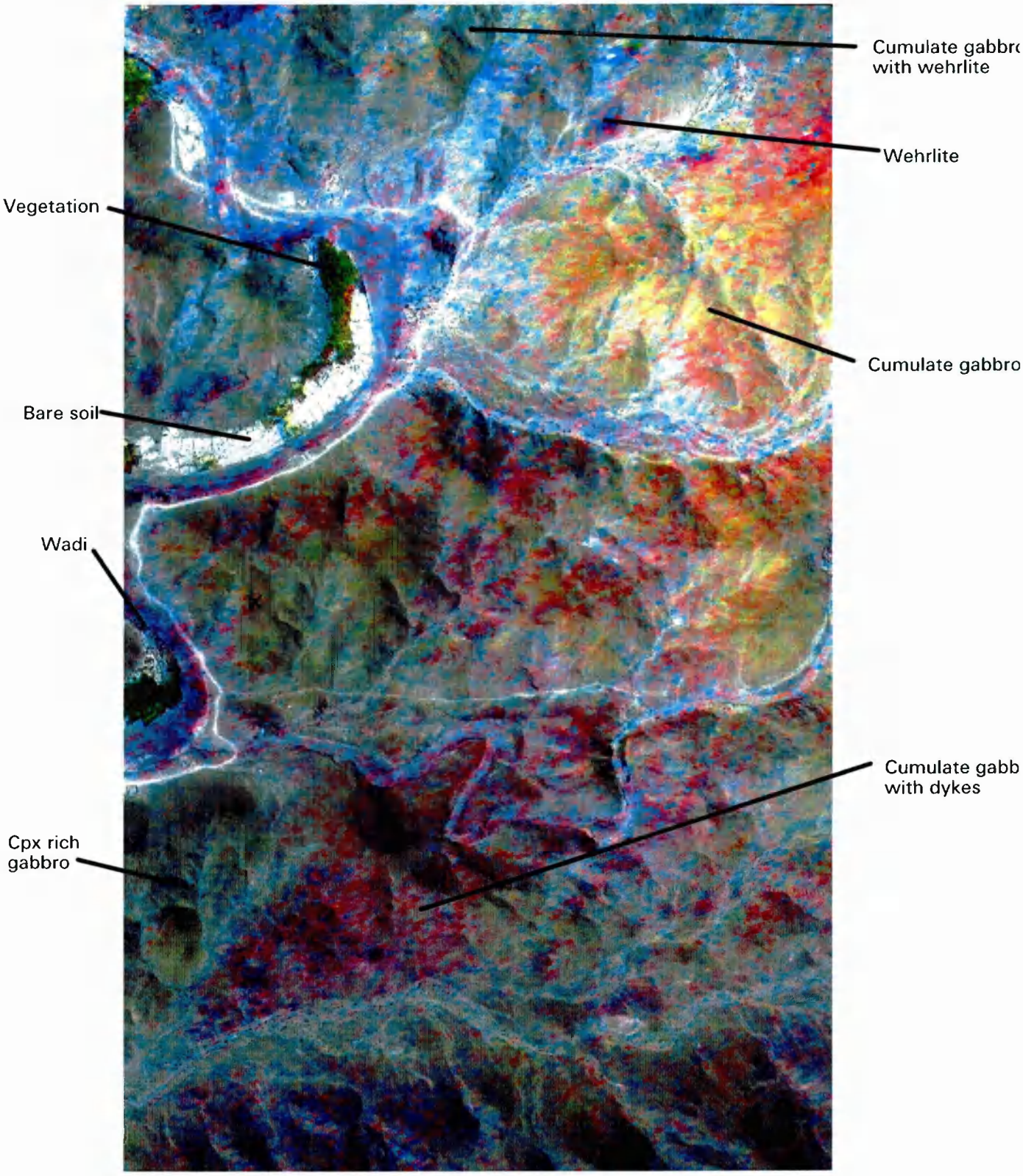

Plate 5.42 Merge of air photograph with OPS 852 composite. Size approximately 2.5 km by 4.0 km. Refer to text for a full description.

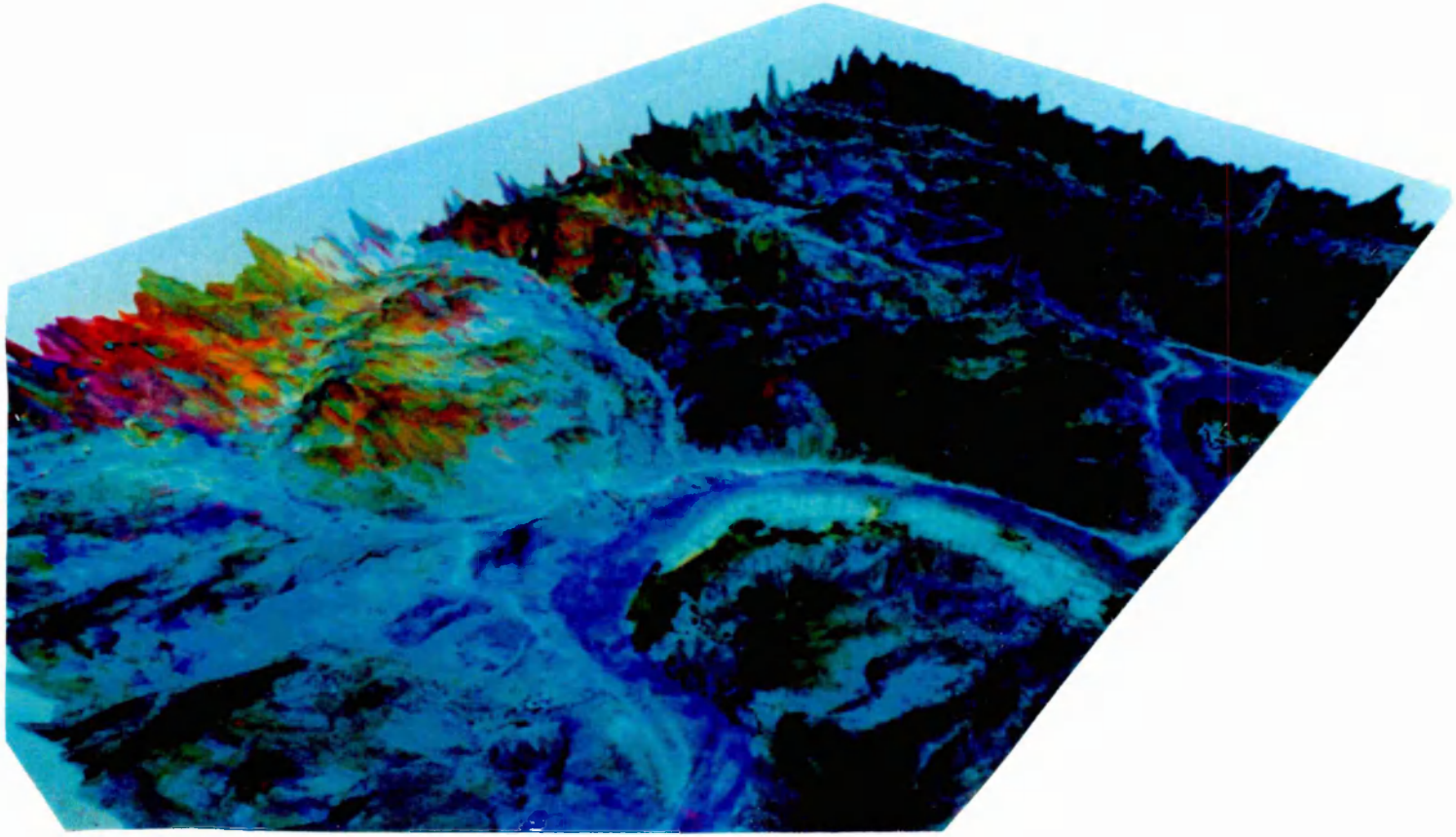

Plate 5.43 Perspective view of OPS 852 draped over DEM derived from stereo air photography. Refer to text for a full description.

5.6 Salahi Study region

5.6.1 An introduction

The second study area used to compare TM and OPS data was in the Salahi block located to the north of Maqsad, see Figure 4.3. This area exhibits very similar lithologies to those encountered in the Maqsad region so they will not be described again. Topography and exposure in this area are almost identical to that in the Maqsad region. This block was mapped as a part of the O.U. mapping project, with the Salahi block being mapped by Lippard (1980) and Lippard and Rothery (1981). This map shows that the strike of the ophiolite sequence is approximately north-south, with mantle lithologies exposed in the western section of the block and crustal lithologies in the eastern side. A transect from west to east would pass through lower mantle, upper mantle, cumulate gabbro and cumulate peridotite, before passing into a well formed sheeted dyke complex. The outcrop pattern of lithological contacts is far simpler than in the Maqsad area.

5.6.2 TM processing

TM imagery of the Salahi block has already been studied by Abrams *et al.* (1988), who concluded that a TM 754 decorrelation stretched image offered the best lithological discrimination of the region. Discrimination on this image was so good it resulted in the O.U. map being revised. Major modifications included the subdivision of the mantle into upper and lower units, the addition of some peridotite bodies within an area mapped as cumulate gabbro and refined boundaries associated with isotropic gabbro. This revision based on TM imagery also resulted in more structural information being added to the map, including the extension of a large fault, initially mapped as discontinuous by Lippard (1980).

5.6.3 OPS processing

OPS imagery of the Salahi block (scene 212-260) were available on two dates with two different gain settings, however the high gain data were severely saturated (as described in section 2.5.3), so only the normal gain data were used in this study. The quality of this imagery was very similar to that of the Maqsad area, with OPS 1 and OPS 3 showing poor dynamic ranges, whilst spectral data in OPS 6 and OPS 7 were severely reduced compared with the other channels. Plates 5.44 (a) to (d) show the

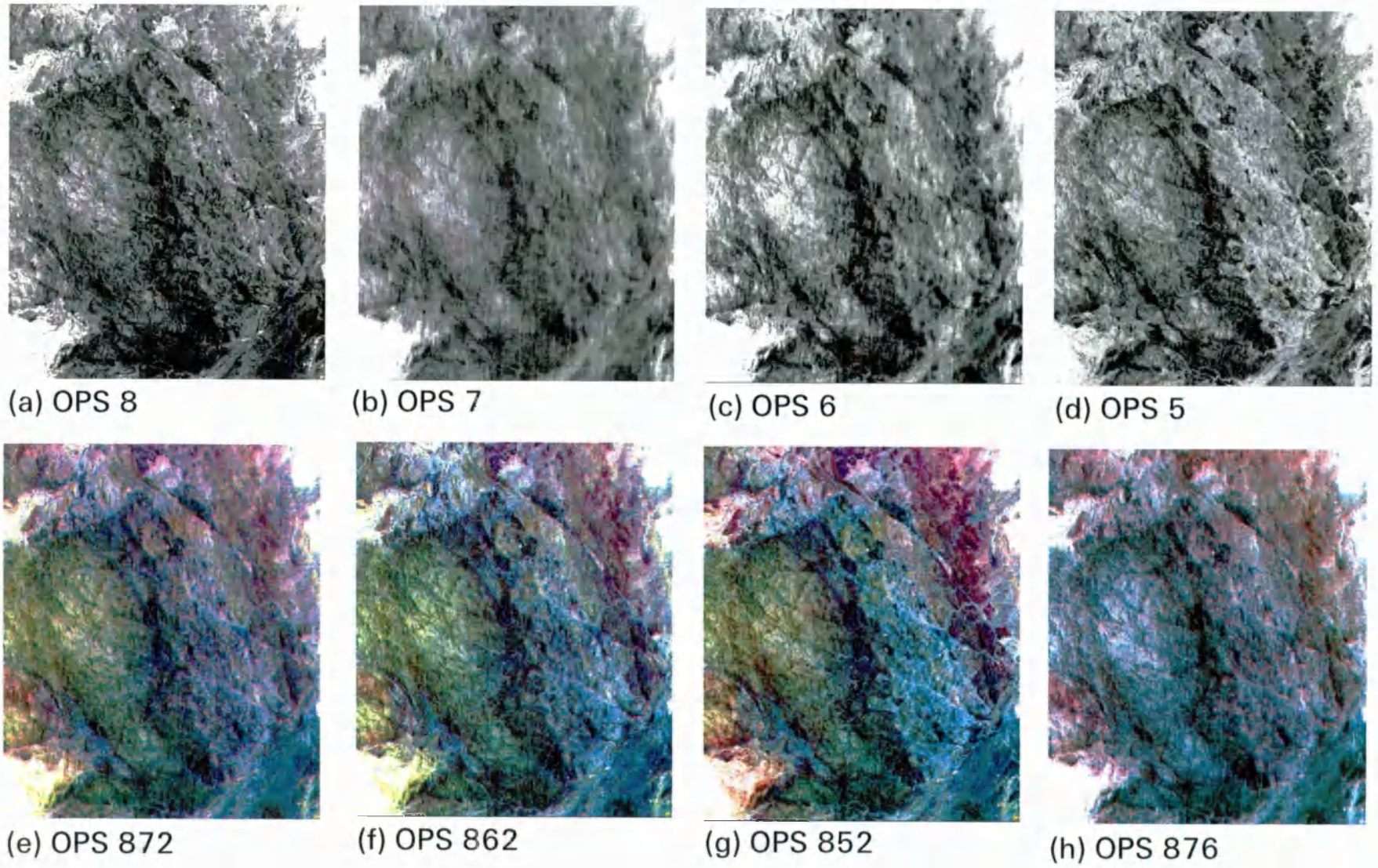

Plate 5.44 Salahi OPS imagery, (a) to (d) single band SWIR channels, (e) to (h) colour composites of SWIR channels. Size approximately 31 km by 37 km. Refer to text for a full description.

four OPS SWIR channels for the Salahi block after they had been cleaned in the frequency domain. Examining these plates it can be seen that OPS 8 and OPS 5 exhibit the best image quality, with OPS 7 and OPS 6 showing reasonable quality (compared with the Maqsad data). Comparing these four plates side-by-side the high degree of spectral correlation between them becomes obvious. This high correlation was predicted by the analysis of convolved lab spectra in section 4.5.1 (see Figures 4.48 (b) and (c). All four plates exhibit low intensities associated with the upper mantle (approximately central in Plate 5.44), whilst some spectral variation can be seen between OPS 8 (a) and OPS 5 (d) in the sheeted dyke complex and pillow lavas (righthand side of image). Combining in turn, OPS 7, OPS 6 and OPS 5 with OPS 8 and OPS 2, produces three very similar colour composite (Plates 5.44 (e), (f) and (g)). Discrimination on these three images is very similar, but the superior quality of OPS 852 is apparent. Combing the three narrow SWIR channels (OPS 8, OPS 7 and OPS 6) results in a very poor image, both in terms of image quality and spectral information. The lack of colour variation on this image confirms the spectral similarity of these channels.

Plate 5.45 (a) is an OPS 852 composite of the entire of the Salahi block, Wadi Jizi is just to the north of the image whilst Wadi Ahin is visible in the south. Because the ophiolite lithologies encountered in this region are mineralogically equivalent to those in the Maqsad region the colours they exhibit on this composite are fairly similar to those on the Maqsad composite. Plate 5.45 shows a large area of mantle lithologies in various shades of green along the lefthand side of the imagery, these represent the lower mantle. The upper mantle is defined by the dark blue-purple zone running almost centrally down the image. This region abuts the crustal section exposed on the righthand side of the image. The crustal section is primarily divided into two major zones; initially a zone of mixed cumulate gabbro (yellow-brown), cumulate peridotite (pale blue-cyan), wehrlite (very dark blue), isotopic gabbro (pink-brown) and secondly a large zone of sheeted dyke complex (brown-red) and finally a zone of lavas (red-magenta). Interspersed within these zones are small areas of trondhjemite (white-pink). A more complete description of these units will be given later. The majority of the image processing techniques tested on the Maqsad data were also applied to these data. The small thumbnail images on Plate 5.45 give an indication of the effectiveness of some of these enhancements. Plate 5.45 (b) is a false colour composite of OPS 256 in RGB. This image shows an enlargement of an area dominated by exposures of very heavily weathered serpentinite. This lithology is discriminated in shades of orange-red on this composite making it more distinct than on the OPS 852 composite. The bright red nature of this lithology indicates that the spectral response of

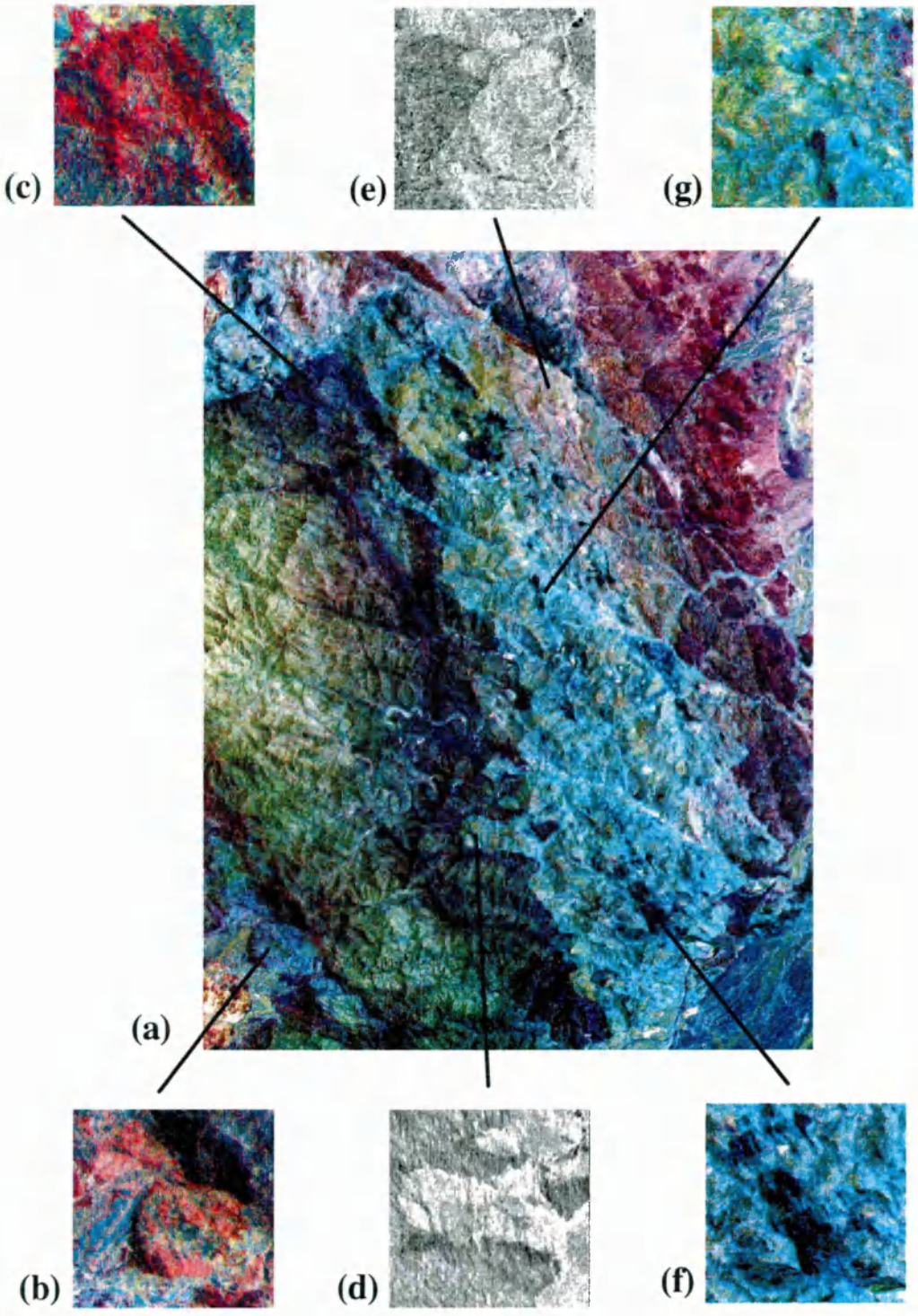

Plate 5.45 (a) OPS 852 composite (same area as Plate 5.44), (b) to (g) various OPS composites of specific features (x2 enlargements). Refer to text for a full description.

serpentinite is far higher in OPS 2 than OPS 5 or OPS 6. This would suggest that OPS 5 and OPS 6 are being affected by a rapid drop in reflectance associated with a large Mg-OH absorption in OPS 8. This idea is supported by varying amounts of red being evident in this region on the OPS 852 (a) composite, indicating that reflectance in this area is being controlled by the strength of serpentine absorptions affecting OPS 8. Plate 5.18 (c) is an extract of an OPS 256 decorrelation stretched image. Like the OPS 256 composite this image very clearly identifies the serpentinite bodies, however the decorrelation stretched image also highlights some parts of the upper mantle in similar colours. This indicates that some parts of the upper mantle are so severely affected by serpentine they exhibit a similar spectral response to that of basal serpentinite units.

Applying a principal component transform to this subscene of data produced interesting results. The most useful PCs were PC 2 (Plate 5.45 (d) and PC 5 (Plate 5.45 (e)). PC 2 very clearly discriminated between crustal gabbros (high PC intensities) and the upper mantle sequence (low intensities), allowing the boundary between the mantle and crust to be mapped very accurately. PC 5 enhanced the boundary between isotropic gabbro (high intensities) and cumulate gabbro (low intensities), allowing intrusive isotropic gabbro to be mapped more precisely. The other PCs did not show any major lithological discrimination.

As for the Maqsad composite the OPS 852 image (Plate 5.45 (a) and (f)) was extremely good at discriminating large wehrlite bodies. These units can be very clearly seen on this composite as discrete bodies scattered throughout the crustal gabbro sequence. This composite also showed reasonable discrimination between cumulate gabbro and cumulate peridotite. However this distinction could be further enhanced by performing a decorrelation stretch on OPS 852 (Plate 5.45 (g)). On the decorrelation stretched image wehrlite remains dark blue, but cumulate gabbro becomes more yellow-green and cumulate peridotite more cyan-blue. These slightly changed colours greatly enhance discrimination between these lithologies.

5.6.4 Comparison of TM and OPS processed imagery

In order to compare the lithological discrimination of TM and OPS data in the Salahi area, a small subscene of data, covering the majority of the lithologies has been extracted for interpretation (Plates 5.46 (a) and (c)). Plate 5.46 (a) is a TM 754 decorrelation stretched composite as described by Abrams *et al.*, (1988), the

Plate 5.46 Subscene of Salahi approximately 10km by 14km. (a) TM 754 decorrelation stretched composite, (b) TM interpretation map, (c) OPS 852 decorrelation stretched composite and (d) OPS interpretation map. Legend gives details of lithological units, full description in text.

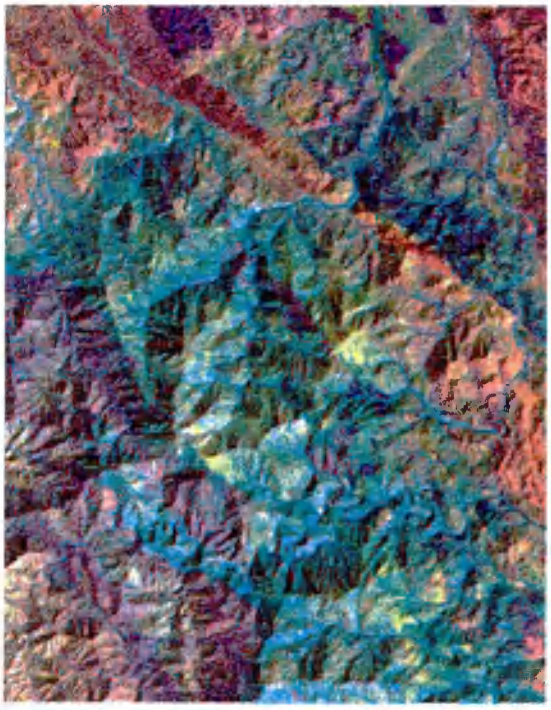

(a)

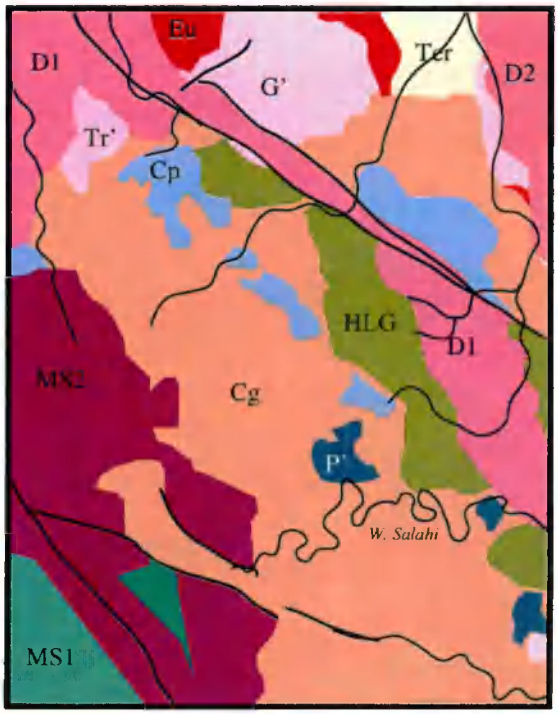

(b)

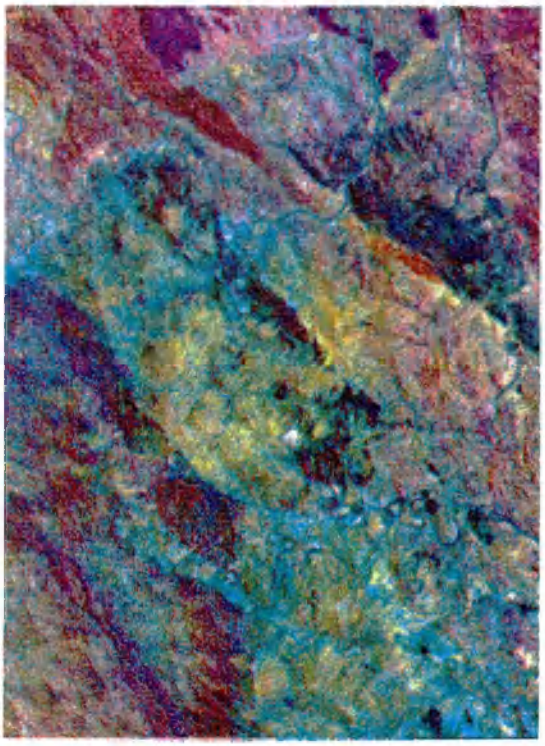

(c)

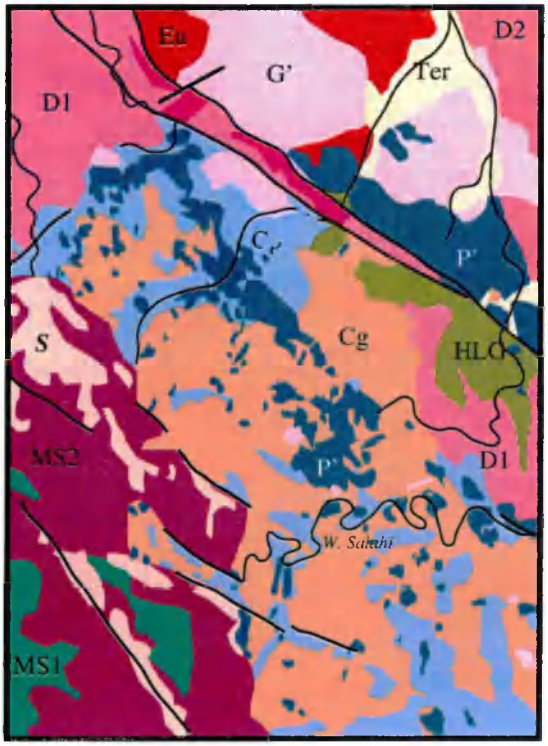

(d)

Ter	Terraces	G'	Felsic gabbro	Cp	Cumulate peridotite
Eu	Extrusives	Tr'	Trondhjemite	Cg	Cumulate gabbro
D1	Dyke complex 1	HLG	High level gabbro	S	Serpentinite
D2	Dyke complex 2	P'	Peridotite	MS1	Lower mantle
				MS2	Upper mantle

corresponding lithological map is shown in (b). This map is an approximation of that produced by Abrams *et al.*, (1988) for this region. Lithological discrimination on this TM 754 image is very similar to that seen on the Maqsad imagery, with most lithologies exhibiting similar colours to those seen earlier. The only slight difference is that isotropic gabbro (referred to as HLG on the map) appears more pink-brown whilst sheeted dykes (D1) appear more orange-brown. The sheeted dyke complex has been subdivided according to Lippard (1986) into a second unit (D2) which appears more magenta-red. D1 represents 30-70% dykes in gabbro whilst D2 represents >70% dykes. Additional lithologies not seen in Maqsad are; felsic gabbro (G') and trondhjemite (Tr').

A decorrelation stretched OPS 852 image is shown in Plate 5.46 (c) for comparison. The colours exhibited on this image are very similar to those on the TM 754 composite. One major difference between these two images is the lack of shadow information on the OPS data. This greatly reduces topographic information. Plate 5.46 (d) shows the lithological interpretation map derived from this imagery, note that the image has been mapped according to the units defined by Abrams *et al.*, (1988). The overall distribution of lithologies on this imagery is broadly equivalent to that seen on the TM map (b), however the OPS map shows more detail. The boundary between mantle and crustal lithologies can be detected equally well on both composites, however the upper mantle on the OPS composite can be further sub-divided into serpentine rich areas. The majority of the differences between these two maps occur within the area mapped as cumulate gabbro. On the TM map this is fairly homogeneous with only a couple of areas mapped as either peridotite or cumulate peridotite. On the OPS data this region is very different as a significant number of peridotite (wehrlite) bodies can be distinguished and mapped. Note how these units occur in a linear zone which is approximately parallel to the mantle-crust boundary. The remaining area is sub-divided between cumulate gabbro and cumulate peridotite. Field checks along Wadi Salahi have shown that this discrimination of the TM mapped cumulate gabbro into cumulate gabbro. peridotite and cumulate peridotite is correct. The OPS 852 imagery also distinguishes a couple of small trondhjemite bodies within this region. The northeast corner of the OPS map is more similar to that of the TM map, except that the OPS data appears to show a large area of wehrlite, which is mapped as cumulate peridotite on the Abrams *et al.*, (1988) map. Discrimination of the two sheeted dyke units on the OPS data is difficult as they are spectrally similar, the boundary of these units with that off felsic gabbro is especially hard to distinguish.

5.6.5 Salahi area summary

The TM 754 composite appears to discriminate the ophiolite lithologies slightly better in this region than in Maqsad, this may in part be due to the simpler structural relationships of the units. However despite the high levels of discrimination on the TM data the OPS data are better still. The OPS 852 composite adds new geological information regarding the extent of serpentinisation within the upper mantle and with respect to sub-dividing the crustal region. Areas previously mapped as cumulate gabbro by Lippard (1980), and Lippard and Rothery (1981), can be clearly divided into large areas of peridotite (wehrlite), cumulate gabbro and cumulate peridotite as shown on Plate 5.46 (d). Discrimination of the other lithologies is approximately equivalent across the two composites, although interpretation of the OPS imagery may improve with additional field checks.

5.7 Fizh study area

5.7.1 Introduction

A third study area from the Fizh block (Figure 4.3) was also used to compare TM and OPS data. The aim of looking at this region was to compare both normal and high gain OPS data with the TM data. Lithologically and structurally the ophiolite complex here is very similar to that seen in the Salahi block, so will not be discussed here. This block was mapped by the O.U. Oman mapping program (Gass *et al.*, 1979).

5.7.2 TM image processing

A TM 754 false colour composite and a TM 754 decorrelation stretched image are shown in Plates 5.47 (a) and (b). Like the other regions studied the discrimination on the TM 754 composite, especially the decorrelation stretched image, is good. All lithologies are distinguished in the colours shown in the other regions.

5.7.3 OPS image processing

The main aim of including this study area was to compare normal gain OPS data with high gain data. Both gain settings were available for scene 212-259 (Fizh area) as per scene 212-260 (Salahi), but unlike the Salahi data the high gain Fizh data were not badly saturated. OPS 6 and OPS 8 were both usable from the high gain SWIR data,

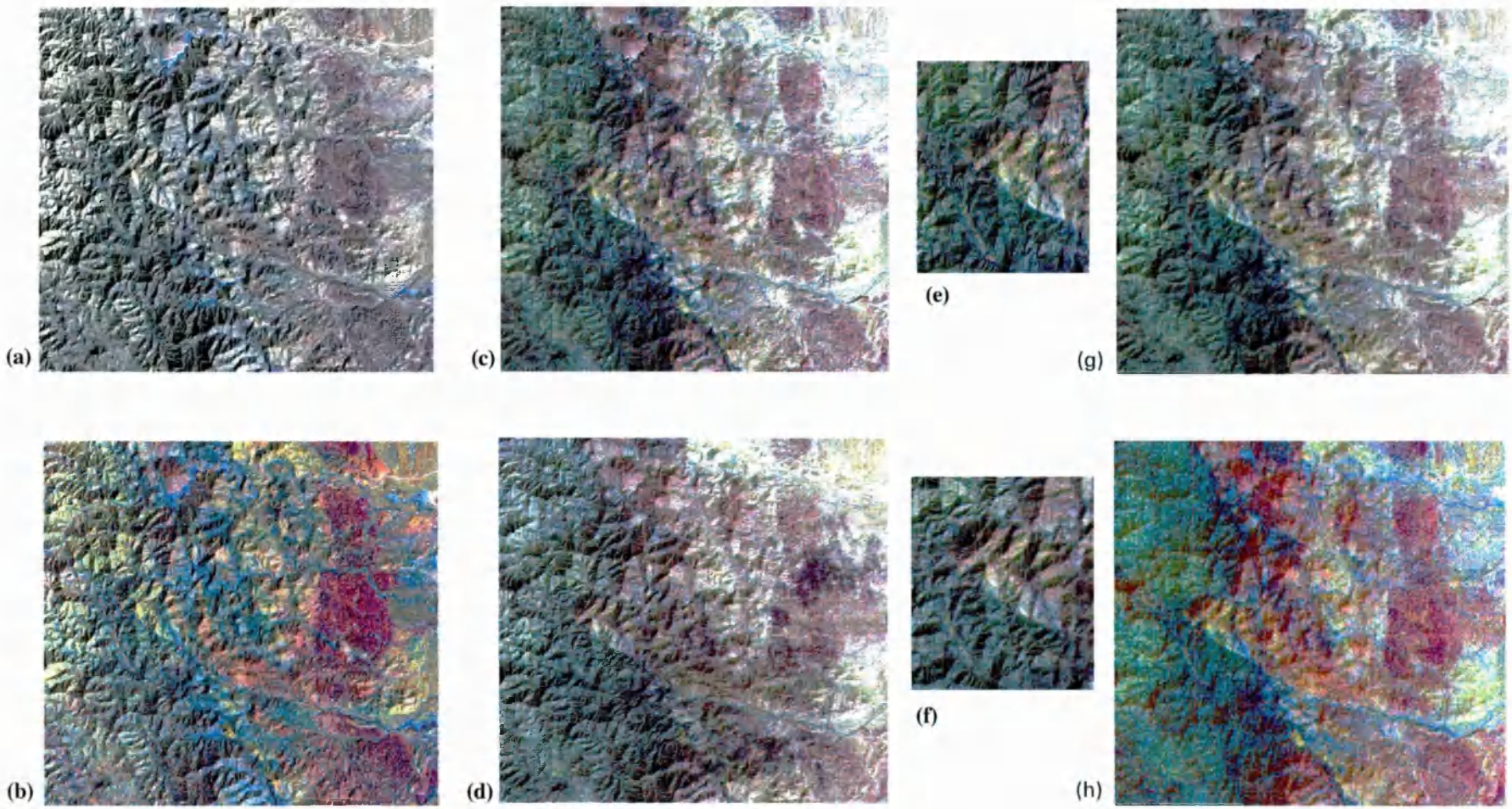

Plate 5.47 Fizh TM and OPS composites. (a) TM 754 colour composite, (b) TM 754 decorrelation stretched composite, (c) OPS 862 high gain composite, (d) OPS 862 normal gain composite, (e) enlargement of OPS 862 high gain, (f) enlargement of OPS 862 normal gain, (g) OPS 862 composite derived from averaging high and normal gain data and (h) OPS merged data with decorrelation stretch applied. Size approximately 18 km by 16 km (x1.5 enlargements). Refer to text for a full description.

although OPS 5 and OPS 7 were completely saturated. This meant that the OPS 852 composite used in the other two study regions could not be used here so instead an OPS 862 composite was produced. All data have been atmospherically corrected and cleaned using FFT techniques.

The high gain OPS 862 composite can be seen in Plate 5.47 (c) and the low gain composite in (d). Initial comparison of these two images shows that they are very similar, with the exception of a dark cloud shadow on the normal gain data (righthand side centre). The high gain data (c) tend to show more colour variation in the mantle lithologies; note how there is more discrimination between the upper (dark blue) and lower mantle (green) on this imagery compared with the low gain image (d). Conversely, the high gain image shows less information within the crustal lithologies, some areas of cumulate gabbro, trondhjemite and metamorphics being saturated. Overall spectral variations between the normal and high gain data are minimal.

Both these composites are of an extremely poor quality (see enlargments (e) and (f)), even after noise removal because OPS 8 and OPS 6 are both affected by the along-track image blur. To try to reduce this effect a composite image was produced by merging both the high and low gain OPS 8, OPS 6 and OPS 2 channels together, Plate 5.47 (g). This involved co-registering the high and low gain scenes, prior to deriving an average intensity image for each channel (for example; (OPS 8 high gain + OPS 8 low gain)/2). The derived composite image is of a slightly better quality than either the low or high gain composites, although at large scales it still shows the characteristic along-track image blur. This composite image was then transformed using a decorrelation stretch (h) for comparison with the TM data.

5.7.4 Comparison of OPS and TM imagery

Plate 5.48 compares the TM 754 decorrelation stretched image (a) with the combined OPS 862 decorrelation stretched image (b). A decorrelation stretch was applied to the OPS composite to try to improve colour saturation. The use of high-gain data has given the OPS 862 composite a slightly 'washed-out' appearance. When comparing slightly enlarged composites the poor quality of the OPS data becomes obvious. Discrimination on the TM imagery is as expected although the mantle-crust boundary is not particularly easy to detect in the north of the scene. Discrimination on the OPS composite is far worse than that seen in the other study areas. The general location and spectral variation between the crust and mantle lithologies can be detected on this

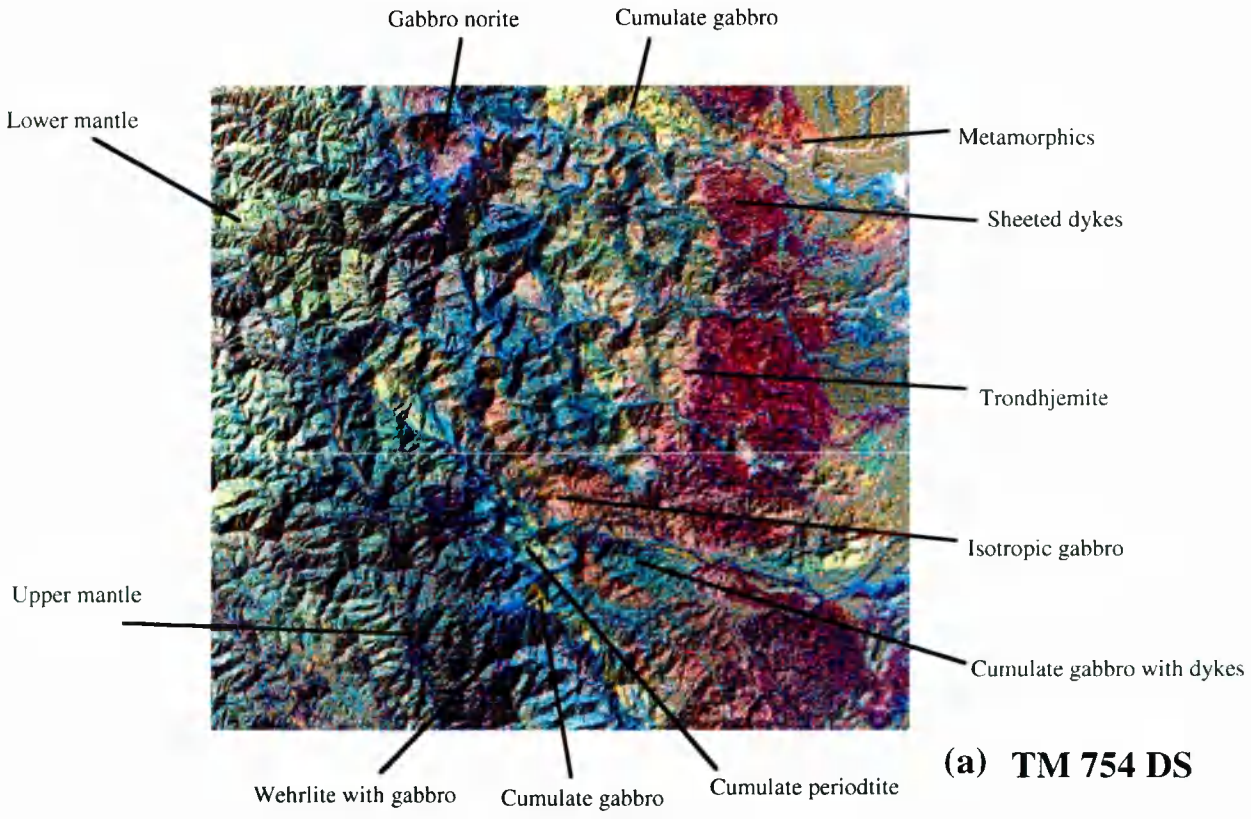

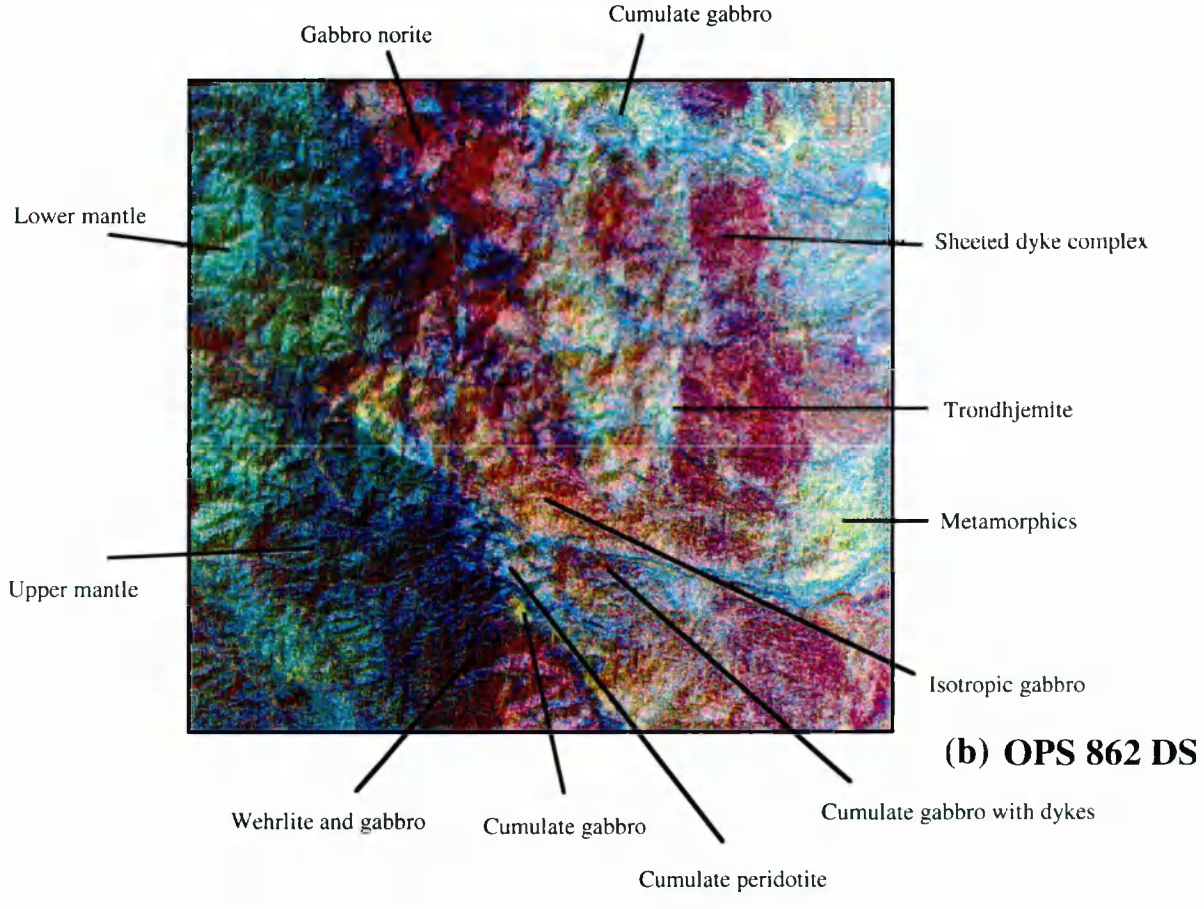

Plate 5.48 (a) TM 754 decorrelation stretched composite, (b) OPS 862 decorrelation stretched composite, derived from averaged high and normal gain data. Refer to text for a full description.

composite, however boundaries can only be placed approximately because of the highly degraded spatial resolution. This image would not really be suitable for interpretation purposes, despite it showing the majority of the spectral variations seen on the TM data. Note how the colours on this OPS 862 image are almost identical to those seen on an OPS 852 decorrelation stretched image. This supports the findings in the Salahi block that OPS 6, OPS 7 and OPS 5 are spectrally similar.

5.8 Summary

This chapter has examined a number of OPS and TM composites for three study areas. The quality and level of spectral discrimination on the TM data have been fairly consistent across these three regions, where those of OPS data have not been so consistent. Excluding the very poor OPS quality seen in the Fizh block, OPS data has shown that despite its associated noise problems it is capable of enhanced discrimination of the ophiolite lithologies (Denniss *et al.*, 1993, 1994 and 1995). In the Maqsad and Salahi study areas OPS data have demonstrated that they can discriminate more lithologies than TM data, including dunite, serpentinite, cumulate gabbro, wehrlite and cumulate peridotite. However it has also shown that some problems exist discriminating isotropic gabbro, sheeted dykes and pillow lavas. This additional discrimination is almost entirely due to the spectrally distinct information recorded by OPS 8 (2.27-2.40 μm), relating to the intensity of Mg-OH absorptions, which the broad-band nature of TM 7 is not capable of recording. The unusually high reflectance of dunite in OPS 2 (0.63-0.69 μm) causes it to be distinct on the OPS 852 composite.

The higher spatial resolution of OPS data coupled with the narrow bandwidth of OPS 8, means that significantly more lithological information is discernible on an OPS composite. OPS 8 is the major channel responsible for the increased spectral information visible on the OPS composites, information not available on TM composites. However, this thesis has shown that the range of usable OPS band composites and image enhancements is extremely limited compared with those of TM data. It has also shown the extremely variable nature of the data, both between scenes and between channels, and the intense noise removal pre-processing required.

6.0 Application of OPS data for volcano monitoring

As described in chapter 1, this chapter is presented in the form of two refereed papers, reprinted without change. I am the principal author on both papers, although the papers have been co-authored to incorporate expert volcanological information on Lascar. The first paper is a general introduction to the suitability of JERS-1 OPS data for volcano monitoring. The second paper is a more complete analysis of two types of remotely sensed data, for volcano monitoring. The AVHRR image processing and thermal analysis in this paper was undertaken by Andrew Harris, the work is included in this thesis to maintain the content of the paper as submitted to IJRS.

6.1 Paper 1 - The 1993 Lascar pyroclastic flow imaged by JERS-1

(International Journal of Remote Sensing, (1995),Vol. 17, No 11, p1975-80)

A. M. Denniss, A. J. L. Harris, D. A. Rothery, P. W. Francis and R. W. Carlton

Department of Earth Sciences, The Open University, Milton Keynes, MK7 6AA, UK.

6.1.1 Introduction

The cover image (as per Plate 6.1.1) shows four false colour composites of Lascar volcano, Chile, constructed using visible and near infrared bands imaged by the Optical Systems (OPS) of the Japanese Earth Resources Satellite (JERS-1). The series of images was acquired between 11 December 1992 and 15 October 1993, straddling an explosive eruption which occurred on 18 April 1993. They clearly show the emplacement and subsequent erosion of pyroclastic flows associated with this event, which was the largest eruption of Lascar for 9,000 years and was probably the largest eruption in the Central Andes since 1601.

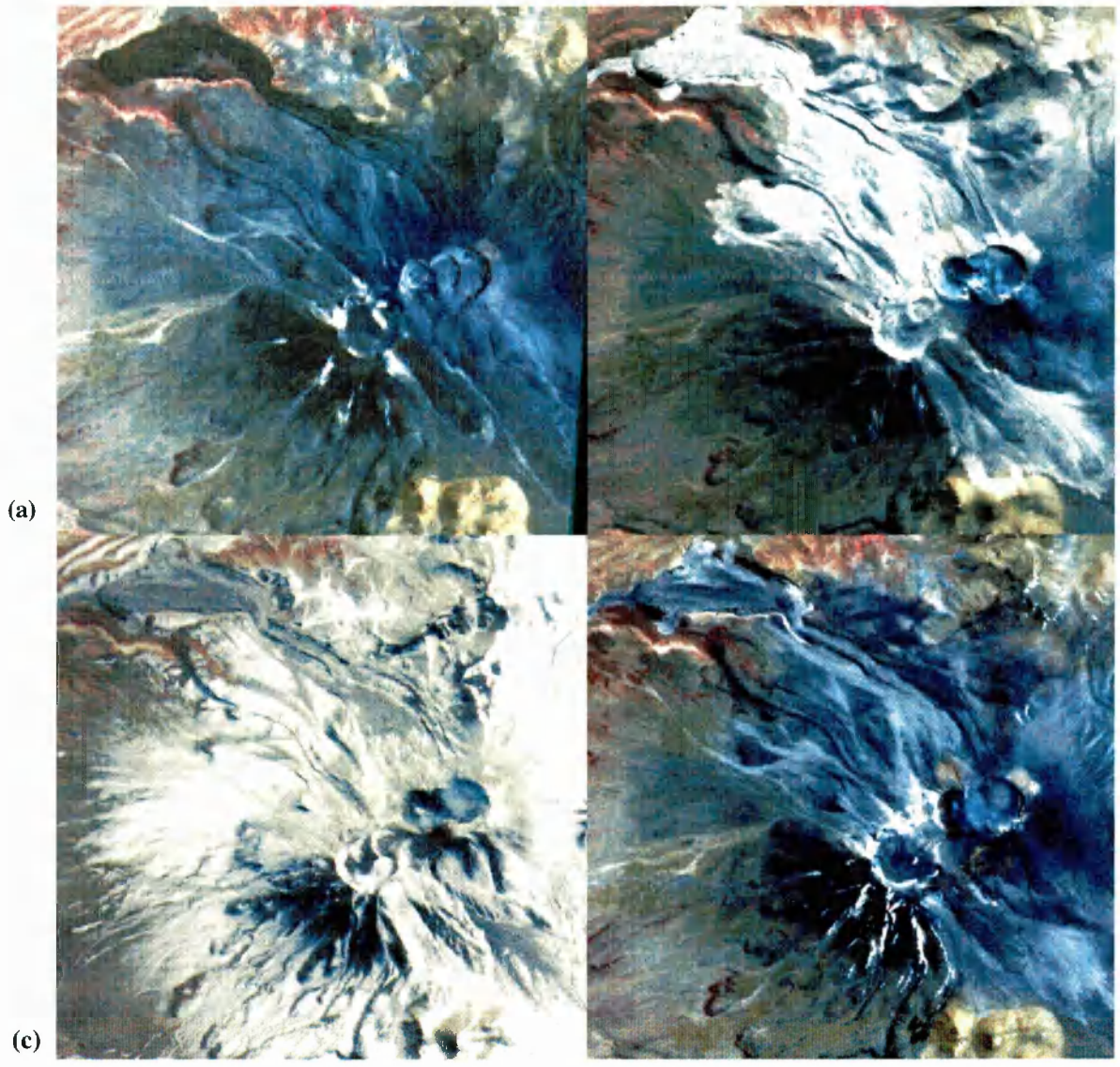

Plate 6.1.1 JERS-1 OPS composites of channels 321 in RGB of Lascar volcano (images approximately 10 km square), (a) 11 December 1992 prior to the eruption, (b) 22 April 1993, one day after the eruption ceased, new pyroclastic flows (light tones) are visible both north and south of the active crater, (c) 19 July 1993 the composite is mainly snow-covered, although in some places the pyroclastic flow can be seen, suggesting that the flow still has enough residual heat to prevent show settling in these areas, (d) 15 October 1993, this image shows that the pyroclastic flow has been significantly modified by erosional processes, this is particularly apparent when comparing the NW edge of the flow to that in Figure 6.1.3 (b).

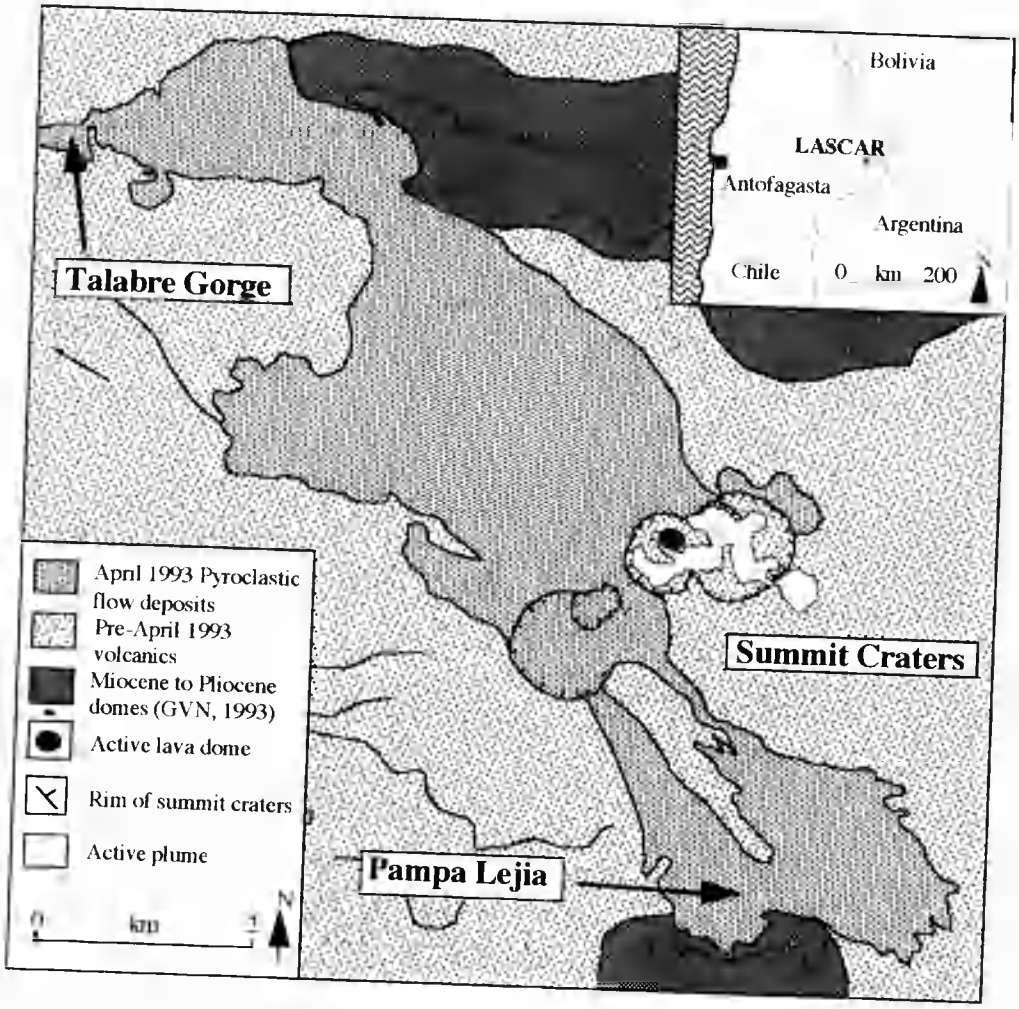

Figure 6.1.1 A preliminary map showing the extent of the pyroclastic flows from the April 1993 eruption of Lascar, as mapped from a JERS-1 OPS 321 composite acquired on 22 April 1993. Inset map shows the location of Lascar volcano.

6.1.2 Lascar and the April 1993 eruption

Lascar is a 5450 metre high volcano in the Chilean Andes (Figure 6.1.1 inset). Over the past several decades Lascar has been continually active, characterised by lava dome extrusion within the summit crater system (Figure 6.1.1), punctuated by periodic explosive ash eruptions creating localised pyroclastic flows and widespread ash fall deposits.

The largest historical eruption of Lascar occurred late on April 18, 1993 and lasted for two days (GVN, 1993). During this time numerous ash columns rose above the crater and a number of pyroclastic flows were erupted. The largest ash column reached 20-

22 km above the crater, resulting in light ash falls (<0.1 mm in depth) as far away as Buenos Aires, Argentina, 1500 km southeast of Lascar. Collapse of a 10 km high ash column on 20 April 1993 resulted in the emplacement of the largest pyroclastic flow, which extended 7.5 km down the NW flank of Lascar. Four smaller superimposed pyroclastic flows where also emplaced ESE of the crater rim; these extended for 3-4 km and reached the Pampa Lejia plain, where they were 1.2-1.5 m thick (GVN, 1993), Figure 6.1.1.

6.1.3 Remote Sensing of volcanoes using JERS-1 OPS

Because of the remote geographical location of Lascar, remote sensing techniques have provided the most continuous source of information of Lascar volcano since 1984 (Rothery *et al.*, 1988, Glaze *et al.*, 1989). In particular, Landsat Thematic Mapper (TM) data have been used to monitor thermal events within the active crater, detecting short wavelength infrared radiance (SWIR) associated with lava dome extrusion (Oppenheimer *et al.*, 1993). Other sensors such as GOES and AVHRR have been used to detect, locate and monitor eruption plumes (Glaze *et al.*, 1989). Since Lascar is infrequently visited, such remotely sensed observations have been an invaluable source of information for activity at this volcano.

JERS-1 OPS has higher spatial and spectral resolution (Table 6.1.1) than Landsat TM (Nishidai, 1993). It was therefore hoped that the thermal changes within Lascar's active crater could be measured more accurately than is possible using TM. However, despite JERS-1 OPS subdividing the wavelength range equivalent to TM band 7 into three narrow SWIR channels (OPS 6, 7 and 8) this has not proved possible, because of the poor data quality associated with JERS-1 OPS imagery (see De Souza *et al.*, 1996).

Data acquired by the SWIR sensor onboard JERS-1 (OPS 5, 6, 7 and 8) are severely affected by complex noise structures such as mis-registration, image blurring and both along and across-track striping. Visible and near-infrared channels (OPS 1, 2 and 3) tend to be less severely affected by noise, although the original 6-bit nature of the data results in the imagery having a low dynamic range (De Souza *et al.*, 1996). The images presented here are Level 2 data with no de-blurring or de-striping applied. The OPS data have not been cleaned to ensure that the thermal features are not modified in any way.

Parameter	Value	Comment
Launch Date	11 February 1992	
Orbit Type	Sun-Synchronous	moving westwards
Orbit Altitude	568 km	above equator
Revisit Period	44 Days	
Local Solar Time	10.30 - 11.00 a.m.	descending orbit
OPS Observation Wavelengths	OPS 1 0.52 - 0.60 μm OPS 2 0.63 - 0.69 μm OPS 3 0.76 - 0.86 μm OPS 4 0.76 - 0.86 μm OPS 5 1.60 - 1.71 μm OPS 6 2.01 - 2.12 μm OPS 7 2.13 - 2.25 μm OPS 8 2.27 - 2.40 μm	forward looking 15.33°
Ground Resolution	18.3 x 24.2 metres	resampled to 18 metre pixels
Swath Width	75 km	
Quantization Level	6 bit	

Table 6.1.1 A summary of JERS-1 orbit and optical parameters.

6.1.4 Monitoring activity at Lascar using JERS-1 imagery

1) Thermal Activity

Despite the poor data quality, we found images from the JERS-1 OPS to be valuable for a qualitative analysis of the intra-crater thermal structure, revealing changes in the thermal structure over nine months, particularly because this period coincided with the time when Landsat TM data for Lascar ceased to be available to us. False colour composites of channels OPS 851, in RGB, show qualitative variations in the location and size of hot spots within the active crater. Plates 6.1.2 (a) to (d) show the locations of the crater hot spots on 11 December 1992, 22 April 1993, 19 July 1993 and 15 October 1993 respectively.

Plate 6.1.2 JERS-1 OPS composites of channels 851 in RGB of the Lascar summit craters (images approximately 3 km square), (a) 11 December 1992, (b) 22 April 1993, (c) 19 July 1993, and (d) 15 October 1993. Thermal hotspots are depicted as red and yellow areas. Severe noise structures are visible in these images, especially vertical and horizontal stripes, these are particularly distinct around the thermal hotspots.

In the December 1992 (Plate 6.1.2 (a)) image two major hot spots are radiant in both OPS 8 and OPS 5 whilst six small hot spots can be seen around these which are radiant in OPS 8 only. Radiance in OPS 5 indicates a minimum surface temperature of ~265 - 285° C, or higher if the hot source is of sub-pixel resolution (as is likely), whereas radiance in OPS 8 indicates a minimum surface temperature of ~160 - 170° C. Probably the highest temperature radiant sources contributing to the signal are at several hundred degrees. The 22 April 1993 image (Plate 6.1.2 (b)), acquired only one day after major eruption activity ceased, shows only one large source of short wavelength infrared thermal flux at the centre of the crater radiant in both OPS 8 and OPS 5. By 19 July 1993, (Plate 6.1.2 (c)) the thermal activity within the crater had greatly diminished with only a small single hot spot evident in OPS 8.

By 15 October 1993 (Figure 6.1.2 (d)) thermal activity had once again increased, with a large area evident as being radiant in OPS 8 whilst two smaller localised hot spots within this region are radiant in OPS 5. Changes in the thermal structure may relate to growth and evolution of a 'lava dome' mostly covered by chilled crust but radiating intensely from cracks, similar to the findings of Oppenheimer *et al.*, (1993) using Landsat TM data.

2) Pyroclastic Flow Mapping

False colour composites of OPS 321 in RGB depict very clearly the nature and extent of the pyroclastic flows emplaced during the April 1993 eruption period (Plate 6.1.1) and allow new pyroclastic flows to be mapped, Figure 6.1.1.

The image in Plate 6.1.1 was acquired prior to the April 1993 eruption, so it serves as a baseline image against which subsequent post eruption images can be compared. Older historical pyroclastic and lava flows can be easily seen spreading out from the summit craters. The Figure 6.1.1 image was acquired just after the April 1993 eruption activity ceased and shows very clearly the extent of the newly emplaced pyroclastic flows (lighter tones) on the N, NW and SE flanks of the crater.

In some places, such as on the NW flank new flows completely cover the older pyroclastic and lava flows, such as within the Talabre Gorge, whilst to the SE they run part way up the north side of pre-existing domes and spread onto the edge of the Pampa Lejia plain (Plate 6.1.1). Pyroclastic flows consist of pumice and fine ash, emplaced from vertically convecting eruption columns which collapse under gravity.

Flows surmount the surrounding topography to the extent their kinetic energy permits. A small plume of gas or steam or aerosols can be detected on this image to the SE of the crater, probably resulting from post eruption fumarolic activity or degassing.

During the 19 July 1993 pass (Plate 6.1.1) the Lascar region was snow covered, so little information regarding the extent of weathering of the flows can be obtained. Snow free patches on the flows suggest that nearly three months after emplacement the flows still have sufficient residual heat to cause snow melt. These snow-free regions correlate with regions where existing topographic features have resulted in the new pyroclastic material being 'ponded' into thicker localised deposits, these thicker deposits retaining their heat for longer than the thinner deposits.

An image acquired on 15 October 1993 shows that considerable changes have occurred around the edges of the flows, less than four months after they were emplaced. This is particularly evident on the large lobe which extends westwards from the flow on the northern flank of the crater and on the flows extending SE from the crater. The flow edge at both of these locations has been severely affected by erosional processes. Initial image interpretation suggests that the fine grained unconsolidated material at these locations, and on high ground to the east, has been removed by wind erosion. It is unlikely that much material has been redistributed by snow melt, as our observations in this area are that snowcover is removed by sublimation rather than melting and surface run-off.

The spectral response of the pyroclastic flows has also changed during this period. They appear much darker on the October composite than they do on the April composite (compare Plates 6.1.1 (a) and 6.1.1 (d)). This would suggest that during this four month period weathering has been severe enough to produce a mineralogical or water-content change significant enough to affect the spectral reflectance.

6.1.5 Summary

This note shows that a large amount of volcanologically useful information can be extracted from JERS-1 OPS data despite the noise problems associated with this data. Such remotely sensed information is invaluable for monitoring volcanoes such as Lascar, which may otherwise go un-monitored.

6.1.6 Acknowledgements

The JERS-1 OPS data were kindly supplied by ERSDAC. Anthony Denniss is funded by a NERC award whilst Andy Harris is funded by an Open University PhD grant. Peter Francis and Dave Rothery were principal investigators for JERS-1 system verification programme projects J-0116 and J-0101 respectively, with which this report is connected. The authors would like to thank Takashi Nishidai for his generous assistance, and the reviewers of this paper whose suggestions prompted us to clarify our description.

6.2 Paper 2 - Satellite observations of the April 1993 eruption of Lascar volcano

(International Journal of Remote Sensing, (1998),Vol. 19, No 5, p801-821)

A. M. Denniss, A. J. L. Harris, D. A. Rothery, P. W. Francis and R. W. Carlton

Department of Earth Sciences, The Open University, Milton Keynes, MK7 6AA, UK.

6.2.1 Abstract

The largest historic eruption of Lascar volcano, Chile, occurred during April 1993. The eruption lasted two days, producing pyroclastic flows, covering an 18.5 km^2 area, and a major ash plume, leading to widespread ash-fall. Here we demonstrate how combined observations from the Japanese Earth Observation (JERS-1) and the National Oceanographic and Atmospheric Administration (NOAA) satellites were used to document this eruption. These two satellite platforms provide complementary data, giving high resolution spatial (JERS-1), spectral (JERS-1) and temporal information (NOAA). Such an integrated remote sensing approach offers a valuable means of easily and safely monitoring large, dangerous, volcanic eruptions and post eruption processes.

6.2.2 Volcano monitoring using remote sensing

Between April 1960, when the United States launched the first satellite in the Television and InfraRed Observation Satellite (TIROS) series, and December 1993, approximately 1520 eruptions occurred (Simkin and Siebert, 1994). Some of these,

due to remoteness, danger or lack of resources, were poorly documented, and others were missed altogether. However, satellite remote sensing offers a means of regularly monitoring all of the world's sub-aerial volcanoes, providing data for an entire volcano or volcanic complex including inaccessible or dangerous areas. Data from high spatial resolution instruments, such as the 30 m pixel data from Landsat's Thematic Mapper (TM), have proved capable of identifying and measuring active features such as lava lakes, domes and flows (e.g., Rothery *et al.*, 1988; Pieri *et al.*, 1990; Oppenheimer, 1991; Oppenheimer *et al.*, 1993; Flynn *et al.*, 1994). However Landsat's 16 day return period means that many volcanic events or cloud free imaging opportunities are missed.

Satellites such as the National Oceanic and Atmospheric Administration (NOAA) series and the GOES / Meteosat series allow more frequent imaging of the Earth's surface (every 6 hours and every 30 minutes, respectively), and have been invaluable sources of data for locating, tracking and measuring eruption plumes (e.g. Sawada, 1989; Kienle *et al.*, 1990; Holasek & Rose, 1991; Holasek & Self, 1995).

However, the disadvantage of improved temporal resolution is decreased spatial resolution: the Advanced Very High Resolution Radiometer (AVHRR) flown onboard the NOAA series of satellites has a nominal spatial resolution of 1 km (at nadir), and that of the scanning radiometer flown on GOES is nominally 2.5 km (visible channels) and 5 km (infrared channels). Such low spatial resolution data have proved capable of detecting and monitoring active lavas (e.g. Wiesnet & D'Aguanno, 1982; Harris *et al.*, 1995a), but higher spatial resolution is always desirable.

Many studies that have used satellite data to monitor volcanoes have used a single data source, allowing either spatial or temporal detail, but not both. An integrated approach, using two data sets, one with high spatial resolution and one with high temporal resolution, allows a more complete analysis. Here we demonstrate this by using high spatial resolution data from the OPtical Scanner (OPS) flown on the Japanese Earth Resources Satellite (JERS-1) in conjunction with high temporal resolution data from NOAA-AVHRR to document the April 1993 eruption of Lascar volcano, Chile.

6.2.3 Activity at Lascar

Lascar, located in an arid environment, is an ideal remote sensing target. As a result, numerous sensors in recent years have provided valuable information about this

geographically remote volcano (e.g. Glaze *et al.*, 1989; Oppenheimer, 1993; Denniss *et al.*, 1996; Wooster and Rothery, 1997). Lascar is a 5450 metre high composite volcano located in the Antofagasta region of the Chilean Andes (Figure 6.2.1 inset), approximately 34 km southeast of the village of Toconao, at 23°22' S, 67°44' W (Oppenheimer 1991). Lascar has erupted intermittently since a Volcano Explosivity Index (VEI) 3 event in September 1986. Activity is characterised by phases of lava dome growth and collapse, followed by explosive eruptions from the active crater (Matthews *et al.*, 1997, Wooster and Rothery, 1997).

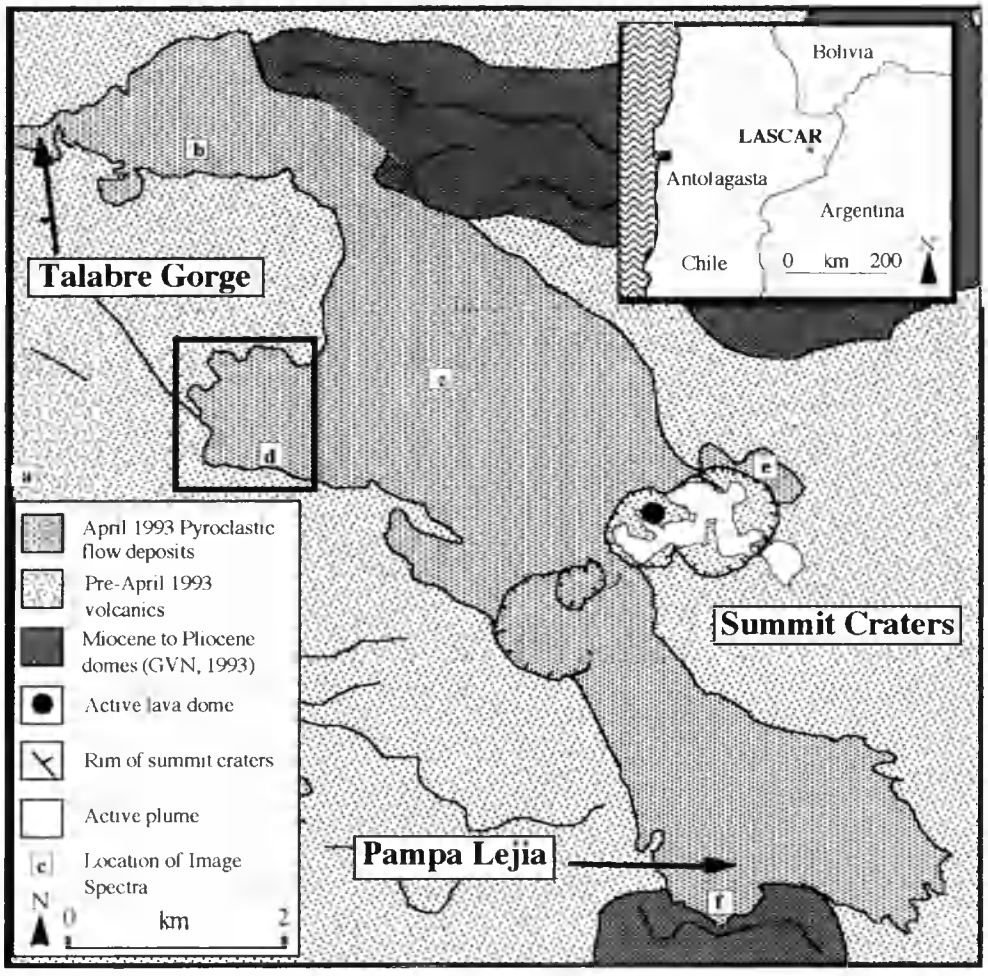

Figure 6.2.1. Inset map shows the location of Lascar volcano, Chile. Main figure shows the extent of the new pyroclastic flows, emplaced during the April 1993 eruption. These flows have been mapped from a JERS-1 OPS 831 False Colour Composite acquired on 22 April 1993. Letters in boxes refer to the location of image spectra seen in Figure 6.2.3 and 6.2.4. Box shows the approximate extent of Plate 6.2.2.

At the time of writing the most recent such eruption resulted in a 700 m high ash plume on 20 July 1995 (GVN 1995). The largest event, in April 1993, produced ash columns up to 22 km high (VEI 4) and associated fast moving (100-700 km h^{-1}) high temperature (100-800 °C) pyroclastic flows (GVN 1993). Prior to the current series of eruptions, the historic record (which extends to 1848, but is likely to be incomplete) shows no events greater than VEI 2 (Simkin and Siebert 1994).

Lascar's prehistoric activity has involved the migration of activity through a series of six overlapping craters which trend roughly northeast (Figure 6.2.1). The current active crater is near the middle of the chain and is approximately 800 m in diameter and 150 m deep (Glaze *et al.*, 1989). As well as pyroclastic deposits, there are many andesitic-dacitic lava flows extending from the crater rims (though none appear to have come from the currently-active crater). The longest, and apparently the youngest, of these extends for 6 km down the northern flank and is suggested by Casertano and Barozzi (1961), though on doubtful grounds, to date from the nineteenth century.

Lascar's April 1993 eruption was its largest for 9000 years and lasted for two days (GVN, 1993). During this time numerous ash columns rose above the crater with the largest reaching 20-22 km above the crater rim. This resulted in light ash falls (<0.1 mm in depth) as far away as Buenos Aires, Argentina, 1500 km southeast of Lascar. A pyroclastic flow extending 7.5 km down the NW flank was emplaced on 20 April 1993, when a 10 km high ash column collapsed. Four smaller pyroclastic flows extending 3-4 km ESE of the crater rim were also emplaced (GVN, 1993).

6.2.4 The remote sensing data set

1) JERS-1 OPS: characteristics and capabilities

JERS-1, launched on 11 February 1992, is a Japanese Earth observation satellite, and is the first satellite to carry both a Synthetic Aperture Radar (SAR) and a pushbroom scanner (OPS) on the same platform (Nishidai, 1993). Both sensors are capable of producing volcanologically useful information. Rowland *et al.*, (1994) and Massonett *et al.*, (1995) have demonstrated the potential of SAR for volcanological studies. In this paper we consider only the capabilities of the optical sensor (Table 6.2.1).

Parameter	Value	Comment
Launch Date	11 February 1992	
Orbit Type	Sun-Synchronous	moving westwards
Orbit Altitude	568 km	above equator
Revisit Period	44 Days	
Local Solar Time	10.30 - 11.00 a.m.	descending orbit
OPS Observation Wavelengths	OPS 1 0.52 - 0.60 μm OPS 2 0.63 - 0.69 μm OPS 3 0.76 - 0.86 μm OPS 4 0.76 - 0.86 μm OPS 5 1.60 - 1.71 μm OPS 6 2.01 - 2.12 μm OPS 7 2.13 - 2.25 μm OPS 8 2.27 - 2.40 μm	forward looking 15.33°
Ground Resolution	18.3 x 24.2 metres	resampled to 18 metre pixels
Swath Width	75 km	
Quantization Level	6 bit	

Table 6.2.1. A summary of JERS-1 orbital and optical parameters.

JERS-1 OPS data offer significantly higher spatial and spectral resolution than Landsat TM, as well as along-track stereoscopic capabilities. OPS data have a pixel size of 18 m x 18 m (resampled during pre-processing from an original 18.3 m x 24.2 m), compared with 30 m x 30 m for TM. This smaller pixel size has the advantage of increasing image detail. This is especially important in many kinds of thermal study of volcanoes, where radiant sources are usually distributed across very few pixels, and high temperature features typically occupy <1 % of a pixel (see Rothery *et al.*, 1988). Unfortunately, JERS-1 revisits each 75 km x 75 km scene-equivalent ground area only once in every 44 days. This is a major disadvantage when studying dynamic and transient phenomena (note that the 1993 Lascar eruption lasted just 2 days, with pyroclastic flow events lasting <30 minutes).

The JERS-1 OPS also offers higher spectral resolution than Landsat TM. It records images in eight narrow channels between 0.52 μm and 2.40 μm, four in the visible and near infrared (VNIR), OPS 1 to 4, and four in the short wavelength infrared (SWIR), OPS 5 to 8 (Table 6.2.1). OPS 4 occupies the same spectral range as OPS 3 and is used to acquire stereoscopic data looking 15.33° ahead along-track. Tanaka and Sugimura (1995) demonstrate the potential of OPS stereoscopic data on Mount Sakurajima, Japan.

JERS-1 OPS data have higher spectral resolution than Landsat TM data, primarily because of the subdivision of the geologically important 2.0 μm to 2.4 μm region of the spectrum (broadly equivalent to TM 7), into three narrow channels, OPS 6, 7 and 8. This region of the spectrum is important in geological mapping studies, providing additional spectral information which helps to differentiate between mineralogically similar lithologies, as demonstrated in the Oman ophiolite by Denniss *et al.*, (1994).

2) OPS data quality

It was hoped in this study that the superior spectral resolution of the JERS-1 OPS data would allow better quantitative measurements of the flow thermal parameters, than TM studies using just two SWIR channels (Rothery *et al.*, 1988, Oppenheimer *et al.*, 1993). However poor data quality means that only a qualitative analysis of these data is possible.

For quantitative analysis Level 0 data must be used, to avoid the loss in data integrity caused by pixel re-sampling during the geometric transformation to Level 2. Unfortunately, the quality of the Level 0 data was degraded by a variety of sensor problems:

(1) Dynamic ranges of all OPS channels, especially the SWIR channels, tend to be very low. SWIR channels OPS 6 and OPS 7 often occupy dynamic ranges of less than 15 DN (Digital Number) values.

(2) Along- and across-track striping cause complex noise structures affecting all OPS channels (see Plates 6.2.3 (a) to (d)). Across-track striping is more severe on VNIR channels although SWIR channels, especially OPS 8, are often affected. Across-track stripes modulate lines of data by ± 2 DN, alternating in frequency between zones of 3-4 lines and 7-8 lines. Along-track striping is very severe on SWIR channels, alternate columns of data being modulated along their entire length by ± 1 DN.

(3) Image blur parallel to the along-track direction is severe in all SWIR channels. This occurs when a sharp change in radiance is encountered, for example at a thermal hot-spot (Plate 6.2.3 (b) shows this very clearly) or a marked reflectance contrast. At such an abrupt boundary the Charge Coupled Devices (CCDs) used in the sensor array fail to respond immediately to the changed radiance level. This results in the previous radiance level being smeared along-track for a number of lines before the new radiance level is detected. This smearing effect is further exaggerated by the differing response functions of odd and even detectors (Nishidai 1993), causing sharp radiance boundaries to be offset across-track by odd and even detectors, resulting in a jagged boundary.

(4) Problems also result from misregistration between individual OPS channels and between the VNIR and SWIR radiometers. Registration errors as large as 300 lines and / or samples (i.e. > 5 km) often have to be corrected on Level 0 data. Considerably smaller errors exist in Level 2 data, which can be easily identified and an appropriate translation calculated to co-register each channel.

Data quality varies greatly both between channels, scenes and Levels. Generally the SWIR channels, especially OPS 6 and 7, tend to be most severely affected by noise. The Level 0 noise problems described are further exaggerated in Level 2 data by the geometrical transformation applied as a part of the pre-processing. Data quality can be improved in some cases by implementing frequency domain noise removal techniques (De Souza *et al.*, 1996), although OPS 6 and OPS 7 are often beyond recovery. Removal techniques also destroy the integrity of the data, precluding any quantitative analysis.

3) AVHRR: characteristics and capabilities

The AVHRR is a scanning radiometer flown aboard the NOAA series of polar orbiting satellites, which has been operational since 1979. For volcano monitoring the temporal resolution, spectral capabilities, image size and low cost of AVHRR data offers a number of benefits:

(1) Temporal resolution. Each NOAA satellite has a return period of 12 hours at the equator, significantly less than the 16 days of Landsat and 44 days of JERS-1. Further, NOAA aims to keep two platforms in orbit at any one time separated by an

interval of 6 to 7 hours. This means that every sub-aerial volcano will be over-flown at-least 4 times a day, greatly increasing the chances of an image coinciding with a cloud-free interval or volcanic event.

(2) Spectral capabilities. AVHRR has two channels in the visible and near infrared (AVHRR 1; 0.58 - 0.68 μm & AVHRR 2; 0.725 - 1.10 μm), one channel in the mid-infrared (AVHRR 3; 3.55 - 3.93 μm) and two in the thermal infrared (AVHRR 4; 10.3 - 11.3 μm & AVHRR 5; 11.5 - 12.5 μm). With the launch of NOAA-K a sixth channel at 1.58 - 1.64 μm will be available. In each of the thermal channels apparent brightness temperature for any pixel can be determined using the calibration data and Planck's radiation equation (Kidwell, 1991), and a correction to take into account the non-linear response of the sensor following Weinreb *et al.*, (1990). AVHRR thermal channels have proved capable of detecting, monitoring and measuring volcanic ash plumes (e.g., Prata, 1989; Kienle *et al.*, 1990; Holasek and Rose, 1991), and the visible channels have been applied to determine the extent of ash fall and its effect on vegetation (Tucker & Matson, 1985; Jeyaseelan & Thiruvengadachari, 1993). The thermal channels have also proved capable of detecting and monitoring active lavas (Weisnet & D'Aguanno, 1982; Harris *et al.*, 1995a; Harris and Rothery, 1995).

(3) Image size. Ground coverage for an overhead pass is 3000 x 6000 km. Such large image areas are appropriate for viewing the whole of volcanic clouds extending for hundreds of kilometers. The large area coverage also enables volcanoes over a wide region to be analysed using just one image. However, the pixel size, 1 km at nadir decreasing to around 7 x 3 km at the scan edge, means that less detail can be extracted than from Landsat TM or JERS-1 OPS data. In spite of this, thermal maps, lava area and thermal flux estimates produced from time series of AVHRR data have been shown capable of reliably documenting events at an active lava flow field (Harris *et al.*, 1995a).

(4) Real-time capabilities, safety and data costs. AVHRR data are freely and immediately available using cheap to install receiving stations. This allows analysis on reception and real time monitoring from a safe vantage point. Installation of the hardware and software for receiving data are relatively cheap (US$ 4000 to 60,000, depending on sophistication), and allows near-real-time monitoring. This contrasts favourably with the US$ 3300 price-tag for a single, up to date, Landsat TM full scene, which in practice takes weeks or months to arrive from a commercial supplier.

6.2.5 Pre- and post-eruption JERS-1 OPS observations

Four cloud-free OPS scenes, straddling the April 1993 eruption, were available for this study (Table 6.2.2), in both Level 0 format (raw data) and Level 2 format (radiometric and geometric corrections applied). No noise removal techniques have been applied to the images in this paper. Level 2 data were used for this study because the inter-channel misregistration was less severe than that of the Level 0 data (Section 6.2.4(4)) and could be corrected with a simple translation. A translation was applied to all data ensuring that the thermal point sources were correctly registered between channels.

Despite the poor OPS data quality, we demonstrate that the high spatial and spectral resolution of the data allows valuable quantitative spatial information, as well as qualitative thermal information, to be extracted.

Date	Gain Setting	Comment	Data Used
11 / 12 / 92	Normal	Cloud Free	✔
24 / 01 / 93	Normal	Cloudy	
22 / 04 / 93	Normal	Cloud Free	✔
19 / 07 / 93	Normal	Snow Covered	✔
01 / 09 / 93	High	Saturated	
15 / 10 / 93	Normal	Cloud Free	✔
28 / 11 / 93	Normal	Not Available	
24 / 02 / 94	Normal	Visible Only	
23 / 05 / 94	Normal	Visible Only	
19 / 08 / 94	Normal	Visible Only	

Table 6.2.2 Chronological listing of JERS-1 OPS data, scene 421-340 covering Lascar volcano, Chile. The last three scenes listed contain only visible data (OPS 1, OPS 2 and OPS 3) as these where acquired after the SWIR sensor on-board JERS-1 stopped working in December 1993. Data used in this study are indicated.

1) Mapping the eruption products

False colour composites of OPS 831 in RGB (Plates 6.2.1 (a) to (d)) show very clearly the extent of the pyroclastic flows emplaced during the April 1993 eruption, allowing them to be mapped (Figure 6.2.1). This band combination also highlights

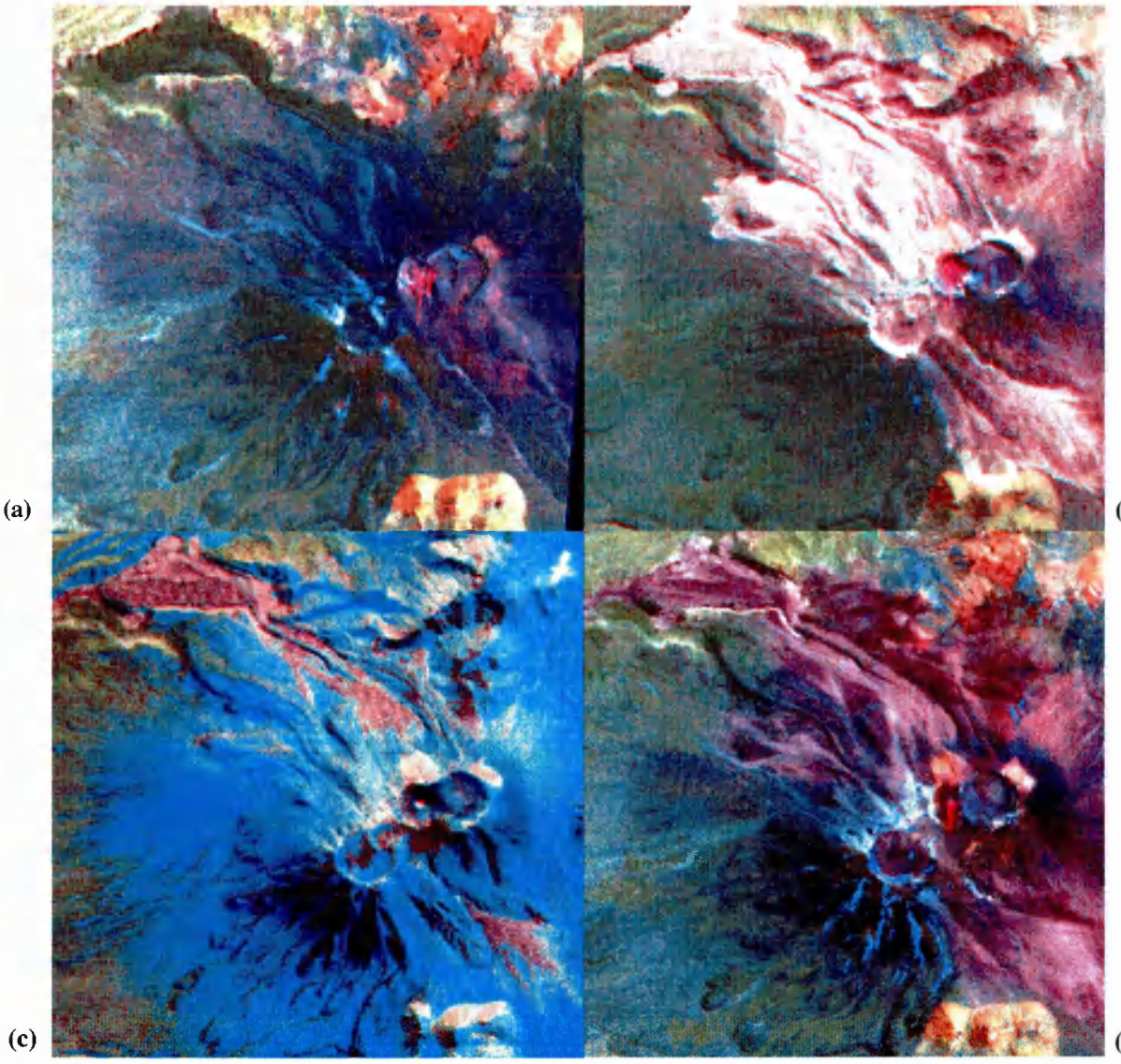

Plates 6.2.1 JERS-1 OPS composites of channels 831 in RGB of Lascar volcano, Chile (images approximately 10km square), (a) 11 December 1992 prior to the eruption, (b) 22 April 1993, one day after the eruption ceased, showing new pyroclastic flows (light tones), (c) 19 July 1993 the Lascar region is snow covered although some parts of the flow (mid brown tones) appear to have enough residual heat to prevent snow settling, (d) 15 October 1993 this image shows that the pyroclastic flow has been significantly modified by erosional processes, compare with (b). Note also the changing thermal structure seen in the centre of the active crater, see Plate 6.2.2 for details.

thermal anomalies in the central crater (see section 6.2.5 (3)). Because Lascar is in an unusually arid environment, it offers the opportunity for exceptional studies of pyroclastic deposits, unlike Pinatubo- or Mount St. Helens-type environments where rapid post-eruption erosion occurs.

Plate 6.2.1 (a) was acquired prior to the April eruption (11 December 1992), and serves as a baseline against which post eruption images can be compared. Older lava flows can be seen extending from the summit craters. Plate 6.2.1 (b), acquired on 22 April 1993, two days after the eruption ceased, shows very clearly the new pyroclastic flows (lighter tones) emplaced on the N, NW and SE flanks of the crater. The northern flow extends for approximately 7.2 km and has been channelled by the existing topography of the Talabre Gorge (Figure 6.2.1). With the exception of one small area, all the old lava flow within the Talabre Gorge has been covered by this pyroclastic flow. To the south of the crater the flows extend 3-4 km and can be seen to run part way up the opposing (northern) flanks of the pre-existing domes. They also spread onto the Pampa Lejia plain (Figure 6.2.1).

The OPS image shows that new pyroclastic flow material covers a total area of approximately 18.5 km^2 (14.2 km^2 north of the crater and 4.3 km^2 south of it). Viramonte (GVN 1993) reports that these flows were between 1.5 - 2 m thick, and were blanketed by a thin co-ignimbrite air fall deposit, 5 - 30 cm thick. The image shows that 4.9 km^2 area to the NNE of the crater, on the slopes of Aguas Calientes (Figure 6.2.1) appears to be covered by air fall material from the plume. Flows tend to be ponded by existing topographic features into thicker deposits, whereas air fall ash mantles the terrain uniformly, except on steep slopes. A small plume of gas or steam can be detected on this image to the SE of the crater, probably resulting from post eruption fumarolic activity.

Plate 6.2.1 (c) shows that the Lascar region is snow covered (blue tones) on 19 July 1993, so little information regarding the extent of weathering of the flows can be obtained. However, this image does indicate that almost three months after emplacement the flows have enough residual heat to cause partial snow melt. Snow free regions (pale brown tones) correlate with regions of thicker deposits, which tend to be located on the less-steep slopes. Snow-free areas represent a total of 6.1 km^2 on the northern flow and 1.1 km^2 on the southern flows, approximately 40% of the total flow area.

The final image (Plate 6.2.1 (d)) acquired on 15 October 1993 shows that considerable changes have occurred on both the north and south flows in the four months since emplacement. These changes are particularly apparent at the flow boundaries. For example, in April the large western lobe on the northern flow (Plate 6.2.2 (a)) had a distinctly lobate structure, but by October (Plate 6.2.2 (b)) this had completely gone. This suggests that the feature consisted almost totally of fine co-ignimbrite fallout which, during the 4 months since emplacement, was removed by action of wind, water and / or snow-melt. Similar changes can also be seen on southern flow margins where material emplaced on the side of small pre-existing domes has also been completely removed (compare Plates 6.2.1 (b) and 6.2.1 (d)). The air fall ash material covering the 4.9 km^2 region to the NNE of the crater also disappeared in the 4 months following the eruption, suggesting that the deposit in this region was very thin and easily removed by aeolian and / or fluvial processes.

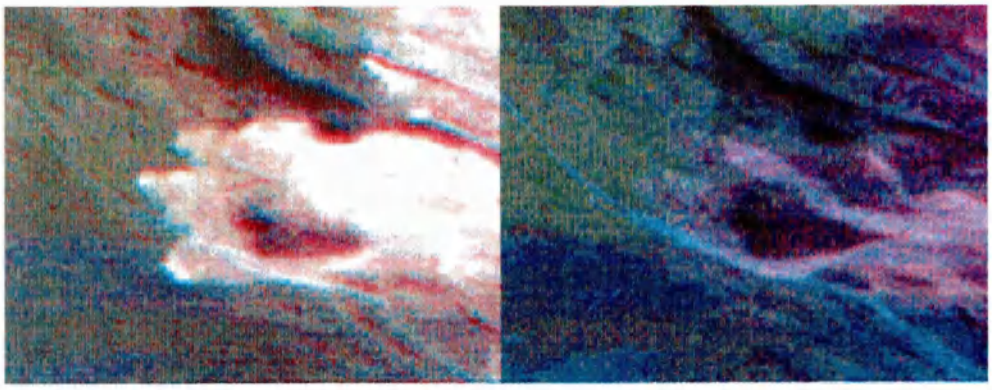

Plates 6.2.2 Enlargement of lobate structure on western edge of northern flow. (a) on 22 April 1993 and (b) 15 October 1993. Note how the majority of the pyroclastic flow seen in (a) has been removed in the 5 month period prior to image (b) this suggests rapid reworking of a surface ash deposit.

2) *Spectral Observations*

The OPS time series shows distinct spectral changes during the 10 month period of data coverage. Figure 6.2.2 (a) shows the lab reflectance spectra (measured using a GER IRIS Mk IV spectroradiometer) for samples of ash and pumice erupted at Lascar in April 1993. The pumice spectrum is fairly flat with low reflectance levels between 15 and 22 %. In comparison, the ash spectrum is more varied, reflectance levels rising from around 15% in the visible to about 43% in the SWIR. This spectrum also shows more pronounced absorption features at 0.5, 0.8, 1.95 and 2.25 μm. In Figure 6.2.2b the lab spectra have been resampled to JERS-1 OPS wavelengths, and therefore comprise of just seven measurements (one for each OPS channel) within the 0.4 - 2.4 μm range. Despite this reduction in detail, the ash and pumice spectra can still be easily distinguished by their relative reflectance ranges, but the individual absorption features cannot be detected.

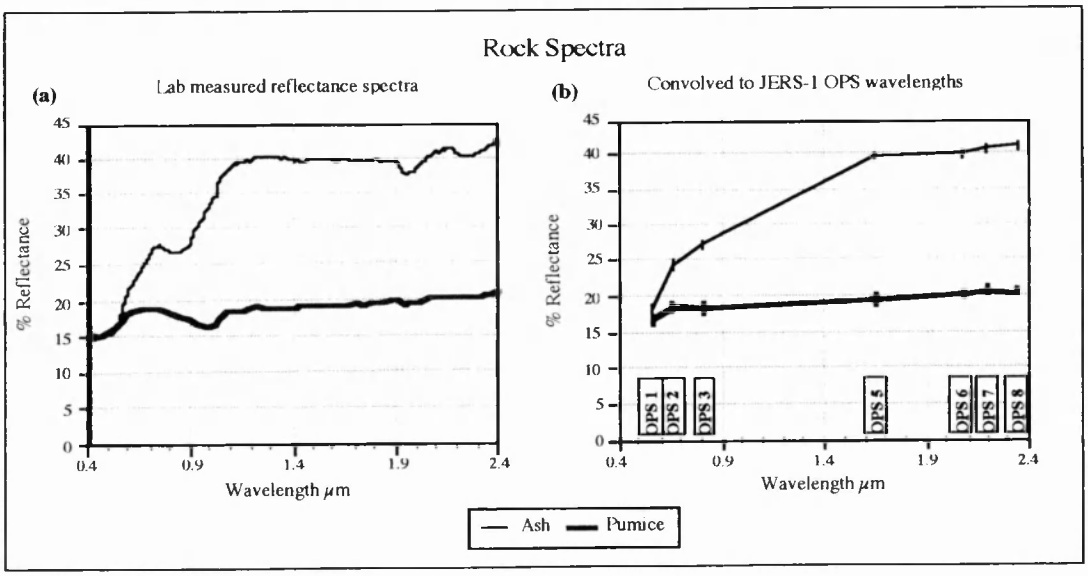

Figure 6.2.2 (a) Lab based reflectance spectra for samples of ash and pumice from Lascar, (b) lab based spectra convolved over OPS bandwidths.

The image-derived spectra in Figures 6.2.3 (a) to (f) and 6.2.4 (a) to (f) have been atmospherically corrected using the technique outlined by Chavez (1988) and converted to semi-quantitative reflectance using the gains and offsets for OPS data given by Shimada and Nakai (1993). The resulting reflectance values are only semi-quantitative as this technique does not take into account variations in surface slope and aspect. Each spectrum illustrated is an average calculated from ten neighbouring sample locations.

In order to constrain the effects of seasonal and / or sensor changes on the image-derived spectra, spectral variations within a region outside that affected by the 1993 eruption were examined (Figure 6.2.3 (a)). During the 10 month period, all four spectra have very similar profiles but their relative reflectances vary considerably. Since the 11 December 1992 and 15 October 1993 spectra tend to be brighter than the 22 April 1993 and 17 July 1993, spectral variation is probably due to seasonal changes in scene illumination, rather than sensor degradation or misregistration of sample location. Without an illumination correction the reflectance spectra from the December imagery tend to be as bright as the April and October ones (Figure 6.2.3 (b) to (f)) if not brighter (Figure 6.2.3 (d)). This is not apparent when comparing the image data (Plates 6.2.1 (a) and 6.2.1 (b)) because these images were individually contrast stretched to give a pleasing appearance. In order to compare image spectra a correction based on Figure 6.2.3 (a) was applied to remove seasonal illumination differences. The corrections applied to the April and October spectra are illustrated in Figure 6.2.4(a).

Figures 6.2.4 (b) to (f) represent illumination-corrected image spectra extracted from areas affected by the April 1993 eruption (see Figure 6.2.1 for sample location sites). Image-derived spectra for the main pyroclastic flow (Figure 6.2.1 (b), (c) and (d)) are very similar. They compare well with the lab-based pumice spectrum (Figure 6.2.2 (b)), the major difference being in the SWIR, where OPS 7 exhibits an unexpected reflectance peak. OPS 7 is very severely affected by noise, and we interpret this spectral peak as a noise characteristic rather than a spectral feature. Excluding this spurious SWIR peak increases the similarity with the lab-based pumice spectrum. Differences such as the rapid increases in reflectance across the visible channels (OPS 1, OPS 2 and OPS 3) suggests that these spectra are partially influenced by the spectral features of ash. Therefore the image-derived spectra represent a mixed spectral response of both pumice and ash.

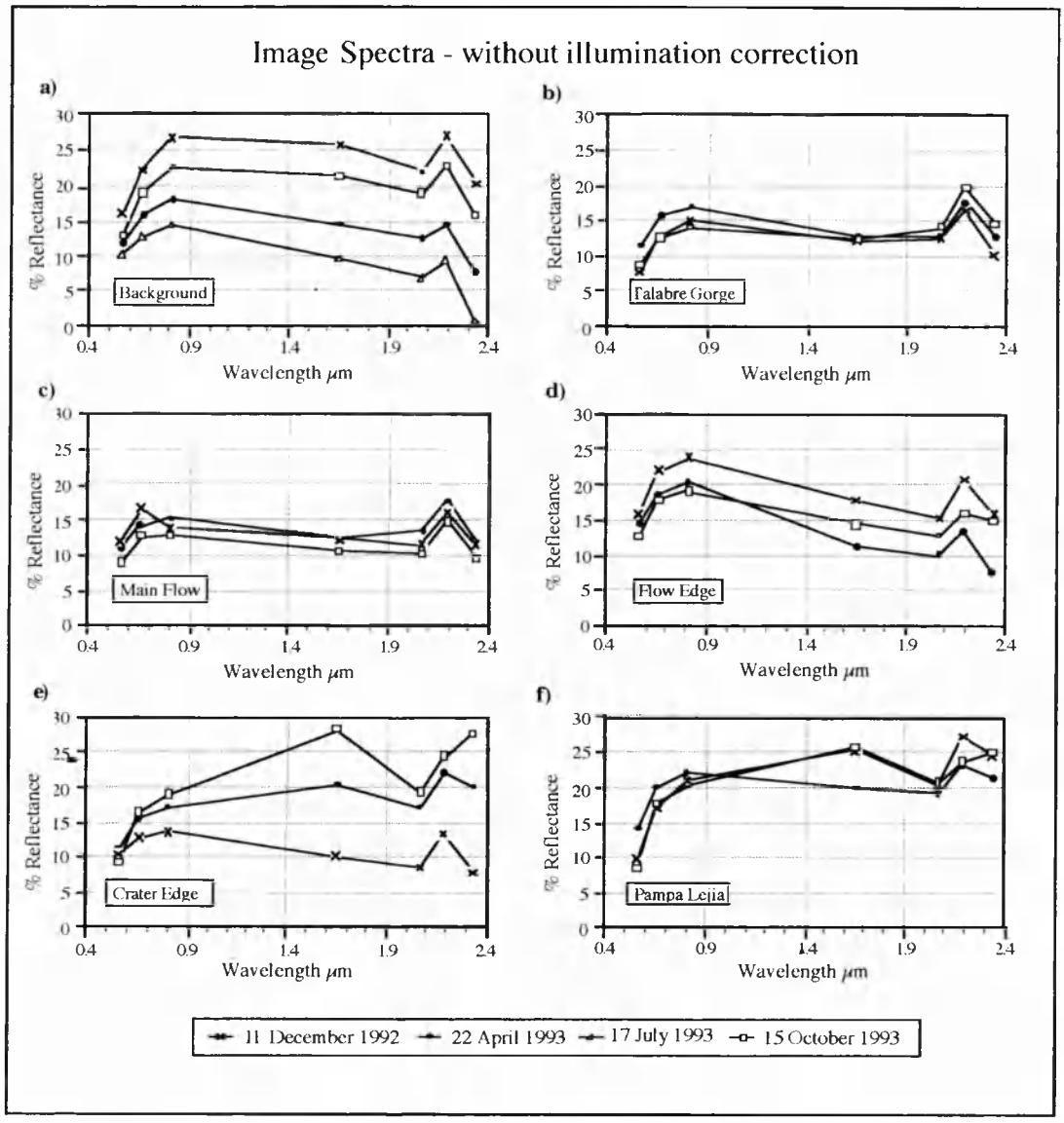

Figure 6.2.3 (a) to (f) Image spectra derived from atmospherically corrected OPS data, for different parts of the pyroclastic flow. These spectra are dominated by seasonal illumination differences as seen in (a). Refer to text for a full description. (Note spectra from the 17th July are not shown in plots (b) to (f) as the region was snow covered on this date). Refer to Figure 6.2.1 for location of spectra.

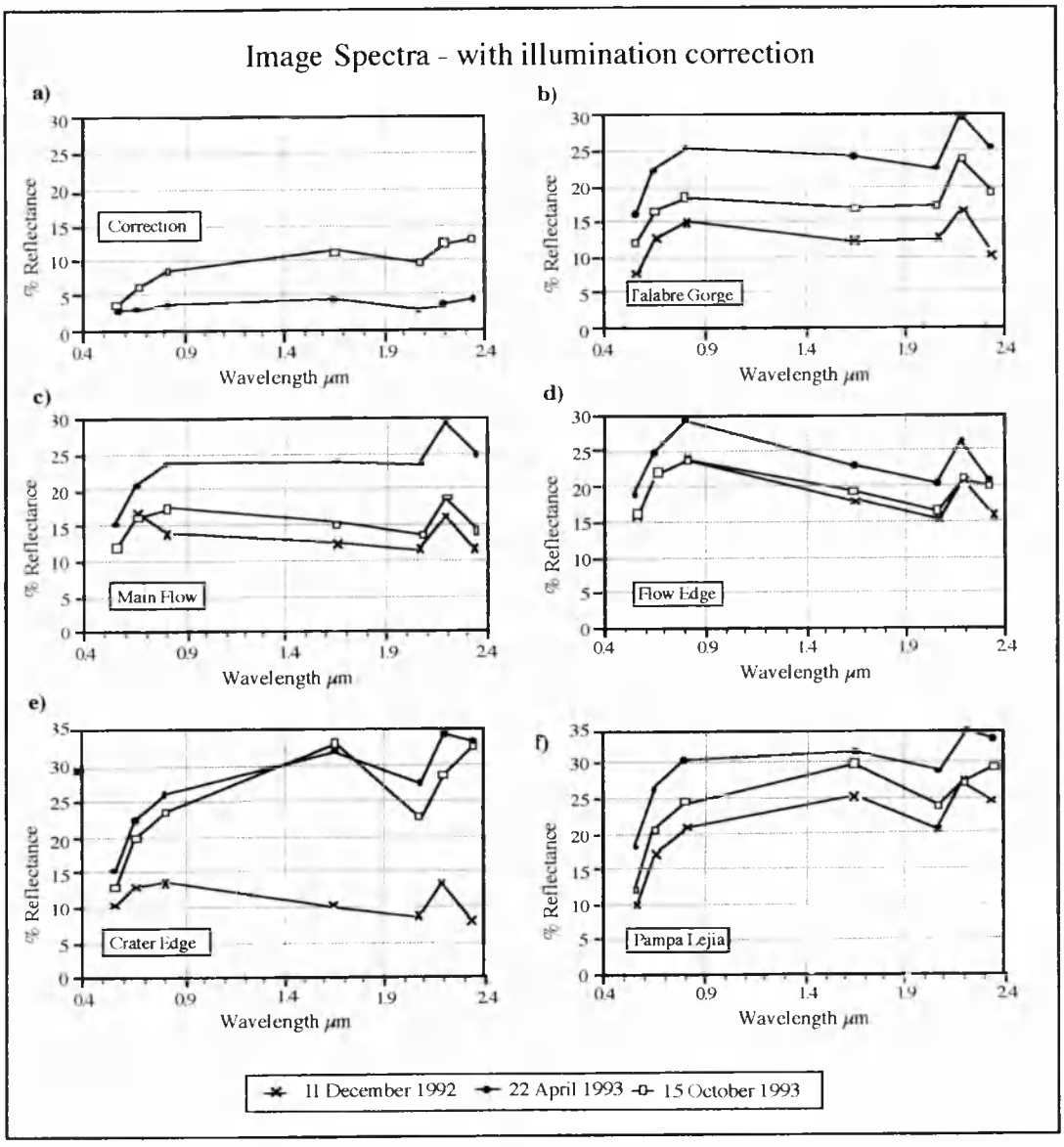

Figure 6.2.4 (a) Illumination correction factors. (b) to (f) Image spectra derived from atmospherically corrected OPS data with a seasonal illumination correction applied. Refer to text for a full description.

The corrected spectra show that the April spectra are much brighter than the December ones, whilst the October ones vary depending on their location. October spectra from the edge of the flow (Figure 6.2.4 (d)) are almost identical to the original December spectra, suggesting that the April variation seen at these locations was caused primarily by ash, material which has been removed from the flow edges on the October imagery. This rapid removal of material is illustrated in Plates 6.2.2 (a) and (b) which show very obvious changes from a region on the western edge of the northern flow (see Figure 6.2.1 for location).

Image-based spectra from near the active crater edge (Sample site 'e', Figure 6.2.1) show the most marked temporal variations, these being particularly apparent in OPS 5 (Figure 6.2.4 (e). This is a location of a persistent bright area and snow-melt (Plates 6.2.1 (a) to (d)), indicating the presence of a persistently active fumarole field. These spectra are therefore influenced by the effects of fumarolic alteration and deposition of sublimates. The Pampa Leija spectra illustrate most clearly the spectral changes caused by the 22 April eruption (Figure 6.2.4 (f)). The April imagery shows this region to be ash covered, whereas it is almost ash-free on the December and October images. The image-derived spectra support this, the April spectrum being markedly higher than the December spectrum, showing high visible reflectance levels caused by the overlying ash deposit. By October the reflectance levels have started to decline because the ash deposit has been partially removed by erosional processes.

3) Thermal observations

If a pixel were entirely filled by a surface at a uniform temperature, to be radiant in OPS 8 the surface temperature would have to be at least ~120-160 °C. However, where the hot source occupies only a fraction of a pixel, as is more likely, its temperature must be greater. Similarly, radiance in OPS 5 indicates a minimum surface temperature of ~265-185 °C.

Inspection of the thermal anomalies in the JERS-1 OPS time-series reveals marked changes in the size and structure of the anomaly through time (Plates 6.2.3 (a) to (d). Two major hot spots radiant in both OPS 5 and OPS 8 can be seen in the December 1992 composite (Plate 6.2.3 (a), accompanied by six smaller hot spots radiant in OPS 8 only. The 22 April 1993 image (Plate 6.2.3 (b) shows one large hot spot radiant in both OPS 5 and OPS 8 at the centre of the crater.

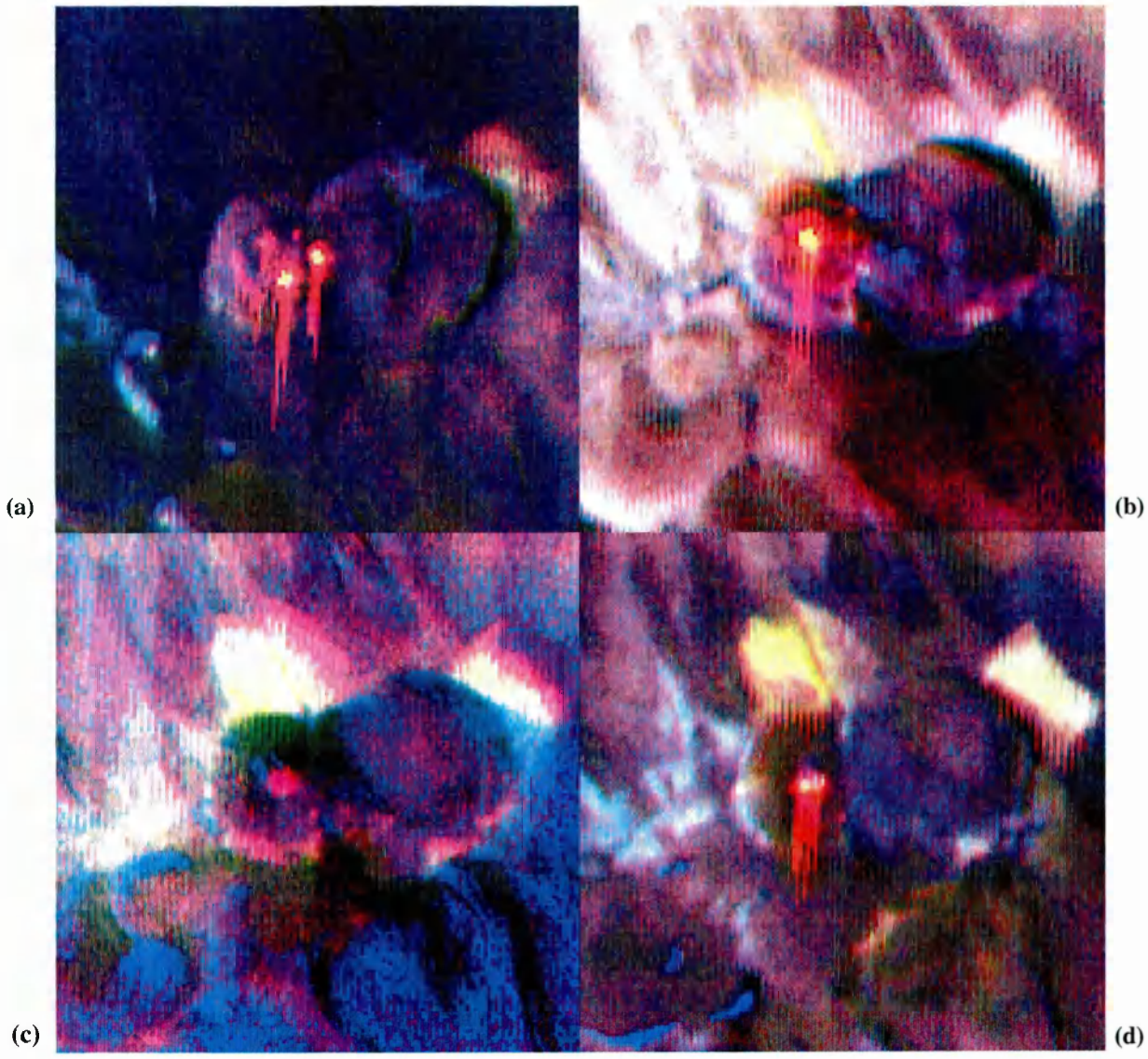

Plate 6.2.3 JERS-1 OPS composites of channels 851 in RGB of the Lascar summit craters (images approximately 3km square), (a) 11 December 1992, (b) 22 April 1993, (c) 19 July 1993, and (d) 15 October 1993. Thermal hot spots are depicted as yellow areas if they are radiant in both OPS 8 and OPS 5 (hottest point sources) or red if only radiant in OPS 8. Note that severe noise structures are visible in these images, especially vertical and horizontal stripes, and along-track blurring.

By 19 July 1993 (Plate 6.2.3 (c)) thermal radiance had greatly diminished, with a single hot spot radiant in OPS 8 only. Unlike the other three composites, the hot spot in this image has not been smeared along-track, indicating that the radiance contrast between the crater background and the hot spot is not as great as on the other images. By 15 October 1993 (Plate 6.2.3 (d)) thermal radiance had once again increased, with an area radiant in OPS 5 and OPS 8.

Since the hot spots are affected by along-track noise and image blur, we do not attempt to use the spectral radiances to derive temperatures and sizes of the sub-pixel radiance sources in the manner previously achieved by Rothery *et al.*, (1988) and Oppenheimer *et al.*, (1993) using TM images of Lascar. However, the data are consistent with radiance sources at magmatic or near-magmatic temperatures occupying small areas (perhaps less than 1% of each affected pixel). On the pre-eruption image (Plate 6.2.3 (a)), the more central of the two hottest sources probably corresponds to the collapsed dome over the vent (Matthews *et al.*,. 1997), whereas the other radiant sources are fumeroles. We note that there was an unusually hot fumerole near the eastern rim of the active crater. The post-eruption images (Plate 6.2.3 (b) to (d)) all show essentially a single radiant source in the middle of the active crater. The persistence and confined nature of this anomaly suggests that it is a lava dome or lake, field observations confirm this body to be a dome (Matthews *et al.*, 1997). Figures 6.2.5 (a) and (b) indicate the structure of the lava dome within the active crater.

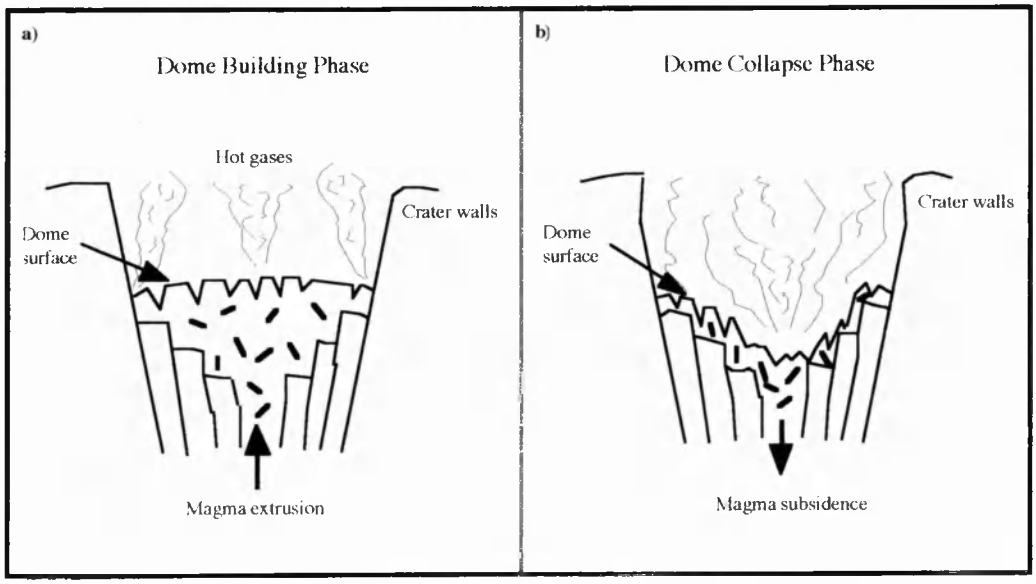

Figure 6.2.5 Schematic diagram (after Matthews *et al.*, 1997) showing the phases of (a) dome building and (b) dome collapse, within the active crater.

Changes in thermal structure over this eight month period (Figure 6.2.6) suggest the following course of events:

(i) An active lava dome was sited within the active crater until at-least 5 months prior to the April 1993 eruption. The presence of a lava dome is confirmed by ground observations, however these note dome collapse after November 1992, with the dome completely disappearing by March 1993 (Matthews *et al.*, 1997). That the dome was collapsing during December 1992 may explain the fragmented nature of the main anomaly on the December image (Plate 6.2.3 (a)).

(ii) The dome was immediately re-established following its destruction during the April 1993 eruption. Extrusion of a new dome as early as 20 April was inferred from the position of the eruption column, with the first definite observation on 26 April (Matthews *et al.*, 1997). The 22 April image confirms re-establishment of the dome 4 days earlier than was possible from the ground (Plate 6.2.3 (b)).

(iii) A return to a phase of dome collapse had occurred by July, this being indicated by the decay of the anomaly by 19 July (Plate 6.2.3 (b)). Ground observations show collapse began on 19 May, was continuing on the 11 June and was followed by a small explosive eruption in August (Matthews *et al.*, 1997).

(iv) Subsequently the dome re-established, once again being apparent as an anomaly by the October image (Plate 6.2.3 (d)). The lower radiance in July 1993 than in either April or October is consistent with the trend extracted from a more temporally detailed time series of measurements of the 1.6 μm flux made using ATSR-1 data (Wooster and Rothery, 1997).

This dome growth-collapse-explosion cycle of activity is consistent with the model given for Lascar by Matthews *et al.*, (1997). They suggest that extrusion of a dome is accompanied by vigorous degassing. Degassing lowers the magma volume and permeability. Dome collapse, initiated by this decrease in magma volume, further restricts gas flow and results in pressure build-up. When gas pressure exceeds the strength of the collapsed dome an explosive eruption occurs, initiating a new cycle.

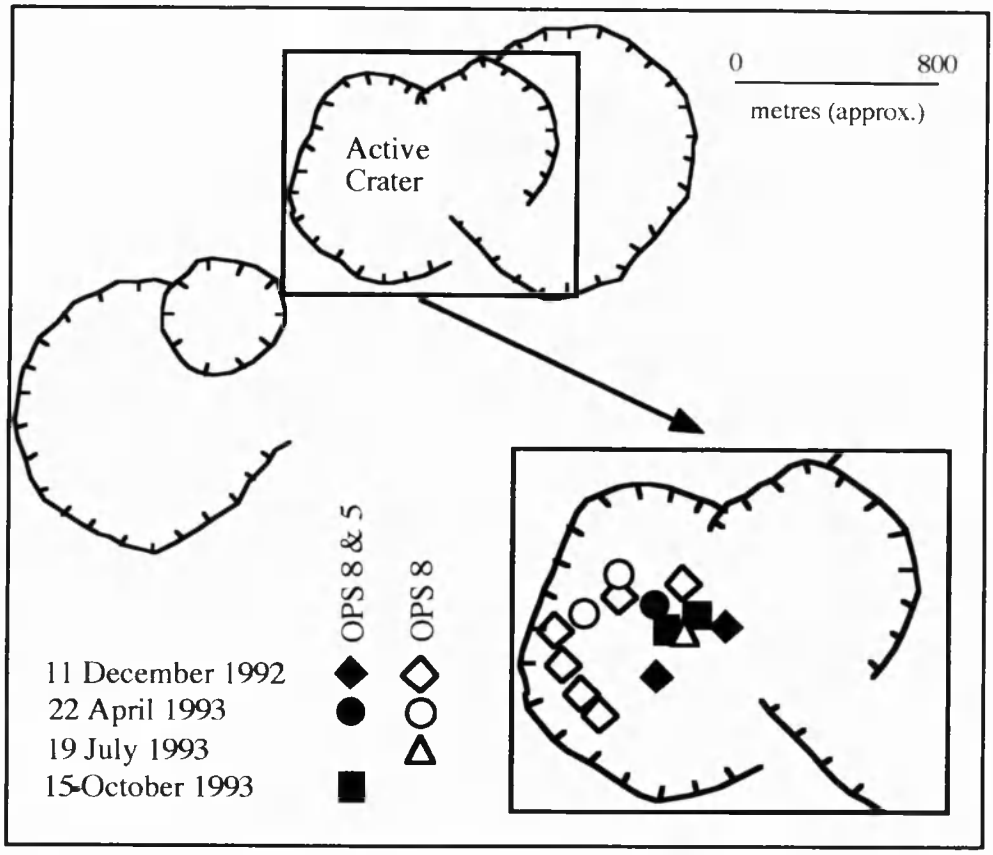

Figure 6.2.6 A map of thermal activity within the central crater as derived from the four OPS scenes. Pixels radiant in both OPS 8 and OPS 5 (high temperatures) are located in the centre of the crater, whilst pixels only radiant in OPS 8 (cooler temperatures) are located around the north and western edge of the crater. The hotter anomalies represent the active lava dome whilst the cooler ones represent fumeroles, with the exception of one 'hot' December feature (Eastern edge of crater) which is a fumerole.

6.2.6 AVHRR observations during the eruption

Although the spatial resolution of the JERS-1 OPS allowed us to map the pyroclastic deposits accurately, the return period meant that no images were coincident with activity. However, cloud-free AVHRR images were available during and just after the eruption, on 20 and 21 April respectively.

1) Plume observations

On 20 April three large explosions were reported. The first two explosions occurred at 06:28 and 09:20 (all times = GMT + 4 hours), producing columns ~10 km high. The columns remained at 2 to 4 km until the third explosion at 13:02 sent a column to 8.5 km, which drifted NE. By 15:00 the column height had decreased to 3.5 to 4 km, and persisted at this height until 19:15 when darkness prevented further ground

observations (GVN, 1993). Our 20 April image was acquired during this final phase at 16:53, and showed that the column had changed direction, drifting from its source at Lascar SE before turning SSE.

The plume is evident in all AVHRR channels, but is clearer as a negative thermal anomaly in AVHRR 4 and 5 than as a reflectance anomaly in AVHRR 1 and 2. This is explained by low plume top temperatures due to adiabatic cooling with plume rise. We have estimated the instantaneous plume dimensions using the simple trigonometric relationships shown in Figure 6.2.7, and plume height using shadow length measured parallel with the solar azimuth angle, in the trigonometric relationship given by Holasek and Self (1995).

At the time of the 20 April image, the plume extended SE for ~245 km, reaching a maximum height of 3.8 km, before turning SSE for ~223 km, placing the plume front roughly over Monteros (Argentina). Along this length, the plume widens in a roughly linear fashion until the final 100 km, where the plume shows a marked bulge (Figure 6.2.8). This suggests an initial explosive pulse, followed by a continuous, more or less steady, eruption rate. Regular "puff" structures were observed in the plume along the entire SE trending segment, evidence that the steady eruption rate is punctuated by regular pulses. Close to the vent a second minor plume, to the north of and sub-parallel to the main plume, was also identified.

Following the 13:02 explosion two columns were observed rising from the crater (GVN, 1993), the AVHRR observation confirms that the eruption continued to feed two columns: a minor northern column, and a much larger southern column at least until ~17:00. To the extreme east of the image a detached dispersing plume was observed, indicating a previous phase of activity, punctuated by a pause, before the current phase. The AVHRR image acquired on the following day at 16:41 shows no sign of a plume, indicating that the eruption had ended.

Such synoptic observations of plume location and extent are of great importance for air traffic safety. Ash plumes can cause engine failure, as well as extensive damage to aircraft bodies and windows (Hastrum & Watson, 1983; Prata, 1989; Kienle *et al.*, 1990).

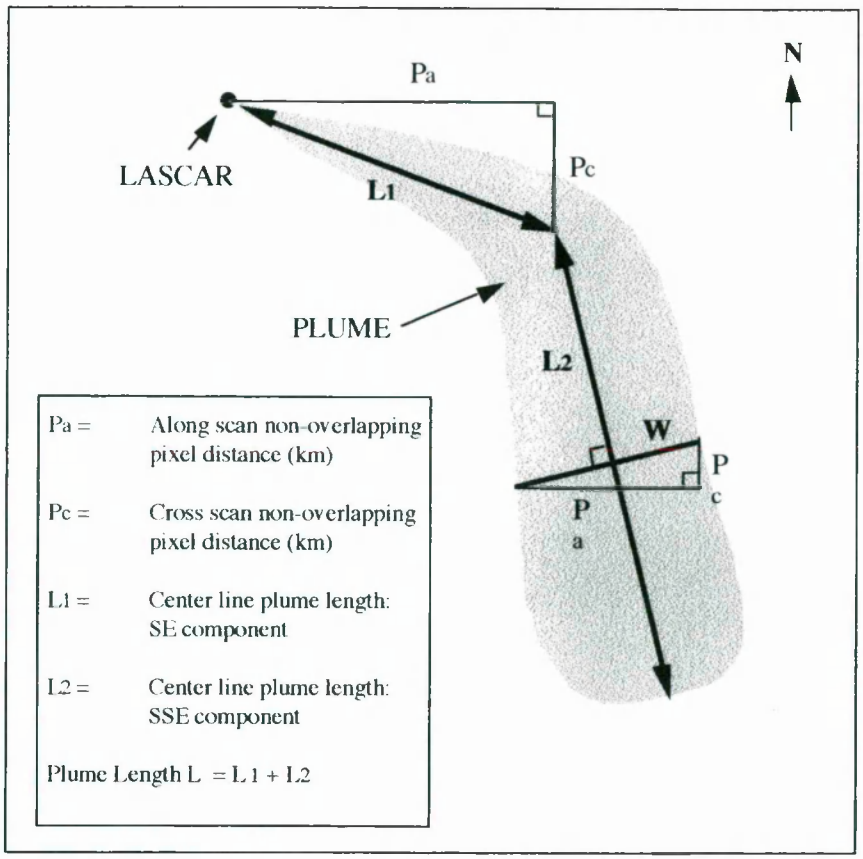

Figure 6.2.7 Geometric relationships used to estimate plume dimensions on the AVHRR imagery. Because the plume is bent, its total length is the sum of L_1 and L_2.

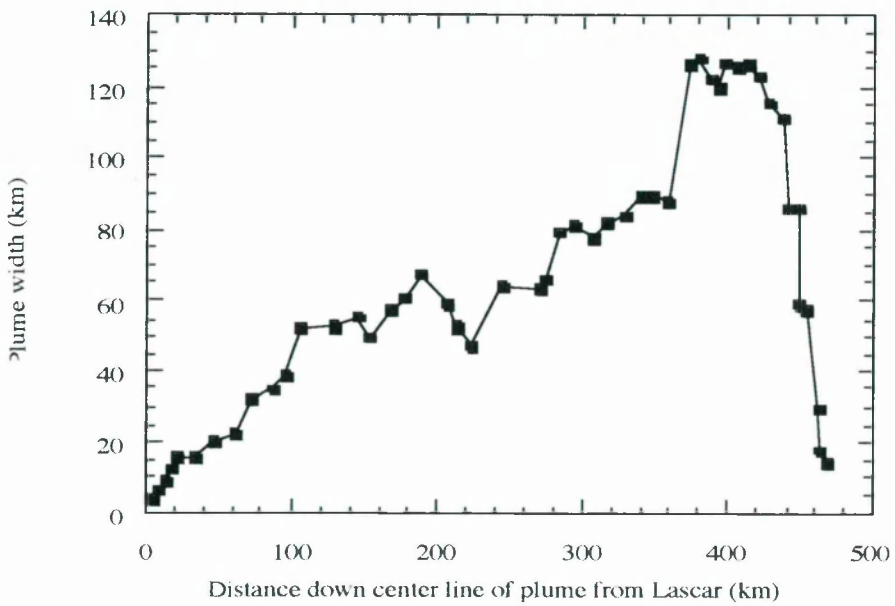

Figure 6.2.8 Plume width variations with distance down-plume at 16:53 on 20 April 1993, derived from AVHRR image analysis.

2) Pyroclastic flows

The pyroclastic flows were clearly evident as a thermal anomaly in AVHRR on the 20 and 21 April images. The anomaly indicates extensive pyroclastic flows extending down the NE flank of the volcano, with a shorter, narrower, anomaly on the S flank. In agreement with ground-based and JERS-1 OPS observations, the anomaly extends <7.8 km to the NE and <3.1 km to the S.

The thermally anomalous pixels are assumed to contain two thermal surfaces: high temperature pyroclastic flow at temperature T_h which occupies portion p of the pixel and cooler, flow-free, ground at temperature T_c which occupies the remainder $(1-p)$ of the pixel. This assumption allows the simultaneous equations, first given by Dozier (1981) to measure the size and temperature of sub-pixel hot spots in AVHRR data, to be applied:

$$R_3 = \varepsilon_3 \tau_3 [p\, L_3(T_h) + (1-p)\, L_3(T_c)] \quad (1)$$

$$R_4 = \varepsilon_4 \tau_4 [p\, L_4(T_h) + (1-p)\, L_4(T_c)] \quad (2)$$

In which R_3 and R_4 are the at-satellite radiances in AVHRR 3 and 4, ε_3, ε_4, τ_3 and τ_4 are the emissivities of the surface and transmissivities in each channel, and $L_3(T)$ and $L_4(T)$ are the Planck function spectral radiances for a blackbody of temperature T in AVHRR 3 and 4 respectively. To be solvable, only two unknowns are allowed in Equations 1 and 2. R_3 and R_4 are already known, ε_3 and ε_4 are set to 0.96 and 0.93 respectively using the emissivity of andesite given by Salisbury and D'Aria (1994), τ_3 and τ_4 are calculated using the widely-used atmospheric transmissivity model LOWTRAN, and T_c is estimated using the mean temperature of the nearest flow-free pixels. This allows T_h and p to be estimated.

If AVHRR 3 is saturated Equations 1 and 2 cannot be solved. AVHRR 3 saturates at a range of apparent (pixel-integrated) T_3 between ~47 and 50 °C (Setzer and Verstraete, 1995; Harris *et al.*, 1995b). A source at just 100 °C occupying ~0.2 of a pixel, against a background of 0 °C, will achieve this saturation temperature in AVHRR 3, so it is not surprising that 13 of the 22 thermally anomalous pixels on the 20 April image were saturated. For these pixels we set T_h using the maximum T_h from surrounding flow

pixels for which Equations 1 and 2 are solvable, and estimate p, following Oppenheimer (1991), from:

$$p = \{[R_4 / \varepsilon_4 \tau_4] - L_4(T_c)\} / \{L_4(T_h) - L_4(T_c)\} \quad (3)$$

Using the results of Equations 1, 2 and 3 we estimate that newly emplaced high temperature pyroclastic flow covered ~13 ±2 km^2 on 20 April. This compares well with a total area of 18.5 km^2 using the 22 April JERS-1 OPS image. The discrepancy could be due to a number of reasons, including: (1) Weakness in the assumption that the pixel is occupied by just two thermal components, and that the pyroclastic flow surface is isothermal across the pixel. Although we believe the assumption to be broadly valid since Banks and Hoblitt (1981) measured variations of just ~100 °C over the final 3 km of the 18 May 1980 pyroclastic flow from Mount St. Helens. (2) The AVHRR estimate is a measure of the radiant area, rather than the total area. Flow units emplaced during 18 and 19 April, on which rapid cooling was observed (GVN, 1993), may already have cooled closer to the ambient background, especially in thinner parts of the flow. The thermal signal from the flow may also be masked by ash fall deposits on the flow surface. (3) Masking of portions of the flow by the eruption plume.

Using the sharpening method given by Harris *et al.*, (1995a), we mapped radiative flux from the flow (R_{flow}) using

$$R_{flow} = \sigma \varepsilon T_h^4 \quad (4)$$

in which σ is the Stefan-Boltzmann constant (5.67 x 10-8 Wm^{-2} K^{-4}) and ε is emissivity integrated over all wavelengths [in this case we use 0.9897, the mean infrared emissivity of andesite from Salisbury and D'Aria (1992)]. Figure 6.2.9 shows that highest radiance occupies a small region in the vicinity of the summit craters. Radiance then decreases down-flow. This is in agreement with the ground based thermal observations of the pyroclastic flows made by Banks and Hoblitt (1981) following the May 1980 Mount St. Helens eruption.

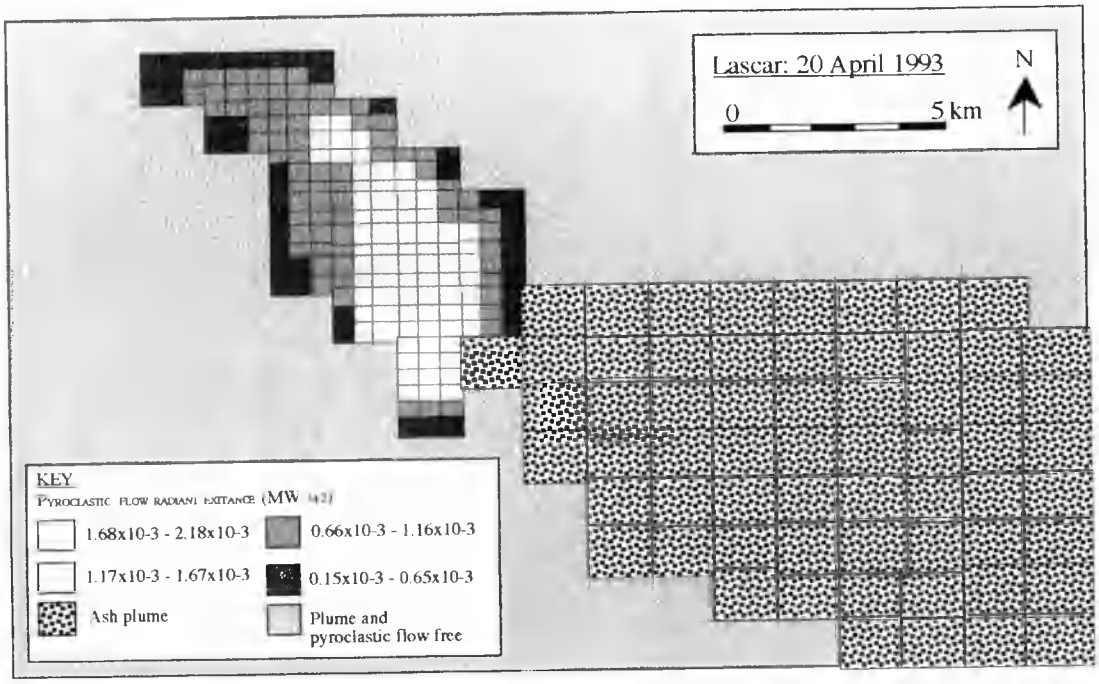

Figure 6.2.9 Thermal map of the April 1993 flow derived from AVHRR imagery.

They found rapid decreases in emplacement temperature in the first few hundred meters of travel followed by less substantial temperature decreases over the remainder of the flow, suggesting rapid initial cooling of the flow due to entrainment of air and adiabatic cooling, after which very little cooling occurs. The trend (N then W) of the thermal anomaly mapped in Figure 6.2.9 is consistent with the flow trend seen in the JERS-1 OPS image, Figure 6.2.1b.

6.2.6 Conclusion

For the April 1993 eruption at Lascar the combined JERS-1 OPS and NOAA-AVHRR data sets provide complementary data allowing a moderately complete analysis of this geographically remote volcanic event. NOAA-AVHRR image acquisition coincided with the event and was able to provide reliable information for the eruption in progress, and JERS-1 OPS allowed a detailed analysis of the pyroclastic flow after its emplacement and of pre- and post-eruption intra-crater activity.

We suggest that remote sensing data can be most usefully used by volcanologists as an integrated data source, taking advantage of data collected by a number of complementary sensors, each with their own contribution, either temporal, spectral or spatial. Using current sensors an integrated approach would consider: (1) Geostationary satellite observations (e.g. METEOSAT), to locate a major plume or

thermal anomaly within 30 minutes of an eruption (2) AVHRR, to supply an initial report for the activity within 6 hours (depending on cloud-cover), and (3) A JERS-1 OPS type sensor, to provide a detailed analysis within a month.

We note that a number of volcanologically useful satellites will add to the current data pool by the end of the century. For example: EOS-MODIS (Earth Observing System - Moderate Resolution Imaging Spectrometer) will provide 250 - 1000 m pixel data at 36 spectral bands every one to two days, EOS-HIRIS (High Resolution Imaging Spectrometer) will provide 30 m SWIR data and MSG-SEVIRI (Meteosat Second Generation - Spinning Enhanced Visible and Infrared Imager) will give thermal data every 15 minutes. The Advanced Along Track Scanning Radiometer (AATSR) to be carried by Envisat (1998) offers several advantages over current AVHRR and ATSR instruments, as will the improved AVHRR (AVHRR/3).

We hope that these new data sources will also be of improved quality, most importantly with reduced noise and higher dynamic ranges providing quantitatively and qualitatively usable, un-saturated, data over hot targets. For near-real time monitoring, either direct data reception or minimal data supply time delays must be achieved with these new sensors, if the advantages of remotely sensed data are to be fully realised. Full or semi-automation of volcanic event detection must also be a goal if all available data are to be utilised in a timely and efficient way, because the repeated analysis of data from numerous satellites over hundreds of active volcanic targets is not possible using only manual techniques.

6.2.7 Acknowledgements

The authors would like to thank Takashi Nishidai for his considerable assistance in locating JERS-1 data for this study, and Steve Matthews for generously loaning rock samples collected at Lascar. The kind assistance of NERC-EPFS for providing access to a spectroradiometer is also acknowledged. This work was undertaken by Anthony Denniss whilst funded by a NERC PhD award, and Andy Harris whilst funded by an Open University PhD grant. Dave Rothery was principal investigator of JERS-1 evaluation project J-0101.

7.0 Suitability of JERS-1 OPS and future sensors for geological mapping and volcano monitoring

7.1 Suitability of JERS-1 OPS for:

7.1.1 Lithological mapping

The design of the optical sensor on JERS-1 promised to increase lithological discrimination from satellite data significantly. Pre-launch simulation studies (Yamaguchi, 1988) showed that three narrow bands in the 2.0 to 2.5 μm part of the spectrum would allow the important Al-OH, Mg-OH and CO_3 absorption features to be detected and discriminated between, a level of detection and discrimination (as demonstrated in section 2.4.2) not available from any other satellite platform. Unfortunately numerous problems with the OPS sensor, and in particular with the SWIR subsystem, meant that the data acquired by JERS-1 were not at the multispectral resolution anticipated.

This thesis has shown (chapter 2) that OPS data quality is extremely variable from both scene to scene and from channel to channel. Sensor induced noise artefacts, combined with poor dynamic ranges, and gross inter-channel and inter-sensor misregistration problems have resulted in the majority of OPS data being of little use for most applications. Despite these problems, this thesis has shown that noise removal techniques (chapter 3) can improve significantly the quality of some OPS channels. However, these techniques cannot solve all the problems associated with OPS data, for example noise removal does not improve the poor dynamic ranges associated with OPS 6 and OPS 7. The seriousness of some noise artefacts results in only four or five channels of OPS data being usable instead of the expected seven. This had the effect of reducing significantly the spectral differences between TM and OPS data. The poor quality of OPS data also meant that it is difficult to apply intensive image processing functions without rapidly degrading the data quality further. In the case of this thesis, only four channels of data (OPS 2, OPS 5, OPS 6 and OPS 8), were used to produce colour composites suitable for analysis of the three

study areas. These channels were used because after applying noise removal techniques they provided the highest quality spectral data.

The choice of OPS channel combinations for the three study regions in this thesis were restricted to either OPS 852 or OPS 862. OPS 852 was the superior composite with respect to data quality and spectral information. OPS 862 tended to be used as a substitute composite when OPS 5 was particularly noisy. Despite data quality induced restrictions, these channels, especially OPS 852, have shown that they contain very useful geological information. This in part can be attributed to the high quality of these three channels when compared with the other OPS channels, and in turn to the success of noise removal techniques applied to these channels. However the main reason why these 'good' channels are useful for geological applications is due to their locations at distinct parts of the electromagnetic spectrum; 0.63-0.69 μm (OPS 2); 1.60-1.71 μm (OPS 5) and 2.27-2.4 μm (OPS 8). These three channels correspond to parts of the spectrum dominated by both iron (OPS 2) and Mg-OH (OPS 8) absorptions, and to varying peaks in reflectance (OPS 5). These three channels are ideally situated to record varying reflectance information for the majority of ophiolite lithologies and may well have been the three channels of choice even if all OPS channels were available at high quality.

Chapter 5 illustrated the effectiveness of an OPS 852 colour composite for discriminating the majority of the ophiolite lithologies. It also clearly demonstrated that the OPS composite provided more geological information than the equivalent Landsat TM composite. Comparing the OPS 852 composite to a TM 754 decorrelation stretched image (deemed the best TM composite for lithologic discrimination) a number of key geological features where identified on the OPS composite that were not visible on the TM composite, i.e., dunite, wehrlite, cumulate gabbro, cumulate peridotite and serpentinite. This increased discrimination on the OPS composite was a direct result of:

- the wavelength range of OPS 8 (2.27-2.40 μm) extending further into the SWIR than TM 7 (2.08-2.35 μm)
- the narrow bandwidth of OPS 8 (0.13 μm) compared with the broad bandwidth of TM 7 (0.27 μm)
- the dominant effect of Mg-OH (hydroxyl) absorptions on OPS 8 compared with their limited effect on TM 7 response

- the narrow bandwidth of OPS 5 (0.11 μm) compared with the broader bandwidth of TM 5 (0.20 μm)
- the significantly increased spatial resolution of OPS (18 m pixels) compared with TM (30 m pixels)

The five factors listed above are the main reasons why OPS data significantly increased lithological discrimination in the three study regions examined in this thesis. A sixth minor factor which was advantageous was the reduced topographic shadow in the OPS composites compared with the TM composites. The reduced shadow on the OPS imagery prevented spectral information being lost in the bottom of some wadis, areas which were often in dark shadow on the winter TM imagery. The disadvantage of this was that some textural information used to help distinguish areas of mantle and crustal lithologies was lost on the OPS imagery. However this problem can be overcome by merging OPS data with topography derived from TM, SPOT or aerial photography.

Prior to launch it was anticipated that OPS data would improve lithological discrimination significantly within the Oman ophiolite. Subsequent data inspection indicated that this might not be the case due to the severity of the noise problems associated with these data. However, despite these problems, OPS data have been very effective at discriminating the ophiolite lithologies in all three study regions examined during the course of this thesis. In all three areas the limited combination of three 'good' OPS channels has provided more geological information than provided by all six TM bands (not including TM 6). This increased discrimination proves the importance of having narrow spectral channels coincident with major spectral absorption features.

During the course of this study I was consulted by a number of companies regarding the suitability of OPS data for geological applications. In all cases I advised that OPS data quality varies considerably from scene to scene, therefore requiring all archived data covering an area of interest to be checked for suitability. Obtaining high quality data is therefore the major acquisition requirement, overriding any other acquisition requirements, e.g., a preferred time of year. Providing that at least three 'good' channels, including one of either OPS 6, OPS 7 or OPS 8 were available for the area of interest, it would be possible to produce a composite offering significant discrimination advantages over TM data. The additional processing time required to

register and clean individual channels of data would be offset by the increased geological information derived from the final composite.

7.1.2 Volcano monitoring

Within this thesis the use of JERS-1 OPS data for volcano monitoring has concentrated on the qualitative analysis of a time series of four OPS scenes, which straddled the 18 April 1993 eruption of Lascar volcano, Chile. These data allowed the extent of the pyroclastic flows emplaced during this major eruption to be clearly mapped, which allowed the area of the flows to be measured. They also showed significant spectral variation associated with the rapid erosion of fine ash material.

Analysis of these data also contributed important information about the intra-crater thermal activity during the 10 month period of data availability. During this period the high spatial resolution of the OPS data allowed a clear picture of the distribution of thermal hot-spots within the crater to be mapped. This included the identification of numerous small hot-spots around the crater edge (fumaroles), as well as a large central thermal anomaly (active dome). The identification of the small hot-spots associated with fumaroles is a direct result of the high spatial resolution of OPS data. It is doubtful if Landsat TM would have been capable of distinguishing these features as distinct thermal point sources. Unfortunately no contemporaneous Landsat TM data were available to compare with the OPS data so this cannot be confirmed. Without the availability of ground information, the identification of these additional smaller thermal sources helps the volcanologist to understand what is happening within the crater, i.e., cycles of dome growth or dome collapse. Deriving information like this directly from remotely sensed data is extremely important, especially when monitoring geographically remote volcanoes.

Prior to JERS-1 being launched it was predicted that the increased spectral resolution of OPS in the SWIR would allow the thermal emission from volcanic targets to be more effectively defined (Openheimer 1991). This would use an OPS multi-band approach to calculate surface temperatures of sub-pixel sized thermal sources as opposed to the dual-band technique implemented with TM data (Rothery *et al.*, 1988 and Openheimer 1991). During the course of this study the quantitative thermal analysis of the OPS hot-spots was not attempted due to severe along-track noise, image blur, poor dynamic ranges and misregistration affecting the data. It was felt that

uncertainties induced by these noise artefacts would make the end result very unreliable.

The potential offered by OPS data for the quantitative thermal analysis of volcanoes has never materialised due to the poor quality of the data. However, OPS data have proved to be useful for deriving semi-quantitative volcanological information, which may not have been discernible on lower resolution TM data. Unfortunately the potential of OPS for volcano monitoring was short lived as the effectiveness of OPS for even semi-quantitative thermal studies ceased with the failure of the SWIR sensor in December 1993 (Takata, 1995).

7.2 Geological potential of future optical sensors

7.2.1 Introduction

In recent years the application of optical remote sensing to geological studies has become rather stale because of the lack of new sensors and the reliance of the industry on Landsat 5. The launch of JERS-1 should have changed this situation, as it promised to offer significantly higher spatial and spectral resolution multispectral data, instead it signalled another disappointment in the space industry. This thesis has shown that JERS-1 was not a complete failure as it is possible to obtain significantly more geological information from OPS imagery than from the equivalent TM imagery. However obtaining this extra information is not a simple task because of the complex pre-processing required to remove or reduce noise artefacts, prior to interpretation. The poor quality associated with OPS data has resulted in the sensor having a bad reputation within the remote sensing industry. As a result very little work, especially geological work, has been attempted with OPS data. This problem has been compounded by the lack of data availability and poor commercial data distribution.

During the course of this thesis there have been some notable developments in optical remote sensing as well as some serious set-backs, most significantly the failure of Landsat 6, carrying the Enhanced Thematic Mapper (ETM) to reach a stable orbit, resulting in its demise in the Indian Ocean shortly after launch in 1995. SPOT-3 was launched successfully in September 1993, but has since ceased to operate after only a 4 year life span. A more successful story came from the Indian space industry which developed and launched both its first remote sensing satellite (IRS-1C) on December 28th, 1995 and its second (IRS-1D) on September 25th, 1997. These satellites are

identical, both carry three sensors acquiring imagery across five spectral bands at three different resolutions (see Table 7.1). Three of these bands (B2, B3 and B4) are spectrally equivalent to TM 2, TM 3 and TM 4, although at a slightly higher spatial resolution of 23.5 m. The major differences are the availability of a high resolution (5.8 m) panchromatic band (B1) and the capability of acquiring across-track stereoscopic data, with a five day repeat frequency. Repeat frequency for all other channels is 24 days, including the coarse resolution (188 m) B5 equivalent (spectrally) to TM 5. Data quality appears to be reasonable although poor radiometric resolution has slightly degraded the 5.8m resolution data. Geological applications of these data are limited because of the lack of SWIR bands. These satellites were primarily designed for vegetation studies. Currently data availability is extremely limited due to the small capacity of the on board recorder and the limited access to ground receiving stations, although this is due to change in the near future.

Indian IRS-1C and IRS-1D satellites			
Launched	28 December 1995, 25 September 1997		
Sensors	PAN	LISS-III	WIFS
Resolution	5.8 m	23.5 m	188 m
Swath width	70 km	142 km	810 km
Spectral resolution	(B1) 500-750 nm	(B2) 520-590 nm (B3) 620-680 nm (B4) 770-860 nm	(B5)1550-1700 nm
Stereoscopic ?	Yes	No	No
Repeat frequency	5 days	24 days	5 days
Orbit	817 km, 98.69°	817 km, 98.69°	817 km, 98.69°
Local image time	10.30 AM	10.30 AM	10.30 AM
Quantisation	6 bit	7 bit	7 bit

Table 7.1 Specifications of the sensors on board IRS-1C

A rather surprising development during the course of this project has come not from a new sensor but from existing military ones which were declassified (Mcdonald, 1995a, 1995b). This resulted in vast amounts of high resolution space-borne photography becoming available from both American and Russian platforms (Tables 7.2 and 7.3). Data from both the Russian and American systems are of mixed quality

	Russian Military Systems			
Name	KFA-1000	KFA-3000	KVR-1000	MK-4
Launched	1974	1978	1986	1988
Swath	80 x 80 km	21 x 21 km	40 x 40 km	170x170km
Resolution	5 m	2 m	2 m	8 m & 15 m
Wavelength	Panchromatic	Panchromatic	Panchromatic	0.51-0.56 μm 0.63-0.69 μm 0.81-0.90 μm

Table 7.2 Specification of Russian military spaceborne camera systems which are now available to civilian users.

	American Military Systems				
Name	KH 1-4	KH 4A	KH 4B	KH 5	KH 6
Launched	1959 - 63	1963 - 69	1967 - 72	1961 - 64	1963
Swath (~ km)	4 x 59 or 118 x 164	4 x 65	4 x 53	135 x 135	3 x 18
Resolution	8 m	3 m	2 m	150 m	2 m
Film type	B & W	B & W	B & W + Colour	B & W	B & W

Table 7.3 Specification of American military spaceborne camera systems which are now available to civilian users. Note the colour photography on KH 4B was a very limited trial, all other imagery is black and white.

and often appear to have a lower spatial resolution than specified. This is due to the images being captured initially in an analogue format (photographic) and then being digitised using a high resolution scanner.

The suitability of these data for geological applications varies considerably due to both quality and availability. Despite large data archives being available to the public (so far the Americans have declassified 860,000 images), available imagery tends to be concentrated in regions of the world which were once of military importance. Only KH 5 acquired imagery for routine mapping purposes. Despite the lack of geographic coverage these sensors provide some of the earliest spaceborne remotely sensed

imagery, which can be extremely important in change detection studies. The data are also very cheap compared with current commercial image prices.

Geological remote sensing may undergo a new lease of life over the next five years when a whole host of new satellite platforms will be launched. These can be roughly divided into high spatial and high spectral resolution optical sensors.

7.2.2 High spatial resolution sensors

The majority of the new satellite platforms to be launched over the next few years will carry very high spatial resolution sensors. These platforms will be used to produce panchromatic and multispectral space imagery at a resolution equivalent to aerial photography (see Table 7.4 for specifications). All of these satellites will be commercially owned and operated, and they will include:

1) Space Imaging

Space Imaging plan to launch a constellation of satellites starting in late 1997, with the aim of providing the first commercial data in January 1998. These satellites will capture data at two resolutions; single band panchromatic at 0.82 m and four band multispectral at 4.0 m (see Table 7.3 for wavelengths). A combined panchromatic and multispectral product (CARTERRA) will be available from these data. The CARTERRA product will be georeferenced using accurate orbit information, allowing the production of ortho-images which are geographically correct to +/- 12m in standard mode and +/- 1.5m in precision mode. Swath width will be 11 km and revisit time will be 4 days. Along-track stereoscopic data will also be available, from which Digital Elevation Models can be produced.

2) Orbimage / Orbview

Orbimage plan a series of new satellites including Orbview-2 which is similar in design to AVHRR. Orbview-3 is the high spatial resolution satellite which will be launched in late 1997. Orbview-3 will produce panchromatic data at 1 m and 2 m, and four band multispectral data at 4 m resolution (see Table 7.3 for wavelengths). Swath width will be 8 km and revisit time will be 3 days.

3) EarthWatch

EarthWatch are developing two different constellations of satellites; EarlyBird and QuickBird. The first satellites developed will be the EarlyBird series, with the first being launched during 1997. These satellites will carry two sensors a 3 m single band panchromatic and 15 m three channel multispectral scanner (see Table 7.3 for wavelengths). Standard swath widths will be 3 km for the panchromatic and 15 km for the multispectral. EarlyBird will also be able to collect single images up to 30 km x 30 km by using a special focal plane array. The imaging array can be pointed 28° across-track and 30° fore-aft, allowing images to be captured over a broad area. This movement also allows along-track and across-track stereo images to be acquired. Since time of writing EarlyBird has failed (June 1998) to reach a stable orbit. The second series of satellites, QuickBird, will be launched late in 1998. These satellites will have both panchromatic and multispectral sensors although these will be of a higher resolution than those on EarlyBird. The QuickBird panchromatic sensor will have a resolution of 0.82 m and 3.28 m for the four band multispectral sensor, both of these will have a 22 km swath width. Like EarlyBird, QuickBird is designed to allow the collection of data over broad areas, ranging from 484 km^2 to 40,500 km^2. Both of these sensors will have the ability to store vast amounts of data on board prior to being downloaded to the next available ground station.

4) Satellite Probatoire d'Observation de la Terre (SPOT)

The SPOT series of satellites will also continue to be developed with the launch of SPOT-4 in late 1997 and SPOT-5 in late 2001. Spot-4 will be like its predecessors except that it will have a new multispectral band approximately equivalent to TM 5 at 1.58 - 1.75 μm. Band 2 (0.61-0.68) has been duplicated at both 10 m and 20 m resolution to allow easy registration of all bands. This change has been made at the expense of removing band 1. The only other major change is the addition of two HRV-IR instruments designed for vegetation monitoring. Spatial resolution comparable to the satellites described above will not become available until the launch of SPOT-5 in 2001, which will have a 5 m panchromatic mode. SPOT-5 will also see an increase in the multispectral resolution from 20 m to 10 m. Otherwise SPOT-5 will be fairly similar to SPOT-4.

Specification	Space Imaging	OrbView-3	EarthWatch EarlyBird	EarthWatch QuickBird	SPOT-5
Launch date	Autumn 1997	NA	Spring 1997 (delayed)	Autumn 1998	Late 2001
Sensor types	Pan, MS	Pan, MS	Pan, MS	Pan, MS	Pan, MS
Resolution					
- Panchromatic	0.82 m	1 m and 2 m	3 m	0.82 m	5 m
- Multispectral	4 m	4 m	5 m	3.2 m	10 m
Wavelengths					
- Panchromatic	NA	0.45-0.90 μm	0.42-0.70 μm	0.45-0.90 μm	0.51-0.73 μm
- Multispectral -1		0.45-0.52 μm	0.40-0.60 μm	0.45-0.52 μm	0.50-0.59 μm
- Multispectral -2		0.52-0.60 μm	0.61-0.70 μm	0.52-0.60 μm	0.61-0.68 μm
- Multispectral -3		0.63-0.69 μm	0.79-0.87 μm	0.63-0.69 μm	0.79-0.89 μm
- Multispectral -4		0.76-0.90 μm	NA	0.76-0.90 μm	1.58-1.75 μm
Swath width					
- Panchromatic	11 x 11 km	8 x 8 km	3 x 3 km	22 x 22 km	60 x 60 km
- Multispectral	11 x 11 km	8 x 8 km	15 x 15 km	22 x 22 km	60 x 60 km
Stereoscopic ?	Along-track	NA	Along-track	Along-track	TBA
Orbit	NA	470 km, NA	470 km, 97.3°	600 km, 52°	830 km, NA
Repeat freq.	4 days	< 3 days	2 - 5 days	1 - 4 days	NA
Local image time	NA	10.30 AM	10.30-11 AM	variable	10.30 AM
Location accuracy	~12 m (X,Y) ~1.5 m (X,Y)	NA	~ 150 m (X,Y)	~ 23 m (X,Y) ~ 17 m (Z)	~ 10 m (X,Y) ~ 5 m (Z)
On board storage	NA	NA	2 Gbytes	~ 137 Gbytes	NA
Quantisation	NA	NA	8 bit	11 bit	8 bit

Table 7.4 Specifications of new high resolution satellites due to be launched over the next few years. SPOT-4 is not included as its spatial resolution is not comparable with the other platforms described. All technical information has been obtained directly from the satellite manufacturers and may be subject to alteration prior to launch. NA denotes technical parameter not available at time of writing.

7.2.3 Geological significance of high spatial resolution data

All of the platforms described above have been designed primarily to supply imagery equivalent in resolution and quality to that of aerial photography. The major consumer market for this type of data will be service and utility industries, particularly those which require up-to-date geographic information in rapidly developing urban environments. All of these platforms will use a mixture of on board GPS, altitude sensors and star sensors to determine their precise orbit position at the time of image acquisition. This results in images whose position on the Earth's surface are known to within meters without the need for ground control points (GCPs). Space Imaging anticipate being able to geometrically rectify their imagery to a scale of 1:2400 without the use of additional GCPs. Image geometry can be further improved by using the DEM, derived from along-track stereoscopic data, to rectify the nadir image and produce an orthorectified image.

1) Geological mapping

The major benefits of high spatial resolution data in the context of geological mapping will be;

i) In arid areas where exposure is good these data will provide vast amounts of textural and structural information. Information which has previously only been available from air photographs, which are often not available for remote parts of the world, or are of a poor quality if available.

ii) The extremely small pixel size (< 1 m) will produce an order of magnitude improvement with respect to the scale of geological features discernible, for example increased detection of bedding, faulting and intrusions.

iii) Spectrally these satellites will provide data approximately equivalent to TM 1, TM 2, TM 3 and TM 4, thereby providing some geologically useful spectral information, such as vegetation anomalies and iron variations.

iv) In temperate climates winter imagery will provide new spectral and textural information relating to surface soils.

v) The majority of these sensors will have a 10.30 AM local image acquisition time, resulting in good relief and structural information on winter imagery.

vi) Acquisition of along-track stereoscopic data is also of use to the geologist. The production of an accurate DEM (*c.* 2-3 m in Z) for an area of interest, provides the geologist with additional information about the third dimension. Information which allows quantitative analysis of an integrated DEM and image product in order to

determine strikes, dips and structural contours. In some terrains the direct analysis of the DEM will also provide geologically useful information.

vii) High resolution rectified imagery will provide geometrically accurate base-images for areas where base maps do not exist. These products will allow other field information to be recorded accurately.

High spatial resolution imagery will also have disadvantages for geological mapping, including;

i) Very high resolution data does not produce a synoptic overview. Large amounts of data have to be processed and mosaiced to derive information for even small to moderate scale geological features. A process which is both time consuming and expensive.

ii) Colour composites derived from these sensors will be spectrally very poor, equivalent to a TM True Colour Composite (TCC).

iii) The 'new' nature of these sensors will mean that a long period of time may be required before sufficient imagery of an area of interest exists. A problem which will be far worse in temperate climates where cloud cover will cause severe acquisition problems.

iv) The high spatial resolution of these images will greatly increase file sizes, a QuickBird four band multispectral image may equal as much as 4 Gbytes. This will have the knock on effect of increasing both computer processing and storage requirements.

2) Volcano monitoring

High spatial resolution data will also offer specific advantages for volcano monitoring, including;

i) Providing detailed information within active craters, allowing the spatial extent of lava lakes and fumarole fields to be mapped (conditions permitting).

ii) All these satellites will have rapid revisit frequencies (< 5 days) compared with Landsat TM (16 days) and JERS-1 (44 days). This will vastly increase the imaging opportunities over volcanic targets, increasing the chances of acquiring good data. By utilising data from all of the different platforms (once they are all operational) it may be possible, depending on orbit configurations, to image a volcanic target daily.

iii) Increased data availability will significantly improve the temporal resolution of volcanic observations. Multi-temporal image analysis will be used to detect changes within an active crater and to monitor long term changes in lava lakes and fumarole fields.

iv) The high spatial resolution at visible wavelengths will allow small gas and steam plumes to be detected, information which is of interest to the aviation community as well as the science community.

v) DEMs derived from these sensors may be of a high enough resolution to detect dome growth (albeit on a large scale) prior to an eruption.

vi) All of the new satellite operators plan to offer a fast-track supply of raw data via Internet connections. This will hopefully mean that digital data are available to the end user within hours of being collected instead of days, weeks or even months later. It may even be possible to acquire data in almost real time, an option OrbView is considering.

vii) The high spatial and temporal resolution of these sensors will mean that regularly updated maps of volcanic targets can be quickly and easily produced. The availability of such maps is extremely important for disaster planning during times of crisis, both prior to and after an eruption.

The disadvantages of high spatial resolution imagery for volcano monitoring will include;

i) In many cases it will be difficult to obtain crater imagery which is not obscured by clouds, gas or steam plumes. This is a problem which affects all optical remote sensing platforms. To some degree it is less of a problem for these new sensors because of the significant increase in imaging opportunities offered by their rapid repeat frequencies, for example, a 5-day repeat frequency gives 72 imaging opportunities a year compared with only 23 for a 16-day repeat frequency (as per Landsat TM). The along- and across-track pointable nature of these sensors may increase imaging opportunities even further.

ii) Visible wavelength data are not suitable for observing thermal features. SWIR data are required to extract quantitative thermal information.

iii) Repeat acquisitions of volcanic targets will mean that data cost will become a significant factor determining the usefulness of high resolution data.

iv) Data volumes may also be a problem if imagery is being acquired for a volcanic target every few days, although this can be alleviated by extracting only specific areas of interest and disregarding the remainder of the scene.

3) Summary of the usefulness of high spatial resolution sensors

Data from these satellites may not be ideal for the mapping geologist but it should prove useful in a number of situations. Primarily high resolution data will be used to obtain detailed structural information about small specific sites, which have been identified using coarser resolution multispectral imagery. In remote locations the orthorectified quality of these images will be very important. It will be possible to use the imagery in conjunction with GPS to locate features precisely, a task which is sometimes difficult without using aerial photographs. The availability of accurate DEMs will also aid geological interpretations. In remote locations the DEM may also prove valuable for determining access routes to field areas or planning seismic surveys.

The volcanologist may find these data valuable for monitoring geographically remote volcanoes, because for the first time imagery at the resolution of aerial photography will be available on a regular basis. This will allow active craters to be regularly monitored for change detection on a scale never before possible. The analysis of this imagery, combined with along-track derived DEMs will significantly improve the level of routine monitoring for cloud-free active volcanoes, hopefully resulting in an improvement in eruption prediction. High spatial resolution imagery will be especially useful during times of volcanic activity, by using all the different satellite platforms it will be possible to acquire high resolution imagery of an eruption site within days, if not hours of the event. This will be especially important for post-eruption monitoring and disaster planning. The rapid acquisition of imagery will help in assessing the level of damage in the vicinity of an active volcano.

7.2.4 High spectral resolution sensors

The spectral resolution of satellite sensors is also due to improve over the next few years with the launch of four new multi- and hyper-spectral sensors. These can be divided into 'higher' spectral resolution sensors (such as the Advanced Spaceborne Thermal Emission and Reflectance Radiometer (ASTER) and the Medium Resolution

Imaging Spectrometer (MERIS) and 'hyperspectral' sensors (such as the Hyper-Spectral Imager (HSI) and the Australian Resource Information and Environment Satellite (ARIES-1).

1) ASTER and MERIS

These two new sensors will provide 9 and 15 channels of data respectively. ASTER is due to be launched in June 1998 (Kahle *et al.*, 1991) and MERIS is scheduled for mid-1999. Neither of these sensors has been designed specifically for geological applications, but they will produce data useful for geological studies. Comparing the sensor specifications listed in Table 7.5, ASTER will provide the most geologically relevant data of these two sensors, because of its combination of spatial and spectral resolution. MERIS will provide some geologically useful information but this will be confined to VNIR wavelengths.

ASTER is a joint Japan-USA project and can be regarded as the next generation Japanese sensor which will replace JERS-1. In many ways ASTER is similar to JERS-1 except that the 2.0-2.5 μm part of the spectrum is further subdivided into 5 channels (Fujisada, 1991). Spatial resolution has improved in the VNIR to 15 m but degraded in the SWIR to 30 m. The other major difference is the inclusion of 5 Thermal Infrared (TIR) channels covering the 8-12 μm range. ASTER will also differ from JERS-1 because a wide range of pre-processed data products will be available, such as;

i) Level 0 - Raw data

ii) Level 1A - Reconstructed unprocessed data

iii) Level 1B - Radiance at sensor

iv) Level 2 - Base products without atmospheric correction (relative emissivity & relative reflectance)

v) Level 2 - Base products with atmospheric corrections (surface radiance, surface temperature, surface emissivity and surface reflectance)

vi) Level 4 - DEM products

Parameters to determine an atmospheric correction will be derived from the Moderate Resolution Imaging Spectroradiometer (MODIS) and Multi-angle Imaging Spectroradiometer (MISR), instruments carried on the same platform (EOS-AM 1) as ASTER. The availability of this additional information should allow an accurate

Specification	ASTER	MERIS
Launch date	June 1998	Mid-1999
Sensor types	VNIR, SWIR, TIR	VNIR
Resolution	- VNIR: 15 m - SWIR: 30 m - TIR: 90 m	300 m above ground station 1200 m rest of orbit
Wavelengths	- VNIR -1: 0.52-0.60 μm - VNIR -2: 0.63-0.69 μm - VNIR -3: 0.76-0.86 μm - SWIR -1: 1.60-1.70 μm - SWIR -2: 2.145-2.185 μm - SWIR -3: 2.185-2.225 μm - SWIR -4: 2.235-2.285 μm - SWIR -5: 2.295-2.365 μm - SWIR -6: 2.360-2.430 μm - TIR -1: 8.125-8.475 μm - TIR -2: 8.475-8.25 μm - TIR -3: 8.925-9.275 μm - TIR -4: 10.25-10.95 μm - TIR -5: 10.95-11.65 μm	- VNIR -1: 0.412 μm (0.01 μm) - VNIR -2: 0.442 μm (0.01 μm) - VNIR -3: 0.490 μm (0.01 μm) - VNIR -4: 0.510 μm (0.01 μm) - VNIR -5: 0.560 μm (0.01 μm) - VNIR -6: 0.620 μm (0.01 μm) - VNIR -7: 0.665 μm (0.01 μm) - VNIR -8: 0.681 μm (0.007 μm) - VNIR -9: 0.705 μm (0.01 μm) - VNIR -10: 0.753 μm (0.007 μm) - VNIR -11: 0.760 μm (0.002 μm) - VNIR -12: 0.765 μm (0.005 μm) - VNIR -13: 0.775 μm (0.015 μm) - VNIR -14: 0.865 μm (0.01 μm) - VNIR -15 0.890 μm (0.01 μm) - VNIR -16: 0.900 μm (0.01 μm)
Swath width	60 x 60 km	NA
Stereoscopic ?	Along-track	No
Orbit	NA	800 km, 98.5°
Repeat freq.	NA	35 days
Local image time	NA	10.00 AM
Quantisation	8 bit	NA

Table 7.5 Specifications of ASTER and MERIS sensors. Note that only 15 of the 16 MERIS channels will be used on the final instrument. MERIS channel details are given as band centre wavelength and bandwidth. NA denotes technical specification not yet known.

atmospheric correction to be applied, thereby increasing the quality of the subsequent products derived from the data.

2) HSI and ARIES-1

The HSI is being developed by NASA as a part of its Small Spacecraft and Technology Initiative (SSTI). This programme aims to reduce the costs associated with satellite design, integration, launch and operation. LEWIS is one satellite being developed as a part of this program and it will carry the HSI sensor. The HSI will record data in 384 channels with a 30 m resolution over the 0.4 - 2.5 μm range. LEWIS was originally planned for launch during 1996 but was delayed until August 1997. Table 7.6 details the launch specification of the HSI. Since writing the LEWIS platform has failed, see page 366.

Specification	HSI	ARIES-1
Launch date	August 1997	1999, operational 2000
Sensor types	Pan, Hyperspectral	Pan, Hyperspectral
Resolution	5 m, 30 m	10 m, 30m
Wavelengths	0.4 - 2.5 μm	0.4 - 2.5 μm
N°. of channels	384	67 from 105 (including 3 atmospheric calibration channels)
Channel resolution	0.01 μm	VNIR 0.02 μm, SWIR 0.016 μm
Swath width	NA	15 km
Stereoscopic ?	No	No
Orbit	523 km, 97.4°	NA
Repeat freq.	7 days	7 days at 30° off nadir
Local image time	10.30 AM	solar noon ± 1 hour
Quantisation	NA	NA

Table 7.6 Specification details of HSI and ARIES-1 as available. NA denotes technical parameter not available at time of writing.

ARIES-1 is a hyperspectral platform which is currently being developed in Australia (Huntington, *pers. comm.*). This platform is only the second satellite (after JERS-1) designed primarily to acquire data for geologists. The main role of this satellite will be to supply aircraft quality imaging spectrometer data for use in mineral exploration

projects. Currently the ARIES-1 project is at the feasibility stage, so the final sensor configuration is yet to be confirmed. Table 7.6 details the most likely configuration for ARIES-1.

ARIES-1 will carry one VNIR (0.4 -1.1 μm) sensor and two SWIR sensors (1.0-2.0 μm and 2.0-2.5 μm), along with a panchromatic band and two additional bands at 0.94 μm and 1.14 μm. These two additional channels will be used specifically for determining atmospheric correction parameters. Unlike the HSI spectral coverage across the 0.4-2.5 μm wavelength range will not be contiguous; instead channel centres (especially SWIR channels) will located to take full advantage of mineral absorption features.

7.2.5 Geological significance of high spectral resolution data

The four spaceborne sensors described above will all acquire multispectral data far exceeding the spectral resolution of any current satellite platform. This will result in these data being extremely important for both geological mapping and volcano monitoring.

1) Geological Mapping

ASTER represents the next major development in multispectral geological remote sensing as it will offer both moderate spatial and spectral resolution data. If these data, are free from the noise artefacts that plagued JERS-1, they will represent a significant improvement over Landsat TM data. The availability of five channels of data from the important 2.0-2.5 μm part of the spectrum will allow very clear discrimination between Al-OH, Mg-OH and CO^{3+} absorption features. Figure 7.1 illustrates the level of discrimination between some common minerals. Comparing Figure 7.1 with Figure 4.28 (b) and (c) the increased discrimination potential of ASTER can be clearly seen. Mineralogical discrimination at ASTER resolution will be far higher than that of either TM or OPS. The ASTER resolution spectra in Figure 7.1 are a far closer approximation to the lab spectra seen in Figure 4.28 (a). The increased resolution in the 2.0-2.5 μm part of the spectrum allows important distinguishing absorption features to be recorded in individual channels. This is very clearly indicated by the muscovite Al-OH absorption (Figure 4.28 (a)) which is not recorded at TM resolution (Figure 4.28 (b)), is only just visible at OPS resolution (Figure 4.28 (c)), but is clearly visible at ASTER resolution (Figure 7.1). This enhanced spectral resolution will not only increase lithological discrimination it will also allow remote mineralogical

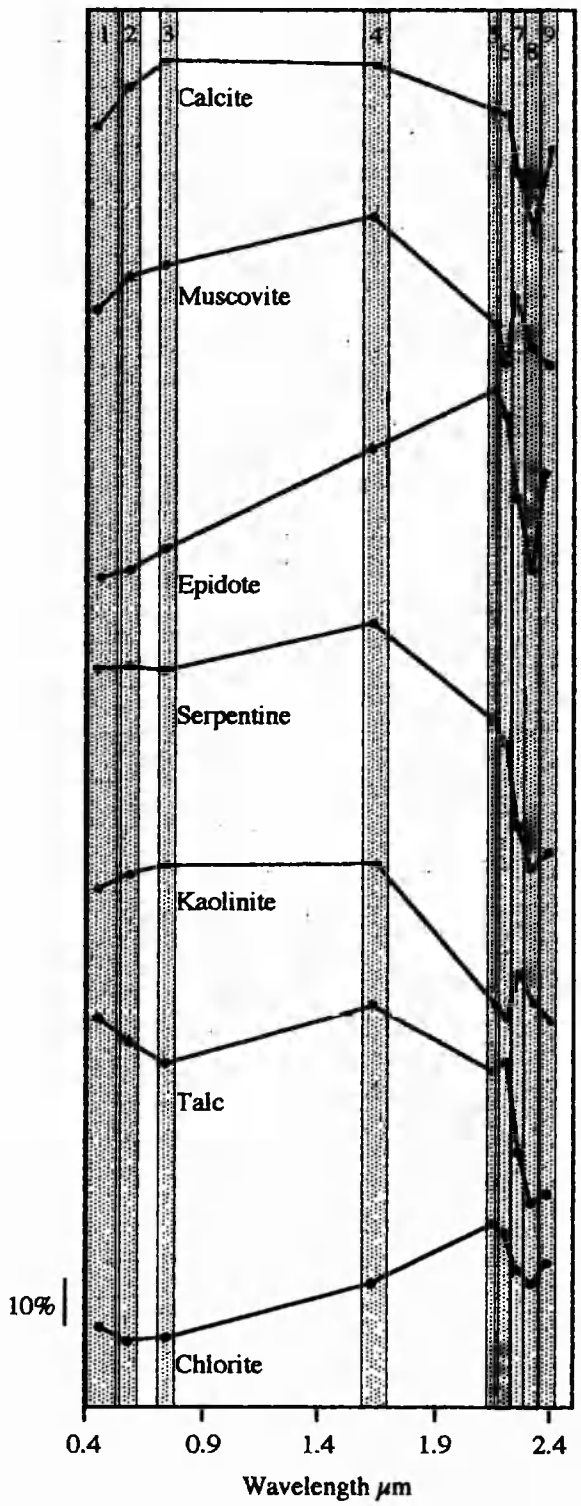

Figure 7.1 Pure mineral spectra (Grove *et al.*, 1992) resampled to the spectral resolution of ASTER. These reflectance spectra are only approximate because without the actual sensor response functions, I have assumed a constant response over each channels width. Numbers refer to VNIR and SWIR channels as listed in Table 7.5. Compare these spectra with ones resampled to TM and OPS spectral resolution in Figures 4.27 and 4.28.

identification to occur. ASTER will also provide 5 channels of data from the thermal infrared (8.1-11.6 μm) with a 90 m pixel size.

MERIS will also provide some useful data for geological mapping, but the spatial resolution of this data, combined with its visible wavelength range will mean that these data are best suited for large area reconnaissance mapping as opposed to detailed lithological discrimination. The high spectral resolution (at visible wavelengths) may prove useful for detecting vegetation stress associated with underlying geological features.

With the launch of the hyperspectral sensors ARIES-1 and the HSI an entirely new era of spaceborne geological remote sensing should begin. Unfortunately shortly after launch NASA lost control of the LEWIS platform carrying the HSI. The failure of LEWIS to reach a stable orbit (at time of writing) will probably result in the HSI entering the Earth's atmosphere without acquiring any data. The failure of LEWIS is a major set-back for spaceborne hyperspectral remote sensing. The HSI would have been the first satellite with contiguous spectral coverage from 0.4 μm to 2.5 μm. It would have been capable, not withstanding poor data quality, of producing spectral data at almost lab resolution. Data of that resolution would have been capable of distinguishing and identifying a vast array of minerals. The task of providing the first spaceborne hyperspectral data now rests with the development and launch of ARIES-1.

Despite ARIES-1 having less than a third of the channels of the HSI it will probably be capable of the same level of mineralogical discrimination. This is because ARIES-1 has been specifically designed for geological remote sensing. The bandpasses and bandcentres of both the VNIR and SWIR, channels have been carefully chosen, to maximise spectral information relating to mineralogical absorption features. Table 7.7 lists the major minerals that ARIES-1 has been designed to identify. Mineral identification on this scale is not at all comparable with any existing satellite sensor, only with current airborne imaging spectrometers. Hyperspectral data at ARIES-1 resolution should be invaluable for lithological discrimination and mineral mapping.

Micas	**Resistate minerals**	**Carbonates**
Muscovite	*Topaz*	*Calcite*
Paragonite	*Tourmaline*	*Dolomite*
Phengite	*Garnets*	*Ankerite*
Illite	**Chlorites**	*Siderite*
Biotite	*Mg-Chlorite*	*Magnesite*
Phlogopite	*Fe-Chlorite*	**Clays (Smectites)**
Al-OH	**Sulphates, arsentates**	*Montmorillonite*
Pyrophyllite	*Alunite*	*Saponite*
Mg-OH	*Jarosite*	**Clays (Kandites)**
Epidote	*Gypsum*	*Kaolinite*
Talc	*Scorodite*	*Dickite*
Antigorite	**Fe oxides**	*Halloysite*
Amphiboles	*Haematite*	**Silica**
Tremolite	*Goethite*	*Hyrothermal quartz*
Riebeckite	**NH4-bearing minerals**	*Opaline silica*
Actinolite	*Buddingtonite*	**REE-bearing minerals**
Hornblende	*Ammonium illite*	*Neodymium*

Table 7.7 Major minerals which ARIES-1 hopes to distinguish (Huntington, *Pers. comm.*). The extent to which these minerals can be distinguished from each other and their local background will depend on both the system spectral resolution and data quality.

2) Volcano monitoring

High spectral resolution sensors will also have potential in volcanological studies both for flow mapping and thermal studies. Oppenheimer (1991) commented on the suitability of ASTER for thermal studies, noting that ASTER should be able to constrain thermal models in a similar way to OPS data, with the finer SWIR resolution constraining errors in calculations using Planck's function even further. In practice ASTER may allow the OPS multi-band thermal modelling described by Oppenheimer (1991) to be actually tested, as this technique has not yet been tested due to the poor quality of OPS data. The higher spatial resolution of the VNIR channels (15 m) will also prove useful, as these will allow the spatial distribution of features within an active crater to be accurately mapped, as demonstrated in chapter 6 with OPS data. The TIR channels on ASTER will have little significance for volcano monitoring.

Oppenheimer (1991) and Oppenheimer *et al.*, (1993) showed that it will be possible to determine ground temperatures using spaceborne imaging spectrometer data. The additional channels of data provided by hyperspectral sensors like ARIES-1 will allow

better fitting of Planck's curves, allowing surface temperatures to be derived more accurately. ARIES-1 will also provide new data at wavelengths suitable for thermal studies (i.e. 1.2 μm) not currently imaged by any existing platform.

An additional use for hyperspectral data within a volcanic environment is the detection and estimation of specific volcanic gas species within an eruption plume. The high spectral resolution of these data will allow distinct absorption features associated with volcanic gases to be detected. This will provide valuable new information from satellite remotely sensed data. Visible wavelength MERIS data may also be useful for detecting and monitoring the movement of eruption plumes.

3) Summary of the usefulness of high spectral resolution sensors

Data from these new multi- and hyper- spectral sensors should be extremely useful for both geological mapping and volcano monitoring. ASTER data will represent a significant step forward for geological remote sensing, providing that data quality is better than that of JERS-1. ASTER resolution will allow the discrimination of Al-OH, Mg-OH and CO^{3+} absorptions. Detection of these important mineralogical absorptions in discrete channels should vastly improve mineral mapping and lithological discrimination. The advent of hyperspectral sensors, in particular ARIES-1, will see the start of a completely new era of spaceborne geological remote sensing. It will be possible, for the first time, to acquire aircraft resolution imaging spectrometer data for anywhere on the Earth's surface. The availability of such data will revolutionise mineral identification and lithological mapping in arid and semi-arid terrains. Satellite-derived mineral abundance maps will become a common part of mineral exploration programmes.

High spectral resolution sensors will also be a new source of valuable information for the remote sensing volcanologist. These data should allow the accurate derivation of surface temperatures for sub-pixel thermal anomalies, and useful spectral information to be gathered relating to the chemical composition of eruption plumes. Overall, high spectral resolution sensors should refine the quantifiable output parameters derivable from remotely sensed data for volcanic targets. In turn these parameters will help to refine eruption models.

7.3 Summary

This project has shown that despite the many problems associated with JERS-1 OPS data they do offer a significant improvement over TM data for lithological discrimination and mapping within the Oman ophiolite. This increase is due primarily to the narrower bandpasses of the OPS channels compared with those of TM, in particular that of OPS 8. The narrow bandpass of OPS 8, combined with the fact that it extends further into the SWIR than TM 7, means that it is extremely responsive to Mg-OH absorptions. Absorption features which are partially lost in the broad TM 7 bandpass. In the very near future the wavelength range equivalent to TM 7 will be subdivided into 5 channels by ASTER and then into as many as 16 channels by ARIES-1. This thesis has shown that considerable improvements in lithological discrimination can be obtained by dividing this geologically important part of the spectrum into three narrow channels, allowing important absorption features to be fully detected. The level of improvement that 5 or 16 channels will bring is yet to be demonstrated.

The previous section showed that satellite sensor technology is developing at a rapid rate. Soon vast amounts of high spatial and high spectral resolution data will be routinely acquired. These higher resolution sensors, combined with repeat frequencies of a few days, will increase data volumes by an order of magnitude. In order to take full advantage of these new data, computer processing and storage technologies as well as data distribution networks will have to develop at a comparable rate. Data processing strategies will also have to develop, as it will no longer be possible to rely on the visual interpretation of three band composites; instead data interpretation will have to become more quantitative. Data produced by ARIES-1 and future hyperspectral sensors will have to be analysed using a spectral approach, like that already demonstrated by Kruse and Boardman (1996). The 'image' context of the data will only be used to show the geographic location and context of mineral occurrences. The processing of hyperspectral data for geological applications will result in the development of new spectral interpretation software packages, atmospheric correction routines, spectral libraries and closer links to ground based spectroscopy.

Geological remote sensing promises to leap into the 21st Century with a whole host of new sensors that will revolutionise geological mapping, mineral exploration and volcano monitoring. However these new sensors are still to be launched and the possibility of failure (as demonstrated very recently with the loss of the HSI) is high, as all of these sensors are pushing spaceborne optical and electronic technology to its

limits. Hopefully the transition to high spatial and spectral resolution remote sensing will be a successful one, opening the doors for a new era of quantitative geological remote sensing.

References

Abrams, M.J., Brown, D., Lepley, L. and Sadowski, R., 1983, Remote sensing for porphyry copper deposits in southern Arizona, *Econom. Geol.*, 78,591-604.

Abrams, M.J., 1986, Mapping in the Oman ophiolite using TM data, *Proc. of the Fifth Thematic Conference on Remote Sensing for Exploration Geology*, 29 Sept.-2 Oct. 1986, Reno, Nevada, 85-95.

Abrams, M.J., Rothery, D.A. and Pontual, A., 1988, Mapping in the Oman ophiolite using enhanced Landsat Thematic Mapper images, *Tectonophysics*, Vol. 151, 387-401.

Abrams, M.J., Glaze, L. and Sheridan, M., 1991, Monitoring Colima volcano, Mexico, using satellite data, *Bull. Volcanol.*, 53, 571-574.

Akiyama, Y., Komai, J., Yokyama, T. and Okada, 1989, Preliminary assessment of JERS-1 optical sensor based on the simulated airborne data. Proc. of Seventh Thematic conference on remote sensing for exploration geology, Calgary, Canada, 2-6 Oct. 1989, 519-529.

Amri, I., 1995, Étude pétrologique et structurale d'une dorsale oceanique fossile, massif de Sumail (Opiolite D'Oman), implications pour les méchanismes d'accr étion océaniques. Unpubl. Ph.D. thesis, Université Paul Sabatier de Toulouse, 199p.

Andrews, H.C., 1970, *Computer Techniques in Image Processing* (New York, Academic Press), 187p.

Andrews, H.C., and Hunt, B.R., 1977, *Digital Image Restoration* (New Jersey, Prentice Hall), 238p.

Ahern, F.J., Goodenough, D.G., Jain, S.C., Rao, V.R. and Rochon, G., 1977, Landsat atmospheric corrections at CCRS, In *Proceedings of the Fourth Canadian Symposium on Remote Sensing*, Quebec City, May, 583-595.

Arvensen, J.C., Griffin, R.N. and Pearson, B.D., 1969, Determination of extraterrestrial solar spectral irradiance from a research aircraft, *Applied Optics*, Vol. 8, No. 11, 2215-2232.

Ball. E., Boudier, F., Nicolas, A. and Reuber, I., 1988, Structural map of the Oman ophiolite (South Sheet).

Ballard, D.H. and Brown, C.M., 1982, *Computer Vision*, (New Jersey, Prentice Hall), 523p.

Banks, H.G. and Hoblitt, R. P., 1981, Summary of temperature studies of 1980 deposits. *U.S. Geological Survey Prof. paper 1250*, pp 295-313.

Benn, K., Nicolas, A. and Reuber, I., 1988, Mantle-crust transition zone and origin of wehrlitic magmas: evidence from the Oman ophiolite. *Tectonophysics*, 151, 75-85.

Bizz, S., Arino, O. and Goryl, P., 1996, Operational algorithm to correct the along-track and across-track striping in JERS-1 OPS images, *Intl. J. Remote Sensing*, Vol.17, No. 10, pp 1963-1968.

Blom, R.G., Abrams, M.J. and Adams, H.G., 1980, Spectral reflectance and discrimination of plutonic rocks in the 0.45 to 2.45 μm region, *Journal Geoph. Res.*, Vol. 85, No. B5, 2638-2648.

Carlson, G. G. and Stobier, R.E., 1977, Geologic mapping by computer analysis of digital Landsat data. *Geol. Soc. Am., 1977 Annual Meeting, Seattle, WA, Program with Abstracts*. p.1234.

Casterano, L. and Barozzi, R., 1961. Informe sobre el sistema volcanica del Lascar. *Inst. Geol. Publ.*, 23, 304-315.

Castleman, K.R., 1979, *Digital Image Processing* (New Jersey, Prentice Hall), 429p.

Ceuleneer, G., 1991, Evidence for a palaeo-spreading centre in the Oman ophiolite: Mantle structure in the Maqsad area. In: *Opiolite Genesis and Evolution of the Oceanic Lithosphere*, (Eds. T.J. Peters.), Klvever Academic Publishers, 147-173.

Ceuleneer, G., Monnereau, M. and Rabinowicz, M. 1993, Thermal and petrological consequences of melt migration within mantle plumes. *Phil. Trans. Royal Soc. London*

Ceuleneer, G., Monnereau, M. and Amri., I., 1996, Thermal structure of a fossil mantle diapir inferred from the distribution of mafic cumulates. *Nature*, Vol. 379, 149-153.

Ceuleneer, G. and Nicolas, G., 1988, Mantle diapirism in Oman ophiolite and ridge segmentation, *EOS Transactions of the American Geophysical Union*, Vol.69, No. 44, p.1425 (abstract only).

Ceuleneer, G., Nicolas, G. and Boudier, F., 1988, Mantle flow patterns at an oceanic spreading centre: The Oman peridotites record. *Tectonophysics*, 151, 1-26.

Ceuleneer, G., Rabinowicz, M. and Rosemberg, C., 1990, 3-D models of mantle plumes: thermal and petrological consequences, EOS, Vol. 71, No. 43, 1625 (Abstract only).

Chapman, B., Alves, M. and Freeman, A., 1995, Validation and calibration of JERS-1 SAR imagery. Published by Ministry of International Trade and Industry, Japan. Vol 1. 75-93.

Chavez, P.S., Graydon, B.L. and Sowers, L.B., 1982, Statistical technique for selecting Landsat MSS ratios, *Journal of Applied Photographic Engineering*, Vol. 8, No. 1, 23-30.

Chavez, P.S., 1988, An improved dark-object subtraction technique for atmospheric scattering correction of multispectral data, *Rem. Sens. Environ.*, 24, 459-479.

Chevrel, S., Chevremont, P., Wyns, R., Le Metour, J., Al Toba, A. and Beurrier, M., 1991, The use of digitally processed Spot data in the geological mapping of the Ophiolite of Northern Oman. Ophiolite Genesis and Evolution of the Oceanic Lithosphere, T.J. Peters et al., (Eds), p853-870.

Coleman , R.G., 1977, Ophiolites: Ancient oceanic lithosphere. Springer-Verlag, Berlin, 221p.

Crippen, R.E., Ford, J.P., Blom, R.G. and Dokka, R.K., (1994), An evaluation of Fuyo-1 (JERS-1) optical data for geologic interpretation, *Proc. of the Tenth Thematic Conference on Geologic Remote Sensing*, 9-12 May 1994, San Antonio, Texas, p. 606 (abstract only).

Crippen, R.E., 1989, Selection of Landsat TM bands and band ratio combinations to maximise lithologic information in colour composite displays, *Proc. Seventh Thematic Conference on Remote Sensing for Exploration Geology*, 2-6 Oct. 1989,Calgary, Alberta, 917-921.

Crist, E.P., and Cicone, R.C., 1984, A physically based transformation of thematic mapper data- the TM tasseled cap, *I.E.E.E Trans. on Geoscience and Rem. Sens.*, Vol. Ge 22, No. 3, 256-263.

Crosta, A.P and Moore, J., 1989, Geological mapping using Landsat Thematic Mapper imagery in Almeria Province, south-east Spain, *Intl. J. Remote Sensing*, Vol.10, No. 3, 505-514.

Davis, J.C., 1973, *Statistics and DataAnalysis in Geology*. Wiley, New York.

Davis, P.A. and Berlin, G.L., 1989, Rock discrimination in the complex geologic environment of Jabal Salma, Saudia Arabia, using Landsat Thematic Mapper data, *Photogrammetry, Engineering and Remote Sensing* Vol. 55, No.8, 1147-1160.

Denniss, A.M., De Souza, C.R., Rothery, D.A. and Drury, S.A., 1993, Lithological discrimination using Landsat TM and JERS-1 SWIR data, initial results in the Oman ophiolite, Proc. of Rem. Sens. Soc. Conference, Chester, 16-17 Sept. 1993, 8p.

Denniss, A.M., Rothery, D.A., Ceuleneer, G., and Amri, I, 1994, Lithological discrimination using Landsat and JERS-1 SWIR data in the Oman ophiolite, Proc. Tenth Thematic Conference on Geological Remote Sensing, 9-12 May, San Antonio, Texas, 97-108.

Denniss, A.M., Rothery, D.A., Carlton, R.W., Ceuleneer, G. and Amri, I., 1995. A comparison of lithological discrimination in the Oman ophiolite using JERS-1 and Landsat TM data. *Final report of JERS-1/ERS-1 system verification program*, Vol. 1, 223-231.

Denniss, A.M., Harris, A.J.L., Carlton, R.W., Francis, P.W., and Rothery, D.A. 1995. The 1993 Lascar pyroclastic flow imaged by JERS-1. *Int. J. Remote Sensing*, Vol.17, No. 11, 1975-1980.

Denniss, A.M., Harris, A.J.L., Rothery, D.A., Francis, P.W and Carlton, R.W., 1998, Satellite observations of the April 1993 eruption of Lascar volcano, *Int. J. Remote Sensing*, Vol. 19, No. 5, 801-821.

De Souza, C.R., 1995, Remote sensing and the tectonic evolution of Northern Eritrea. Unpublished. Ph.D. thesis, Open University, 276p.

De Souza, C.R., Denniss., A.M., Drury., S.A.D., Rothery., D.A. and Carlton., R.W., 1996, Restoration of noise-corrupted Optical Fuyo-1 (JERS-1) data using frequency domain techniques, *Photogrammetry, Engineering and Remote Sensing* Vol. 62, No.9, 1037-1047.

Dozier, J., 1981, A method for satellite identification of surface temperature fields of sub-pixel resolution. Remote. Sens. Environ. Vol. 11, 221-229.

Drury, S.A., 1987, *Image Interpretation in Geology* (London, Allen and Unwin), 243p.

Drury, S.A. and Berhe, S.M., 1993, Accretion tectonics in northern Eritrea revealed by remotely sensed imagery, *Geol. Mag.*, 130(2), 177-190.

Edwards, K, and Davis, P.A., 1994, The use of Intensity-Hue-Saturation transformation for producing colour shaded relief images, *Photogrammetry, Engineering and Remote Sensing*, Vol. 60, No.11, 1369-1374.

Elvidge, C.D. and Lyon, R.J.P., 1984, Mapping clay alteration in the Virginia Range-Camstock Lode, Nevada with airborne thematic mapper imagery. *Proc. of International Symposium of Remote Sensing of Environment, Third Thematic Conference, Remote sensing for Exploration Geology*, Colorado Springs, Colorado, USA, 16-19 April, 161-170.

Engel, J.L. and Weinstein, O., 1983, The Thematic Mapper - an overview, *I.E.E.E Transactions on Geoscience and Remote Sensing*, Vol. Ge-21, No.3, 258-265.

Fleet, A.J. and Roberston, A.H.F., 1980, Ocean-ridge metalliferous and pelagic sediments of the Semail Nappe Oman, *Journal of Geological Soc. London*, Vol.137, 403-422.

Flynn, L. P., Mouginis-Mark, P. J and Horton, K. A., 1994. Distribution of thermal areas on an active lava flow field: Landsat observations of Kilauea, Hawaii, July 1991. *Bull. Volcanol.*, 56, 283-296.

Frazer, S.J., 1991, Discrimination and identification of ferric oxides using satellite Thematic Mapper data: A Newman case study. *Int. J. Remote Sensing*, Vol. 12, No. 3, 635-641.

Fujisada, H. and Ono, A., 1991. Overview of ASTER design concept. *SPIE*, Vol. 1490. 244-254.

Gass, I.G., 1990, Open University ophiolite project maps 1 and 2. Open University.

Gillespie, A.R., Kahle, A.B., and Walker, R.E., 1986, Colour Enhancement of highly correlated images. I. Decorrelation and HSI contrast stretches, *Remote Sensing of Environ.* 20: 209-235.

Glaze, L. S., Francis, P. W., Self, S. and Rothery, D. A., 1989. The 16 September 1986 eruption of Lascar volcano, north Chile: satellite investigations. *Bull. Volcanol.*, 51, pp 146-160.

Glennie, K.W., Boeuf, M.G.A., Hughes-Clarke, M.W., Moody-Stuart, M., Pilaar, W.F.F. and Reinhardt, B.M., 1974, The geology of the Oman Mountains. *Ver. Konin. Ned. Geol. Mijn. Geno.*, Vol.31, 423.

Gnos, E., Wyder, R. and Rothery, D.A., 1991, Comparison between mapping at 1:25000 scale and decorrelation stretched Landsat Thematic Mapper images in the Wuqbah Block (Oman Mountains). Ophiolite Genesis and Evolution of the Oceanic Lithosphere, T.J. Peters et al., (Eds), p875-885.

Gramont, X., Metour, J. and Villey M., 1986a, Geological map of Oman Mountains at 1:100 000 - Sheet NF 40-7C, Samad. Bureau de Reserches Géologiques et Minères, France.

Gramont, X., Metour, J. and Villey M., 1986b, Geological map of Oman Mountains at 1:100 000 - Sheet NF 40-7C, Samad: Explanatory notes. Bureau de Reserches Géologiques et Minères, France.

Green, A.A., Berman, M., Switzer, P. and Craig, M.D., 1988, A transformation for ordering multispectral data in terms of image quality with implictaions for noise removal, *IEEE transactions on Geoscience and Remote Sensing*, Vol. 26, No. 1, 65-74.

Grove, C.I., Hook, S.J. and Paylor, E.D., 1992. Laboratory reflectance spectra of 160 minerals, 0.4 to 2.5 micrometers. Jet Propulsion Laboratory Publication 92-2, 355p.

Gonzalez, R.C. and Wintz, P., 1977, *Digital Image Processing* (Massachusetts, Addison-Wesley), 502p.

GVN, 1993. Lascar. Smithsonian Institution Global Volcanism Network, 18(4).

GVN, 1995. Lascar. Smithsonian Institution Global Volcanism Network, 20(6).

Harding, D.J., and Bird, J.M., Mapping ultramafic rock using Landsat Data: The Josephine peridotite, Oregon , California, *Proc. of International Symposium on Remote Sensing of Environment, Third Thematic Conference*, 16-19 April, 1984, Colorado Springs, Colorado, 695-709.

Harris, A. J. L. and Rothery, D. A., 1995. Thermal monitoring of volcanoes using data from the AVHRR. *Proceedings of the 21st Annual Conference of the Remote Sensing Society*, 11-14 September 1995, Southampton, UK, 528-535.

Harris, A. J. L., Vaughan, R. A. and Rothery, D. A., 1995a. Volcano detection and monitoring using AVHRR data: the Krafla eruption, 1984. *Int. J. Remote Sensing*, 16, 1001-1020.

Harris, A. J. L., Rothery, D. A., Carlton, R. W., Langaas, S. and Mannstein, H., 1995b. Non-zero saturation of AVHRR thermal channels over high temperature targets: evidence from volcano data and a possible explanation. *Int. J. Remote Sensing*, 16, 89-196.

Hastrum, B.N. and Watson, A.S., 1983, A case study of two eruptions of Mount Galunggung and an investigation of volcanic eruption cloud characteristics using remote sensing techniques. *Aust. Met. Mag.* Vol. 31, 171-177.

Haydn, R., Darke, G.W., Henkel, J. and Bare. J.E., 1982, Application of the IHS colour transform to the processing of multisensor data and image enhancement. *Proc. of International symposium on remote sensing of arid and semi-arid lands*, Cairo, Egypt, Jan. 1982, 599-615.

Holasek, R. E. and Rose, W. I., 1991, Anatomy of 1986 Augustine volcano eruptions as recorded by multispectral image processing of digital AVHRR weather satellite data. *Bull. Volcanol.*, 53, 429-435.

Holasek, R. E. and Self, S., 1995, GOES weather satellite observations and measurements of the May 18, 1980, Mount St. Helens eruption. *J. Geophys. Res.*, 100(B5), 8469-8487.

Hopson, C.A., and Pallister, J.S., 1980, Semail ophiolite magma chamber: I. Evidence from gabbro phase variation, internal structure and layering. *Proc. of the International Ophiolite Symposium*, 1979, Cyprus, 402-404.

Hummer-Miller, S., 1990, Techniques for noise removal and registration of TIMS data, *Photogrammetric Engineering and Remote Sensing*, Vol. 56, No.1, pp 49-53.

Hunt, G.A., Drury, S.A. and Rothery, D.A., 1986, Techniques for choosing optimum Thematic Mapper channel combinations for lithological mapping in semi-arid terrains, *Proc. of the International Symposium on Mapping from Modern Imagery*, Sept. 1986, Edinburgh, 637-646.

Hunt, G.R., 1977, Spectral signatures of particulate minerals in the visible and near infrared, *Geophysics*, Vol. 42, No.3, pp 501-513.

Hunt, G.R., and Salisbury, J.W., 1970, Visible and Near-infrared spectra of minerals and rocks: I. Silicate minerals, Modern Geology, Vol. 1, 283-300.

Hunt, G.R., Salisbury, J.W., and Lenhoff, C.J., 1971, Visible and near-infrared spectra of minerals and rocks: III. Oxides and hydroxides. *Modern Geology*, Vol.2, 195-205.

Hunt, G.R., Salisbury, J.W., and Lenhoff, C.J., 1971, Visible and near-infrared spectra of minerals and rocks: IV. Additional silicates. *Modern Geology*, Vol. 4, 85-106.

Hutin, G., Bechennec, F., Beurrier, M. and Rabu, D., 1986a, Geological map of Oman Mountains at 1:100 000 - Sheet NF 40-7B, Birkat Al Mawz: Bureau de Reserches Géologiques et Minères, France.

Hutin, G., Bechennec, F., Beurrier, M. and Rabu, D., 1986b, Geological map of Oman Mountains at 1:100 000 - Sheet NF 40-7B, Birkat Al Mawz: Explanatory notes. Bureau de Reserches Géologiques et Minères, France.

Jackson, R.D., 1983, Spectral indices in n-space, *Remote Sensing of Environment*, 13: 409-421.

Jain, A.K., 1989, *Fundamentals of Digital Image Processing* (London, Prentice-Hall), 385p.

Jeyaseelan, A. T. and Thiruvengadachari, S., 1993, Suspected Mt. Pinatubo aerosol impact on the NOAA AVHRR NDVI over India. *Int. J. Remote Sensing*, 14, 603-608.

Kahle, A.B., Palluconi, F.D., Hook, S.J., Realmuto, V.J. and Bothwell, G., 1991, The Advanced Spaceborne Thermal Emission and Reflectance Radiometer (ASTER). *Int. J. of Imaging Systems and Technology*, Vol. 3, 144-156.

Kaufmann, H., 1988, Mineral exploration along the Aqaba-Levant structure by use of TM data, , *Int. J. Remote Sensing*, Vol.9, No. 10/11, pp 1639-1658.

Kauth, R.J. and Thomas, G.S., 1976, The Tasseled Cap - a graphic description of the spectra-temporal development of agricultural crops as seen by Landsat. *Proc. of the Symposium on Machine Processing of Remotely Sensed Data*, Lars, Purdue University, West Lafayette, 441-451.

Kidwell, K., 1991. NOAA polar orbiter data users guide. NOAA/NESDIS, Washington DC.

Kienle, J., Dean, K. G., Garbeil, H. and Rose, W. I., 1990. Satellite surveillance of volcanic ash plumes, application to air safety. *EOS*, 71(7), 266.

Kruse, F.A and Boardman, J.W., 1996, Hyperspectral data analysis and image processing workshop manual. Unpublished workshop manual, Analytical Imaging and Geophysics Ltd.

Lillesand, T.M. and Kiefer, K.W., 1994, Remote sensing and image interpretation. (John Wiley and Sons), New York, 749p.

Lippard, S.J., (Ed.) 1980, Wadi Jizi Oman geological ophiolite project, Map 2. Dir. Overseas Surv. Open University, Milton Keynes.

Lippard, S.J. and Rothery, D.A., (Eds.), 1981, Wadi Ahin-Yanqul Oman geological ophiolite project, Map 3. Open University, Milton Keynes.

Lippard, S.J., Shelton, A.W. and Gass, I.G., 1986, The Ophiolite of Northern Oman. Geol. Soc. Lon. Memoirs 11, 178p.

Madeira, J., Bedidi, A., Çervelle, B., Pouget, M. and Flay, N., 1996, Visible spectrometric indices of hematite (Hm) and goethite (Gt) content in lateritic soils: the application of a Thematic Mapper (TM) image for soil-mapping in Brasilia, Brazil. *Int. J. Remote Sensing*, Vol. 18, No. 13, 2835-2852.

Malila, W.A. and Meyers, T.J., 1995, Initial tasseled-cap transform for JERS-1 OPS multispectral data. *Final report of JERS-1/ERS-1 system verification program, Vol. 1*. 171-178.

Markham, B.L. and Barker, J.L., 1986, Spectral characterisation of the Landsat Thematic Mapper sensor, , *Intl. J. Remote Sensing*, Vol.6, No. 5, 697-716.

Massonnet, D., Briole, P. and Arnaud, A., 1995. Deflation of Mount Etna monitored by spaceborne radar interferometry. *Nature*, 375, 567-570.

Matthews, S. J., Gardeweg M. C. and Sparks, R. S. J., 1997. Crater collapse and explosive eruptions as a result of magma degassing; the 1984 to 1986 cyclic activity of Lascar Volcano, Northern Chile. Bull. *Volcanol.*, Vol. 59, 72-82.

Matsui, K., 1995, JERS-1 status of satellite bus. *Final report of JERS-1/ERS-1 system verification program*, Vol. 1. 17.

McDonald, R.A., 1995a, Opening the cold war sky to the public: Declassifying satellite reconnaissance imagery. *Photogrammetry, Engineering and Remote Sensing* Vol.61, No.5, 385-390.

McDonald, R.A., 1995b, CORONA: Success for space reconnaissance, a look into the cold war and a revolution for intelligence. *Photogrammetry, Engineering and Remote Sensing* Vol. 61, No.6, pp 689-720.

Miller, N.L. and Elvidge, C.D., 1985, The iron absorption index: A comparison of ratio-based and baseline-based techniques for the mapping of iron oxides.

Proc. of Fourth Thematic Conference, Remote Sensing for Exploration Geology, San Francisco, California, 405-415.

Moody J.D., 1974, Late Cretaceous Nappes in the Oman Mountains and their Geologic Evolution: Disscussion. Am. Ass. Petrol. Geol. Bull. Vol. 58, 889-895.

Mukai, Y., Nakayam, Y., Hasegawa, I. and Suga, Y., 1995. Verification of observation capability of radiometric intensity by JERS-1 OPS. *Final report of JERS-1/ERS-1 system verification program*, Vol 1. 197-206.

NASDA, 1994, JERS-1 Data users handbook. Alby Consulting Co. (Eds), 296p.

Niblack, W., 1986, *An introduction to Image Processing* (New Jersey, Prentice Hall), 316p.

Nicolas, A., Ceuleneer, G. and Benn, K., 1988, Coupling between tectonic and magmatic processes in the Oman ophiolite. I. Melt extraction from diapirs. *EOS Transactions of American Geophysical Union.* p.1476 (Abstract Only).

Nicolas, A., Ceuleneer, G., Boudier, F., and Misseri, M., 1988. Structural mapping in the Oman ophiolites: Mantle diapirism along an oceanic ridge. *Tectonophysics*, 151, 27-56.

Nicolas, A., Freydier, C., Godard, M. and Vauchez, 1993, Magma chambers at oceanic ridges: How Large ? *Geology*, Vol. 21, 53-56.

Nishidai, T., 1993, Early results from Fuyo-1, Japan's Earth Resources Satellite (JERS-1), , *Intl. J. Remote Sensing*, Vol.14, No. 9, 1825-1833.

Nishidai, T., Yoshie, T. and Tsu, H., 1995, Overall results of the Earth Resources Satellite 'Fuyo-1' data evaluation. *Final report of JERS-1/ERS-1 system verification program*, Vol. 1. 33-61.

Ogasawara, M., 1995, Evaluation of JERS-1 OPS data for geological interpretation in the Halls Creek Mobile Zone, Western Australia: comparison of OPS high and normal gain data. *Final report of JERS-1/ERS-1 system verification program*, Vol. 1, 529-538.

Oppenheimer, C.M.M, 1991, Volcanology from space: applications of infrared remote sensing. Unpublished Ph.D. thesis, Open University

Oppenheimer, C.M.M. and Rothery, D.A., 1991, Infrared monitoring of volcanoes by satellite, *Journal of Geol. Soc. Lon.*, Vol. 148, 563-569.

Oppenheimer, C.M.M., 1991, Lava flow cooling estimated from Landsat Thematic Mapper Infrared data: the Lonquimay eruption (Chile, 1989). *J. Geophys. Res.*, 96(B13), 21865-21878.

Oppenheimer, C., Francis, P. W., Rothery, D. A., Carlton, R. W. and Glaze, L.S., 1993. Infrared image analysis of volcanic thermal features: Lascar volcano, Chile, 1984-1992, *J. Geophys. Res.*, 98(B3), 4269-4286.

Oppenheimer, C., Rothery, D.A., Pieri, D.C., Abrams, M.J. and Carrere V.,1993, Analysis of Airborne Visible-Infrared Imaging Spectrometer (AVIRIS) data of volcanic hotspots. *Int. J. Rem. Sens*, Vol. 14, No. 16, 2919-2934.

Peli, T. and Verly, J.G., 1983, Digital line-artefact removal, *Optical Engineering*, Vol. 22, No.4, 479-484.

Pierce, L., Smith, J.R. and Webb, W.C., 1979, Landsat-D: Data acquisition and processing, *Proceedings of the Machine Processing of Remotely Sensed Data Symposium*, 15-20.

Pieri, D.C., Glaze, L.S. and Abrams, M.J., 1990, Thermal radiance observations of an active lava flow during the June 1984 eruption of Mount Etna, *Geology*, 18, 1018-1022.

Pohn, H.A., Offield, T.W. and Watson, K., 1974, Thermal inertia mapping from satellite - discrimination of geologic units in Oman, *Jour. Res. U.S. Geol. Surv.* Vol .2, No.2, 147-158.

Pontual , A., 1990, Lithological information in remotely sensed images and surface weathering in arid regions. Unpublished Ph.D. Thesis, Open University, 421p.

Prata, A. J., 1989, Observations of volcanic ash clouds in the 10-12 μm window using AVHRR/2 data. *Int J. Remote Sensing*, 10, 751-761.

Pratt, W.K., 1978, *Digital Image Processing* (New York, Wiley-Interscience), 749p.

Qari, M.Y.H.T., 1989, Lithological mapping and structural analysis of Proterozoic rocks in part of the southern Arabian Shield using Landsat images. *Intl. J. Remote Sensing*, Vol.10, No. 3, 499-503.

Rabinowicz, M., Ceuleneer, G. and Nicolas, A., 1986, Melt segregation and asthenospheric flow in diapirs below spreading centres: Evidence from Oman ophiolite. *EOS Transactions of the American Geophysical Union*, Vol. 67, No.16, p.409 (Abstract only).

Rabu, D., Bechennec, F., Beurrier, M. and Hutin, G., 1986a, Geological map of Nakhl, Sheet NF 40-3E. Bureau de Reserches Géologiques et Minères, France.

Rabu, D., Bechennec, F., Beurrier, M. and Hutin, G., 1986b, Géological map of Nakhl, Sheet NF 40-3E: Explanatory Notes. Bureau de Reserches Geologiques et Minères, France.

Raggam, J., Almer, A. and Tarsi, T., 1995, Geometric assessment of JERS-1 optical and SAR data in comparison and in combination with European SPOT and ERS-1 data. *Final report of JERS-1/ERS-1 system verification program*, Vol 1. 120-135.

Rees, W.G., 1990, *Physical Principles in Remote Sensing* (Cambridge, Cambridge University Press), 247p.

Reuber, I., 1988, Complexity of the crustal sequence in the northern Oman ophiolite (Fizh and southern Aswad blocks): The effect of early slicing? Tectonophysics, 151, 137-165.

Rose, J.F., 1989, Spatial Interference in the AVIRIS Imaging Spectrometer, *Photogrammetric Engineering and Remote Sensing*, Vol. 55, No. 5, pp 1339-1346.

Rothery, D.A., 1982, Remote sensing in Oman. Unpublished. Ph.D. thesis, Open University.

Rothery, D.A., 1984, Reflectances of ophiolite rocks in the Landsat MSS bands: relevance to lithological mapping by remote sensing. *J. Geol. Soc. London*, Vol. 141, 933-939.

Rothery, D.A., 1987a, Decorrelation stretching as an aid to image interpretation, *Intl. J. Remote Sensing*, Vol.8, No. 9, 1253-1254.

Rothery, D.A., 1987b, Decorrelation stretching and reflectance techniques as an aid to image interpretation in geology. *Proc. Thirteenth Annual Conf. Remote Sensing Soc.*, Nottingham, England.

Rothery, D.A., Francis, P.W. and Wood, C.A, 1988, Volcano monitoring using short wavelength infrared data from satellites, *Journal of Geoph. Res.*, Vol. 93, No. B7., 7993-8008.

Rothery, D.A. and Hunt., G., 1990, A simple way to perform decorrelation stretching and related techniques on menu driven image processing systems, *Intl. J. Remote Sensing*, Vol.11, No. 1, 135-137.

Rowland, S. K., Smith, G. A. and Mouginis-Mark, P. J., 1994. Preliminary ERS-1 observations of Alaskan and Aleutian Volcanoes. *Remote Sensing Environ.*, 48, 358-369.

Salisbury, J. W. and D. M. D'Aria, 1992, Emissivity of Terrestrial materials in the 8-14 μm atmospheric window. Remote Sensing *Environ.*, 42, 83-106.

Salisbury, J. W. and D'Aria, D. M., 1994, Emissivity of Terrestrial materials in the 3-5 μm atmospheric window. *Remote Sensing Environ.*, 47, 345-361.

Sawada, Y., 1989, The detection capability of explosive eruptions using GMS imagery, and the behaviour of dispersing eruption clouds. IAVCEI proceedings in Volcanology 1 (Springer-Verlag: Berlin), 233-245.

Schowengerdt, R.A., 1983, *Techniques for Image Processing and Classification in Remote Sensing* (London, Academic Press), 245p.

Segal, D.B. and Merin, I.S., 1989, Successful use of Landsat Thematic Mapper data for mapping hydrocarbon microseepage - induced mineralogic alteration, Lisbon Valley, Utah, *Photogrammetric Engineering and Remote Sensing*, Vol. 55, No. 8, 1137 1145.

Setzer, A. W. and Verstraete, M. M., 1994. Fire and glint in AVHRR's channel 3: a possible reason for the non-saturation mystery. *Int. J. Remote Sensing*, 15, 711-718.

Sheffield, C., 1985, Selecting band combinations from multispectral data, *Photogrammetry Engineering and Remote Sensing*, Vol.51, No.6 681-687

Shimada, M., 1993, Image quality of SAR / OPS. *Proc. of JERS-1 information exchange meeting (Presentation Materials)*, Kogakuin University, Tokyo, Japan, 16-17 August, 1993, 90-132.

Shimada, M., 1995, Image quality of SAR/OPS. Published by Ministry of International Trade and Industry, Japan. Vol 1. 21.

Simkin, T. and L. Siebert, 1994, Volcanoes of the world. (Geoscience Press: Tuscon).

Simpson, J.J. and Yhann, S.R., 1994, Reduction of noise in AVHRR channel 3 data with minimum distortion, *IEEE Transactions on Geoscience and Remote Sensing*, Vol. 32, No. 2, 315-328.

Sultan , M., Arvidson, R.E. and Sturchio, N.C., 1986, Mapping serpentinites in the Eastern desert of Egypt using Landsat Thematic Mapper data. *Geology*, Vol.4, 995-999.

Sultan, M., Arvidson, R.E., Sturchio, N.C. and Guinness, E.A., 1987, Lithologic mapping in arid regions with Landsat Thematic Mapper data: Meatiq dome, Egypt, *Geol. Soc. of Amer. Bull.*, Vol. 99, 748-762.

Sultan , M., Arvidson, R.E., Duncan, I.J., Stern, R.J. and Kaliouby, B.E., 1988, Extension of the Najd shear system from Saudi Arabia to the central eastern desert of Egypt based on integrated field and Landsat Observations. *Tectonics*, Vol. 7, No. 6, 1291-1306.

Takata, N., 1995, SAR / OPS characteristics and status *Final report of JERS-1/ERS-1 system verification program*, Vol 1, 9-14.

Tanaka, S., and Sugimura, T., 1995, Bird's eye view of Mount Sakurajima from JERS-1 / OPS. *Int. J. Remote Sensing*, 16, 1179-1181.

Tucker, C. J. and Matson, M., 1985, Determination of volcanic dust deposition from El Chichon using ground and satellite data. *Int. J. Remote Sensing*, 6, 619-627.

Villey , M., Metour, J. and Gramont, X., 1986a, Geological map of the Oman Mountains at 1:100 00 - Sheet NF 40-3F, Fanjah. Bureau de Reserches Géologiques et Minères, France.

Villey , M., Metour, J. and Gramont, X., 1986a, Geological map of the Oman Mountains at 1:100 00 - Sheet NF 40-3F, Fanjah. Explanatory notes.Bureau de Reserches Géologiques et Minères, France.

Weinreb, M. P., Hamilton, G., Brown, S. and Koczor, R. J., 1990, Nonlinearity corrections in calibration of Advanced Very High Resolution Radiometer infrared channels. *J. Geophys. Res.*, 95(C5), 7381-7388.

Weisnet, D. R. and D'Aguanno, J., 1982, Thermal imagery of Mount Erebus from the NOAA-6 satellite. *Antarctic J. U.S.*, 17, 32-34.

Welland, M.J.P. and Mitchell, A.H.G, 1977, Emplacement of the Oman ophiolite: A mechanism related to subduction and collision. *Geological Soc. of America Bulletin*, Vol. 88, 1081-1088.

Westin, T., 1990, Filters for removing coherent noise of period 2 in SPOT imagery, *Intl. J. Remote Sensing*, Vol.11, No. 2, 351-357.

Wilson, H.H., 1969, Late Cretaceous eugosynclinal sedimentation, gravity tectonics and ophiolite emplacement in Oman Mountians, southeast Arabia. *Bull. Am. Ass. Petrol. Geol.* Vol. 53, 626-671.

Wooster, M. J. and Rothery, D. A., 1997, Thermal monitoring of Lascar volcano, Northern Chile, using infrared data at high temporal resolution: a 1992 to 1995 time-series using the Along Track Scanning Radiometer. *Bull. Volcanol.*, Vol. 58, 566-579.

Yamaguchi, Y., 1987, Possible techniques for lithological discrimination using the short-wavelength infrared bands of the Japanese ERS-1, *Remote Sensing of Environment*, 23, 117-129.

Yamaguchi, Y., 1988, Spectral indices for vegetation and rock type discrimination using the optical sensor of the Japanese ERS-1. *Proc. Sixth thematic conference remote sensing for exploration geology*, Houston, Texas, 16-19 May, 1988. 159-167.

Yamaguchi, Y., Tsuchida, S., Matsunaga, T., Sato, I., Urai, M., Ninomiya, Y., Miyazaki, Y, and Lyon, R.J.P., 1995, Evaluation of OPS capability for lithologic mapping. *Final report of JERS-1/ERS-1 system verification program*, Vol 1. 510-520.

Zink, M., 1995, JERS-1 external calibration experiments. *Final report of JERS-1/ERS-1 system verification program*, Vol 1. 94-101.

Acronyms and abbreviations

AATSR	Advanced Along Track Scanning Radiometer
ARIES-1	Australian Resource Information and Environment Satellite-1
ASP	Analogue Signal Processor
ASTER	Advanced Spaceborne Thermal Emission and Reflectance Radiometer
ATSR-1	Along Track Scanning Radiometer
AVHRR	Advanced Very High Resolution Radiometer
AVIRIS	Airborne Visual Infrared Imaging Spectrometer
B/H	Base to Height ratio
BOT	Beginning of Tape
BRGM	Bureau de Recherches Géologiques et Minières
CCD	Charge Coupled Device
dB	Decibel
DEM	Digital Elevation Model
DN	Digital Number
DS	Decorrelation Stretching
DSP	Digital Signal Processor
EM	Electromagnetic
EMR	Electromagnetic Radiation
EMV	Ellipsoid of Maximum Variance
EOC	Earth Observation Centre
EOS-MODIS	Earth Observation System - Moderate Resolution Imaging Spectrometer
EOT	End of Tape
ERSDAC	Earth Remote Sensing Data Analysis Centre
ETM	Enhanced Thematic Mapper
FCC	False Colour Composite
FFT	Fast Fourier Transform
Gbytes	Giga-bytes
GCP	Ground Control Point
GF	Gradient Filter
GMT	Greenwich Mean Time

GOES	Geostationary Operational Environment Satellite
GPS	Global Positioning System
GRS	Ground Reference System
HH	Horizontal -transmit, Horizontal receive
HRIR	High Resolution Infrared Radiometer
HRV-IR	High Resolution Visible-Infrared Radiometer
HSI	Hyper Spectral Imager
IAI	Iron Absorption Index
IDIMS	Interactive Digital Image Manipulation System
IFT	Inverse Fourier Transform
IRS-1C	Indian Remote Sensing Satellite
JERS-1	Japanese Earth Resources Satellite-1
K	Kelvin
km	Kilometre
MAI	Mineral Absorption Index
Mb	Megabyte
Mbps	Mega bits per second
MDR	Mission Data Recorder
MDT	Mission Data Transmitter
MERIS	Medium Resolution Imaging Spectrometer
MHz	Mega-Hertz
MISR	Multi-angle Imaging SpectroRadiometer
MNF	Maximum Noise Fraction
MSG-SEVIRI	Meteosat Second Generation - Spinning Enhanced Visible & Infrared Imager
MSS	Multispectral Scanner
NASDA	National Aeronautical and Space Development Agency
NERC-EPFS	Natural Environment Research Council - Equipment Pool for Field Spectroscopy
NIR	Near-Infrared
NOAA	National Oceanographic and Atmospheric Administration
OIF	Optimum Index Factor
OPS	OPtical Sensor
PAN	Panchromatic
PC	Principal Component
PCA	Principal Component Analysis
PI	Principal Investigator
PS	Polar Stereo
SAR	Synthetic Aperture Radar
SI	Spectral Indices

SNR	Signal to Noise Ratio
SOM	Space Oblique Mercator
SPOT	Satellite Probatoire d'Observation de la Terre
SSTI	Small Spacecraft Technology Initiative
SWIR	Short Wave Infrared
TACC	Tracking And Control Centre
TC	Tasseled Cap
TCU	Thermal Control Unit
TCC	True Colour Composite
THIR	Temperature Humidity Infrared Radiometer
TI	Three-dimensional Index
TIMS	Thermal Infrared Multispectral Scanner
TIR	Thermal InfraRed
TIROS	Television and Infrared Observation Satellite
TM	Thematic Mapper
TU	Transport Unit
UTM	Universal Transverse Mercator
VEI	Volcano Explosivity Index
VNIR	Very Near Infrared
ZNF	Zonal Notch Filter

Appendix 1

A1.1 Atmospheric attenuation

Attenuation of EMR by the atmosphere is a very complex process and only a very basic outline of these processes will be given here, more in depth descriptions can be found in the literature, for example, Rees (1990). Reflected radiation recorded by passive sensors (i.e., TM and OPS) has to make two journeys through the Earth's atmosphere prior to being detected. On each of these journeys the electromagnetic radiation undergoes both absorption and scattering. In some parts of the spectrum the amount of attenuation is so great the atmosphere can be regarded as being opaque. As a result satellite sensors are confined to wavelengths where the atmosphere is fairly transparent, known as atmospheric windows. Even in these relatively transparent regions the interaction of electromagnetic radiation with the atmosphere results in some attenuation.

The atmosphere contains mainly nitrogen and oxygen with significant amounts of water vapour, ozone, carbon dioxide and airborne dust. Combined vibrational and rotational transitions in these components result in well defined absorptions at specific wavelengths, for example the 1.4 μm and 1.9 μm water absorptions. As well as absorption the interaction of radiation with water, air molecules and dust particles results in atmospheric scattering. During atmospheric scattering, energy is not lost from the system, merely redirected within it. The redirection of energy back towards the sensor results in an additive effect causing increased scene brightness. Scattering depends on the size of the scattering particles relative to the wavelength of the radiation (Rees, 1990). If the particles are smaller than the wavelength of the EMR (such as oxygen or nitrogen molecules) the degree of scattering is inversely proportional to the fourth power of the wavelength, this is known as Rayleigh Scattering (Drury, 1987). This type of scattering is very significant at short wavelengths (i.e., in the blue part of the spectrum) where it swamps the real reflected blue component with a very high scattered component. If the particles are a similar size to the wavelength, or larger, for example water droplets or dust particles, Mie scattering occurs, which is inversely

proportional to wavelength. Mie scattering affects longer wavelengths than blue light and is mainly a problem in clear but humid or dusty atmospheres (Drury, 1987).

A1.2 Atmospheric correction

Numerous techniques exist to correct for atmospheric scattering, with the most complex requiring ground based reflectance measurements to be made simultaneously with the satellite overpass (Ahern *et al.*, 1977, Otterman and Robinove, 1981). Alternative techniques use computer programs (i.e., LOWTRAN) to model the atmosphere on the day of image acquisition. The problem with both of these techniques is that they require information 'external' to that which is contained within the image data. This is often not available to the end data user, especially when working with old archived data.

A1.1.2 Dark object subtraction correction

A very simple and effective correction method which requires no information other than the image data is the 'dark object subtraction' technique (Chavez, 1975). Because Oman has a very dry atmosphere and it can be assumed that the main atmospheric attenuation affecting satellite imagery will be caused by Rayleigh scattering. This affect can be seen on imagery by viewing regions of dark shadow, which should ideally appear black (i.e., zero DN) as there is no spectral reflectance occurring. However in practise these regions appear grey (i.e., low DN values) due to the additive affects of atmospheric scattering. A very simple way to determine this additive affect and to correct for it is to derive a minimum shadow DN value for each channel. This 'scatter offset' value, which represents the additive atmospheric affect, is then subtracted from all of the other DN values in the channel. Independent scatter offset values are required for each channel as the amount of atmospheric scattering will vary with wavelength. The offset value will be at its highest in the visible channels rapidly decreasing to almost zero in the SWIR channels.

Figure A1.1a shows the offset DN values derived from shadow areas on the Landsat TM scene 158-044 (Maqsad region). The offset values are very high in the visible channel (TM 1) but rapidly decrease with increasing wavelength to very low values in the SWIR channels (TM 5 and TM 7). For comparison Figure A1.1b shows the additive atmospheric scattering values which have been calculated using only the

extracted TM 1 shadow offset value as a starting point. The offset values for channels TM 2 to TM 7 are derived by using a Relative Scattering Model (RSM) as described by Chavez (1988). This model states that relative scattering is inversely proportional to wavelength between λ^{-4} for very clear atmospheric conditions and $\lambda^{-0.5}$ for very hazy conditions. Atmospheric scattering in the clear atmosphere of Oman has been approximated by λ^{-1}, where λ represents the average wavelength of each TM channel. It can be seen from Figure A1.1 that this is a reasonable assumption as the calculated curve closely matches the observed curve. Using this technique can slightly improve the dark object subtraction technique as it reduces problems encountered at the analysis stage determining minimum values for each channel, as only one shadow value is required. For this scene of TM data there is little difference between the image shadow derived offset values and the calculated ones (see Figure A1.1), with the exception of TM 2 which shows a slightly larger calculated offset .

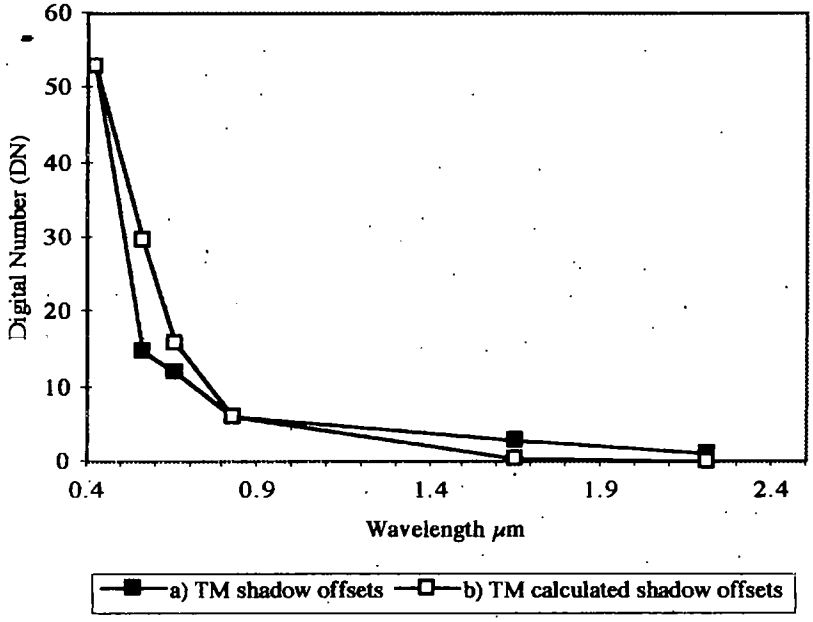

Figure A1.1 Plot of DN values representing atmospheric scatter in each TM channel; (a) derived from areas of shadow,(b) calculated using Chavez (1988) atmospheric model.

Figure A1.2 (a) shows the offset DN values derived from the shadow regions of the JERS-1 OPS scene 208-262 (Maqsad region). It is immediately apparent that these values do not plot to give the characteristic rapid decrease in scatter with increasing wavelength. Instead they produce a highly variable plot which shows high scatter values for all channels. Obviously the scatter offset values derived from the shadow

regions have been modified by an unknown effect. This modification may be as a result of the 6 bit to 8 bit conversion (Mukai *et al.*, 1995). If this conversion includes an additive component which varies by channel a highly variable plot such as this (Figure A1.2 (a)) may result.

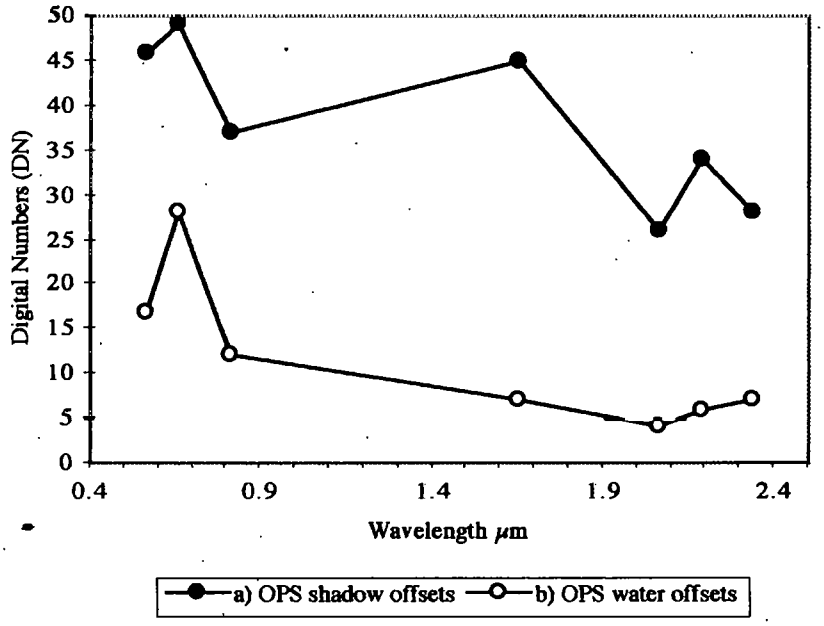

Figure A1.2 Plot of DN values in each OPS channel representing atmospheric scatter; (a) derived from regions of shadow, (b) from regions of water.

This idea can be tested by comparing the shadow offset curve with one derived from the minimum channel DN values extracted over a water body (Figure A1.2 (b)). Like regions of shadow, deep water has virtually zero spectral reflectance and should therefore appear black (i.e., zero DN), any non-zero DN values can be used in the visible and SWIR regions to approximate atmospheric scattering. The water offset curve (Figure A1.2 (b)) does not exhibit the highly variable nature seen in the shadow offset curve (Figure A1.2 (a)) despite the fact that it comes from the same scene of data. Instead it exhibits a shape similar to that seen in the TM plots (Figure A1.1) where the offset values decease with increasing wavelength, although OPS 1 shows an unusual low DN value. Because this curve does not show the same variable nature as the shadow curve it is doubtful that the 6 bit to 8 bit transformation is responsible for the modified shape of the shadow curve. If it was responsible both curves should exhibit similar profiles as they both represent DN values of pixels which have no added surface reflectance component.

The non-characteristic profile of the shadow curve must be as a result of sensor noise (as described in chapter 3). It is possible that the variation between these two curves represents different amounts of additive noise between land and water targets. This would imply that noise structures are related to the activity level of the sensors, i.e., rapid changes in radiance levels over a land target may induce more system noise than the fairly constant radiance levels encountered over a water target. This is certainly true of the 'image blur' noise structure (described in chapter 2, section 2.5.3) which occurs as a direct result of sharp changes in radiance levels and therefore does not occur over water targets. However the visual inspection of images covering both land and water suggests that this is not the case as both seem to have fairly consistent levels of noise. The differences between these two curves may therefore be a result of variations in sample size. Due to the limited area of image shadow encountered on any scene, it is possible that all of the pixels within shadow regions are affected by additive noise, making it impossible to extract DN values which are truly representative of only atmospheric scattering. In comparison areas of water tend to be very large and it is doubtful that all of the pixels within these regions are affected by noise. Thereby making it possible to extract DN values with no additive noise component which are truly representative of atmospheric scattering.

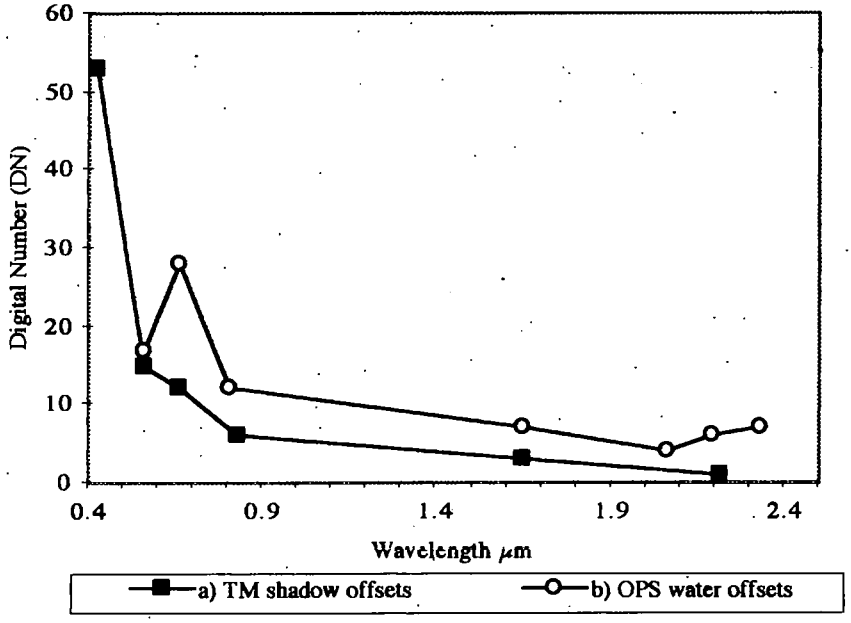

Figure A1.3 Comparison of atmospheric scatter correction derived from (a) TM shadow regions and (b) OPS water regions.

As a result the water curve (Figure A1.3 (b)) probably best represents the atmospheric scattering component of this OPS scene. An approximation of the accuracy of this curve can be established by comparing it to the TM shadow scatter curve (Figure A1.3

(a)). Obviously this is only an approximate comparison as there are a number of variables between the two data sets, for example, sensor radiometric resolution, channel location, bandwidth and atmospheric changes due to different image acquisition dates. Ignoring these variables the two curves roughly approximate each other except for OPS 2 which shows an unusually high value of scatter. So assuming that the OPS 1 scatter value is correct, which it appears to be as it coincides with the TM values, the offset values for the other channels can be calculated using the Chavez (1988) method, by substituting the average TM channel wavelength with the average OPS wavelength. The resultant calculated curve Figure A1.4 (b) can be seen to resemble the profile of the TM shadow curve (Fig 1.4 (a)). The scatter offset value for OPS 2 is now comparable with the value of TM3.

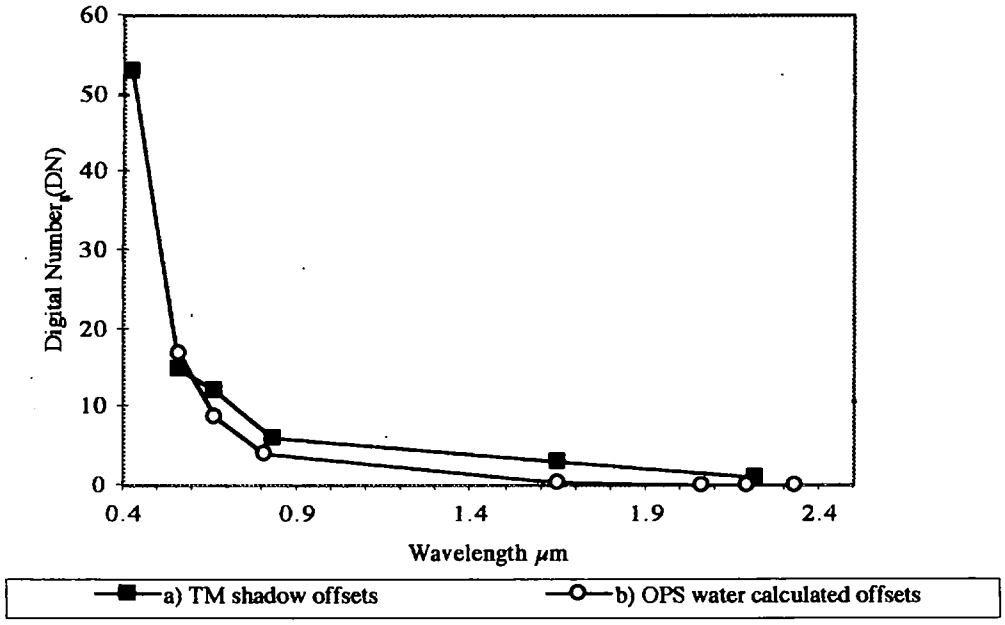

Figure A1.4 Plot showing the atmospheric scatter (a) derived from areas of shadow on TM data and (b) calculated from OPS 1 water scatter offset value.

By comparing the OPS scatter curves with the TM scatter curves it would appear that the OPS curve calculated from the water DN extracted from OPS 1 is the best approximation to the levels of atmospheric scatter for scene 208-262. This can be checked by taking the DN values for an area of homogeneous lithology (for example, harzburgite) and transforming these values to percentage reflectance, after applying each of the OPS scatter corrections discussed above. The technique for converting image DN to percentage reflectance is outlined in Appendix 2 for both TM and OPS and will not be discussed here.

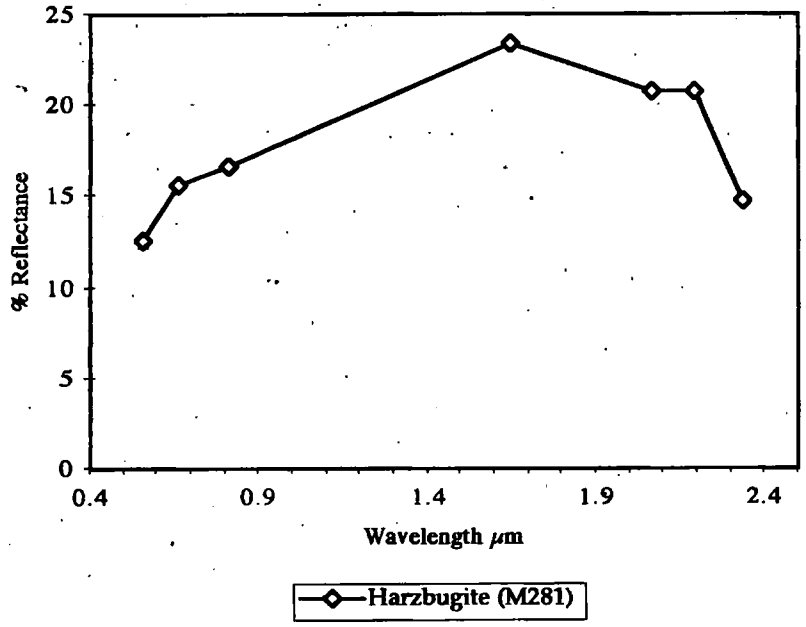

Figure A1.5 Lab reflectance spectra of a sample of harzbugite, convolved to OPS bandwidths.

Figure A1.5 shows for reference the lab reflectance spectrum of a weathered harzbugite sample convolved to the OPS bandwidths. Ideally the OPS image spectrum should approximate this if a correct atmospheric correction is applied. Converting the image DN values to reflectance without applying an atmospheric correction produces a fairly flat spectrum (Figure A1.6 (a)) with channels OPS 1, OPS 2 and OPS 3 showing high reflectance values, characteristic of the additive effects of atmospheric scatter. Applying the scatter offset DN values derived from areas of shadow produces a very strange spectrum (Figure A1.6 (b)). The shape of this spectrum which has negative reflectance values for channels OPS 6, OPS 7 and OPS 8 indicates that the offset value established from the image shadow regions are too high, due to the additive noise component. Using the shadow value from OPS 1 to calculate an atmospheric correction using the Chavez (1988) method produces an image spectrum with a reasonable profile (Figure A1.6 (c)), except that the reflectance values in channels OPS 1 and OPS 2 appear to be over corrected. This suggests that the initial starting value established from OPS 1 was a poor approximation to atmospheric scattering. Applying the scatter offset values derived from an area of water (Figure A1.7) also results in slight over correction.

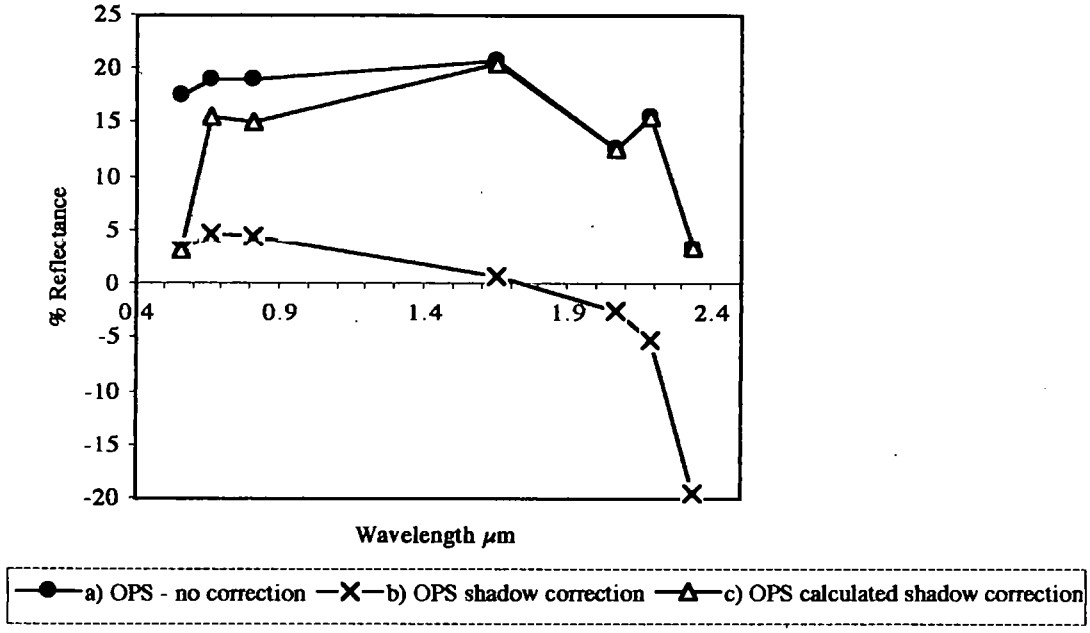

Figure A1.6 OPS image spectrum for a region of harzburgite outcrop with (a) no atmospheric correction applied, (b) with an OPS shadow correction applied and (c) with a calculated atmospheric correction applied, derived from the OPS 1 shadow value.

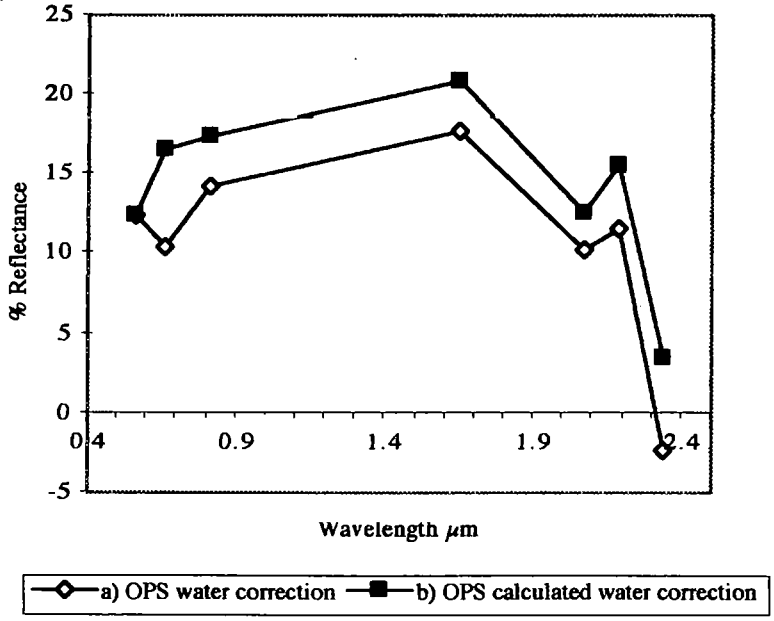

Figure 1.7 OPS image reflectance spectrum for an area of harzburrgite with (a) atmospheric correction applied from an area of water and (b) with an atmospheric correction calculated from OPS 1 over water.

This is especially apparent in OPS 2 which shows a sudden decrease in reflectance, confirming that the extracted water DN value for OPS 2 is anomalously high. Using the water value from OPS 1 to calculate an atmospheric scatter correction for all channels produces an image profile which is a very close match to the lab spectrum.

This confirms that the calculated atmospheric scattering model based on a water scatter DN value extracted from OPS 1 is probably the best correction to apply. This model can be further improved by taking into account sensor gain and offset values. However in practice it was found that this additional processing made very little difference to the calculated offset values. Table A1.1 summarises the offset coefficients applied to both the TM and OPS imagery.

TM Image Data (Scene 158 - 044)		OPS Image Data (Scene 208-262)	
Band	Offset (DN)	Band	Offset (DN)
TM 1	53	OPS 1	17
TM 2	15	OPS 2	9
TM 3	12	OPS 3	4
TM 4	6	OPS 5	0
TM 5	3	OPS 6	0
TM 7	1	OPS 7	0
		OPS 8	0

Table A1.2 Offset values in DN applied to Maqsad data, TM scene 158-044 and OPS scene 208-262.

Appendix 2

A2.1 Methodology for pixel data calibration

This appendix outlines the methodology used to convert Landsat TM and JERS-1 OPS image DN values to semi-calibrated reflectance values. The purpose of this is to allow lithological spectral information extracted from image data to be compared directly with convolved lab spectra. Prior to this conversion, both the TM and OPS data were corrected for atmospheric scatter as described in Appendix 1.

A2.2 Calibration of extracted pixel DN values to radiance

The calibration of atmospherically corrected TM and OPS pixel values is a two part process. The first part converts the DN values to spectral radiance and the second part converts them to semi-calibrated reflectance by normalising for solar irradiance. The resultant values are regarded as only semi-calibrated because variations in topographic slope angle are not taken into consideration.

A2.2.1 Conversion from DN to spectral radiance

TM and OPS data can be converted to spectral radiance by using the formula (after Markham and Barker, 1986):

$$\text{Spectral Radiance}\,(R_\lambda) = (DN_\lambda * GAIN_\lambda) + OFFSET_\lambda \qquad (1)$$

where:

DN_A = pixel DN corrected for atmospheric scatter

$GAIN_\lambda$ = sensor gain value

$OFFSET_\lambda$ = sensor offset value

R_λ = spectral radiance value (in $mWcm^{-2}ster^{-1}\mu m^{-1}$)

The values of $GAIN_\lambda$ and $OFFSET_\lambda$ will vary with wavelength. The gain and offset parameters for both the TM sensor and the OPS sensor are listed in Table A2.1.

TM Sensor			OPS Sensor		
Band	Gain	Offset	Band	Gain	Offset
TM 1	0.0602353	- 0.15	OPS 1	0.16143118	- 0.0692
TM 2	0.1174902	- 0.28	OPS 2	0.12869565	- 0.4445
TM 3	0.0805882	- 0.12	OPS 3	0.12253829	- 0.4066
TM 4	0.081451	- 0.15	OPS 5	0.02932935	- 0.6162
TM 5	0.01080784	- 0.037	OPS 6	0.01673193	- 0.2585
TM 7	0.005698	- 0.015	OPS 7	0.01482986	- 0.3213
			OPS 8	0.01464364	- 0.4502

Table A2.1 Sensor dynamic range values to use in formula (1). The TM values are taken from Markham and Barker (1986) and can be used with any TM data acquired after January 15th 1984. The OPS values are revised values established in December 1992 by an AVIRIS underflight, taken from Shimada and Nakai (1993). All values in $mWcm^{-2}ster^{-1}\mu m^{-1}$.

A2.2.2 Normalisation for solar irradiance

To remove the effects of the solar irradiance curve, the spectral radiance value (as calculated by (1) for each pixel is normalised by the exoatmospheric solar irradiance values convolved across the sensor bandwidths. The equation used is after Markham and Barker (1986):

$$\text{At satellite planetary reflectance}(\%) = \frac{R_\lambda * d * \pi * 100}{E_{sun} * \cos \phi} \quad (2)$$

where:

E_{sun} = mean solar exoatmospheric irradiance across the satellite channel

d = Earth - sun distance in astronomical units

ϕ = solar zenith angle

The mean solar irradiance values for the TM sensor are from Markham and Barker (1986). The mean solar irradiance values for JERS-1 were calculated by convolving the irradiance values given by Arvesen *et al.* (1969) by the OPS sensor response functions. The resulting E_{sun} values are:

TM Sensor		OPS Sensor	
TM Band	Exoatmospheric irradiance (E_{sun})	OPS Band	Exoatmospheric irradiance (E_{sun})
TM 1	195.7	OPS 1	188.07
TM 2	182.1	OPS 2	160.13
TM 3	155.7	OPS 3	114.56
TM 4	104.7	OPS 5	23.49
TM 5	21.9	OPS 6	10.35
TM 7	7.4	OPS 7	8.08
		OPS 8	6.33

Table A2.2 Solar irradiance values across TM and OPS bandwidths, TM values taken from Markham and Barker (1986), OPS values convolved using irradiance values extracted from Arvesen *et al.*, (1969). All values in $mWcm^{-2}ster^{-1}\mu m^{-1}$.

The d values were derived from the Astronomical Almanac as being 0.9971 for the TM scene and 1.033 for the OPS scene (Astronomical Units). The solar zenith angles were derived from the header information supplied with each scene, these were 38° for the TM scene and 27° for the OPS scene.

Appendix 3

A3.1 Maqsad ground truthing and sample localities

The Maqsad field region was visited on two occasions during the course of this study (February 1993 and November 1993), for a period of approximately four weeks each visit. These field visits were spent checking spectral anomolies on both the Landsat TM and JERS-1 OPS data and collecting hand samples for laboratory based spectral analysis. Throughout both field visits considerable assistance and geological information were provided by Georges Ceuleneer and Isma Amri of Paul Sabitier University, Toulouse, France.

Figures A3.1 and A3.2 are JERS-1 OPS 852 composites of the north and south parts of the Maqsad study region. On these two images the locations and numbers of all field localities visited within the Maqsad region are indicated. These localities are distributed throughout the study region although their density is greater in complex crustal regions. Note that a 5km grid has been superimposed on these images.

Table A3.1 lists the major Maqsad localities where lithological samples were collected for laboratory spectral analysis. This table also lists the major lithological type and the filenames of the associated spectral measurements.

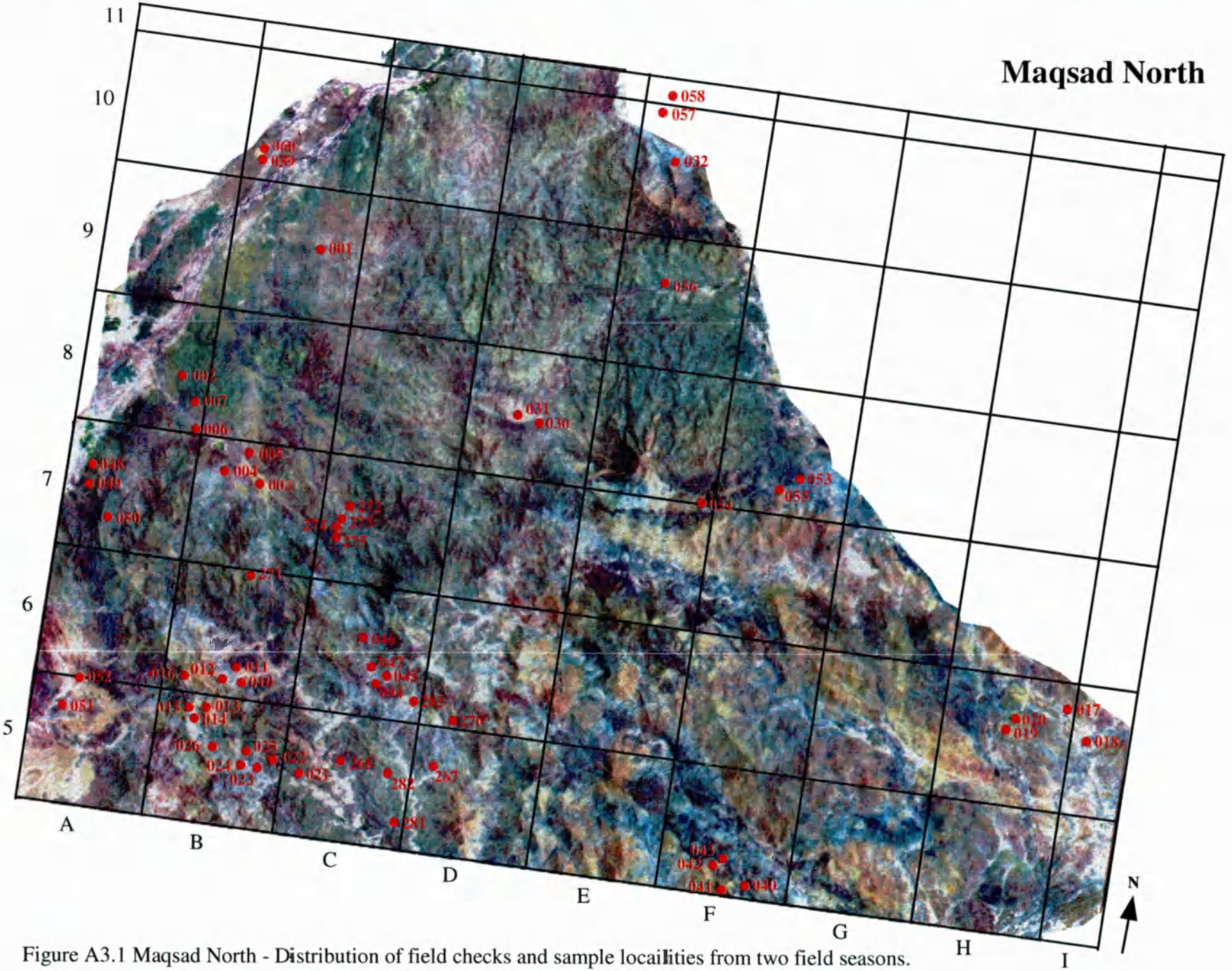

Figure A3.1 Maqsad North - Distribution of field checks and sample locailities from two field seasons. Grid squares are 5 km x 5km.

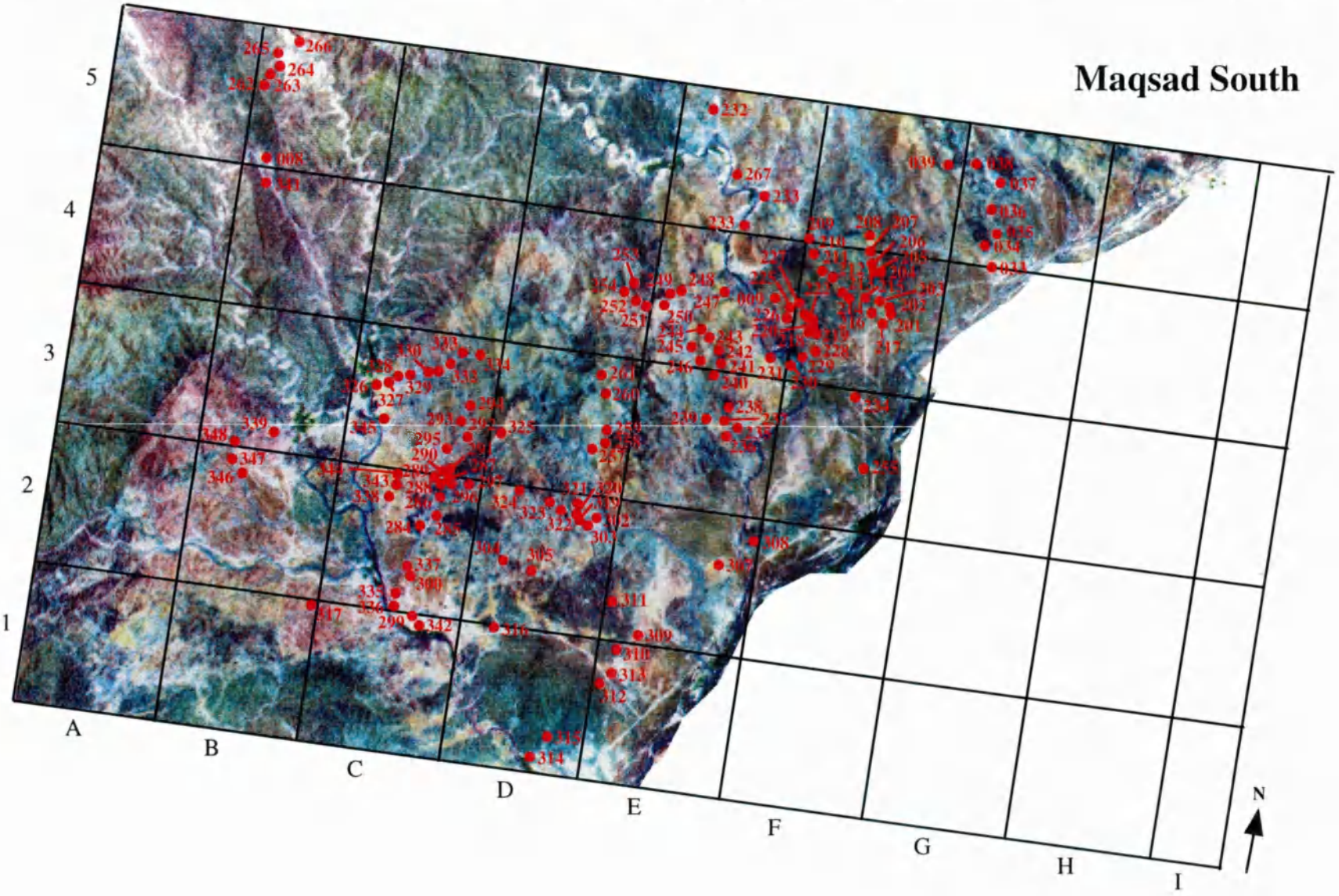

A3.2 Maqsad South - Distribution of field checks and sample locailities from two field seasons. Grid squares 5 km x 5 km.

		Fresh Surface		Weathered Surface	
Location	**Lithology**	**File1**	**File2**	**File3**	**File4**
4	Dunite	MDU011	MDU012	MDU009	MDU010
5	Gabbro	MGA064	MGA065	MGA063	MGA064
6	Harzburgite	MHA013	MHA014	MHA015	MHA016
7	Harzburgite	MHA037	MHA038	MHA039	MHA040
8	Trondhejemite	MPL005	MPL006	MPL007	MPL008
9	Dunite	MDU005	MDU006	MDU007	MDU008
10	Pematic gabbro	MGA041	MGA042	MGA039	MGA040
11A	Dyke			MDY005	MDY006
11B	Dunite			MDU019	MDU020
11C	Gabbro	MGA058	MGA059	MGA056	MGA057
13	wehrlite	MWE015	MWE016	MWE017	MWE018
15A	Trondhjemite	MPL001	MPL002	MPL003	MPL004
15B	Altered gabbro			MGA068	MGA069
17A	Sheeted Dyke	MDY001	MDY002	MDY003	MDY004
17B	Coarse Gabbro	MGA045	MGA046	MGA043	MGA044
17C	Dyke	MDY007	MDY008	MDY009	MDY010
17D	Dyke			MDY023	MDY024
18	Gabbro	MGA031	MGA032	MGA033	MGA034
22A	Harzburgite	MHA009	MHA010	MHA011	MHA012
22B	Vein serpentine	MHA041	MHA042	MHA043	MHA044
22C	Vein serpentine	MHA045	MHA046	MHA047	MHA048
23	Dunite	MDU017	MDU018	MDU015	MDU016
25	wehrlite	MWE011	MWE012	MWE013	MWE014
28	Harzburgite	MHA025	MHA026	MHA027	MHA028
29	Serpentinised harzburgite	MHA005	MHA006	MHA006	MHA007
30A	Harzburgite (sepentinite)	MHA033	MHA034	MHA035	MHA036
30B	Pegmatite	MGE012	MGE013	MGE014	MGE015
34	Gabbro	MGA080	MGA081	MGA082	MGA083
37A	Gabbro	MGA052	MGA053	MGA54	MGA055
37B	wehrlite	MWE007	MWE008	MWE009	MWE010
45	Chromite	MCH009	MCH010	MCH011	MCH012
46	Harzburgite	MHA021	MHA022	MHA023	MHA024
47A	Dunite	MDU001	MDU002	MDU003	MDU004
47B	Cumulate gabbro	MGA029	MGA030	MGA027	MGA028
48	Harzburgite	MHA017	MHA018	MHA019	MHA020
49	Harzburgite	MHA001	MHA002	MHA003	MHA004
52A	Gabbro	MGA048	MGA049	MGA050	MGA051
52B	Dyke	MDY011	MDY012	MDY013	MDY014
54	wehrlite	MWE001	MWE002	MWE003	MWE004
55A	Dunite	MDY015	MDY016	MDY017	MDY018
55B	Dunite	MGE025	MGE026	MGE027	MGE028
55C	Dyke	MDY020	MDY021		
56	Harzburgite	MHA029	MHA030	MHA031	MHA032
57A	Gabbro dyke (coarse)	MGA070	MGA071	MGA072	MGA073
57B	Gabbro dyke (fine)	MGA074	MGA075	MGA072	MGA073
58	Gabbro	MGA056	MGA057	MGA058	MGA059
59	Meta-sediment			MGE005	MGE006
60	Meta-sediment	MGE001	MGE002	MGE003	MGE004
201B	Gabbro	GAR061	GAR062	GAR063	GAR064
203	Dyke	DYR001	DYR002	DYR003	
208	Gabbro	GAR018	GAR019	GAR020	GAR021
227	Epidote and Quartz	LOR041	LOR042	LOR043	LOR044

228	Isotropic gabbro	GAR001	GAR002	GAR003	GAR004
233	Gabbro	GAR049	GAR050	GAR051	
235	Isotropic gabbro	GAR006	GAR007	GAR008	GAR009
246	Gabbro	GAR052	·	GAR056	GAR057
250	Gabbro	GAR58		GAR059	GAR60
256	Dyke	DYR017	DYR018	DYR019	DYR020
264	Wehrlite	LOR012	LOR013	LOR014	LOR015
268	harzburgite	HAR021	HAR022	HAR023	HAR024
270	Chromite	LOR006	LOR007	LOR008	LOR009
272	Harzburgite	HAS011	HAS012	HAS013	HAS014
274	Vein serpentine	HAR040	HAR041	HAR042	HAR043
275	Harzburgite	HAR014	HAR015	HAR016	HAR017
276	Harzburgite	HAR017	HAR018	HAR019	HAR020
280	Dunite	LOR001	LOR002	LOR003	LOR004
281	Harzburgite	HAR002	HAR003	HAR004	HAR005
284	Dyke	DYR008		DYR009	DYR010
295	Gabbro	GAR021	GAR022	GAR023	GAR024
297	Gabbro	GAR025	GAR026	GAR027	GAR028
299	Extrusive	DYR025	DYR026	DYR027	DYR028
300A	Extrusive	DYR029	DYR030	DYR031	DYR032
300B	Extrusive	DYR033	DYR034	DYR035	DYR036
304	wehrlite	LOR018	LOR019	LOR020	LOR021
307	Gabbro	GAR012	GAR013	GAR014	GAR015
311A	Harzburgite	HAR010		HAR011	HAR012
311B	Harzburgite	HAS015	HAS016	HAS017	HAS018
314A	Dunite	HAR008	HAR009	HAR006	HAR007
314B	Harzburgite	HAS019	HAS020	HAS021	HAS022
317A	Gabbro	GAR031	GAR032	GAR033	
317B	Trondhjemite	GAR034	GAR035	GAR036	GAR037
318	Dyke			DYR004	DYR005
325	Gabbro	GAR042	GAR043	GAr044	GAR045
332	Gabbro	GAR028	GAR029	GAR031	GAR032
336	Dyke	DYR011	DYR012	DYR013	DYR014
341A	Harzburgite	HAR027	HAR028	HAR029	HAR030
341B	Vein material	HAR036	HAR037	HAR038	HAR039
341C	Harzburgite	HAS001	HAS002	HAS003	HAS004
346	Trondhjemite	GAR037		GAR038	GAR039
347A	wehrlite	LOR022	LOR023	LOR024	LOR025
347B	Gabbro	LOR026	LOR027	LOR028	LOR029
347C	Pyroxenite	LOR029	LOR030	LOR031	LOR032

Table A3.1 A list of the main Maqsad samples used for spectral analysis.
(Note not all repeat and multi-surface spectral measurements are listed.